ASME
SETTING THE STANDARD

Journal of Fluids Engineering

Published Monthly by ASME

VOLUME 129 • NUMBER 9 • SEPTEMBER 2007

FLUIDS ENGINEERING DIVISION
Editor
J. KATZ (2009)
Assistant to the Editor
L. MURPHY (2009)

Associate Editors
M. J. ANDREWS (2009)
S. BALACHANDAR (2008)
A. BESKOK (2008)
S. L. CECCIO (2009)
D. DRIKAKIS (2008)
P. A. DURBIN (2008)
I. EAMES (2010)
A. GOTO (2007)
C. HAH (2009)
T. J. HEINDEL (2007)
H. JOHARI (2009)
J. KOMPENHANS (2009)
Y. T. LEE (2007)
J. A. LIBURDY (2007)
P. LIGRANI (2008)
R. MITTAL (2009)
T. J. O'HERN (2008)
U. PIOMELLI (2007)
S. ROY (2007)
D. SIGINER (2008)
S. P. VANKA (2007)
Y. ZHOU (2008)

PUBLICATIONS COMMITTEE
Chair, B. RAVANI

OFFICERS OF THE ASME
President, SAM Y. ZAMRIK
Executive Director, V. R. CARTER
Treasurer, T. D. PESTORIUS

PUBLISHING STAFF
Managing Director, Publishing
P. DI VIETRO
Manager, Journals
C. MCATEER
Production Coordinator
A. HEWITT
Production Assistant
M. ANDINO

(Contents continued on inside back cover)

Transactions of the ASME, Journal of Fluids Engineering (ISSN 0098-2202) is published monthly by The American Society of Mechanical Engineers, Three Park Avenue, New York, NY 10016. Periodicals postage paid at New York, NY and additional mailing offices.
POSTMASTER: Send address changes to Transactions of the ASME, Journal of Fluids Engineering, c/o THE AMERICAN SOCIETY OF MECHANICAL ENGINEERS, 22 Law Drive, Box 2300, Fairfield, NJ 07007-2300.
CHANGES OF ADDRESS must be received at Society headquarters seven weeks before they are to be effective. Please send old label and new address.
STATEMENT from By-Laws. The Society shall not be responsible for statements or opinions advanced in papers or ... printed in its publications (B7.1, Par. 3).
COPYRIGHT © 2007 by the American Society of Mechanical Engineers. Authorization to photocopy material for internal or personal use under those circumstances not falling within the fair use provisions of the Copyright Act, contact the Copyright Clearance Center (CCC), 222 Rosewood Drive, Danvers, MA 01923, tel: 978-750-8400, www.copyright.com. Request for special permission or bulk copying should be addressed to Reprints/Permission Department.
Canadian Goods & Services Tax Registration #126148048.

This journal is printed on acid-free paper, which exceeds the ANSI Z39.48-1992 specification for permanence of paper and library materials. ♾™
♻ 85% recycled content, including 10% post-consumer fibers.

Downloaded 03 Jun 2010 to 171.66.16.159. Redistribution subject to ASME license or copyright; see http://www.asme.org/terms/Terms_Use.cfm

(**Contents continued**)

Journal of Fluids Engineering **Volume 129, Number 9** **SEPTEMBER 2007**

TECHNICAL BRIEF

The ASME Journal of Fluids Engineering is abstracted and indexed in the following:

Applied Science & Technology Index, Chemical Abstracts, Chemical Engineering and Biotechnology Abstracts (Electronic equivalent of Process and Chemical Engineering), Civil Engineering Abstracts, Computer & Information Systems Abstracts, Corrosion Abstracts, Current Contents, Ei EncompassLit, Electronics & Communications Abstracts, Engineered Materials Abstracts, Engineering Index, Environmental Engineering Abstracts, Environmental Science and Pollution Management, Excerpta Medica, Fluidex, Index to Scientific Reviews, INSPEC, International Building Services Abstracts, Mechanical & Transportation Engineering Abstracts, Mechanical Engineering Abstracts, METADEX (The electronic equivalent of Metals Abstracts and Alloys Index), Petroleum Abstracts, Process and Chemical Engineering, Referativnyi Zhurnal, Science Citation Index, SciSearch (The electronic equivalent of Science Citation Index), Shock and Vibration Digest, Solid State and Superconductivity Abstracts, Theoretical Chemical Engineering

Downloaded 03 Jun 2010 to 171.66.16.159. Redistribution subject to ASME license or copyright; see http://www.asme.org/terms/Terms_Use.cfm

Determination of Cavity Detachment for Sheet Cavitation

Eduard Amromin
e-mail: amromin@aol.com
Mechmath LLC,
Prior Lake, MN 55372-1283

Sheet cavitation has been traditionally analyzed with ideal fluid theory that employs the cavitation number as the single parameter. However, characteristics of cavitation can significantly depend on location of cavity detachment. According to known experimental data, this location is influenced by the freestream speed and the body/hydrofoil size. As shown in this paper, it takes place because of the combined effect of the Reynolds number and Weber number. Here, sheet cavitation is considered as a special kind of viscous separation caused by the cavity itself. The viscous-inviscid interaction concept is employed to analyze the entire flow. Validation of the suggested approach is provided for hydrofoils and bodies of revolution. The effects of flow speed, the body size, and its surface wettability are illustrated by comparison of computed cavity length/shape to the known experimental data. The difference between cavity detachment in laminar and turbulent boundary layers is discussed. [DOI: 10.1115/1.2754312]

Introduction

Principal time-average characteristics of cavitating flows include lift and drag, cavity length and volume, as well as cavitation inception number. As follows from numerous studies on cavitation of hydrofoils and bodies with smooth shapes, these characteristics substantially depend on the location of cavity detachment points. In the traditional concept (known as the ideal cavitation), the cavitating flows significantly depend on a single parameter: cavitation number. In the framework of this concept, the theoretical analysis could be performed on an ideal fluid, with a preliminary selected cavity closure scheme and cavity detachment point/line. As has been shown (e.g., [1]), using the cavity detachment point at its observed location and tuning the closure scheme allows a satisfactory agreement of ideal cavitation with some sets of experimental data (as experimental data [2] in Fig. 1), though other sets may require another scheme.

There is the classical Brillouin–Villat condition [3] for detachment determination within the ideal cavitation itself but, as is shown by Brennen [4], Arakeri [5], and others, the difference between detachment predictions based on this condition and experimental data can be very significant. Analysis of experimental data has shown that this difference depends on hydrofoil (or body) size and freestream speed. There are also dependencies of other cavitation characteristics on C and U_∞, as is shown by Keller [6] for σ_l. Thus, it is necessary to analyze effects of two parameters and these parameters must depend on both C and U_∞. It seems reasonable to select the Reynolds number as the primary parameter. Currently, there are two main concepts for analyzing viscous cavitating flows.

The first concept (widely used in recent papers on cavitation) is based on consideration of the entirely turbulent flows (by [7–12]). It is named here as the uniform turbulent cavitation concept (UTCC). All above-mentioned versions of the UTCC are very similar. The background of the versions [7,8,10–12] is the κ-ε model of turbulence (with different constants in different papers) and only [9] uses another model of turbulence. These studies do not consider any boundary between the cavity and surrounding liquid. The main computation results are the pressure distributions over the body/hydrofoil surface and the void fractions (two-phase mixture models are used for cavitation modeling in the versions [7–11]).

The main issues in evaluation of the UTCC are interpretation of computational results and its validation. Although the experimental data on void fraction distributions are already available (see [13]), a correspondence of such distributions to the cavity shapes/lengths (traditionally recorded in experiments) is not yet sufficiently certain. Furthermore, validation of the majority of the UTCC versions has been carried out only for the axisymmetric body with hemispherical head at the single $\mathrm{Re}=1.36\times10^5$ in a range of σ from 0.2 to 0.4 and for the hydrofoil NACA66MOD at $\mathrm{Re}=2\times10^6$ in the range $0.84<\sigma<1.0$. These versions disregard the existence of laminar boundary layers over hydrofoils/bodies and consider the entire flow field as the completely turbulent flow. Such simplification is made despite of experimental proofs of existence of laminar boundary layer along streamlines with uniform velocities up to $\mathrm{Re}_X=2\times10^6$ for turbulence level up to 0.2% [14] and along streamlines with increasing velocities for $\mathrm{Re}_X\gg2\times10^6$ [15]. There have been also observations made of laminar separation upstream of cavities on the bodies of revolution at $\mathrm{Re}\gg1.36\times10^5$ (in [5] and other known sources). Besides, as has been shown by Arakeri and Acosta [16], the difference in the boundary layer types is certainly important for the cavity detachment.

For UTCC versions, comparisons of the computed dimensionless pressure coefficient with its values measured in several points have been used as a major validation. The good agreement of computed and measured C_P has been shown in several papers, but, as possible to conclude from Fig. 2, the very different theoretical results may be in good accordance with such experimental data, especially in the vicinity of cavity detachment. Finally, there is no published UTCC computation for a range of Re. Thus, there is no sufficient data yet to validate the ability of the UTCC to analyze the effects of Re on cavitation, and the accumulation of data will take time.

The second concept is matching of the theory of cavitation in ideal fluid with boundary layer approaches ([17–20]). It is named here as the concept of cavitation within viscous layers (CCVL). This concept operates with terms that are traditional for experiments with cavitation (such as cavity length, etc). The CCVL employs the traditional division of the whole flow into viscous layers (boundary layers and wake) and surrounding curl-free flow of ideal fluid. The viscous-inviscid interaction is mainly predetermined by two effects: the influence of the pressure gradient on the thickness of these layers and the inverse influence of this thickness on the shape of boundary between viscous and inviscid parts of the flow. The ability to correctly compute laminar boundary layers upstream of cavity has been proven for the CCVL.

Contributed by the Fluids Engineering Division of ASME for publication in the JOURNAL OF FLUIDS ENGINEERING. Manuscript received September 22, 2005; final manuscript received March 5, 2007. Review conducted by Georges L. Chahine.

 Copyright © 2007 by ASME

Downloaded 03 Jun 2010 to 171.66.16.156. Redistribution subject to ASME license or copyright; see http://www.asme.org/terms/Terms_Use.cfm

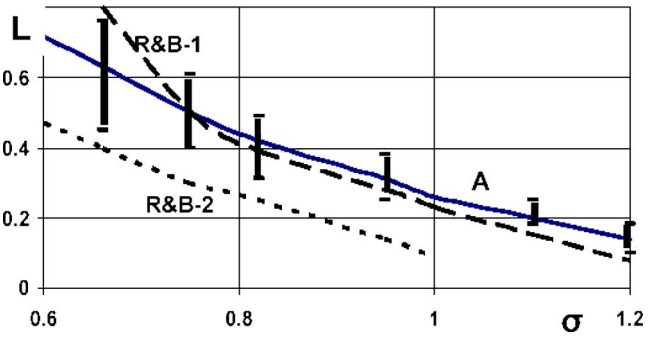

Fig. 1 Cavity length on the EN-hydrofoil at Re=1.5×10⁶, α =4.2 deg: Vertical segments show experimental data with their dispersion. Curve A shows our result obtained with the CCVL. Curves R&B-1 and R&B-2 show results for different cavity closure schemes in ideal fluid [1].

The following analysis of cavity detachment has been carried out with the CCVL. Besides Re, another parameter depending on both D and U_∞ is the Weber number (We), and the surface tension effect in the vicinity of cavity detachment points is included in this concept as an important factor.

CCVL Model of Sheet Cavitation

The CCVL can be looked at as a modification of the ideal cavitation concept and, compared to this traditional concept, can be easily explained. The flow schemes and pressure distributions in the meridian semi-plane for the axisymmetric ITTC body are presented in Fig. 3 for both concepts. There are three parts in the meridian sections shown there: the body section, the cavity section, and the flow section. Although the boundary between the second and third parts is initially unknown, only the flow section is under consideration in both concepts; the cavity impact on flow is limited by replacing the streamlines.

The velocity potential Φ is used in both concepts, but the potential flow does not make contact with the surfaces of the body and cavity in the CCVL; there are boundary layers between them. As observed by Arakeri [5], the boundary layer separation takes place upstream of the attached cavity. Viscous separation upstream of a sheet cavity is not caused by the boundary layer separation on the surface of the cavitation-free body at the same Re. This separation is caused by the cavity itself. Because of the surface tension, the cavity head cannot be infinitely thin. As a result, the cavity provokes separation as a surface irregularity submerged in the boundary layer does. Viscous separation downstream of the cavity is caused by the reentry (reverse) jet. Thus, there are two viscous separation zones between the detachment of the boundary layer and its reattachment to the body, with the cavity located in-between.

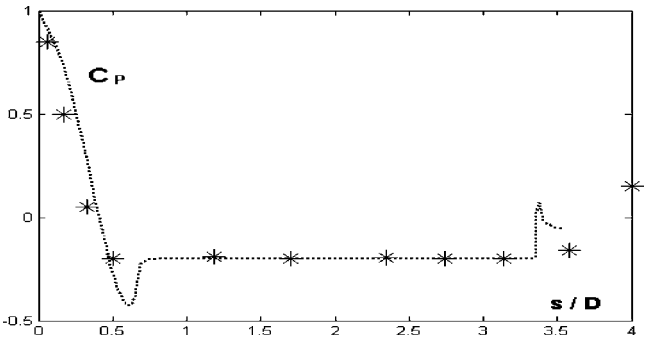

Fig. 2 C_p distributions on the body with hemispherical head computed by the author for Re=1.36×10⁵. Stars show experimental data (after [8]). One can see that a distribution without minimum of C_p may be also in a good accordance with the measured C_p.

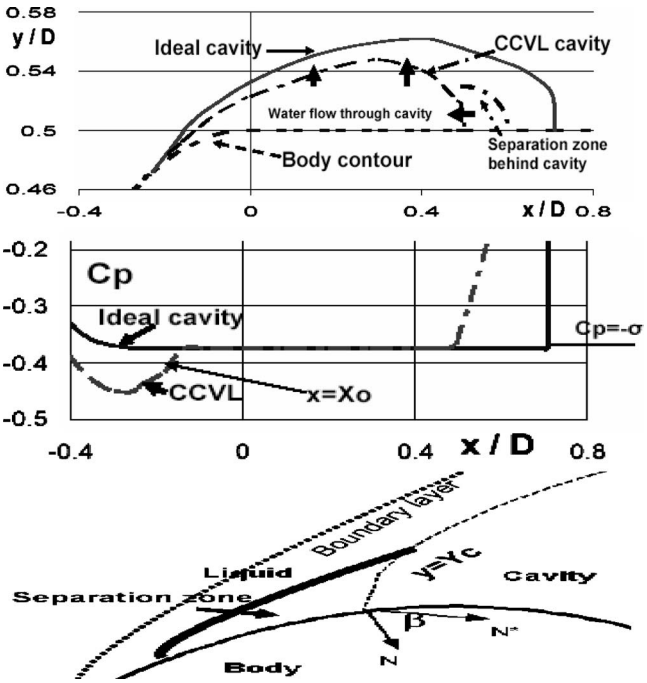

Fig. 3 Comparison of ideal cavitation and the CCVL: The top plot shows cavity shapes; there is the vertical fictitious body in the tail of ideal cavity and separation zone behind the CCVL cavity, whereas the cavity detachment zone is too small to be visible here; arrows show direction of time-average water flux through the cavity in the CCVL. The middle plot presents corresponding pressure distribution over the body in the vicinity of cavity. The bottom plot shows the cavity detachment zone in more detail; here, β is the angle between outer normal to liquid on the liquid-cavity and liquid-body boundaries.

The comparison of two computation results in Fig. 3 is made at the same value of σ. The difference in the cavity lengths and pressure distributions is mainly caused by the difference in the cavity detachment. For the ideal cavitation, the pressure in cavity is the lowest pressure on the body surface and the detachment should be determined from the above-mentioned Brillouin–Villat condition. In contradistinction to this, the cavity detachment in CCVL (and, in fact, in reality) is coupled with the boundary layer separation; therefore, the lowest pressure points are located upstream of cavity in this model.

The cavitation problem in the CCVL is the following free-boundary problem:

$$\Delta\Phi = 0 \tag{1}$$

$$\left.\frac{\partial\Phi}{\partial N}\right|_S = 0 \tag{2}$$

$$|\mathrm{grad}(\Phi)|^2\big|_{S^*} = 1 - C_P^*(x) \tag{3}$$

Equations (1)–(3) are written in dimensionless form, with all lengths being normalized either by D or C. As Fig. 3 illustrates, the right-hand side of Eq. (3) is constant over the major part of S^*. This takes place in ideal cavitation as well, but, unlike the ideal cavitation case, there are pressure increase regions near the edges of the free surface S^*. The function $C_P^*(x)=1-U^2(x)$ can be defined by using undetermined coefficients C_1, C_2 and initially unknown abscissas x^*, X_0, X_3, X_4

$$U = C_1(x-x^*)^2 + \sqrt{1+\sigma} \quad \text{for} \quad X_0 \le x < x^*$$

Downloaded 03 Jun 2010 to 171.66.16.156. Redistribution subject to ASME license or copyright; see http://www.asme.org/terms/Terms_Use.cfm

Table 1 Zones in boundary layer

Wall boundary layer	At $x<X_0$
Separated and reattached boundary layer	At $X_0\le x<x^*$
Cavity boundary layer	At $x^*\le x\le X_2$
Separated and reattached boundary layer	At $X_2<x\le X_3$
Wall boundary layer and wake	At $x>X_3$

$$U=\sqrt{1+\sigma} \quad \text{for} \quad x^*\le x<X_2$$

$$U=C_2\xi^2(3-2\xi)+\sqrt{1+\sigma} \quad \text{for} \quad X_2\le x<X_3 \tag{4}$$

Here, $\xi=(x-X_2)/(X_4-X_2)$ and $x^*>X_1$. Equation (4) is not a theoretical solution but smoothly approximates experimental C_P in cavitating flows. The computed pressure distribution in Figs. 2 and 3 was obtained with Eq. (4).

The above coefficients and abscissas must be found with matching conditions for different flow zones. As shown in Table 1, there are five zones in the boundary layer over a cavitating hydrofoil/body and there should be four matching sections between five zones.

The section $x=X_2$ is ordered at the start of computation, as well as the section $x=X_1$. Determination of the sections $x=X_0$ and $x=X_3$ can be done with semi-empirical criteria of boundary layer separation from the wall used by Castillo et al. [21]. Applying such criteria for boundary layer reattachment to the wall has been already validated by Roberts [22]. The general form of such conditions is as follows:

$$\delta^*\frac{\partial C_P}{\partial s}=a^* \tag{5}$$

Here, a^* is an empirical coefficient that has different values for laminar and turbulent boundary layers, separation, and reattachment. In particular, as the reattachment criterion, $a^*=0.015$ was used. Two criteria (5) can be generally used with both integral and differential methods. There is also the second reattachment condition at X_3 that is the consequence of Prandtl's definition of the body of displacement

$$\delta^*(X_3)=h(X_3) \tag{6}$$

$h(X_3)$ must be obtained by solving Eqs. (1)–(4), whereas δ^* is the result of the computation of the boundary layer with the jumps of δ^* and δ^{**} at $x=X_2$. These jumps are caused by the presence of reverse jet. The jump of δ^* is calculated as $\tau Y_C(X_2)$, with $\tau=0.77$ being used. For the velocity profile being used here, the corresponding δ^{**} jump is 141/845 of the δ^* jump. On the other hand, it is assumed that dU/ds is continuous at $x=X_1$ and this derivative is used for determination of C_1 with Eq. (4).

For determination of x^*, there is the evident condition $\delta^*(x^*)+Y_C(x^*)=h(x^*)$. Here, $Y_C(X_1)=0$ and Y_C is computed by taking into account the surface tension effect. The surface tension over the major cavity part is small, but it is substantial in a region of cavity-liquid-body contact because there the cavity surface curvature is very high (as observed by Arakeri [5], this curvature is $>1/\delta$). The cavity equilibrium has the following form there:

$$C_P^*+\sigma=\frac{2}{\mathrm{We}}\frac{d^2Y_C}{dx^2}\left[1+\left(\frac{dY_C}{dx}\right)^2\right]^{-3/2} \tag{7}$$

The β-dependent value of dY_C/dx on the body surface at $x=X_1$ must be used in integration of Eq. (7).

After determination of the matching section, the general flow parameters must be determined. There are three parameters of attached cavitation in the described model: $\{\sigma,\mathrm{Re},\mathrm{We}\}$. The values of Re, as well as the pair $\{X_1,X_2\}$, must be initialized. The value of We has to be found from Eq. (7) at the point $x=X_1$. σ has to be found from a cavity closure condition. The continuity condition for N at $x=X_3$ can be employed as the closure condition. As noted in [18], determination of h is based on solving the quasilinearized equations (Eqs. (2) and (3)): $\partial\varphi/\partial s=U-U^*$; $q/2=\partial(h^*U^*)/\partial s$. Here, q is the density of φ. It is clear from the second of these equations that such continuity is possible only with a limited q. However, the first equation is a singular integral equation that has a limited solution q with the following existence condition that depends on σ:

$$\int_{s_0}^{s_3}\frac{U-U^*}{\sqrt{(s_3-s)(s-s_0)}}ds=0 \tag{8}$$

Here, s_0 and s_3 are arc coordinates corresponding to X_0 and X_3, and U is defined by Eq. (4).

Thus, the entire problem on sheet cavitation in the CCVL is a superposition of nonlinear problems. The procedure to match the solution of the inviscid flow outside the boundary layer and the solution of the boundary layer is based on tuning the shape of boundary between viscous and inviscid flow to pressure distribution along this boundary by methods of potential theory. This procedure should take into account criteria for the boundary layer that must be yield by this distribution. The procedure of iterative solving of the problem consists of the following steps:

1. For a fixed Re and given pair $\{X_1,X_2\}$, an intermediate cavity shape is determined with Eqs. (1)–(4), C_P is calculated over the entire S with the boundary element method (BEM); the numerical accuracy of the entire solution is predetermined by the accuracy of this C_P calculation.
2. The boundary layer is computed up to $x=X_0$ determined with Eq. (5). We is determined with Eq. (7); the coefficient C_1 is found from continuity condition for dU/ds.
3. The cavitation number σ and coefficient C_2 are found with Eq. (5) at $x=X_0$ and Eq. (8). As explained earlier [18] in more detail, the combination of these equations gives a square equation for C_2. The value of X_3 is corrected to yield Eq. (6); if the correction is not negligible, a new iteration starts with computation of boundary layer parameters downstream of $x=X_0$.

A special feature of attached cavitation is the dependency of the derivative $\partial C_P/\partial s$ in Eq. (5) on the cavity shape. The cavity head is submerged in the boundary layer and influences velocities as a surface irregularity of curvature $1/r^*$. For velocity estimation, such irregularity can be replaced by a source. Such a source induces the normal velocity proportional to $\delta^*\lambda^{-2}r^*(1+\cos\beta)$. This proportionality must be taken into account in calculation of C_P. Therefore, the following form of Eq. (5) describes the separation of laminar boundary layer upstream of cavity:

$$\frac{C_L D}{\delta^*\mathrm{Re}}+\frac{\delta^*}{U}\frac{\partial U}{\partial x}<\frac{[1+\cos(\beta)]^2}{(C_C\lambda/\delta^*)^3} \tag{9}$$

Here, the angle β depends on the body surface wettability. According to the theory of a thin laminar boundary layer, $C_L=1.1$, whereas the value of C_C is the result of tuning to empirical data on cavitating flows.

The BEM numerical technique for determination of derivatives of the potential Φ and integral methods for the wall boundary layer are widely known. The correction procedure for 2D free boundary S^* employing the auxiliary functions φ and h^* has been recently described [18]. Here, let us provide more details on the computation of the cavity boundary layer over cavities. The following dimensionless velocity profile is employed:

Downloaded 03 Jun 2010 to 171.66.16.156. Redistribution subject to ASME license or copyright; see http://www.asme.org/terms/Terms_Use.cfm

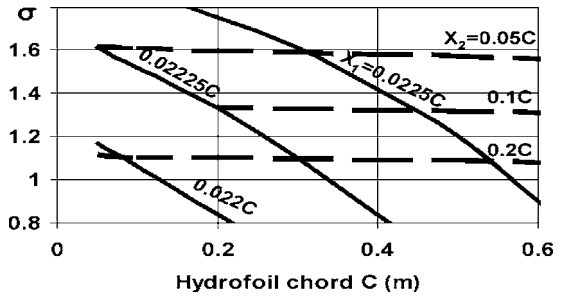

Fig. 4 Correspondence of the variables $\{X_1, X_2\}$ and $\{C, \sigma\}$ for the EN-hydrofoil at Re=1.5×10⁶

$$\bar{u}(\eta) = \frac{u}{U} + \left(1 - \frac{u}{U}\right)\eta^2(3 - 2\eta) \tag{10}$$

Here, $\eta=(y-Yc)/\delta$. For determination of two unknown parameters $u(x)$ and $\delta(x)$, two equations must be employed. The first equation is the Karman equation in the following form,

$$U\frac{dU}{dx}(\delta^* + 2\delta^{**}) + U^2\frac{d\delta^{**}}{dx} + v(U-u) = 0 \tag{11}$$

Here, v is the water velocity component normal to the cavity surface (direction of this velocity through the cavity surface is shown in Fig. 3). One can see in Eq. (11) that the friction on the cavity surface is omitted as negligibly small. The second equation is the momentum differential equation for the zero friction line in the Clauser form,

$$u\frac{du}{dx} = 0.015\frac{(U-u)^3}{U\delta^*} - U\frac{dU}{dx} \tag{12}$$

For different parts of the problem, different grids are used. For computation of U in 2D and axisymmetric flows with BEM, from 60 to 100 boundary elements are typically used, with very different element lengths (from 0.0003 at edge to 0.05); the high-order Gauss quadrature is used within each element. For the S^* correction, another nonuniform 2D grid with 30–40 elements is generated. For the integration of boundary layer differential equations, the grids are denser with a factor from 400 to 8000 (variations of boundary layer parameters between neighbor nodes must be $<1\%$).

As noted above, for the given X_1 and X_2 at the fixed Re, the corresponding pairs $\{\sigma, \mathrm{We}\}$ can be found, but researchers have usually recorded D instead of We. Because $\mathrm{We}=\rho(\nu\mathrm{Re})^2/(\chi D)=\mathrm{const}/D$, the pair $\{\sigma, \mathrm{We}\}$ can be easily replaced by the pair $\{\sigma, D\}$ here.

Nevertheless, there are some common effects, and determination of cavity for a given pair $\{\sigma, D\}$ requires the fit of $\{X_1, X_2\}$ values with maps similar to those plotted in Fig. 4 for the EN-hydrofoil. Returning to Fig. 1, one can see that such a fit leads to numerical results that are in good agreement with measured values of the cavity length L.

One can find out from Fig. 4 that the body size (chord length) very slightly influences dependencies $X_2(\sigma)$, whereas X_1 significantly depends on both σ and body size (chord length). Impact of C_C value on such results depends on $\partial U/\partial x$. For example, for the body with hemispherical head at $\mathrm{Re}=2\times10^6$ with $L=0.45D$, a 30% increase from the used value 0.0164 of C_C in Eq. (9) results in a 30% decrease in the predicted D, with keeping σ practically constant. For $C_C\to\infty$, D would be reduced threefold and σ would be reduced by 2.5%.

Cavity Detachment on Axisymmetric Bodies

Comparisons of the predicted positions of cavity detachment with experiments in axisymmetric flows are given in Figs. 5 and 6. Axisymmetric flows as the primary tests are preferable, in general, because the absence of lift removes additional effects that may introduce difficulties in comparisons.

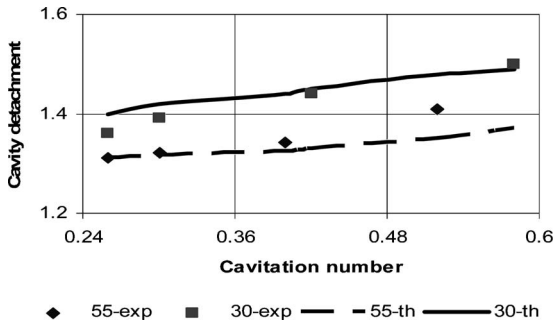

Fig. 5 Comparison of theoretical (lines) and measured positions of cavity detachment points (after [5], shown by symbols) on axisymmetric body of D=0.045 m with hemispherical head. The arc coordinate of detachment point is normalized by the head radius $D/2$. The number in the legend indicates U_∞ (in feet per second)

The cavity detachment abscissa over the slender body with hemispherical head in Fig. 5 is the curvilinear coordinate counted along the meridian section of the body. One can see in Fig. 5 that the presented CCVL version satisfactorily describes the effect of flow speed. The comparison of theoretical results to the experimental data of [23] for the ellipsoid in Fig. 6 has a double significance. First, it is the confirmation of the theory for another body shape. Second, this comparison emphasizes the roles of surface tension and body wettability: The angle β is close to zero for metals, but it is $\sim\pi/2$ for Teflon®.

The difference in the cavity detachment for smooth bodies leads to the difference in the cavity length. For cavities with detachment points shown in Figs. 5 and 6, the detachment effect on cavity length is shown in Fig. 7. The observed [23] cavity length for the Teflon ellipsoid had variations from $1.75D$ at $\sigma=0.2$ down to $L=0.65D$; thus, the advantages of the CCVL relatively ideal cavitation increase with σ. For a body with a hemispherical head, the situation is similar.

The analysis of 3D cavitating flows around axisymmetric bodies is presented here for slightly 3D flows at the small angles of attack α. For these nonaxisymmetric flows, the inviscid flow was computed with the 3D approach, whereas the boundary layer was computed with the 2D equations along the ensemble of 3D streamlines of inviscid flows around these bodies. Furthermore, the 3D cavity pattern is computed as a combination of 2D cavities in the artificial nonuniform 2D incoming flows, with the unperturbed pressure distributions determined from the above 3D inviscid problem. The combined mutual influence of these cavities is

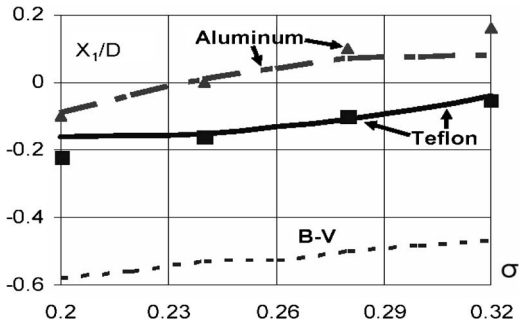

Fig. 6 Computed and measured [23] abscissas of cavity detachment X_0 on ellipsoids $(x/D)^2+(2y/D)^2+(2z/D)^2=1$ made from different materials: D=0.05 m, U_∞=18 m/s. Curve B–V means ideal cavitation with Brillouin–Villat condition.

Downloaded 03 Jun 2010 to 171.66.16.156. Redistribution subject to ASME license or copyright; see http://www.asme.org/terms/Terms_Use.cfm

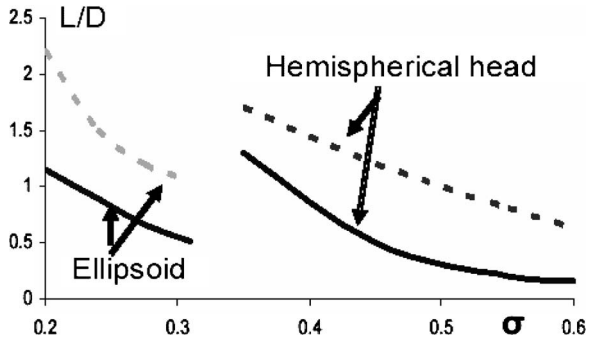

Fig. 7 Effect of cavity detachment on cavity length: Solid curves give results of the CCVL for D and U_∞ employed in Figs. 5 and 6; dashed curves give results of ideal cavitation with Brillouin–Villat condition

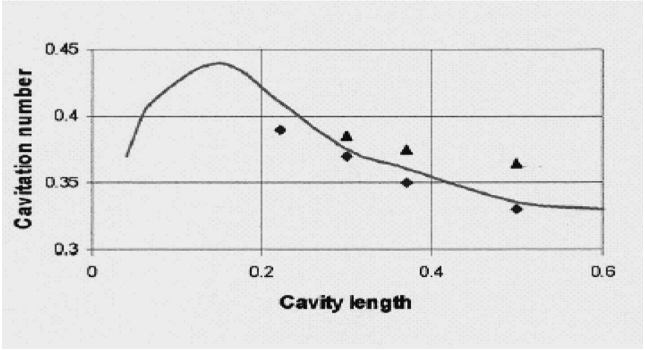

Fig. 9 Cavity length over the ITTC body. Triangles and rhombs show observed maxima and minima of L; the curve is the computation result.

supposed to be negligible here. The application of this approach to a 12 in. torpedo model is compared in Fig. 8 to cavity observations (by Gorshkov in a 1.3 m × 1.3 m test section with smoothed corners of a water tunnel with closed recirculation in the Krylov Ship Research Institute; the wall effect is taken into account in his σ values).

The Reynolds number in this experiment was quite high, but the boundary layer upstream the cavity remains to be laminar (the Michel criterion was used for the prediction of natural transition, as was recently done in [15]). According to computations, there is no significant scale effect on cavity detachment in the upper part of the body, but the observed asymmetry of the cavity should disappear with increase of Re with a factor 11 with and increase of We with a factor 44.

Cavitation Detachment and Cavitation Inception

A challenging problem associated with determination of the cavity location and size is the prediction of the cavitation inception number σ_I, defined here as a maximum possible value of σ in the steady flow at fixed Re and D. This definition is used in both contemporary experimental practice and theoretical studies.

Although the cavitation inception can be significantly affected by the water quality (as explained in [24]) and the presented theory does not take into account the water quality effects, there is a possibility to compare this theory with experimental data obtained in facilities with the low gas content. For such facilities, the gas pressure within appearing cavities differs insignificantly from the vapor pressure and the actual cavitation number is very close to the vapor cavitation number usually employed in presentations of experimental data, as well as in our theory. It is important to emphasize that in the CCVL, the cavity of the highest cavitation number is not a cavity of the minimum size, and there are two solutions for cavity length $L(\sigma)$ within a range of σ. One can see the computed dependency $L(\sigma)$ for International Towing Tanks Committee (ITTC) body with the fixed {Re, We} in Fig. 9. The σ values do increase with L along the low-L branch of the dependency $\sigma(L)$, but this branch only represents a mathematical possibility. In reality, $\sigma(L)$ is a decreasing dependency and the decreasing branch of the computed dependency in Fig. 9 is in a good agreement with the experimental data presented by Ceccio and Brennen [25], taking into account the pulsation of the cavity.

For bodies with the hemispheric head in facilities with low air content, the comparison of our computations with the experimental data on σ_I(Re, D), gathered by Billet and Holl [26] and Arakeri and Acosta [16], is given in Fig. 10. There are two different trends there. The first trend includes results for the body with a turbulence stimulator only. The second trend accumulates all other results.

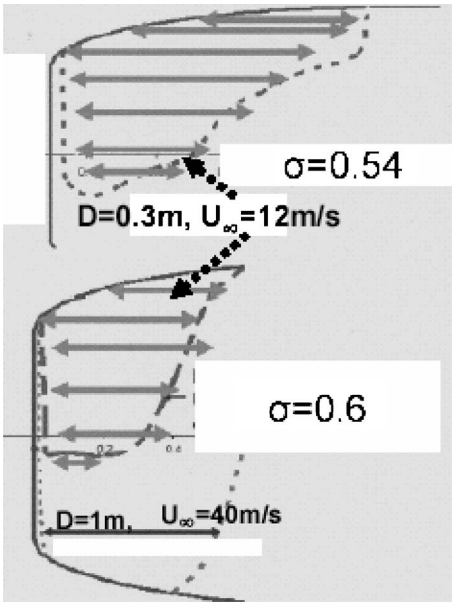

Fig. 8 Cavitation patterns on the body of revolution at α = 3 deg. Body head similar to ITTC body head, but a little bit blunter (its block coefficient, 2.5% greater). Solid lines show the body contour (abscissa is normalized by D). Dashed and dotted curves limit the computed cavity patterns. Observed cavity patterns are shown by double arrows.

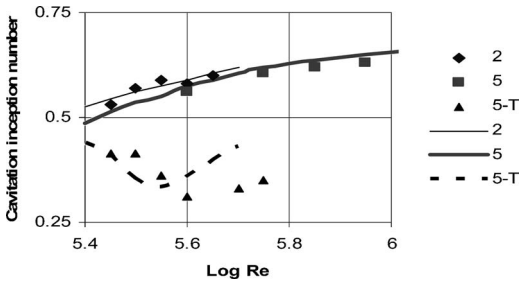

Fig. 10 Cavitation inception number for bodies with hemispherical head versus Reynolds number for different calibers D: "2" shows measurements with low air contain for D = 0.02 m, "5-T" show measurements for D = 0.05 m with a turbulence stimulator, and "5" shows measurements for this body without this stimulator. Indexes of our computational curves correspond to symbol indexes.

Downloaded 03 Jun 2010 to 171.66.16.156. Redistribution subject to ASME license or copyright; see http://www.asme.org/terms/Terms_Use.cfm

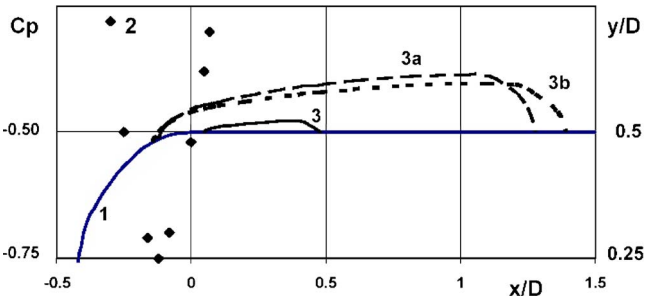

Fig. 11 Boundary layer effect on cavity shapes for $\sigma=0.3$ on the body with hemispherical head. Curve 1 is the body contour; curve 2 is C_p for cavitation-free flow; curve 3 is the cavity section at $Re=5\times10^5$, $D=0.05$ m in turbulent boundary layer; curve 3a is the cavity section at $Re=5\times10^5$, $D=0.05$ m in laminar boundary layer; curve 3b is the cavity section at $Re=10^7$, $D=1$ m turbulent boundary layer.

The first trend is related to the flow with the forced transition at the abnormally low Re values. This trend was obtained with a simplified method of simulating the stimulated transition (by 200% jumps of δ^* at the point of stimulator location) and with the oversimplification of the criterion of turbulent boundary layer separation upstream of the cavity (using this criterion in the form $\lambda=2\delta^*$, after [17]). These simplifications have resulted in a quantitative disagreement between our prediction and the measurements [16], but a qualitative explanation of the effect of stimulated transition on cavitation can be done with the CCVL. As shown in Fig. 11 plotted with the CCVL solutions, for a fixed Re, the turbulent boundary layer can grow without separation upstream of the cavity, with much higher $\partial C_P/\partial s$ than the laminar boundary layer can. Therefore, there is no equilibrium position for the attached cavity in the low-pressure zone of the turbulent boundary layer at low Re, and the cavity inception is delayed at a quite low σ. For the following significant increase of Re and D, the cavity head goes upstream.

The second trend data do not collapse in a single dependency. There is a difference between σ_I(Re) for different D. The larger bodies have lower σ_I(Re) in both the presented theory and experiments (as was noted by Keller [6] as well).

Thus, the demonstrated ability of the CCVL to predict σ_I for sheet cavitation is related to the generally correct prediction of cavity detachment. However, there are two conservation laws in the integral form for 2D and axisymmetric incompressible boundary layers. Therefore, an integral method can work with two unknown functions only (for instance, δ^* and δ^{**}). As a result, the velocity profiles can depend on two parameters only. It limits the accuracy of modeling with the CCVL, as manifested by the trend for stimulated turbulent flow in Fig. 10.

Conclusions

The developed concept of cavitation within viscous layers (CCVL) is an advanced modification of the classical cavitation theory that operates with the traditional characteristics of cavitation and with the traditional scheme of viscous-inviscid interaction. The key point of this concept is that sheet cavitation itself generates viscous separation on the body surface.

As has been shown, incorporating the surface tension effects in consideration of the cavity head has a great significance in analyzing cavitation of the smooth-shaped bodies and hydrofoils. It substantially improves the determination of cavity detachment for hydrofoils and bodies of revolution. It leads to much better computations of cavity sizes and the cavitation inception number.

On the other hand, the presented version of the CCVL employs integral methods for all considered boundary layers. It may be a cause of significant discrepancies between the computed and measured data for some flows because the real cavitation flows are very complex. There are large-scale two-phase turbulence structures, compressibility effects, and zones of massive flow recirculation there. The mathematical UTCC methods generally have a potential to take more of such physics into account. However, it would require replacing the assumption of uniformly turbulent cavitating flow and focusing on small important regions, such as zones of cavity detachment, laminar-turbulent transition, etc.

Nomenclature

C = hydrofoil chord
C_C = empirical coefficient in the separation criterion
$C_P=2(P_\infty-P)/(\rho U_\infty^2)$ = dimensionless pressure coefficient
D = body diameter
h = distance between the body surface and S^*
h^* = variation of h from iteration to iteration
$L=X_2-X_1$ = cavity length
N = normal to S
P_C = pressure within cavity,
P_∞ = unperturbed pressure
$\mathrm{Re}=DU_\infty/\nu$ = Reynolds number
Re_X = abscissa-based Reynolds number
S = the entire boundary of inviscid flow
S^* = part of S at $X_0\leq x\leq X_3$
s = arc abscissa
U = velocity on S
U_∞ = free stream speed
U^* = distribution of U known from previous iteration
u = velocity in the boundary layer
$\mathrm{We}=\rho U_\infty^2 D/\chi$ = Weber number
X_0 = abscissa of boundary layer separation point
X_1 = abscissa of cavity detachment point
X_2 = abscissa of cavity end
X_3 = abscissa of boundary layer reattachment to the body surface downstream of cavity
X_4 = $5/3X_3-2/3X_2$
x^* = abscissa of boundary layer reattachment to the cavity surface
Y_C = ordinate of the cavity surface
δ = boundary layer thickness
δ^* = displacement thickness
δ^{**} = momentum thickness
$\lambda=X_1-X_0$ = separation zone length
χ = surface tension coefficient
$\sigma=2(P_\infty-P_C)/(\rho U_\infty^2)$ = cavitation number
σ_I = cavitation inception number
ρ = liquid density
Φ = velocity potential
φ = auxiliary potential; perturbation of Φ

References

[1] Rowe, A., and Blottiaux, O., 1993, "Aspects of Modeling Partially Cavitating Flows," J. Ship Res., **37**, pp. 39–50.
[2] Yamaguchi, H., and Kato, H., 1983, "Non-Linear Theory for Partially Cavitating Hydrofoils," J. Soc. Nav. Archit. Jpn., **152**, pp. 117–124.
[3] Birkhoff, G., and Zarantonello, E., 1957, *Jets, Wakes and Cavities*, Academic Press, New York.
[4] Brennen, C. E., 1969, "A Numerical Solution for Axisymmetric Cavity Flows," J. Fluid Mech. **37**, pp. 671–688.
[5] Arakeri, V. H., 1975, "Viscous Effects on the Position of Cavitation Separation From Smooth Bodies," J. Fluid Mech., **68**, pp. 779–799.
[6] Keller, A. P., 2001, "Cavitation Scale Effects Empirically Found Relations and

Downloaded 03 Jun 2010 to 171.66.16.156. Redistribution subject to ASME license or copyright; see http://www.asme.org/terms/Terms_Use.cfm

the Correlation of Cavitation Number and Hydrodynamic Coefficients," Cav-2001 Symposium.
[7] Ahuja, V., Hosangadi, A., and Arunajatesan, S., 2001, "Simulation of Cavitating Flows Using Hybrid Unstructured Meshes," ASME J. Fluids Eng., **123**, pp. 331–338.
[8] Lindau, J. W., Kunz, R. F., Boger, D. A., Stinebring, D. R., and Gibeling, H. J., 2002, "High Reynolds Number, Unsteady, Multiphase CFD Modeling of Cavitating Flows," ASME J. Fluids Eng., **124**, pp. 607–617.
[9] Iga, Y., Nonmi, N., Goto, A., Shin, B. R., and Ikohagi, T., 2003, "Numerical Study of Sheet Cavitation Breakoff Phenomenon on a Cascade Hydrofoil," ASME J. Fluids Eng., **125**, pp. 643–650.
[10] Singhal, A. K., Athavale, M. M., Li, H., and Jiang, Y., 2002, "Mathematical Basis and Validation of the Full Cavitation Model," ASME J. Fluids Eng., **124**, pp. 617–624.
[11] Vaidyanathan, S., Senocak, I., Wu, J., and Shyy, W., 2003, "Sensitivity Evaluation of a Transport-Based Turbulent Cavitation Model," ASME J. Fluids Eng., **125**, pp. 447–455.
[12] Qin, Q., Song, C. C. S., and Arndt, R. E. A., 2003, "A Virtual Single-Phase Natural Cavitation Model and Its Application to Cav2003 Hydrofoil," 5th Symp. on Cavitation, Osaka, Paper No. Cav03-OS-1-004.
[13] Gopalan, S., and Katz, J., 2000, "Flow Structure and Modeling Issues in the Closure Region of Attached Cavity," Phys. Fluids, **12**, pp. 895–911.
[14] Schubauer, G. B., and Skramstad, H. K., 1948, "Laminar Boundary-Layer Oscillations and Transition on a Flat Plate," NACA Report No. 909.
[15] Bourgoyne, D. A., Hamel, J. M., Ceccio, S. L., and Dowling, D. R., 2003, "Time-Averaged Flow Over a Hydrofoil at High Reynolds Number," J. Fluid Mech., **496**, pp. 365–404.
[16] Arakeri, V. H., and Acosta, A. J., 1976, "Cavitation Inception Observation on Axisymmetric Bodies at Supercritical Reynolds Numbers," J. Ship Res., **20**, pp. 40–50.
[17] Amromin, E. L., 1985, "On Cavitation Flow Calculation for Viscous Capillary Fluid," Fluid Dyn., **20**, pp. 891–897.
[18] Amromin, E. L., 2002, "Scale Effect of Cavitation Inception on a 2D Eppler Hydrofoil," ASME J. Fluids Eng., **124**, pp. 186–193.
[19] Brewer, W. H., and Kinnas, S. I., 1997, "Experiment and Viscous Flow Analysis on a Partially Cavitating Hydrofoil," J. Ship Res., **41**, pp. 161–171.
[20] Chahine, G. L., and Hsiao, C.-T., 2000, "Modeling 3D Unsteady Sheet Cavities Using a Coupled UnRANS-BEM Code," 23rd Symposium on Naval Hydrodynamics.
[21] Castillo, L., Wang, X., and George, W. K., 2004, "Separation Criterion for Turbulent Boundary Layers via Similarity Analysis," ASME J. Fluids Eng., **126**, pp. 297–304.
[22] Roberts, W. B., 1980, "Calculation of Laminar Separation Bubbles and Their Effect on Airfoil Performances," AIAA J., **18**, pp. 25–31.
[23] Amromin, E. L., and Ivanov, A. N., 1982, "Determination of Cavity Separation Points on Body in Viscous Capillary Fluid," Sov. Phys. Dokl., **262**, pp. 823–826.
[24] Arndt, R. A. E., 2002, "Cavitation in Vortical Flow," Annu. Rev. Fluid Mech., **34**, pp. 143–176.
[25] Ceccio, S. L., and Brennen, C. E., 1992, "Dynamics of Sheet Cavities on Bodies of Revolution," ASME J. Fluids Eng., **114**, pp. 93–99.
[26] Billet, M. L., and Holl, J. W., 1981, "Scale Effects on Various Types of Limited Cavitation," ASME J. Fluids Eng., **103**, pp. 405–414.

Downloaded 03 Jun 2010 to 171.66.16.156. Redistribution subject to ASME license or copyright; see http://www.asme.org/terms/Terms_Use.cfm

Tomaž Rus
Turboinštitut d.d.,
Rovšnikova 7,
1210 Ljubljana-Šentvid, Slovenia
e-mail: tomaz.rus@turboinstitut.si

Matevž Dular[1]
e-mail: matevz.dular@fs.uni-lj.si

Brane Širok
e-mail: brane.sirok@fs.uni-lj.si

Marko Hočevar
e-mail: marko.hocevar@fs.uni-lj.si

Laboratory for Water and Turbine Machines,
University of Ljubljana,
Aškerčeva 6,
1000 Ljubljana, Slovenia

Igor Kern
Turboinštitut d.d., Rovšnikova 7, 1210
Ljubljana-Šentvid, Slovenia
e-mail: igor.kern@turboinstitut.si

An Investigation of the Relationship Between Acoustic Emission, Vibration, Noise, and Cavitation Structures on a Kaplan Turbine

The goal of the study was to explain the relationship between different acoustic signals and visual appearance of cavitation. Measurements of acoustic emission, vibration, and noise were performed on a Kaplan turbine model, with only two blades, in a cavitating condition. Since a model with only two blades was used, most of the side effects were eliminated, and it was concluded that the cavitation itself is the source of the recorded signal. Results showed an interesting relationship between the extent of the cavitation and the recorded data from sensors. At a decreasing cavitation number, the recorded amplitudes from all measurements first rose, experienced a local maximum, then fell to a local minimum, and finally rose again. The cavitation was also visually observed. It was concluded from the measurements that there are distinct correlations between acoustic emission, vibration, and noise on one side and the topology, extent, and type of cavitation structures on the other side. A physical explanation for the phenomenon was introduced and included in a semi-empirical model that links the visual appearance of cavitation on the blade of the turbine to the generated noise and vibration. [DOI: 10.1115/1.2754313]

1 Introduction

The phenomenon of cavitation, characterized by vapor generation and condensation, occurs frequently in hydraulic machines. It causes vibration, increase of hydrodynamic drag, changes in the flow hydrodynamics, erosion, thermal and light effects (such as luminescence), generation of noise, and acoustic emission.

The most commonly used method for identifying the presence of cavitation in hydraulic machines is based on observations of the drop in efficiency. It must be noted that cavitation starts to develop before the usual "critical" point, the 1% drop in efficiency in turbine model testing. It is generally accepted that the pressure for inception of cavitation is not constant and varies with fluid physical properties and the surface roughness of the hydraulic equipment. Other techniques, such as vibration analysis [1–3], hydrophone observations, and application of the high-frequency acoustic emission technique [4–6] in condition monitoring of rotating machinery, have been growing over recent years. Typical frequencies associated with these techniques range from 5 kHz to 1 MHz. On the other hand, in model testing, visualization of cavitation is becoming an important aspect of cavitation research [7–9]. The interesting trend, where when the cavitation number is decreased, the measured signal first rises, experiences a local maximum, then falls to the local minimum, and rises again, is actually well known and was first reported by Pearsall [10] who investigated cavitation noise and vibration in a centrifugal pump. A similar trend on an inducer pump was also measured by Gopalakrishan [11]. However, a thorough explanation of the trend was never given.

This paper discusses the measurements of acoustic emission, vibration, and noise on a two-bladed Kaplan turbine. Parallel to conventional measurements, images of cavitation structures were recorded. It was discovered that a correlation exists between the acoustic emission, vibration, and noise on one side, and topology, type, and extent of cavitation structures on the other side. Finding deterministic links between the acoustical signal and the cavitation structures could lead to improvement of the monitoring and control of hydraulic machines.

A physical explanation of the processes involved in the noise generation is given in this paper. To quantify our observations, the conclusions drawn from the results of experiment are introduced as a semi-empirical model that also includes theories of cavitation cloud collapse [12,13] and attenuation of the pressure wave [14]. A similar model was previously successfully used for the prediction of cavitation erosion on different geometries [15,16]. The present model could be used to predict the cavitation noise and also to determine the type of cavitation that appears in turbines.

2 Experimental Setup

Experiments were performed at the low head closed-loop test rig for Kaplan turbines (Fig. 1). Model tests were performed according to IEC 60193 standard [17]. The flow rate was measured with an absolute accuracy of ±0.16% of the measured value (Venturimeter calibrated with volumetric method) and ±0.20% of the measured value (electromagnetic flowmeter). The head was measured with an uncertainty of less than ±0.1% of the measured value.

Experiments were first conducted on a four-bladed Kaplan turbine model with specific speed $n_q=3.21$ and nominal outside diameter of 350 mm. The Reynolds number was held constant during the experiment $\mathrm{Re}=2.6\times10^6$ (based on the blade tip velocity and the blade chord length).

Because of the distorted signals from noise, the measured acoustic signals from the four-bladed turbine show an unclear cavitation trend from the interaction of multiple blades. This unclear trend is also demonstrated from the visual measurements. In order to isolate the cavitation features, a two-bladed Kaplan tur-

[1]Corresponding author.

Contributed by the Fluids Engineering Division of ASME for publication in the JOURNAL OF FLUIDS ENGINEERING. Manuscript received June 21, 2006; final manuscript received April 2, 2007. Review conducted by Yu-Tai Lee. Paper presented at Euronoise 2006.

 Copyright © 2007 by ASME

Downloaded 03 Jun 2010 to 171.66.16.156. Redistribution subject to ASME license or copyright; see http://www.asme.org/terms/Terms_Use.cfm

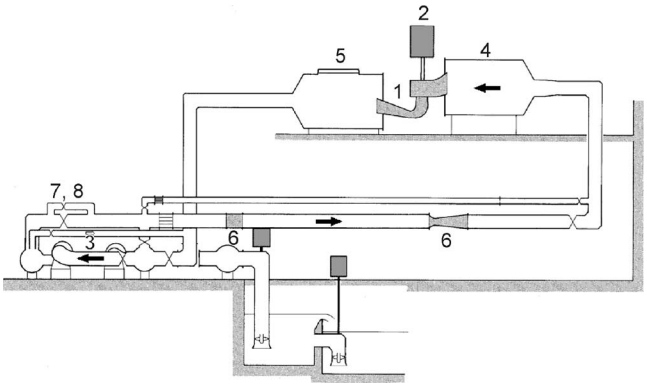

Fig. 1 Low head closed-loop test rig for Kaplan turbine testing: 1, model turbine; 2, motor-generator; 3, circuit pumps; 4, pressure tank; 5, suction tank; 6, flowmeters; and 7 and 8, regulation and by-pass valves, respectively

bine was therefore constructed from the original four-blade configuration by removing two blades. The two-bladed turbine has, of course, higher specific speed than the original. The efficiency of the two-bladed turbine certainly deviates from the original design. However, a similar cavitation condition and phenomena would be expected with the same revolution speed, guide vane opening, flow rate, cavitation number, and lower head as for the original four-bladed turbine.

Because of the physical nature of cavitation, sensors with a large frequency range were used. The acoustic emission sensor and accelerometer were mounted on the flange in the horizontal plane at the beginning of the suction tube. The hydrophone was mounted on the suction tube close to the impeller. Actual positions of the sensors, stroboscopic light, and the charge-coupled device (CCD) camera can be seen in Fig. 2.

2.1 Acoustic Emission Sensor. For the detection of the high-frequency noise, an acoustic emission sensor Kistler 8152A1 was used. It contains a piezoelectric element that detects acoustical waves in solids with a frequency ranging from 50 kHz to 400 kHz (±10 dB). The sensor was mounted according to ASTM E 650-85 standard [18]. It was connected to the signal-conditioning device, a Kistler AE-Piezotron Coupler 5125A, which contains the sensor's current supply, the amplifier, a two-pole Butterworth high-pass (50 kHz cutoff frequency), and low-pass (1 MHz cutoff frequency) filters.

2.2 Hydrophone. A Bruel and Kjær (B & K) type 8103 high-frequency hydrophone was used. It can be used for sound measurements with a frequency ranging from 0.1 Hz to 180 kHz. (±12.5 dB). The hydrophone was connected to the charge amplifier B&K-type 2635. The hydrophone was submerged in a small container filled with water and attached to the outside surface of the draft tube. The acoustical signal was transmitted from the flow field, through the Plexiglas and water to the hydrophone. To improve the amplitude resolution of the high-frequency component before A/D conversion, the low-frequency signal (up to 2 kHz) was removed with an analog filter KEMO VBF42.

2.3 Accelerometer. A Bruel and Kjær type 4393 accelerometer was used. It has a flat frequency response from 0.1 Hz to ~15 kHz. The typical mounted resonance frequency is ~55 kHz. The calibration curve was considered so that the vibrations could be measured almost up to the accelerometer resonance region (frequency range 30–50 kHz (±7 dB)). Despite this deficiency, the results were similar to those of the acoustic emission and hydrophone measurements. The accelerometer was connected to the amplifier B&K-type 2635.

2.4 Data Acquisition. The acoustic emission, hydrophone, accelerometer, and trigger signals were simultaneously sampled at a 12-bit resolution with a 1 MHz sampling rate for 20 s to preserve the full frequency range of each transducer for further analysis. To avoid the possible aliasing phenomenon, the sampling frequency was at least five times higher than the observed frequency range. PC-based sampling was carried out simultaneously over four channels using a National Instruments PCI-6110E A/D converter card. Data sampling and post-processing were performed with software developed in LABVIEW on 2×10^7 samples of complete acquired signal from each transducer.

2.5 Blade-Passage Modulation Level. Amplitude demodulation (or envelope analysis) is a method of signal analysis, which includes elements of signal treatment in the time and frequency domain. Shaft rotation in hydraulic machinery is a fundamental motion that influences all other phenomena. Turbine blades encounter a nonuniform and nonsteady flow field at the entrance. The dominant frequency contained in the cavitation signal is the blade-passage frequency (BPF). The cavitation signal is modulated by the blade-passage frequency. In order to demodulate signal, bandpass filters are used to extract the other frequencies. The filtered signal is then processed by the Hilbert transform or by full wave rectification to obtain the envelope signal. The Fourier transform of the envelope represents the demodulated spectrum $G_M(f)$. The modulated intensity (power) I_M is then

$$I_M = \int_{f_1}^{f_2} G_M(f)df \tag{1}$$

Abbot et al. [3] showed that the blade-passage modulation level (BPML) can be used as a measure of cavitation intensity on the blade

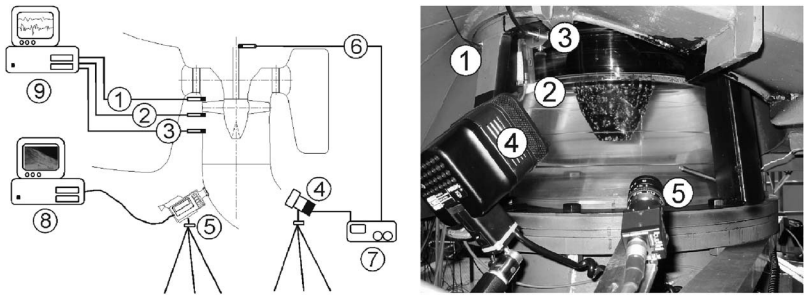

Fig. 2 Experimental setup: 1, accelerometer; 2, hydrophone; 3, AE sensor; 4, stroboscopic light; 5, CCD camera; 6, trigger; 7, stroboscopic main unit; 8, PC with video grabber card; and 9, PC with data acquisition

Downloaded 03 Jun 2010 to 171.66.16.156. Redistribution subject to ASME license or copyright; see http://www.asme.org/terms/Terms_Use.cfm

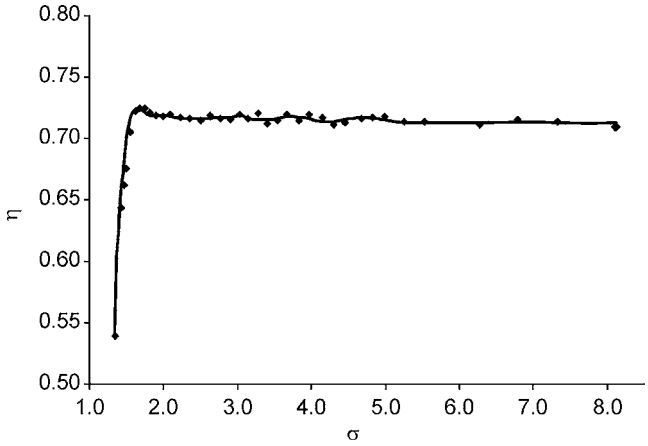

Fig. 3 Two-bladed impeller model efficiency at various cavitation numbers

$$\mathrm{BPML} = \sum_{i=1}^{n} G_M(f_i) \tag{2}$$

where BPML is a sum over blade-passage frequency harmonic lines f_i given in the demodulated spectrum.

The method can disclose the presence of amplitude modulation of the high-frequency noise in hydraulic machinery. Since it is sometimes difficult to distinguish between the basic flow noise (structural and noncavitating) and the cavitation noise, it is useful to apply the same technique also to signals of the noncavitating flow [9].

2.6 Model Turbine Operation Conditions. The present study concentrates on the most severe cavitation conditions, i.e., at the operating point with a full turbine discharge and a minimum full-size turbine operating head. Cavitation measurements were performed at a fixed model turbine head (5.4 m), flow rate (0.44 m^3/s), and rotational speed (900 rpm). Only the cavitation number was changed by adjusting the absolute pressure in the turbine draft tube. The definition of the cavitation number as used in water turbine testing is

$$\sigma = \frac{H_b - H_s - H_v}{H} \tag{3}$$

where H_b is the atmospheric pressure, H_s is the suction head, H_v gives the vapor pressure of water, and H is the net head applied to the turbine.

At first, a negative suction head was achieved by applying overpressure in the draft tube (measuring points with cavitation number σ higher than 4.6 in Fig. 3), then a vacuum pump was used to achieve positive suction head up to the point of full impeller cavitation. In this way, the full range of cavitation conditions was tested.

3 Results of Measurements

Previous studies showed that signals of acoustical emission, noise, and vibration will rise with decreasing cavitation number, reach a maximum, and then fall in a very low cavitation number region [9]. With the highly cavitating flow, the signal drops because highly compressible two-phase flow attenuates the pressure wave and causes the fall of the measured signal.

In another commonly found trend of the acoustical signal with the cavitation number, one would first observe a rise of the signal to a local maximum, a fall to a local minimum, and a rise again [10,11]. A clear and plausible explanation of such a phenomenon was never given. Present measurements show a similar trend, and this study focuses on explaining this phenomenon.

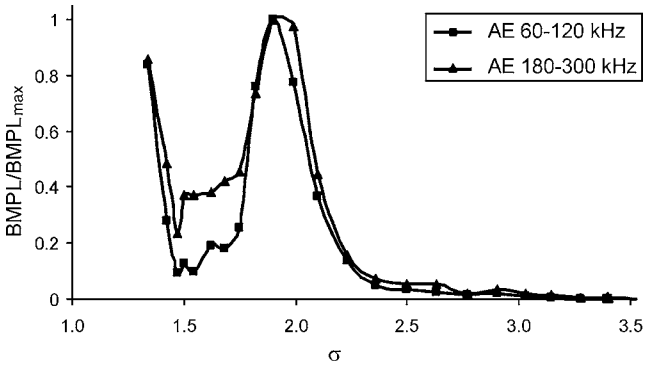

Fig. 4 Results of measurements with acoustical emission sensor

Diagrams of measured signals with three sensors, i.e., the acoustic emission sensor shown in Fig. 4, the hydrophone shown in Fig. 5, and the accelerometer shown in Fig. 6, in different frequency ranges are presented. The data obtained from the acoustic emission sensor, the hydrophone, and the accelerometer are normalized by their maximal values (BPML/BPML$_{max}$).

3.1 Results of Acoustic Emission Measurements. For the acoustical emission measurements (Fig. 4), the frequency range plays no role for the cases with higher cavitation numbers. Both signals (in the frequency ranges of 60–120 kHz and 180–300 kHz) begin to rise at approximately $\sigma = 3.4$, where cavitation first occurs. A maximum of both signals is reached at $\sigma = 1.9$. After that, the amplitude of the signals drops significantly until a local minimum is reached at $\sigma = 1.5$. The amplitude of the signal with the frequency range 180–300 kHz drops slightly slower in this region, probably because the majority of the eigenfrequencies of the pressure waves that are emitted during the cavi-

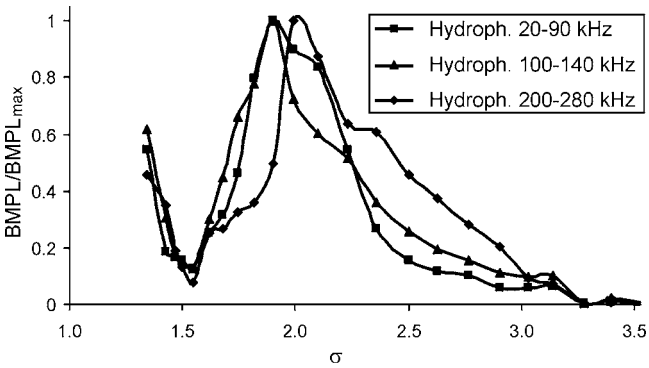

Fig. 5 Results of measurements with a hydrophone

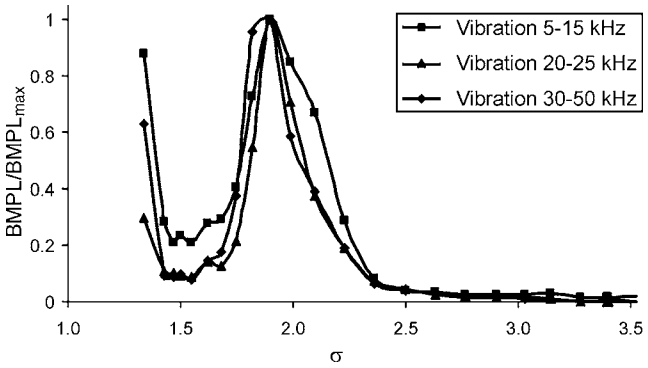

Fig. 6 Results of measurements with accelerometer

Downloaded 03 Jun 2010 to 171.66.16.156. Redistribution subject to ASME license or copyright; see http://www.asme.org/terms/Terms_Use.cfm

tation cloud collapse also lie in this range [12,13]. At even lower cavitation numbers ($\sigma < 1.5$), both signals rise again.

3.2 Results of Hydrophone Measurements. For hydrophone measurements (Fig. 5), the frequency range has greater influence on the measured signal amplitude. Similarly to the acoustic emission measurements, the signals begin to rise at incipient cavitation ($\sigma \approx 3.5$). The signal with the frequency from 200 kHz to 280 kHz rises the fastest since it is the closest to the eigenfrequencies of the pressure waves that are emitted during the collapse of vapor structures. The maximum of the three signals is not reached at the same cavitation number—while the signals with the ranges of 20–90 kHz and 100–140 kHz reach it at $\sigma = 1.9$, the signal with the range of 200–280 kHz reaches it at approximately $\sigma = 2.1$. The signal amplitudes drop when the cavitation number is further decreased. Interestingly, the signal with the frequency range of 200–280 kHz drops the fastest. The local minimum is the same for all the frequency ranges at approximately $\sigma = 1.5$. Also, similar signals can be seen in a region with $\sigma < 1.5$.

It seems that the frequency range plays a major role in hydrophone measurements. The sensor responds much quicker (at lower signal magnitude) when the range of frequencies is closer to the eigenfrequency of the measured pressure waves.

It is possible that the structural response of the turbine and other components might affect the measurements, but we believe these effects are negligible in comparison to the signal of cavitation. This is concluded from a noise measurement of nearly as low as 40 dB for a noncavitating condition.

3.3 Results of Vibration Measurements. Accelerometer measurements (Fig. 6) are again less dependent on the range of frequencies. No significant influence can be seen even in the range of 30–50 kHz, where the sensor resonant frequency could have an effect. The signals begin to rise after the incipient cavitation occurs ($\sigma \approx 3.4$). The maximum of all signals is reached at $\sigma = 1.9$, and the local minimum occurs at $\sigma = 1.5$. The signals rise when the cavitation number is further reduced ($\sigma < 1.5$).

It is clear that a sufficient explanation of signal trends cannot be given at this stage. The local minima probably correspond to the increased compressibility of the developed cavitating flow. Visualization of cavitation was employed to determine the reason for the increase of the amplitude at very low cavitation numbers.

4 Visualization of Cavitation Structures

A Sony HC-HR50 progressive scan monochrome CCD camera (internal/external synchronization for capturing up to 60 noninterlaced frames per second at maximum resolution of 659×494 pixels) with Pentax C-mount lenses 12 mm f/1.2 and a stroboscopic light were used for image capturing and illumination, respectively. The stroboscopic light and the camera were triggered at a specific rotation angle of the turbine shaft using an inductive sensor. Images of the suction side of one blade were taken simultaneously with the acoustic measurements. For each operating point, 600 images of the same turbine blade were taken during 40 s of data acquisition (turbine revolution speed was 900 rpm). Images were digitalized in real time with a National Instruments PCI-1409 image acquisition board in an eight-bit color depth (256 levels of gray level). In further analysis, only 500 images were retained (100 images with the most differences from the average were further discarded).

Figure 7 shows a typical image for the blade cavitation. One can see the suction side of the blade. The cavitating flow can occur at three typical positions:

- near the impeller hub-hub cavitation
- on the suction side of the blade-blade cavitation
- on the tip of the blade-tip cavitation

It is not necessary for the cavitation to be present at all three positions. The blade cavitation, for example, occurs much later (at a lower cavitation number) than the hub and tip cavitation. The arc that can be seen in the bottom part of the image is the edge of the suction tube (the same applies for the images in Figs. 8–10).

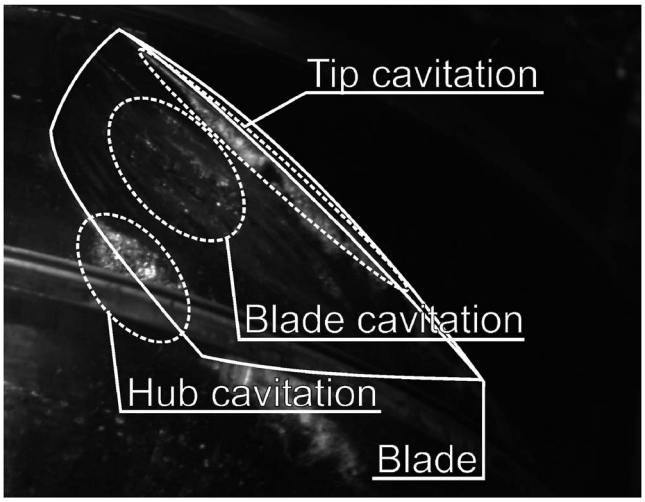

Fig. 7 A typical image with noted places of cavitation occurrence on the blade

Figure 8 shows typical images of cavitation on the blade at different cavitation numbers. The first operating point at cavitation number $\sigma = 8.11$ displays one-phase liquid flow. Cavitation first appears at cavitation number $\sigma = 3.4$ ($\sigma_{incipient} = 3.4$). At first, cavitation on the hub and on the tip of the blade is present (Fig. 8). The cavitation pockets are first attached to the solid body (to the blade and the hub). The separation of the cavitation clouds occurs

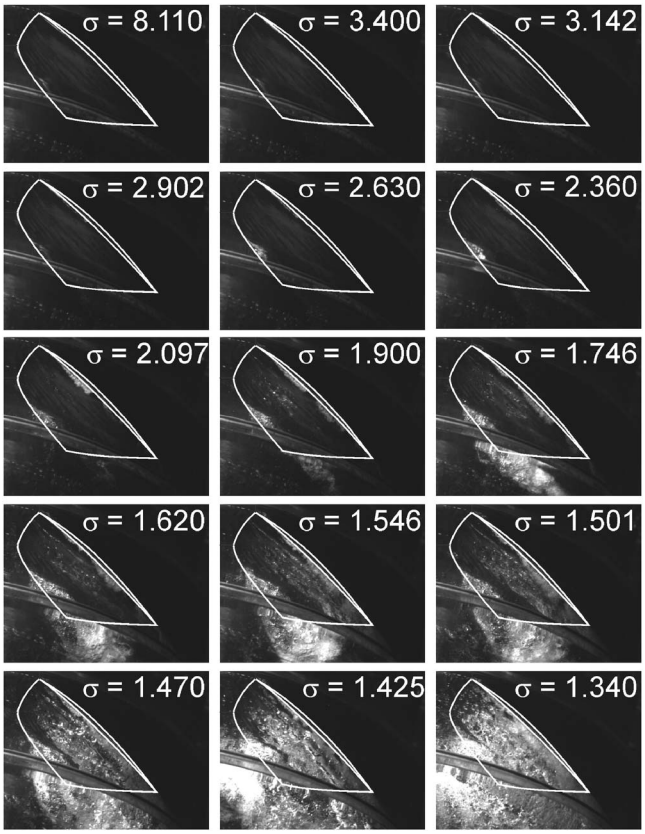

Fig. 8 Typical images of vapor structures at different cavitation numbers

Downloaded 03 Jun 2010 to 171.66.16.156. Redistribution subject to ASME license or copyright; see http://www.asme.org/terms/Terms_Use.cfm

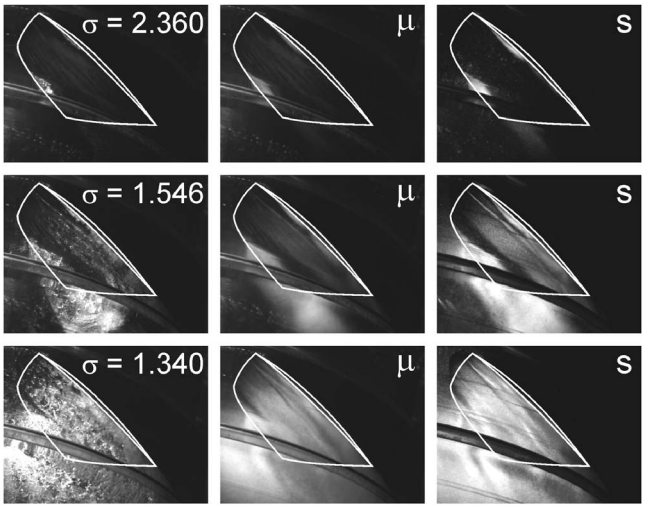

Fig. 9 Image from the series (left), mean value of gray level μ (middle), and standard deviation of gray level *s* (right) for three cavitation numbers

when the pressure is further decreased—at approximately $\sigma = 2.63$. The position and type of the cavitation remain unchanged until the cavitation number $\sigma = 2.097$ is reached. At this stage, the hub cavitation changes its type from cloud to bubble cavitation—macroscopic bubbles (radii > 1 mm) appear. Meanwhile, the tip cavitation remains cloudy.

With the decreasing pressure, the cavitation on the hub and the tip grows. At cavitation number $\sigma = 1.9$, the cavitation on the surface of the blade appears in the form of macroscopic bubbles (bubble cavitation). The types of cavitation remain the same (hub bubble cavitation, blade bubble cavitation, and tip cloud cavitation) until the pressure is decreased to the limit where supercavitation on the blade occurs. The first glimpse of supercavitation can be seen at cavitation number $\sigma = 1.425$; the cavitation covers entirely the blade at cavitation number 1.34. Meanwhile, it seems that the tip cavitation remains cloudy and the cavitation on the hub remains bubbly.

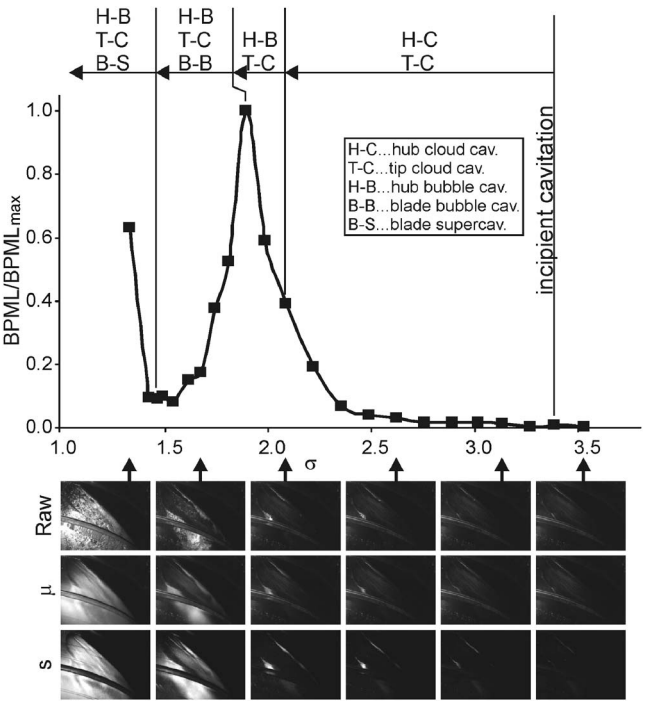

Fig. 10 A typical diagram of acoustical measurements with noted corresponding cavitation types and positions

4.1 Image Post-Processing. Image post-processing is based on the fact that image n with ij pixels can be presented as a matrix with ij elements. With eight-bit resolution, there are 256 levels of gray level for $A(i,j,n)$, in which the matrix element can be 0 for black pixel and 255 for white pixel

$$A(i,j,n) \in \{0,1,\ldots 255\} \tag{4}$$

Each image is presented as a matrix

$$\text{Image}(n) = \begin{pmatrix} A(1,1,n) & \cdots & A(i,1,n) \\ A(1,2,n) & \cdots & A(i,2,n) \\ \vdots & \ddots & \vdots \\ A(1,j,n) & \cdots & A(i,j,n) \end{pmatrix} \tag{5}$$

Interesting parameters are the mean value of gray level, $\mu(i,j)$, and the standard deviation of gray level, $s(i,j)$, of the ijth matrix element in the series of N images

$$\mu(i,j) = \frac{1}{N}\sum_{n=1}^{N} A(i,j,n) \tag{6}$$

$$s(i,j) = \sqrt{\frac{1}{N-1}\sum_{n=1}^{N} [A(i,j,n) - \mu(i,j)]^2} \tag{7}$$

Results of functions $\mu(i,j)$ and $s(i,j)$ are best presented as contour diagrams in matrix form,

$$\mu(i,j) = \begin{pmatrix} \mu(1,1) & \cdots & \mu(i,1) \\ \mu(1,2) & \cdots & \mu(i,2) \\ \vdots & \ddots & \vdots \\ \mu(1,j) & \cdots & \mu(i,j) \end{pmatrix} \tag{8}$$

$$s(i,j) = \begin{pmatrix} s(1,1) & \cdots & s(i,1) \\ s(1,2) & \cdots & s(i,2) \\ \vdots & \ddots & \vdots \\ s(1,j) & \cdots & s(i,j) \end{pmatrix} \tag{9}$$

Convergence of the mean value and the standard deviation of gray level was studied to determine the minimum number of images that need to be included in the post-processing. The uncertainty level of $<1\%$ for the mean value and $<1.5\%$ for the standard deviation was estimated for the case with 50 images [8].

4.2 Results of Image Post-Processing. In all, 500 images for each operating point were used for the statistical evaluation of cavitation. The mean value and standard deviation of gray level of images were calculated. Figure 9 shows results of statistical evaluation of images for three characteristic cavitation numbers ($\sigma = 2.36$, 1.546, and 1.340). The left image in Fig. 9 is from each series, the middle image represents the mean value of gray level μ, and the right one represents the standard deviation of gray level s. We can interpret the mean value of the gray level as a parameter that is related to the mean vapor volume fraction. Similarly, one can look at the standard deviation of the gray level as a parameter that defines the activity (dynamics) of cavitation. We can conclude that both the vapor volume fraction and the dynamics of cavitation increase as the cavitation number is reduced.

It is known that the cavitation appearance becomes stable as the state of supercavitation is reached. In contrast to this, the standard deviation increases. This is probably because the steady free surface between the liquid and the vapor phase is still slightly oscillating, but not in a form of cavitation cloud separations. This phenomenon was more thoroughly investigated by Dular et al. [8].

Besides an expected increase of cavitation aggressiveness, the

Downloaded 03 Jun 2010 to 171.66.16.156. Redistribution subject to ASME license or copyright; see http://www.asme.org/terms/Terms_Use.cfm

damping effects, which can be related to the vapor volume fraction [14], will also increase. In the following sections, a discussion of the effect of the increase in attenuation as a possible reason for the measured signal trend is presented.

5 Discussion

Since the signals of acoustical measurements (Figs. 4–6) do not vary significantly, the explanation and discussion of the relationships between the acoustical measurements and cavitation appearance are, in essence, the same for all the measured signals. Hence, only the relation between the hydrophone measurements in the range of 100–140 kHz and cavitation images is thoroughly discussed. The conclusions stated in this section are also valid for other measurements (vibration, acoustic emission, and other hydrophone measurements).

Figure 10 shows the measured evolution of the hydrophone signal (100–140 kHz) and the corresponding cavitation types and positions. Inset pictures show raw images, mean values, and standard deviations at specific operating points.

The signal starts to rise after the incipient cavitation occurs (at $\sigma=3.4$). As mentioned before, first the cavitation on the hub of the impeller and on the tip of the blade occur. Both regions of cavitation are cloudy (the bubble sizes are up to 20 μm) and attached. The signal rises exponentially as the cavity grows, and the cloud separations begin to occur. At approximately $\sigma=2.1$, the cloud cavitation on the hub becomes partially bubbly—macroscopic bubbles appear, the diameter of which are on the order of a few millimeters. It is known that an implosion of a single macroscopic bubble is usually less aggressive than an implosion of a cloud of microscopic bubbles [13]. This is probably the reason that a small decrease in the gradient of the amplitude versus σ can be seen in the diagram at this point (Fig. 10, and also in other diagrams of acoustical measurements, Figs. 4–6). The gradient increases again, after the tip cavitation grows slightly (at $\sigma\approx 2$). At cavitation number $\sigma=1.9$, a maximum of the acoustical signal is reached. At this stage, the blade starts to cavitate in the form of macroscopic bubbles. If we move to the next operating point ($\sigma=1.746$), then the acoustical signal falls dramatically. The cavitation on the other hand grows. The reason probably lies in the fact that the hub cavitation grows to the point when it "chokes" itself—the pressure wave that is emitted at a cloud collapse is attenuated in a highly compressible two-phase bubbly flow region. The pressure wave amplitude that comes from the hub cavitation is, in fact, smaller at $\sigma=1.746$ than at $\sigma=1.9$, where the cavitation extent is smaller. The gradient of the acoustical curve decreases when the cavitation number is decreased. This is because the extent of the cavitation increases—while the part of the detected signal from thehub cavitation decreases, parts of the signal from the tip and the blade cavitation increase. They are not influenced by the attenuation of the two-phase bubbly flow. The local minimum is reached at approximately $\sigma=1.5$. When the cavitation number is further reduced, the cavitation pocket covers the whole blade—supercavitation occurs. Here (at $\sigma<1.5$), a free surface between the liquid and vapor phase exists. This situation is unique, since the compressibility of individual phases is much smaller than that of the bubbly two-phase flow, which was present at higher cavitation numbers. The emitted pressure waves are again faced with a smaller attenuation; hence, the detected amplitudes are higher at very small cavitation numbers.

6 Model Development

On the basis of the above-mentioned interpretations, we can formulate a physical model that links the information gained by the visualization of cavitation structures to the results of measurements of cavitation noise and vibration. This model is very similar to the cavitation erosion model developed by Dular et al. [15,16] that uses data from visualization as input for the prediction of the distribution and the magnitude of damage. This can be done because the processes of cavitation erosion and cavitation noise and vibration are strongly linked [19].

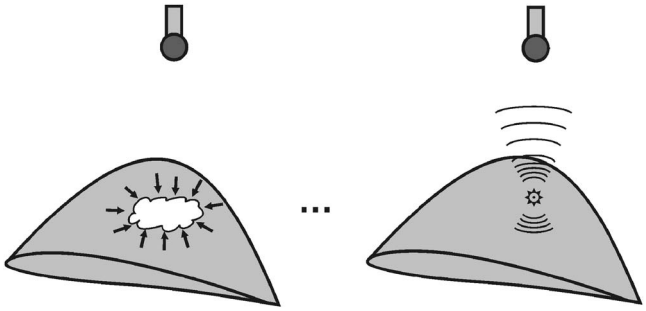

Fig. 11 Principle on which the model is based

The phenomenon of cavitation noise generation is complex and can be looked on as a sequence of several processes. The presented theory explains it in the following way (Fig. 11):

- Collapse of the cavitation cloud causes a shock wave that spreads in the fluid.
- The magnitude of the shock wave is attenuated as it travels through the fluid.
- The attenuation of the shock wave is predominately a function of the vapor volume fraction of the region through which it travels.

Although results of acoustic measurements imply otherwise, the cavitation aggressiveness (which would be manifested in effects such as cavitation erosion) probably gradually increases as the cavitation number is decreased and does not follow the trend measured by acoustical sensors, which are positioned "far" away [8,19]. This hypothesis was partially confirmed by erosion tests from previous studies on similar geometries, where increase in erosion was found when the cavitation number was lowered [20,21]. The measured trend is very probably solely a result of attenuation of the pressure wave by the region between the cavitation and the sensor.

6.1 Amplitude of the Emitted Pressure Wave. The power and, consequently, the magnitude of the emitted pressure wave are closely related to the velocity of the change of the vapor cloud volume (velocity of cavitation cloud collapse) and to the surrounding pressure [22]. We can write the following relation:

$$P_{\text{wave}} = \Delta p\left(\frac{dV}{dt}\right) \tag{10}$$

where Δp is the difference between the surrounding pressure and vapor pressure ($p_{\text{sur}}-p_v$) and dV/dt is the change of the vapor cloud volume in time t.

The magnitude of the emitted pressure wave is proportional to the square root of its power ($p_0 \propto \sqrt{P_{\text{wave}}}$). If we consider the surrounding pressure to remain approximately constant, then we can write that the distribution of the mean change in cavitation cloud volume reveals the mean distribution of amplitude of the pressure wave that is emitted by the cavitation cloud collapse.

Since the measurements of the instantaneous change of the cavitation cloud volume is not possible (the image-capturing frequency was much lower than the frequency of vapor cloud shedding), a standard deviation of gray level was used as the parameter to be related to the power of the emitted pressure wave. Standard deviation can be used in this manner since it is a function of the change of the gray level in the image as well as the cavitation cloud volume. This hypothesis was confirmed by comparing results of the standard deviation and the time derivative of a sequence of images using high-speed movie [23].

Downloaded 03 Jun 2010 to 171.66.16.156. Redistribution subject to ASME license or copyright; see http://www.asme.org/terms/Terms_Use.cfm

$$\text{gray level} = f(V) \Rightarrow s \propto \left(\frac{dV}{dt}\right) \tag{11}$$

The hypothesis is that the relation between the time derivative of vapor cloud volume and the distributions of standard deviation of gray level exists. A measure of the emitted pressure wave power P_{wave} can be simply formulated in the following way:

$$P_{\text{wave}} \propto \Delta p \sum_i \sum_j s_{ij} \tag{12}$$

where Δp is the mean pressure difference and s is the standard deviation of a pixel in the series of images. It was found by comparison of model predictions and from results of experimental measurements of the emitted pressure wave magnitude by Hofmann [24] that a linear function shows the best correlation to the experimental results [15,16],

$$p_0 = k\sqrt{P_{\text{wave}}} = k\sqrt{\Delta p \sum_i \sum_j s_{ij}} = k_1 \frac{\sqrt{\Delta p \sum_i \sum_j s_{ij}}}{\left[\sqrt{\Delta p \sum_i \sum_j s_{ij}}\right]_{\max}} \tag{13}$$

In order to simplify the calculation at each operating point, the expression inside the square root was normalized by its maximal value (in this case, it occurred at the cavitation number $\sigma = 1.34$).

6.2 Attenuation of the Pressure Wave. As the pressure wave travels away from its source, its energy is gradually converted into heat. For our problem, the main energy loss mechanism is the viscous losses generated from the friction within the fluid itself [14]. In the present case, the pressure wave passes a highly compressible two-phase region and also a single (liquid) phase region before it arrives at the sensor (except for the last three operating points, where supercavitation is present and only two regions with small compressibility exist). The wave magnitude is attenuated with distance x from the source according to

$$p = p_0 e^{-(2/3)(\omega^2/\rho c^3)\eta x} \tag{14}$$

where ω is the pressure wave frequency, η and ρ are the viscosity and the density of the fluid through which the pressure wave travels, respectively, and c is the sonic velocity within the fluid through which the pressure wave travels. The quantities ρ, η, and c, are functions of the local vapor volume fraction α. The vapor volume fraction α of the region where the pressure wave travels through (the region between the cavitation cloud and the sensor) can be related to the mean value of the gray level of the cavitation images [25]. For the present study, the following relation was used:

$$\alpha = f(\mu) = k \sum_i \sum_j \mu_{ij} = k_2 \frac{\sum_i \sum_j \mu_{ij}}{\left[\sum_i \sum_j \mu_{ij}\right]_{\max}} \tag{15}$$

A maximal value was used to normalize the function.

6.3 Consideration of Sonic Velocity and Fluid Properties. Experimental results show obvious influences of fluid properties on cavitation aggressiveness. For example, it was shown that when the experiment was conducted in water with high gas content cavitation aggressiveness (the amplitude of acoustical signals) was smaller [8]. The main reason lies in the fact that the sonic velocity is lower in water with high gas content. Consequently, compressibility and pressure wave attenuation are higher. To consider these effects, one has to introduce the properties of two-phase bubbly mixture to the model.

The sonic velocity of fluid with the presence of gas bubbles is given by [12]

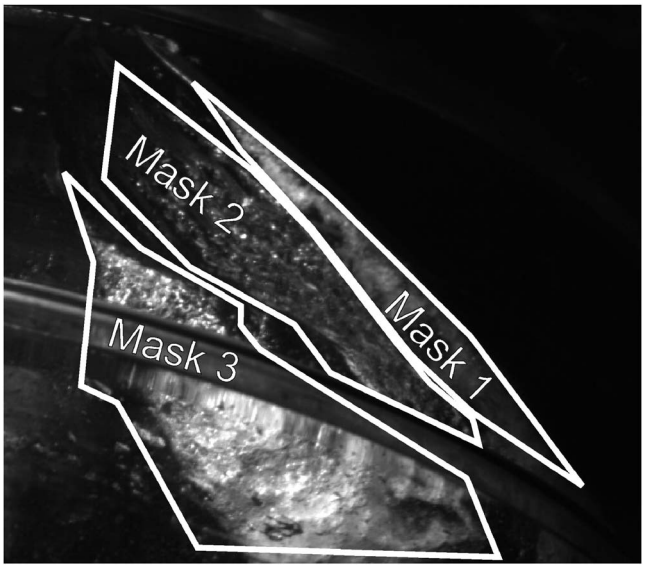

Fig. 12 Positions of masks that define different positions of cavitation occurrence

$$c = \left\{ [\rho_l(1-\alpha) + \rho_g \alpha] \left(\frac{\alpha}{\kappa p_{\text{sur}}} + \frac{1-\alpha}{\rho_l c_l^2} \right) \right\}^{-(1/2)} \tag{16}$$

where ρ_l and ρ_g are the density of the liquid and gas, respectively, α is the gas volume fraction, and κ the polytropic constant of the gas. The density and viscosity of the fluid considering the presence of gases are

$$\rho = \alpha \rho_g + (1-\alpha)\rho_l \tag{17}$$

and

$$\eta = \alpha \eta_g + (1-\alpha)\eta_l \tag{18}$$

Results of Eqs. (16)–(18) are included in the "final model equation"—Eq. (20), where parameters of the fluid (sonic velocity, density, and viscosity) through which the pressure wave travels are considered.

6.4 Formulation of the Integral Pressure Wave Amplitude. The noise or vibration detected contains signals from cavitation from the hub, blade, and tip. We must consider that pressure wave first travels through a two-phase flow and then also through a single-phase liquid flow before it reaches the sensor. The pressure wave from a specific cavitation location is in respect to attenuation rate (Eq. (14)); therefore,

$$p_{\text{sig}} = \left(p_0 e^{-(2/3)(\omega^2/\rho_{2p} c_{2p}^3)\eta_{2p} x_{2p}}\right) e^{-(2/3)(\omega^2/\rho_l c_l^3)\eta_l x_l} \tag{19}$$

The expression in the parentheses defines the amplitude of the pressure wave on the boundary of the cavitation pocket (variables ρ, η, c, and x correspond to two-phase fluid—index $2p$). The added exponential function defines additional attenuation of the pressure wave amplitude due to friction in single (pure liquid) flow (variables ρ, η, c, and x correspond to pure liquid fluid—index l). Finally, the pressure wave amplitude can be defined as the sum of the pressures from specific locations defined by the mask (Fig. 12) (from hub, blade, and tip)

$$\begin{aligned} p_\Sigma = {} & \left(p_{0,\text{hub}} e^{-(2/3)(\omega^2/\rho_{2p,\text{hub}} c_{2p,\text{hub}}^3)\eta_{2p,\text{hub}} x_{2p,\text{hub}}}\right) e^{-(2/3)(\omega^2/\rho_l c_l^3)\eta_l x_{l,\text{hub}}} \\ & + \left(p_{0,\text{blade}} e^{-(2/3)(\omega^2/\rho_{2p,\text{blade}} c_{2p,\text{blade}}^3)\eta_{2p,\text{blade}} x_{2p,\text{blade}}}\right) \\ & \times e^{-(2/3)(\omega^2/\rho_l c_l^3)\eta_l x_{l,\text{blade}}} \\ & + \left(p_{0,\text{tip}} e^{-(2/3)(\omega^2/\rho_{2p,tip} c_{2p,tip}^3)\eta_{2p,\text{tip}} x_{2p,\text{tip}}}\right) e^{-(2/3)(\omega^2/\rho_l c_l^3)\mu_l x_{l,\text{tip}}} \end{aligned} \tag{20}$$

Downloaded 03 Jun 2010 to 171.66.16.156. Redistribution subject to ASME license or copyright; see http://www.asme.org/terms/Terms_Use.cfm

Table 1 Values of parameters used in the model

Region/coefficient	k_1 (Pa)	k_2	k_3 (m)	x_1 (m)
Hub cavitation	6×10^6	0.3	0.07	0.2
Blade cavitation	6×10^6	0.987	0.03	0.1
Tip cavitation	6×10^6	0.241	0.01	0.01

The acoustical path considered in Eq. (20) does not entirely reflect the complicated physical situation with the pressure waves bouncing from different solid surfaces. The simplification is, however, reasonable since the possible reflected pressure wave is for an order of magnitude smaller because of the high frequency and additional viscous attenuation and energy loss at reflection.

6.5 Relation Between the Pressure Wave Amplitude and the Acoustic Pressure. The acoustic pressure is by definition the pressure variation around the mean pressure. We presumed that the acoustic pressure amplitude is proportional to the pressure wave amplitude p_Σ (the acoustic pressure amplitude rises with increasing pressure wave amplitude).

One can make such an assumption, since it is the pressure wave p_Σ that causes cavitation effects (such as erosion) and, therefore, noise generation. The aggressiveness of these effects (and, consequently, the generation of noise) is proportional to the amplitude of the pressure wave p_Σ [19].

6.6 Acquiring the Data From the Images. As we can see (Eqs. (13) and (15)), we need to acquire the data composed of the mean values and the standard deviations of the gray level to determine the parameters of vapor volume fraction and the intensity of cavitation implosion at the specific region (hub, blade, and tip). For this purpose, masks were used so that only the gray level from the desired region was considered for post processing (Fig. 12).

Another problem occurs when the shock wave travels through the cavitation cloud. The thickness of the cavitation cloud defined as $x_{2p,\mathrm{hub}}$, $x_{2p,\mathrm{blade}}$, and $x_{2p,\mathrm{tip}}$ in Eq. (20) are approximated as the functions of the mean value of the gray level in the region and expressed as

$$x_{2p} = k\sum_i\sum_j \mu_{ij} = k_3\frac{\sum_i\sum_j \mu_{ij}}{\left[\sum_i\sum_j \mu_{ij}\right]_{\max}} \tag{21}$$

Again normalized values were used. Values of coefficients k_1, k_2, k_3, and the distances between the cavitation at the specific region and the sensor $x_{l,\mathrm{hub}}$, $x_{l,\mathrm{blade}}$, and $x_{l,\mathrm{tip}}$ are given in Table 1.

To determine the values of coefficients k_1, k_2, and k_3 that are used in Eqs. (13), (15), and (21) information from literature and some iterations are required. The shock wave magnitude at its origin has not yet been experimentally determined because of the effect of attenuation, but theoretical work by Brennen [12] and Shimada et al. [13] set it on the order of 6 MPa. Some help was also gained from experimental measurements of the shock waves on similar geometries from Hofmann [24]. It was also shown by the present authors [8] that using the value of 6 MPa works well for prediction of the pressure wave amplitude. The coefficient k_1 was chosen to fulfill the physical and empirical (from past studies [12,13,24]) considerations of the shock wave values, so the maximum pressure wave amplitude of 6 MPa was assumed (k_1 =6 MPa).

The coefficient k_2 varies significantly from one region to another, since the vapor volume fraction varies according to the type of cavitation (Fig. 8). The values were derived by iteration, but physical background was considered. It can be seen from the single images (Fig. 8) that, for the case of hub and tip cavitation, maximal volume fraction does not reach values near to unity. This is because the vapor volume fraction is relatively low in cloud and bubble cavitation. For example, Stutz and Reboud [26] report on measurements of void fractions, where maximal values of up to α=0.4 for the case of cloud cavitation were found. Hence, a maximum value of vapor volume fraction (coefficient k_2) of α=0.4 ($k_{2,\max}$=0.4) for these two regions was expected and also found. On the other hand, in the region of blade cavitation, almost a single vapor phase was approximated, since a supercavitation region exists here in the case of a maximum (Fig. 8). The final values of coefficient k_2 were then determined by iteration until the best correlation between the experiment and the model prediction was found. The values are in agreement with experimental data from past measurements of vapor volume fraction in cavitating flow [26]. The evolution of values of k_2 for each iteration step are presented in Fig. 13. One can see that the values $k_{2,\mathrm{hub}}$, $k_{2,\mathrm{blade}}$, and $k_{2,\mathrm{tip}}$ converge to the final values regardless of the initial value (cases for initial values of 0.1 and 0.9 are presented). The coefficient k_3 defines the maximal thickness of cavitation—values were measured directly from the images. The values of densities and viscosities of water and water vapor (ρ_l, ρ_v, ν_l, ν_v) and the sonic velocity (c_l) and water vapor pressure (p_v) correspond to the ambient temperature of 20°C. The system (surrounding) pressure was p_{sur}=22,500 Pa.

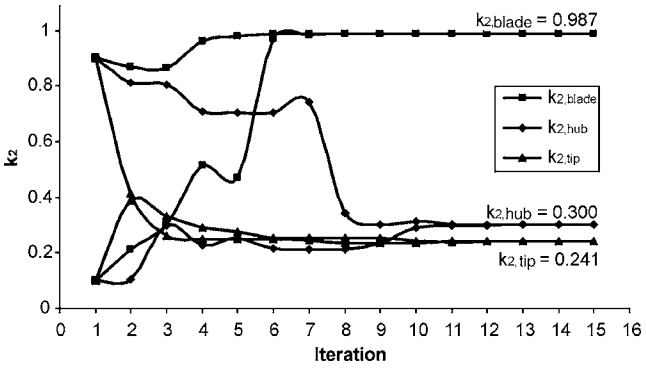

Fig. 13 Evolution of values of parameter k_2 during iterations

A value of f=0.5 MHz for frequency of the pressure wave was chosen on the basis of studies of Shimada et al. [13] and Lohrberg et al. [19] and also on the basis of measurements of pressure waves on similar geometries done by Hofmann [24].

In order to present the model in a clearer way, Fig. 14 shows the whole path from image capturing to the prediction of the pressure wave amplitude for one operating point (one cavitation number):

1. 500 images of cavitation structures are captured (Fig. 8).
2. By means of statistical evaluation (Eqs. (5)–(9)), the mean value and the standard deviation of the images are determined (Fig. 9).
3. Masks that determine the position of cavitation are generated (Fig. 12).
4. Parameters in Table 1 (k_1, k_2, k_3, and x_l) are determined on the basis of references, iteration and present experiment (see Sec. 6.6).
5. p_0 ($p_{0,\mathrm{hub}}$, $p_{0,\mathrm{blade}}$, $p_{0,\mathrm{tip}}$) is calculated by Eq. (13), where matrix of standard deviation is used as an input. Masks and parameters from Table 1 are also used in this step.
6. Void fractions α for each region (hub, blade, and tip) are calculated by Eq. (15), where matrix of mean value is used as an input. Masks and parameters from Table 1 are also used in this step.
7. Physical properties and void fractions α are used to determine the properties of the two-phase flow region through which the acoustic wave travels ($\eta_{2p,\mathrm{hub}}$, $\eta_{2p,\mathrm{blade}}$, $\eta_{2p,\mathrm{tip}}$, $\rho_{2p,\mathrm{hub}}$, $\rho_{2p,\mathrm{blade}}$, $\rho_{2p,\mathrm{tip}}$, $c_{2p,\mathrm{hub}}$, $c_{2p,\mathrm{blade}}$, $c_{2p,\mathrm{tip}}$) (Eqs. (16)–(18)).

Downloaded 03 Jun 2010 to 171.66.16.156. Redistribution subject to ASME license or copyright; see http://www.asme.org/terms/Terms_Use.cfm

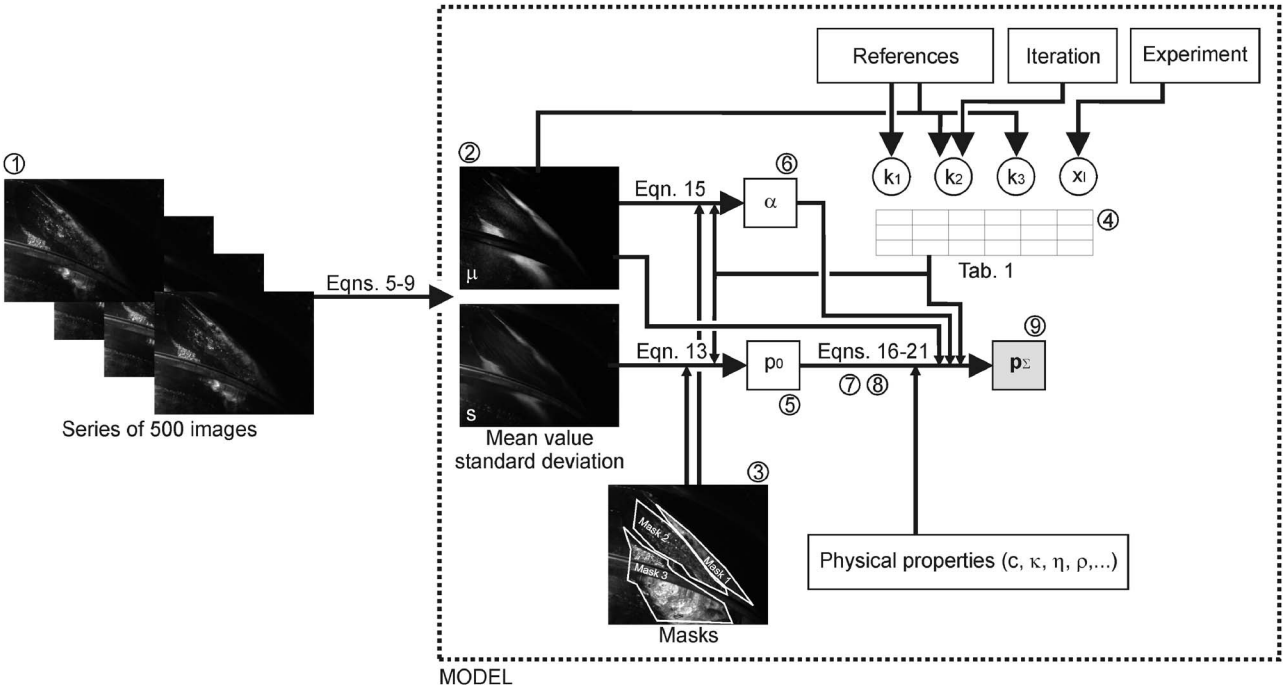

Fig. 14 Graphical representation of the model structure

8. The thickness of the cavity ($x_{2p,\text{hub}}$, $x_{2p,\text{blade}}$, $x_{2p,\text{tip}}$) is calculated by Eq. (21), where parameters from Table 1 are used as an input.
9. By introducing parameters of single (pure liquid) fluid (η_l, ρ_l, c_l) and distances between the cavity and the sensors ($x_{l,\text{hub}}$, $x_{l,\text{blade}}$, $x_{l,\text{tip}}$), attenuation rate and, finally, the sum of the pressure wave amplitude are calculated by Eq. (20).

7 Results of Predictions

As already mentioned, we made a presumption that the acoustic pressure amplitude is proportional to the pressure wave amplitude p_Σ and that the acoustic pressure amplitude rises with increasing pressure wave amplitude. Hence, a comparison of results of measurements of acoustic emission in the frequency range from 60 kHz to 120 kHz and the model prediction of the pressure wave amplitude is shown in Fig. 15.

One can obviously see the resemblance of the two curves. The model predicts that the pressure wave amplitude begins to rise as cavitation first appears (at cavitation number $\sigma=3.4$). The predicted pressure wave amplitude exponentially rises as the cavitation number is decreased and reaches a maximum at the same operating condition at which the maximum of acoustic emission was measured (at cavitation number $\sigma=1.9$). The model then correctly predicts the decrease in pressure wave amplitude and later an increase as the operating pressure (cavitation number) is lowered. The maximal predicted amplitude of the pressure wave is ~2.4 MPa, which corresponds very well to the measurements of Hoffman [24].

For better understanding of how the model works, it is convenient to plot the individual contributions of each cavitation region (hub, tip, and blade), which adds to the sum of the pressure wave amplitude (Fig. 16). The model predicts that the pressure wave from the tip cavitation will rise exponentially as the cavitation number decreases. It will reach a maximum at approximately $\sigma=1.9$. Then a sudden decrease occurs as a result of "choking." Its predicted amplitude falls to almost 0 at $\sigma=1.5$. After that, supercavitation occurs and a signal of higher amplitude is predicted. As can be expected, the cavitation on the tip of the blade adds the

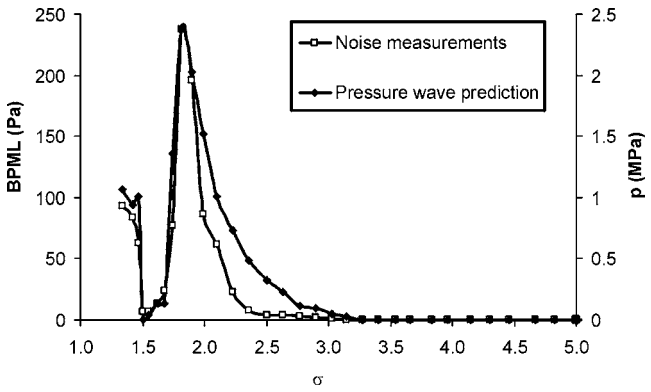

Fig. 15 Results of noise measurements and model predictions of the pressure wave amplitude

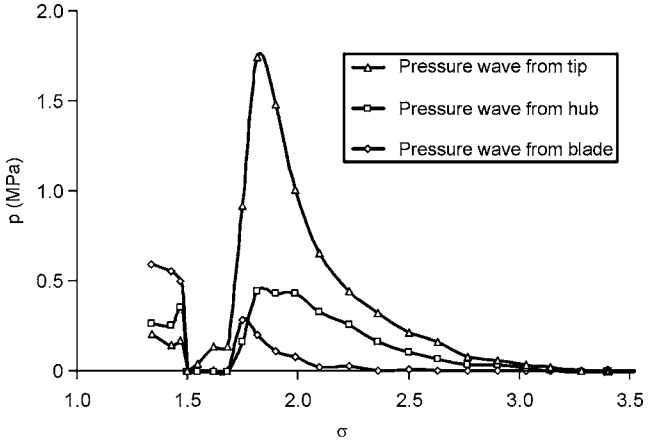

Fig. 16 Predicted pressure wave contributions of each cavitation region

Downloaded 03 Jun 2010 to 171.66.16.156. Redistribution subject to ASME license or copyright; see http://www.asme.org/terms/Terms_Use.cfm

biggest portion to the sum of the predicted pressure wave amplitude. This is because it is the closest to the sensors' location, and therefore, the attenuation is the smallest.

In the case of hub cavitation, the model predicts a monotone increase of cavitation intensity until a plateau is reached at $\sigma = 2.0$. The predicted pressure wave from this region stays almost constant until $\sigma = 1.8$ is reached and then falls to a negligible value. Similarly to the case of tip cavitation, a pressure wave is predicted as the cavitation in this region takes the form of supercavitation.

In contrast to hub and tip cavitation, the blade cavitation occurs later (at a lower cavitation number). Its influence is first predicted at $\sigma = 2.3$, but the pressure wave amplitude does not increase significantly until $\sigma = 1.8$. After that, the intensity decreases to almost 0. Again at $\sigma = 1.5$ in the regime of supercavitation, an increase of the pressure wave amplitude was predicted.

8 Conclusions

A study of acoustical measurements on a two-bladed Kaplan turbine model in various cavitating conditions was presented. Interesting results that could not be unveiled previously were obtained. As the cavitation number was decreased, all signals experienced a maximum, local minimum, and later (at even lower cavitation numbers) another increase in amplitude. Visualization of the cavitation was done, and a relatively simple statistical evaluation of captured images was performed. A hypothesis that the mean value of the gray level is related to the local vapor volume fraction and that the standard deviation of the gray level is related to the dynamics of cavitation was made on the basis of previous studies.

The inspection of single images revealed that different cavitation types exist at various positions on the turbine blade as a function of cavitation number. This fact indicates a possible explanation of the variation of acoustic emission, noise, and vibration based on the topological structure and the position of cavitation.

It is hypothesized that the attenuation of the pressure wave causes the distinctive signal trend and the cavitation aggressiveness increases while the cavitation number is lowered. This was done on the basis of previous experiments [20,21]. A corresponding semi-empirical model was developed, and its prediction result agrees very well with the measured signals.

Nomenclature

A = gray level value of pixel
BPML = blade-passage modulation level (Pa)
$\mathrm{BPML}_{\max}$ = maximal blade-passage modulation level (Pa)
c = sonic velocity (m/s)
c_l = liquid sonic velocity (m/s)
f = frequency (Hz)
G_M = demodulated spectrum
H = net head (m)
H_b = barometric head (m)
H_s = suction head (m)
H_v = vapor head (m)
i = pixel coordinate
I_M = modulated intensity
j = pixel coordinate
k_1 = empirical coefficient (Pa)
k_2 = empirical coefficient
k_3 = empirical coefficient (m)
l = blade chord length (m)
n = image number
n_q = turbine specific speed $n_q = \omega\sqrt{Q} \Big/ \sqrt[4]{(gH)^3}$
N = number of images
p = pressure wave amplitude (Pa)
p_{sig} = pressure wave amplitude from a specific location (Pa)
p_{sur} = surrounding pressure (Pa)
p_v = vapor pressure (Pa)
p_Σ = integral pressure wave amplitude (Pa)
Δp = pressure difference (Pa)
p_0 = pressure wave amplitude at its source (Pa)
P_{wave} = pressure wave power (W)
Q = volume flow (m^3/s)
Re = Reynolds number $\mathrm{Re} = ul/\nu$
s = standard deviation
t = time (s)
V = volume (m^3)
u = blade tip velocity (m/s)
x = distance (m)
x_l = distance in liquid (m)
x_{2p} = distance in two-phase flow (m)
α = vapor volume fraction
η = dynamic viscosity or efficiency (Pa s)
η_l = liquid dynamic viscosity (Pa s)
η_v = vapor dynamic viscosity (Pa s)
κ = polytropic constant
μ = mean value
ν = kinematic viscosity (m^2/s)
ρ = density (kg/m^3)
ρ_l = liquid density (kg/m^3)
ρ_v = vapor density (kg/m^3)
σ = cavitation number (Eq. (1))
ω = pressure wave frequency and revolution speed (rad/s)

References

[1] Castellini, P., and Santolini, C., 1998, "Vibration Measurements on Blades of a Naval Propeller Rotating in Water With Tracking Laser Vibrometer," Measurement, **24**(1), pp. 43–54.
[2] Bajic, B., 1996, "Vibroacustical Diagnosis of Hydroturbine Cavitation: Some Measurement and Analysis Methods, Modelling," Testing & Monitoring for Hydro Powerplants Conference Papers, Lausanne, pp. 169–178.
[3] Abbot, A., Gedney, C. J., and Greeley, S. D., 1986, "Cavitation Monitoring of Two Axial-Flow Hydroturbines Using Novel Acoustic and Vibration Methods," *13th IAHR Symposium Proceedings*, vol. 1, Paper 23, Montreal.
[4] Neill, G. D., Reuben, R. L., and Sandford, P. M., 1997, "Detection of Incipient Cavitation in Pumps Using Acoustic Emission," Proc. Inst. Mech. Eng., Part E: J. Process Mech. Eng., **211**(4), pp. 267–277.
[5] Alfayez, L., Mba, D., and Dyson, G., 2005, "The Application of Acoustic Emission for Detecting Incipient Cavitation and the Best Efficiency Point of a 60 kW Centrifugal Pump: Case Study," NDT & E Int., **38**(5), pp. 354–358.
[6] Kaye, M., Holenstein, A., Dupont, P., and Rettich, J., 1996, "Acoustic Methods for Monitoring Mechanical Seal Condition and Cavitation Erosion in Hydro Machinery," Modelling, Testing & Monitoring for Hydro Powerplants Conference Papers, Lausanne, pp. 179–188.
[7] Pereira, F., Avellan, F., and Dorey, J. M., 1995, "Cavitation Erosion: Statistical Analysis of Transient Cavities," Int. Symp. on Cavitation—Cav'95, Deauville.
[8] Dular, M., Bachert, B., Stoffel, B., and Sirok, B., 2004, "Relationship Between Cavitation Structures and Cavitation Damage," Wear, **257**(11), pp. 1176–1184.
[9] Kern, I., Rus, T., Hocevar, M., Djelic, V., and Sirok, B., 1999, "Study of Topological Structures of Cavitation With Dynamical Analysis and Computer Aided Visualization," 20th IAHR WG1 Meeting, Brno.
[10] Pearsall, I. S., 1966, "Acoustic Detection of Cavitation," Proc. Inst. Mech. Eng., 1-A66-67, **181**, Part 3A, Paper No. 14.
[11] Gopalakrishan, S., 1985, "Modern Cavitation Criteria for Centrifugal Pumps," 2nd International Pump Symposium, College Station.
[12] Brennen, C. E., 1995, *Cavitation and Bubble Dynamics*, Oxford University Press, New York.
[13] Shimada, M., Kobayashi, T., and Matsumuto, Y., 1999, "Dynamics of Cloud Cavitation and Cavitation Erosion," *Proc. of ASME/JSME Fluids Engineering Division Summer Meeting*, San Francisco, CA, FEDSM99-6775.
[14] Beranek, L. L., 1996, *Acoustics*, Acoustical Society of America, New York.
[15] Dular, M., Stoffel, B., and Širok, B., 2005, "Method for Cavitation Erosion Prediction—Model Development," ASME Fluids Engineering Division Summer Meeting, Houston.
[16] Dular, M., Stoffel, B., and Širok, B., 2006, "Development of a Cavitation Erosion Model," Wear, **261**(5/6), pp. 642–655.
[17] IEC, 1999, *International Standard IEC 60193: Hydraulic Turbines, Storage Pumps and Pump-Turbines—Model Acceptance Tests*, 2nd ed. The International Electrotechnical Commission, Geneva, Switzerland.
[18] ANSI, 2002, *ASTM E650-97: Standard Guide for Mounting Piezoelectric*

Downloaded 03 Jun 2010 to 171.66.16.156. Redistribution subject to ASME license or copyright; see http://www.asme.org/terms/Terms_Use.cfm

Acoustic Emission Sensors, American National Standards Institute, West Conshohocken, PA.
[19] Lohrberg, H., Voss, B., Schlachta, C., Stoffel, B., and Glesner, M., 2002, "Impeller Integrated Measurement of Cavitation Erosive Aggressiveness," Mechatronics, **12**(8), pp. 1047–1057.
[20] Bachert, B., Ludwig, G., Stoffel, B., Širok, B., and Novak, M., 2003, "Experimental Investigations Concerning Erosive Aggressiveness of Cavitation in Radial Test Pump With the Aid of Adhesive Copper Films," 5th International Symposium on Cavitation, Osaka.
[21] Bachert, B., 2004, "Zusammenhang zwischen visueller Erscheinung und erosiver Agressivität kavitierenden Strömungen," Ph.D thesis, Technische Universität, Darmstadt.
[22] Fortes-Patella, R., Reboud, J. L., and Briancon-Marjollet, L., 2004, "A Phenomenological and Numerical Model for Scaling the Flow Aggressiveness in Cavitation Erosion," Workshop on Cavitation Erosion, Bassin d'essais des carenes, Val de Reuil.
[23] Dular, M., 2005 "Development of a Method for the Prediction of Cavitation Erosion in Hydraulic Machines," Ph.D thesis, University of Ljubljana.
[24] Hofmann, M., 2001, "Ein Beitrag zur Verminderung des erosiven Potentials kavitierender Stömungen," Ph.D thesis, Technische Universität Darmstadt.
[25] Wosnik, M., and Arndt, R. E. A., 2006, "Measurements in High Void-Fraction Bubbly Wakes Created by Ventilated Supercavitation," 6th International Symposium on Cavitation, Wageningen.
[26] Stutz, B., and Reboud, J. L., 2000, "Measurements Within Unsteady Cavitation," Exp. Fluids, **29**(6), pp. 545–552.

Downloaded 03 Jun 2010 to 171.66.16.156. Redistribution subject to ASME license or copyright; see http://www.asme.org/terms/Terms_Use.cfm

Satoshi Watanabe
Associate Professor
Mem. ASME
Faculty of Engineering,
Kyushu University,
744 Motooka, Nishi-ku,
Fukuoka 819-0395 Japan
e-mail: fmnabe@mech.kyushu-u.ac.jp

Tatsuya Hidaka
Graduate Student

Hironori Horiguchi
Associate Professor

Graduate School of Engineering Science,
Osaka University,
1-3 Machikaneyama,
Toyonaka, 560-8531 Japan

Akinori Furukawa
Professor
Faculty of Engineering
Kyushu University
744 Motooka,
Nishi-ku, Fukuoka 819-0395 Japan

Yoshinobu Tsujimoto
Professor
Mem. ASME
Graduate School of Engineering Science,
Osaka University,
1-3 Machikaneyama,
Toyonaka, 560-8531 Japan

Analysis of Thermodynamic Effects on Cavitation Instabilities

The suction performance of turbopumps in cryogenic fluids is basically much better than that in cold water because of the thermodynamic effect of cavitation. However, it is not still clear how the thermodynamic effect works on cavitation instabilities, such as rotating cavitation and cavitation surge. In the present study, the unsteady heat exchange between the cavity and the surrounding liquid is taken into account in a stability analysis using a singularity method. The results are qualitatively compared to existing experiments to clarify the research needs for deeper understanding. [DOI: 10.1115/1.2754326]

Keywords: rotating cavitation, thermodynamic effect, cascade, closed-cavity model, singularity method

Introduction

Vapor production from cavitation extracts the latent heat of evaporation from the surrounding liquid. This decreases the local temperature and then the local vapor pressure in the vicinity of the cavity. This is called the thermodynamic/thermal effect of cavitation. The thermodynamic effect of cavitation could be ignored for usual applications, especially with water at ambient temperature, but is much more important for cryogenic fluids, such as liquid oxygen (LOX) and liquid hydrogen (LH2). For example, the suction performance of a turbopump inducer for a liquid propellant rocket engine is much better if operated with cryogenic fluids than in water. The development of the cavities is suppressed because of the lowered local vapor pressure due to the thermodynamic effect of cavitation.

The installation of an inducer just upstream of main impeller is one of the most effective ways to improve the suction performance of turbopumps, and most liquid propellant rocket engines, such as SSME, ARIAN V, and LE-7, employ an inducer for LOX and LH2 turbopumps. However, it is well known that the cavitating inducer often causes cavitation instabilities, such as rotating cavitation and cavitation surge [1]. Thus, in order to achieve more reliable turbopumps, it is important to understand the thermodynamic effect of cavitation on the cavitation instabilities for cryogenic fluids as well as the quantitative evaluation of the suction performance.

Many studies have been done to clarify the thermodynamic effect of cavitation. The most important study especially for the thermodynamic effects in pumps might be Stepanoff's [2]. In this work, the *B*-factor is defined to correlate the suction performance with the thermodynamic properties of working fluids with the idea of the latent heat exchange between vapor and liquid phases. Ruggeri and Moore [3] also derived an empirical formula to estimate the thermodynamic effect mainly for turbopump inducers of rocket engines. Recently, Franc et al. [4] experimentally investigated the thermodynamic effect of cavitation in a four-bladed inducer by using Freon R-114 instead of cryogens as a thermosensible working fluid. They found that the thermodynamic effect in R-114 is significant for the development of the leading-edge cavity, while there is a critical cavity length for both cold water and R-114 at which the alternate blade cavitation starts to occur. Cervone et al. [5] also examined a cavitating helical inducer with cold water at 293 K and hot water at 343 K to investigate the thermodynamic effect on cavitation instabilities. Yoshida et al. [6] investigated the thermodynamic effect in a three-bladed inducer by using liquid nitrogen (LN2). In their inducer, the cavitation surge was observed in the cold water operation, whereas it never occurred in the LN2 case. Then, in general, the occurrence of cavitation instabilities is considered to be dependent on the thermody-

Contributed by the Fluids Engineering Division of ASME for publication in the JOURNAL OF FLUIDS ENGINEERING. Manuscript received August 30, 2006; final manuscript received April 10, 2007. Review conducted by Georges L. Chahine. Paper presented at 2006 ASME Fluids Engineering Division Summer Meeting and Exhibition (FEDSM2006), July 17–20, 2006, Miami, FL.

 Copyright © 2007 by ASME

Downloaded 03 Jun 2010 to 171.66.16.156. Redistribution subject to ASME license or copyright; see http://www.asme.org/terms/Terms_Use.cfm

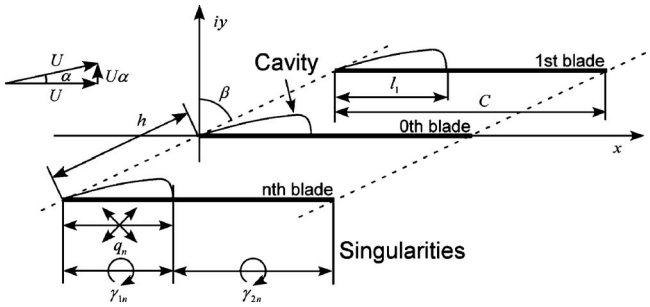

Fig. 1 Model for present analysis

namic effect of cavitation. Probably because an experimental study using the real cryogenic fluids is technically and economically difficult, information on unsteady cavitating flow in cryogenic inducers has been insufficient. In such a situation, it is difficult to understand the thermodynamic effect on cavitation instabilities only from experiments.

From the numerical/analytical point of view, Billet and Weir [7] and, later, Fruman et al. [8] constructed a vapor entrainment model to predict the thermodynamic effect based on the experimental correlation between the vapor flow rate and the gas flow rate in a ventilated cavity geometrically analogous to a natural cavity. Kato [9] proposed a simple model expressing the heat transfer around the sheet cavity as a one-dimensional partial differential equation of unsteady heat conduction. Tokumasu et al. [10] investigated the thermodynamic effect on closed sheet cavities by combining Reynolds Averaged Navier-Stokes (RANS) simulation with Kato's model. Tani and Nagashima [11] simulated the cavitating flow around a hydrofoil with cryogenic fluids by a bubbly flow model based on the Rayleigh Plesset equation. More recently, Hosangadi et al. [12] succeeded in simulating the cavitating flow in a flat plate inducer with liquid hydrogen, and compared the performance to that with cold water. Many numerical simulations are being developed. However, most of them are limited to steady analysis, and the impact of the thermodynamic effect on cavitation instabilities, such as rotating cavitation and cavitation surge, is still unclear.

We have already reported an analytical method of the thermodynamic effect on steady, partially cavitating flow [13]. In this work, a singularity analysis is combined with a heat transfer model proposed by Kato [9], which expresses the heat transfer outside of the cavity by a one-dimensional unsteady heat conduction model. In the present paper, we extend the study into the unsteady analysis to examine the thermodynamic effects on rotating cavitation. The results are qualitatively compared to existing experiments to clarify the research needs for deeper understanding.

Fundamental Flow Field

We consider a flat plate cascade with the chord length C, the spacing h, and the stagger angle β, as shown in Fig. 1. We assume that the flow far upstream is uniform with the magnitude U and the angle of attack α. We define the blade index n by taking into account the number of blades N; the blade on the x-axis is given the index $n=0$, and the index increases in the y direction and returns to $n=0$ at the Nth blade. We consider the partial cavitation with cavity length l_n on each blade fluctuating with a complex angular frequency ω. Assuming the interblade phase difference of fluctuations, $\Delta\phi=2\pi m/N$ (m: number of cells), we can simulate the circumferential propagation of fluctuations in rotating cavitation.

The flow disturbance due to the cavities and blades is expressed by source distributions q_n representing the cavity thickness, bound vortex distributions γ_{1n} and γ_{2n} representing the blade loading, and trailing vortex distributions γ_{tn} representing the free vortices from the blades. These singularities are distributed along the blades and their extensions downstream, assuming both steady and unsteady flow disturbances are small. Then, the complex potential W and the complex conjugate velocity w can be written as follows:

$$W(z,t) = Ue^{-i\alpha}z + \frac{1}{2\pi}\sum_{n=0}^{N-1}\left[\int_0^{l_n}(q_n + i\gamma_{1n})F_n(z,\xi)d\xi + i\int_{l_n}^{C}\gamma_{2n}F_n\{z,\xi\}d\xi + i\int_C^{\infty}\gamma_{tn}F_n(z,\xi)d\xi\right] \quad (1)$$

$$F_n(z,\xi) = \log\left\{\sin\left[\frac{\pi}{Nh}(z-\xi)e^{-i(\pi/2-\beta)} - \frac{n\pi}{N}\right]\right\} + \frac{\pi}{Nh}e^{i\beta}z \quad (2)$$

$$w(z,t) = \frac{\partial W}{\partial z} = u - iv = Ue^{-i\alpha} + \frac{1}{2\pi}\sum_{n=0}^{N-1}\left[\int_0^{l_n}(q_n + i\gamma_{1n})f_n(z,\xi)d\xi + i\int_{l_n}^{C}\gamma_{2n}f_n(z,\xi)d\xi + i\int_C^{\infty}\gamma_{tn}f_n(z,\xi)d\xi\right] \quad (3)$$

$$f_n(z,\xi) = \frac{\pi}{Nh}e^{-i(\pi/2-\beta)}\cot\left[\frac{\pi}{Nh}(z-\xi)e^{-i(\pi/2-\beta)} - \frac{n\pi}{N}\right] + \frac{\pi}{Nh}e^{i\beta} \quad (4)$$

where i denotes the imaginary unit in space. We introduce the following coordinates s_1 and s_2 along the cavity and the blade, to take account the fluctuating cavity length l_n,

$$\xi = l_n s_1 \quad (\text{for} \quad 0 < \xi < l_n, \quad 0 < s_1 < 1)$$
$$\xi = (C - l_n)s_2 + (2l_n - C) \quad (\text{for} \quad l_n < \xi < C, \quad 1 < s_2 < 2) \quad (5)$$

We define the all strength of singularities in these coordinates and divide them into steady and unsteady components as follows:

$$q_n(s_1,t) = q_s(s_1) + \tilde{q}(s_1)\exp j(\omega t - n\Delta\varphi)$$
$$\gamma_{1n}(s_1,t) = \gamma_{1s}(s_1) + \tilde{\gamma}_1(s_1)\exp j(\omega t - n\Delta\varphi)$$
$$\gamma_2 n(s_2,t) = \gamma_{2s}(s_2) + \tilde{\gamma}_2(s_2)\exp j(\omega t - n\Delta\varphi) \quad (6)$$
$$\gamma_{tn}(\xi,t) = \tilde{\gamma}_t(\xi)\exp j(\omega t - n\Delta\varphi)$$
$$l_n(t) = l_s + \tilde{l}\exp j(\omega t - n\Delta\varphi)$$

We have already assumed that the steady components are identical for all cavities and blades; thus, the fluctuations around the steady flow with identical cavities for all blades are considered. The imaginary unit in time j has been introduced in Eq. (6), and we should note that $ii=jj=-1$ but $ij\neq -1$.

After substituting Eqs. (5) and (6) into Eq. (3), we divide the velocity into the uniform steady velocity $Ue^{-i\alpha}$, the steady disturbance (u_s, v_s), and the unsteady velocity disturbance $(\tilde{u},\tilde{v})$ as follows:

$$u = U + u_s + \tilde{u}e^{j\omega t}, \quad v = U\alpha + v_s + \tilde{v}e^{j\omega t} \quad (7)$$

where we have assumed $\alpha \ll 1$. We further assume that $|\tilde{u}|, |\tilde{v}| \ll |u_s|, |v_s| \ll U$. Linearizations are made throughout the present study based on these assumptions.

Boundary and Complementary Conditions

We assume that the cavity is sufficiently thin so that all boundary conditions are applied on the blade surfaces. Because of the periodicity, the boundary and complementary conditions for the 0th blade are just satisfactory to solve the problem and are applied in the coordinates fixed to the fluctuating cavity defined by Eq. (5). Because the boundary and complementary conditions for the

Downloaded 03 Jun 2010 to 171.66.16.156. Redistribution subject to ASME license or copyright; see http://www.asme.org/terms/Terms_Use.cfm

steady components are the same as in the previous study [13], we concentrate mainly on the unsteady components in the following subsections.

Boundary Condition on Cavity Surface. We assume that the pressure on the cavity surface is equal to the vapor pressure. Under the presence of the thermodynamic effect of cavitation, the vapor pressure is locally different due to the temperature depression around the cavity surface. We assume that, for simplicity, the equilibrium condition is locally sustained during the evaporation and condensation processes and employ the Clausius–Clapeyron equation to relate the vapor pressure to the temperature. Applying the Clapeyron–Clausius equation on the cavity surface at ξ along the blade from the leading edge, we obtain,

$$\tilde{P}_V(\xi) = \frac{L}{T_\infty}\rho_V \tilde{\theta}_c(\xi)$$

where $\tilde{P}_V(\xi)$ and $\tilde{\theta}_c(\xi)$, respectively, denote the amplitudes of unsteady vapor pressure and temperature on the cavity surface, and L, ρ_V, and T_∞ are the latent heat of evaporation, the density of vapor phase, and the temperature at the upstream infinity. Substituting the above equation into the linearized momentum equation on the cavity surface, we obtain

$$j\frac{\omega}{U}\frac{\tilde{u}_c'(\xi)}{U} + \frac{\partial}{\partial\xi}\left(\frac{\tilde{u}_c'(\xi)}{U}\right) = -\left(\frac{\rho_V}{\rho_L}\right)\frac{L}{U^2}\frac{d}{d\xi}\left(\frac{\tilde{\theta}_c(\xi)}{T_\infty}\right) \tag{8}$$

where $\tilde{u}_c'(s_1)$ denotes the amplitude of the unsteady velocity on the cavity surface defined in the stationary coordinate. To solve Eq. (8), we need the boundary value of the unsteady component of the velocity $\tilde{u}_c'$ on the cavity at the leading edge (ξ=0), which is obtained by applying the unsteady Bernoulli's equation between the cavity leading edge and the upstream infinity.

$$\frac{\partial[\mathrm{Re}\{W(-\infty) - W(0)\}]}{\partial t} + U\tilde{u}_c'(0) = 0 \tag{9}$$

By using $\tilde{u}_c'(\xi)$, the boundary condition on the cavity surface in the coordinate fixed to the fluctuating cavity can be expressed as follows:

$$\tilde{u}(l_0 s_1 + 0i) = \tilde{u}_c(s_1) = \tilde{u}_c'(l_s s_1) + s_1\frac{du_{cs}}{ds_1}\frac{\tilde{l}}{l_s} \tag{10}$$

where $u_{cs}(s_1)$ denotes the steady component of the velocity on the cavity surface and $\tilde{u}_c(s_1)$ denotes the amplitude of the unsteady velocity on the cavity surface defined in the coordinate s_1 fixed to the fluctuating cavity.

Boundary Condition on a Wetted Surface. We employ the following flow tangency condition on the wetted blade surfaces:

$$\begin{aligned}\tilde{v}(l_0 s_1 + 0i) &= 0\\ \tilde{v}[(C - l_0)s_2 + 2(l_0 - C) \pm 0i] &= 0\end{aligned} \tag{11}$$

Kutta's Condition. We assume that the pressure difference across the blade vanishes at the trailing edge. This condition can be obtained by applying the linearized momentum equation on both surfaces of the blades and expressed as follows:

$$\frac{d}{dt}\left[\int_0^1 \gamma_{10}(s_1)l_0 ds_1 + \int_1^2 \gamma_{20}(s_2)(C - l_0)ds_2\right] + U\gamma_{20}(2) = 0$$

This equation is equivalent to the Kelvin's circulation conservation law and determines the strength of the free vortex $\gamma_{20}(2)$ shed on the main flow U from the trailing edge in accordance with the change in the blade circulation. Assuming that the trailing free vortices are transported by the main flow U, we obtain the following free vortex distribution:

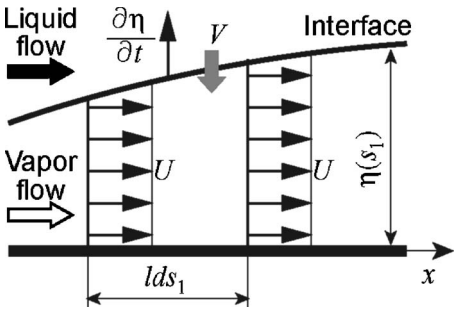

Fig. 2 Control volume for continuity equation

$$\tilde{\gamma}_t = \tilde{\gamma}_2(2)\exp\left[\frac{-j\omega(\xi - C)}{U}\right] \tag{12}$$

Cavity Closure Condition. We employ the closed-cavity model for its simplicity. The cavity thickness $\eta_0(s_1,t)$ should be determined to satisfy the following kinematic boundary condition on the cavity surface:

$$\frac{\partial\eta_0}{\partial t} + \frac{1}{l_0}\left(U - s_1\frac{dl_0}{dt}\right)\frac{\partial\eta_0}{\partial s_1} = v(l_0 s_1 + 0i) = q_0(s_1)$$

After dividing this equation into the steady and unsteady parts, we linearize and integrate them. Then, we can obtain the steady and unsteady components of cavity thickness. The unsteady cavity thickness $\tilde{\eta}(s_1)$ is expressed as follows:

$$\tilde{\eta}(s_1) = \frac{l_s}{U}\int_0^{s_1}\tilde{q}(s_1')e^{-j\omega l_s(s_1 - s_1')/U}ds_1' + \frac{\tilde{l}}{U}\int_0^{s_1}(1 + j\omega l_s s_1' U)q_s(s_1')e^{-j\omega l_s(s_1 - s_1')/U}ds_1'$$

Imposing the condition of zero cavity thickness at the cavity trailing edge, we obtain the following cavity closure condition:

$$\tilde{\eta}(1) = 0 \tag{13}$$

Heat Exchange Between Cavity and Surrounding Liquid. Vapor production from cavitation extracts the latent heat of evaporation from the surrounding liquid. This is called the thermodynamic effect of cavitation. In the previous report for steady cavity [13], we have modeled the thermodynamic effect of cavitation, using the heat conduction model developed by Kato [9] for the liquid flow external to the cavity to evaluate the rate of evaporation. In the present study, we extend the model for unsteady flows.

In the original model proposed by Kato [9], a parabolic velocity profile is assumed for the vapor flow inside the cavity. However, for simplicity, we herein assume that the flow inside the cavity is uniform in the y direction with the velocity on the cavity surface. For more accurate calculations, we must model the velocity profile inside the cavity, which satisfies the momentum balance, taking account of the above-mentioned vapor pressure distribution. At the same time, we should consider the fact that, in many cases, we have the two-phase (liquid–vapor) structure inside the cavity rather than the single-phase cavity as a vapor pocket. Modeling these physical aspects is still a challenging problem, and we would like to investigate it in our future study.

Considering the continuity relation in the control volume inside the cavity as shown in Fig. 2, we can relate the local evaporation velocity V_0 with the source distribution q_0 as follows:

$$V_0 = -\left[\frac{\partial\eta_0}{\partial t} + \frac{1}{l_0}\left(U - s_1\frac{dl_0}{dt}\right)\frac{\partial\eta_0}{\partial s_1}\right] = -q_0(s_1,t)$$

Then, the unsteady heat flux $\tilde{q}_T(s_1)$ across the cavity surface, defined in the coordinate s_1 fixed to the cavity, can be related with

Downloaded 03 Jun 2010 to 171.66.16.156. Redistribution subject to ASME license or copyright; see http://www.asme.org/terms/Terms_Use.cfm

the unsteady source distribution $\tilde{q}(s_1)$, as follows:

$$\tilde{q}_T(s_1) = \rho_V L \tilde{V} = -\rho_V L \tilde{q}(s_1) \tag{14}$$

where L denotes the latent heat of evaporation.

Because of the heat flux across the cavity surface, there appears a temperature distribution around the cavity. We assume that the heat conduction in the main flow direction (x) is negligibly small and consider the heat conduction only in the normal direction (y) of the cavity surface. The temperature increase (in actual flow, decrease with negative quantity) ΔT due to the cavity development should satisfy the following linearized energy equation for inviscid flow.

$$\frac{\partial \Delta T}{\partial t} + U\frac{\partial \Delta T}{\partial x} = \varepsilon a \frac{\partial^2 \Delta T}{\partial y^2}$$

where a denotes a thermal diffusivity. The turbulent diffusivity factor ε [9] has been employed to take account of the enhancement of thermal diffusion due to the turbulent flow around the cavity.

We divide the temperature increase ΔT into steady and unsteady components ΔT_s and $\tilde{\theta}(x,y)$ as follows:

$$\Delta T = \Delta T_s(x,y) + \tilde{\theta}(x,y) \exp j\omega t$$

Applying the above energy equation to the flow field around the cavity on the 0th blade and solving it analytically under the boundary condition of $\Delta T = 0$ at the leading edge of the cavity, we obtain the amplitude of unsteady temperature increase $\tilde{\theta}(x,y)$ as follows:

$$\tilde{\theta}(x,y) = \frac{y}{2\sqrt{\pi \kappa_p}} \int_0^x \tilde{\theta}_c(\xi) e^{-j(\omega/U)(x-\xi)} \frac{\exp\left(-\dfrac{y^2}{4K_p(x-\xi)}\right)}{(x-\xi)^{3/2}} d\xi$$

where K_p is defined here as $K_p = \varepsilon a / U$. In this equation, we have defined the temperature increase along the cavity surface as follows:

$$\Delta T_n(\xi,t) = \theta_{cs}(\xi) + \tilde{\theta}_c(\xi) \exp j(\omega t - n\Delta\varphi)$$

where $\theta_{cs}(\xi)$ denotes the steady temperature increase and $\tilde{\theta}_c(\xi)$ denotes the amplitude of the unsteady temperature on the cavity surface. Then, the temperature gradient normal to the cavity surface is derived as

$$\lim_{y\to 0} \frac{d\tilde{\theta}(x,y)}{dy} = -\frac{1}{\sqrt{\pi K_p}} \left[\int_0^x \frac{d\tilde{\theta}_c(\xi)}{d\xi} + j\frac{\omega}{U}\tilde{\theta}_c(\xi) \right] \frac{e^{-j(\omega/U)(x-\xi)}}{(x-\xi)^{1/2}} d\xi \tag{15}$$

By equating the heat flux $q_{Tn} = -\varepsilon\lambda(\partial T_n/\partial y)|_{y=0}$ with Eq. (14), we obtain

$$\int_0^x \left[\frac{d\tilde{\theta}_c(\xi)}{d\xi} + j\frac{\omega}{U}\tilde{\theta}_c(\xi) \right] \frac{e^{-j(\omega/U)(x-\xi)}}{T_\infty (x-\xi)^{-1/2}} d\xi = -\frac{L}{C_P T_\infty} \left(\frac{\rho_V}{\rho_L}\right) \sqrt{\frac{\pi}{K_P}} \left[\frac{\tilde{q}}{U} - \frac{s_1}{U}\frac{dq_s}{ds_1}\frac{\tilde{l}}{l_s} \right] \tag{16}$$

Analytical Method

The unknown quantities in this problem are the steady and unsteady components of $q_n(s_1,t)$, $\gamma_{1n}(s_1,t)$, $\gamma_{12n}(s_1,t)$, $\gamma_{tn}(\xi,t)$, $l_n(t)$, $u_{cn}(s_1,t)$, and $\Delta T_n(\xi,t)$. Discretizations of singularities distributed along the blades and cavities are made in the same manner as in the previous report [13]. The nodes are distributed more densely near the leading and trailing edges of the blades and cavities. The control points, where boundary conditions are applied, are placed at the midpoints between each node.

Table 1 Values of Σ^* estimated for the other studies

Researcher	Application	Liquid	T_∞ (K)	U_∞ (m/s)	Σ^*
Hord [15]	Hydrofoil	LH2	22.15	66.8	753
Tagaya et al. [16]	Hydrofoil	H2O	413.15	14	118
Fruman et al. [8]	Venturi	R-114	310	31.0	204
Franc et al. [4]	Inducer	R-114	310	34.0	202
Franc et al. [4]	Inducer	H2O	290	34.0	0.013
Yoshida et al. [6]	Inducer	LN2	80	150.4	14.16
Yoshida et al. [6]	Inducer	LN2	76	150.4	6.88
Tokumasu et al. [10]	Hydrofoil	LOX	90	11.11	134
Tani and Nagashima [11]	Hydrofoil	LN2	77	5	924

The analytical method to obtain the steady components, including the steady temperature distribution, is the same as that described in the previous report [13]. It has been found that the steady quantities are functions of $\sigma/2\alpha$, where σ is a cavitation number defined as $\sigma = 2[P_\infty - P_v(T_\infty)]/\rho_L U^2$.

The unsteady components are determined from the boundary and complementary conditions Eqs. (8)–(16). After the discretizations, we obtain a set of linear equations for the unsteady components as follows:

$$[A_u(l_s,\omega)]\tilde{Q} = 0$$

$$\tilde{Q} = \{\tilde{q}, \ldots, \tilde{\gamma}_1, \ldots, \tilde{\gamma}_2, \ldots, \tilde{\gamma}_t, \alpha\tilde{l}, \tilde{u}_c, \ldots, \tilde{\theta}_c, \ldots\}^T \tag{17}$$

where $A_u(l_s,\omega)$ denotes a coefficient matrix. For the existence of nontrivial solutions, the determinant should be equal to zero. This condition gives the characteristic equation, from which we can obtain the complex angular frequency ω. The complex propagation velocity in the reference frame moving with the cascade is defined as

$$k = k_R + jk_I = \frac{\omega/(2\pi)}{U_T/(Nh)}$$

where U_T denotes the moving velocity of the cascade. Then the complex propagation velocity in the absolute frame, k^*, can be obtained as follows:

$$k^* = k_R^* + jk_I^* = (1 - k_R) + jk_I \tag{18}$$

where the real part k_R^* denotes the propagation velocity ratio in the absolute frame, defined as the propagation velocity of fluctuations normalized by the moving velocity of the cascade. The value with $k_R^* > 1$ means that the corresponding mode is the forward rotating mode, in which the fluctuations propagate faster than the impeller rotation. This mode is often observed in experiments. The imaginary part k_I^* denotes the decay rate, and $k_I^* < 0$ means that the corresponding mode is destabilizing.

We can find from Eqs. (8), (10), and (16) that the unsteady velocity on the cavity surface $\tilde{u}_c(s_1)$ is directly related to the unsteady temperature distribution. Then, the thermodynamic effect of cavitation can be represented by the following thermodynamic parameter Σ^*:

$$\Sigma^* = \frac{L^2}{C_P T_\infty} \left(\frac{\rho_V}{\rho_L}\right)^2 \sqrt{\frac{C}{aU^3}} \tag{19}$$

Because the unknowns representing the steady flow, including the cavity length l_s, are functions of $\sigma/2\alpha$ and Σ^*, we can conclude from Eq. (17) that the complex angular frequency ω as well as the unsteady components are also functions of $\sigma/2\alpha$ and Σ^*.

The parameter Σ^* is equivalent to Brennen's Σ^* [14], which is derived from the thermodynamics of a bubble flowing along the suction surface of the blade. It can be also obtained by normalizing the Stepanoff's B-factor $B = C_p T_\infty / L^2(\rho_L/\rho_V)^2$. Table 1 summarizes the values of Σ^* estimated for various studies, from which

Downloaded 03 Jun 2010 to 171.66.16.156. Redistribution subject to ASME license or copyright; see http://www.asme.org/terms/Terms_Use.cfm

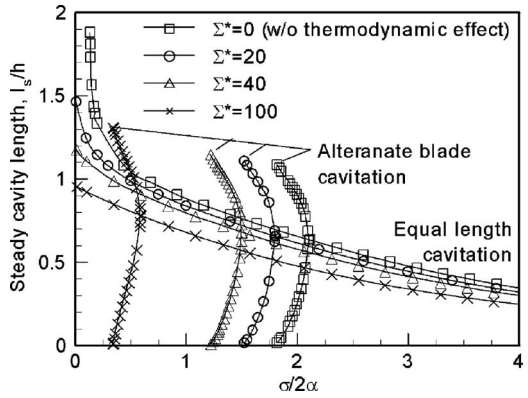

Fig. 3 Steady cavity length versus $\sigma/2\alpha$

we can find that Σ^* takes 0–1000. Note that the larger value of Σ^* can be seen in the experiments with hydrofoils. For cryogenic inducers, Σ^* takes a relatively smaller value because the rotational speed is quite large.

In the present study, geometrical parameters of the cascade are set as the solidity of $C/h=2.0$, the stagger of $\beta=75.0$ deg, and the number of blades of $N=3$ and 4. The angle of attack $\alpha=5.0$ deg is used when needed. The turbulence diffusion factor ε is unknown, but is set to be $\varepsilon=4000$ throughout the present study. This value is smaller than Kato's $\varepsilon=10^5$, but is still quite large for the turbulent diffusivity factor. One of the possible explanations for this is that we treat the filmlike cavity as being filled with vapor. If we have the liquid phase inside the cavity (e.g., bubbly flow or vapor flow containing many droplets), then a smaller amount of evaporation will be needed for a cavity of the same size to be formed. Then, less diffusivity will be required.

The thermodynamic parameter Σ^* is set to be 0, 20, 40, and 100. We have confirmed that the results for $\Sigma^*=0$ agrees with those obtained by Watanabe et al. [17], where the thermodynamic effect is not considered. The numbers of nodes for the discretization of singularity distributions are 37 both for cavity and wetted surfaces of each blade. It is confirmed that the numerical uncertainty is within 1% of the solutions.

Results and Discussions

Figure 3 shows the cavity length plotted against the cavitation number obtained by the present analysis for the case with $N=4$. The cavity length is normalized by the blade spacing h. We have two sets of solutions; one of them corresponds to the equal length cavitation, where the cavities are identical on all blades. The other is the alternate blade cavitation where the cavity length on the blade changes alternatively from blade to blade, obtained in the case of even blade number. We can see that, as Σ^* increases, the growth of equal length cavitation is suppressed and the onset region of the alternate blade cavitation moves toward a smaller cavitation number region. The transition from the equal length to the alternate blade cavitation occurs with $l/h\approx0.65$ for $\Sigma^*=0$. The cavity length for the transition slightly increases with the increase of Σ^*.

Various modes of cavitation instabilities are obtained from the characteristic equation derived from Eq. (17) representing the fluctuation around the steady solution of the equal length cavitation shown in Fig. 3. Rotating cavitation is one of those modes propagating from blade to blade with a phase difference $\Delta\phi$ between blades. We hereafter concentrate on the lowest mode of forward rotating cavitation, which is often observed in the experiments.

Figures 4(a) and 4(b) show the propagation velocity ratio k_R^* and the decay rate k_I^* for the cases with the blade number of $N=3$ and 4, respectively. The region with the negative value of k_I^*

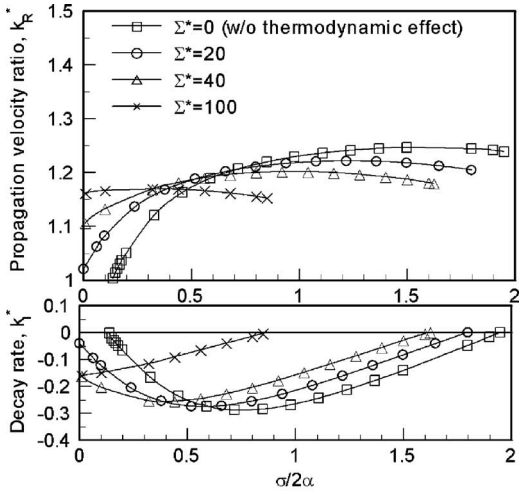

(*a*)

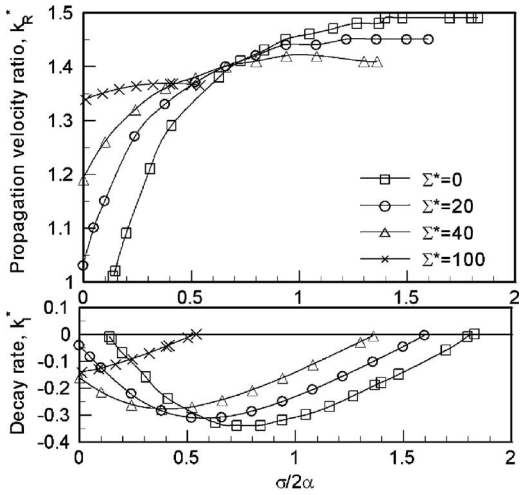

(*b*)

Fig. 4 Solutions corresponding to conventional forward rotating cavitation for various values of Σ^* and $\sigma/2\alpha$: (*a*) $N=3$ and (*b*) $N=4$

shows the onset region of rotating cavitation. From k_I^*, we can find that the inception point of rotating cavitation ($k_I^*=0$) shifts toward the lower cavitation number as Σ^* increases, implying that the thermodynamic effect of cavitation delays the inception of rotating cavitation for lower cavitation number. The propagation velocity ratio k_R^* at the inception decreases as Σ^* increases.

Figure 5 shows the propagation velocity ratio k_R^* plotted against the normalized cavity length l_s/h. Apparently, the propagation velocity ratio is larger for $N=4$ than for $N=3$. Although the propagation velocity ratio near the inception differs for the different values of Σ^*, it becomes independent of Σ^* as the cavity becomes longer. The onset point of rotating cavitation in terms of cavity length changes from $l/h\approx0.65$ for $\Sigma^*=0$ to the slightly larger cavity length with the increase of Σ^*, which is similar to that of alternate blade cavitation as shown in Fig. 3.

To focus on the thermodynamic effect on the inception of cavitation instabilities, the cavity shapes at the inception of rotating cavitation are shown in Fig. 6. The cavity shapes for two extreme cases with $\Sigma^*=0$ and 100 are plotted for the case with the blade number of $N=3$. The inception points of rotating cavitation are $\sigma/2\alpha=1.95$ ($l_s/h=0.66$) for $\Sigma^*=0$ and $\sigma/2\alpha=0.85$ ($l_s/h=0.71$) for $\Sigma^*=100$. As shown in Fig. 6, the maximum cavity thickness is located closer to the leading edge for $\Sigma^*=100$ than that for Σ^*

Downloaded 03 Jun 2010 to 171.66.16.156. Redistribution subject to ASME license or copyright; see http://www.asme.org/terms/Terms_Use.cfm

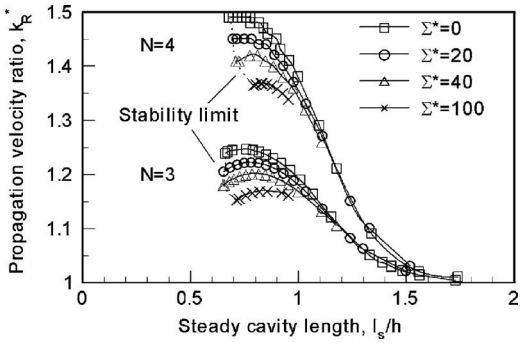

Fig. 5 Propagation velocity ratio plotted against steady cavity length with various values of Σ^* for blade number of $N=3$ and 4

=0. Moreover, the maximum thickness is larger for $\Sigma^*=0$ than $\Sigma^*=100$ despite the fact that the cavity is longer for $\Sigma^*=100$. It is also found that the cavity thickness near the trailing edge of the cavity is smaller for $\Sigma^*=100$ due to the thermodynamic effect of cavitation; the latent heat due to the strong condensation increases the temperature, hence, increases the vapor pressure, preventing the cavity from terminating.

Horiguchi et al. [18] has pointed out by the singularity analysis that rotating cavitation and alternate blade cavitation are triggered when the flow near the leading edge is strongly influenced by the flow around the trailing edge of the cavity on the next blade. Our model employs a linear closed-cavity model with a small cavity thickness, whose blockage effect is to be small. However, even with this linear cavity model, the interaction between the cavity trailing edge and the flow around the leading edge of the next blade is significant, due to the strong singularity of the trailing edge of the closed cavity. Then, this interaction is still considered to be essential for the onset of cavitation instabilities. It has been seen in Figs. 3–5 that the cavity length at the inception points of rotating cavitation and alternate blade cavitation becomes larger as Σ^* increases. The reason for this can be also explained as follows, by the interaction of the cavity trailing edge to the flow around the next blade. The thermodynamic effect of cavitation

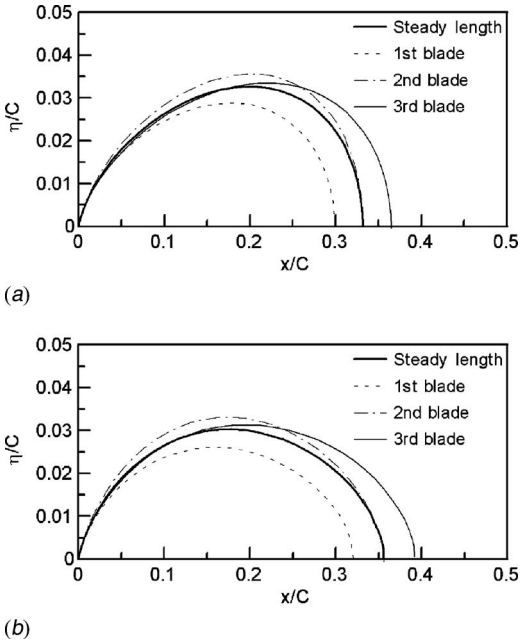

Fig. 6 Steady and temporal cavity shapes at stability limit for $N=3$ (*a*) $\Sigma^*=0$, $\sigma/2\alpha=1.95$ and (*b*) $\Sigma^*=100$, $\sigma/2\alpha=0.85$

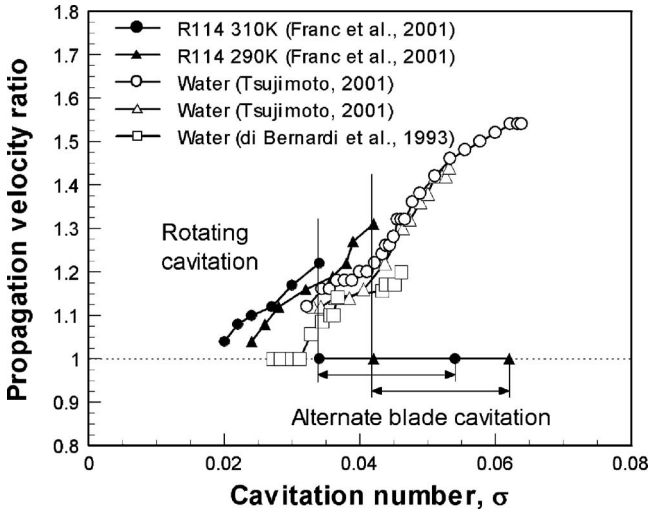

Fig. 7 Experimental results of propagation velocity ratio of rotating cavitation from the literature

makes the cavity thinner around its trailing edge. The interaction is weakened, and then the inception is delayed for longer cavitation.

Figure 7 summarizes the propagation velocity ratio in the absolute frame k_R^* of rotating cavitation for four-bladed inducers, obtained by the experiments. We can see that the onset region for Freon R114 obtained by Franc et al. [19] lies in a lower cavitation number region than that for cold water obtained by the other researchers [20,21]. This trend is well captured by the present analysis, as shown in Fig. 4(*b*). The trend of the propagation velocity ratio k_R^* shows a good agreement between the present analysis and the experiments, indicating that the Kato's heat transfer model [9] we applied to the present analysis is applicable even for the unsteady flow in rotating cavitation.

As referred in the previous report [13], Franc et al. [4] has experimentally obtained the onset region of rotating cavitation and alternate blade cavitation for both Freon R114 and cold water. The result shows that the cavity length at the inception point of alternate blade cavitation is almost independent of the working fluid, which agrees with the result of the present analysis, as shown in Fig. 3. However, the inception of rotating cavitation strongly depended on the working fluid in the experiment and rotating cavitation occurred for shorter cavity under the existence of the thermodynamic effect of cavitation, which disagrees with the present analysis. The reason for this discrepancy might be because, in the present study, we consider the fluctuations around the equal length cavitation, whereas, in the Franc et al.'s experiment, the rotating cavitation starts to occur in the transition from the alternate blade cavitation. Under such conditions, the flow is more complicated, and we need to take account of the other forms of cavitation, such as tip-leakage cavitation and backflow cavitation in addition to the sheet cavitation, which is analyzed by the present study.

Conclusions

Kato's heat transfer model [9] has been extended to treat the unsteady heat conduction and combined with a singularity method for the analysis of thermodynamic effects on cavitation instabilities. As an example of the analysis, the thermodynamic effects on alternate blade cavitation and rotating cavitation are discussed. The results are summarized as follows:

(a) The thermodynamic effect is included in the unsteady analysis only through one thermodynamic parameter Σ^* as well as in the steady analysis.

Downloaded 03 Jun 2010 to 171.66.16.156. Redistribution subject to ASME license or copyright; see http://www.asme.org/terms/Terms_Use.cfm

(b) As Σ^* increases, the inception point of rotating cavitation moves toward lower cavitation number.
(c) The inception point of alternate blade cavitation obtained by the steady analysis moves toward lower cavitation number as Σ^* increases.
(d) The cavity length at the inception points of rotating cavitation and alternate blade cavitation becomes slightly larger due to the thermodynamic effect of cavitation. The reason for this is that the cavity becomes thin around the trailing edge due to the thermodynamic effect and the influence of cavity trailing edge on the flow around the next blade is weakened.
(e) The propagation velocity ratio of rotating cavitation becomes smaller due to the thermodynamic effect of cavitation.

Since the present analysis can simulate rotating cavitation in different working fluids qualitatively well, we conclude that the unsteady version of the heat transfer model is useful for the analysis of cavitation instabilities. However, the turbulence diffusion factor ε used in the model is unknown and should be explored by future study. Especially, the flow structure inside the cavity should be taken into account for a more accurate simulation with the reasonable value of ε. Moreover, the real flow in the cavitating inducer is more complicated, with tip leakage and backflow cavitations in addition to the blade surface cavitation treated here. Those cavitations might play important roles for rotating cavitation and should be also explored by the future study.

Acknowledgment

First of all, we would like to express the sincere gratitude to the reviewers, who gave us valuable discussions and suggestions to improve the paper. We also would like to thank Daisuke Yumiba for his great help and many valuable discussions on the present study. This study is partly supported by the Grant-in-Aid for Scientific Research for the Ministry of Education, Science, Sports and Culture.

Nomenclature

A_u = coefficient matrix in Eq. (17)
a = thermal diffusivity
C = chord length
C_p = specific heat
F,f = kernel functions, defined by Eqs. (2) and (4)
h = blade spacing
i = imaginary unit
j = imaginary unit in time
K_P = $\varepsilon a/U$
k = complex propagation velocity ratio in reference frame moving with cascade
k^* = complex propagation velocity ratio in absolute frame
k_R^* = propagation velocity ratio in absolute frame
k_I^* = decay rate
L = latent heat of evaporation
l = cavity length
m = number of cells
N = number of blades
n = blade index
P_V = vapor pressure
Q = vector of unknowns
q = source strength representing cavity thickness
q_T = heat flux on cavity surface
T = temperature
U = main flow velocity
U_T = moving velocity of cascade
V = local evaporation velocity
u,v = velocity components in x and y directions
u_c = tangential velocity disturbance on cavity surface
u_s,v_s = steady velocity disturbances in x and y directions
W = complex potential
w = complex conjugate velocity
x,y = coordinates
z = complex coordinate, $=x+iy$
α = angle of attack
β = stagger angle
γ_1,γ_2 = bound vortices representing blade loading
ΔT = temperature increase (depression)
$\Delta\varphi$ = inter-blade phase difference
ε = turbulent diffusion factor
η = cavity thickness
λ = thermal conductivity
θ = temperature increase
ρ_L,ρ_V = densities of liquid and vapor phases
Σ^* = thermodynamic parameters, defined by Eq. (19)
σ = cavitation number
ω = complex angular frequency of fluctuations
ξ = distance along the blade from the leading edge

Superscripts

$\sim$ = amplitude of unsteady component

Subscripts

c = cavity surface
s = steady component
n = blade index
∞ = upstream infinity

References

[1] Tsujimoto, Y., Yoshida, Y., Maekawa, Y., Watanabe, S., and Hashimoto, T., 1997, "Observations of Oscillating Cavitations of an Inducer," ASME J. Fluids Eng., **119**, pp. 775–781.
[2] Stepanoff, A. J., 1964, "Cavitation Properties of Liquids," ASME J. Eng. Power, **86**, pp. 195–200.
[3] Ruggeri, R. S., and Moore, R. D., 1969, "Method for Prediction of Pump Cavitation Performance for Various Liquids, Liquid Temperatures, Rotative Speeds," NASA TN D-5292.
[4] Franc, J.-P., Rebattet, C., and Coukon, A., 2004, "An Experimental Investigation of Thermal Effects in a Cavitating Inducer," ASME J. Fluids Eng., **126**, pp. 716–723.
[5] Cervone, A., Testa, R., and d'Agostino, L., 2005, "Thermal Effects on Cavitation Instabilities in Helical Inducers," J. Propul. Power, **21**, pp. 893–899.
[6] Yoshida, Y., Kikuta, K., Watanabe, M., Hashimoto, T., Nagaura, K., and Ohira, K., 2006, "Thermodynamic Effect on Cavitation Performances and Cavitation Instabilities in an Inducer," *Proc. of 6th International Symposium on Cavitation*, Wageningen, The Netherland, Paper No. 38, pp. 1–9.
[7] Billet, M. L., and Weir, D. S., 1975, "The Effect of Gas Diffusion on the Flow Coefficient for a Ventilated Cavity," ASME J. Fluids Eng., **97**, pp. 501–506.
[8] Fruman, D. H., Reboud, J.-L., and Stutz, B., 1999, "Estimation of Thermal Effects in Cavitation of Thermosensible Liquids," Int. J. Heat Mass Transfer, **42**, pp. 3195–3204.
[9] Kato, H., 1984, "Thermodynamic Effect on Incipient and Development of Sheet Cavitation," ASME FED-Vol. 16, pp. 127–136.
[10] Tokumasu, T., Sekino, Y., and Kamijo, K., 2003, "A New Modeling of Sheet Cavitation Considering the Thermodynamic Effects," *CD-ROM Proc. of 5th International Symposium on Cavitation*, Osaka, Japan, Paper No. Cav03-GS-16-003.
[11] Tani, N., and Nagashima, T., 2002, "Numerical Analysis of Cryogenic Cavitating Flow on Hydrofoil—Comparison Between Water and Cryogenic Fluids," *CD-ROM Proc. of 4th International Conference of Launcher Technology*, Liege, Belgium, Paper No. 27.
[12] Hosangadi, A., Ahuja, V., Ungewitter, R. J., and Busby, J., 2006, "Numerical Study of a Flat Plate Inducer: Comparison of Performance in Liquid Hydrogen and Water," *Proc. of 42nd AIAA/ASME/SAE/ASEE Joint Propulsion Conference & Exhibit*, AIAA, Washington, DC, AIAA Paper No. AIAA-2006-5070, pp. 1–13.
[13] Watanabe, S., Hidaka, T., Horiguchi, H., Furukawa, A., and Tsujimoto, Y., 2007, "Steady Analysis of the Partial Cavitation Using the Singularity Method," ASME J. Fluids Eng., **129**, pp. 121–127.
[14] Brennen, C. E., 1995, *Hydrodynamics of Pumps*, Concepts ETI, Inc., and Oxford University Press, London.

Downloaded 03 Jun 2010 to 171.66.16.156. Redistribution subject to ASME license or copyright; see http://www.asme.org/terms/Terms_Use.cfm

[15] Hord, J., 1973, "Cavitation in Liquid Cryogens: II Hydrofoil," NASA CR-2156.
[16] Tagaya, Y., Kato, H., Yamaguchi, H., and Maeda, M., 1999, "Thermodynamic Effect on a Sheet Cavitation," ASME Paper No. FEDSM 99-6772.
[17] Watanabe, S., Sato, K., Tsujimoto, Y., and Kamijo, K., 1999, "Analysis of Rotating Cavitation in a Finite Pitch Cascade Using a Closed Cavity Model and a Singularity Method," ASME J. Fluids Eng., **121**, pp. 834–840.
[18] Horiguchi, H., Watanabe, S., Tsujimoto, Y., and Aoki, M., 2000, "A Theoretical Analysis of Alternate Blade Cavitation in Inducers," ASME J. Fluids Eng., **122**, pp. 156–163.
[19] Franc, J.-P., Janson, E., Morel, P., Rebattet, C., and Riondet, M., 2001, "Visualizations of Leading Edge Cavitation in an Inducer at Different Temperatures," *Proc. of 4th International Symposium on Cavitation*, Pasadena, CA, Paper No. CAV2001:B7.002.
[20] Yoshida, Y., Tsujimoto, Y., Kataoka, D., Horiguchi, H., and Wahl, H., 2001, "Effects of Alternate Leading Edge Cutback on Unsteady Cavitation in 4-Bladed Inducers," ASME J. Fluids Eng., **123**, pp. 762–770.
[21] de Bernardi, j., Joussellin, F., and Von Kaenel, A., 1993, "Experimental Analysis of Instabilities Related to Cavitation in a Turbopump Inducer," *Proc. of 1st Int. Symposium on Pump Noise and Vibrations*, Paris, France, pp. 1–9.

Downloaded 03 Jun 2010 to 171.66.16.156. Redistribution subject to ASME license or copyright; see http://www.asme.org/terms/Terms_Use.cfm

Dielectrophoretic Control of Bubble Transport in Mesochannels—Experimental Study

C. Helberg

J. E. Bryan

Department of Mechanical & Aerospace Engineering,
University of Missouri,
Columbia, MO 65211

Using electrostatic fields to manipulate and/or pump fluids on the microscale is a promising method for the advancement in microfluidics. Preliminary analysis showed that unidirectional bubble motion could be achieved if the polarization (dielectrophoretic) force could overcome surface tension and viscous forces. Results are presented for the development and fundamental study of dielectrophoretic control of bubble transport in mesochannels. Electrode array configurations were manufactured using printed circuit board technology and mated with an acrylic channel. Bubble velocity, acceleration, and deformation were investigated for a range of bubble sizes, two electrode array configurations, two working fluids—pentane and a 20/80 mixture by mass of ethanol and pentane, two switching frequencies, and a range of +DC pulse applied voltages. A maximum average velocity of 6.6 mm/s *and a maximum local velocity of* 30 mm/s *were achieved. For the results presented, both the switching frequency and bubble size affected the velocity for a given applied voltage. Of the two fluids tested, there was no measurable difference in the bubble velocity even though the bubble deformation was significantly different for the two fluids. It was concluded that bubble deformation reduced the unidirectional bubble motion effectiveness. Bubble deformation could be reduced by lowering the applied voltage without significantly reducing the velocity of the bubble.*
[DOI: 10.1115/1.2754310]

Keywords: electrohydrodynamics, two-phase flow, microfluidics

Introduction

Continued advances in microelectronics and microelectromechanical systems (MEMS) is opening up new science and market opportunities in areas of chemistry, biology, medicine, cooling of high-power microelectronic systems, and chemical processing. Many of these applications will require fluid flow control, pumping/dispensing, and flow monitoring. The new technological devices developed will have to be capable of pumping and/or accurately controlling flow on the meso- to microscale. When a liquid and gas (vapor) are present, the ability to control flow becomes more complicated. There have been a few studies investigating nonmechanical means to create bubble motion in capillaries or use phase change to create bulk fluid motion.

The most common way to manipulate liquid-gas mediums in capillary geometry has been through the use of controlled heating. One method, thermocapillary pumping (TCP), is achieved by creating a capillary pressure imbalance with discreet resistance heating at the interface of a liquid/vapor plug. Sammarco and Burns [1] performed a thorough investigation of TCP to move liquid plugs of several different fluids with varying surface tension and viscosity. They measured velocities up to 0.33 mm/s in a 34 μm by 500 μm wide channel for several liquids at temperature differences between 10°C and 70°C. From experimental and theoretical analysis, they found the velocity was proportional to the temperature difference between the liquid plug ends. The required temperature difference depended on the channel shape, plug length, viscosity, surface tension, and contact angle hysteresis. A second method to create pumping is achieved by controlled growth of a vapor bubble, again by discreet resistive heating within a microchannel. Jun and Kim [2] demonstrated controlled pumping of isopropanol in a 2 μm by 30 μm (3.4 μm hydraulic diameter) microchannel, producing velocities to 0.16 mm/s with 58 mW heater pulses at 0.5 s intervals. The actuation mechanism was determined to be due to vapor pressure variations caused by the discreet heating. Song and Zhao [3], using a similar approach, demonstrated pumping of water at 300 μl/min by sequenced pulsing of 12 discreet heaters at 8–12 W for 3 s each. They found at higher heating powers, >12 W, there existed an optimum heater pulse time for maximum flow. Tsai and Lin [4], utilizing the same method of discreet heating, created a thermal bubble micropump to develop an active microfluidic mixer by growth and collapse of a bubble. The degree of mixing could be controlled by controlling the heater pulse rate. Optimal mixing was demonstrated at a heater pulse frequency of 200 Hz. This corresponded to a flow rate of 6.5 μl/min with a mixture of isopropyl alcohol and blue food dye in a 50 μm by 200 μm wide channel. Geng et al. [5] use focused Joule heating to control the growth and collapse of a bubble in a conductive salt-water solution to produce pumping in the range of 100 μl/min in channels diameters of 1 mm.

Another method to manipulate liquid-gas mediums in microfluidics is through the use of electrostatic forces. Electrostatic micropumps have some of the same advantages as thermal activated micropumps, such as low power consumption and no moving parts. Most electrostatic (electrokinetic, EHD, etc.) micropumps have been studied using liquid only as the working fluid. A few studies have investigated the use of electrostatic forces to move a liquid-vapor interface or pump bubbles. Using parallel electrodes, various researchers have utilized the polarization force to drive a liquid-vapor interface. Jones et al. [6] demonstrated creation of a

Contributed by the Fluids Engineering Division of ASME for publication in the JOURNAL OF FLUIDS ENGINEERING. Manuscript received August 9, 2005; final manuscript received April 4, 2007. Review conducted by Kenneth Breuer. Paper presented at the 2005 ASME International Mechanical Engineering Congress (IMECE2005), November 5–11, 2005, Orlando, FL.

 Copyright © 2007 by ASME

Downloaded 03 Jun 2010 to 171.66.16.156. Redistribution subject to ASME license or copyright; see http://www.asme.org/terms/Terms_Use.cfm

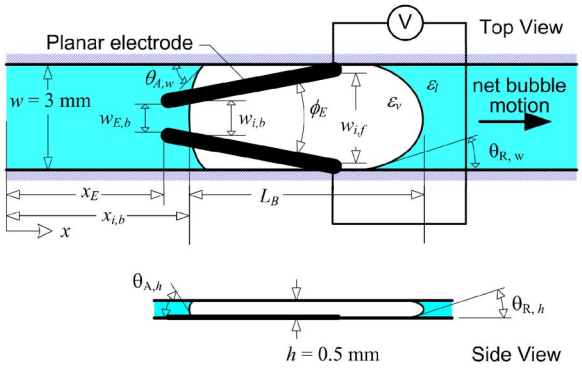

Fig. 1 Simple electrode geometry to evaluate the potential of bubble motion due to DEP (polarization) force

water filament along parallel electrodes using an AC field. Applying 700 V rms at 10^5 Hz at an electrode spacing of 100 μm, a water finger was formed over 6 cm at a velocity exceeding 10 cm/s (corresponding to $\sim$1 μl/s). Yu et al. [7] pumped pentane between parallel electrodes to drive a micro heat pipe. They achieved 5 W (5x enhancement) transport at 9.5 kV/mm in a 28 mm long by 14 mm wide flat plate heat pipe. In a similar approach, Darabi et al. [8], using R-134a, demonstrated a microcooling device that utilized the polarization force to supply the working fluid to the evaporating surface. The device was able to dissipate 65 W/cm^2 with a pressure head of 250 Pa. The only known study to pump liquid and gas (vapor) plugs in microchannels was by Chang [9]. Utilizing electroosmosis, pumping of a bubble was achieved by building up a high liquid pressure region behind the bubble to drive it. By applying 70 V and using KCl/H_2SO_4 as the working fluid a maximum bubble velocity of 0.14 mm/s was achieved in a 5 cm long capillary with a 1.0 mm i.d.

We began a study to determine if two-phase (liquid and gas) flow could be created and controlled in meso- to micro-channels using electrostatic forces, ideally, the polarization force. Our motivation was the potential to manipulate a wide range of fluids at much higher rates than can be achieved with thermal activated techniques. In this study, we provide initial results on the use of the dielectrophoretic force to control motion of bubbles in mesochannels.

Liquid-Vapor Interface Manipulation With Polarization Force

Fluid dynamic motion can be created and manipulated by two electrostatic forces: the Coulomb force and polarization force; see Melcher [10], Pohl [11], and Jones [12] for range of examples. These two forces can be represented through a force density equation as

$$\vec{f}_E = q_e\vec{E} - \frac{1}{2}E^2\nabla\varepsilon + \nabla\left(\frac{1}{2}\rho\frac{\partial\varepsilon}{\partial\rho}E^2\right). \tag{1}$$

The first term on the right-hand side is the Coulomb force. The second and third terms in Eq. (1) represent the polarization force. The Coulomb force arises in fluids when free charges interact with either uniform or nonuniform electric fields. Polarization forces, on the other hand, are created when permittivity gradients exist within in a nonuniform electrical field.

To create two-phase motion in capillary geometry, the electrostatic forces must overcome surface tension, viscous, and inertial forces. A simple analysis can be performed to determine the necessary electrostatic force needed to maintain bubble motion in a capillary geometry. Referring to Fig. 1, a simple electrode concept will create a nonuniform electric field in which the field intensity is increasing in the $-x$ direction, perpendicular to the field lines. Ideally, using only the dielectrophoretic (DEP) force, bubble motion can be maintained if surface tension and viscous forces are overcome, approximated here as

$$\frac{1}{2}V^2(\varepsilon_l - \varepsilon_v)\left[\frac{h}{w_{i,b}} - \frac{h}{w_{i,f}}\right] = 5w(u_v\mu)^{2/3}\sigma^{1/3} + \frac{13.408w\mu u_l L_l}{h} \tag{2}$$

assuming negligible bubble compressibility. The inertial forces of the liquid and bubble are ignored at this time as the interest is to determine the necessary DEP force to maintain steady motion.

The left-hand side term in Eq. (2) is the net DEP force, assuming the bubble back and front are within and electrode pair. The DEP force, second term in Eq. (1), per interface area is determined at the liquid ε_l and bubble ε_v interface [10] and depends on the permittivity difference, applied voltage V, the position of the interface from the vertex of the electrode pair at angle ϕ_E, and the bubble length L_B. It is important to note that the size and position of the bubble relative to the electrode pair will determine the net DEP force available to maintain motion. For the configuration shown in Fig. 1, the DEP force is an approximation as the electrode pair is planar and lies beneath the bubble.

The first term on the right-hand side in Eq. (2) represents the retarding surface tension and viscous force by a moving bubble. This term is based work by Bretherton [13] and Chang [9], using lubrication approximation and matched asymptotic method for steady motion of a long bubble between parallel plates. The assumptions are: (i) the viscous liquid wets the channel (zero contact angle at the wall); (ii) the surface tension σ is well defined and constant; and (iii) the channel height h is so small that gravitational effects are negligible.

The second term on the right-hand side of Eq. (2) represents the retarding viscous force in the liquid segment. We start by considering a problem of steady pressure-driven flow of incompressible Newtonian fluid in a rectangular channel with width w and height h. This term is based on the well-known Poiseuille flow for steady pressure-driven flow [14]. The constant of 13.408 is obtained for a rectangular channel 3 mm wide by 0.5 mm high, which is used in this work.

If the net DEP force is greater than the surface tension and viscous forces, then bubble motion in the $+x$ direction (see Fig. 1) is maintained. Equation (2) can be simplified to

$$\frac{1}{2}\frac{V^2(\varepsilon_l - \varepsilon_v)h}{w_{E,b}} = 5w(u_v\mu)^{2/3}\sigma^{1/3} + \frac{13.408w\mu u_v L_l}{h} \tag{3}$$

assuming the bubble is longer than the electrode pair and located at the back edge of the electrode pair and the bubble and liquid velocity are the same. Equation (3) can be used as a first-order approximation to determine the required voltage to maintain bubble motion for a given fluid and channel geometry. Results for pentane (κ=2 and $\sigma_e = 10^{-11}$ S/m), ethanol (κ=26 and $\sigma_e = 5 \times 10^{-6}$ S/m), and water (κ=80 and $\sigma_e = 10^{-4}$ S/m) are shown in Fig. 2(*a*) for a channel 3 mm wide by 0.5 mm high with ϕ_E =20 deg, $w_{E,b}$=0.7 mm, L_l=146 mm, which are applicable to the experimental conditions to be presented. Dielectric fluids, such as pentane, can be affected by DC fields, but more polar fluids, such as water, may require frequency dependent AC fields to realize DEP force actuation [12]. Ethanol properties lie in-between pentane and water; thus, it is not known what field type will be best.

The application of a voltage to an electrode pair within a fluid medium will result in current flow, increasing the liquid temperature due to Joule heating. This increase in temperature can be approximated as [15]

$$\Delta T \sim \frac{\sigma_e V^2}{k} \tag{4}$$

where k is the liquid thermal conductivity. Results for the same three fluids are shown in Fig. 2(*b*).

Downloaded 03 Jun 2010 to 171.66.16.156. Redistribution subject to ASME license or copyright; see http://www.asme.org/terms/Terms_Use.cfm

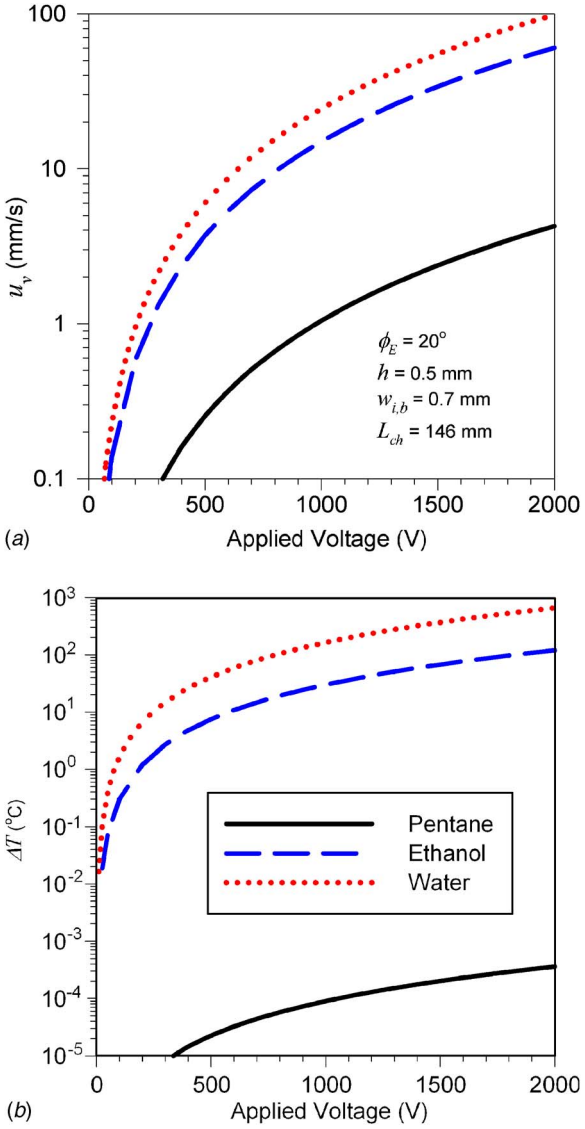

Fig. 2 Graphs showing the effect of DEP force on three fluids: (*a*) bubble velocity as function of constant applied DEP force and (*b*) resulting Joule heating as a function of constant applied voltage

Three important observations can be made from inspection of Fig. 2. First, the DEP force scales as a function of the electric field squared, where the surface tension force is a constant at a given temperature, but the viscous force will scale with bubble and liquid velocity. Additionally, the electric field and viscous force are a function of the reciprocal of the characteristic length squared. This means that as the dimensional scale is reduced, the DEP force and viscous force become significant driving and retarding forces, respectively. Second, as the fluid becomes more conductive, the required voltage to initiate bubble motion decreases; however, joule heating increases significantly. Typically, as the permittivity of a pure fluid increases so does the conductivity. Polar fluids, such as water and ethanol, have high κ and σ_e, whereas nonpolar fluids, such as pentane, have low κ and σ_e. Thus, to practically realize bubble motion in water, for example, will require dielectric insulation between the electrode and fluid. This will increase the required electric field for bubble actuation. Some joule heating can be advantageous because it will reduce the local surface tension and viscous forces leading to greater efficiency of the DEP force. The third observation is if bubble motion is initiated, then it will be a very dynamic process because once the bubble moves in the channel the force on the interface will change. The degree to which the DEP forces changes will depend on the electrode design and position of the bubble over the electrode pair.

Based on the above first-order analysis, a study was initiated to investigate DEP-induced bubble motion. By creating an array of simple electrode designs, similar to that shown in Fig. 1, it was believed that controlled motion could be achieved by applying an electric field in the proper sequence.

The dimensions of the geometry presented in Fig. 1 were chosen based on capillary effects and ease of fabrication of the experimental system to demonstrate controlled bubble motion. The channel width of 3 mm was determined from [16]

$$L_c \leq 2\sqrt{\frac{\sigma}{g(\rho_l - \rho_v)}} \tag{5}$$

For pentane, ethanol, and water at 25°C, L_c is 2.9 mm, 3.2 mm, and 5.0 mm, respectively. At a channel width of 3 mm, capillary effects begin to be significant; thus, the effect of electrostatic forces on interface deformation can be studied and related to the ability to create and control two-phase fluid motion. Furthermore, this dimension allowed for various electrode designs to be easily created with printed circuit board technology to study the effect of the DEP force. A channel height of 0.5 mm, 6× smaller than the channel width, was chosen to decrease the nonuniformity of the electric field in channel height dimension due to the planar electrodes; thus, focusing the nonuniformity of the electric field in desired flow direction. Knowledge gained at the mesoscale dimension can then be more effectively applied at the microscale dimension.

Experimental Setup and Procedure

An experimental system, as shown in Fig. 3, was developed to study electrostatic force control in meso- and microfluidic phenomena. The system consists of the test card housing, repeatability dispensers connected to microsyringes, unique four-channel programmable high-voltage power supply, four-channel digital oscilloscope, and stereo microscope with high-speed digital camera. The power supply contains a programmable chip for controlling the switching frequency of the four channels. A key feature of the system is an 8 cm by 5 cm area where test cards (see Fig. 3(*b*)) are placed, allowing for discrete amounts of liquid and/or air to be injected and source of power to be applied. The test card is created by patterning an electrode array on a printed circuit board (PCB) or glass slide. The fluidic channels are created on the test card. For the research presented here, the test card consists of an acrylic top with fluidic channels epoxied to the PCB. Additional connections are epoxied to the card to introduce and control discrete amounts of liquid and air.

The typical output from the programmable high-voltage power supply is shown in Fig. 4. This voltage behavior is the same for the different electrode array configurations (EACs) tested. From Fig. 4, it is seen that one of the four switches in the power supply is different. The switch applied to electrode pair 4 (EP4) resulted in a much more precise field application and practically no stored capacitance. Switches on EP1–EP3 had stored electrical capacitance. This stored capacitance resulted in a decay rate of ~5.6 V/ms and residual applied voltage on EP1–EP3 ranging from ~200 to 500 V. It is not clear how much this affected bubble motion.

Results will be presented for two different electrode array configurations, as shown in Fig 5. With these two configurations, the effect of the electrostatic forces on bubble motion is evaluated. EAC 1, as shown in Fig. 5, consisted of four overlapping electrode pairs, 6.59 mm in length and ϕ_E=20 deg angle between the high-voltage electrode and ground. EAC 2 consisted of four electrode pairs in series at 0.51 mm spacing, 5.71 mm in length, and ϕ_E=4 deg angle between the high-voltage electrode and ground.

Downloaded 03 Jun 2010 to 171.66.16.156. Redistribution subject to ASME license or copyright; see http://www.asme.org/terms/Terms_Use.cfm

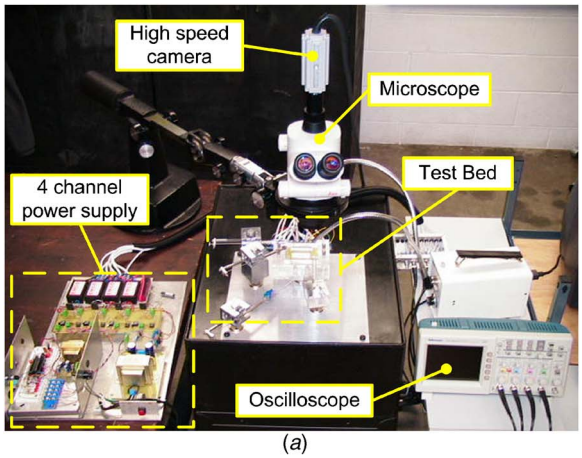

(*a*)

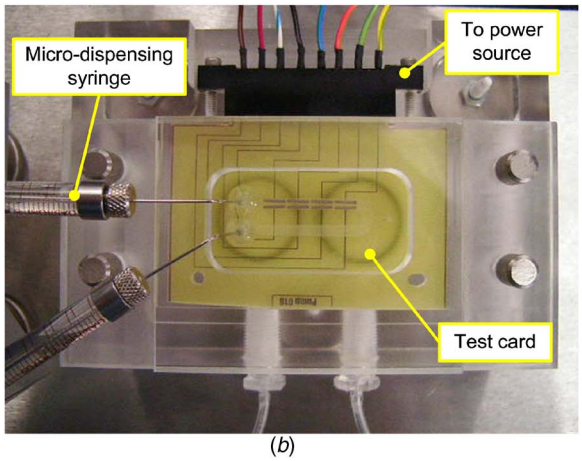

(*b*)

Fig. 3 Experimental system to study electrostatic force control in small scale fluidic phenomena: (*a*) test system and (*b*) test card support

In both configurations, the electrode arrays were placed beneath a 3 mm wide by 0.5 mm high channel. Additionally, no dielectric layer covered the electrode arrays. Each configuration was evaluated with different bubble sizes, two working fluids, and two switching frequencies (0.4 Hz and 1 Hz). The two working fluids were pentane and a 20%/80% by mass mixture of ethanol in pentane. The fluids were chosen based on their dielectric properties, compatibility, and ease of use in the test system.

Experiments were performed by first filling channels with the test fluid and then introducing the discrete bubble size at the location of interest in the test card EAC. Because of surface tension, the test card geometry, and the actuator on the repeatability dispensers, bubble lengths could vary ±1 mm per dispenser actuation. Thus, all experiments were repeated at least three different times to verify repeatability, and typically more when the effect of bubble size influenced the measured results. Furthermore, tests were repeated by introducing new fluid into the EAC and testing under same conditions on different days. All presented results are based on visual analysis of digital high-speed video images. The performance of each EAC was compared by measuring the velocity, acceleration, and deformation of the different bubbles.

The velocity and acceleration were measured at the front and back of the bubble along the centerline of the channel using tracking software. The measurement resolution was 0.025 mm for tracking the bubble interface with worst-case interface location error at ±0.08 mm. This error was due to light quality, which affected the ability to clearly locate the bubble interface. The results presented are confined to single bubble motion through four electrode pairs. The electrode pairs are referred to as EP1, EP2, EP3, and EP4. To accurately measure bubble movement and deformation, the field of view was confined to the last two electrode pairs, EP3 and EP4. Experimental data presented were measured in two forms. First, the velocity and acceleration were measured for the front and back of the bubble at 0.0167 s time intervals, corresponding to 60 frames per second. Second, average velocity was determined by measuring the time required for the bubble front to move through the field of view.

Bubble length affected the initial bubble placement and in some cases the measured velocity across the electrodes. At the start of each test the bubble was placed on EP1. Before the electric field was applied, the bubble would migrate and sit between EP1 and EP2 for both electrode array configurations. The electrode array (circuit on PCB) is raised 0.025 mm above the circuit board surface, which affects the resting position of the bubbles within the electrode array.

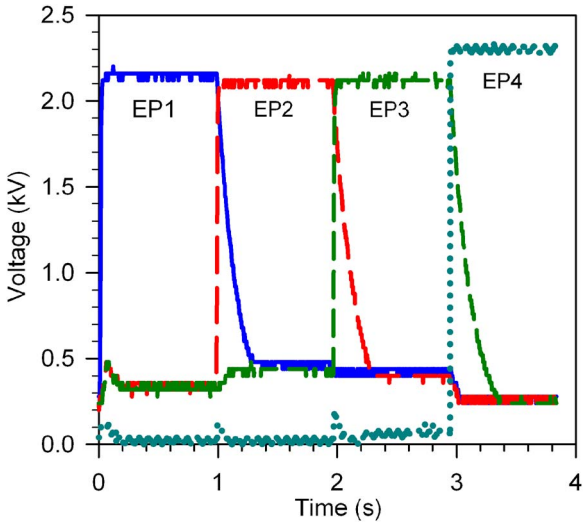

Fig. 4 The measured voltage during one sequence at 1 Hz pulse to a four-pair electrode array configuration (EAC)

Experimental Results and Discussion

To achieve unidirectional bubble motion, each electrode pair was energized in sequence starting from EP1 to EP4 for a preset frequency of 0.4 Hz (2.5 s time interval) or 1 Hz (1 s). Once EP4 was energized, the sequence would start again at EP1. The energizing sequence was repeated because at certain operating conditions a bubble may only move a certain distance within an EAC. The bubble motion will depend on the location of the liquid-vapor interface over an electrode pair at any given time relative to when the electrode pair is energized. Creating effective unidirectional bubble motion through a channel will depend on how well a bubble can be manipulated through an electrode array. A sequence of bubble deformation images are shown in Figs. 6 and 7 for EAC 1 and EAC 2, respectively. In all cases, the applied voltage to the electrode pair is 2.1 kV +DC and the switching frequency is 1 Hz. Examples of bubble motion through EAC 1 and EAC 2 are shown in Figs. 6(*b*) and 7(*b*). From first inspection of the images, bubble deformation occurs under all conditions when an electrode pair is energized. Furthermore, the nature of the deformation is different in the two fluids. The diverging angle of EAC 1 and EAC 2 were ideally designed to create a DEP force parallel to the flow channel. This assumes that the bubble lies in-between the two diverging electrodes, not necessarily above them. If a bubble were positioned between a diverging electrode pair, the polarization force would drive the bubble to the region of lowest field strength. From the images shown in Figs. 6 and 7 for pentane, the electrostatic force appears to drive the bubble off the high-voltage electrode

Downloaded 03 Jun 2010 to 171.66.16.156. Redistribution subject to ASME license or copyright; see http://www.asme.org/terms/Terms_Use.cfm

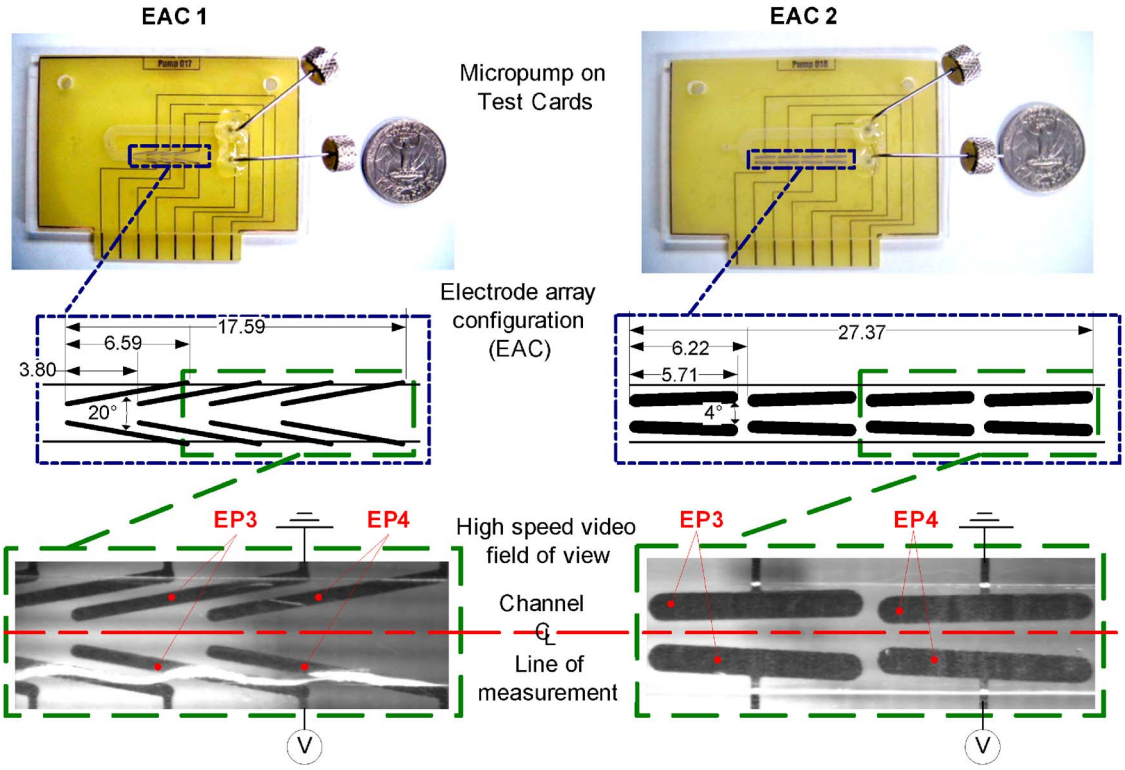

Fig. 5 Photographs and drawings of EAC 1 and EAC 2; top pictures show test card with the corresponding electrode array; middle drawing is the electrode array with dimensions in millimeter; and the bottom is the image field of view from the high-speed camera.

toward the grounded electrode. The diverging electrode pair configuration results in a nonuniform squeezing of the bubble, driving it down stream (+x direction). When ethanol is added to pentane, a binary mixture is created resulting in different bubble deformation. The difference in the deformation between the pure pentane and the 20/80 mixture of ethanol in pentane is not well understood at this time. Based on the results shown in Figs. 6 and 7, EAC 1 and EAC 2 were investigated further to obtain a better understanding of how the intensity of the electric field affected bubble deformation and bubble velocity.

EAC 2 required at least 1.5 kV to drive a bubble to the next electrode pair. EAC 1, because of the overlapping array design, could produce continuous bubble motion at 1 kV. Average velocity versus voltage results for EAC 1 are shown in Fig. 8 for a range of bubble sizes (4.32–6.84 mm) with pentane and the 20/80 mixture operating at 1 Hz switching frequency. The average velocity was calculated by measuring the time for the bubble front to pass through the field of view. In all cases, the average velocity increased with increasing bubble size and increasing voltage. In general, there is no measurable difference in the average bubble velocity between pentane and the 20/80 mixture even though the bubble deformation is different between the two fluids. A minimum voltage of 1.25 kV and 1 kV was required to create and maintain axial bubble motion in pentane and the 20/80 mixture, respectively, but the bubble is 1 mm longer for the 20/80 mixture. Additionally, for the 20/80 mixture, the average velocity appears to be a function of bubble size only between 1.5 kV and 2 kV. Thus, bubble size has an impact on the bubble motion produced. This is explored further later in this section.

Additional insight can be gained by comparing the results presented in Fig. 2 to Fig. 8. An applied voltage of 1.25 kV was needed to maintain bubble motion at an average velocity of 3.7 mm/s for a 5 mm bubble. It was predicted that 1.9 kV would be required to achieve bubble motion of 3.8 mm/s. If the liquid velocity is assumed to be half the bubble velocity, then it is pre-

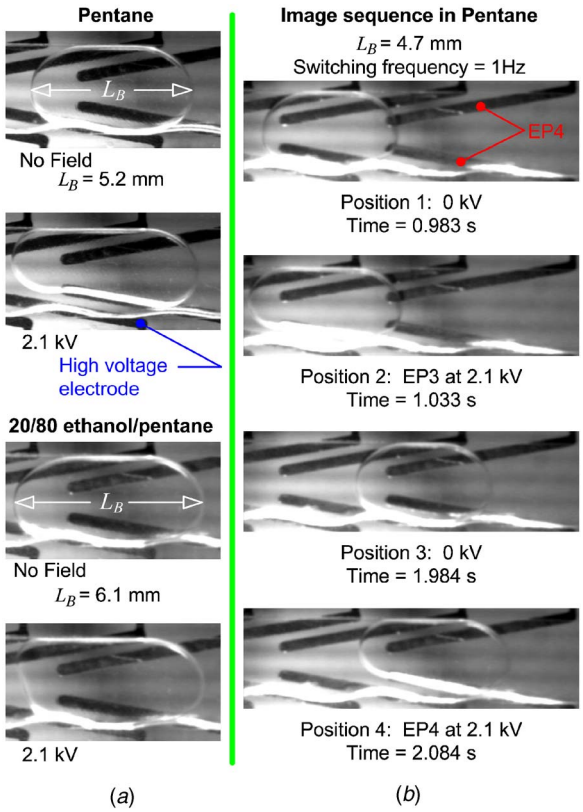

Fig. 6 Bubble deformation and motion in EAC 1: (*a*) bubble deformation with and without an applied field for pentane (top) and the 20/80 mixture (bottom) and (*b*) image sequence of induced bubble motion in pentane

Downloaded 03 Jun 2010 to 171.66.16.156. Redistribution subject to ASME license or copyright; see http://www.asme.org/terms/Terms_Use.cfm

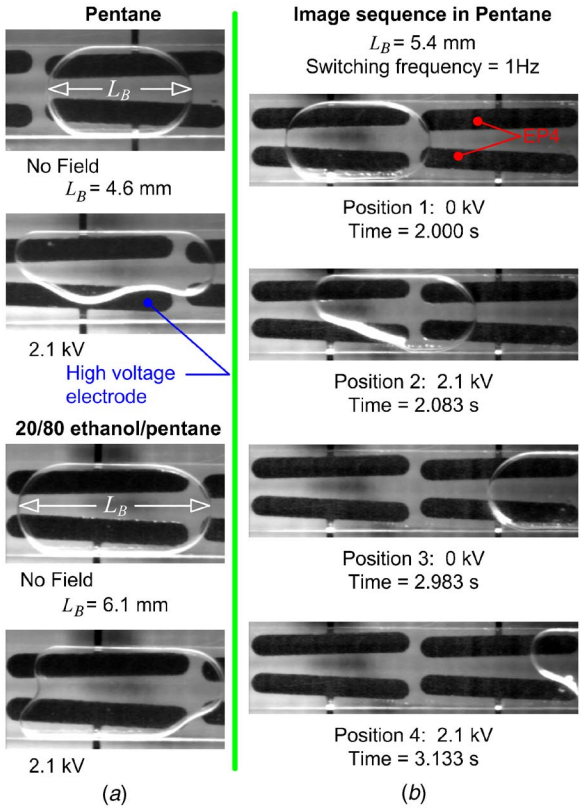

Fig. 7 Bubble deformation and motion in EAC 2: (*a*) bubble deformation with and without an applied field for pentane (top) and the 20/80 mixture (bottom) and (*b*) image sequence of induced bubble motion in pentane

dicted that 1.36 kV is required to maintain the bubble motion at 3.8 mm/s. The average velocity predicted by Eq. (3) is shown in Fig. 8 for $u_v = u_l$ and $u_l = 0.5u_v$. The bubble will "slip" by the liquid at a higher rate due to deformation, channel geometry, and wetting. The process of producing bubble motion is very dynamic, which is not represented by Eq. (2) or Eq. (3). Experimentally, continuous bubble motion through EAC 1 could not be achieved below 1.25 kV for bubbles of <5 mm in size because the net DEP force was not great enough to overcome surface tension and viscous forces to keep the bubble moving to the next electrode pair. Once bubble motion is created, there will be a nonlinear decay in the DEP force as the bubble interface moves through the electrode pair, which is not represented in Eq. (2) or Eq. (3). The prediction assumes that the DEP force is constant and a maximum acting only at the back of the bubble, which is not the case. The net DEP force (difference between back and front) will continuously change as the bubble moves through an EAC. Furthermore, the bubble and liquid motion will be a function of the bubble deformation, location, size, gap between the channel and bubble, switching frequency, and acceleration of the bubble (and liquid) as a function of position and time. Although Eq. (2) cannot predict the dynamic behavior of the bubble motion, it can be used to determine the voltage range to maintain bubble motion. Predictions are not made for the 20/80 mixture because the electrical permittivity is unknown. Inspection of Fig. 2 shows that ethanol requires much lower voltage to achieve the same bubble motion. Based on the results shown in Fig. 8 there is not clear evidence that the 20/80 mixture produces in a similar bubble velocity at a lower voltage because bubble size plays a role.

To better understand the dynamic bubble motion, selected results using a midsize ($L_B \sim 5.5$ mm) bubble in pentane at a switching frequency of 1 Hz for EAC 1 and EAC 2 are shown in Fig. 9. Within the field of view (approximately two electrode pairs), the interface velocity and acceleration at the back of the bubble and the normalized deformation of the bubble were measured and compared for EAC 1 and EAC 2. The data presented in Fig. 9 are the average result from three trials that were conducted over a one-week period. The standard deviation among the trials is shown as the shaded region in interface velocity graphs. Results for EAC 1 were very repeatable even at the point of greatest deformation. Results for EAC 2 were repeatable, but greater variation occurred when an electrode pair was energized and the bubble deformation was the greatest. The images in Fig. 9 were taken at the point of greatest deformation during each trial, where it is clear that more variation occurred in EAC 2. The normalized

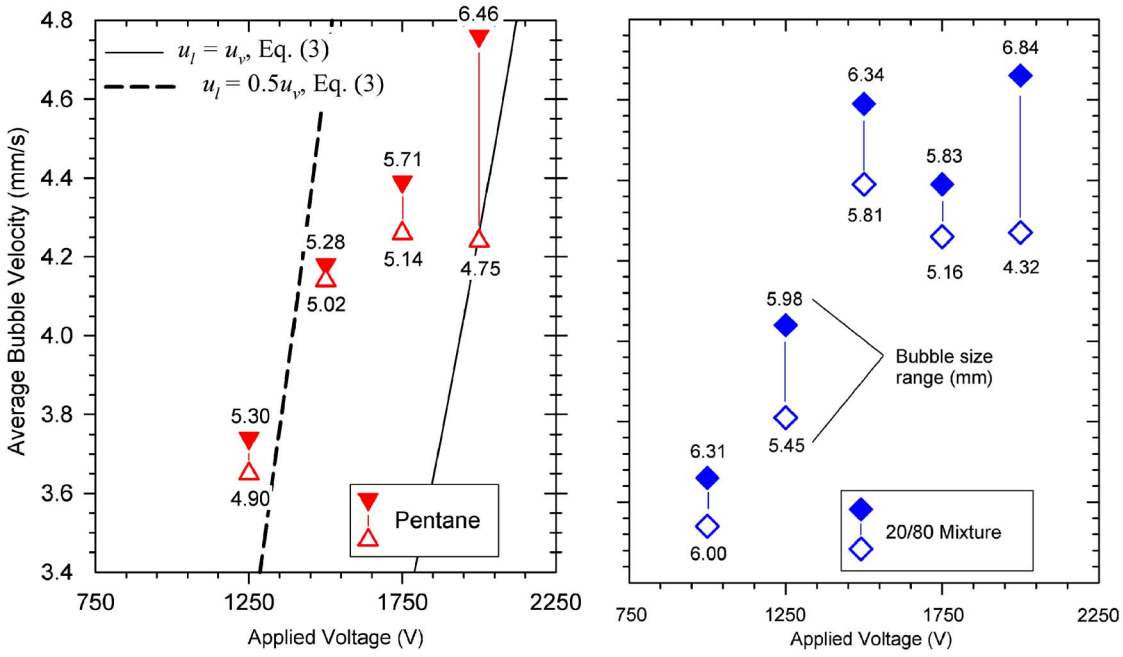

Fig. 8 Graph of the average velocity through the field of view versus applied voltage for EAC 1

Downloaded 03 Jun 2010 to 171.66.16.156. Redistribution subject to ASME license or copyright; see http://www.asme.org/terms/Terms_Use.cfm

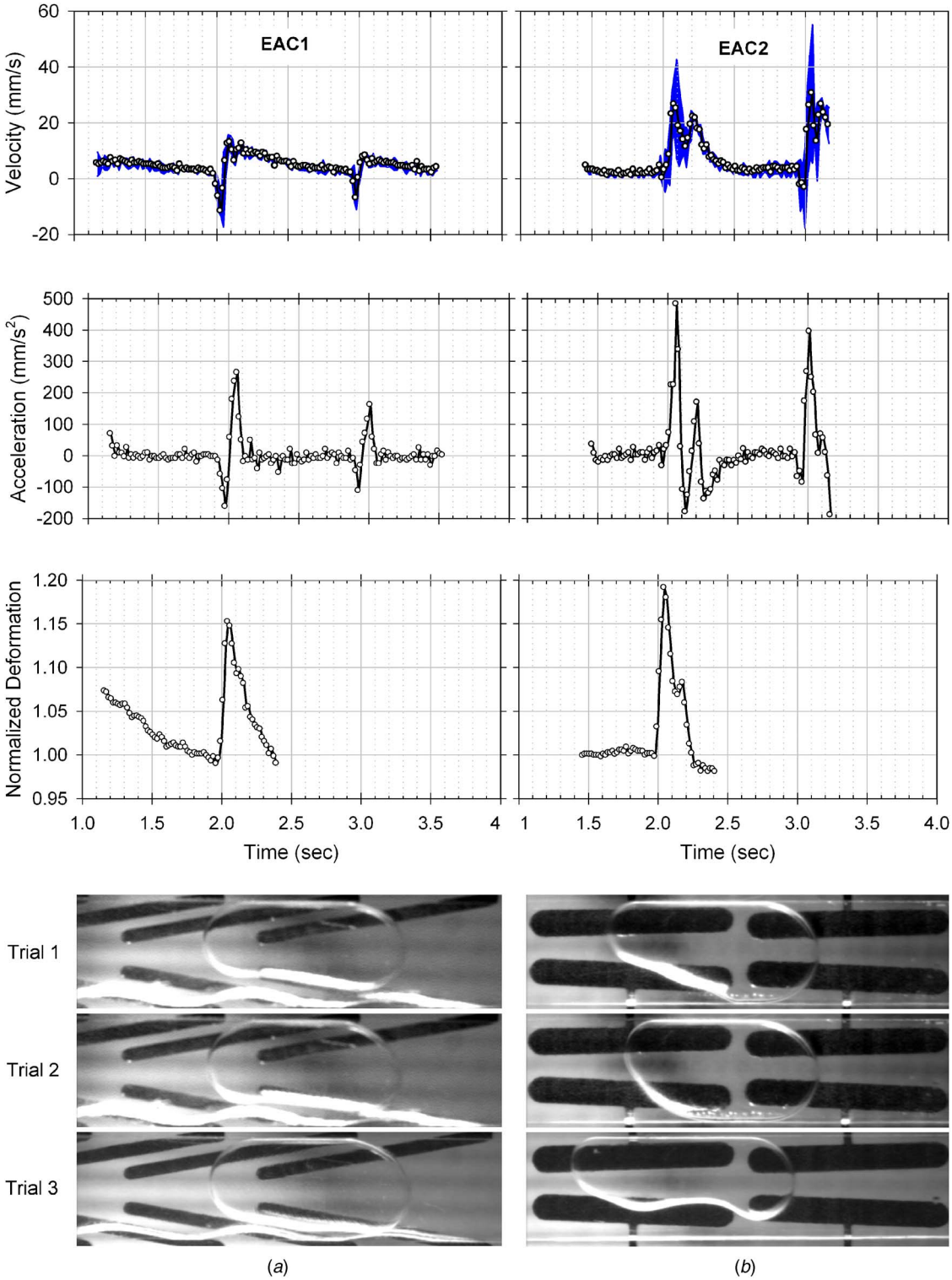

Fig. 9 Comparison of interface velocity, interface acceleration, and normalized bubble deformation averaged over three trials for a midsize bubble (~5.5 mm) at 1 Hz switching frequency and 2.1 kV applied voltage in pentane: (*a*) results for EAC 1 and (*b*) results for EAC 2

variation was determined as the ratio of the deformed bubble length to the bubble length at rest with no force applied. The bubble length was measured at the centerline of the channel. The normalized deformation calculated as the ratio of the bubble lengths was used instead of the ratio of the bubble perimeters because it was easier to calculate and resulted in the same trend and very similar deformation magnitude. The normalized deformation is only shown for one position on EP3 because the bubble front moves out of the field of view on EP4.

From inspection of Fig. 9, it is seen that unidirectional bubble motion is created for both EAC 1 and EAC 2 operating at 2.1 kV+DC. However, the bubble motion through EAC 1 and

Downloaded 03 Jun 2010 to 171.66.16.156. Redistribution subject to ASME license or copyright; see http://www.asme.org/terms/Terms_Use.cfm

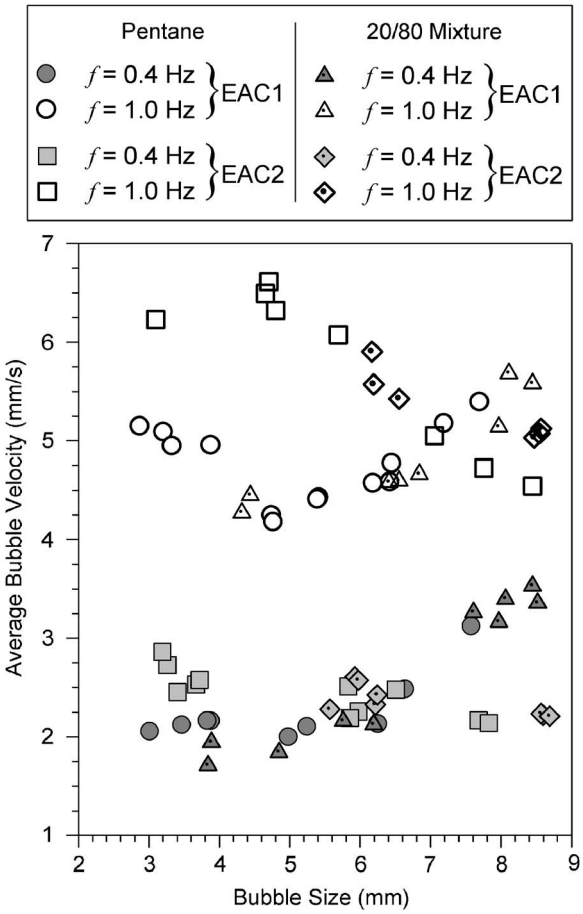

Fig. 10 Average velocity through field of view for different bubble sizes at 2.1 kV DC voltage pulse for different conditions: (1) frequency of 0.4 Hz and 1 Hz, (2) EAC 1 and EAC 2, and (3) pentane and the 20/80 mixture

EAC 2 is not constant, but very dynamic as evidenced by the bubble acceleration and normalized deformation. As the bubble moves over an electrode pair and the pair is energized at a set frequency, the bubble deforms and accelerates, pulsing forward to the next electrode pair. The bubble motion was faster on average through EAC 2 than EAC 1, ~7 mm/s compared to 4 mm/s. This appears to be due to the electrode design resulting in peak acceleration in EAC 2 of about two times that of EAC 1. Thus, EAC two may be a more effective configuration because it results in greater bubble motion for the given applied voltage, bubble size, and switching frequency. However, it is important to note that since the current was not measured, it is unknown at this time which EAC is more efficient.

The DEP force produces net bubble motion down the channel (+*x* direction), but with significant deformation at the point when an electrode pair is first energized. It is interesting to note that as the bubble is driven across EP3 to EP4, the normalized deformation rapidly changes from greater than 1 to slightly less than 1. This provides evidence that as the bubble front moves onto EP4, it "slips" less by the liquid and begins pushing more liquid at the bubble front. The interaction between the changing DEP, viscous, surface tension, and inertia forces results in the very dynamic motion shown in Fig. 9 for both EAC 1 and EAC 2.

The effect of bubble size was also evaluated in EAC 1 and EAC 2 with pentane and the 20/80 mixture. The results for average velocity at the front of the bubble through the field of view are shown in Fig. 10 for pentane and the 20/80 mixture. The average velocity was measured for a range of bubble sizes at two switching frequencies of 0.4 Hz and 1.0 Hz at 2.1 kV. From inspection of Fig. 10, three general observations can be made. First, as switching frequency increased, bubble motion increased. From 0.4 Hz to 1 Hz, in both electrode configurations for all bubble sizes, the bubble interface moved faster to the next electrode pair before that pair was energized. As the frequency increased, there appears to be a greater affect of bubble size on velocity in both EAC 1 and EAC 2. The optimum frequency to maximize bubble motion will depend on electrode pair design, applied voltage, fluid, channel geometry, and bubble size. Second, the trend in bubble velocity versus bubble size is different for EAC 1 compared to EAC 2. As the bubble size increased greater than 4.5 mm, the bubble velocity increased in EAC 1 and decreased in EAC 2. The reason for this is not well understood at this time because the effect of the bubble deformation and electrical capacitance from neighboring electrode pairs is not known. Third, for the conditions tested there is no measurable difference in the bubble velocity in pentane compared to the 20/80 mixture even though the bubble deformation (see Figs. 6 and 7) is significantly different.

The electrode pair design within the channel will have a significant effect on the achievable bubble motion. Only bubble sizes 3 mm and greater produced unidirectional motion, shown in Fig. 10, through the entire electrode array configuration, whereas all bubble sizes less than 3 mm never made it all the way through the array. As the bubble size changes, the driving and opposing DEP forces at the back and front of the bubble, respectively, will change depending on the electrode pair angle and size. The electrode angle creates a challenge because, as the angle decreases, the force at the bubble interface will increase. If the bubble is smaller than the electrode pair, then the net DEP force to drive the bubble will decrease as the electrode angle decreases. The spacing from one electrode pair to the next is another issue that will influence motion and be sensitive to switching frequency. For example, in EAC 2, the net DEP force for a given bubble size must be great enough to move the bubble 6.5 mm before the next pair is energized, compared to only 3.7 mm for EAC 1.

Conclusions

Preliminary analysis showed that motion of bubbles could be maintained if the DEP force could overcome surface tension and viscous forces. An experimental investigation was carried out confirming that bubble motion on the mesoscale could be produced by discreet application of a polarization (DEP) force. Using a unique experimental system, two electrode array configurations were developed and tested. Unidirectional bubble motion was demonstrated and measured over a range of bubble sizes for both electrode array configurations with two working fluids, and two switching frequencies. Experimental results indicate that an average bubble velocity ranging from 2 mm/s to 6.5 mm/s could be achieved in the different electrode array configurations for both pentane and a 20/80 mixture by mass of ethanol in pentane. The bubble motion achieved was affected by bubble deformation. Additionally, electrode array configuration design had a significant effect on bubble velocity, acceleration, and deformation. Furthermore, the velocity of the bubble could be considerably affected by increasing or decreasing the switching frequency and bubble size.

In this work, only a single bubble through an electrode array configuration was studied. To realize applications such as pumping, continuous motion of multiple and different-sized bubbles must be investigated and understood. Additionally, more conductive fluids, such as pure ethanol and water, were not studied. Future research requires investigating these areas as well as developing a model to more accurately predict the dynamic bubble motion as a function of electrode array design, bubble size, bubble deformation, switching frequency, and fluid properties.

Acknowledgment

We would like to acknowledge Richard Oberto for his time and commitment in building a novel four-channel programmable high-

Downloaded 03 Jun 2010 to 171.66.16.156. Redistribution subject to ASME license or copyright; see http://www.asme.org/terms/Terms_Use.cfm

voltage power supply and Jenny Jackson for her help in analyzing some of the results. Funding for this research was supported in part by the University of Missouri Research Board.

Nomenclature

E = electric field strength (V/m)
$\vec{f}_E$ = EHD force density (N/m^3)
g = gravity (m/s^2)
h = channel height (mm)
k = thermal conductivity (W/m K)
L_B = bubble length (mm)
L_c = characteristic length (mm)
L_l = liquid plug length (mm)
q_e = charge density (C/m^3)
T = temperature (°C)
u = velocity (mm/s)
μ = dynamic viscosity ($N\ s/m^2$)
V = applied voltage (V)
x = channel position (mm)
w = width (mm)

Greek Symbols

ε = permittivity (pF/m)
ϕ_E = angle between electrodes
κ = dielectric constant
θ = contact angle
ρ = density (kg/m^3)
σ = surface tension (N/m)
σ_e = electrical conductivity (S/m)

Subscripts

A = advancing
b = back
E = electrode
f = front
C = capillary
h = height
i = interface
l = liquid
r = radial direction
R = receding
v = vapor
w = width

References

[1] Sammarco, T. S., and Burns, M. A., 1999, "Thermocapillary Pumping of Discrete Drops in Microfabricated Analysis Devices," AIChE J., **45**(2), pp. 350–366.
[2] Jun, T. K., and Kim, C. J., 1998, "Valveless Pumping Using Traversing Vapor Bubbles in Microchannels," J. Appl. Phys., **83**(11), pp. 5658–5664.
[3] Song, Y. J., and Zhao, T. S., 2001, "Modelling and Test of a Thermally-Driven Phase-Change Nonmechanical Micropump," J. Micromech. Microeng., **11**, pp. 713–719.
[4] Tsai, J. H., and Lin, L., 2002, "Active Microfluidic Mixer and Gas Bubble Filter Driven by Thermal Bubble Micropump," Sens. Actuators, A, **97-98**, pp. 665–671.
[5] Geng, X., Yuan, H., Oguz, H. N., and Prosperetti, A., 2001, "Bubble-Based Micropump for Electrically Conducting Liquids," J. Micromech. Microeng., **11**, pp. 270–276.
[6] Jones, T. B., Gunji, M., Washizu, M., and Feldman, M. J., 2001, "Dielectrophoretic Liquid Actuation and Nanodroplet Formation," J. Appl. Phys., **89**(2), pp. 1441–1448.
[7] Yu, Z., Hallinani, K., Bhagat, W., and Kashani, R., 2002, "Electrohydrodynamically Augmented Micro Heat Pipes," J. Thermophys. Heat Transfer, **16**(2), pp. 180–186.
[8] Darabi, J., Ohadi, M. M., and DeVoe, D., 2001, "An Electrohydrodynamic Polarization Micropump for Electronic Cooling," J. Microelectromech. Syst., **10** (1), pp. 98–106.
[9] Chang, H., 2001, *The MEMS Handbook*, Gad-el-hak, M., ed., CRC Press, Boca Raton, Ch. 11.
[10] Melcher, J. R., 1981, *Continuum Electromechanics*, MIT Press, Cambridge, MA.
[11] Pohl, H. A., 1978, *Dielectrophoresis*, Cambridge University Press, Cambridge, England.
[12] Jones, T. B., 1995, *Electromechanics of Particles*, Cambridge University Press, Cambridge, England.
[13] Bretherton, F. P., 1961, "The Motion of Long Bubbles in Tubes," J. Fluid Mech., **10**, pp. 166–188.
[14] Papanastasiou, T. C., Georgiou, G. C., and Alexandrou, A. N., 2000, *Viscous Fluid Flow*, CRC Press, Boca Raton.
[15] Ramos, A., Morgan, H., Green, N. G., and Castellanos, A., 1998, "AC Electrokinetics: A Review of Forces in Microelectrode Structures," J. Phys. D, **31**, pp. 2338–2353.
[16] Kew, P., and Cornwell, K., 1997, "Correlations for the Prediction of Boiling Heat Transfer in Small Diameter Channels," Appl. Therm. Eng., **17**, pp. 705–715.

Downloaded 03 Jun 2010 to 171.66.16.156. Redistribution subject to ASME license or copyright; see http://www.asme.org/terms/Terms_Use.cfm

Nonequilibrium Molecular Dynamics Approach for Nanoelectromechanical Systems: Nanofluidics and Its Applications

Changsung Sean Kim
e-mail: csean.kim@samsung.com

Corporate R&D Institute,
Samsung Electro-Mechanics Co. Ltd.,
Suwon, 443-743 Korea

Molecular dynamics (MD) simulations have been performed to provide the basic knowledge of nanofluidics and its applications at the molecular level. A nonequilibrium molecular dynamics (NEMD) code was developed and verified by comparing a micro Poiseuille flow with the classical Navier–Stokes solution with nonslip wall boundary conditions. Liquid argon fluids in a platinum nanotube were simulated to characterize the homogeneous fluid system. Also, positively charged particles were mixed with solvent particles to study the non-Newtonian behavior of the heterogeneous fluid. At equilibration state, the macroscopic parameters were calculated using the statistical calculation. As an application of MD simulation, the nanojetting mechanism was identified by simulating the full process of droplet ejection, breakup, wetting on the surface, and natural drying. For an electrowetting phenomenon, a fluid droplet with positive charges moving on the ultrathin film with negative charges was simulated and then compared to the macroscopic experiments. A conceptual nanopumping system using the electrowetting phenomenon was also simulated to prove its feasibility. The molecular dynamics code developed here showed its potential applicability to the novel concept design of nano- and microelectromechanical systems. [DOI: 10.1115/1.2754311]

Introduction

Recently, the molecular level understanding becomes more important in information and biological technology. With the advance of supercomputing resource, molecular dynamics (MD) simulations have been one of the most promising methods to provide a clear and fundamental understanding of microscopic mass and heat transfer at the molecular level. Classical Navier–Stokes solutions mimicking macroscopic flows have been widely used in numerous fluid engineering fields. However, some MD simulations have shown that the Navier–Stokes theory shows a significant deviation from MD simulations and its hypotheses are not satisfied.

Numerous MD studies (i.e., [1–3]) have shown that the velocity profile in nanochannels deviates from that of the classical Poiseuille flow due to the wall slip boundary. Travis et al. [4] noted that the classical Navier–Stokes behavior for a channel width larger than 10 M dia. Thompson and Troian [5] simulated Couette flow and found that the wall slip boundary condition depends on the strength of fluid-wall coupling and the commensurability of fluid and wall densities. They presented MD simulations of Newtonian liquids under shear that indicate there exists a general nonlinear relationship between the amount of slip and local shear rate at a solid surface. Nagayama and Cheng [6] studied the effect of the interface wettability on the pressure-driven flow in a nanochannel with a width of 16 M and showed a plug flow velocity profile for a hydrophobic surface. They also found that the interface wettability results in nonuniform temperature and pressure profiles near the solid walls.

As applications of MD simulation, Moseler and Landman [7] simulated the formation of nanojets with velocities up to 400 m/s, created by pressurized injection of fluid propane through nanoscale convergent gold nozzles. Xue and Shu [8] simulated the equilibration of heat conduction in a very thin film in order to understand the macroscopic behavior from the standpoint of molecular dynamics motions. Maruyama [1] pointed out that surface tension is one of the benchmark properties to examine the applicability of the MD method to the liquid-vapor interface and the potential function model. Actually, he simulated a water droplet on a platinum solid surface as a more practical simulation of solid-liquid-vapor interaction.

The objectives of the present study can be summarized as: (i) to develop a nonequilibrium molecular dynamics code named as NEM^{3}D (nanoelectromechanics multiphase molecular dynamics), (ii) to probe the effect of characteristic length on the deviation between the capillary flow pattern in a nanotube and the classical Navier–Stokes solution, and (iii) to apply the NEM^{3}D code to simulate nanojetting and electrowetting phenomena. A brief introduction of the molecular dynamics approach adopted in NEM^{3}D is presented in the next section, followed by Computed Results and the Conclusion.

Molecular Dynamics Approach

The NEM^{3}D code [9] adopts an effective pair potential of the system with the sum of the Lennard–Jones potential, ϕ_{LJ} and the Coulomb potential, ϕ_C within the cutoff distance, r_c as

$$\Phi = \sum_i \sum_j \phi^{LJ}(r_{ij}) + \sum_i \sum_j \phi^{C}(r_{ij})$$

$$\phi^{LJ}(r_{ij}) = 4\epsilon\left[\left(\frac{\sigma}{r_{ij}}\right)^{12} - \left(\frac{\sigma}{r_{ij}}\right)^{6} - \left(\frac{\sigma}{r_c}\right)^{12} + \left(\frac{\sigma}{r_c}\right)^{6}\right]$$

$$\phi^{C}(r_{ij}) = \frac{q_i q_j}{4\pi\epsilon_0}\left[\frac{1}{r_{ij}} - \frac{1}{r_c}\left(1 - \frac{r_{ij} - r_c}{r_c}\right)\right] \quad (1)$$

where σ and ϵ are the distance and energy parameters, r is the distance between two interacting particles, q is the electric charge, and ϵ_0 is the electric permittivity of vacuum. For liquid-solid in-

Contributed by the Fluids Engineering Division of ASME for publication in the JOURNAL OF FLUIDS ENGINEERING. Manuscript received April 1, 2006; final manuscript received March 26, 2007. Review conducted by Ali Beskok. Paper presented at the 2005 ASME International Mechanical Engineering Congress (IMECE2005), November 5–11, 2005, Orlando, FL.

 Copyright © 2007 by ASME

Downloaded 03 Jun 2010 to 171.66.16.156. Redistribution subject to ASME license or copyright; see http://www.asme.org/terms/Terms_Use.cfm

teraction, the Lennard–Jones potential in Eq. (1) was modified as

$$\phi_{ls}^{LJ}(r_{ij}) = 4\epsilon_{ls}\left[\left(\frac{\sigma_{ls}}{r_{ij}}\right)^{12} - \beta\left(\frac{\sigma_{ls}}{r_{ij}}\right)^{6} - \left(\frac{\sigma_{ls}}{r_c}\right)^{12} + \beta\left(\frac{\sigma_{ls}}{r_c}\right)^{6}\right] \quad (2)$$

where the intermolecular parameters between liquid and solid are given by $\epsilon_{ls}=\alpha\sqrt{\epsilon_l\epsilon_s}$ and $\sigma_{ls}=(\sigma_l+\sigma_s)/2$ based on the Lorentz–Berthelot combination [10]. And α and β were tested to study the dynamic intermolecular behavior (hydrophilic or hydrophobic) near the wall boundary layer. The values of α and β can be determined as $\sqrt{\epsilon_l/\epsilon_s}\sim 1.0$ and 0–1.0, respectively.

The interacting force is derived by differentiating Eq. (1) as

$$\vec{F} = -\nabla\Phi = 24\epsilon\sum_i\sum_j\left[2\left(\frac{\sigma}{r_{ij}}\right)^{12} - \left(\frac{\sigma}{r_{ij}}\right)^{6}\right]\frac{\vec{r}_{ij}}{|r_{ij}|^2} + \sum_i\sum_j\frac{q_i q_j}{4\pi\epsilon_0 r_{ij}^2}\frac{\vec{r}_{ij}}{|r_{ij}|} \quad (3)$$

Then, the equation of motion of a particle can be written as

$$m\vec{a} = \vec{F} + m\vec{g} \quad (4)$$

where $m\vec{g}$ is an external force, such as gravitational force.

For time integration, the Verlet's algorithm [11] and Beeman's algorithm [12] were verified as

$$\vec{r}(t+\Delta t) = \vec{r}(t) + \vec{v}(t)\Delta t + \frac{[C_{r1}\vec{a}(t) + C_{r2}\vec{a}(t-\Delta t)]}{6}(\Delta t)^2 \quad (5)$$

$$\vec{v}(t+\Delta t) = \vec{v}(t) + \frac{[C_{v1}\vec{a}(t+\Delta t) + C_{v2}\vec{a}(t) + C_{v3}\vec{a}(t-\Delta t)]}{6}(\Delta t) \quad (6)$$

where $\vec{r}$ is displacement, $\vec{v}$ is velocity, $\vec{a}$ is acceleration vectors, t is the time, $C_{r1}=3$, $C_{r2}=0$, $C_{v1}=3$, $C_{v2}=3$, and $C_{v3}=0$ for Verlet's algorithm, and $C_{r1}=4$, $C_{r2}=-1$, $C_{v1}=2$, and $C_{v2}=5$, and $C_{v3}=-1$ for Beeman's algorithm, respectively. It was found that the latter is more accurate to update the velocity components than the former. Thus, the Beeman's algorithm was used for all computations in the present study. A Berendsen thermostat [13,14] was adopted to avoid viscous heating, and then velocities were rescaled as

$$\vec{v}' = \chi\vec{v}, \quad \chi = \left[1 - \frac{\Delta t}{\tau}\left(\frac{T_{\text{tar}}}{T} - 1\right)\right]^{1/2}$$

where T is the temperature, T_{tar} is the target temperature, and τ is a time constant of the rescaling. The equation of motion was nondimensionalized with respect to σ, ϵ, and m as

$$t^* = \frac{t}{\tau} = \frac{t}{(\sigma\sqrt{m/\epsilon})}, \quad r^* = \frac{r}{\sigma}$$

$$v^* = \frac{v}{\sqrt{\epsilon/m}}, \quad a^* = \frac{a}{\sigma/\tau^2}, \quad \phi^* = \frac{\phi}{\epsilon}$$

$$F^* = \frac{F}{\epsilon/\sigma}, \quad T^* = \frac{T}{\epsilon/k_B} \quad (7)$$

Periodic boundary conditions have been reasonably used to reduce surface effects. The computational domain in the center box is surrounded by its periodic images as shown in Fig. 1. The potentials and forces from the image domain should be included in the primary domain. The cutoff distance r_c was given by 2.5σ and the neighboring particles within the nearest distance $r_{NL}=3.75\sigma$ were stored in neighbor lists. Compared to the full computing case without cutoff distance and neighbor lists, for capillary flow in a nanotube with total number of 3200 particles, computing time using neighbor lists was reduced by 1/24 time, as shown in Fig. 2. Computations were performed on a HP Workstation xw8200 with 3.6 GH CPU.

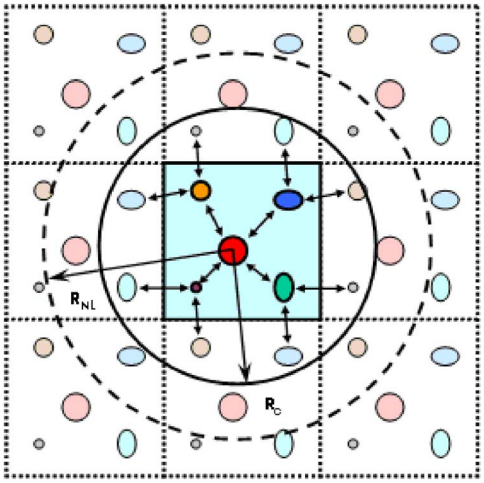

Fig. 1 Cutoff distance (r_c) and neighbor lists (r_{NL}) with periodic boundary conditions

Computed Results and Discussion

Code Verification. The NEM^{3}D code was validated by simulating the micro Poiseuille flow for liquid argon in a nanoscale channel and then compared with the previous molecular dynamics (MD) study. Liquid argon particles are flowing in a platinum channel with two solid walls with the face-centered-cubic (fcc) structure as shown in Fig. 3. The liquid calculation domain is set to be $5.83\times3.85\times7.22$ nm^3. The total number of particles is 5088:2400 for fluid particles (density of 21.45×10^3 Kg/m^3) and 2688 for wall particles. At a temperature of 100 K, the Lennard-Jones parameters are $\epsilon_l=1.67\times10^{-21}$ J, $\sigma_l=0.34$ nm for liquid argon, $\epsilon_s=8.35\times10^{-22}$ J and $\sigma_s=0.248$ nm for platinum walls. The interaction between liquid argon particles and platinum molecules follows Eq. (2) with $\alpha=1$, $\beta=1$, as also suggested by Nagayama and Cheng [6]. Figure 4 shows axial velocity profiles in the z direction along the nanochannel for two different driving forces (9.80 pN and 1.96 pN). The present results show a good agreement with their MD simulations.

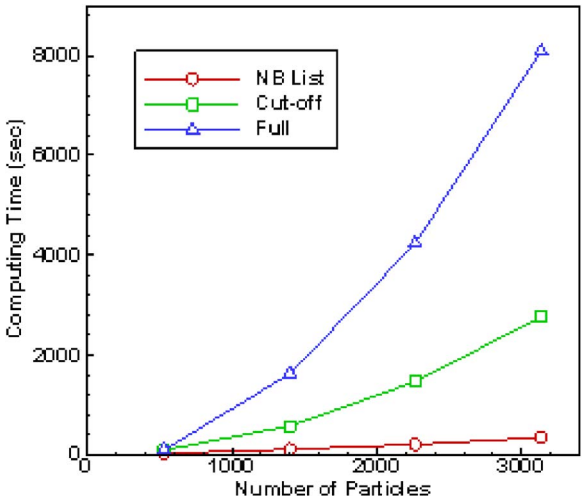

Fig. 2 Computing time versus number of particles

Downloaded 03 Jun 2010 to 171.66.16.156. Redistribution subject to ASME license or copyright; see http://www.asme.org/terms/Terms_Use.cfm

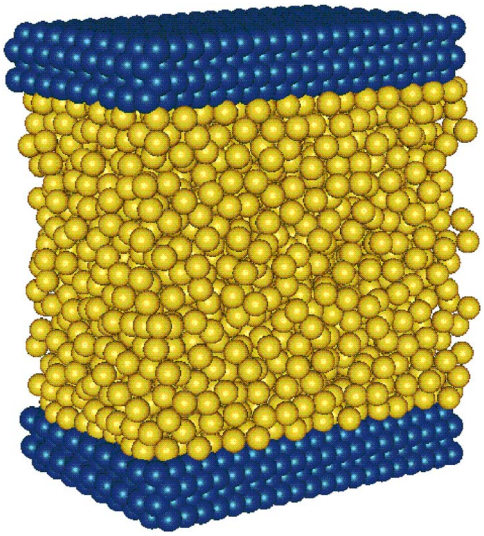

Fig. 3 Modeling of a Poiseuille flow in a nanochannel

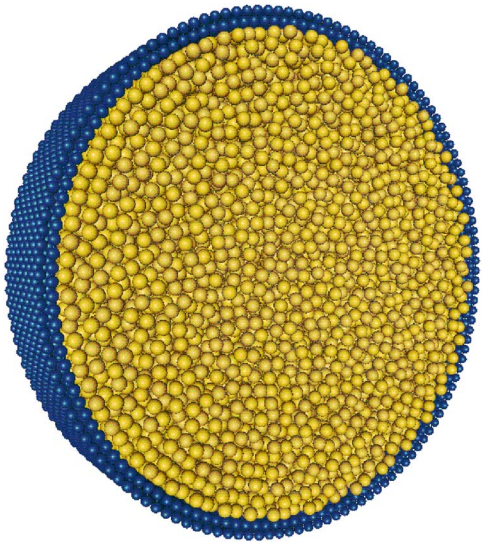

Fig. 5 Liquid argon flowing through a platinum nanotube of 12 nm dia

Homogeneous Flow in a Nanotube. Single-component fluids flowing through three different nanotubes of 3 nm dia, 6 nm dia, and 12 nm dia were simulated to investigate the validity of the classical Navier–Stokes solution for nanoscale flow regime. The fluid is liquid argon, and the wall material of nanotubes is platinum. At a temperature of 85 K, liquid argon particles are bounded by platinum wall particles within a diameter of 12 nm, as shown in Fig. 5. The total number of particles is 10,284:7044 for fluid particles (number density is 0.64) and 3240 for wall particles. The Lennard–Jones parameters are $\epsilon_l = 1.67 \times 10^{-21}$ J, $\sigma_l = 0.3410$ nm for liquid argon, $\epsilon_s = 83.5 \times 10^{-21}$ J and $\sigma_s = 0.248$ nm for platinum walls. Coulomb potential and forces between fluid-fluid and fluid-wall interaction were excluded for this case. The interaction between liquid argon particles and platinum molecules follows Eq. (2), with $\alpha = 1$, $\beta = 1$ to provide the nonslip boundary conditions.

External forces are applied in the streamwise direction to drive fluid particles. The periodic boundary condition was used in the streamwise direction with 3 nm distance. Figure 6 shows the time-averaged axial velocity profiles for 3 ns (or 0.3×10^6 time steps). The axial velocity profile using neighbor lists and cutoff distance of 2.2σ shows a good agreement with 2.5 and 3.5σ cases. When using 10,284 particles, the cutoff distance of 2.2σ shows a speedup as much as 2.4 times faster than the 3.5σ case with minor loss of accuracy.

Because of strong interaction between fluid and wall particles, MD solutions show a noticeable discrepancy near wall surfaces from the classical Navier–Stokes solution of Poiseuille flow with nonslip wall boundary condition. Axial velocity component, $u(r)$ can be written as

$$u(r) = U_{\max}\left[1 - \left(\frac{r}{R}\right)^2\right], \quad U_{\max} = \frac{R^2}{4\mu L}\Delta p \tag{8}$$

where $U_{\max}$ is the maximum value in axial velocity, R is the tube radius, L is length, μ is fluid viscosity, and Δp is pressure difference between inlet and outlet. Those wall effects become more serious as the diameter decreases from 12 nm to 3 nm, as shown in Fig. 7. The magnitude of velocity and diameter were normalized for fair comparison. The Navier–Stokes solution deviates from MD results, showing non-Newtonian fluid behavior.

Electrowettability in a Charged Nanotube. Multicomponent fluids in a nanotube of 9 nm dia were simulated to examine the surface wettability due to electric charges imposed at the wall. The solvent is modeled as in Refs. [6,9], and the wall material of the nanotube is platinum. At a temperature of 275 K, solvent particles are bounded by platinum wall particles within a diameter of 9 nm, as shown in Fig. 8. Total number of particles is 9337:4772 for fluid particles, 2141 for counterions, and 2424 for wall particles. The Lennard–Jones parameters are $\epsilon_l = 1.08 \times 10^{-21}$ J, $\sigma_l = 0.317$ nm for the solvent fluids, $\epsilon_q = 1.08 \times 10^{-21}$ J, σ_q

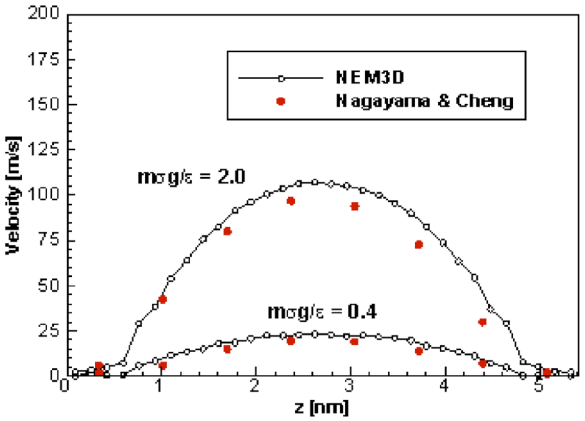

Fig. 4 Velocity profiles in the z direction of two pressure-driven flows

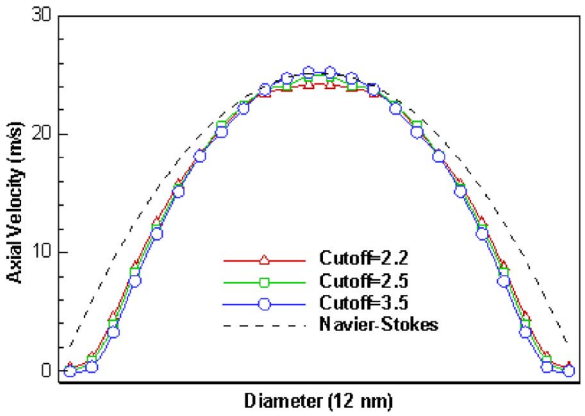

Fig. 6 Axial velocity profiles due to cutoff distance

Downloaded 03 Jun 2010 to 171.66.16.156. Redistribution subject to ASME license or copyright; see http://www.asme.org/terms/Terms_Use.cfm

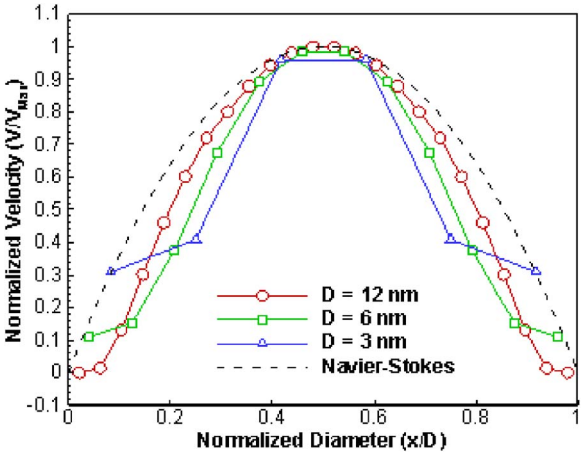

Fig. 7 Axial velocity profiles due to nanotube diameter

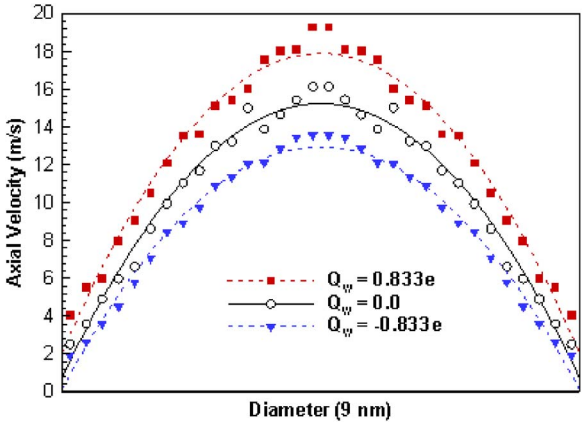

Fig. 9 Axial velocity profiles due to surface charges at wall

=0.194 nm for counterions, and $\epsilon_s = 83.5 \times 10^{-21}$ J, $\sigma_s = 0.248$ nm for platinum walls. The interaction between liquid argon particles and platinum molecules follows Eq. (2) with $\alpha = 0.5$, $\beta = 0.5$. Coulomb potential and forces between fluid-fluid and fluid-wall interaction were also included to take electrostatic effects into account. Cutoff schemes for electrostatic interactions might be inaccurate, even if cutoff distance is over $4.5\sigma_l$. In the present study, however, we have used cutoff distance of $4.5\sigma_l$, which can provide an obvious discrimination between the effects of electric charged walls on axial velocity profiles in Fig. 9. Solvent particles have no charge, and each counterion is positively charged by $1e = 1.602 \times 10^{-19}$ C. Each wall particle has $-0.883e$ to balance the surface charge density with that of counterions.

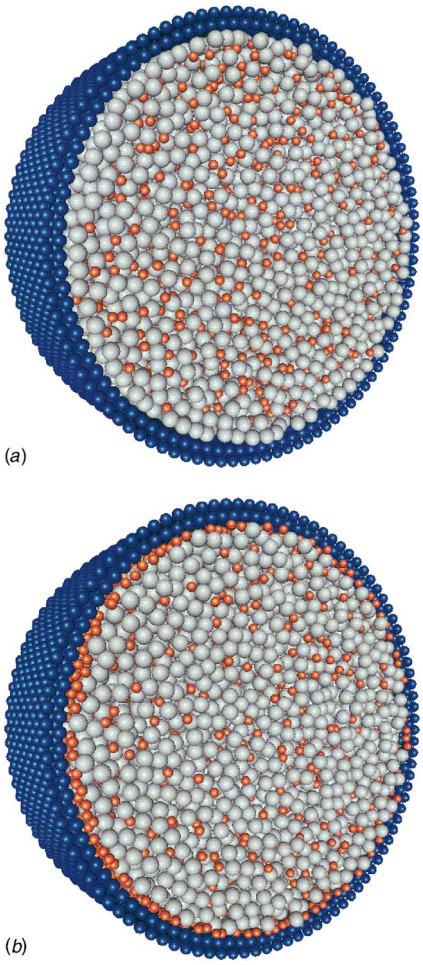

Fig. 8 Electrostatic flows in a nanotube of 9 nm dia: (*a*) $q_w = +0.833e$ and (*b*) $q_w = -0.833e$

Periodic boundary condition was used in streamwise direction with 3 nm distance. Because of the heterogeneous rheology, a longer time of 10 ns was required for time-averaged flow quantities. The negative surface charges, opposite to the charge of counterions, result in adhesive forces near the wall surface, and then counterions are attached to the wall surface. On the other hand, repulsive forces are induced between fluid and wall particles, which causes the slip flow at wall surface. It is found that the sign of wall surface charge determines the flow resistance that is inversely proportional to flow rate while applying the same driving force per sectional area (i.e., pressure difference).

Nanojetting Physics. The NEM^{3}D code was then applied to identify the nanojetting mechanism from droplet ejection, breakup, wetting, and the drying process. A single droplet of liquid argon was ejected into vacuum through the nozzle outlet of 3 nm dia. The nozzle wall material was assumed as platinum. The temperature of the system was maintained at 85 K. The Lennard–Jones parameters are $\epsilon_l = 1.67 \times 10^{-21}$ J, $\sigma_l = 0.3410$ nm for liquid argon, $\epsilon_s = 83.5 \times 10^{-21}$ J and $\sigma_s = 0.248$ nm for platinum walls. The interaction between liquid argon particles and platinum molecules follows Eq. (2), with $\alpha = 0.5$, $\beta = 0.5$. A pressure of 900 MPa is applied inside the nozzle, only for 0.125 ns to eject a single droplet of interest. The droplet approaches the platinum substrate located at 50 nm below, in the z direction. Periodic boundary conditions were given the in the x and y directions.

Figure 10 shows nine snap shots of full process in nanojetting from droplet ejection to wetting on the surface. After 0.125 ns, the sudden drop of ejecting pressure results in breakup and droplet formation. Initial ejecting velocity through the nozzle was ~94 m/s. Figures 10(*a*)–10(*c*) show the breakup process to make a single droplet accompanied by molecular evaporation and formation of necking instabilities, as observed in Ref. [7]. Because of the strong capillary force in nanotube, as shown in Figs. 10(*d*)–10(*f*), the remainder of the liquid particles at exit start moving back to the nozzle. Figure 10(*f*) shows a moment of interest when the droplet collides with the substrate surface. Sudden repulsive forces between fluid and wall particles give rise to a temporary unstable state as shown in Fig. 10(*g*).

Consequently, the droplet has been fully wetted on the substrate surface as shown in Fig. 10(*i*). The full wetting (hydrophilic) condition was applied to the surface by using $\beta = 1.0$, from Eq. (2). Some portion of satellite particles are floating about from the sur-

Downloaded 03 Jun 2010 to 171.66.16.156. Redistribution subject to ASME license or copyright; see http://www.asme.org/terms/Terms_Use.cfm

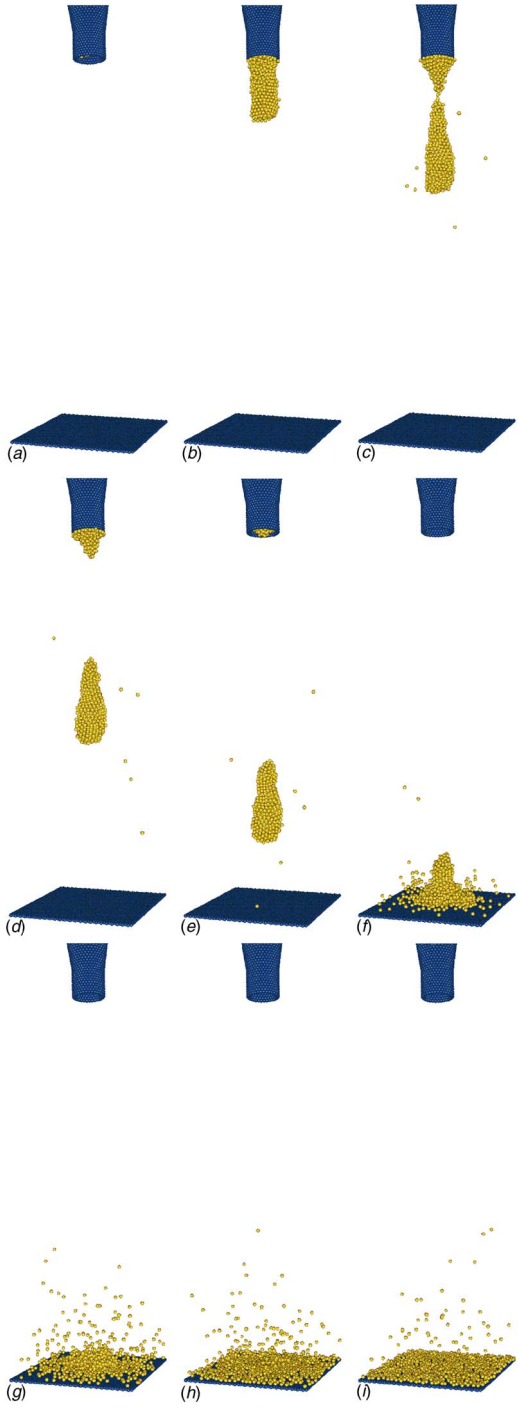

Fig. 10 Evolution of nanojetting from droplet ejection to surface wetting: (*a*) t=0.084 ns, (*b*) t=0.116 ns, (*c*) t=0.148 ns, (*d*) t=0.180 ns, (*e*) t=0.212 ns, (*f*) t=0.244 ns, (*g*) t=0.276 ns, (*h*) t=0.324 ns, and (*i*) t=0.368 ns

face until reaching a new equilibration state, which is considered to provide an illustrative understanding of drying (or molecular evaporation) mechanism in nanoscale.

Surface Wettability on Ultrathin Film. Three types of typical wetting phenomena were simulated to understand the effects of intermolecular forces on the surface tension and contact angle. The droplet with 4.5 nm dia ejected from the nanojet in the previous example was used as an initial condition for the ultrathin film with three different surface energies. Figure 11(*a*) shows examples full wetting, Fig. 11(*b*) intermediate wetting, and Fig. 11(*c*) no wetting phenomena at equilibration state using β=1.0, 0.25, and 0.1 from Eq. (2), respectively.

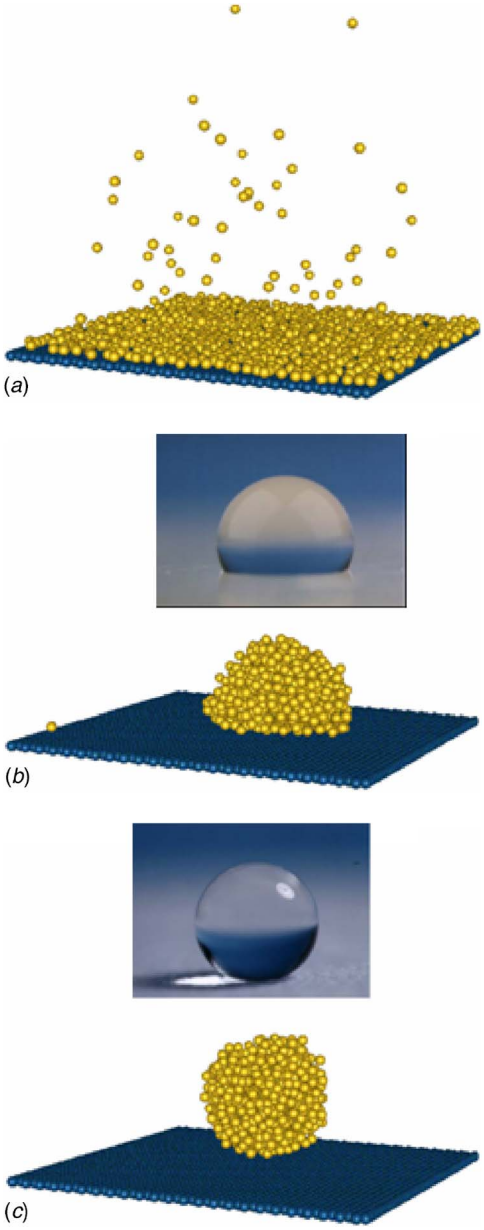

Fig. 11 Contact angle (CA) and surface wettability at equilibration state (Both photographs with permission of Prof. K. Tsujii at Hokkaido University [15]): (*a*) CA=0 deg (fully wetting, α=1, β=1), (*b*) CA≅109 deg (α=1, β=0.25), and (*c*) CA≅174 deg (Hydrophobic, α=1, β=0.1)

The full wetting (hydrophilic) condition gives rise to a contact angle of 0 deg as shown in Fig. 11(*a*). With an increase of the contact angle, the droplet on the substrate reforms in spherical shape in order to minimize the surface energy along the phase line. Two nanodroplets in Figs. 11(*b*) and 11(*c*) show the similar shapes with photographs of water droplets (~1 mm dia) on the flat surface and the super water-repellent surface by fractal concept, respectively. Surface wettability with a liquid is enhanced by the surface roughness, in particular, by the presence of fractal structures. More details on super water-repellent fractal surfaces can be found in Ref. [15]. Nevertheless, of the drastic difference

Downloaded 03 Jun 2010 to 171.66.16.156. Redistribution subject to ASME license or copyright; see http://www.asme.org/terms/Terms_Use.cfm

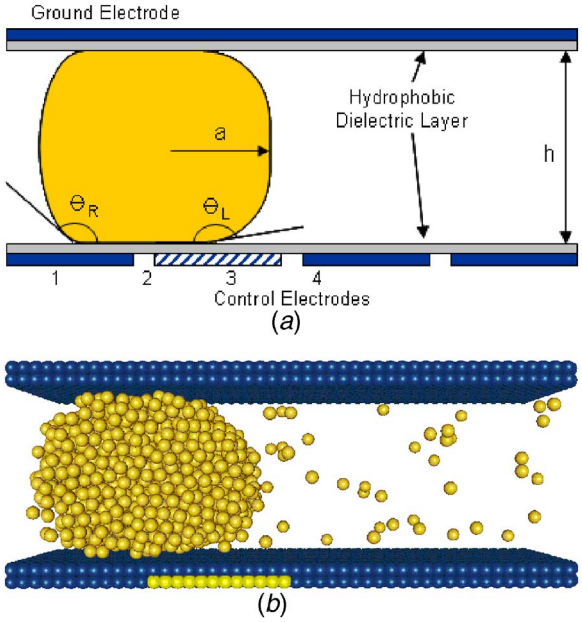

Fig. 12 Concept design for nanopumping system (*a*) Schematics of an electrowetting pump and (b) Simplified modeling of a nanopump

in diameter size, it is found that both nanodroplets and water droplets form in spherical shape as contact angle increases over 90 deg.

Conceptual Nanopumping System. As another application, a charged droplet moving between the upper and lower electrowetting plates was simulated as illustrated in Fig. 12(*a*). To simplify the nanoscale system, the dielectric layers and electrodes are modeled as thin films whose material is assumed as platinum. The nanodroplet moves along the channel in the z direction, and periodic boundary conditions are given in the y and z directions, as shown in Fig. 12(*b*). The periodic boundary condition is used in the z direction with a 15 nm distance. The Lennard–Jones parameters are $\epsilon_l = 1.67 \times 10^{-21}$ J, $\sigma_l = 0.3410$ nm for liquid droplet, $\epsilon_s = 83.5 \times 10^{-21}$ J and $\sigma_s = 0.248$ nm for the platinum surface. Coulomb potential and forces between fluid-fluid and fluid-wall interaction were also included to simulate electrowetting phenomenon. The interaction between liquid argon particles and platinum molecules follows Eq. (2) with $\alpha = 0.5$, $\beta = 0.1$ to mimic the hydrophobic surfaces on the electrodes. Initially, surface particles have no charge, whereas liquid particles are positively charged by $0.01e = 1.602 \times 10^{-21}$ C.

The surface tension over the droplet and the viscous force at wall surfaces, respectively, can be expressed as

$$F_{\text{surf}} = 2a\gamma_{LV}(\cos\theta_R - \cos\theta_L) \tag{9}$$

$$F_{\text{visc}} = 2\tau_w \pi a^2 = \frac{12\mu U_d \pi a^2}{h} \tag{10}$$

where γ_{LV} is the surface tension, μ is the viscosity, and the shear stress is given by $\tau_w = 6\mu U_d / h$, assuming a plane Poiseuille flow. By equating Eqs. (9) and (10) the axial velocity of the droplet can be approximated as

$$U_d = \frac{\gamma_{LV} h}{6\pi\mu a}(\cos\theta_R - \cos\theta_L) \tag{11}$$

Before the negative charges are applied to the hydrophobic surface of the control electrodes, the droplet forms a spherical shape to minimize the surface energy. For a nanosecond, the negative charges ($-0.01e = -1.602 \times 10^{-21}$ C) are applied to the second

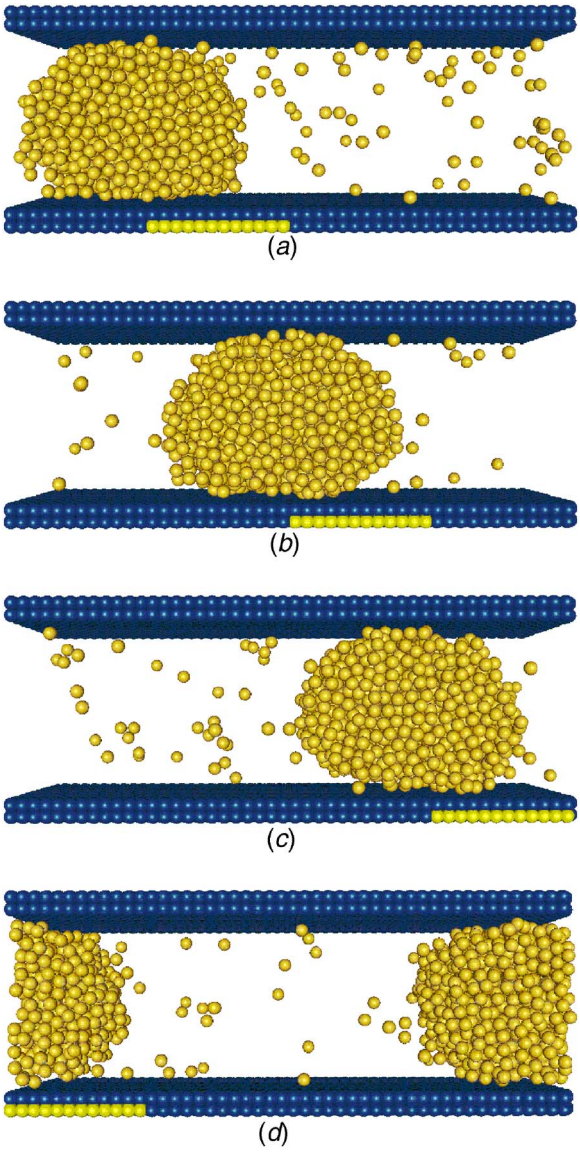

Fig. 13 Nano-pump using electrowetting phenomenon: (*a*) *t* = 0.6 ns (electrode 2), (*b*) *t* = 1.6 ns (electrode 3), (*c*) *t* = 2.6 ns (electrode 4), and (*d*) *t* = 3.6 ns (electrode 1)

control electrode from the left (electrode 2) as yellow colored in Fig. 13(*a*), and then the contact angle of the left half of the droplet θ_L becomes larger than θ_R. The difference in the contact angles results in the net force between surface tension and viscous wall-shear force, which is the driving force of the droplet moving along the channel in the z direction.

The same negative charges are switched to the neighboring control electrode in order to keep the droplet moving on the surfaces. Consequently, the second droplet moves in with electrode 1, negatively charged, while the first one moving out as observed in Fig. 13(*d*). Figure 14 shows the instantaneous velocity vectors of all the fluid particles at $t = 0.6$ ns and 1.6 ns, respectively. Also, the sum of velocity components of the droplet indicates its simultaneous mode of rolling and transition on the surfaces. The averaged magnitude of the axial velocity with respect to time is plotted in Fig. 15. One by one, each control electrode holds negative charges for the same interval of a nanosecond. At the beginning phase of each interval, the droplet accelerates due to the adhesive force between the fluid particles and wall particles on the electrode until it reaches the midpoint of the electrode, and then its moving speed

Downloaded 03 Jun 2010 to 171.66.16.156. Redistribution subject to ASME license or copyright; see http://www.asme.org/terms/Terms_Use.cfm

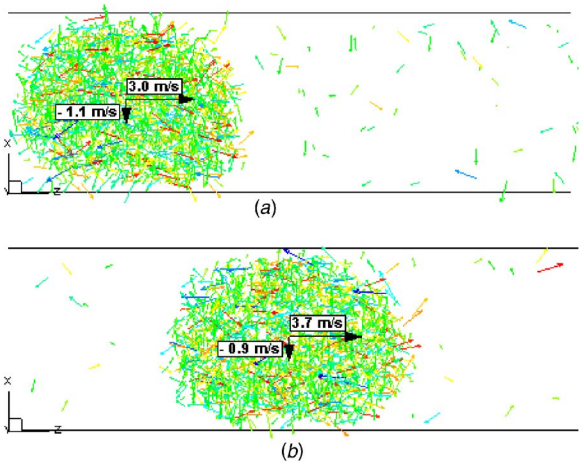

Fig. 14 Instantaneous velocity vectors of the droplet in motion: (*a*) *t*=0.6 ns and (*b*) *t*=1.6 ns

suddenly drops. Based on the present simulations, it is reconfirmed that electrowetting phenomenon could be one of the promising ideas for nano-/micropumping systems.

Conclusion

The NEM^{3}D code has been developed and applied to provide fundamental understandings of nanofluidics. The statistical flow quantities, such as time-averaged velocity profiles, showed the discrepancy from the Navier–Stokes solution in nanoscale. Counterions were mixed with liquid argon to illustrate the non-Newtonian behavior of the heterogeneous fluid. In addition, electrostatic flows in a charged nanotube were also examined to compare to noncharged fluids. It is found that the sign of wall surface charge determines the flow resistance that is inversely proportional to flow rate while applying the same driving force per sectional area. As an application, full nanojetting process was simulated for droplet ejection, wetting, and drying phenomena in a consequent manner. In addition, a conceptual nano-pumping system was successfully simulated using the electrowetting phenomenon. The present molecular dynamics approach showed its potential applicability to the wide range of nano-/microelectromechanical engineering fields.

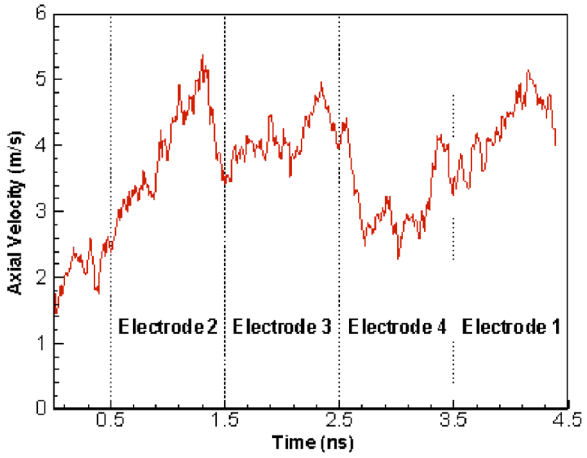

Fig. 15 Averaged magnitude of axial velocity of the droplet

Acknowledgment

The author would like to express special thanks to Dr. Dochan Kwak at NASA Ames Research Center and Dr. Timur Halicioglu at Stanford University for their insightful guidance to micro-/biofluids and nonequilibrium molecular dynamics, respectively.

References

[1] Maruyama, S., 2000, "Molecular Dynamics Method for Microscale Heat Transfer," *Advances in Numerical Heat Transfer*, Vol. 2, Minkowycz, W. J., and Sparrow, E. M., eds., Taylor & Francis, New York, pp. 189–226.
[2] Xu, J. L., and Zhou, Z. Q., 2004, "Molecular Dynamics Simulation of Liquid Argon Flow at Platinum Surfaces," Heat Mass Transfer, **40**, pp. 859–869.
[3] Thompson, A. P., 2003, "Nonequilibrium Molecular Dynamics Simulation of Electro-Osmotic Flow in a Charged Nanopore," J. Chem. Phys., **119**(14), pp. 7503–7511.
[4] Travis, K. P., Todd, B. D., and Evans, D. J., 1997, "Departure From Navier–Stokes Hydrodynamics in Confined Liquids," Phys. Rev. E, **55**, pp. 4288–4295.
[5] Thomson, P. A., and Troian, S., 1997, "A General Boundary Condition for Liquid Flow at Solid Surfaces," Nature (London), **389**, pp. 360–362.
[6] Nagayama, G., and Cheng, P., 2004, "Effects of Interface Wettability on Microscale Flow by Molecular Dynamics Simulations," Int. J. Heat Mass Transfer, **47**, pp. 501–513.
[7] Moseler, M., and Landman, U., 2000, "Formation, Stability, and Breakup of Nanojets," Science, **289**, pp. 1165–1169.
[8] Xue, H., and Shu, C., 1999, "Equilibration of Heat Conduction Simulation in a Very Thin Film Using Molecular Dynamics," Int. J. Numer. Methods Heat Fluid Flow, **9**(1), pp. 60–71.
[9] Kim, C. S., 2005, "Non-Equilibrium Molecular Dynamics Approach for Nano-Electro-Mechanical Systems: Nanofluidics and Its Applications," ASME Conference, IMECE 2005-79628, Orlando, Florida, Nov.
[10] Delhommelle, J., and Millie, P., 2001, "Inadequacy of the Lorentz-Berthelot Combining Rules for Accurate Predictions of Equilibrium Properties by Molecular Simulations," Mol. Phys., **99**(8), pp. 619–625.
[11] Verlet, L., 1967, "Computer 'Experiments' on Classical Fluids. I. Thermodynamical Properties of Lennard–Jones Molecules," Phys. Rev., **159**(98), pp. 98–103, or see also **165**, pp. 201–214.
[12] Beeman, D., 1976, "Some Multistep Methods for Use in Molecular Dynamics Calculations," J. Comput. Phys., **20**(2), pp. 130–139.
[13] Berendsen, H. J. C., Postma, J. P. M., van Gunsteren, W. F., DiNola, A., and Haak, J. R., 1984, "Molecular Dynamics With Coupling to an External Bath," J. Chem. Phys., **81**, pp. 3684–3690.
[14] Kotsalis, E. M., Walther, J. H., and Koumoutsakos, P., 2004, "Multipase Water Flow Iniside Carbon Nanotubes," Int. J. Multiphase Flow, **30**, pp. 995–1010.
[15] Onda, T., Shibuichi, S., Satoh, N., and Tsujii, K., 1996, "Super Water-Repellent Fractal Surfaces," Langmuir, **12**(9), pp. 2125–2127.

Downloaded 03 Jun 2010 to 171.66.16.156. Redistribution subject to ASME license or copyright; see http://www.asme.org/terms/Terms_Use.cfm

Scaling of the Wall Pressure Field Around Surface-Mounted Pyramids and Other Bluff Bodies

Robert Martinuzzi
Department of Mechanical and Manufacturing Engineering,
University of Calgary,
Calgary, AB, T2N 1N4, Canada

Mazen AbuOmar
Stantec Consulting Ltd.,
3260 Devon Drive,
Windsor, ON, N8X 4L4, Canada

Eric Savory
Department of Mechanical and Materials Engineering,
University of Western Ontario,
London, ON, N6A 5B9, Canada

The turbulent flow around square-based, surface-mounted pyramids, of height h, in thin and thick boundary layers was experimentally investigated. The influence of apex angle ζ and angle of attack α was ascertained from mean surface flow patterns and ground plane pressure measurements taken at a Reynolds number of 3.3×10^4 based on h. For both boundary layer flows, it was found that the normalized ground plane pressure distributions in the wakes of all the pyramids for all angles of attack may be scaled using an attachment length (X_a') measured from the upstream origin of the separated shear layer to the near-wake attachment point on the ground plane. It was also shown that this scaling is applicable to data reported in the literature for other bluff body shapes, namely, cubes, cones, and hemispheres. The ground plane pressure coefficient distributions in the upstream separated flow region, for all the shapes and angles of attack examined, were found to collapse onto two curves by scaling their streamwise location using a length scale (X_u), which is a function of the frontal projected width of the body (w') and the height of the body. These two curves were for cases where $\delta/h<1$ ("thin" boundary layer) or $\delta/h\geq1$ ("thick" boundary layer), where δ is the oncoming boundary layer thickness. Further work is required to provide a more detailed statement on the influence of boundary layer thickness (or state) on the upstream pressure field scaling.
[DOI: 10.1115/1.2754325]

Keywords: surface-mounted bluff body, pyramid, surface pressure distribution, scaling, topology, separation, attachment

1 Introduction

The study of separated, turbulent flows around even simple, surface-mounted, three-dimensional bluff bodies is fundamentally important for providing diagnostic tools to understand and predict more complex flows of industrial and environmental relevance. Generally, the flow separation process upstream of the obstacle and on the obstacle faces gives rise to complex, large-scale vortical structures [1–4], the relevance of which ranges from wind effects on buildings [5–10], dispersion of pollutants and changing wind patterns over rough terrain [11–14], to the cooling of electronic heat sinks [15,16]. Unlike flows over nominally two-dimensional surface-mounted bluff bodies, the mean orientation for the vortical structures may change downstream of the obstacle, giving rise to highly three-dimensional and much more complex flow patterns [1,3]. Yet, three-dimensional bluff body flows have received much less attention than their two-dimensional counterparts.

At moderate and high Reynolds numbers, the flow around different surface-mounted bluff bodies, such as rectangular obstacles [4–7,9,15], hemispheres [2,17,18], cones [12,13,19], or vertical cylinders [1,20–22], share many qualitative features. Typically, the adverse pressure gradient imposed by the obstacle causes the upstream separation of the oncoming flow, giving rise to a horseshoe vortex system, fed by the vorticity generated at the leading edge of the plate [1,22], which extends downstream on either side of the body [1–4,17–25]. A comprehensive review [22] of the separated flow structure upstream of rectangular bluff bodies and symmetrical, vertical cylinders of different cross-sectional shapes shows that the effect of body geometry and boundary layer conditions are both dependent on whether the incident flow is laminar or turbulent. For a turbulent boundary layer, the location of the upstream separation and of the primary core of the horseshoe vortex system in the plane of symmetry depend mainly on the body width. On closer inspection, blunt bodies, such as prisms, give rise to a longer separation region than more streamlined bodies, such as airfoils, of the same width. For obstacles of width w and height h, it is found that the location of the upstream separation, when measured from a point $w/2$ downstream of the frontal wall body junction, scales with boundary layer thickness δ for $h/w>1$. However, for $h/w<1$, the influence of the body geometry is significant, while the influence of the boundary layer thickness is very small. For laminar boundary layers, it is found that both the displacement thickness-to-body height ratio and the Reynolds number (based on the displacement thickness) are also significant parameters. To the authors' knowledge, a similar comparative study has not been published for tapered bodies, such as cones or hemispheres.

The flow structure in the wake of three-dimensional bluff bodies strongly depends on the obstacle shape, since the vorticity is mainly generated at the separation point on the obstacle faces [1,3]. For rectangular bluff bodies with $h/w<1$ [3], the wake flow structure corresponds to an owl-face pattern of the second kind, This mean wake flow pattern is characterized: (i) in the vertical plane of symmetry by a recirculation vortex (node) formed by a hairpin vortex extending downstream on either side of the plane of symmetry, and (ii) on the ground plane (wall) by two nodes on at the leeward base of the obstacle (a vortex tube extends downstream from each), an attachment node on the plane of symmetry, and two saddle points on each side as defined in [25]. The attachment length X_a along the line of symmetry depends on h/w and the oncoming boundary layer thickness-to-obstacle height ratio [3]. Furthermore, a partial streamwise collapse of the mean surface pressure distribution along the line of symmetry in the obstacle wake can be obtained, when the streamwise variable is

Contributed by the Fluids Engineering Division of ASME for publication in the JOURNAL OF FLUIDS ENGINEERING. Manuscript received September 6, 2006; final manuscript received March 20, 2007. Review conducted by Timothy J. O'Hern.

 Copyright © 2007 by ASME

Downloaded 03 Jun 2010 to 171.66.16.156. Redistribution subject to ASME license or copyright; see http://www.asme.org/terms/Terms_Use.cfm

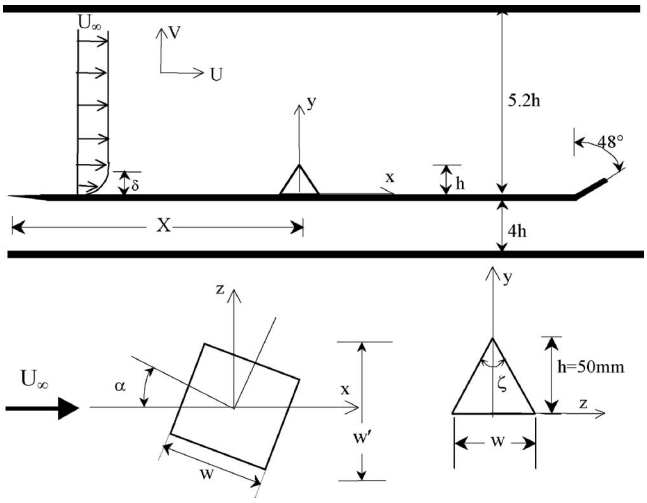

Fig. 1 Experimental setup and geometry

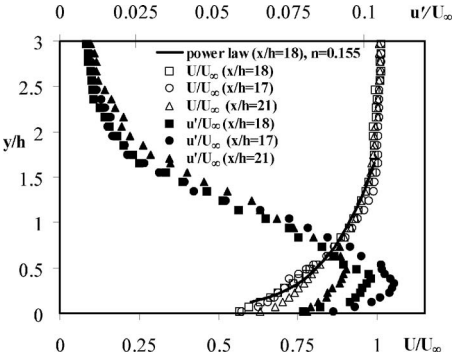

Fig. 2 Mean velocity, U/U_∞, and turbulence intensity, u'/U_∞, profiles of approach flow in a thick boundary layer at $X=17h$ and $X=18h$ as well as $X=21h$ (downstream of obstacle) as measured prior to placement of obstacle with apex at $X=20h$. Power-law fit is provided for $X=18h$ ($U_\infty=10$ m/s)

normalized by X_a, defined from the obstacle leading edge [3,15]. Tapered geometries, such as cones [12,13,19] or pyramids [10,23], are found to result in the generation of oblique shear layers. The influence of the resulting tilted vortical structures on wake mixing is still poorly understood. The generation of large hairpin vortices behind hemispheres [2,17,18] results in mean flow patterns topologically different from those behind rectangular bluff bodies [3,4]. For cones or pyramids, previous studies have concentrated mainly on qualitative observations of the flow structure and measurements of heat and mass transfer [10,12,16,19] or shedding characteristics [13,23]. The wake flow structure has not been extensively studied, and the program of research by the present authors is intended to examine the effect of the body geometry on pyramid wake flows.

The present paper focuses on the surface pressure distributions on the ground plane around differently tapered pyramids, together with the mean surface flow patterns deduced from oil-film surface visualization. The pyramid shape was selected for this study because it is fundamentally distinct. Because of the wall taper, its detailed wake structure is expected to differ from that of rectangular prismatic obstacles. Unlike cones or hemispheres, however, the separation point is fixed at the sharp edges and the wake should be less dependent on Reynolds number effects or oncoming turbulence level. The principal aim was to find appropriate scaling parameters for the upstream and downstream separated flow regions that may be applicable to all pyramid geometries, flow angles of attack and approach flow boundary layer conditions. A second aim was to ascertain whether such parametrization would also be applicable to other bluff body shapes. Because of the change in flow pattern (and shear layer separation location) with angle of attack, it was hypothesized that such a universal spatial scaling for the near wake wall pressure distribution would necessitate a length scale related to the distance from separation of the shear layer from the body to the reattachment point on the ground plane, rather than the conventional scaling from the geometrical center of the body to reattachment.

2 Experimental Details

The surface flow field was investigated for three different square-based, sharp-edged, surface-mounted pyramids placed in a thin and a thick boundary layer at Reynolds numbers, Re, ranging from 1.0×10^4 to 5.0×10^4, based on the pyramid height h and the freestream velocity U_∞. The flow geometry and nomenclature are shown schematically in Fig. 1. The experiments were carried out in a 460 mm$\times$460 mm cross-section, open-circuit suction-type wind tunnel with an inlet contraction ratio of 4:1, and a test section length of 800 mm. The freestream velocity ranged between $U_\infty=3$ m/s to $U_\infty=15$ m/s, and the freestream turbulence intensity u'/U_∞ was around 1.0%. Three pyramids of tip (apex) angles: $\zeta=45$ deg, 60 deg, and 90 deg, were tested at six angles of attack: $\alpha=0$ deg (one face normal to the flow), $\alpha=10$ deg, $\alpha=15$ deg, $\alpha=22.5$ deg, $\alpha=35$ deg, and $\alpha=45$ deg (one base tip aligned with the flow). The pyramids were of height $h=50$ mm, giving a maximum blockage ratio, based on the obstacle frontal area, of $\sim$2.7%, such that no blockage corrections were required for the data presented. A further model, namely, a cone of height 100 mm and apex angle $\zeta=28$ deg, had also been tested in the same thin laminar boundary used in the present study and, thus, those data were included in the analysis presented here.

Preliminary measurements of the undisturbed (i.e., in the absence of the obstacle) boundary layer velocity distribution were conducted using a Model TSI-1210 cylindrical straight probe single-wire hot-wire anemometer (HWA), with the freestream reference velocity being monitored by a linearized, ruggedized single probe (Model TSI-1266). The outputs from both probes were sampled at 1000 Hz. For the thin boundary layer experiments, the HWA measurements showed that the undisturbed boundary layer was laminar and the velocity distribution followed the Blasius profile with a boundary layer thickness of $\delta\approx0.1h$ at $X=6h$. The obstacles were mounted with the apex at $X=6h$ downstream of the plate leading edge.

The thick, turbulent boundary layer was created by a 9 mm high horizontal barrier at the plate leading edge, followed by a fetch ($9h$ length) comprising three 5 mm wide and 3 mm high two-dimensional rectangular block roughness elements spaced 90 mm apart in the streamwise direction and spanning the working section, followed by three rows of 5 mm wide and 2 mm high two-dimensional rectangular block roughness elements spaced 80 mm apart in the streamwise direction, also spanning the test section. The mean velocity and turbulence intensity profiles at $X=18h$ downstream of the plate leading edge are shown in Fig. 2. At this location, the boundary layer thickness was $\delta\approx2h$, whereas the displacement and momentum thickness were $0.25h$ and $0.18h$, respectively. The mean velocity profile followed a power-law distribution with coefficient 0.155. The maximum turbulence intensity was 11% and occurred at $\approx0.45h$ above the plate. The value of the surface roughness parameter z_o for the boundary layer was 0.089 mm, and the normalized friction velocity u_*/U_∞, was 0.038, as determined by fitting the standard logarithmic-law relationship $U/u_*=2.5\ln([y-d]/z_o)$, to the experimental data, while choosing the zero plane displacement value d to give the best fit near the wall. The pyramids were placed on a smooth section of the plate, with the pyramid tip located at $X=20h$ from the leading edge and

Downloaded 03 Jun 2010 to 171.66.16.156. Redistribution subject to ASME license or copyright; see http://www.asme.org/terms/Terms_Use.cfm

$6h$ from the last roughness element. Also included in Fig. 2 are the velocity and turbulence intensity distributions at $X=17h$ and $X=21h$.

A total of 550 pressure taps of 0.8 mm dia were uniformly distributed on the plate around the pyramid at intervals of 5 mm and 10 mm in the spanwise and the streamwise directions, respectively. The frequency response of the pressure-sensor-tapping-tube system to imposed pressures at different discrete frequencies produced through a speaker was determined to be flat to 100 Hz (3 dB cutoff at 140 Hz). Sixteen Data Instruments DCA4 differential pressure transducers were used to measure the pressure, simultaneously, at different locations. The continuous signal was acquired with a 12-bit, 16-channel A/D acquisition card at sampling rates of 1000 Hz for 10 s record lengths. The freestream velocity U_∞ was also measured with the HWA during each set of pressure measurements, using the same sampling rate and recording length, with the uncertainty for U_∞ being ±0.7%. The differential pressure transducer had a range of 0–250 Pa and a resolution of ±0.26 Pa. The standard deviation of the pressure signal calibration curve, based on linear regression analysis, was ±0.8% of the full scale. The digitization uncertainty based on the acquisition card was ±0.4 Pa. Mean pressure P results are shown in terms of the pressure coefficient, $Cp=(P-P_\infty)/(1/2)\rho U_\infty^2$, where ρ is the air density and P_∞ is the reference static pressure from a freestream pitot-static tube. The fluctuating pressures are given by $Cp_{\rm rms}=p'/(1/2)\rho U_\infty^2$, where p' is the standard deviation (rms) of the pressure fluctuations. The resulting uncertainty in $Cp=\pm 0.035$ and in $Cp_{\rm rms}=\pm 0.015$ at $\mathrm{Re}=3.3\times 10^4$, and these are shown as error bars in the figures.

Preliminary measurements showed that the pressure distribution was symmetric about the X-axis with the model at $\alpha=0$ deg and 45 deg. Hence, symmetry was assumed for all the $\alpha=0$ deg and 45 deg cases, with pressure measurements taken over only one side of the ground plane.

Oil-film surface flow visualization, following the principles given in [26], was carried out in order to provide the mean surface flow shear patterns from which the near-wall large-scale flow structure could be deduced. Approximately 10 ml of graphite powder (photocopier machine toner) was added to 100 ml of light transmission oil. Then, 20 ml of kerosene was added to the mixture, which was immediately painted on the ground plane and the wind tunnel switched on. These visualizations were recorded on a digital camera and used in conjunction with topological principles [1,25] to ascertain the surface flow structure, including the mean locations of flow separation and attachment that were determined to within ±3 mm ($\pm 0.06h$).

3 Results and Discussion

The characteristics of the mean flow and pressure field around square-based, sharp-edged, surface-mounted pyramids in thin and thick boundary layers are presented. Tests were conducted for three different pyramids (apex angles: $\zeta=45$ deg, 60 deg and 90 deg) at six angles of attack: $0\ \mathrm{deg}\le\alpha\le 45$ deg, for $1.0\times 10^4<\mathrm{Re}<5.0\times 10^4$ in thin ($\delta/h\approx 0.1$) and thick ($\delta/h\approx 2.0$) boundary layers. The influence of Re in this range was found to be small, within experimental uncertainty, and so only data from the case with $\mathrm{Re}=3.3\times 10^4$ (that is, with a freestream velocity of 10 m/s) are presented in this paper.

The present authors have previously shown [23] that, based on the wake flow periodicity and mean velocity distribution for the thin boundary layer case, the pyramids can be classified as slender ($\zeta<75$ deg) or broad ($\zeta\ge 75$ deg). For slender pyramids, it was shown that wake periodicity occurs only for thin boundary layers and is related to the regular shedding of vortices formed on the obstacle side faces and base region. The shedding frequency scales with $L=w'/\sqrt[4]{w'/h}$, where w' is the frontal projected width of the pyramid base. For the broad pyramids, it is observed that the periodic vortex shedding occurs only for thin boundary layers and above a critical angle of attack α. In this section, the mean ground plane flow patterns and pressure distributions for slender pyramids in thick and thin boundary layers are compared. Subsequently, the influence of the apex angle ζ and angle of attack α are discussed.

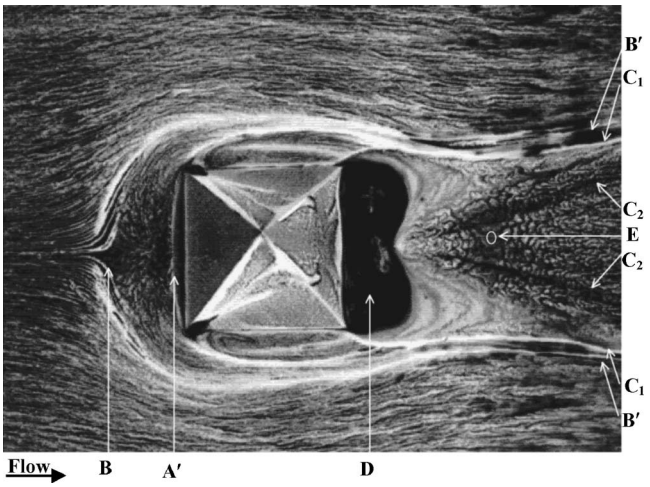

Fig. 3 Oil-film flow patterns around pyramid $\zeta=60$ deg for $\alpha=0$ deg in thin boundary layer ($\mathrm{Re}=3.3\times 10^4$)

3.1 Wall Flow Around Slender Pyramids ($\zeta<75$ deg) at $\alpha=0$ deg. It was found [23] that the flow around pyramids mounted normal to the flow, $\alpha=0$ deg, is similar for all slender pyramids ($\zeta<75$ deg) and so the $\zeta=60$ deg pyramid case only is used here as an example for discussion.

3.1.1 Thin Boundary Layer Case. The mean flow pattern obtained with the oil-film visualization technique is shown in Fig. 3 for the thin boundary layer case. The mean Cp and fluctuating $Cp_{\rm rms}$ pressure coefficients are shown in Fig. 4. The oncoming flow separates along the pigment accumulation line originating at the saddle point, marked **B** in Fig. 3, due to the rapid increase in the adverse pressure gradient (Fig. 4(*b*); marked B in P1). The separated shear layer roles up to form a horseshoe vortex similar to those observed for cubes [3,4,6], hemispheres [2,18], and cones [12,16,19]. The core of the primary horseshoe vortex is located downstream of the separation line, slightly upstream of the white band marked **A′** in Fig. 3. This white band results from the pigment being swept away due to the high shear rates induced by the vortex motion. This motion also results in the slight pressure drop upstream of the obstacle observed in Fig. 4(*b*), P1. Several counterrotating secondary vortices are located between the separation line **B′**, extending from the saddle point at **B**, and the primary horseshoe vortex (**A′**). Such secondary structures have been observed for other bluff bodies in thin, laminar boundary layers [2,19,22–24]. These secondary structures are entrained into the primary horseshoe vortex as the system is deflected downstream [22].The separation line **B′** is deflected downstream and is a negative bifurcation line (flow converges). The core of the horseshoe vortex extension is roughly located above this line.

In the near wake, the oil-film results show two vorticity concentration nodes, with their centres marked **D** in Fig. 3. These nodes are the footprints of two counterrotating vortex tubes and the Cp contours (Fig. 4(*a*) and 4(*b*), P3) at $x/h=0.75$ show that a high suction pressure exists there, together with high-pressure fluctuations, $Cp_{\rm rms}$, in Fig. 4(*b*), P3. Further downstream, the flow attaches at the node marked **E** in Fig. 3. The present authors' previous velocity measurements [23] show that the flow along $z/h=0$ is a *downwash* directed toward the ground plane. The impinging mass flux forces the wake to expand, forming a necklace pattern downstream of the attachment point **E**. As a result, there is

Downloaded 03 Jun 2010 to 171.66.16.156. Redistribution subject to ASME license or copyright; see http://www.asme.org/terms/Terms_Use.cfm

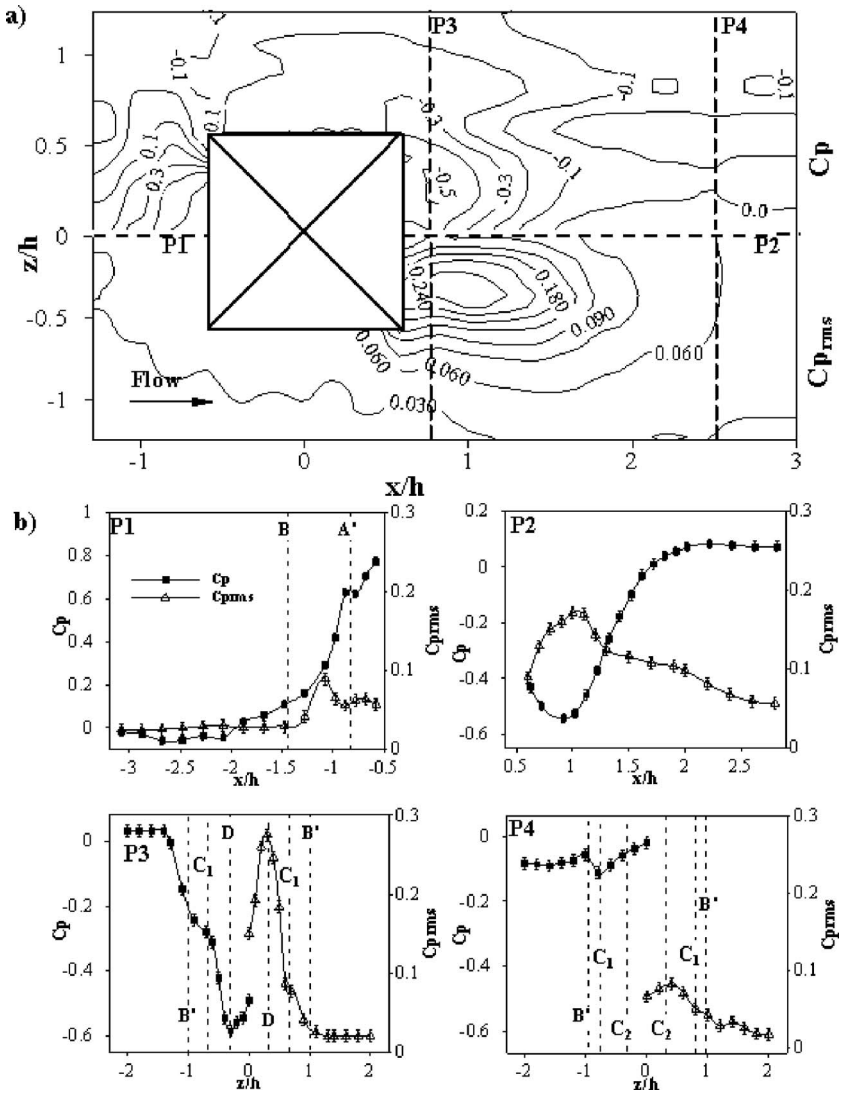

Fig. 4 (*a*) *Cp* and Cp_{rms} contours around pyramid $\zeta=60$ deg at $\alpha=0$ deg and Re $=3.3\times10^4$ in thin boundary layer and (*b*) profiles along different sections labeled in (*a*). Letters correspond to flow structures in Fig. 3.

a positive bifurcation line along $z/h=0$. Since the vorticity concentrations about the node **D** cause fluid to move towards the plane $z/h=0$, two saddle points must exist, located symmetrically about **E**, from which the two negative bifurcation lines, $\mathbf{C_2}$, extend downstream. Since the flow and, hence, the pigment, converge along these lines, these appear as slightly darker traces. The nature of the lines $\mathbf{C_2}$ was verified using different color pigments (not shown here). The pigments could be observed to converge but not cross these critical lines. Following previous work [1,25], to be topologically consistent, a positive bifurcation line (flow diverges) must exist between $\mathbf{B}'$ and $\mathbf{C_2}$. This line matches the low-pigment (white) line indicated as $\mathbf{C_1}$ in Fig. 3, and it coincides with the location of the slight depression in the *Cp* distribution for profile P4 shown in Fig. 4(*b*). The pressure distribution along $z/h=0$ in the wake initially shows a pressure drop. The minimum is located roughly at the downstream location of the center of nodes marked **D**. Further downstream, there is a pressure recovery. The Cp_{rms} distribution shows a maximum close to the minimum *Cp* streamwise location (Fig. 4(*b*), P2).

3.1.2 Thick Boundary Layer Case. The oil-film surface flow visualization for the pyramid $\zeta=60$ deg at $\alpha=0$ deg in the thick boundary layer is shown in Fig. 5. The flow patterns due to the upstream separation and the downstream extension of the horseshoe vortex are qualitatively similar to those for thin boundary layers. The location of the separation point **B** changes little with δ, this behavior being similar to that observed for vertically mounted cylinders of different shapes [22]. The position of the line $\mathbf{A}'$, which is associated with the location of the primary horseshoe vortex (and a local pressure drop along P1 in Fig. 6(*a*)), occurs closer to the obstacle for larger δ. This observation is consistent with earlier work (reviewed in [22]) showing that, for turbulent boundary layers, the location of the primary vortex core is generally closer to the obstacle and relatively insensitive to the oncoming boundary layer thickness when compared to laminar boundary layers.

In the wake, for thick boundary layers, the nodes **D** are located closer to the obstacle than for the thin case. Further downstream only one (positive) bifurcation line $\mathbf{C}'$ is observed. As a result, the bifurcation line along the plane of symmetry ($z/h=0$) is now a negative bifurcation. During the oil-film experiments, it was confirmed that pigment is entrained from $\mathbf{C}'$ to the plane of symmetry. These observations suggest that there is a general *upwash* along $z/h=0$ downstream of the attachment node **E**, as can be inferred from measurements made in atmospheric boundary layers

Downloaded 03 Jun 2010 to 171.66.16.156. Redistribution subject to ASME license or copyright; see http://www.asme.org/terms/Terms_Use.cfm

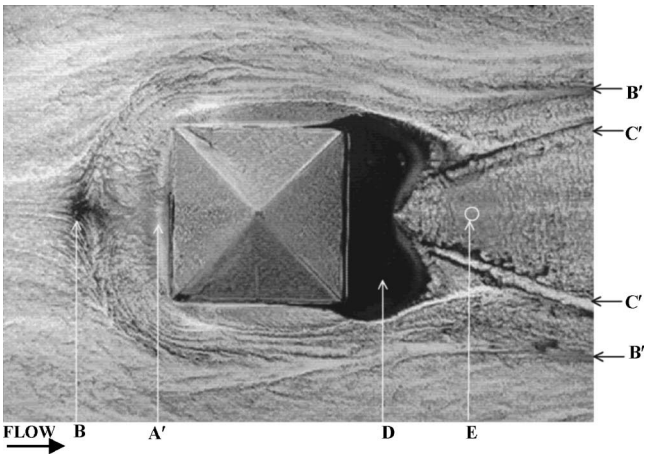

Fig. 5 Oil-film flow patterns around pyramid ζ=60 deg and α =0 deg in thick boundary layer

for similar pyramid apex angles [10]. The line **C′** appears to originate between the node **D** and the plane of symmetry, while the line $\mathbf{C_1}$, for the thin boundary layer case (shown in Fig. 3), originates at the trailing-edge corner of the pyramid, suggesting that these lines arise differently. Thus, the wake structure is significantly different from that for the thin boundary layer case.

The wall pressure distribution for the pyramid ζ=60 deg at α =0 deg in the thick boundary layer is shown in Fig. 6. The patterns of Cp and Cp_{rms} contours are generally similar to those observed for thin boundary layers (see Fig. 4), but their magnitudes are much less for the thick boundary layer case. For example, along z/h=0, Cp upstream of the pyramid approaches 0.80 and the minimum in the wake trough approaches −0.55 for the thin boundary layer. For the thick boundary layer case, these values are reduced to 0.25 and −0.30, respectively.

A similar observation is made for Cp_{rms}. The difference in Cp and Cp_{rms} levels can be related to the flow inertia. For thin boundary layers, the pyramid extends above the wall layer and, there-

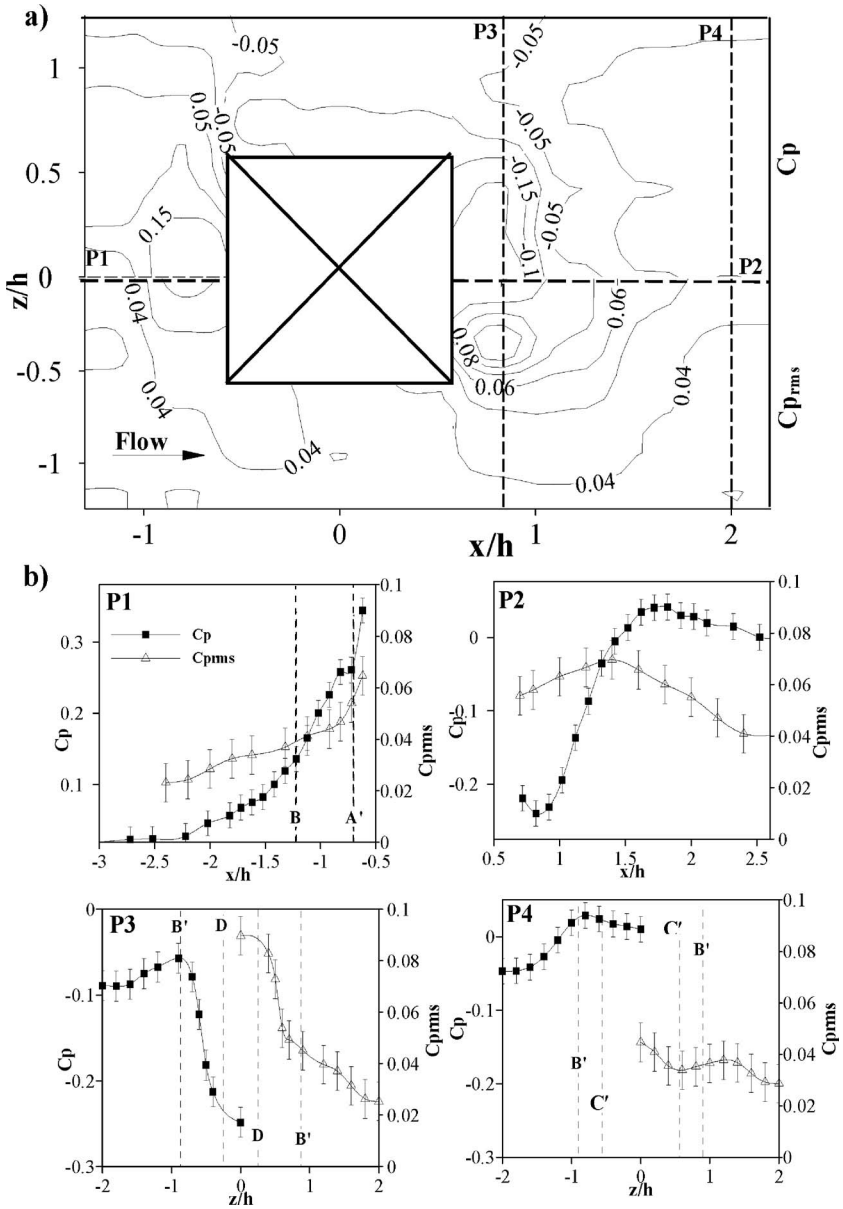

Fig. 6 (*a*) *Cp* and Cp_{rms} contours around pyramid ζ=60 deg at α=0 deg and Re =3.3×10^4 in thick boundary layer and (*b*) profiles along different sections labelled in (*a*). Letters correspond to flow structures in Fig. 5.

Downloaded 03 Jun 2010 to 171.66.16.156. Redistribution subject to ASME license or copyright; see http://www.asme.org/terms/Terms_Use.cfm

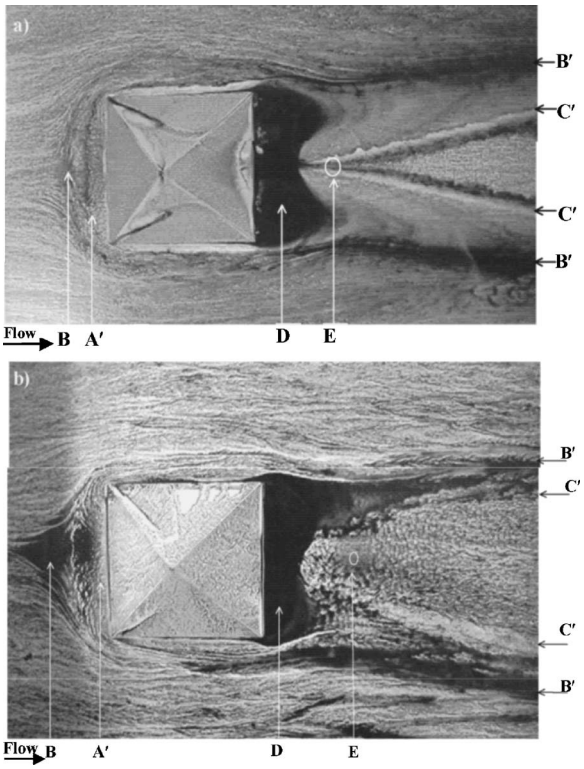

Fig. 7 Oil-film picture for pyramid ζ=90 deg for α=0 deg in (*a*) thin boundary layer and (*b*) thick boundary layer (Re=3.3 $\times 10^4$)

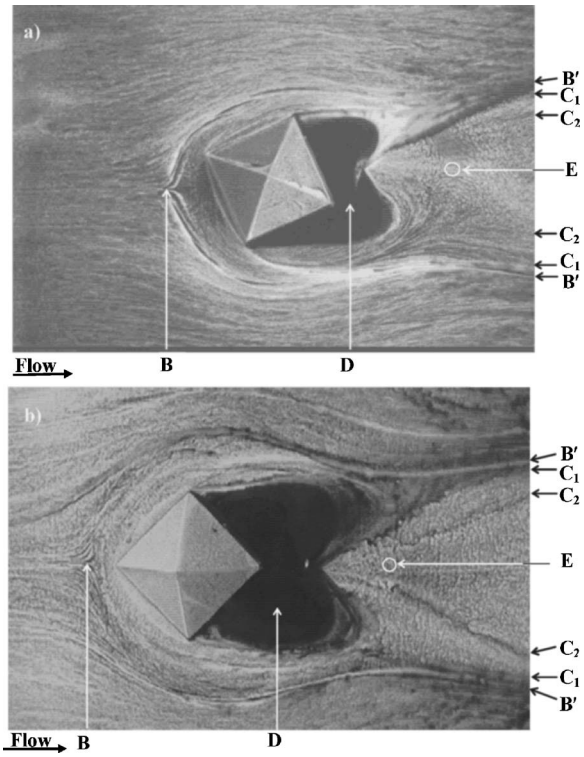

Fig. 8 Oil-film flow pattern for pyramid ζ=60 deg in thin boundary layer at (*a*) α=22.5 deg and (*b*) α=45 deg

fore, is exposed to high inertia fluid. For the thick boundary layer case, the pyramid is immersed in lower-momentum fluid. It follows that the energy content and, thus, the maximum resulting pressure fluctuations, will be lower relative to the kinetic energy of the freestream flow. From the above results, it may be noted that the Cp and Cp_{rms} distributions over the center line, z/h=0 are representative of the changes in magnitude of the entire wall surface field. Therefore, the pressure coefficient along z/h=0 will be used for further comparisons in this paper.

3.2 Wall Flow Around Broad Pyramids (ζ>75 deg) at α =0 deg. As noted above, for a given oncoming boundary layer, the flow patterns are very similar for the slender pyramids (ζ <75 deg) at α=0 deg. In addition, periodic vortex shedding form the obstacle side faces is observed in the thin but not for the thick boundary layer case [23]. For broad pyramids, however, (ζ >75 deg) at α=0 deg, there is no evidence of periodic vortex shedding for either boundary layer case. In this section, it will be shown that the resulting flow patterns for broad pyramids are similar for both boundary layers and are more akin to those observed around slender pyramids for the thick (turbulent) boundary layer case.

Oil-film images of the surface flow patterns observed for the broad pyramids are similar to those for ζ=90 deg pyramid at α =0 deg shown in Figs. 7(*a*) and 7(*b*) for the thin and thick boundary layers, respectively. In each case, the footprint of the horseshoe vortex system is easily identified upstream and to the sides of the obstacle. The concentration nodes **D** and the negative (converging flow) bifurcation line **B′** are easily recognized. Similarly to the slender pyramids in the thick boundary layer case, there is a single positive bifurcation line **C′** between **B′** and the negative (converging) bifurcation line along z/h=0. This pattern indicates a general *upwash* in the wake along $\mathbf{z/h}$=0, as confirmed by the previous velocity measurements along the plane of symmetry [23]. Hence, the surface flow patterns for the broad pyramids in both the thin and thick boundary layer are similar to those of the slender pyramids in the thick boundary layer (see Fig. 5). This indicates that where periodic vortex shedding is not present, the flow structure is always similar but different to that observed when vortex shedding occurs.

3.3 Influence of Angle of Attack (α). Figure 8 provides an illustration of the effect of changing the flow angle of attack and shows the oil-film surface flow patterns for a slender pyramid (ζ =60 deg) at α=22.5 deg and 45 deg in the thin boundary layer. Considering first the case of α=45 deg, shown in Fig. 8(*b*), it may be seen that the topology of the flow patterns is similar to that observed for α=0 deg. The footprint of the horseshoe vortex (line **B′**) and the wake vortices (marked **D**) are easily recognized. Careful inspection allows identification of the positive and negative bifurcation lines, $\mathbf{C_1}$ and $\mathbf{C_2}$, respectively, from which it can be inferred that a positive bifurcation occurs at z/h=0 (implying a downwash in the wake). For α=22.5 deg, these features can also be identified but are distorted due to the inherent asymmetry as shown in Fig. 8(*a*).

Inspection of the oil-film surface flow patterns for the other cases studied (not shown here) allows similar observations. For slender pyramids in thick boundary layers and for broad pyramids in both thin and thick boundary layers, the flow topology at α =22.5 deg and α=45 deg is similar to that observed for α =0 deg, for the same flow conditions. The line **B′** and the nodes marked **D** are easily recognized and only the positive bifurcation line **C′** is observed in the wake (see Figs. 5 and 7).

The pressure distributions on the ground plane around the obstacle provide a good indication of the extents of the upstream and downstream flow recirculation regions. Hence, the question of whether the changes in these distributions (reflecting the near-wall flow structure) with angle of attack, model geometry, and boundary layer conditions can be taken into account by use of suitable scaling variables is addressed in Sec. 3.4.

Downloaded 03 Jun 2010 to 171.66.16.156. Redistribution subject to ASME license or copyright; see http://www.asme.org/terms/Terms_Use.cfm

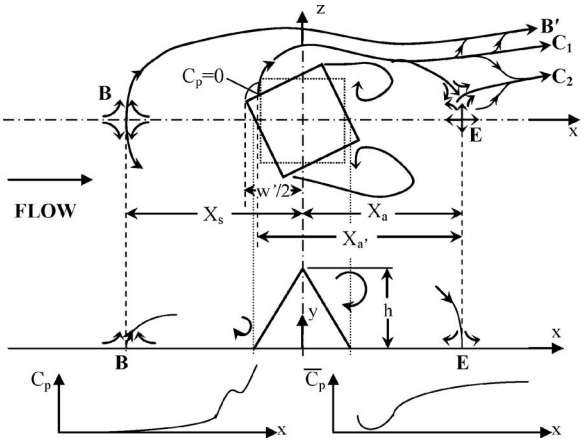

Fig. 9 Schematic representation of the more pertinent length scales in relation to the main topological features and geometric parameters

3.4 Scaling of the Ground Plane Pressure Distributions. The choice of suitable length scales for the ground plane mean pressure distribution along a line passing through the obstacle geometric center is discussed in this section. It will be shown that the chosen upstream and downstream length scales are appropriate for scaling results from different geometries and conditions. To facilitate the ensuing discussion, Fig. 9 provides a summary of the more pertinent length scales in relation to the main topological features and geometric parameters.

3.4.1 Pressure Distribution in the Upstream Separated Flow Region. Figures 10(*a*) and 10(*b*) show the mean pressure coefficient distribution along $z=0$ for the pyramid at all the measured angles of attack in the thin and thick boundary layers, respectively. In the figure legends, the data series are referenced first by the apex angle, with the angle of attack after the hyphen. The x location is scaled by the length of the upstream separated flow region X_s, measured from the point of separation (marked **B** in Figs. 3, 5, 7, and 8) to the center of the obstacle, as determined from the oil-film images. It was found that the alternative approach of measuring X_s from separation to the upstream edge of the base of the obstacle along $z=0$ produced a much poorer collapse of the data. Also included are relevant data from other workers for a cone with $\delta/h=0.16$ [19], a cube with $\delta/h=0.99$ [6], and a hemisphere with both $\delta/h=1.23$ and 2.47 [18]. Although the collapse is not particularly good, especially for the cube data, it may be seen that the data fall into either the "thin" or "thick" boundary layer categories, depending on whether $\delta/h<1$ ("thin") or $\delta/h\geq 1$ ("thick"). Ballio et al. [22] investigated the location of the upstream separation point for different surface-mounted, symmetrical, vertical (i.e., nontapered) obstacles of height h and width w'. They found that, for a given geometry, X_s/w' depends only on h/w' when $\delta_*/w'>0.01$, where δ_* is the boundary layer displacement thickness and X_s is referenced to $w'/2$ downstream of the leading face. However, this scaling does not appear to be appropriate for collapsing the data from the wide range of different shapes studied in the present work.

It is likely that the length of the upstream ground plane pressure distribution will scale with some measure of the bluffness, or blockage, of the obstacle. Renormalizing x by $A^{1/2}$, where A is the projected frontal area of the obstacle, produces an improved scaling (not shown here) for all the pyramid data, within each of the two δ/h categories. However, there must be a restriction on the applicability of this simple area scaling in terms of body aspect ratio, w'/h (the data presented here being within $0.8<w'/h<3$), since very broad (nominally 2D) or very tall bodies will have upstream pressure distributions that are eventually independent of aspect ratio. To account for the obstacle shape and aspect ratio, the scaling $X_u=\sqrt{\bar{w}/w'}\bullet(\bar{w}/h/\bar{w}/h+1)h$ was developed, where $\bar{w}=A/h$ represents an average obstacle width, $\bar{w}/w'$ is a shape factor (with w' being defined as the projected width of the base of the obstacle) and $\bar{w}/h\bar{w}/h+1$ represents the influence of the aspect ratio. As required, in the limit of very broad or very tall bodies, X_u scales with h or w', respectively, and with $A^{1/2}$ for aspect ratios close to 1. Scaling the data with X_u provides a good collapse of the upstream pressure distribution for the different bodies and angles of attack for a given δ/h category, as shown in Figs. 11(*a*) and 11(*b*).

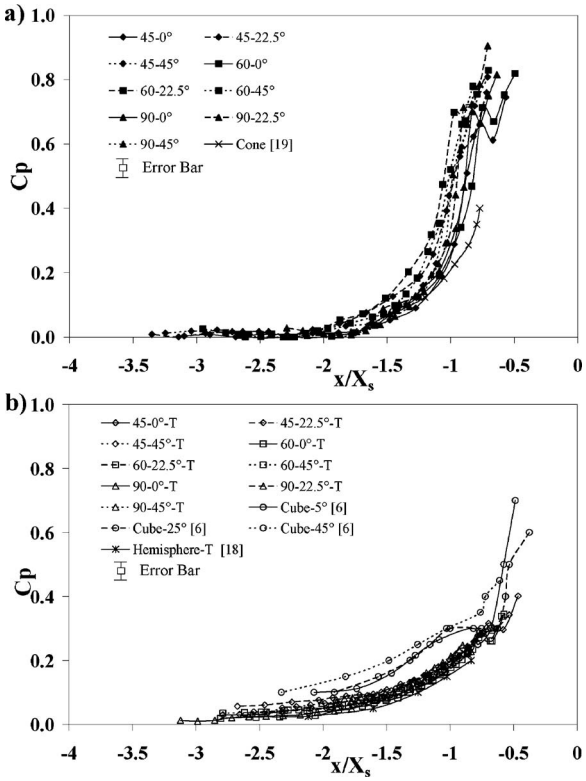

Fig. 10 *Cp* distribution along $z/h=0$, with position scaled using length of separated flow region X_s, for the bluff bodies in (*a*) thin boundary layer and (*b*) thick boundary layer (*T* is used to indicate thick boundary layer data)

It was not possible to find a suitable scaling for these pressure coefficient distributions that will collapse all the experimental data from both boundary layer categories onto a single curve, whether by using the stagnation pressure on the front face of the body, the dynamic pressure of the boundary layer at $y=h$, or the wall shear stress, based on u_*.

3.4.2 Pressure Distribution in the Near Wake Region. It has been shown previously that reexpressing the wall pressure coefficient distribution in terms of a modified coefficient, defined as $\bar{C}p=[(\mathrm{Cp}-\mathrm{Cp}_{\min})/(\mathrm{Cp}_{\max}-\mathrm{Cp}_{\min})]$, leads to a collapse of the Cp distribution in the near wake of several different 2D bluff body geometries [27]. Here, $Cp_{\min}$ is the minimum pressure located in the recirculation zone and $Cp_{\max}$ is the pressure at the end of the recovery region. The wake wall pressure distributions along $z=0$ for the bodies discussed in Sec. 3.4.1, expressed in terms of $\bar{C}p$, are presented in Figs. 12(*a*) and 12(*b*), for the two boundary layer categories, respectively. The legends Fig. 12 are defined in the same way as in the earlier figures. The conventional normalizing length scale for x has been used here, namely, the attachment length X_a, measured from the center of the obstacle to the point of mean reattachment of the shear layer, as determined from flow

Downloaded 03 Jun 2010 to 171.66.16.156. Redistribution subject to ASME license or copyright; see http://www.asme.org/terms/Terms_Use.cfm

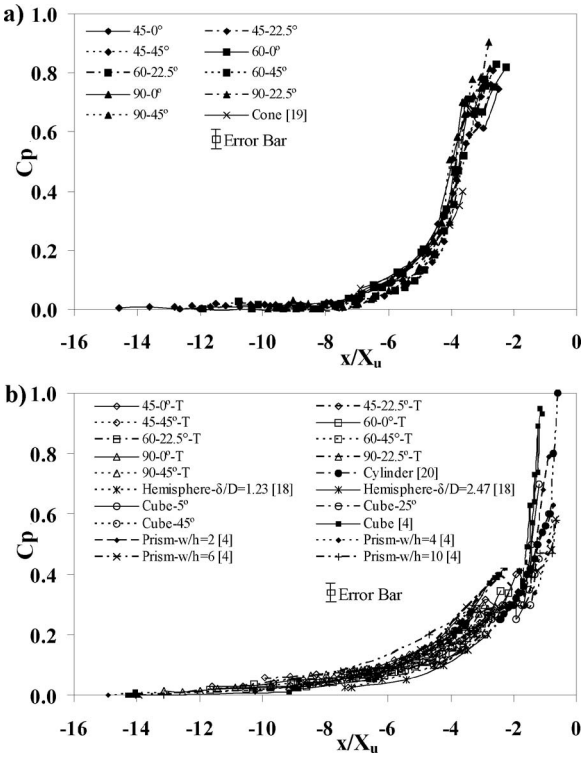

Fig. 11 Upstream Cp distribution along $z/h=0$ with position scaled using X_u for bluff bodies in (*a*) thin boundary layer and (*b*) thick boundary layer

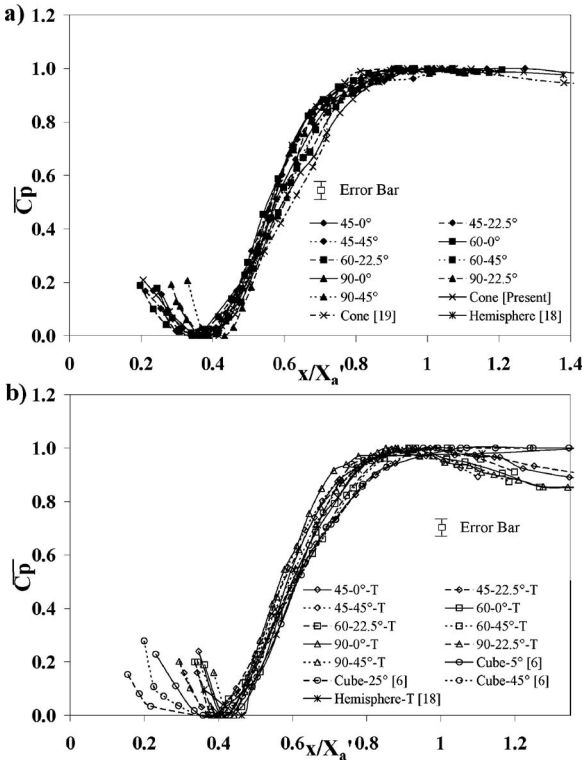

Fig. 13 Ground plane pressure distribution downstream of the bluff bodies, $\bar{C}p=[(Cp-Cp_{min})/(Cp_{max}-Cp_{min})]$, with location scaled by X'_a in (*a*) thin boundary layer and (*b*) thick boundary layer

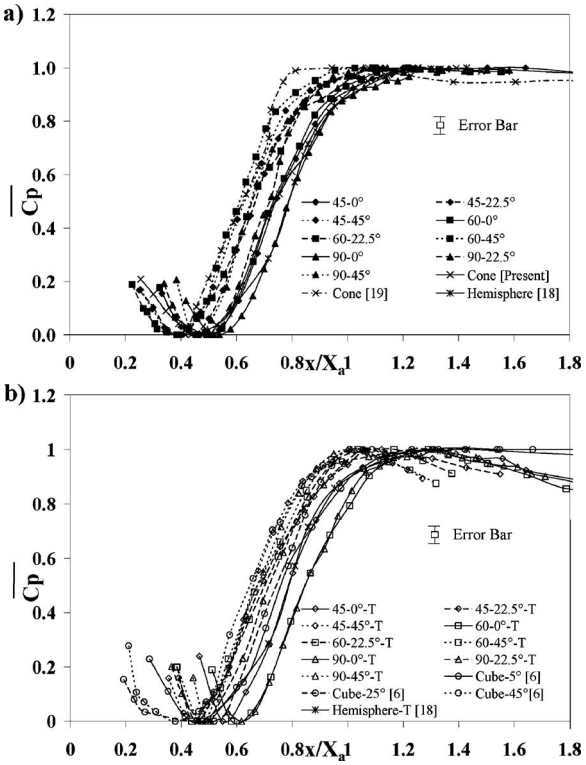

Fig. 12 Ground plane pressure distribution downstream of the bluff bodies, $\bar{C}p=[(Cp-Cp_{min})/(Cp_{max}-Cp_{min})]$, with location scaled by X_a in (*a*) thin boundary layer and (*b*) thick boundary layer

visualization images. When comparing the distributions for the different obstacles and different angles of attack, it may be seen that the collapse is extremely poor and greatly in excess of any experimental uncertainty. This is, perhaps, unsurprising since choosing a fixed point (the center of the obstacle) for scaling X_a is not appropriate when it is evident that the location of the shear layer separation from the body will vary with both body shape and angle of attack. Hence, a more suitable scaling has been sought that reflects the complete length of the recirculation region from the origin of the separated shear layer to its subsequent reattachment. It was found that the streamwise length X'_a, measured from the mean attachment point to the location where $Cp=0$ on the ground plane adjacent to the most upstream face of the obstacle resulted in a greatly improved collapse of the data sets for all the bodies, as shown in Figs. 13(*a*) and 13(*b*). The $Cp=0$ location provides a sensible and consistent reference point since it is approximately at the center of the strong pressure gradient region, where the shear layer vorticity near the ground is being generated immediately prior to separation. Not only does X'_a scale the pressure distributions within the different δ/h categories, it may be seen from Figs. 14(*a*) and 14(*b*) that it also makes the distributions (except very close to the body where the local geometry will be important) practically independent of boundary layer conditions (Fig. 14(*b*)). This is not the case when the conventional scaling by X_a is used (Fig. 14(*a*)). This finding suggests that, irrespective of the differences in the formation of the shear layer due to different boundary layer conditions, the resulting ground plane pressure distribution is strongly correlated with the streamwise extent of that shear layer after separation.

4 Concluding Remarks

The influence of obstacle taper on the mean near-wall flow around surface-mounted, sharp-edged, square-based pyramids was

Downloaded 03 Jun 2010 to 171.66.16.156. Redistribution subject to ASME license or copyright; see http://www.asme.org/terms/Terms_Use.cfm

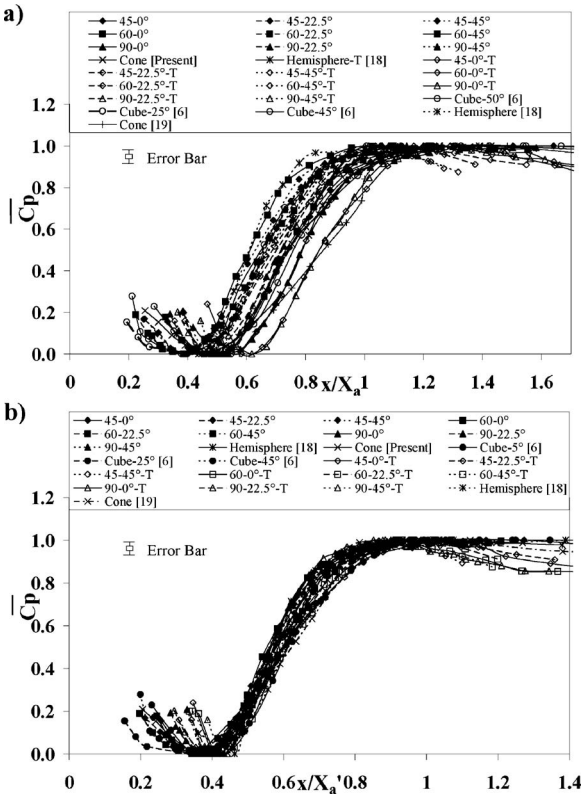

Fig. 14 Ground plane pressure distribution, $\bar{C}p=[(Cp-Cp_{min})/(Cp_{max}-Cp_{min})]$, downstream of all the bodies in all the boundary layers, with location scaled by (*a*) X_a and (*b*) X'_a

experimentally investigated. Surface pressure distributions and mean surface flow patterns for several pyramids of different apex angle ζ as a function of the angle of attack α in a thin and a thick oncoming boundary layer were measured, with the surface pressure data compared to those obtained for other bluff body shapes, namely, a cone, a hemisphere, a cube, and square cross-sectional prisms ($w/h \leq 10$).

Differences in the surface flow patterns downstream of the pyramids in the thick and thin boundary layers suggest significant topological differences in the mean wake flow structure. In particular, for those cases where periodic vortex shedding was previously found to occur [23], namely, slender pyramids ($\zeta < 75$ deg) in a thin boundary layer, the surface flow topology presented here, together with previous flow field velocity measurements, demonstrate that downwash occurs on the wake centerline. In contrast, for broad pyramids ($\zeta \geq 75$ deg) in a thin boundary layer, and all pyramids in a thick boundary layer, where vortex shedding was found not to occur, there is an upwash in the near-wake centerline.

Irrespective of the detail of the near-wake structure, this paper has shown that a suitable scaling approach may be used to achieve a collapse of the mean ground plane surface pressure distributions around a wide range of different surface-mounted bluff bodies, based on geometrical considerations (namely, a simple function of the frontal projected width of the base and the height of the body for the upstream wall pressure distribution) and a first-order assessment of the length of the separated shear layer from the body (namely, the overall streamwise extent of the separated flow region for the near-wake wall pressure distribution). However, the present scaling for the pressure distribution upstream of bluff obstacles is still incomplete since the influence of the oncoming boundary layer thickness (or state) could not be quantified. Furthermore, additional work is required in order to fully describe the near-wake formation processes and flow topologies associated with the various pyramid configurations discussed here and this will be the subject of a subsequent paper.

Nomenclature

A = frontal projected area of body
Cp = mean pressure coefficient
Cp_{rms} = rms pressure coefficient
h = height of body
P = pressure
p' = rms of pressure fluctuations
Re = Reynolds number$=hU_\infty/\nu$
U = streamwise velocity component
U_∞ = freestream velocity
u' = rms of the streamwise velocity component
u_* = friction velocity
w = width of base of body
$\bar{w}$ = average projected width of body
w' = frontal projected width of base of body
x = distance along streamwise axis from center of body
X = distance from leading edge on ground plane
X_a = attachment length (from geometrical center of body)
X'_a = attachment length (from location of separation on upstream side of body)
X_s = upstream separation length (from geometrical center of body)
X_u = scaling parameter for upstream pressure distribution
y = distance along vertical axis
z = distance along lateral axis
α = angle of attack
δ = boundary layer thickness
δ_* = boundary layer displacement thickness
ν = kinematic viscosity of fluid
ρ = density of fluid
ζ = pyramid or cone tip (apex) angle

References

[1] Hunt, J. C. R., Abell, C. J., Paterka, J. A., and Woo, H., 1978, "Kinematical Studies of the Flow Around Free or Surface-Mounted Obstacles; Applying Topology to Flow Visualization," J. Fluid Mech., **86**, pp. 179–200.
[2] Acarlar, M. S., and Smith, C. R., 1987, "A Study of Hairpin Vortices in a Laminar Boundary Layer. Part 1. Hairpin Vortices Generated by a Hemisphere Protuberance," J. Fluid Mech., **175**, pp. 1–41.
[3] Schofield, W., and Logan, E., 1990, "Turbulent Shear Flow Over Surface Mounted Obstacles," ASME J. Fluids Eng., **112**, pp. 376–385.
[4] Martinuzzi, R., and Tropea, C., 1993, "The Flow Around Surface-Mounted, Prismatic Obstacles Placed in a Fully Developed Channel Flow," ASME J. Fluids Eng., **115**, pp. 85–92.
[5] Bearman, P. W., and Obasaju, E. D., 1982, "An Experimental Study of Pressure Fluctuations on Fixed and Oscillating Square-Section Cylinders," J. Fluid Mech., **119**, pp. 297–321.
[6] Sakamoto, H., 1982, "Flow Around a Cubic Body Immersed in a Turbulent Boundary Layer," J. Wind. Eng. Ind. Aerodyn., **9**, pp. 275–293.
[7] Kanda, J., and Choi, H., 1992, "Correlating Dynamic Wind Force Components on 3-D Cylinders," J. Wind. Eng. Ind. Aerodyn., **41–44**, pp. 758–796.
[8] Tieleman, H. W., Surry, D., and Lin, J. X., 1994, "Characteristics of Mean and Fluctuating Pressure Coefficients Under Corner (Delta Wing) Vortices," J. Wind. Eng. Ind. Aerodyn., **52**, pp. 263–275.
[9] Lin, J. X., Surry, D., and Tieleman, H. W., 1995, "The Distribution of Pressure Near Roof Corners of Flat Roof Low Buildings," J. Wind. Eng. Ind. Aerodyn., **56**, pp. 235–265.
[10] Ikhwan, M., and Ruck, B., 2006, "Flow and Pressure Field Characteristics Around Pyramidal Buildings," J. Wind. Eng. Ind. Aerodyn., **94**, pp. 745–765.
[11] Heist, D. K., and Gouldin, F. C., 1997, "Turbulent Flow Normal to Triangular Cylinder," J. Fluid Mech., **331**, pp. 107–125.
[12] Vosper, S. B., Castro, I. P., Snyder, W., and Mobb, S. D., 1999, "Experimental Studies of Strongly Stratified Flow Past Three-Dimensional Orography," J. Fluid Mech., **390**, pp. 223–249.
[13] Castro, I. P., Vosper, S., Paisley, M., and Hayden, P., 2001, "Vortex Shedding Behind Tapered Obstacles in Neutral and Stratified Flow," Dyn. Atmos. Oceans, **34**, pp. 145–163.

Downloaded 03 Jun 2010 to 171.66.16.156. Redistribution subject to ASME license or copyright; see http://www.asme.org/terms/Terms_Use.cfm

[14] Castro, I. P., and Rogers, P., 2002, "Vortex Shedding From Tapered Plates," Exp. Fluids, **33**, pp. 66–74.
[15] Igarashi, T., 1985, "Heat Transfer From a Square Prism to an Air Stream," Int. J. Heat Mass Transfer, **28**(1), pp. 175–181.
[16] Chyu, M. K., and Natarajan, V., 1996, "Heat Transfer on the Base of Three-Dimensional Protruding Elements," Int. J. Heat Mass Transfer, **39**(14), pp. 2925–2935.
[17] Savory, E., and Toy, N., 1988, "The Separated Shear Layers Associated With Hemispherical Bodies in Turbulent Boundary Layers," J. Wind. Eng. Ind. Aerodyn., **28**, pp. 291–300.
[18] Taniguchi, S., Sakamoto, H., Kiya, M., and Arie, M., 1982, "Time-Averaged Aerodynamic Forces Acting on a Hemisphere Immersed in a Turbulent Boundary," J. Wind. Eng. Ind. Aerodyn., **9**, pp. 257–273.
[19] Okamoto, T., Yagita, M., and Kataoka, S., 1977, "Flow Past Cone Placed on Flat Plate," Bull. JSME **20**(141), pp. 329–336.
[20] Baker, C. J., 1991, "The Oscillation of Horseshoe Vortex Systems," ASME J. Fluids Eng., **113**, pp. 489–495.
[21] Agui, J. H., and Andreapoulos, J. V., 1992, "Investigation of a Three Dimensional Boundary Layer Flow in the Vicinity of an Upright Wall Mounted Cylinder," ASME J. Fluids Eng., **114**, pp. 566–576.
[22] Ballio, F., Bettoni, G., and Franzetti, S., 1998, "A Survey of Time-Averaged Characteristics of Laminar and Turbulent Horseshoe Vortices," ASME J. Fluids Eng., **120**, pp. 233–242.
[23] Martinuzzi, R. J., and AbuOmar, M., 2003, "Study of the Flow Around Surface-Mounted Pyramids," Exp. Fluids, **34**, pp. 379–389.
[24] Martinuzzi, R. J., and Havel, B., 2000, "Turbulent Flow Around Two Interfering Surface-Mounted Cubic Obstacles in Tandem Arrangement," ASME J. Fluids Eng., **122**, pp. 24–31.
[25] Perry, A. E., and Hornung, H., 1984, "Some Aspects of Three-Dimensional Separation, Part II: Vortex Skeletons," Z. Flugwiss. Weltraumforsch., **8**(3), pp. 155–160.
[26] Merzkirch, W., 1974, *Flow Visualization*, Academic Press, New York, pp. 52–56.
[27] Narayanan, M. A. B., Khadgi, Y. N., and Viswanath, P. R., 1974, "Similarities in Pressure Distribution in Separated Flow Behind Backward-Facing Step," Aeronaut. Q., **25**(4), pp. 305–312.

Downloaded 03 Jun 2010 to 171.66.16.156. Redistribution subject to ASME license or copyright; see http://www.asme.org/terms/Terms_Use.cfm

Simulation of Contaminant Transport in a Fractured Porous Aquifer

Sergei Fomin
Department of Mathematics and Statistics,
California State University,
Chico, CA 95928
e-mail: sfomin@csuchico.edu

Vladimir Chugunov
Department of Applied Mathematics,
Kazan State University,
Kazan, Russia

Toshiyuki Hashida
Fracture & Reliability Research Institute,
School of Engineering,
Tohoku University,
Sendai, Japan

Solute transport in the fractured porous confined aquifer is modeled by the advection-dispersion equation with fractional time derivative of order γ, which may vary from 0 to 1. Accounting for diffusion in the surrounding rock mass leads to the introduction of an additional fractional time derivative of order 1/2 in the equation for solute transport. The closed-form solutions for concentrations in the aquifer and surrounding rocks are obtained for the arbitrary time-dependent source of contamination located in the inlet of the aquifer. Based on these solutions, different regimes of contamination of the aquifers with different physical properties are modeled and analyzed. [DOI: 10.1115/1.2754327]

Keywords: solute transport, contamination, fractured aquifer, porous blocks, fractional-in-time derivative, closed-form solutions

1 Introduction

Water flow and solute transport in fractured rocks gained increasing interest in the last decades because several countries plan to site final repositories for high-level nuclear waste at large depths in rock formations [1–6]. For a number of reasons, some accidents at or damage of nuclear waste repositories may occur and, as a result, groundwater may come into contact with the radioactive waste. Nuclides would then be released and carried by the slowly seeping groundwater to the biosphere. Fortunately, there are mechanisms that retard most of the nuclides of concern. The most important retardation mechanism is caused by the uptake of the nuclides from the flowing water in the fractures into the (slightly) porous rock matrix in the rock blocks between the conducting fractures. The retardation effect can be tremendous for the sorbing nuclides and can result in significant reduction of radioactivity of the waste [1,2]. Besides the granular porous medium, which contains fluid in the intergranular pore space, in fractured rocks fluid flow takes place in a network of interconnecting fractures. A fractured porous medium is made up of blocks of an ordinary porous medium, possessing the nonzero porosity of blocks and high hydraulic conductivity of the network of fissures. Therefore, for a fractured porous medium, it can be said that the fluid is stored in the porous elements and transported along the fissures. Water flow and solute transport by the seeping groundwater are relatively slow, and it is not possible to make experiments over the thousands of years and hundreds of meters of interest. Instead, one has to rely on models that describe the processes and mechanisms that will be dominant over long times. Recently, Schumer et al. [7] suggested a relatively simple mobile/immobile model, with fractal retention times, capable of simulating the anomalous character of solute concentration distributions for the flows in heterogeneous media of fractal geometry. In the field experiments carried out by Becker and Shapiro [8], Haggerty et al. [9], and Reimus et al. [10] for the solute transport in highly heterogeneous media, the solute concentration profiles exhibited anomalous non-Fickian growth rates, skewness, and sharp leading edges. These effects cannot be predicted by the conventional mass transport equations. It was demonstrated in a number of publications [7,11–15] that fractional differential equations can simulate the anomalous character of solute transport in highly heterogeneous media. Suggesting inclusion of a fractional time derivative into the mass transport equation (in addition to the conventional derivative with respect to time), Schumer et al. [7] referred to the conceptual model of multirate diffusion into immobile zones, which had been described by Cunningham et al. [16], Haggerty and Gorelick [17], Carrera et al. [18], and Haggerty et al. [9]. On the basis of the model suggested by Schumer et al. [7], in the present study the effect of retardation of the contaminant transport caused by diffusion into the confining rocks and into the porous blocks within the fractured porous aquifer is analyzed. Along with diffusion into the porous blocks within the aquifer, diffusion into surrounding rocks appeared to be an important factor that retards contamination. It is shown that accounting for diffusion into the confining rocks leads to an emerging additional fractional time derivative of the order 1/2 in a solute transport equation. This once again justifies applicability of the fractional time derivatives for modeling the diffusion in porous blocks and for accounting for the memory effects in the solute transport. Hence, along with nonfractured porous blocks within the aquifer, the confining from above and below rocks can be treated as huge infinite porous blocks, which significantly contribute to the memory effects.

2 System Model and Analysis

2.1 Basic Assumptions and Governing Equations. A schematic sketch of the fractured porous aquifer is presented in Fig. 1. Cartesian coordinates (x,y) are chosen in such a manner that fluid in the aquifer flows in the x direction and that the coordinate y is directed upward. Since the goal of the present study is to qualitatively estimate the effect of non-Fickian diffusion into the surrounding rocks on the solute transport in the aquifer (rather than to simulate the performance of concrete aquifer within the specific rock formation), it is assumed for simplicity that rocks below and above the aquifer have the same physical properties. The latter assumption makes the process symmetrical with regard to the median line of the aquifer $y=-h$ (dashed line in Fig. 1). Therefore, the mass flux equals to 0 at $y=-h$, and the solution of the problem in the subdomain below this line is identical to the solution in the upper subdomain. Hence, only the upper half of the domain ($y \geq -h$) can be considered. Thus, due to the above assumptions, the differential equation describing the diffusive transport in the upper rocks can be presented in the following form:

Contributed by the Fluids Engineering Division of ASME for publication in the JOURNAL OF FLUIDS ENGINEERING. Manuscript received August 27, 2006; final manuscript received March 30, 2007. Review conducted by Dennis Siginer.

 Copyright © 2007 by ASME

Downloaded 03 Jun 2010 to 171.66.16.156. Redistribution subject to ASME license or copyright; see http://www.asme.org/terms/Terms_Use.cfm

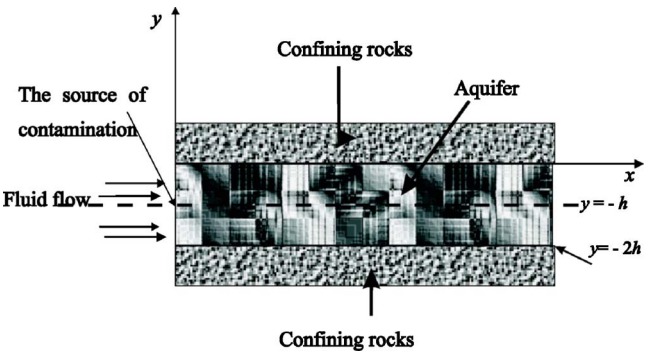

Fig. 1 Schematic of the model

$$\frac{\partial c_1}{\partial \tau} = D_1\left(\frac{\partial^2 c_1}{\partial x^2} + \frac{\partial^2 c_1}{\partial y^2}\right) \quad (0 < x < \infty; \quad 0 < y < \infty; \quad \tau > 0) \tag{1}$$

Following the approach suggested in [7], the advection–dispersion process in the fracture porous aquifer can be described

$$\frac{\partial c_2}{\partial \tau} + \beta\frac{\partial^\gamma c_2}{\partial \tau^\gamma} = D_2\left(\frac{\partial^2 c_2}{\partial x^2} + \frac{\partial^2 c_2}{\partial y^2}\right) - v\frac{\partial c_2}{\partial x}$$

$$(-h < y < 0, \quad 0 < x < \infty, \quad \tau > 0) \tag{2}$$

where c_1 and c_2 are concentrations of solute in the confining rocks and aquifer, respectively; D_1 and D_2 are the coefficients of effective diffusivity (which account for dispersion and diffusion) in the rocks and aquifer, respectively; h is a half thickness of the aquifer; v is the fluid velocity, β is the capacity coefficient, which accounts for the ratio of immobile mass to mobile mass and physical properties of the blocks of porous rocks within the aquifer [17] and τ is time. The fractional time derivative $\partial^\gamma c_2/\partial\tau^\gamma$ can be defined through the Laplace transformation L as [19] $L[\partial^\gamma c_2/\partial\tau^\gamma] = s^\gamma L[c_2] - s^{\gamma-1}c_2(x,0)$. When $0<\gamma<1$ the fractional time derivative predicts continual transfer of mass from the mobile (fissures) to the immobile (porous blocks) phase. It can be readily shown that in many situations the contaminant transport within the aquifer in direction of the mainstream flow (x direction) is predominantly determined by the advection mechanism [1,2,9] and that in surrounding rocks, confining the aquifer from below and above, concentration gradients in the x direction are much smaller than in direction orthogonal to the aquifer [10,20], i.e., $\partial c_1/\partial x \ll \partial c_1/\partial y$. Then, letting $c = 1/h\int_{-h}^{0} c_2 dy$ and assuming that $c_1 = c$ at $y = 0$ reduce Eqs. (1) and (2) as follows:

$$\frac{\partial c_1}{\partial \tau} = D_1\frac{\partial^2 c_1}{\partial y^2} \quad 0 < y < \infty; \quad \tau > 0 \tag{3}$$

$$\frac{\partial c}{\partial \tau} + \beta\frac{\partial^\gamma c}{\partial \tau^\gamma} = D_1\frac{1}{h}\left.\frac{\partial c_1}{\partial y}\right|_{y=0} - v\frac{\partial c}{\partial x}, \quad 0 < y < \infty; \quad \tau > 0 \tag{4}$$

Introducing the nondimensional coordinates as

$$C_1 = \frac{c_1}{c_0(0)}; \quad C = \frac{c}{c_0(0)}; \quad C_0 = \frac{c_0(\tau)}{c_0(0)}; \quad t = \frac{\tau D_1}{h^2}; \quad \mathrm{Pe} = \frac{vh}{D_1};$$

$$b = \beta\left(\frac{h^2}{D_1}\right)^{1-\gamma}; \quad X = \frac{x}{h}; \quad Y = \frac{y}{h} \tag{5}$$

and imposing the relevant boundary condition, the mathematical model of the process can be presented in the following form:

$$\frac{\partial C_1}{\partial t} = \frac{\partial^2 C_1}{\partial Y^2}; \quad 0 < Y < \infty; \quad \tau > 0 \tag{6}$$

$$\frac{\partial C}{\partial t} + b\frac{\partial^\gamma C}{\partial t^\gamma} = \left.\frac{\partial C_1}{\partial Y}\right|_{Y=0} - \mathrm{Pe}\frac{\partial C}{\partial X}; \quad 0 < X < \infty; \quad \tau > 0 \tag{7}$$

$$t = 0, \quad C = 0 \tag{8}$$

$$X = 0, \quad C = C_0(t) \tag{9}$$

$$Y = 0, \quad C_1 = C; \quad Y \to \infty, \quad C_1 \to 0 \tag{10}$$

where $C_0(t)$ is concentration in the inlet of the aquifer.

2.2 Analytical Solution of the Problem. Considering the auxiliary problem for the function u, which satisfies Eq. (6), initial condition (8), boundary condition at $Y=0$, $u=1$, and vanishes in infinity ($Y\to\infty$, $u\to 0$), it can be readily seen that its solution is defined by the formula $u(Y,t) = \mathrm{erfc}(Y/2\sqrt{t})$. Then, utilizing the Duhamel's theorem, the solution for C_1 can be given by the following integral: $C_1(t,X,Y) = (\partial/\partial t)\int_0^t C(t,X)u(Y,t-p)dp$. Hence, an equation that couples C_1 and C can be presented in the following form:

$$C_1(t,X,Y) = \frac{\partial}{\partial t}\int_0^t C(t,X)\,\mathrm{erfc}\left(\frac{y}{2\sqrt{t-p}}\right)dp \tag{11}$$

From Eq. (11), the concentration flux on the aquifer-rock interface can be presented as follows:

$$\left.\frac{\partial C_1}{\partial Y}\right|_{Y=0} = -\frac{\partial}{\partial t}\int_0^t C(t,X)\frac{dp}{\sqrt{\pi(t-p)}} \tag{12}$$

Applying the Laplace transformation to the formula (12) gives $L[-\partial C_1/\partial Y|_{Y=0}] = s^{1/2}L[C]$, and hence, in a view of definition of the fractional derivative, (12) can be converted to the following form:

$$\left.\frac{\partial C_1}{\partial Y}\right|_{Y=0} = -\frac{\partial^{1/2} C}{\partial t^{1/2}} \tag{13}$$

Accounting for the latter formula, the boundary value problem for the solute transport in the aquifer C can be rewritten as follows:

$$\frac{\partial C}{\partial t} + b\frac{\partial^\gamma C}{\partial t^\gamma} + \frac{\partial^{1/2} C}{\partial t^{1/2}} = -\mathrm{Pe}\frac{\partial C}{\partial X}; \quad 0 < X < \infty; \quad t > 0 \tag{14}$$

$$t = 0, \quad C = 0 \tag{15}$$

$$X = 0, \quad C = C_0(t) \tag{16}$$

It is worth noting that in contrast to the model discussed in [7], the problem formulated by Eqs. (14)–(16) accounts for the variable-in-time source of contamination (boundary condition (16)) and contains an additional fractional time derivative of order 1/2 (third term in the left-hand side of Eq. (14)), which models diffusion into surrounding porous rocks.

The boundary value problem (14)–(16) can be solved by the Laplace transformation with respect to t. For the transforms, the problem (14)–(16) reduces to

$$\frac{d\bar{C}}{dX} = -\bar{C}\frac{s + s^{1/2} + s^\gamma}{\mathrm{Pe}} \tag{17}$$

$$X = 0, \quad \bar{C} = \bar{C}_0 \tag{18}$$

where $\bar{C} = L[C]$.

The solution of Eq. (17) with boundary condition (18) has the form

$$\bar{C} = s\bar{C}_0\bar{\varphi}(s,X)\exp\left(-\frac{X}{Pe}s\right) \tag{19}$$

where

Downloaded 03 Jun 2010 to 171.66.16.156. Redistribution subject to ASME license or copyright; see http://www.asme.org/terms/Terms_Use.cfm

$$\bar{\varphi}(s,X) = \frac{1}{s}\exp\left(-\frac{s^{1/2}+bs^{\gamma}}{\mathrm{Pe}}X\right) \tag{20}$$

The original of the function $\bar{\varphi}(s,X)$ can be presented through the stable subordinator $g_{\gamma}(t)$ as

$$\varphi(t,X) = \int_0^t \mathrm{erfc}\left[\frac{X}{2\mathrm{Pe}\sqrt{p}}\right]\left(\frac{\mathrm{Pe}}{bX}\right)^{1/\gamma} g_{\gamma}\left[\frac{(t-p)\mathrm{Pe}^{1/\gamma}}{(bX)^{1/\lambda}}\right]dp \tag{21}$$

where $g_{\gamma}(t)$ (with Laplace transform $\bar{g}(s)=\exp(-s^{\gamma})$) is the probability density function of the limit of many heavy-tailed waiting times [7,13]. Although the properties of function $g_{\gamma}(t)$ are well documented and some asymptotic approximations are obtained, to the best of our knowledge there are no explicit expressions for this function available in literature. To this end, it is more convenient to proceed with straightforward calculation of the inverse Laplace transform L^{-1} for the function $\bar{\varphi}(s,X)$ defined by the formula (20). As a result, it can be readily shown that

$$\varphi(t,X) = 1 - \frac{1}{\pi}\int_0^{\infty} \exp\left[-\xi t - \frac{X}{\mathrm{Pe}}b\xi^{\gamma}\cos(\pi\gamma)\right] \times \sin\left[\frac{X}{\mathrm{Pe}}(b\xi^{\gamma}\sin(\pi\gamma)+\xi^{1/2})\right]\frac{d\xi}{\xi} \tag{22}$$

It is worth mentioning that function $g_{\gamma}(t)$ is a particular instance of the representation (22). Namely, assuming in (20) $bX/\mathrm{Pe}=A$ and $X/\mathrm{Pe}=B$, then putting $B=0$ and $A=1$, yields $\bar{\varphi}_{B=0,A=1}=\exp(-s^{\gamma})/s$, which is equal to $L[g_{\gamma}(t)]/s$. On the other hand for $B=0$ and $A=1$, Eq. (22) leads to the expression $L^{-1}[e^{-s\gamma}/s]=1-(1/\pi)\int_0^{\infty}e^{-\xi t-\xi^{\gamma}\cos(\pi\gamma)}\sin[\xi^{\gamma}\sin(\pi\gamma)](d\xi/\xi)$, from where, accounting for the well-documented properties of Laplace transformation, it follows that:

$$g_{\gamma}(t) = \frac{\partial}{\partial t}L^{-1}\left[\frac{e^{-s\gamma}}{s}\right] = \frac{1}{\pi}\int_0^{\infty} e^{-\xi t-\xi^{\gamma}\cos(\pi\gamma)}\sin[\xi^{\gamma}\sin(\pi\gamma)]\frac{d\xi}{\xi} \tag{23}$$

An explicit expression for the probability density function (23) is relatively simple and can be readily evaluated numerically; for instance, it can be done by the computer algebra system MATHEMATICA. To this end, formula (23) can be recommended for computations based on solutions obtained in [7], where this function is widely utilized in the expressions of the closed-form solutions. However, in our case, direct application of the formula (22) is more convenient for numerical computations. Calculating the inverse Laplace transform of expressions (19) and (22) and accounting for the Duhamel's theorem, solution of the boundary value problem (14)–(16) can be presented as follows:

$$C(t,X) = \frac{\partial}{\partial t}\int_0^t C_0(t-p)\,\eta\left(p-\frac{X}{\mathrm{Pe}}\right)\varphi\left(p-\frac{X}{\mathrm{Pe}},X\right)dp \tag{24}$$

where $\eta(\tau)$ is the unit step function and function φ is defined by Eqs. (21) and (22).

For the arbitrary γ and $C_0=1$, which models the uniform contaminant source at $X=0$, solution (24) can be converted to the following form:

$$C(t,X) = \eta\left(t-\frac{X}{\mathrm{Pe}}\right)\varphi\left(t-\frac{X}{\mathrm{Pe}},X\right) \tag{25}$$

In the particular case of $C_0=1$ and $\gamma=1/2$, solution (25) reduces to the well-documented formula

$$C(t,X) = \eta\left(t-\frac{X}{\mathrm{Pe}}\right)\mathrm{erfc}\left[\frac{X(1+b)}{2\mathrm{Pe}\sqrt{t-\frac{X}{\mathrm{Pe}}}}\right] \tag{26}$$

The important practical case when contaminant leakage at $X=0$ occurs by accident and continues until a specified moment of time t^*, after which the source of contamination is eliminated and the flow of clean water resumes, can be modeled by assuming that $C_0(t)=1$ for t from the interval $(0,t^*)$ and that $C_0(t)=0$ for $t>t^*$. Then, for this case, solution (24) can be converted to the following form:

$$C(t,X) = \eta\left(t-\frac{X}{\mathrm{Pe}}\right)\varphi\left(t-\frac{X}{\mathrm{Pe}},X\right) - \eta\left(t-\frac{X+\mathrm{Pe}T}{\mathrm{Pe}}\right)\varphi\left(t-\frac{X+\mathrm{Pe}T}{\mathrm{Pe}},X\right) \tag{27}$$

If the solution for concentration in the aquifer C is found, then the concentration in the surrounding rock C_1 can be immediately obtained from Eq. (11). However, even in the particular cases when C is defined by Eqs. (25) and (27), this will lead to rather bulky formulas. A much simpler solution for C_1 can be obtained applying the Laplace transform to Eq. (11), which results in the following expression: $\bar{C}_1=\bar{C}\exp(-Y\sqrt{s})$. Accounting for Eqs. (19) and (20) and also assuming that $C_0=1$, the expression for $\bar{C}_1$ can be presented in the following form:

$$\bar{C}_1 = \frac{1}{s}\exp\left[-\frac{X+\mathrm{Pe}Y}{\mathrm{Pe}}\left(s^{1/2}+\frac{bX}{X+\mathrm{Pe}Y}s^{\gamma}\right)\right]\exp\left(-\frac{X}{\mathrm{Pe}}s\right) \tag{28}$$

Calculating the inverse Laplace transform, it yields

$$C_1(t,X) = \eta\left(t-\frac{X}{\mathrm{Pe}}\right)\varphi_1\left(t-\frac{X}{\mathrm{Pe}},X,Y\right) \tag{29}$$

where

$$\varphi_1(t,X,Y) = 1 - \frac{1}{\pi\nu}\int_0^{\infty}\exp\left[-\zeta^{1/\nu}t - \frac{X}{\mathrm{Pe}}b\zeta^{\gamma/\nu}\cos(\pi\gamma)\right] \times \sin\left[\frac{X}{\mathrm{Pe}}b\zeta^{\gamma/\nu}\sin(\pi\gamma)+\frac{X+Y\mathrm{Pe}}{\mathrm{Pe}}\xi^{1/(2\nu)}\right]\frac{d\xi}{\xi} \tag{30}$$

and $\nu=\min(\gamma,1/2)$.

In the case described by formula (27), i.e., when at $X=0$, $C_0(t)=1$ for $0<t<t^*$, and $C_0(t)=0$ for $t>t^*$, the concentration in the surrounding rocks can be presented by the following expression:

$$C_1(t,X) = \eta\left(t-\frac{X}{\mathrm{Pe}}\right)\varphi_1\left(t-\frac{X}{\mathrm{Pe}},X,Y\right) - \eta\left(t-\frac{X+\mathrm{Pe}T}{\mathrm{Pe}}\right)\varphi_1\left(t-\frac{X+\mathrm{Pe}T}{\mathrm{Pe}},X,Y\right) \tag{31}$$

2.3 Discussion of the Analytical Solutions and Their Implications. Solutions obtained for concentrations in the aquifer and surrounding rock matrix are rather simple and do not present any difficulties for numerical computations, especially if MATHEMATICA is applied. The accuracy of the numerical evaluation of the integrals in the solutions presented in general form can be easily verified by comparison to the simple solution (26) obtained for the particular case when $C_0=1$ and $\gamma=1/2$.

Prior to numerical computations, some conclusions can already be made solely on the basis of the governing equations derived above. For instance, the additional fractional time derivative of the order 1/2 in Eq. (14), which appeared as a result of accounting

Downloaded 03 Jun 2010 to 171.66.16.156. Redistribution subject to ASME license or copyright; see http://www.asme.org/terms/Terms_Use.cfm

for diffusion in the surrounding confining rocks, once again substantiates the model of Schumer et al. [7]. According to this approach, solute in the fissures within the fractured porous aquifer can be considered as a mobile phase and in the randomly distributed porous blocks that constitute the aquifer can be considered as an immobile phase, where the mass transport is only determined by diffusion. Interaction of mobile and immobile phases in the aquifer can be modeled by the fractional time derivative $b(\partial^{\gamma}C/\partial t^{\gamma})$ (second term on the left-hand side of Eq. (14)), where the capacity parameter b is determined by the ratio of mass in the immobile and mobile phases at the equilibrium and by the diffusivity, porosity, geometry, and sizes of the blocks, and the order of fractional derivative γ is determined by the geometry of the pores and their distribution in the blocks and by the adopted model of mass transfer in the blocks [17]. From the above solution for C and C_1, it can be readily seen that for the constant concentration in the inlet of the aquifer, $C_0(t)=1$, the late-time concentrations in the aquifer and surrounding rocks behave as follows:

$$C \sim 1 - \frac{Xt^{-1/2}}{\mathrm{Pe}\Gamma(1/2)} - \frac{bXt^{-\gamma}}{\mathrm{Pe}\Gamma(-\gamma+1)} \tag{32}$$

$$C_1 \sim 1 - \frac{(X+\mathrm{Pe}Y)t^{-1/2}}{\mathrm{Pe}\Gamma(1/2)} - \frac{bXt^{-\gamma}}{\mathrm{Pe}\Gamma(-\gamma+1)} \tag{33}$$

where $\Gamma(x)$ is Gamma function. Note that Eqs. (33) and (32) are valid for $X=O(\mathrm{Pe})$ and $Y=O(1)$. Hence, if contamination continues with time and the source of concentration is not eventually eliminated, concentrations in the aquifer and in the neighboring rock masses tend to the concentration in the inlet. For $\gamma<1/2$, distributions of concentrations are determined by the diffusion in the porous blocks in the aquifer; otherwise (for $\gamma>1/2$), the effect of diffusion in the surrounding rocks will dominate. In the other particular case of practical importance, contamination may occur due to the instantaneous injection of fluid at $X=0$. This can be modeled by the Dirac δ-function assuming that $C_0=\delta(t)$. In this case, the late-time asymptotic solutions decay as follows:

$$C \sim \frac{Xt^{-3/2}}{\mathrm{Pe}\Gamma(-1/2)} + \frac{bXt^{-1-\gamma}}{\mathrm{Pe}\Gamma(-\gamma)} \tag{34}$$

$$C_1 \sim \frac{(X+\mathrm{Pe}Y)t^{-3/2}}{\mathrm{Pe}\Gamma(1/2)} + \frac{bXt^{-1-\gamma}}{\mathrm{Pe}\Gamma(-\gamma)} \tag{35}$$

Again, in this case for $\gamma<1/2$ the decay of concentrations takes place as a result of diffusion in the porous blocks within the aquifer, whereas for $\gamma>1/2$ it happens mostly due to diffusion in the surrounding rock. Note, however, that in all situations Eqs. (34) and (35) predict more rapid asymptotic decline of concentration than late-time variation of concentration in the case of constant inlet concentration described by Eqs. (32) and (33). It is also interesting to note that, if the effect of diffusion in the surrounding rocks is ignored (first term on the right-hand side is omitted), Eq. (34) coincides with asymptotic presentation for C obtained by Schumer et al. [7] for the nonconfined flow.

3 Numerical Results and Discussion

3.1 Concentration of Solute in Aquifer in the Case of the Permanent Source of Contamination. Distributions of solute concentrations in the aquifer, with respect to the stream-wise distance X from a permanent source of contamination, $C_0=1$ at $X=0$, for various orders of derivative γ and for various contaminating period durations are shown in Fig. 2. Computations for $\gamma=1/2$ were performed by a simple formula (26), which corresponds to the case when diffusion in the porous blocks within the aquifer, similarly to the diffusion in the confining rocks, is Fickian. It is worth noting that the model with $\gamma=1/2$ is valid for the aquifer, which is composed of the relatively large porous blocks, so that concentration fronts within each block, moving from the different faces of each block to its center, do not overlap. For γ equal to 0.2 and 0.8, computations were carried out by Eq. (25). For relatively long periods of time, $t>5$, the corresponding concentration distributions vary according to the asymptotic formula (32). Namely, for $\gamma=0.2$, the value of the last term on the right-hand side of expression (32) is greater than in the case when $\gamma=0.5$ and, therefore, the concentration is lower for $\gamma=0.2$, whereas for $\gamma=0.8$ the same term in expression (32) becomes smaller, which leads to the higher values of concentration. In other words, for relatively long periods of time, the smaller values of γ simulate the solute transition from mobile into immobile phase in greater amounts, i.e., penetration of the greater amount of solute into the porous blocks within the aquifer, and therefore, concentration of solute in the mobile phase decreases. For the shorter periods of time ($t<1$), due to the definition of fractional derivative, the mass flux into a porous medium behaves asymptotically as $t^{-\gamma}/\Gamma(1-\gamma)$ and, therefore, for the greater values of γ the amount of solute transferred into the immobile phase increases. As a result, concentration of the solute in the mobile phase, C, becomes smaller. This effect for $t=0.2$ is illustrated by the dashed line in Fig. 2. For the intermediate times, these two effects (one dominates for the short and the other for long times) begin to interact, leading to the non-trivial distributions of concentrations, which is illustrated in Fig. 2 by the curves computed at $t=1$.

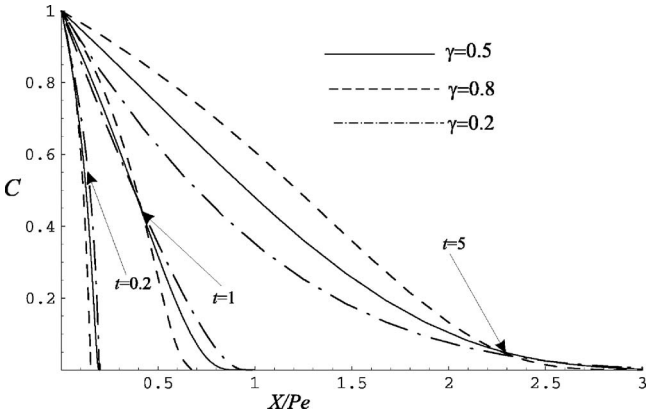

Fig. 2 Variation of concentration in the aquifer C in stream-wise direction for the permanent uniform source of concentration $C_0=1$ in the inlet of the aquifer

3.2 Concentration of Solute in the Confining Rocks, C_1, and in the Aquifer, C, for the Case of the Temporary Source of Contamination. Figures 3 and 4 illustrate the distribution of concentration C_1 in the rock matrix, confining the aquifer from the above, in the direction orthogonal to the aquifer (coordinate Y). Results presented in Figs. 3 and 4 are computed by formula (31), which models two regimes: (i) the regime of contamination from the source located at $X=0$ over the finite period of time $(0,t^*)$ and (ii) the consequent regime of clean water flow after elimination of the source of contamination, which begins since $t=t^*$. Comparison of the corresponding plots in Fig. 3 shows that smaller values of the parameter γ lead to the lower concentrations of solute in the rock matrix for the both regimes (contamination for $t<t^*$ and cleaning for $t>t^*$) and these discrepancies become more pronounced for the longer times. As it has been already mentioned above, the lower concentrations of solute in the aquifer, C, are typical for the smaller values of γ. It can be attributed to the fact that in this case the greater amount of solute diffused into the porous blocks. As a result of the lower solute concentration of contaminant in the aquifer, concentration of the solute in the confining rocks also decreases. Computations presented in Fig. 4(a) for the smaller value of the parameter $b=0.1$ and their comparison with plots in Fig. 3 at $b=1$ indicate that reduction of this param-

Downloaded 03 Jun 2010 to 171.66.16.156. Redistribution subject to ASME license or copyright; see http://www.asme.org/terms/Terms_Use.cfm

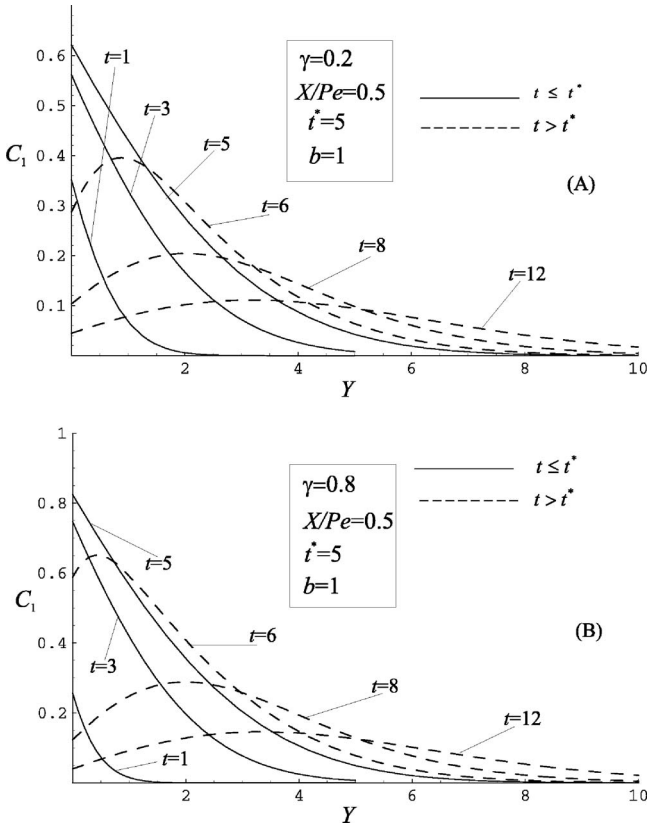

Fig. 3 Distributions of concentrations in the confining porous rocks C_1 with respect to transverse coordinate Y over the period of contamination, $0<t<t^*$ (solid lines), and after the elimination of the source of contamination, $t>t^*$ (dashed lines) at $X/\mathrm{Pe}=0.5$, $b=1$ and different γ: (*a*) $\gamma=0.2$ and (*b*) $\gamma=0.8$

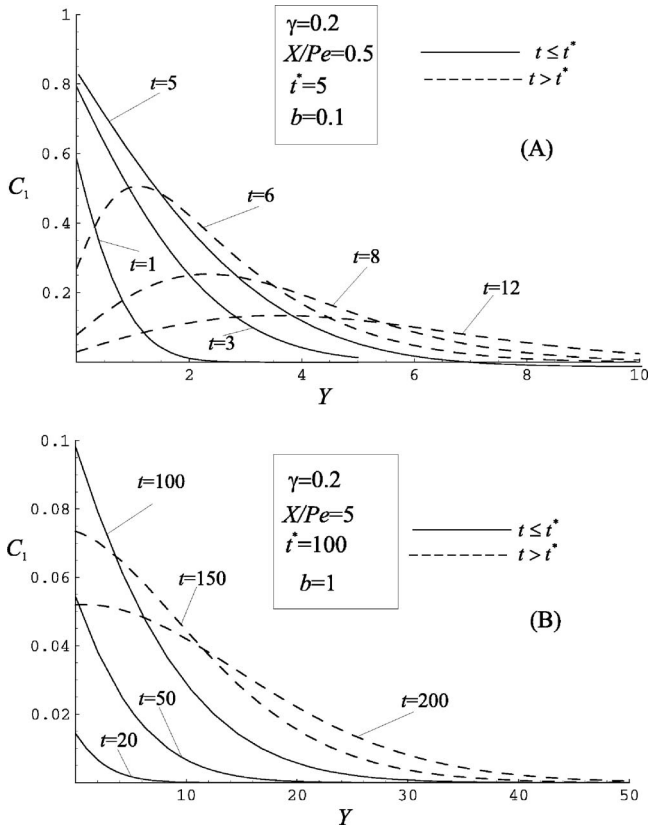

Fig. 4 Distributions of concentrations in the confining from above porous rocks C_1 with respect to transverse coordinate Y over the period of contamination, $0<t<t^*$ (solid lines), and after the elimination of the source of contamination, $t>t^*$ (dashed lines) for $\gamma=0.2$ and different t^*, X, and b

eter leads to the higher concentrations in the confining rock matrix. Obviously, smaller values of the parameter b model smaller volumes of porous blocks (immobile phase) in the aquifer and/or lower absorbing capacity of these blocks, which results in higher concentration within the mobile phase C, and the latter leads to the higher solute concentration in the confining rocks. It is worth noting that the deeper penetration of the contaminant by diffusion in the confining from above rock matrix may lead with time to contamination of the upper subterranean strata and finally may affect the areas in the vicinity of the earth surface. Figure 4(*b*) illustrates variations of concentrations at the longer distance from the source of contamination, $X/\mathrm{Pe}=5$, where concentration is lower even for the significantly longer period of contamination ($t^*=100$). Qualitatively, distributions of concentrations at $X/\mathrm{Pe}=5$ are very similar to the concentration profiles obtained for the shorter distances from the source of contamination (inlet of the aquifer), though the values of concentrations, as it could be expected, are much lower in this case. Results presented in Fig. 5 are obtained from the solution (27), which models concentration in the aquifer C. Solid lines correspond to the stage of continuing contamination and dashed lines represent the regime of clean water flow after elimination of the source of contamination. Similarly to what has been observed for the concentration in the confining rocks surrounding the aquifer (see Figs. 3 and 4), in the aquifer itself higher concentrations C are obtained for the higher orders of the time derivative γ, e.g., for $\gamma=0.8$, which simulates the less intensive diffusion into the porous blocks within the aquifer. High concentrations C can be also sustained for the smaller values of parameter b. The latter corresponds to the smaller fraction of the immobile phase, i.e., smaller total volume of porous blocks or low porosity of these blocks, which reduces the effective diffusivities of the blocks within the aquifer.

Sensitivity analysis of the proposed mathematical model provided above demonstrates that variations of the controlling parameters b and γ can significantly affect the computed contaminant concentrations in the aquifer and in the surrounding rocks. Hence, assigning the proper values of parameters b and γ is of crucial importance for the further application of the mathematical model and for predicting the consequences of contamination of the particular water aquifers. Different types of fractured porous aquifers and rocks can be identified by the corresponding values of these parameters: parameter γ characterizes the geometry of the pore distribution within the blocks of the aquifer and the specific character of diffusion in these blocks, whereas parameter b characterizes the configuration of the major fracture network, the volume and the shape of the blocks. Calibration of the theoretical model (i.e., obtaining the corresponding values of the controlling parameters) can be carried out by comparison of the computations based on the closed-form analytical solution with the tracer breakthrough curves obtained in the laboratory or field experiments. The calibrated solutions can be readily used for predicting the possible outcome of the particular aquifer contamination, for calculating the maximal distances of the contaminant migration within the certain time range, and for assessing the amounts of contaminant absorbed by the porous blocks and surrounding rocks and the amounts of contaminant carried by the groundwater to the biosphere. Furthermore, since it is a well-documented fact that the order of the fractional derivative γ is directly related to fractal dimension of the porous medium that can be considered as fractal [21], calibrating the mathematical model and specifying the value of parameter γ can allow the modeler to calculate the fractal di-

Downloaded 03 Jun 2010 to 171.66.16.156. Redistribution subject to ASME license or copyright; see http://www.asme.org/terms/Terms_Use.cfm

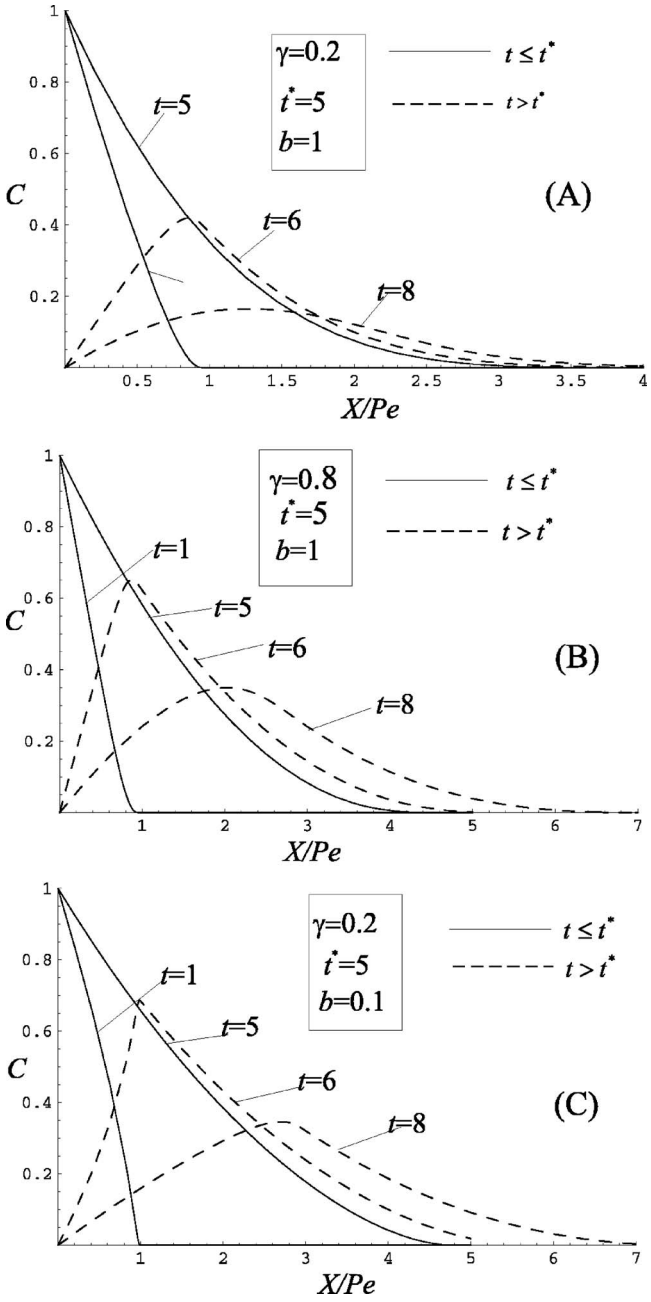

Fig. 5 Distributions of concentrations in the aquifer *C* along the aquifer over the period of contamination, $0<t<t^*$ (solid lines), and after the elimination of the source of contamination, $t>t^*$ (dashed lines), for different *b* and γ: (*a*) *b*=1, γ=0.2; (*b*) *b*=1, γ=0.8; (*c*) *b*=0.1, γ=0.2

mension of the porous matrix and therefore can provide important information about the geological structure of the rocks.

4 Conclusions

The following conclusions are drawn:

1. Using the fractional time model suggested by Schumer et al. [7], the closed-form solutions for the contaminant transport in the confined fractured porous aquifer are obtained.
2. Representation of the mass flux into the confining surrounding rock masses by the fractional time derivative of order 1/2 in the governing equation for the aquifer, once again confirms the applicability of the approach of Schumer et al. [7] for modeling the solute transport in rocks by equations with fractional time derivatives.
3. Introducing the fractional time derivative of the arbitrary order into equation of mass transport in fractured porous medium leads to a simple and efficient model for the mechanisms of fluid-rock interaction within the fractured aquifer of complex geological structure.
4. The parameters that allow simulating different regimes of fluid-rock interactions and different properties of the porous blocks within the aquifer are determined and their influence on the solution behavior is analyzed. For instance, the late-time behavior of the concentration suggests that low values of γ, with the same capacity coefficient *b*, have the reduced values of concentrations in both aquifer and surrounding rocks, whereas the lower values of the coefficient *b* lead to the higher concentrations.
5. After the proper calibration based on comparison to the experimentally obtained tracer breakthrough curves, the closed-form solutions can be used for predicting the consequences of contamination of these aquifers.

References

[1] Neretnieks, I., 1980, "Diffusion in the Rock Matrix: An Important Factor in Radionuclide Retardation," J. Geophys. Res., **85**(B8), pp. 4379–4397.

[2] Neretnieks, I., 1993, "Solute Transport in Fractured Rock: Applications to Radionuclide Waste Repositories," *Flow and Contaminant Transport in Fractured Rock*, Academic Press, New York, J. Bear, C. F. Tsang, and G. de Marsily, eds., pp. 39–127.

[3] Birkholzer, J. T., Li, G., Tsang, C. F., and Tsang, Y., 1999, "Modeling Studies and Analysis of Seepage Into Drifts at Yucca Mountain," J. Contam. Hydrol., **38**, pp. 349–384.

[4] Tsang, Y. W., and Birkholzer, J. T., 1999, "Predictions and Observations of the Thermal-Hydrological Conditions in the Single Heater Test at Yucca Mountain," J. Contam. Hydrol., **38**, pp. 385–425.

[5] Tsang, Y. W., and Tsang, C. F., 1987, "Channel Model of Flow Through Fractured Media," Water Resour. Res., **23**(3), pp. 467–479.

[6] Tsang, Y. W., and Tsang, C. F., 2001, "A Particle-Tracking Method for Advective Transport in Fractures With Diffusion Into Finite Matrix Blocks," Water Resour. Res., **37**(3), pp. 831–836.

[7] Schumer, R., Benson, D. A., Meerschaert, M. M., and Baeumer, B., 2003, "Fractal Mobile/Immobile Transport," Water Resour. Res., **39**(10), 1296, pp. SBH13(1)–SBH13(12).

[8] Becker, M. W., and Shapiro, A. M., 2000, "Tracer Transport in Fractured Crystalline Rock: Evidence of Non-Diffusive Breakthrough Tailing," Water Resour. Res., **36**(7), pp. 1677–1686.

[9] Haggerty, R., McKenna, S. A., and Meigs, L. C., 2000, "On the Late-Time Behavior of Tracer Test Breakthrough Curves," Water Resour. Res., **36**(12), pp. 3467–3479.

[10] Reimus, P. W., Pohll, G., Mihevc, T., Chapman, J., Haga, M., Lyles, B., Kosinski, S., Niswonger, R., and Sanders, P., 2003, "Testing and Parameterizing a Conceptual Model for Solute Transport in a Fractured Granite Using Multiple Tracers in a Forced Gradient Test," Water Resour. Res., **39**(12), 1356, pp. SBH14(1)–SBH14(15).

[11] Benson, D. A., Wheatcraft, S. W., and Meerschaert, M. M., 2000, "Application of a Fractional Advection-Dispersion Equation," Water Resour. Res., **36**(6), pp. 1403–1412.

[12] Benson, D. A., Schumer, R., Meerschaert, M. M., and Wheatcraft, S. W., 2001, "Fractional Dispersion, Levy Motion, and the MADE Tracer Tests," Transp. Porous Media, **42**, pp. 211–240.

[13] Baeumer, B., Meerschaert, M. M., Benson, D. A., and Wheatcraft, S. W., 2001, "Subordinated Advection-Dispersion Equation for Contaminant Transport," Water Resour. Res., **37**(6), pp. 1543–1550.

[14] Herrick, M., Benson, D., Meerschaert, M., and McCall, K., 2002, "Hydraulic Conductivity, Velocity, and the Order of the Fractional Dispersion Derivative in a Highly Heterogeneous System," Water Resour. Res., **38**(11), pp. 1227–1239.

[15] Meerschaert, M. M., Benson, D. A., and Baeumer, B., 1999, "Multidimensional Advection and Fractional Dispersion," Phys. Rev. E, **59**, pp. 5026–5028.

[16] Cunningham, J. A., Werth, C. J., Reinhard, M., and Roberts, P. V., 1997, "Effects of Grain-Scale Mass Transfer on the Transport of Volatile Organics Through Sediments: 1. Model Development," Water Resour. Res., **33**(12), pp. 2713–2726.

Downloaded 03 Jun 2010 to 171.66.16.156. Redistribution subject to ASME license or copyright; see http://www.asme.org/terms/Terms_Use.cfm

[17] Haggerty, R., and Gorelick, S. M., 1995, "Multiple-Rate Mass Transfer for Modeling Diffusion and Surface Reactions in Media With Pore-scale Heterogeneity," Water Resour. Res., **31**(10), pp. 2383–2400.
[18] Carrera, J., Sanchez-Vila, X., Benet, I., Medina, A., Galarza, G., and Guimera, J., 1998, "On Matrix Diffusion: Formulations, Solution Methods and Qualitative Effects," Hydrogeol. J., **6**, pp. 178–190.
[19] Samko, S. G., Kilbas, A. A., and Marichev, O. I., 1993, *Fractional Integrals and Derivatives: Theory and Applications*, Gordon and Breach, London.
[20] Kennedy, C. A., and Lennox, W. C., 1995, "A Control Volume Model of Solute Transport in a Single Fracture," Water Resour. Res., **31**(2), pp. 313–322.
[21] Giona, M., and Roman, H. E., 1992, "Fractional Diffusion Equation on Fractals: One-Dimensional Case and Asymptotic Behavior," J. Phys. A, **25**, pp. 2093–2105.

Downloaded 03 Jun 2010 to 171.66.16.156. Redistribution subject to ASME license or copyright; see http://www.asme.org/terms/Terms_Use.cfm

Turbulent Flow Downstream of a Perforated Plate: Sharp-Edged Orifice Versus Finite-Thickness Holes

Rui Liu

David S.-K. Ting[1]
e-mail: dting@uwindsor.ca

Mechanical, Automotive & Materials Engineering,
University of Windsor,
Windsor, ON, N9B 3P4, Canada

In this study, perforated plates with sharp-edged orificed openings and finite-thickness straight openings were applied to produce nearly isotropic turbulence in a wind tunnel. At the same nominal velocity, the orificed perforated plate was able to produce a higher level of turbulence due to the well-defined flow separation from its sharp edge openings. The integral length, L was found to be related to the square root of the turbulence decay coefficient in the power law decay of turbulence kinetic energy, A. The larger A associated with the orificed perforated plate gave rise to a larger L. The corresponding streamwise autocorrelation functions for the two perforated plates behaved differently, confirming the quantitative disparity in L and further indicates some qualitative difference in the large-scale structures generated. [DOI: 10.1115/1.2754314]

Introduction

A perforated plate with multiple openings has been widely utilized in the study of turbulence and related subjects for experimentally simulating nearly isotropic turbulence (e.g., [1,2]). The flow downstream of a perforated plate can generally be divided into different regions of distinct flow characteristics. Immediately downstream of the perforated plate, the flow embodies a complex interaction between the multiple jets issued from the plate openings. These jets are coupled with the wakes formed behind the solid portion of the plate. Significant turbulence generation results from the strong shearing flow in this region. Farther downstream, the jet-wake interaction homogenizes the flow and beyond a critical distance, no jet or wake can be distinguished from the flow. The turbulent flow in this region can either be uniform, decaying, nearly isotropic, or of an oscillating nature, determined largely by the perforated plate solidity ratio [3], $\sigma \equiv$ solid area/total area.

The far field flow region of the perforated plate bears a great resemblance to that downstream of a grid constructed from solid bars. A considerable number of studies have been conducted on the grid wind/water tunnel turbulence since the pioneering work of Taylor [4]. The turbulent flow beyond the developing region downstream of the grid was found to be nearly isotropic [5], making grid/perforated plates a suitable device in generating isotropic turbulence and verifying the associated theories. Conventional grid turbulence generators were constructed with solid bars in a biplane pattern. The grid geometry is characterized by parameters such as the bar shape (round or square), bar diameter, mesh size, and grid solidity. The turbulence level downstream of the grid depends directly on the grid solidity, which has been summarized in Ref. [6] to follow a logarithmic relationship. Uberoi and Wallis [7] investigated the effect of grid geometry on the decay of grid turbulence using a biplane grid, an inclined-rods grid, and a honeycomb grid. For all the grids considered, the isotropy level, which depends on the grid geometry, was found to remain essentially constant during the decay. This implies that the rate of decay depends on the initial energy spectrum and the energy containing eddies remain self-similar during the decay. Lavoie et al. [8] studied the effect of the grid geometry using grids composed of square and round bars of different solidities. It was found that, over the range of conditions investigated in that study, the bar shape exerts a stronger influence on the energy containing scales than the grid solidity, which has little effect on the scales ranging from Kolmogorov length to Taylor microscale.

It should be noted that all the existing studies on grid/perforated plate turbulence utilized turbulence generators of finite thickness. The thickness effect on empirical grid turbulence has long been ignored, or assumed to be negligible. None of the previous studies included a contrast of the effect of sharp-edged orifices and holes of constant diameter. Gan and Riffat [9] found that the pressure drop coefficient of a perforated plate with a *single* perforation decreases with increasing plate thickness and remains nearly unchanged beyond a particular range of thickness. Given the fact that perplexing multiple-jet interactions occur immediately downstream of the perforated plate with multiple openings, the plate thickness effect for a perforated plate turbulence generator is expected to be more complex than it is for a single opening plate. This speculation is strengthened by the fact that the evolution and decay of isotropic turbulence depend strongly on the initial and boundary conditions as demonstrated by independent analytical studies [10,11].

Experimental Details

The experiments were conducted in a wind tunnel of closed-circuit type. The working section of this wind tunnel measures 6 m long with a square cross section of 0.76 m by 0.76 m at the entrance. The cross-sectional area increases gradually to incorporate the buildup of the boundary layer on the walls. Consequently, the end portion of the working section measures 0.80 m by 0.80 m. The maximum achievable mean velocity is $\sim$15 m/s. A preliminary test was carried out at a mean velocity of 10 m/s, where the background turbulence level was found to be $<0.5\%$.

An orificed perforated plate (OPP) with aligned hole network (Figs. 1(*a*) and 1(*b*)) and a 25.4 mm thick, straight hole perforated plate (SHPP) with aligned hole network (Fig. 1(*c*)) were utilized to experimentally simulate nearly isotropic turbulence in the wind tunnel. Both perforated plates measure 0.76 m by 0.76 m. During the test, one of these perforated plates was secured at 0.38 m downstream of the entrance of the working section. The perforation was made of 38.1 mm diameter holes, and the aligned hole

[1]Corresponding author.

Contributed by the Fluids Engineering Division of ASME for publication in the JOURNAL OF FLUIDS ENGINEERING. Manuscript received February 18, 2006; final manuscript received March 28, 2007. Review conducted by Joseph Katz.

 Copyright © 2007 by ASME

Downloaded 03 Jun 2010 to 171.66.16.156. Redistribution subject to ASME license or copyright; see http://www.asme.org/terms/Terms_Use.cfm

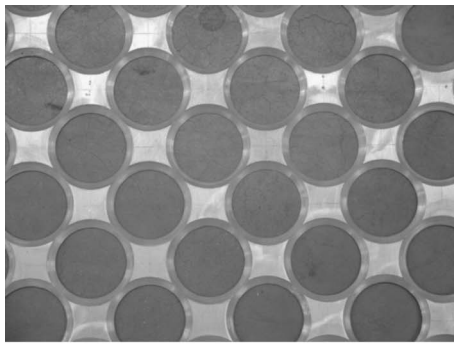

(*a*)

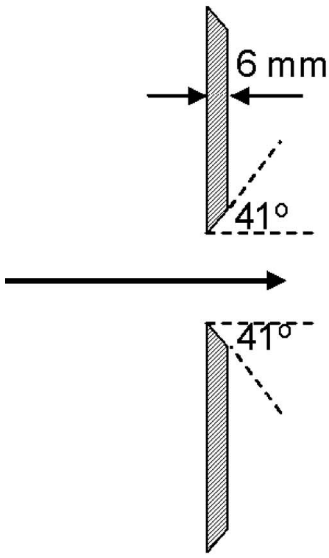

(*b*)

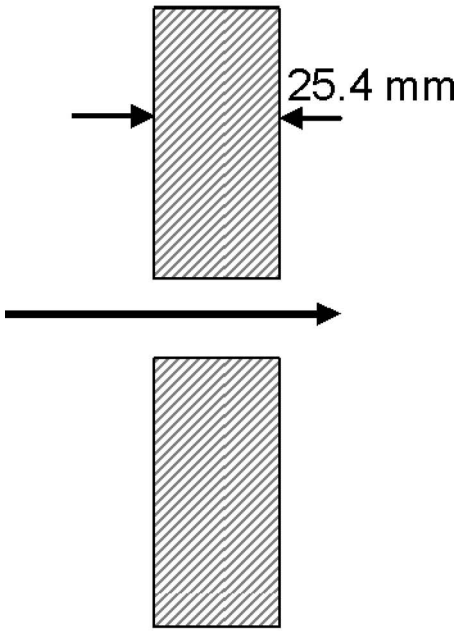

(*c*)

Fig. 1 (*a*) Close-up view of the orificed perforated plate, (*b*) cross-sectional view of the OPP, and (*c*) cross-sectional view of the 25.4 mm thick straight-hole perforated plate

network of each perforated plate was arranged so that the diagonal center-to-center hole distance M was 45 mm. This gave rise to a material plate solidity ratio σ of ~0.43. This solidity is comparable to the largest value (0.44) tested in conventional grid turbulence study [12]. The OPP was made of a 6 mm thick aluminum sheet. The orificed holes in the OPP have 41 deg inclined openings; see Fig. 1(*b*). The SHPP, on the other hand, was made of 25.4 mm thick plastic board, and the drilled surfaces have an average surface finish of 32.

Instantaneous flow velocities were measured with a Dantec Streamline® 55C90 constant temperature anemometer (CTA) and a DISA 55P61 X-configuration hot-wire probe. The sensors on the probe were two 1.25 mm long, platinum-coated tungsten wires with a diameter of 5 μm. The analog signals from the CTA were picked up by a National Instrument SC-2040 sample-and-hold board and then digitized via a 12-bit National Instrument multifunctional A/D converter. All the velocity data were collected at a sampling rate of 40 kHz and low passed at 10 kHz to avoid the aliasing problem. The hot-wire probe was calibrated within the potential core of an in-house jet facility. The nominal velocity was given by a digital manometer with a resolution of 0.0254 mm of water. A thermistor-type temperature probe was placed close to the hot-wire probe to provide the temperature reading necessary for small temperature correction. The correction procedure is as follows.

The ambient temperature T_{amb} measured by the thermister was applied in the following formula to estimate the temperature correction factor T_{corr} as

$$T_{\text{corr}} = \left(\frac{T_w - T_{\text{ref}}}{T_w - T_{\text{amb}}} \right)^{0.5(1\pm m)} \tag{1a}$$

where T_w is the constant temperature of the hot-wire sensor, T_{ref} is the temperature at which the cold wire resistance has been measured, and m is the temperature load coefficient (=0.2 for air). The ultimate correction was made to the instantaneous voltage reading, E_i from the hot-wire sensor as

$$E_{\text{corr}} = T_{\text{corr}} E_i \tag{1b}$$

Typically, the value of T_{corr} for a given test was ~1.03.

For each perforated plate, the instantaneous flow velocities were measured along the centerline at three different nominal mean flow velocities, namely, 5.8 m/s, 7.8 m/s, and 10.8 m/s. The nominal mean velocity was set with the assistance of a Pitot-static tube positioned at 15D upstream of the perforated plate. The mean velocity set in this way was double-checked with the pressure drop across the wind tunnel contraction section located immediately upstream of the working section. At each mean flow velocity, in order to reduce the statistical error associated with the subsequent curve-fitting process, the turbulence measurements were taken at 121 evenly separated (ΔX=25.4 mm) streamwise locations from 20D to 104D downstream of the perforated plate.

To ensure reliable turbulence decay data along the centerline of the wind tunnel, one has to make sure the flow over the cross section normal to the mean flow is uniform. Thus, verification tests were conducted at a nominal mean velocity of 10.8 m/s over five evenly separated cross sections from 20D to 100D downstream of each perforated plate. Each cross section measures 254×254 mm^2, centering at the middle of the working section. The measuring locations over each cross section were separated 12.7 mm from one another, giving a total of 441 measurement points. The flow fields over these cross sections were found to be approximately uniform (within ±5% of the corresponding centerline value) in terms of $\bar{U}$ (the time-averaged mean velocity), u' (the root-mean-square value of the streamwise turbulence fluctuation velocity), and v' (the root-mean-square value of the lateral turbulence fluctuation velocity). Moreover, the turbulent flows were found to be nearly isotropic as indicated by $u'/v' \approx 1.0$.

Downloaded 03 Jun 2010 to 171.66.16.156. Redistribution subject to ASME license or copyright; see http://www.asme.org/terms/Terms_Use.cfm

The uncertainties in the present measurements were estimated in the following steps. First, the uncertainty in the instantaneous flow velocity was estimated since it was the starting point of the subsequent calculation of all the turbulence parameters. The uncertainties in the other parameters were estimated using the uncertainty propagation theory. The actual calculation of the uncertainties was accomplished with a MATLAB® code dedicated for this purpose.

Decay of Turbulence Kinetic Energy

Since there is no kinetic energy input from the mean flow in the absence of mean shear, the nearly isotropic turbulent flow downstream of the perforated plate, beyond the wake-jet interaction near-field region, decays monotonically with the distance from the turbulence generator. Theoretical analysis of decaying isotropic turbulence has demonstrated, under different levels of self-preservation assumptions, that the turbulence decay obeys the power-law relationship for which the decay exponent varies from 1 to 10/7 among different studies [11,13–18]. Many empirical results from grid turbulence studies confirmed this scatter, with the value of the decay exponent ranging from 1 to 1.4 [12,19,20]. In the present work, the turbulence decay is expressed in the form of the time variation of turbulence kinetic energy K, i.e.,

$$K \equiv \frac{u'^2 + 2v'^2}{2} = A(t - t_o)^{-n} \tag{2}$$

where $t = X/U$ indicates the elapsing time when one observes the turbulence decay in the coordinate system moving with the mean flow. The uncertainty in K was estimated to be ±7%, following the guideline in Ref. [21].

The conventional approach to estimate the decay parameters A, t_o, and n is by computing the values of A and n at systematically varying t_o values. The set of values that give the highest curve fit confidence level are chosen to represent the decay of turbulence. Graphically, this can be determined by plotting the curve fit residues against the corresponding t_o values, the t_o at the saddle point is chosen as the ultimate curve fit result. The drawback of this approach is that the curve fit confidence levels corresponding to different sets of decay parameters are numerically too close to each other to lead to a definitive decision [20].

To address this issue, we adopted a nonlinear curve fitting technique as opposed to the linear technique used in the conventional grid turbulence studies. This nonlinear technique has been widely applied in estimating the power-law curve fitting parameters of hot-wire calibration data. The advantage of this technique is that one can simultaneously obtain the values of all three curve fitting parameters, A, t_o, and n, which give the best possible power-law form. The nonlinear curve fitting method is available in commercial software packages, e.g., MATLAB. However, in this study, a dedicated C code has been written for this purpose.

Figure 2 presents in logarithmic scale the variation of the turbulence kinetic energy, K with $t - t_o$, the time after the virtual origin t_o. Figure 2 clearly depicts an increase in the turbulence kinetic energy with increasing mean flow velocity. It is also noted in Fig. 2 that, for the same nominal mean velocity, the OPP gives rise to a higher level of turbulence. Nonetheless, the decay exponent n appears to be the same for both perforated plates for all three mean velocities considered; as all six sets of data points line up parallel to each other. This observation is confirmed by the curve fitting results listed in Table 1, where the value of n varies from 1.12 to 1.16, that is, by $<4\%$.

Figure 3 presents the variation the relative turbulence intensity, $\mathrm{Tu} = [(2K/3)^{3/2}/U] \times 100\%$ with respect to the downstream distance X. The relative turbulence intensity seems to be unaffected by the changes in U from 5.8 m/s to 10.8 m/s. A comparison of the Tu values for the OPP and SHPP shows that, on average, the relative turbulence intensity downstream of the OPP is ~25% higher than that of the SHPP. This may be explained, following

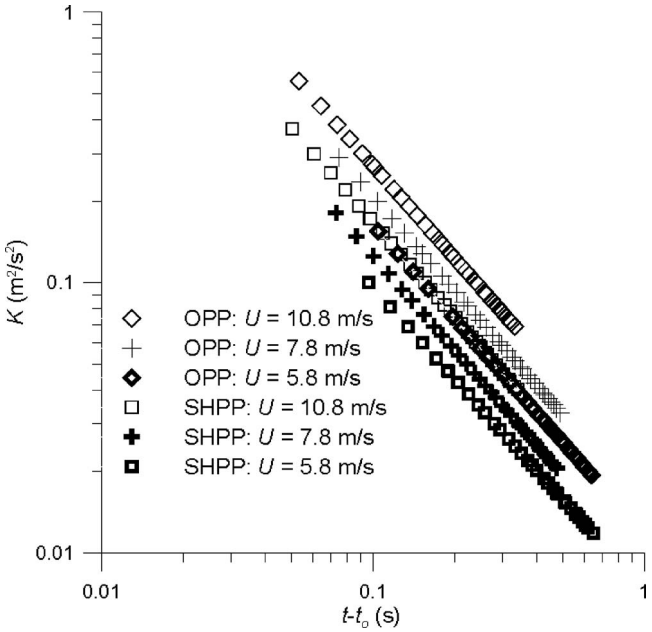

Fig. 2 Variation of *K* with the time measured in the coordinate system moving with the mean flow

Ref. [22], in terms of the effective fluid dynamic solidity of the turbulence generator. Even though both perforated plates have exactly the same material solidity ($\sigma = 0.43$) and hole diameter, the flow field immediately downstream of the leading edge of each hole opening is expected to be different as postulated in Fig. 4. In the case of the SHPP, the recirculation field formed in between the vena contracta and the solid boundary of the hole tends to reduce the effective fluid dynamics solidity. This phenomenon is not present when utilizing the OPP of virtually zero plate thickness. In other words, the OPP has a larger effective, fluid dynamics solidity than the SHPP and thus gives rise to a higher level of turbulence at the same mean velocity.

Variation of Integral Length Scale

The turbulence integral length scale L is an important parameter that signifies the average size of the energy containing eddies. Various schemes have been proposed for the estimation of L [23]. The approach adopted in this study is based on the Taylor's frozen turbulence hypothesis, where L is defined as

$$L = 2\int_0^\infty g(r)dr \tag{3}$$

The integration process was terminated at the first zero crossing. This approach is slightly different from that described by Barrett and Hollingsworth [23] in the sense that the lateral autocorrelation function $g(r)$ was utilized here in place of the streamwise autocorrelation function $f(r)$. This is because both theoretical and experimental results have shown that the autocorrelation function $g(r)$ has a clear zero crossing point, which is not generally observed in $f(r)$. The consistent zero crossing nature of $g(r)$ ensures both the feasibility and reliability in estimating the integral scale L. The uncertainties in $f(r)$ and $g(r)$ are approximately ±0.001, which gives rise to an uncertainty in L of approximately ±0.5 mm.

An alternative approach in calculating L is to assume the applicability of the relationship

Downloaded 03 Jun 2010 to 171.66.16.156. Redistribution subject to ASME license or copyright; see http://www.asme.org/terms/Terms_Use.cfm

Table 1 Curve fitting results to Eq. (2)

	OPP			SHPP		
	U: 10.8 m/s	U: 7.8 m/s	U: 5.8 m/s	U: 10.8 m/s	U: 7.8 m/s	U: 5.8 m/s
A (m^2 s^{n-2})	0.0196	0.0145	0.0116	0.0110	0.0087	0.0073
n	1.14	1.16	1.14	1.16	1.16	1.12
t_o (s)	0.0191	0.0267	0.0368	0.0229	0.0322	0.0484

$$L = B\frac{u'^3}{\varepsilon} \tag{4}$$

where ε is the turbulence dissipation rate, which can be estimated as

$$\varepsilon \equiv -\frac{dK}{dt} = nA(t-t_o)^{-n-1} \tag{5}$$

Equation (4) is based on the assumption that the time scale of the energy dissipation, u'^2/ε is of the same order of magnitude as the characteristic time scale of the energy containing eddies L/u'. Coefficient B has been found to be of the order of one [24,25]. To verify the applicability of Eq. (4), the variation of the dimensionless length scale, $B=L\varepsilon/u'^3=L\varepsilon(2K/3)^{3/2}$ is presented in Fig. 5 for both perforated plates with a nominal mean velocity of 10.8 m/s. Herein, L values were estimated from Eq. (3). The dimensionless length scales at the other two mean velocities (7.8 m/s and 5.8 m/s) behave similarly; these values are not plotted to avoid clustering of the data points. Figure 5 demonstrates that, notwithstanding some fluctuation and/or scatter, the value of $L\varepsilon/(2K/3)^{3/2}$ stays within 1 to 1.2 for both the OPP and SHPP cases. More precisely, the average value of $L\varepsilon/(2K/3)^{3/2}$ is 1.08 with a standard deviation of 0.03 for the OPP case, and 1.11 with a standard deviation of 0.03 for the SHPP case.

Replacing u' in Eq. (4) with $(2K/3)^{3/2}$ and utilizing Eqs. (2) and (5) gives rise to the following relationship:

$$L = B\frac{(2K/3)^{3/2}}{\varepsilon} = B\frac{[A(t-t_o)^{-n}2/3]^{3/2}}{nA(t-t_o)^{-n-1}} = \left(\frac{2}{3}\right)^{3/2} B\frac{A^{1/2}}{n}(t-t_o)^{1-0.5n} \tag{6}$$

Equation (6) states that the evolution of the turbulence integral length scale can be described by the same set of power-law parameters that depicts the decay of turbulence kinetic energy. Specifically, when two isotropic turbulent flows have the same decay exponent n and proportional coefficient B the one with the larger decay coefficient A has a larger integral length scale at any given elapsed time.

The $L \propto A^{1/2}$ relationship can be verified by considering the ratio of the respective integral length scales downstream of the OPP and SHPP at the same mean velocity. Figure 6 presents the variation of such a ratio with the downstream distance, i.e., the decaying time, at 10.8 m/s. The listed values in Table 1 show that $(A_{\mathrm{OPP,10.8\ m/s}}/A_{\mathrm{SHPP,10.8\ m/s}})^{1/2}=1.33$. This value (shown as a solid straight line in Fig. 6) falls within the scatter of $L_{\mathrm{OPP}}/L_{\mathrm{SHPP}}$, corroborating the $L \propto A^{1/2}$ prediction.

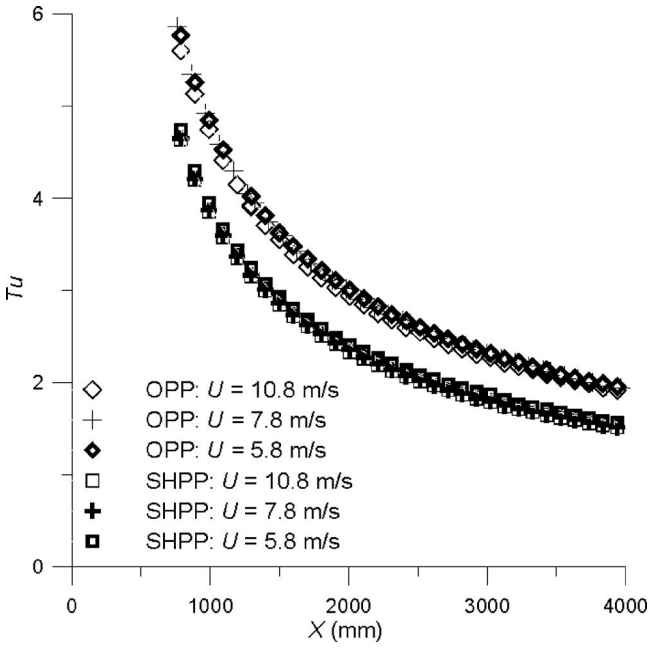

Fig. 3 Variation of Tu with the downstream distance from the perforated plates

Similarity of Autocorrelation Functions

Table 1 shows that the turbulence decay exponent remains nearly unchanged under all the test conditions considered in this study. This leads naturally to the expectation that the decaying turbulent flows downstream of the OPP and the SHPP are similar as implied by the study of George [10], who claimed that the decay exponent depends on the initial condition and is not necessarily universal. The flow similarity between these two perforated plates can be readily verified or challenged by examining the corresponding autocorrelation functions.

Figures 7(*a*) and 7(*b*) present the variation of the streamwise autocorrelation function with the downstream distance ($X/D=20$, 60, and 100) for the OPP and SHPP cases, respectively. As expected, the area underneath $f(r)$ increases with the downstream distance, indicating the increase in the integral length scale. Note that $\lim_{r\to\infty} f(r)_{\mathrm{OPP}} \to 0$ for $X/D=20$ and 60, as would be expected; there is, however, a slight indication that this limit does not go to 0 for $X/D=100$. The lack of approach to 0 is more pronounced for the SHPP case at $X/D=100$, where $\lim_{r\to\infty} f(r)_{\mathrm{OPP}} \to 0.08$. This seems to suggest that there may be a low-frequency fluctuation in the velocity.

The typical behavior of the autocorrelation function $f(r)$ for the OPP is shown in Fig. 8(*a*). The plot clearly reveals that $f(r)$ has a small negative portion. This behavior is consistent with the measurement of van Atta and Chen [26], but differs from that of Frenkiel and Klebanoff [27] who observed that $f(r)$ remains nonnegative over the range of r they considered. It should be noted that the nominal test conditions in the studies of van Atta and Chen [26] and Frenkiel and Klebanoff [27] were the same; both are, however, quite different from the current study in terms of the type of turbulence generator. In both of these previous studies, a biplane grid with a mesh size of 25.4 mm and a bar diameter of 5 mm were utilized. This corresponds to a grid material solidity of ~0.35. Another feature of Fig. 8(*a*) is that the three autocorrelations associated with the three different mean velocities at the same downstream location collapse onto a single curve. This leads

Downloaded 03 Jun 2010 to 171.66.16.156. Redistribution subject to ASME license or copyright; see http://www.asme.org/terms/Terms_Use.cfm

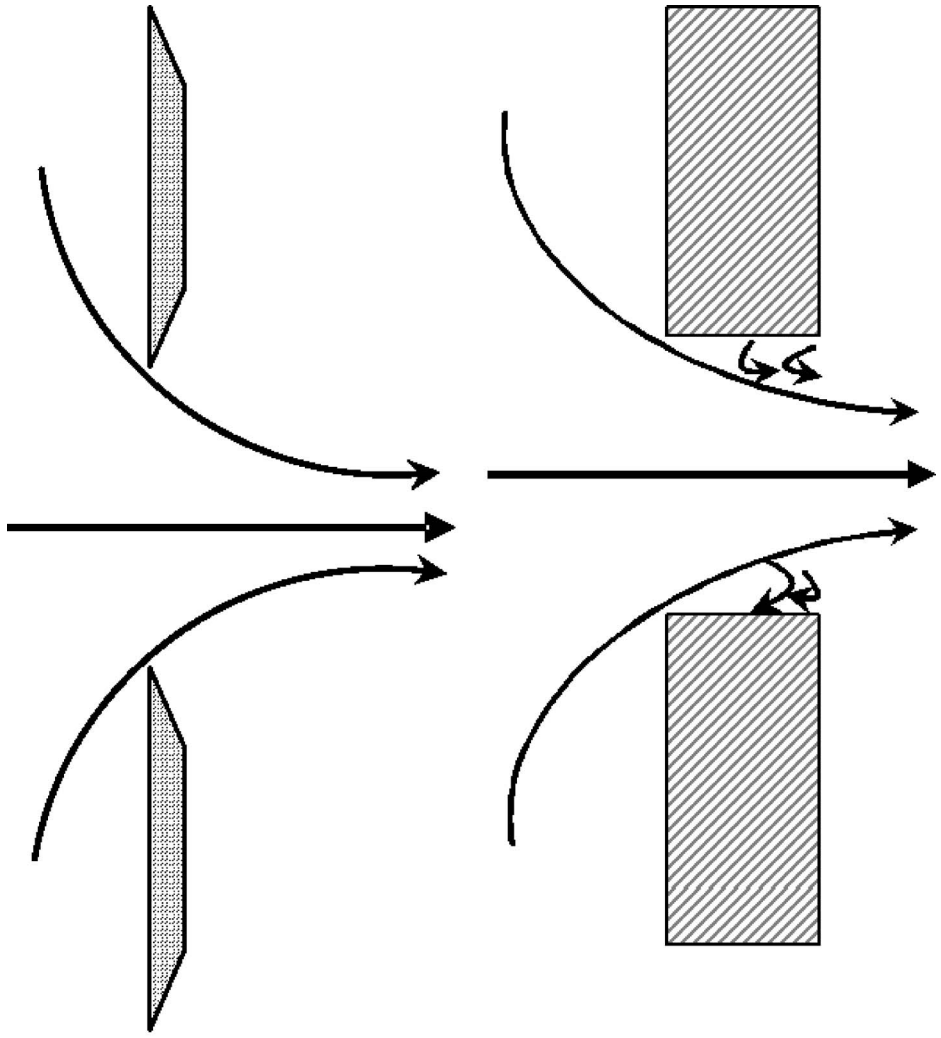

Fig. 4 Illustration of the flow fields immediately downstream of the leading edges of (*a*) the orificed perforated plate and (*b*) the straight hole perforated plate

immediately to the impression that the turbulence integral length scale at a particular location downstream of the perforated plate is determined exclusively by the geometrical feature(s) of the turbulence generator and is independent of the mean velocity. This is confirmed by the observation that the lateral autocorrelation functions shown in Fig. 8(*b*) collapse onto one single curve for $X/D=60$ at $U=5.8$ m/s, 7.8 m/s, and 10.8 m/s.

Figure 9(*a*) presents the variation of $f(r)$ for the SHPP for $X/D=60$ at $U=5.8$ m/s, 7.8 m/s, and 10.8 m/s. Just as in the OPP case the three autocorrelation functions collapse onto each other, which, again, corroborates the aforementioned dependence of the integral turbulence length scale on the geometry of turbulence generator. The unique feature of Fig. 9(*a*) is that the streamwise autocorrelation function $f(r)$ does not have the negative portion, as observed for the OPP case in Fig. 8(*a*). It is worth mentioning that there is no general agreement among turbulent experts as per the overall shape of $f(r)$, let alone the existence of a negative portion. The results of the present study seem to indicate that the shape of $f(r)$ is dependent on the initial conditions, among which the geometry of the turbulence generator is an important factor. The behavior of the lateral autocorrelation function for the SHPP is demonstrated in Fig. 9(*b*), which, similar to Fig. 8(*b*), shows that the $g(r)$ function in this study has a clear negative

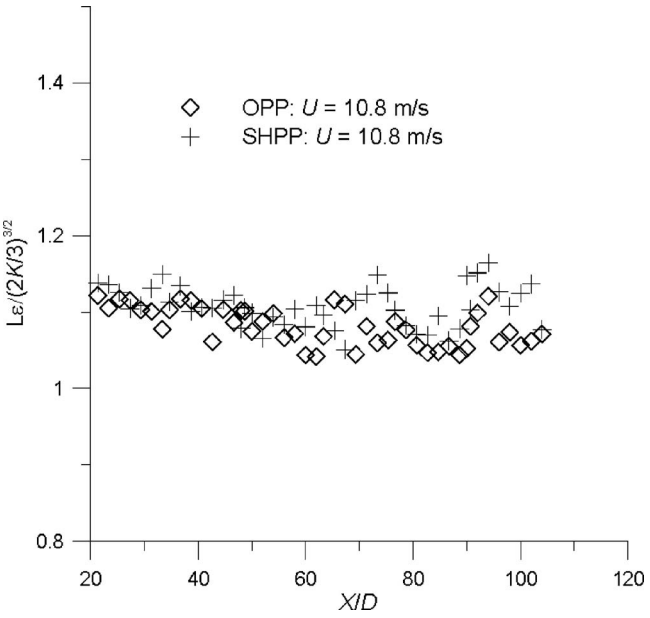

Fig. 5 Variations of dimensionless parameter $L\varepsilon/(2K/3)^{3/2}$ for OPP and SHPP

Downloaded 03 Jun 2010 to 171.66.16.156. Redistribution subject to ASME license or copyright; see http://www.asme.org/terms/Terms_Use.cfm

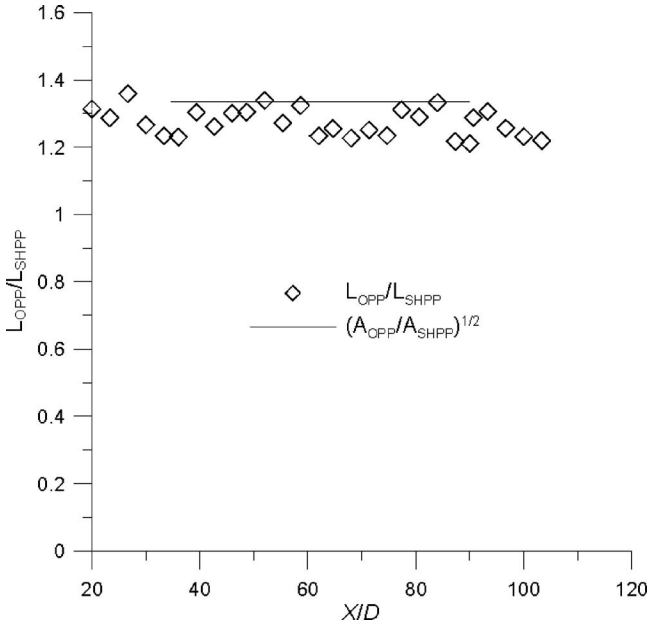

Fig. 6 Verification of $L \propto A^{1/2}$ relationship at $U=10.8$ m/s

portion. This is consistent with the results of many conventional grid turbulence studies [e.g., [28,29]] as well as that from analytical prediction [30].

Conclusions

A comparison study has been conducted to investigate the decaying, nearly isotropic turbulent flow downstream of a perforated plate. The test has been carried out using two different perforated plates with the same perforation pattern and material solidity. The major geometrical feature that differentiates the two turbulence generators is the effective plate thickness seen by the oncoming flow. The thickness disparity has been found to lead to differences in several corresponding turbulence parameters, namely, the turbulence intensity Tu, the turbulence integral length scale L, and the streamwise turbulence autocorrelation $f(r)$.

The experimental data of the current study show that (at any given downstream location) the turbulence intensity Tu is higher in the OPP case and remains approximately unchanged with variation of velocity from 5.8 m/s to 10.8 m/s. A probable explanation for OPP's enhanced turbulence generation ability is its larger effective fluid dynamics solidity.

Conventional studies on the decaying isotropic turbulence have shown that the size of the turbulence integral length scale increases with the decay time for which a mathematical relationship in the form of the power law applies. The analysis in this study further reveals that the integral length is proportional to the square root of A, i.e.,

$$L \propto \left(\frac{2}{3}\right)^{3/2} \frac{A^{1/2}}{n} (t - t_o)^{1-0.5n}$$

The turbulence integral length scale at any location downstream of the perforated plate was found to be exclusively determined by the effective plate thickness and is not a function of the mean velocity. The streamwise autocorrelation function crosses zero into negative, in the case of OPP, whereas it remains non-negative for the SHPP. This indicates that the large-scale structures downstream of the two perforated plates are also qualitatively different.

Notwithstanding the aforementioned disparities in turbulence intensity and length scale, the nearly isotropic turbulent flows downstream of the two different perforated plates decay at almost the same rate, as indicated by the negligible difference in the decay exponents corresponding to these two perforated plates.

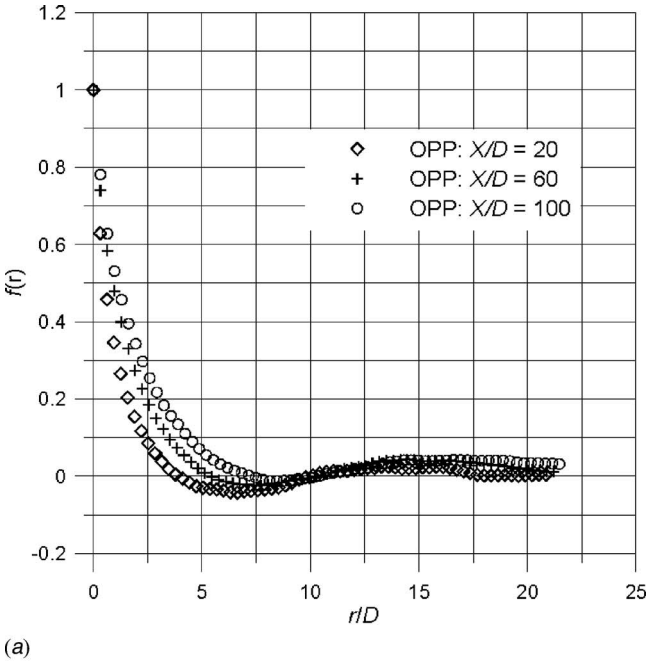

(*a*)

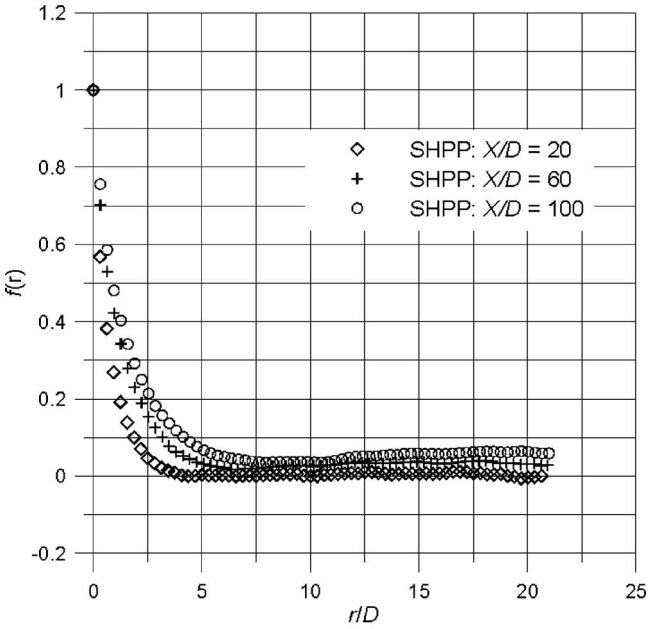

(*b*)

Fig. 7 (*a*) Streamwise autocorrelation function $f(r)$ at 20D, 60D, and 100D downstream of the OPP at $U=10.8$ m/s, and (*b*) streamwise autocorrelation function $f(r)$ at 20D, 60D, and 100D downstream of the SHPP at $U=10.8$ m/s

This implies the possible existence of universal self-similarity between the two seemingly different turbulent flows.

It should be noted that the turbulent flows generated in this study are low Reynolds number nearly isotropic turbulence. At the highest time-averaged flow velocity, the Taylor microscale Reynolds number Re_λ decreases from ~108 to 94 for the OPP, and from 85 to 72 for the SHPP. Further study at higher Re_λ is necessary to depict a more complete picture of the plate thickness effect.

Acknowledgment

This project was sponsored by the Natural Sciences and Engineering Research Consul of Canada (NSERC). The lead author

Downloaded 03 Jun 2010 to 171.66.16.156. Redistribution subject to ASME license or copyright; see http://www.asme.org/terms/Terms_Use.cfm

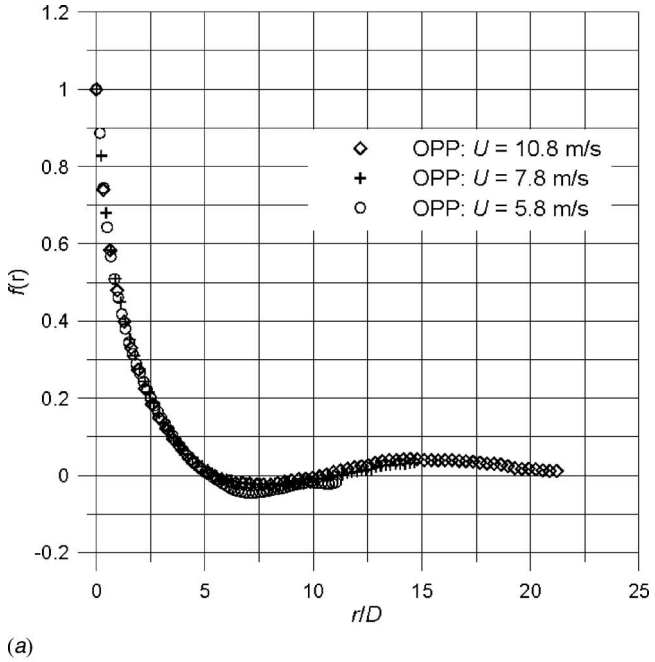

(a)

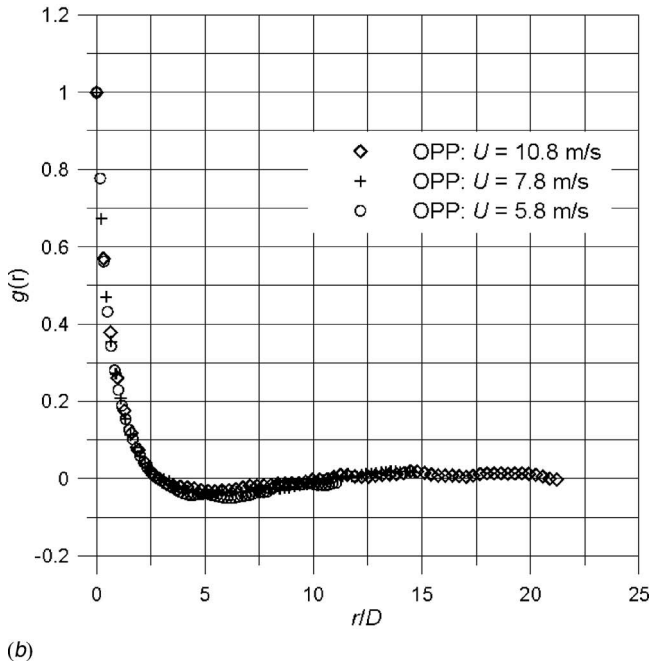

(b)

Fig. 8 (*a*) Streamwise autocorrelation function *f*(*r*) at 60*D* downstream of the OPP at *U*=5.8 m/s, 7.8 m/s, and 10.8 m/s, and (*b*) lateral autocorrelation function *g*(*r*) at 60*D* downstream of the OPP at *U*=5.8 m/s, 7.8 m/s, and 10.8 m/s

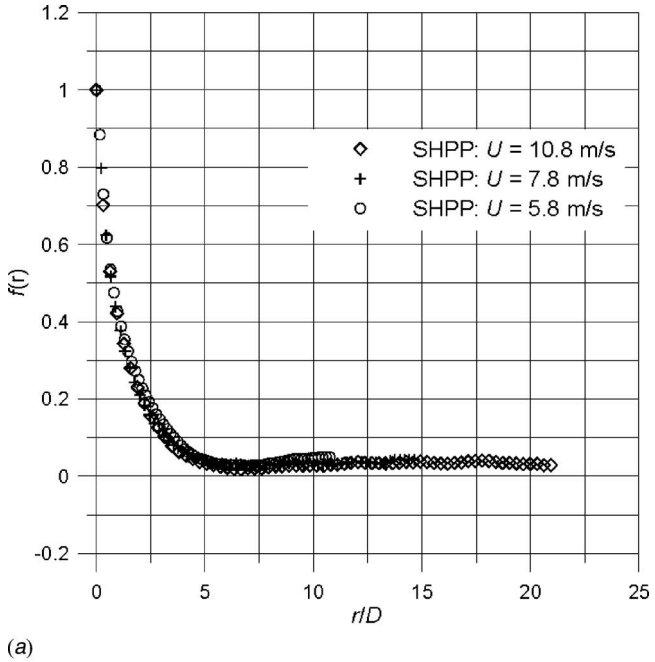

(a)

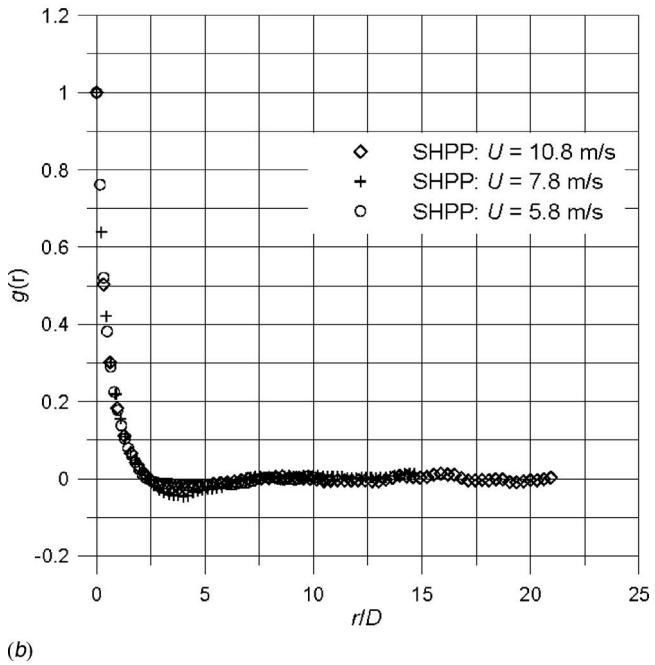

(b)

Fig. 9 (*a*) Streamwise autocorrelation function *f*(*r*) at 60*D* downstream of the SHPP at *U*=5.8 m/s, 7.8 m/s, and 10.8 m/s, and (*b*) lateral autocorrelation function *g*(*r*) at 60*D* downstream of the SHPP at *U*=5.8 m/s, 7.8 m/s, and 10.8 m/s

gratefully acknowledges Ontario Student Assistance Program (OSAP) for an Ontario Graduate Scholarship (OGS).

Nomenclature

A = decay power law coefficient ($m^2\ s^{n-2}$)
B = proportional coefficient in $L=B(u'^3/\varepsilon)$
D = plate hole diameter (D=38.1 mm)
E_i = instantaneous voltage reading
E_{corr} = instantaneous voltage reading with temperature correction
f = streamwise autocorrelation function of u, $f(r)=\overline{u*u(r)}/u'^2$
g = streamwise autocorrelation function of v, $g(r)=\overline{v*v(r)}/v'^2$
K = turbulence kinetic energy per unit mass (m^2/s^2)
L = turbulence integral length scale (mm)
M = mesh size of grid/OPP turbulence generator (M=45 mm)
m = temperature load coefficient
n = decay power exponent
OPP = orificed perforated plate

Downloaded 03 Jun 2010 to 171.66.16.156. Redistribution subject to ASME license or copyright; see http://www.asme.org/terms/Terms_Use.cfm

r = streamwise separation ($=U\tau$ m)
Re_λ = Taylor microscale Reynolds number
rms = root mean square
SHPP = straight hole perforated plate
T_{amb} = ambient temperature
T_{corr} = temperature correction factor
T_{ref} = cold wire reference temperature
T_w = constant hot-wire sensor temperature
Tu = Relative turbulence intensity, $\mathrm{Tu}=[(2K/3)^{3/2}/U]\times 100\%$
t = converted elapsing time (s)
U = local time-averaged flow velocity (m/s)
u' = streamwise rms turbulence fluctuation velocity (m/s)
v' = lateral rms turbulence fluctuation velocity (m/s)

Greek Symbols

σ = solidity ratio ($\sigma=0.43$)
τ = separation in time (s)

References

[1] Villermaux, E., and Hopfinger, E. J., 1994, "Periodically Arranged Co-Flowing Jets," J. Fluid Mech., **263**, pp. 63–92.
[2] Geers, L. F. G., Tummers, M. J., and Hanjalic, K., 2004, "Experimental Investigation of Impinging Jet Arrays," Exp. Fluids, **36**, pp. 946–958.
[3] Baines, W. D., and Peterson, E. G., 1951, "An Investigation of Flow Through Screens," ASME J. Appl. Mech., **73**, pp. 467–478.
[4] Taylor, G. I., 1935, "Statistical Theory of Turbulence," Proc. R. Soc. London, Ser. A, **151**, pp. 421–444.
[5] Tresso, R., and Munoz, D. R., 2000, "Homogeneous, Isotropic Flow in Grid Generated Turbulence," ASME J. Fluids Eng., **122**, pp. 51–56.
[6] Liu, R., Ting, D.S.-K., and Rankin, G. W., 2004, "On the Generation of Turbulence With a Perforated Plate," Exp. Therm. Fluid Sci., **28**, pp. 307–316.
[7] Uberoi, M. S., and Wallis, S., 1967, "Effect of Grid Geometry on Turbulence Decay," Phys. Fluids, **10**, pp. 1216–1224.
[8] Lavoie, P., Antonia, R. A., and Djenidi, L., 2004, "Effect of Grid Geometry on the Scale-by-Scale Budget of Decaying Grid Turbulence," 15th Australasian Fluid Mechanics Conference, The University of Sydney, Sydney.
[9] Gan, G., and Riffat, S., 1997, "Pressure Loss Characteristics of Orifice and Perforated Plates," Exp. Therm. Fluid Sci., **14**, pp. 160–165.
[10] George, W. K., 1992, "The Decay of Homogeneous Isotropic Turbulence," Phys. Fluids A., **4**(7), pp. 1492–1509.
[11] Speziale, C. G., and Bernard, P. S., 1992, "The Energy Decay in Self-Preserving Isotropic Turbulence Revisited," J. Fluid Mech., **241**, pp. 645–667.
[12] Comte-Bellot, G., and Corrsin, S., 1966, "The Use of a Contraction to Improve the Isotropy of Grid-Generated Turbulence," J. Fluid Mech., **25**, pp. 657–682.
[13] von Karman, T., and Howarth, L., 1938, "On the Statistical Theory of Isotropic Turbulence," Proc. R. Soc. London, Ser. A, **164**, pp. 192–215.
[14] Dryden, H. L., 1943, "A Review of the Statistical Theory of Turbulence," Q. Appl. Math., **1**, pp. 7–42.
[15] Batchelor, G. K., 1948, "Energy Decay and Self-Preserving Correlation Functions in Isotropic Turbulence," Q. Appl. Math., **6**, pp. 97–116.
[16] Lin, C. C., 1948, "Note on the Law of Decay of Isotropic Turbulence," Proc. Natl. Acad. Sci. U.S.A., **34**, pp. 230–233.
[17] Saffman, P. G., 1967, "The Large Scale Structure of Homogeneous Turbulence," J. Fluid Mech., **27**, pp. 581–593.
[18] Antonia, R. A., Smalley, R. J., Zhou, T., Anselmet, F., and Danaila, L., 2003, "Similarity of Energy Structure Functions in Decaying Homogeneous Isotropic Turbulence," J. Fluid Mech., **487**, pp. 245–269.
[19] Stewart, R. W., and Townsend, A. A., 1951, "Similarity and Self-Preservation in Isotropic Turbulence," Philos. Trans. R. Soc. London, Ser. A, **243**, pp. 359–386.
[20] Mohamed, M. S., and LaRue, J. C., 1990, "The Decay Power Law in Grid-Generated Turbulence," J. Fluid Mech., **219**, pp. 195–214.
[21] Abernethy, R. B., Benedict, R. P., and Dowdell, R. B., 1985, "ASME Measurement Uncertainty," ASME J. Fluids Eng., **107**, pp. 161–164.
[22] Gad-El-Hak, M., and Corrsin, S., 1974, "Measurements of the Nearly Isotropic Turbulence Behind a Uniform Jet Grid," J. Fluid Mech., **62**, pp. 115–143.
[23] Barrett, M. J., and Hollingsworth, D. K., 2001, "On the Calculation of Length Scales for Turbulent Heat Transfer Correlation," ASME J. Heat Transfer, **123**, pp. 878–883.
[24] Sreenivasan, K. R., 1984, "On the Scaling of Turbulence Energy Dissipation Rate," Phys. Fluids, **27**, pp. 1048–1051.
[25] Burratini, P., Lavoie, P., and Antonia, R. A., 2005, "On the Normalized Turbulent Energy Dissipation Rate," Phys. Fluids, **17**, Paper No. 0908103, pp. 1–4.
[26] van Atta, C. W., and Chen, R., 1968, "Correlation Measurements in Grid Turbulence Using Digital Harmonic Analysis," J. Fluid Mech., **34**, pp. 497–515.
[27] Frenkiel, F. N., and Klebanoff, P. S., 1967, "Correlation Measurement in a Turbulent Flow Using High-Speed Computing Method," Phys. Fluids, **10**, pp. 1737–1747.
[28] Monin, A. S., and Yaglom, A. M., 1975, *Statistical Fluid Mechanics*, Lumley, J. L., ed., MIT Press, Cambridge, MA, vol. 2.
[29] Comte-Bellot, G., and Corrsin, S., 1971, "Simple Eulerian Time Correlation of Full- and Barrow-Band Velocity Signals in Grid-Generated, 'Isotropic' Turbulence," J. Fluid Mech., **48**, pp. 273–337.
[30] Mathieu, J., and Scott, J., 2000, *An Introduction to Turbulent Flow*, Cambridge University Press, Cambridge, England.

Downloaded 03 Jun 2010 to 171.66.16.156. Redistribution subject to ASME license or copyright; see http://www.asme.org/terms/Terms_Use.cfm

Numerical Investigation of Steady Density Currents Flowing Down an Incline Using $\overline{v^2}-f$ Turbulence Model

Nima Khakzad[1]
Graduate student
e-mail: nimakhakzad@yahoo.com

Bahar Firoozabadi
Assistant Professor
e-mail: firoozabadi@sharif.ir

Bijan Farhanieh
Professor
e-mail: bifa@sharif.ir

School of Mechanical Engineering,
Sharif University of Technology,
Azadi Ave., P.O.Box 11365-9567,
Tehran, Iran

The governing equations of two-dimensional steady density currents are solved numerically using a finite volume method. The $\overline{v^2}-f$ turbulence model, based on standard $k-\varepsilon$ model, is used for the turbulence closure. In this method, all Reynolds stress equations are replaced with both a transport equation for $\overline{v^2}$ and an elliptic relaxation equation for f, a parameter closely related to the pressure strain redistribution term. The Simple-C procedure is used for pressure-velocity coupling. In addition, Boussinesq's approximation is used to obtain the momentum equation. The computed height of the progressive density current is compared to the measured data in the literature, resulting in good agreement. The present results show that the flow rate is the most dominant parameter among those affecting the density currents hydrodynamics. The results also show that the $\overline{v^2}-f$ turbulence model is able to predict and simulate the characteristics of the low Reynolds turbulent density currents successfully, although it is based on a high Reynolds number turbulence model, i.e., the standard $k-\varepsilon$ model. The use of boundary layer convention, saying that the density current's height is a height at which the concentration is ~1% of the inlet concentration, seems to yield reasonable results.
[DOI: 10.1115/1.2754318]

Keywords: density current, $\overline{v^2}$–f model, standard k–ε model, turbulence, numerical modeling

Introduction

Density current is a subsurface current flowing over a sloping bottom because of the fact that its density is heavier than ambient water. This density difference can arise from temperature, chemicals, suspended solids, etc. These affect the gravity, which is an actual driving force of such flows. Thus, gravity current is another name for this flow. Most density currents are buoyancy conserving, whereas sediment-laden density currents, turbidity currents, are not. In the study of density current hydrodynamics, there are three important components: clear ambient water, density current, and bed. During its movement, the density current entrains clear water into the flow (water entrainment) and, simultaneously, either deposits suspended sediment on the channel bed or entrains bed sediment into the flow (sediment entrainment). Density currents occur in many different environments, including subaerial pyroclastic flow in volcanic environments, density currents in lakes and oceans, thunderstorm outflows in the atmosphere, avalanche of airborne snow, the accidental release of dense gas, and oil spillage [1]. The problem of density current inflows has important applications in reservoir and outflow water quality. Knowing how contaminant in the inflow, e.g., dissolved salts, excess heat, suspended solids, or chemicals, is transported and dispersed enables decisions to be made regarding the selective withdrawal of municipal supply, cooling water, and water for irrigation from different levels within the reservoir. The density current parameters, e.g., propagation speed, thickness, and dilution, can be used to determine the change in water quality at different depths [2]. Because of their widespread occurrence in nature, density currents have recently drawn strong interests from hydraulic engineers and marine geologists.

Laboratory experiments are useful for visualizing patterns of behavior even though there are considerable problems in comparing experiments directly to individual natural density currents. Such experiments are valuable for understanding processes but should only be compared to natural case studies with extreme care, particularly in the light of problems of scaling turbulent mixing. Some previous laboratory experiments of density and turbidity currents include Buckee et al. [1], Alavian [3], Garcia [4], Altinakar et al. [5], Kneller et al. [6], Firoozabadi et al. [7], Best et al. [8], de Rooji and Dalziel [9], and Alexander and Mulder [10].

Field measurements usually only cover a small range of hydrodynamic and sediment transport conditions, and laboratory measurements have other restrictions, such as scale effects. Therefore, researchers have recently focused on numerical models consisting turbulence equations. Numerical modeling has the flexibility to allow for the adjustment of variables to evaluate their interdependence, something not always possible in laboratory experiments because of scaling limitations. It should be noted however, that modeling is neither a more accurate nor a more realistic approach than the others and is therefore not a substitute.

Considerable theoretical [2,11,12] and numerical studies of density and turbidity currents and their deposits have been carried out during the past several decades [13–29]. An important aspect of the density current is the turbulent energy. If the turbulent kinetic energy is not properly balanced, a numerical model may predict physically unrealistic acceleration [14].

Stacey and Bowen [21] investigated the necessary condition for self-maintenance using a mixing length model for the turbulence closure. Their model allowed for the influence of current's interface stability on eddy viscosity and diffusivity. Eidsvik and BrØrs [22] applied the $k-\varepsilon$ turbulence model to turbidity currents and

[1]Corresponding author.

Contributed by the Fluids Engineering Division of ASME for publication in the JOURNAL OF FLUIDS ENGINEERING. Manuscript received May 31, 2006; final manuscript received March 30, 2007. Review conducted by Ugo Piomelli. Paper presented at the 13th Conference of "Fluid Dynamics" 2005, Technical University of Shiraz, Shiraz, Iran.

 Copyright © 2007 by ASME

Downloaded 03 Jun 2010 to 171.66.16.156. Redistribution subject to ASME license or copyright; see http://www.asme.org/terms/Terms_Use.cfm

investigated the possibility of self-acceleration of the currents. The $k-\varepsilon$ model has been adopted by others to simulate two-dimensional density and turbidity currents in reservoirs [23–25], down an inclined surface in a flume [26–28], and recently in submarine channels [29,30]. Other turbulence models, such as Reynolds stress model [31,32], Mellor-Yamada level 2.5 second-order model [33], and $k-\lambda$ [34] has also been applied.

The objective of the present paper is to simulate and qualitatively investigate the vertical structure and bulk properties of two-dimensional, steady, nonparticulate density currents, herein, salt water, developing on a slope in a channel. The $\overline{v^2}-f$ model, a recently proposed turbulence model [35], is used for turbulence closure. Nonparticulate currents have been investigated by numerous researchers both in laboratory experiments (e.g., [1]) and in numerical simulations (e.g., [27]) because such currents are the simplest case and, thus, the best starting point for studying the turbulence structure in the body region of density currents. Similarity profiles of current height by Akiyama et al. [18] are used here for validation the numerical model.

Governing Equations

Density current concentration is assumed to be small enough to use Boussinesq's approximation in the momentum equation. The basic equations are mass conservation, downslope and vertical momentum conservation, and concentration equation, respectively,

$$\frac{\partial u}{\partial x}+\frac{\partial v}{\partial y}=0 \tag{1}$$

$$u\frac{\partial u}{\partial x}+v\frac{\partial u}{\partial y}=-\frac{1}{\rho}\frac{\partial P}{\partial x}+g'\sin\theta+\frac{\partial}{\partial x}\left(\nu_e\frac{\partial u}{\partial x}\right)+\frac{\partial}{\partial y}\left(\nu_e\frac{\partial u}{\partial y}\right) \tag{2}$$

$$u\frac{\partial v}{\partial x}+v\frac{\partial v}{\partial y}=-\frac{1}{\rho}\frac{\partial P}{\partial y}-g'\cos\theta+\frac{\partial}{\partial x}\left(\nu_e\frac{\partial v}{\partial x}\right)+\frac{\partial}{\partial y}\left(\nu_e\frac{\partial v}{\partial y}\right) \tag{3}$$

$$u\frac{\partial c}{\partial x}+v\frac{\partial c}{\partial y}=\frac{\partial}{\partial x}\left(\nu_e\frac{\partial c}{\partial x}\right)+\frac{\partial}{\partial y}\left(\nu_e\frac{\partial c}{\partial y}\right) \tag{4}$$

where x,y=coordinates; u,v=velocity components in the x and y directions, respectively; c=concentration; θ=the slope angle; and P=pressure. Reduced gravitational acceleration g' is defined as

$$g'=\frac{\rho-\rho_w}{\rho_w}g \tag{5}$$

ρ is the density of the current. ρ_s and ρ_w are the density of soluble substance (herein, salt) and the density of water, respectively. Using the normalized $(0\le c\le 1)$ concentration of the fluid

$$\rho=c\rho_s+(1-c)\rho_w \tag{6}$$

ν_e is the effective viscosity, which is the sum of laminar viscosity ν and eddy viscosity ν_t. The dense underflow is diluted in the x direction by entraining the ambient water; thus, the current's height and density vary continuously in the streamwise direction. This is why the pressure gradient cannot be neglected even in the presence of free surface [26]. Numerous turbulence models may be used to estimate the eddy viscosity. Most eddy viscosity-based turbulence models, such as standard $k-\varepsilon$ model, overpredict the turbulent kinetic energy near the solid boundaries. This weakness probably arises because of the fact that such models have been developed for high Reynolds number and isotropic turbulent-viscosity flows. Herein, the $\overline{v^2}-f$ turbulence model was used to evaluate the eddy viscosity by using the following relationship

$$\nu_t=c_\mu\overline{v^2}\eta,\ \text{where}\ \eta=\max\left(\frac{k}{\varepsilon},6\sqrt{\frac{\nu}{\varepsilon}}\right) \tag{7}$$

where η=turbulent time scale, k=turbulent kinetic energy, ε=turbulent kinetic energy dissipation rate, and c_μ=empirical constant. The turbulent quantities k and ε are obtained by solving the following transport equations:

$$u\frac{\partial k}{\partial x}+v\frac{\partial k}{\partial y}=\frac{\partial}{\partial x}\left[\left(\nu+\frac{\nu_t}{\sigma_k}\right)\frac{\partial k}{\partial x}\right]+\frac{\partial}{\partial y}\left[\left(\nu+\frac{\nu_t}{\sigma_k}\right)\frac{\partial k}{\partial y}\right]+P_k-\varepsilon \tag{8}$$

$$u\frac{\partial \varepsilon}{\partial x}+v\frac{\partial \varepsilon}{\partial y}=\frac{\partial}{\partial x}\left[\left(\nu+\frac{\nu_t}{\sigma_\varepsilon}\right)\frac{\partial \varepsilon}{\partial x}\right]+\frac{\partial}{\partial y}\left[\left(\nu+\frac{\nu_t}{\sigma_\varepsilon}\right)\frac{\partial \varepsilon}{\partial y}\right]+\frac{c_{\varepsilon 1}}{\eta}P_k-\frac{c_{\varepsilon 2}}{\eta}\varepsilon \tag{9}$$

where the production term P_k and modified empirical constant $c_{\varepsilon 1}$ are estimated, respectively, by

$$P_k=\nu_t\left[2\left(\frac{\partial u}{\partial x}\right)^2+2\left(\frac{\partial v}{\partial y}\right)^2+\left(\frac{\partial v}{\partial x}+\frac{\partial u}{\partial y}\right)^2\right] \tag{10}$$

$$c_{\varepsilon 1}=1.4\left(1+c_{\varepsilon d}\sqrt{\frac{k}{\overline{v^2}}}\right) \tag{11}$$

The preceding equations contain various empirical constants obtained by comprehensive data fitting for a wide range of turbulent flows. The following standard values from Parneix et al. [36] are also used in the present computation:

$$c_\mu=0.22,\quad \sigma_k=1.00,\quad \sigma_\varepsilon=1.30,\quad c_{\varepsilon d}=0.045,\quad c_{\varepsilon 2}=1.90 \tag{12}$$

During the last few years the $\overline{v^2}-f$ turbulence model, originally suggested by Durbin [35], has become increasingly popular due to its ability to correctly account for near-wall damping without use of so-called damping functions. The reason why these damping functions can be avoided is the availability of an additional turbulent velocity scale, a generic wall normal Reynolds stress component, $\overline{v^2}$. By considering the exact transport equations for the Reynolds stresses in a fully developed channel flow, it can readily be shown that the production of $\overline{uv}$ (the only Reynolds stress component that effects the mean flow field) should be proportional to $\overline{v^2}$ [35,37]. In two equation models, this velocity scale is not explicitly available but is replaced with the turbulent kinetic energy k. Because k has a different wall distance dependency (y^2) than $\overline{v^2}(y^4)$, this modeling is expected to be inaccurate as walls are approached. Durbin [35] showed that by simply replacing k with $\overline{v^2}$ in the definition of the eddy viscosity, results were substantially improved. The main problem with a damping function is that there can be only one and that this function can be tuned to only a limited number of test cases. In $\overline{v^2}-f$ model on the other hand, $\overline{v^2}$ is governed by a separate transport equation and thus has a potential of being applicable to a wider range of flow situations. The wall-normal Reynolds stress component $\overline{v^2}$ is modeled using

$$u\frac{\partial \overline{v^2}}{\partial x}+v\frac{\partial \overline{v^2}}{\partial y}=\frac{\partial}{\partial x}\left[\left(\nu+\frac{\nu_t}{\sigma_k}\right)\frac{\partial \overline{v^2}}{\partial x}\right]+\frac{\partial}{\partial y}\left[\left(\nu+\frac{\nu_t}{\sigma_k}\right)\frac{\partial \overline{v^2}}{\partial y}\right]+k\times f-\frac{\overline{v^2}}{k}\varepsilon \tag{13}$$

$$L^2\frac{\partial^2 f}{\partial x_j^2}-f=\frac{c_1-1}{\eta}\left(\frac{\overline{v^2}}{k}-\frac{2}{3}\right)-c_2\frac{P_k}{k} \tag{14}$$

where f=redistribution parameter. The turbulent length scale L is calculated using

$$L=c_L\max\left(\frac{k^{3/2}}{\varepsilon},c_\eta\frac{\nu^{3/4}}{\varepsilon^{1/4}}\right) \tag{15}$$

The following standard values of turbulence model coefficients are used in the present study [36]:

Downloaded 03 Jun 2010 to 171.66.16.156. Redistribution subject to ASME license or copyright; see http://www.asme.org/terms/Terms_Use.cfm

Table 1 Inlet conditions used for verification of the numerical simulation

Run No.	Ref.	u_{in} (cm/s)	c_{in} (%)	h_{in} (cm)	Slope (%)	Re_{in}	θ (deg)
1	[18]	6.3	1.2	4	14	2538	8.13
2	[18]	6.84	1	5	10	3458	5.71

$$c_1 = 1.40, \quad c_2 = 0.30, \quad c_L = 0.25, \quad c_\eta = 85.00 \tag{16}$$

Boundary Condition

In the present study, various boundary conditions, such as the inlet, the bottom, and the free surface boundary condition, are required. Because in elliptic flows, information at the downstream travels in the upstream direction, an additional boundary condition is necessary, namely, at the outlet. Known quantities are specified at the inlet for inflow velocity u_{in}, concentration c_{in}, and current thickness h_{in}. The turbulent kinetic energy and dissipation rate at the inlet are estimated, respectively, as $k_{in}=10^{-4}u_{in}$ and $\varepsilon_{in}=10k_{in}^{3/2}/h_{in}$ [27]. At the free surface, a symmetry boundary condition (no flux condition) is used. This assumption is typically good unless the dynamics of the free surface affects the propagation of the density current, i.e., the overlying depth of ambient water is greater than about ten times the current thickness. At the bottom, the no-slip condition is imposed. For solute concentration, zero flux is used at the bottom. At the outlet, the flow is assumed fully developed; thus, zero gradient for velocity components and concentration is employed as well as for other variables.

In summary, boundary conditions can be explained using following notations:

$$\text{Bottom boundary: } u = v = 0\big|_{y=0} \quad \text{and} \quad \left.\frac{\partial c}{\partial y} = 0\right|_{y=0} \tag{17}$$

$$\text{Free surface boundary: } v = 0\big|_{y=H} \quad \text{and} \quad \left.\frac{\partial u}{\partial y} = \frac{\partial c}{\partial y} = 0\right|_{y=H} \tag{18}$$

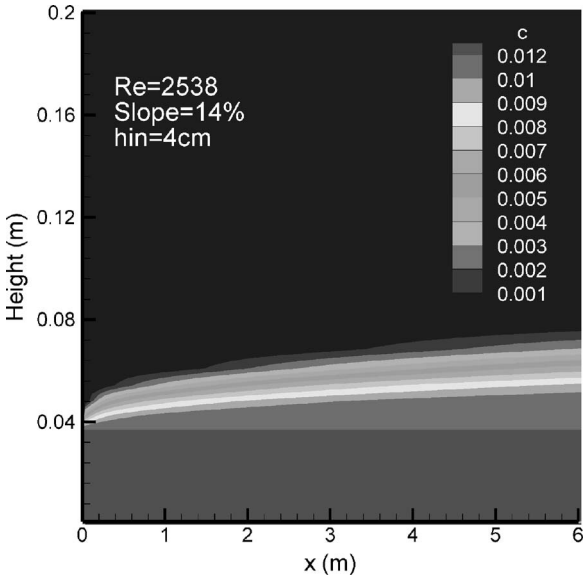

Fig. 1 Concentration contour of saline density current developing on a slope of Run 1

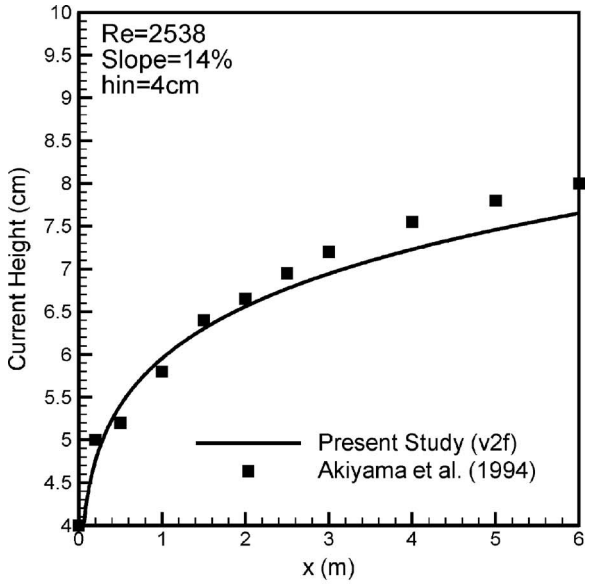

(*a*)

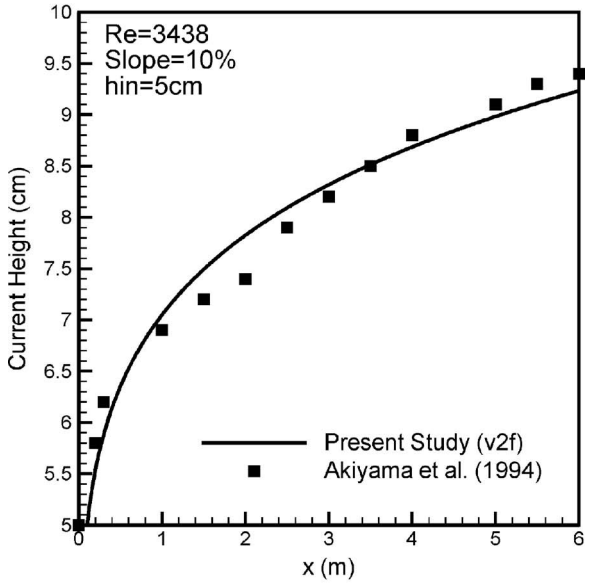

(*b*)

Fig. 2 Comparison of the current height for (*a*) Run 1 and (*b*) Run 2 with experimental data

$$\text{Outlet boundary: } \left.\frac{\partial u}{\partial x} = \frac{\partial v}{\partial x} = \frac{\partial c}{\partial x} = 0\right|_{x=l} \tag{19}$$

where H and l are the total height of ambient water and the length of the flume, respectively.

Solver

A structured finite volume code using the pressure correction scheme Simple-C and a co-located grid arrangement (i.e., all variables are stored at the center of the control volume) was written. The Rhie and Chow interpolation, which computes the velocity components at the control volume faces, was used. The Van Leer scheme (a bounded, second-order upwind scheme) was used to discretize the momentum, turbulence, and concentration equations. The algebraic equations were solved with a tridiagonal matrix solver (TDMA) [38]. The convergence is evaluated based on the residual criterion. In this work, the sum of absolute residuals

Downloaded 03 Jun 2010 to 171.66.16.156. Redistribution subject to ASME license or copyright; see http://www.asme.org/terms/Terms_Use.cfm

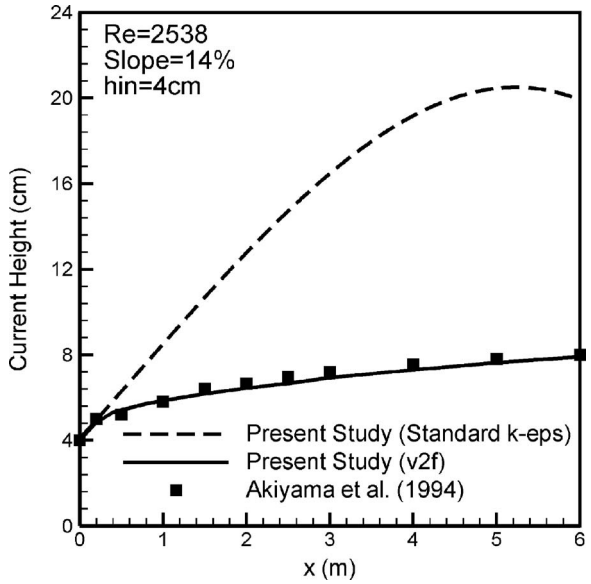

Fig. 3 Comparison of the dense layer height of Run 1 obtained from $\overline{v^2}-f$ model with standard $k-\varepsilon$ model and measurement

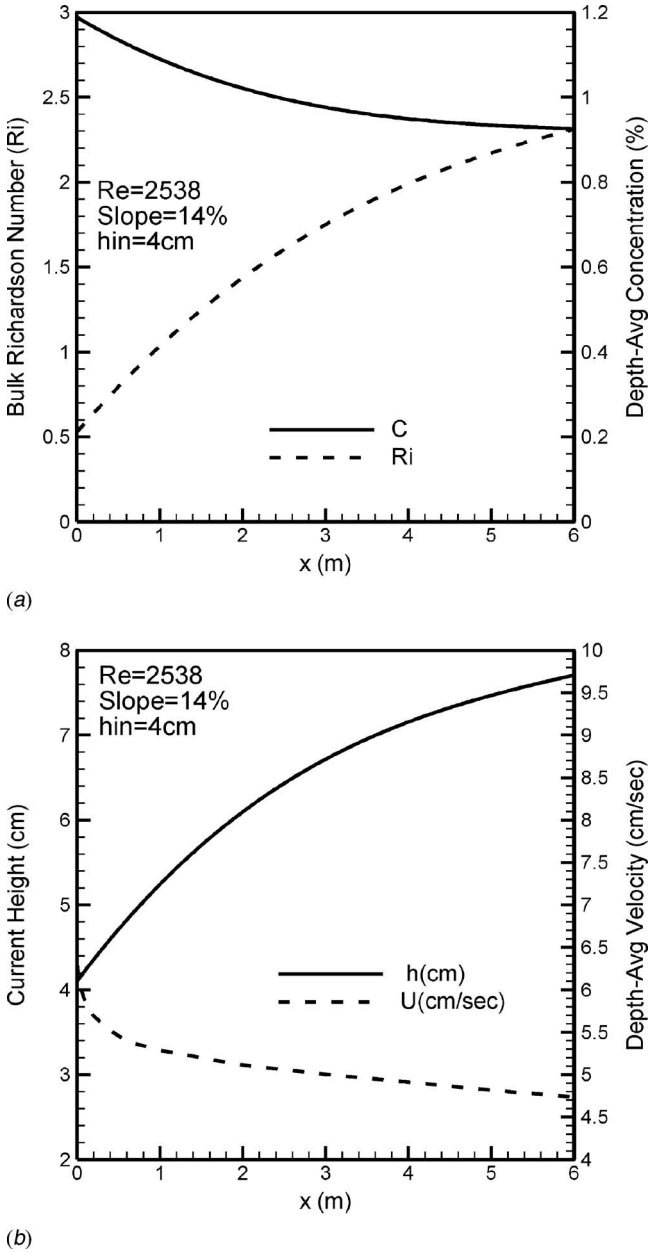

Fig. 4 Distance evolution of the bulk properties of a typical density current: (*a*) depth-averaged bulk Richardson number and concentration, (*b*) depth-averaged velocity and flow height, Run 1

of a variable for all computational control volumes was compared to the inlet flux of that variable. When the sum of normalized residuals for all variables are in the order of 10^{-4}, computation stops. After converging the velocity components and pressure, the scalar transport equations for turbulent kinetic energy, dissipation rate $\overline{v^2}$, and f are solved. Finally, concentration equation along with all previous equations is simultaneously solved and iterations continue until the convergence for all variables is obtained.

Some tests were performed with different grid sizes to seek a grid independent solution. The results show that 102×42 mesh size, in the x and y directions, respectively, is sufficiently fine so that the computed profiles are grid independent. The mesh points are chosen as uniform in the streamwise direction, but in the vertical direction, because of high gradients in the near-bed region, the grid points are distributed in a nonuniform manner with higher density of grids close to the bed. Because of the fact that such models as $\overline{v^2}-f$ use a low Reynolds enhanced treatment particularly near the wall, a grid should be designed with $y^+\leq1$ for them [39]. Thus, in the current numerical simulation, the grid is designed with $y^+\approx1$ at the first cell.

To verify the present model, two experiments of Akiyama et al. [18], which involved a conservative saline density flow discharged through the inlet, were used. The flow develops two- dimensionally on a slope in a 1.0 m deep and 8.0 m long flume. Then, the bulk properties and characteristics of the current under different inlet conditions are qualitatively investigated. In order to be sure that the assumption of fully developed flow at the outlet boundary is true, the length of computation domain is taken 10.0 m.

Results

Inlet conditions of two different experiments of Akiyama et al. [18], which are used to validate the model, are listed in Table 1. In this paper, these two experiments are referred to as Run 1 and Run 2. The interface between a density current and the ambient water is generally defined as the region where the density gradient is at a maximum [2]. In most laboratory experiments, due to intense mixing and high turbulence, it is nearly impossible to define accurately the position of the diffuse top of the density current visually [1]. In fact, in experimental simulations, the interface is at the level above which no concentration can be visualized. The accuracy of the visually identified current thickness is, therefore, highly dependent on the observer, and may vary if the observer is replaced by another. However, to find the current height in the present study, we adopt the convention used in the boundary layer literature where the height of the boundary layer is considered a height at which the local downstream velocity component is about 0.99 of the freestream velocity of the flow. Thus, in this simulation, it has been assumed that the current height is the height at which the concentration is about 0.01 of the inlet concentration c_{in}.

Figure 1 shows a concentration contour of the dense bottom current for Run 1. It can be seen that the current is thickened but is diluted by entraining ambient water along the downstream direction. Figures 2(*a*) and 2(*b*) shows the computed current height for Runs 1 and 2. Experimental data by Akiyama et al. [18] are also plotted in the same figures. The overall agreement between

Downloaded 03 Jun 2010 to 171.66.16.156. Redistribution subject to ASME license or copyright; see http://www.asme.org/terms/Terms_Use.cfm

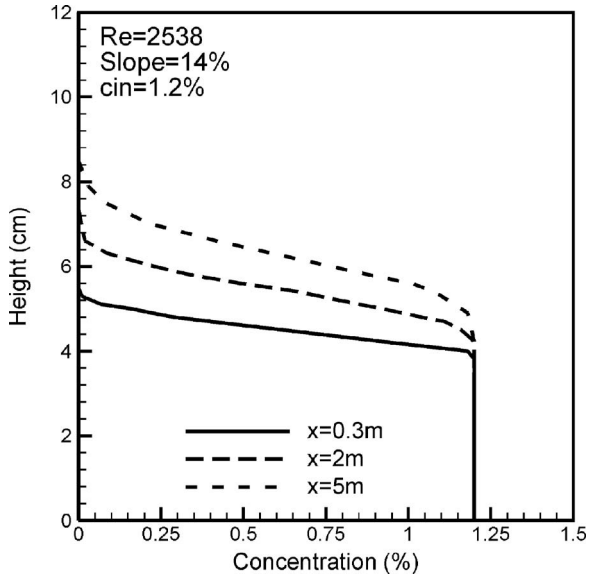

Fig. 5 Vertical profiles of concentration at some distances from the inlet, Run 1 (c_{in}=1.2%, h_{in}=4 cm, and bed slope=14%)

the computed and measured profiles appears good particularly in Fig. 2(*b*). However, in Fig. 2(*a*), the computed height is slightly smaller than the measured one.

Because the present model can handle the turbulence by using either $\overline{v^2}-f$ or $k-\varepsilon$ model, the computed flow heights, which have been calculated by using both $\overline{v^2}-f$ and $k-\varepsilon$ models, have been compared to the measured data of Akiyama et al. [18] in Fig. 3. It can be seen, although neither of the two turbulence models is developed for low Re number flows, the $\overline{v^2}-f$ model has a better performance in modeling of such flows. In order to investigate the depth-averaged variables, the following integrals are used to calculate the depth-averaged velocity U, depth-averaged concentration C, and the bulk Richardson number Ri.

$$U = \frac{\int_0^h u dy}{h} \tag{20}$$

$$C = \frac{\int_0^h c dy}{h} \tag{21}$$

$$\mathrm{Ri} = \frac{g' h \cos\theta}{U^2} \tag{22}$$

The bulk Richardson number Ri is used to assess the stability of the flow boundaries. There have been numerous attempts to relate the entrainment of the ambient water with bulk Richardson number and bed slope [21,27,28]. The entrainment of ambient water into a density current due to turbulence strongly influences the overall flow characteristics. Figure 4(*a*) depicts that the depth-averaged concentration decreases continuously because of the ambient water entrainment [10]. The bulk Richardson number is also plotted in Fig. 4. It can be seen that the bulk Richardson number, which has a specific value at the inlet, gradually increases along the flume in the streamwise direction until it approaches a constant value, namely, the normal Richardson number, within a short distance [2,13,21]. At this condition, the flow is considered to be at a normal state. In a normal state, the bulk Richardson number is independent of x. The flow height also follows a linear increase with distance, and the depth-averaged velocity is constant (Fig. 4(*b*)).

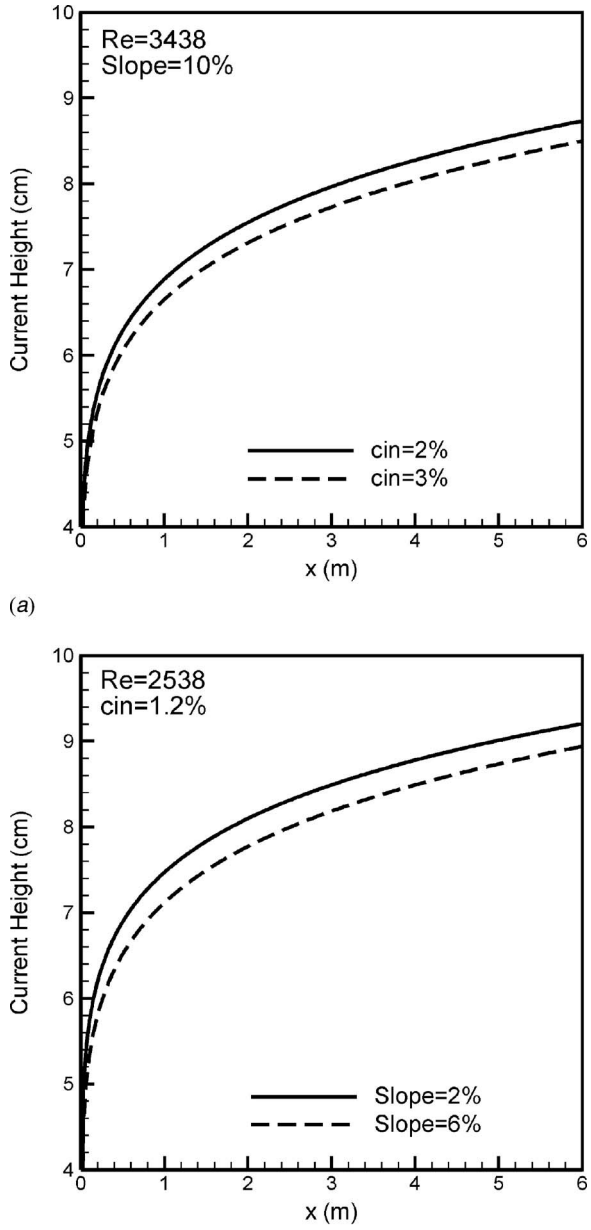

Fig. 6 Flow height of saline density current: (*a*) different inlet concentration and (*b*) different bed slope

The vertical structure of a density current is shown in Fig. 5, which also shows the vertical profile of concentration in some distances from the inlet. The concentration has a uniform value near the bed and decreases rapidly in the vertical direction [2]. In currents that entrain the ambient water rapidly at the upper boundary, there is a reinforcement of the stratification and the stepped concentration profile may become more pronounced; this is consistent with studies in Buckee et al. [1] and Peakall et al. [40].

In order to further investigate of the influence of input variables on the density current characteristics, the flow height is plotted in Fig. 6 under such different conditions as different inlet concentration and bed slope. Figure 6(*a*) shows that the flow height decreases when the inlet concentration increases. Flows with different initial concentrations behave very differently because the flow behavior is governed by the density contrast between the flow and

Downloaded 03 Jun 2010 to 171.66.16.156. Redistribution subject to ASME license or copyright; see http://www.asme.org/terms/Terms_Use.cfm

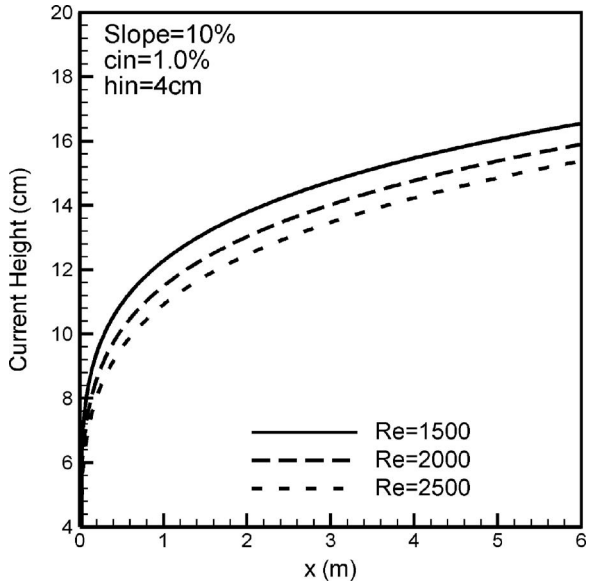

Fig. 7 Flow height obtained using three different values of inlet Reynolds number (c_{in}=1.2%, h_{in}=4 cm, slope=14%)

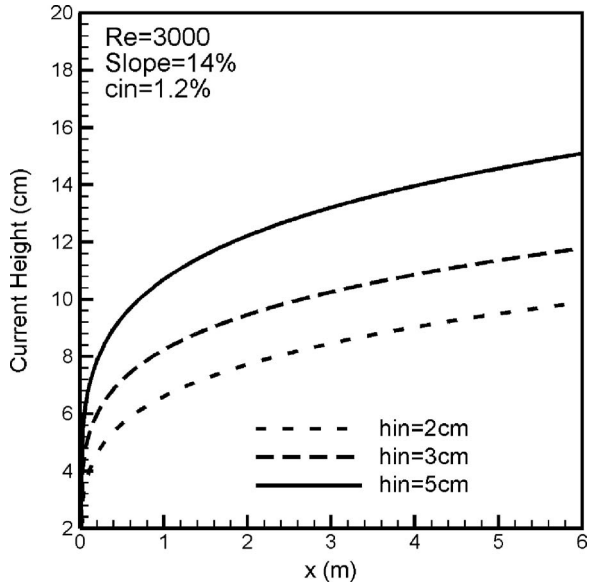

Fig. 8 Flow height of saline density current using three different inlet heights and identical Reynolds number (i.e., Re =3000, c_{in}=1.2%, slope=14%)

the ambient water. Qualitative comparison suggests that if all else is constant, then lower-concentration flows are thicker. When the inlet concentration increases, both density gradient and buoyancy increase. It makes the bulk Richardson number higher, and the water entrainment at the interface, therefore, decreases. Because the water entrainment rate is directly related to the increase in the flow thickness [41], decreasing water entrainment may cause the flow height to increase slowly. In Fig. 6(*b*), the variation of the current height due to different bed slopes is plotted. Runs with different bed slopes suggest that the pattern of flow thickness may be insignificantly different on gentle slopes. However, increasing the bed slope will cause the flow height to decrease.

The flow thickness mainly depends on the discharge. The greater the discharge, the thinner the current becomes. It can be indicated, by comparison, between three runs with identical conditions other than discharge in Fig. 7. Because of the fact that the discharge has a linear relationship with Reynolds number, i.e., $\mathrm{Re}=q/\upsilon$, where q=discharge per unite width, it can be implied that the greater the Reynolds number, the thinner the flow becomes. Because the inlet heights are the same for all three runs, it can be indicated that when a flow has a higher Reynolds number, its velocity is also higher. High velocity will make the bulk Richardson number lower. Decreasing the bulk Richardson number increases the entrainment of the low-momentum fluid into the density current and the current thickness, therefore, is expected to increase. However, Fig. 7 does not prove such a procedure, suggesting the water entrainment is not the only factor affecting the growth of the flow height.

Figure 8, also, confirms the above result. Three different runs are plotted in Fig. 8 to investigate the role of inlet height (or inlet velocity). They differ only in the magnitude of their inlet height, while their Reynolds numbers are the same. In other words, the flow with larger inlet height has a smaller inlet velocity. Qualitative comparison suggests if all else is constant, then lower-velocity flows are thicker.

Conclusion

The $\overline{v^2}-f$ turbulent model has been applied to simulate the nonparticulate dense underflows propagating along the sloped surface in a flume with deep, quiescent ambient water. The governing equations were solved using a finite volume method. The results of saline density currents have been compared to the two-dimensional experimental data. Comparison to experimental measurement of the flow thickness has shown favorable agreement. Specifically, the following conclusion can be drawn:

1. The $\overline{v^2}-f$ model can be used to simulate dilute density flows down a slope. Although the main aim of this paper is not to compare the standard $k-\varepsilon$ model with $\overline{v^2}-f$ model, it is founded that the later model predicts the thickness of the density currents more precisely.
2. Despite the fact that the performance of $\overline{v^2}-f$ model, based on the standard $k-\varepsilon$ model, in simulation of low-Re density currents seems to be good, a $\overline{v^2}-f$ model which is coupled with low-Re $k-\varepsilon$ models, such as Launder–Sharma $k-\varepsilon$ model or buoyancy-extended $k-\varepsilon$ models, may result in more accurate simulation.
3. This study also suggests that the density currents are very dependent on the inlet discharge. The greater the discharge, the thinner the current becomes. Also, in constant discharges, flows that have a larger inlet height become thicker.
4. The boundary layer convention, adopted in the numerical simulation of the flow height, is seen to be effective in simulating changes in the flow height due to different inlet conditions. However, this convention still needs to be tested to determine whether it holds for wider variety of flow conditions, including particulate flows with erosion and deposition.

These results add to the understanding of density current dynamics but leave many questions unanswered. Because it is certainly the first time that the $\overline{v^2}-f$ turbulent model is employed to simulate the density currents, further experimental and numerical works are needed to support the results presented here. After further verification of the model for a wide range of the flow conditions, it may be applied to simulate other characteristics of the density currents and to investigate the turbidity currents.

Acknowledgment

The authors would like to thank the anonymous reviewers whose constructive comments improved the quality of this paper.

Downloaded 03 Jun 2010 to 171.66.16.156. Redistribution subject to ASME license or copyright; see http://www.asme.org/terms/Terms_Use.cfm

Nomenclature

C = depth-averaged concentration
c = concentration
c_{in} = inflow volumetric concentration
c_1, c_2, c_L, c_η = constants in $\overline{v^2}-f$ model
$c_\mu, c_{\varepsilon 1}, c_{\varepsilon 2}, c_{\varepsilon d}$ = empirical constants in $k-\varepsilon$ model
f = redistribution parameter
g = gravitational acceleration
g' = reduced gravitational acceleration
H = total height of the ambient water in the flume
h = density current thickness
h_{in} = inlet height
k = turbulent kinetic energy
k_{in} = inlet turbulent kinetic energy
L = turbulent length scale
l = length of the flume
P = pressure
P_k = production term in $k-\varepsilon$ model
q = discharge per unit width
Re = Reynolds number
Re_{in} = inlet Reynolds number
Ri = bulk Richardson number
U = depth-averaged velocity
u, v = velocity components
$\overline{uv}$ = Reynolds stress
$\overline{v^2}$ = turbulent velocity scale
x, y = Cartesian coordinates
y^+ = dimensionless wall distance
ε = turbulent dissipation rate
ρ = density current density
ρ_s = soluble substance density
ρ_w = water density
ν = kinematic viscosity
ν_t = kinematic eddy viscosity
$\sigma_k, \sigma_\varepsilon$ = model constants for $k-\varepsilon$ model
η = turbulent time scale
θ = slope angle

References

[1] Buckee, C., Kneller, B., and Peakall, J., 2001, "Turbulence Structure in Steady, Solute-Driven Gravity Currents," Spec. Publs. Int. Assn. Sediment., **31**, pp. 173–187.
[2] Alavian, V., Jirka, G. H., Denton, R. A., Johnson, M. C., and Stefan, H. G., 1992, "Density Currents Entering Lakes and Reservoirs," J. Hydraul. Eng., **118**(11), pp. 1464–1489.
[3] Alavian, V., 1986, "Behavior of Density Currents on an Incline," J. Hydraul. Eng., **112**(1), pp. 27–42.
[4] Garcia, M., 1990, "Depositing and Eroding Turbidity Sediment Driven Flows: Turbidity Currents," Project Report No. 306, St. Anthony Falls Hydraulic Lab., Univ. of Minnesota, Minneapolis.
[5] Altinakar, M. S., Graft, W. H., and Hopfinger, E. J., 1996, "Flow Structure in Turbidity Current," J. Hydraul. Res., **34**(5), pp. 713–718.
[6] Kneller, B. C., Bennett, S. J., and McCaffrey, W. D., 1997, "Velocity and Turbulence Structure of Gravity Currents and Internal Solitary Waves," J. Sediment Geol., **122**, pp. 235–250.
[7] Firoozabadi, B., Farhanieh, B., and Rad, M., 2000, "The Propagation of Turbulent Density Currents on Sloping Bed," J. Sci. Iran., **8**(2), pp. 223–235.
[8] Best, J. L., Kirkbride, A. D., and Peakall, J., 2001, "Mean Flow and Turbulence Structure of Sediment-Laden Gravity Currents: New Insights Using Ultrasonic Doppler Velocity Profiling," Spec. Publs. Int. Assn. Sediment., **31**, pp. 159–172.
[9] de Rooji, F., and Dalziel, B., 2001, "Time- and Space-Resolved Measurements of Deposition Under Turbidity Currents," Spec. Publs. Int. Assn. Sediment., **31**, pp. 207–215.
[10] Alexander, J., and Mulder, T., 2002, "Experimental Quasi-Steady Currents," J. Marine Geol., **186**, pp. 195–210.
[11] Luthi, S., 1980, "Some New Aspects of Two-Dimensional Turbidity Currents," J. Sedimentology, **28**, pp. 97–105.
[12] Akiyama, J., and Stefan, H. G., 1984, "Plunging Flow Into Reservoir: Theory," J. Hydraul. Eng., **110**(4), pp. 484–499.
[13] Akiyama, J., and Stefan, H. G., 1985, "Turbidity Current With Erosion and Deposition," J. Hydraul. Eng., **111**(12), pp. 1473–1495.
[14] Parker, G., Fukushima, Y., and Pantin, H. M., 1986. "Self Accelerating Turbidity Currents," J. Fluid Mech., **171**, pp. 145–181.
[15] Akiyama, J., and Stefan, H. G., 1988, "Turbidity Current Simulation in a Diverging Channel," Water Resour. Res., **24**(4), pp. 579–587.
[16] Fukushima, Y., and Watanabe, M., 1990, "Numerical Simulation of Density Underflow by the $k-\varepsilon$ Turbulence Model," J. Hydrosci. Hydr. Eng., **8**, pp. 31–40.
[17] Garcia, M., 1993, "Hydraulic Jumps in Sediment-Driven Bottom Current," J. Hydraul. Eng., **119**(10), pp. 1094–1117.
[18] Akiyama, J., Ura, M., and Wang, W., 1994, "Physical-Based Numerical Model of Inclined Starting Plumes," J. Hydraul. Eng., **120**(10), pp. 1139–1157.
[19] Bradford, S. F., and Katapodes, N., 1999, "Hydrodynamics of Turbid Underflows. II: Aggradation, Avulsion, and Channelization," J. Hydraul. Eng., **125**(10), pp. 1016–1028.
[20] Salaheldin, T. M., Imran, J., Chaudhry, M. H., and Reed, C., 2000, "Role of Fine-Grained Sediment in Turbidity Current Flow Dynamics and Resulting Deposits," J. Marine Geol., **171**, pp. 21–38.
[21] Stacey, M. W., and Bowen, A. J., 1988, "The Vertical Structure of Turbidity Currents and a Necessary Condition for Self-Maintenance," J. Geophys. Res., **93**(C4), pp. 3543–3553.
[22] Eidsvik, K. J., and BrØrs, B., 1989, "Self-Accelerated Turbidity Current Prediction Based Upon $k-\varepsilon$ Model Turbulence," Cont. Shelf Res., **9**(7), pp. 617–627.
[23] Farrell, G. J., and Stefan, H. G., 1988, "Mathematical Modeling of Plunging Reservoir Flows," J. Hydraul. Res., **26**(5), pp. 525–537.
[24] Bournet, P. E., Dartus, D., Tassin, B., and Vincon-Leite, B., 1999, "Numerical Investigation of Plunging Density Current," J. Hydraul. Eng., **125**(6), pp. 584–594.
[25] de Cesare, G., Schleiss, A., and Hermann, F., 2001, "Impact of Turbidity Currents on Reservoir Sedimentation," J. Hydraul. Eng., **127**(1), pp. 6–16.
[26] Firoozabadi, B., Farhanieh, B., and Rad, M., 1998, "Numerical Investigation of the Structure of Density Currents in a Two Dimensional Channel," J. Esteghlal, **2**, pp. 155–169 (in Farsi).
[27] Choi, S., and Garcia, M., 2002, "$k-\varepsilon$ Turbulence Modeling of Density Currents Developing Two Dimensionally on a Slope," J. Hydraul. Eng., **128**(1), pp. 55–63.
[28] Huang, H., Imran, J., and Pirmez, C., 2005, "Numerical Model of Turbidity Currents With a Deforming Bottom Boundary," J. Hydraul. Eng., **131**(4), pp. 283–293.
[29] Imran, J., Kassem, A., and Khan, S. M., 2004, "Three Dimensional Modeling of Density Current. I. Flow in Straight Confined and Unconfined Channels," J. Hydraul. Res., **42**(6), pp. 578–590.
[30] Kassem, A., and Imran, J., 2004, "Three-Dimensional Modeling of Density Current. I. Flow in Straight Confined and Unconfined Channels," J. Hydraul. Res., **42**(6), pp. 591–602.
[31] BrØrs, B., and Eidsvik, K. J., 1992, "Dynamic Reynolds Stress Modeling of Turbidity Currents," J. Geophys. Res., **97**(c6), pp. 9645–9652.
[32] Taulbee, D. B., Mashayek, F., and Barré, C., 1999, "Simulation and Reynolds Stress Modeling of Particle-Laden Turbulent Shear Flows," Int. J. Heat Fluid Flow, **20**, pp. 368–373.
[33] Felix, M., 2001, "A Two-Dimensional Numerical Model for Turbidity Current," Spec. Publs. int. Assn. Sediment., **31**, pp. 71–81.
[34] Drago, M., 2002, "A Coupled Debris Flow-Turbidity Current Model," Ocean Eng., **29**, pp. 1769–1780.
[35] Durbin, P., 1991, "Near-Wall Turbulence Closure Modeling Without 'Damping Functions'," Theor. Comput. Fluid Dyn., **3**, pp. 1–13.
[36] Parneix, S., Durbin, P., and Behnia, M., 1998, "Computation of 3-D Turbulent Boundary Layer Using the $\overline{\nu^2}-f$ Model," Flow, Turbul. Combust., **60**, pp. 19–46.
[37] Sveningsson, A., and Davidson, L., 2004, "Assessment of Realizability Constraints in $\overline{v^2}-f$ Turbulence Models," Int. J. Heat Fluid Flow, **25**, pp. 785–794.
[38] Davidson, L., and Farhanieh, B.,1991, "A Finite Volume Code Employing Collocated Variable Arrangement and Cartesian Velocity Components for Computation of Fluid Flow and Heat Transfer in Complex Three-Dimensional Geometries," Chalmers Univ. of Tech., Sweden.
[39] Heschl, Ch., Sanz, W., and Klanatsky, P., 2005, "Implementation and Comparison of Different Turbulence Models for Three Dimensional Wall Jets With FLUENT," CFD Forum, Bad Nauheim, Deutschland.
[40] Peakall, J., McCaffrey, W. D., and Kneller, B. C., 2000, "A Process Model for the Evolution, Morphology and Architecture of Sinuous Submarine Channels," J. Sediment Res., **70**, pp. 434–448.
[41] Ellison, T. H., and Turner, J. S., 1959, "Turbulent Entrainment in a Stratified Fluid," J. Fluid Mech., **6**, pp. 423–449.

Downloaded 03 Jun 2010 to 171.66.16.156. Redistribution subject to ASME license or copyright; see http://www.asme.org/terms/Terms_Use.cfm

Turbulent Flow Structure in a Cylinder-on-Cone Cyclone

W. O. Wong

X. W. Wang

Y. Zhou

Department of Mechanical Engineering,
The Hong Kong Polytechnic University,
Hong Kong, People's Republic of China

Turbulent flow structure in a cylinder-on-cone cyclone was experimentally investigated. Measurements were conducted at a fixed geometrical swirl number. Experiments were performed at a swirl number of 3 and Reynolds numbers from 37,100 to 74,200, based on the inlet velocity and the cyclone body diameter. The flow field in planes normal to and through the cyclone axis was measured in detail using a two-component laser Doppler velocimetry (LDA) and a particle imaging velocimetry (PIV). Two dominant frequencies of vortical structures were identified based on LDA-measured tangential and axial velocity spectra. Although one of them agreed quite well with those in literature, the other was reported for the first time. One explanation was proposed. [DOI: 10.1115/1.2754315]

1 Introduction

Cyclone separators have been used in various industries for about 100 years and are still one of the most widely used industrial gas-cleaning devices, e.g., vehicle exhaust-gas cleaning devices, vacuum cleaners, incinerators, and boilers. In spite of a long history, the basic design of cyclones has evolved little from its first application, perhaps mainly due to the complexity and inadequate knowledge of the turbulent swirling flow, including the precessing vortex core inside the cyclone. Early experimental investigations of cyclones were conducted using pitot tubes [1] and hot-wire anemometry [2], aiming primarily at understanding the turbulent flow structure and determining the most efficient shape of a cyclone. The two techniques suffer from a few drawbacks, for example, being intrusive to flows and point measurement, giving insufficient information on the overall flow structure. With the advent of nonintrusive laser Doppler velocimetry (LDA), there have been increasing experimental investigations of the gas flow in a cyclone in the last one or two decades. Using LDA, O'Doherty et al. [3] unveiled a very complex flow structure associated with the strongly swirl flow in a cyclone. It is well known that flow with a high swirl number (>0.6) and a high Reynolds number ($\mathrm{Re}=U_{\mathrm{in}}2R/\nu$, where R is the radius of the cyclone chamber, U_{in} the inlet velocity, and ν the kinematic viscosity of fluid) of more than 10^4 in a confined flow produces the onset of vortex breakdown and a low-frequency instability phenomenon due to the precessing motion of the vortex core [4–8]. Alekseenko et al. [9] reported the results of theoretical and experimental investigation of steady helical vortex structures in a swirl flow. They observed a linear relationship between the Strouhal number, St ($\equiv f_{\mathrm{prec}}2R/U_{\mathrm{in}}$, where f_{prec} is the precessing frequency of the vortex in the cyclone), and Re (=14,000–45,000) at a swirl number, S ($\equiv \pi d_e R/2A$, where d_e is the diameter of the cyclone outlet and A is the inlet area), of 1–3.8. Fluid dynamics in a cylinder-on-cone cyclone is different from the helical flow model. The former is, in general, characterized by the presence of a reverse flow, whereas the latter is not. Derksen and Van den Akker [10] noted numerically that the main vortex core moved about the geometrical axis of the reverse flow cyclone in a quasiperiodic manner, and St was found to be 0.53 at Re=14,000 and $S=2.1$. Hoekstra et al. [11] experimentally observed St=0.6 in a cyclone of similar geometry at a comparable Re and $S=3.1$. However, Alekseenko et al. [9] measured St=0.85 at $S=1.9$ and Re=14,000–45,000. Peng et al. [12] also observed experimentally a similar St value at $S=2.0$ and Re=57,300–260,000, and predicted a slightly lower St near the wall just under the vortex finder using a theoretical model of the tangential velocity of the flow at the wall.

In spite of previous investigations, many aspects of fluid dynamics, including the flow instabilities such as the vortex breakdown and precessing vortex core (PVC), within a cyclone have yet to be better understood. These instabilities will generate extra losses and produce a higher pressure drop in the cyclone. In terms of particle separation, the PVC will cause a pressure fluctuation and associated high levels of turbulence and mixing in the cyclone [13]. As a result, there are problems with cyclones in engineering, such as the incorrect prediction of the separation efficiency of submicron particles in common industrial cyclone separator [14]. Previous investigations on PVC and associated instabilities are mostly related to swirl burners [15] and generators [16]; there have been very limited reports on the PVC, which occurs in a cyclone, with a reverse flow. This work aims to improve our understanding of the turbulent flow structure in a cylinder-on-cone cyclone that is characterized by a reverse flow in the core region. Measurements were conducted in an industrial cyclone model using particle imaging velocimetry (PIV) and laser Doppler velocimetry (LDA). Experimental details are given in Sec. 2. Experimental results are presented and discussed in Sec. 3. The work is concluded in Sec. 4.

2 Experimental Details

Experimental investigation was conducted based on a laboratory scale model of cyclones as illustrated in Fig. 1. The cyclone radius R is 47 mm, the outlet diameter d_e is 44 mm, the cyclone cylinder length L is 132 mm, and cross-sectional area of the cylindrical body A is 1100 mm^2. The coordinate system, (r,θ,z), is defined in Fig. 1(a), with its origin at the center of the bottom plane of the cylindrical section of the cyclone body. The velocity components in the r, θ, and z directions are designated by V_r, V_θ, and V_z, respectively. The cylinder-on-cone cyclone was made of transparent acrylic. The inlet flow velocity of the cyclone, measured by a pitot tube, was 8 m/s. Experiments were first conducted at $S=3.0$ and Re=47,000.

A two-component LDA system (Dantec Model 58N40) with an enhanced flow velocity analyzer (FVA) signal processor was used to measure V_θ and V_z along the axis X-X of the measurement plane at $z=R$ (Figs. 1(a) and 1(c)). This section at $z/R=1$ should be quite representative of others, except near the top and bottom of the cyclone, as indicated in PIV data in the (r,z) plane presented later. The flow was seeded by smoke generated by mosquito repellant, which was introduced into cyclone from the inlet. The LDA system was introduced in detail in Wang et al. [17]. The measuring volume formed by laser beams has a minor axis of 1.18 mm and a major axis of 2.48 mm. LDA measurements of V_θ

Contributed by the Fluids Engineering Division of ASME for publication in the JOURNAL OF FLUIDS ENGINEERING. Manuscript received May 11, 2006; final manuscript received April 10, 2007. Review Conducted by Joseph Katz.

 Copyright © 2007 by ASME

Downloaded 03 Jun 2010 to 171.66.16.156. Redistribution subject to ASME license or copyright; see http://www.asme.org/terms/Terms_Use.cfm

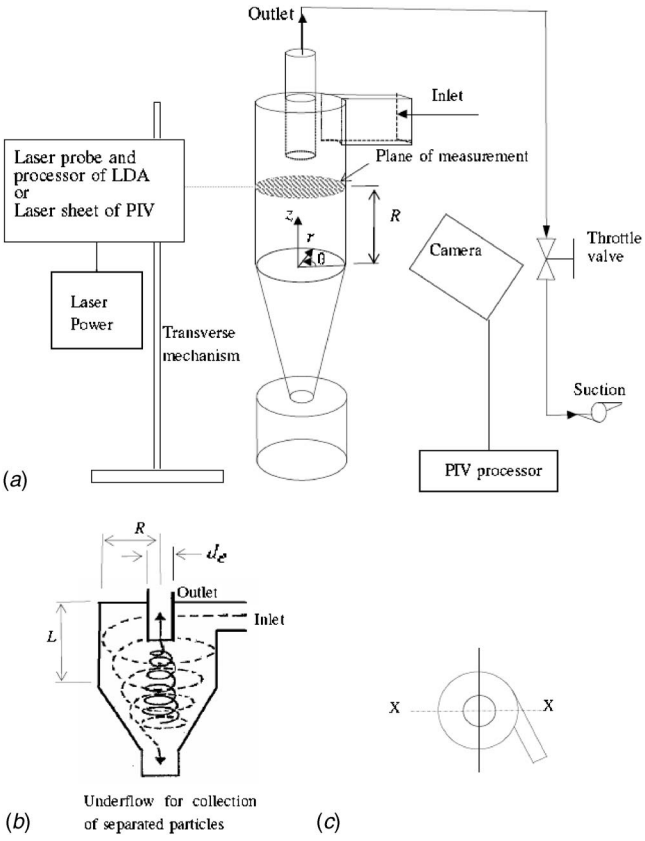

Fig. 1 (*a*) Experimental setup, (*b*) sketch of mean flow in the cyclone, and (*c*) top view of the cyclone

and V_z were made at 38 points of 2 mm uniform spacing along a diametric axis *X-X* of the measurement plane at $z/R=1$ (Figs. 1(*a*) and 1(*c*)). About 50,000 samples were taken for each point of LDA measurements at a sampling rate of about 1500 samples per second, with a typical validation rate of 80–95%. The data were processed using the signal processor of the LDA system (Dantec Model 58N40 with an enhanced FVA signal processor) to obtain the power spectral density function. The selected window size was 2048 points, and the frequency range of the calculated spectrum was from 0 to 1500 Hz. Thus, the frequency resolution was ~0.7 Hz, which was considered to be adequate for the present investigation. Experimental uncertainties are estimated to be within 1% for the mean velocities, $\bar{V}_\theta$ and $\bar{V}_z$, and 3% for the fluctuating velocities, $V_{\theta\text{rms}}$ and $V_{z\text{rms}}$. In this paper, the overbar denotes time averaging, while the subscript rms represents the root-mean-square values.

Another independent technique, i.e., a hot wire, was used to measure the predominant frequencies in the cyclone. A single hot-wire operated on a constant temperature circuit at an overheat ratio of 1.8 was used to measure the fluctuating velocities, V_θ and V_z, inside the cyclone. The hot-wire probe (Dantec type 55P11) is a 1.25 mm long platinum-plated tungsten wire of 5 μm diam, mounted on a 1.9 mm diam and 30 mm long ceramic tube. The hot-wire probe was inserted into the measurement plane at $z/R=1$ (Figs. 1(*a*) and 1(*c*)) and traversed along the diametric axis *X-X*. Since the hot wire was used only to monitor the frequency information inside the cyclone; calibration was not needed. Hot-wire measurements were made at the same location as the LDA measurement. Signals from the circuits were offset, amplified, and then digitized using a 16-channel (12-bit) A/D board and a personal computer at a sampling frequency 3.5 kHz per channel. The sampling duration was 40 s.

A Dantec standard PIV2100 system was used to measure the flow velocities in the (r,θ) plane at $z=R$ and (r,z) plane, which cut through the cyclone along the *X-X* axis. The flow was again seeded by smoke. Seeding particles in PIV measurements were measured using a digital microscope and were found to be a few microns in diameter. The particle Stokes numbers of the seeding particles were calculated to be <0.1. Details of the PIV system were introduced in Hu et al. [18]. The flow illumination was provided by two New Wave standard pulsed laser sources of a wavelength of 532 nm, each having a maximum energy output of 120 mJ. The time interval to capture two sequential images was ~50 μs. Digital particle images were taken using one charge-coupled device (CCD) camera (HiSense type 13, gain $\times 4$, double frames, 1280 pixels $\times$ 1024 pixels). A Dantec FlowMap Processor (PIV2100) was used to synchronize image acquisition and illumination. A wide-angle lens was used so that each image covered an area of 90 mm $\times$ 72 mm of the flow field in the (r,z) plane and an area of 112 mm $\times$ 88 mmin the (r,θ) plane. The longitudinal and lateral image magnifications were identical, i.e., 0.12 mm/pixel. Each laser pulse lasted for 10 ns. An optical filter was used to allow only the green light (the wavelength=532 nm), generated by the laser source, to pass.

The amount of distortion of the PIV images due to the curvature of the transparent cylinder of 3 mm wall thickness was measured by placing a single-frequency sinusoidal transmittance grating (Applied Image, SF-2.0) of two cycles per-millimeter in the (r,z) measurement plane. Image of the grating without cyclone was captured by the camera of the PIV system and another image of the cyclone with the grating placed in the (r,z) measurement plane was also captured by the camera. The distance between the grating and the camera and the zoom ratio of the imaging lens of the camera were kept constant in the two cases. The images were compared carefully using MATLAB, and the maximum distortion of the grating lines due to the curvature of the transparent cylinder was found to be ~1% at the left- and right-end edges of the (r,z) measurement plane.

The thickness of the light sheet of the PIV system is ~2 mm. The time duration between every two images recorded for every velocity vector plot is 20 μs, and the maximum tangential velocity of the flow is ~20 m/s. The maximum distance traveled of the seeding particles due to the tangential velocity is estimated to be 0.4 mm. Therefore, the seeding particles did not leave the light sheet in the recording duration for the velocity vectors in the (r,z) plane. Since the maximum axial velocity is less than that of the tangential velocities (Fig. 2), there is no loss of pairs in the images due to the third velocity component, V_z, for the velocity vectors in the (r,θ) plane.

The PIV data analysis is conducted by a software program, FLOWMANAGER, provided by Dantec. The peak-finding algorithm is PEAK-HEIGHT VALIDATION, which validates or rejects individual vectors based on the values of the peak heights in the correlation data**,**where the raw vector displacement was measured. The cross correlation between the initial and final positions of the flow field, recorded on two consecutive images, was calculated using a cross-correlation algorithm, included in FLOWMANAGER. In the processing of the (r,z)-plane images, 32×64 rectangular interrogation areas were used. Each interrogation area included 32 pixels with 50% overlap with other areas in either of the r and z directions. The overlap is used to minimize the occurrence of erroneous vectors. The in-plane velocity vector field consisted of 79×31 vectors (2449 vectors in total). In the processing of the (r,θ)-plane images, the interrogation area is 32 pixels $\times$32 pixels ($\approx 0.06d_e \times 0.06d_e$) with 25% overlap in either of the radial and tangential directions. The ensuing in-plane velocity vector field consisted of 53×42 vectors (2226 vectors in total). Vectors outside the specified velocity range are most likely to be outliers. *Velocity range validation* and *moving average validation* were applied to remove false vectors (outliers) among raw velocity vectors. The rejected

Downloaded 03 Jun 2010 to 171.66.16.156. Redistribution subject to ASME license or copyright; see http://www.asme.org/terms/Terms_Use.cfm

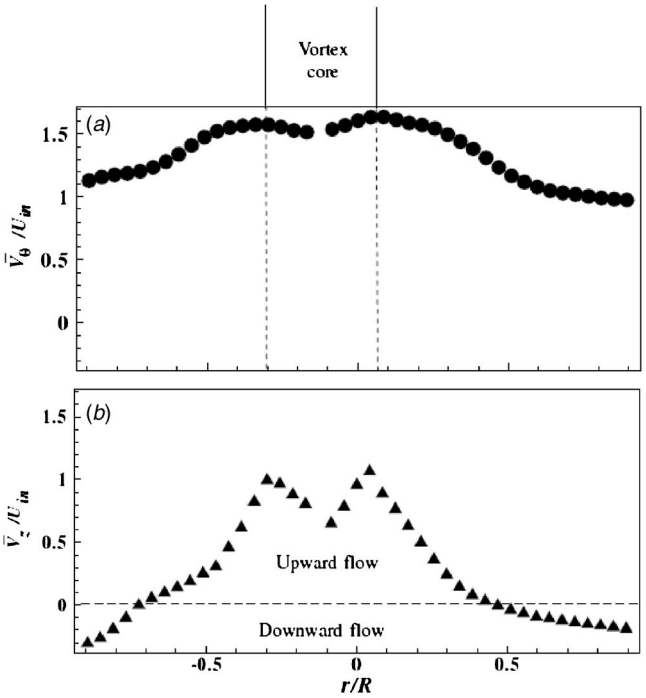

Fig. 2 Radial distribution of (*a*) mean tangential velocity $\bar{V}_\theta$ and (*b*) mean axial velocity $\bar{V}_z$ in the (r, θ) plane ($z/R=1$), Re =47,000

vectors may be replaced by vectors estimated from surrounding values. Subsequently, the *moving average filter* is used for reducing noise in the obtained vectors. In this investigation, about 24 outliers are substituted in a typical vector map, accounting for ~1% of the total number of vectors generated. The uncertainty in the velocity measurement is estimated to be 3%. The vorticity component ω_z in the (r,θ) plane was approximately derived based on particle velocities. The number of the ω_z data was the same as that of velocity vectors. The spatial resolution for ω_z was ~1.86 mm or $0.04d_e$.

3 Presentation of Results and Discussion

The measured $\bar{V}_\theta$ (Fig. 2(*a*)) and $\bar{V}_z$ (Fig. 2(*b*)) are qualitatively agreeable with previous reports, such as [19]. For the convenience of discussion, we designate the value of r/R at $\theta=0$ to be positive and that at $\theta=\pi$ to be negative. Both $\bar{V}_\theta$ and $\bar{V}_z$ display a twin peak distributions, with one peak at $r/R=-0.3$ and the other at $r/R=0.08$. The minimum of the trough in both $\bar{V}_\theta$ and $\bar{V}_z$ indicates the center of the vortex core [20]. This minimum occurs at $r/R \approx -0.1$, suggesting that the center of the vortex core does not coincide with the geometrical center of the cyclone. Furthermore, both $\bar{V}_\theta$ and $\bar{V}_z$ do not appear symmetrical about neither $r/R=0$ nor the center of the vortex core. The observations are reasonable since the flow inlet (Figs. 1(*a*) and 1(*c*)) is located asymmetrically about the geometrical center of the cyclone and the airflow enters the cyclone tangentially. $\bar{V}_\theta$ around the vortex center has not been measured because of insufficient concentration of smoke particles about the vortex center.

The flow field may be separated into two regions, i.e., the outer and inner regions, by the peaks of $\bar{V}_\theta$. In the inner or core region, i.e., $r/R<-0.3$ and $r/R>0.08$, $\bar{V}_\theta$ increases approximately linearly with the distance from the center of the vortex core, displaying similarity to a rigid-body rotation or a forced vortex. In the outer region of the vortex, i.e., $-1<r/R<-0.3$ and $0.08<r/R<1$, $r^{0.7}\bar{V}_\theta \approx$ constant, similar to previous report by Solero and Coghe [19]. The highest $\bar{V}_\theta$ occurs at the interface of the two regions and is ~1.66 U_{in}.

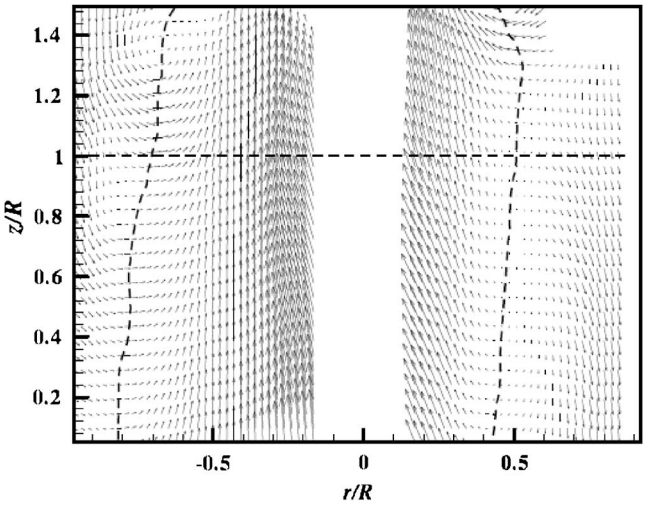

Fig. 3 Averaged velocity vectors in the (r,z)-plane of the cyclone chamber measured using PIV, Re=47,000 and S=3.0

In the central region, the axial velocity $\bar{V}_z$ (Fig. 2(*b*)) points up and is approximately linearly proportional to the distance from the center of the vortex core. The lower axial velocity toward the center of the vortex core reflects the loss of swirl in the exit pipe, resulting in an adverse pressure gradient at the centerline of the cyclone [11]. In the region close to the wall, $\bar{V}_z$ is downward directed toward the conical section in an annular region, i.e., $-1<r/R<-0.72$ and $0.43<r/R<1$, and is otherwise upward directed. The observed distribution of $\bar{V}_z$ is reasonable. Once entering the cyclone tangentially, the airflow moves toward the wall, forming an outer downward vortex flow under the strong action of the centrifugal force. After reaching the bottom, the flow turns upward.

Figure 3 presents the velocity vectors in the (r,z) plane averaged from 278 plots of PIV-measured instantaneous velocity vectors. Two curves indicate the location of zero *axial* velocity, i.e., $\bar{V}_z=0$, indicating the interface between the regions of upward and downward axial flows. Apparently, the location of $\bar{V}_z=0$ depends on z/R. At $z/R=1$, $\bar{V}_z=0$ occurs at $r/R=-0.72$ and 0.47, internally consistent with the radial distribution of LDA-measured $\bar{V}_z$. A close examination of the vectors suggests that the axes of both the upward and downward swirl flows in the cylindrical body of the cyclone are tilted and shifted away from the geometrical axis of the cyclone chamber. Using LDA to measure the flow velocities in a cylinder-on-cone cyclone, Peng et al. [21] also observed the asymmetry of axial velocity of the flow below the vortex finder.

The fluctuating tangential velocity $v_{\theta,\text{rms}}$ (Fig. 4(*a*)), displays a W-shaped distribution, rising markedly near the wall and the core. The results suggest a highly turbulent boundary layer over the cyclone wall and a highly turbulent inner precession vortex core. The large $v_{\theta,\text{rms}}$ toward the inner region is probably linked to the loss of swirl in the exit pipe [11]. In contrast to the variation of $v_{\theta,\text{rms}}$, $v_{z,\text{rms}}$ displays peaks at $r/R \approx -0.3 - -0.4$ and 0.2–0.3, where $\bar{V}_z/U_{\text{in}}$ (Fig. 2(*b*)) exhibits large gradients. The highly sheared flow is associated with an instability, resulting in large-scale vortical structures, as confirmed later by measured instantaneous vorticity contours. These vortical structures should be responsible for the peaks in $v_{z,\text{rms}}$.

Figure 5 presents the power spectral density function, E_{v_θ}, of V_θ

Downloaded 03 Jun 2010 to 171.66.16.156. Redistribution subject to ASME license or copyright; see http://www.asme.org/terms/Terms_Use.cfm

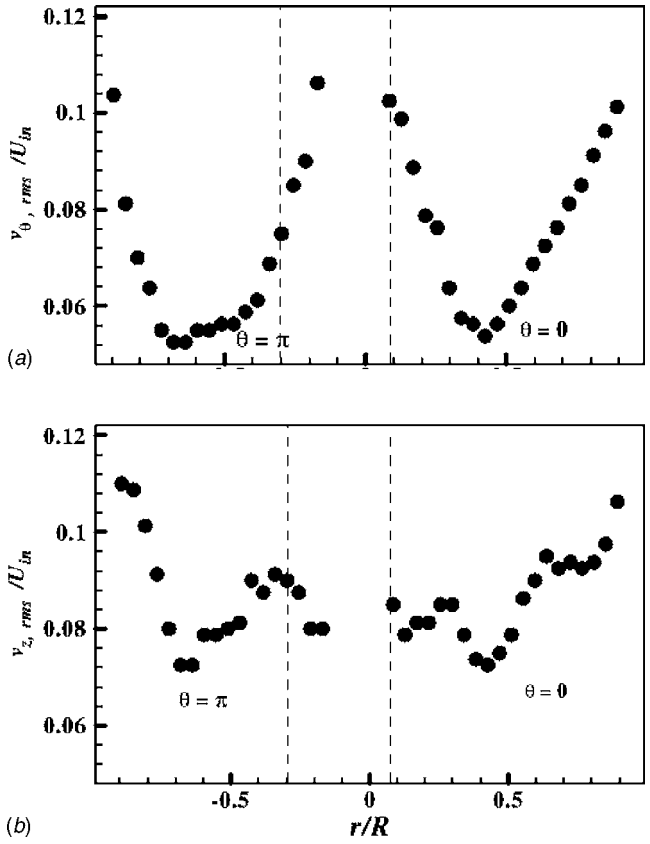

Fig. 4 Radial distribution of (*a*) $V_{\theta,\mathrm{rms}}$ and (b) $V_{z,\mathrm{rms}}$ in the (r, θ) plane ($z/R=1$), Re=47,000

measured using LDA at various r/R along the axis *X-X* of the measurement plane (Fig. 1(*c*)). In Figs, f is frequency (in Hertz). One pronounced peak occurs at $\mathrm{St}_1=f_1 2R/U_{\mathrm{in}}=0.53$ in E_{v_θ} at all positions except $r/R\geq 0.68$. Another pronounced peak is identifiable at $\mathrm{St}_2=f_2 2R/U_{\mathrm{in}}=0.62$ (Fig. 5), though only over the upward

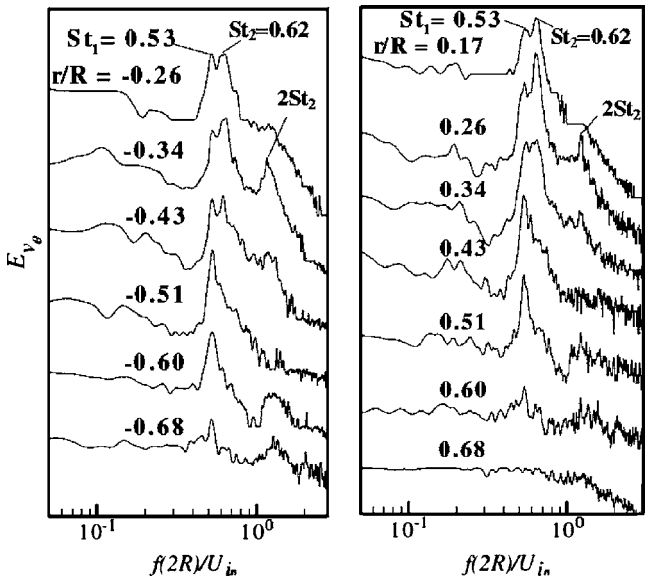

Fig. 5 Power spectral density functions of V_θ, measured along the axis *X-X* (Fig. 1(*c*)) in the (r, θ) plane ($z/R=1$), at various r/R using LDA, Re=47,000

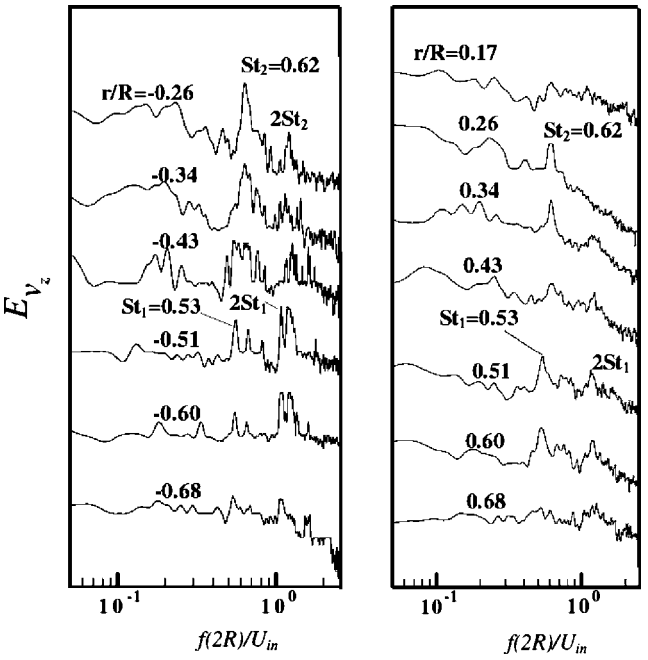

Fig. 6 Power spectral density functions of V_z measured along the axis *X-X* (Fig. 1(*c*)) in the (r, θ) plane ($z/R=1$), at various r/R using LDA, Re=47,000

flow region, i.e., $r/R=0.17-0.47$. The observed St_2 agrees quite well with the Strouhal number (=0.6) of the precessing vortex core in a similar cyclone [11].

Previous investigations [10,11,14,19], on reverse-flow cyclone have reported one dominant frequency only, i.e., the one that is observed only in the upward flow region. A scenario is proposed for the present observation of two dominant frequencies. Under the influence of the tangential flow momentum at the cyclone inlet, the flow within the cyclone is likely to precess as a whole, thus producing the peak in E_{v_θ} at St_1. This precessing flow spirals downward. The region of upward-directed flow also precesses. The two precessions, one spiral down and the other spiral up, are unlikely to have the same precessing frequency. In fact, being relatively small in diameter, the upward-directed flow should have a higher precessing frequency due to the conservation of the moment of momentum if the wall shear force on fluid is neglected. Therefore, in addition to swirling with the whole flow field, the region of the upward-directed flow should precess at St_2, which is higher than St_1. Near the cyclone wall, the peak at St_1 is not discernible probably because of the boundary layer effect. The two precession motions are opposite in the sense of rotation. The two fluid motions, one spiral down and the other spiral up (Fig. 3), are unlikely to have a "black-and-white" border between them; there should be a transition region where both motions could be present. Indeed, we have observed the twin-peak distribution in E_{v_θ} (Figs. 5 and 7) over $r/R\approx 0.26-0.43$ in the upward flow region. However, the proposed explanation has yet to be confirmed by more experimental or numerical data.

The V_z spectrum E_{v_z} (Fig. 6) again displays a peak at St_2 in the region of $r/R\leq 0.47$, where the flow is upward. However, the peak at St_1 is only discernible for $0.47<r/R<0.68$. Furthermore, the peaks are appreciably less pronounced, compared to those in E_{v_θ}. The observation is probably due to the fact that the dominant frequencies, St_1 and St_2, are primarily due to the precessing downward and precessing upward motions, respectively. The precessing motions are sensitive along the V_θ direction, not at the V_z direction. As a result, the peak at St_1 cannot be detected in the region of upward flow and even at $r/R=0.68$, where this peak is clearly

Downloaded 03 Jun 2010 to 171.66.16.156. Redistribution subject to ASME license or copyright; see http://www.asme.org/terms/Terms_Use.cfm

discernible in E_{v_θ} (Fig. 5). Chao et al. [22] observed two dominant frequencies in the axial velocity spectra within a swirl tube. They proposed that one of the frequencies was due to the precessing vortex core and the other to an azimuthal instability connected to the contraction downstream. Apparently, a swirl tube is rather different from a cylinder-on-cone cyclone; there is no reverse flow in the swirl tube, which is distinct from the present flow. Figure 7 shows the spectra of hotwire-measured V_θ and V_z, which display two pronounced peaks at the same frequencies as those given in the LDA data. Derksen [23] mentioned two frequencies were measured by Hoekstra [24] in the vortex core of a cylinder-on-cone cyclone with reverse flow under a flow condition of Re =280,000 and Swirl number=3.9. The two frequencies are St =0.7 and 1.58. The experimental data were given only at one point near the center in the midplane of the conical section of the cyclone; no explanation was given.

Additional experiments were conducted at three different Reynolds numbers Re=37,100, 60,000 and 74,000. The simultaneous presence of two peaks in the spectra was again measured, as shown in Fig. 8. Apparently, the Strouhal numbers appear independent of Re. As it can be noted, the measured St_1 and St_2 appears to be constant for the Re range presently investigated, significantly lower than Alekseenko et al.'s [9] measurements, i.e., St=0.85 at $S=1.9$ and 1.19 at $S=3.8$ (Re=14,000–45,000), which is expected in view of very different fluid dynamics between the flow in a cylinder-on-cone cyclone and a simple helical flow.

In order to gain a better understanding of the turbulent flow structure in the cyclone, the contours of PIV-measured instantaneous vorticity, $\omega_\theta 2R/U_{\text{in}}$, in the (r,z) plane are examined, as illustrated in Fig. 9. The normalized vorticity in the core region is opposite in sign to that in the outer region, suggesting that the precession of the overall flow (spiral downward) in the cyclone chamber is opposite in sense to the precession of the upward flow, which will be reconfirmed by the contours of axial vorticity measured in the (r,θ) plane. The maximum concentrations of vorticity in the outer region occur in the immediate neighborhood of the inner region. This is more evident in the contours of vorticity (Fig. 10) averaged from 278 plots of instantaneous vorticity measurements. The maximum concentrations of vorticity in the outer region coincide with the location, where the maximum gradient of LDA-measured $\bar{V}_z$ occurs.

Figure 11 presents the contours of typical instantaneous axial vorticity, $\omega_z 2R/U_{\text{in}}$, measured in the (r,θ) plane $(z/R=1)$. The inner region is characterized by highly concentrated positive $\omega_z 2R/U_{\text{in}}$, with the maximum occurring about $r/R=0$, exhibiting

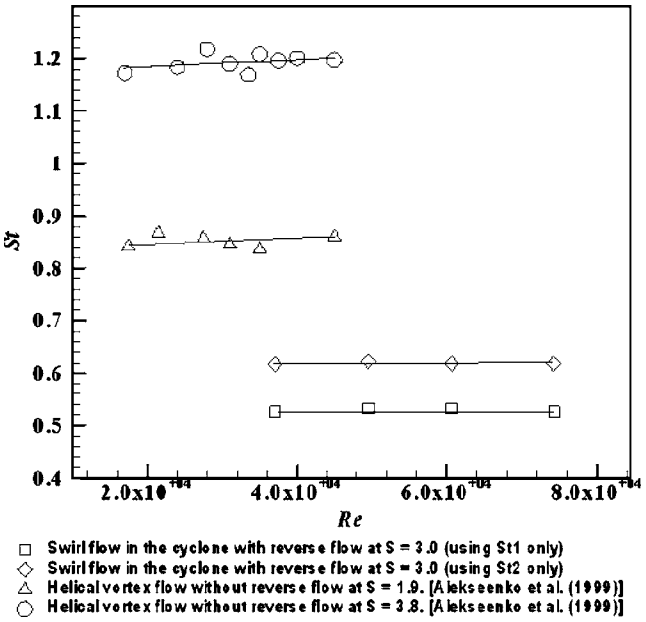

Fig. 8 Strouhal numbers of the swirl flow in the present cyclone at four different Reynolds numbers

the characteristics of the precessing vortex core. On the other hand, the opposite-signed (negative) $\omega_z 2R/U_{\text{in}}$ tends to dominate near the wall $(r/R=1)$, though significantly less concentrated than that in the inner region. Between the wall and inner regions (the outer region), the vortical structures of both signs are evident, again with less concentrated $\omega_z 2R/U_{\text{in}}$ than in the inner region. The observation is consistent with the fact that the two precession motions in the cyclone are opposite in the sense of rotation. The above characteristics are better reflected in the contours of $\bar{\omega}_z 2R/U_{\text{in}}$ (Fig. 12) averaged from 278 plots of instantaneous vorticity data. The maximum $\bar{\omega}_z 2R/U_{\text{in}}$ is shifted by $0.05R$ from the geometric center of the cyclone chamber.

Both the averaged and instantaneous vorticity contours suggest the presence of relatively large-scale structures encircling the vortex core in the annular region $|r/R|<0.8$. These structures appear quasiperiodical and are probably responsible for the pronounced

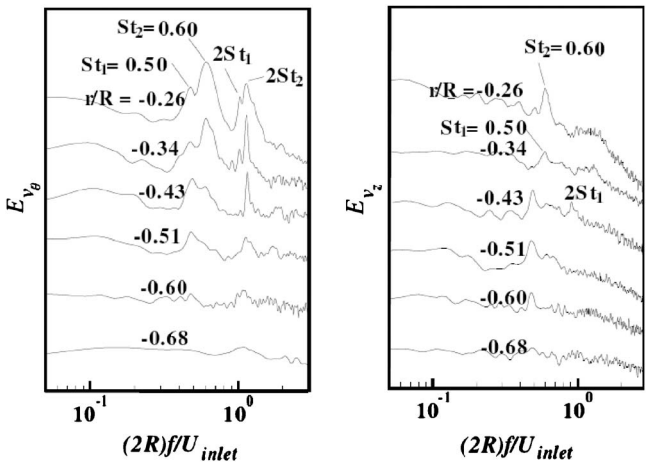

Fig. 7 Power spectral density functions of V_θ and V_z measured along the axis X-X (Fig. 1(c)) in the (r,θ) plane $(z/R=1)$, at various r/R using hot-wire anemometry, Re=47,000

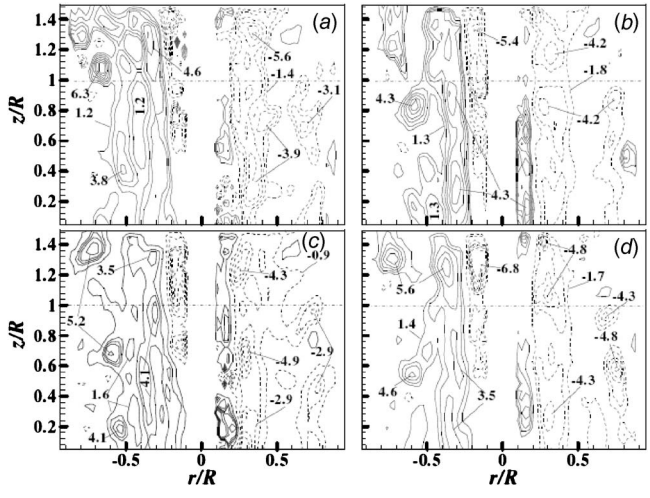

Fig. 9 Contours of PIV-measured instantaneous normalized vorticity in (r, z)-plane, Re=47,000 and $S=3.0$. The (r, θ) plane, where both PIV and LDA measurements were conducted, is marked by the dashed-dotted line.

Downloaded 03 Jun 2010 to 171.66.16.156. Redistribution subject to ASME license or copyright; see http://www.asme.org/terms/Terms_Use.cfm

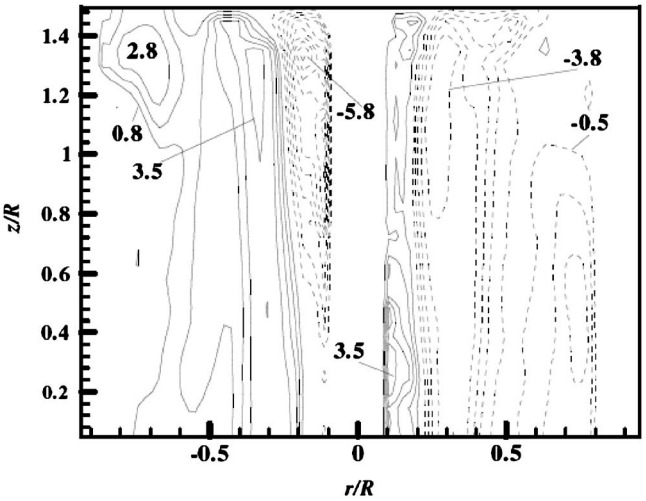

Fig. 10 Averaged vorticity contours measured using PIV in the (r,z) plane of the cylinder chamber, Re=47,000 and S=3.0

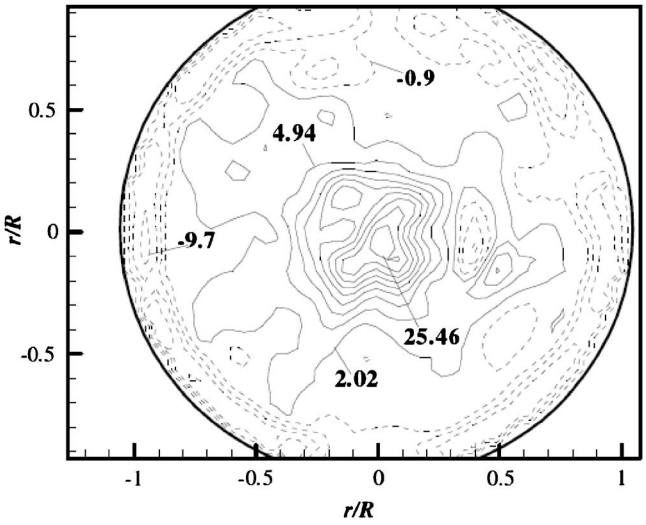

Fig. 12 Averaged vorticity contours in the (r, θ) plane (z/R =1) measured using PIV, Re=47,000 and S=3.0

peak at $St_1=0.53$ in E_{v_θ} (Fig. 5). Meanwhile, strong vortical structures that occur in $|r/R|<0.4$ may account for the peak in E_{v_θ} (Fig. 5) at $St_2=0.62$ that occur for $r/R=0.26-0.47$. Note that the averaged vorticity contours shown in Fig. 12 conform to the distribution of $V_{\theta,\mathrm{rms}}$ (Fig. 4(*a*)). The concentration in $\bar{\omega}_z 2R/U_{\mathrm{in}}$ for $0.8<|r/R|<1$ corresponds to the large $V_{\theta,\mathrm{rms}}$ near the wall; $\bar{\omega}_z 2R/U_{\mathrm{in}}$ appears low in the annular region of $0.4<|r/R|<0.7$, where $V_{\theta,\mathrm{rms}}$ is also small; $\bar{\omega}_z 2R/U_{\mathrm{in}}$ is large for $|r/R|<0.2$, where $V_{\theta,\mathrm{rms}}$ is large.

It has been well known that large-scale vortical structures may result from shear layer instabilities [25–27]. Naturally, the shear layer due to the occurrence of the spiral-up motion and spiral-down motion could lead to the formation of vortical structures. Nevertheless, more experimental evidence is required to confirm the present proposition.

4 Conclusions

The turbulent flow structure within a cyclone was experimentally investigated on a laboratory-scale cylinder-on-cone cyclone model based on LDA and PIV measurements. The work leads to the following conclusions:

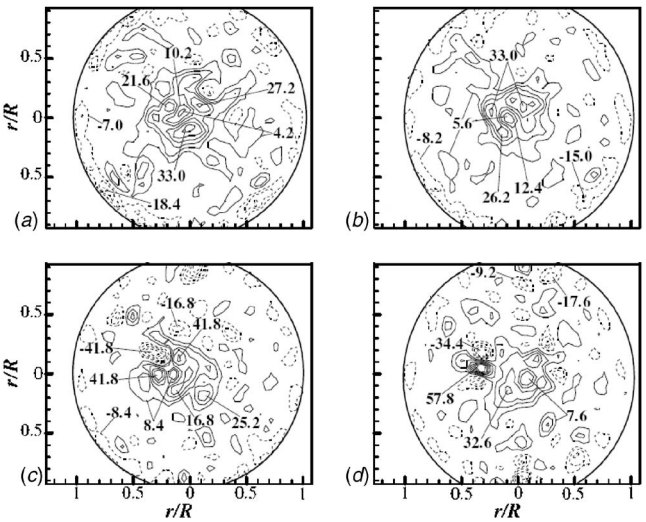

Fig. 11 PIV-measured instantaneous vorticity contours in the (r, θ)-plane (z/R=1), Re=47,000 and S=3.0

1. The flow has been characterized, in detail, in terms of the mean circumferential and axial velocities and their rms values, along with their topological features in the (r,θ) plane and the (r,z) plane. The rms circumferential and axial velocities are both high near the wall because of the turbulent boundary layer. The rms circumferential velocity is large in the core region, while the rms axial velocity displays a peak at $r/R\approx 0.3$, which is ascribed to the instability associated with the large velocity gradient immediately outside the vortex core region. The precession axis of the flow is found to be tilted and displaced from the geometric center of the cyclone. The data obtained from the measurements provide a data base for numerical modeling of the flow in a cylinder-on-cone cyclone.
2. Two dominant frequencies, St_1 and St_2, are observed based on the power spectral density functions of the tangential and axial fluctuating velocities. The lower frequency St_1 is observed in both of the outer and inner regions of the flow. This frequency is ascribed to the downward precession of the flow, within the cyclone, as a whole. To our knowledge, this frequency has been reported for the first time in the flow of a cylinder-on-cone cyclone. The higher frequency St_2 occurs in the vortex core region as a result of the upward precession of the vortex core, as previously reported.

Acknowledgment

The authors wish to acknowledge support given to them by the Central Research Grant of The Hong Kong Polytechnic University through Grants Nos. A-PE55 and No. G-T679.

References

[1] Linden, A. J., 1949, "Investigations Into Cyclone Dust Collectors," Proc. Inst. Mech. Eng., **130**, pp. 233–251.
[2] Ustimenko, B. P., and Bukhman, M. A., 1968, "Turbulent Flow Structure in a Cyclone Chamber," Therm. Eng., [Translation of Teploenergetika (Moscow)], **15**(2) pp. 64–67.
[3] O'Doherty, T., Jaryczewski, R., Bates, C. J., and Syred, N., 1991, *Velocity Characteristics of Cyclone Chambers*, ASME, New York, Vol. 1: Laser Anemometry.
[4] Chanaud, R. C., 1965, "Observations of Oscillatory Motion in Certain Swirling Flows," J. Fluid Mech., **21**, pp. 111–127.
[5] Cassidy, J. J., and Falvey, H. T., 1970, "Observations of Unsteady Flow Arising After Vortex Breakdown," J. Fluid Mech., **41**, pp. 727–736.
[6] Gouldin, F. C., Halthore, R. N., and Vu, B. T., 1984, "Periodic Oscillations Observed in Swirling Flows With and Without Combustion," *Proc. of 20th Symposium (International) on Combustion*, The Combustion Institute, Philadelphia, pp. 269–276.

Downloaded 03 Jun 2010 to 171.66.16.156. Redistribution subject to ASME license or copyright; see http://www.asme.org/terms/Terms_Use.cfm

[7] Harvey, J. K., 1962, "Some Observations of the Vortex Breakdown Phenomenon," J. Fluid Mech., **45**, pp. 585–592.
[8] Sarpkaya, T., 1971, "On Stationary and Traveling Vortex Breakdown," J. Fluid Mech., **45**, pp. 545–559.
[9] Alekseenko, S. W., Kuibin, P. K., Okulov, V. L., and Shtork, S. I., 1999, "Helical Vortex in Swirl Flow," J. Fluid Mech., **382**, pp. 195–243.
[10] Derksen, J. J., and Van den Akker, H. E. A., 2000, "Simulation of Vortex Core Precession in a Reverse-Flow Cyclone," AIChE J., **46**, pp. 1317–1331.
[11] Hoekstra, A. J., Israel, A. T., Derksen, J. J., and Van den Akker, H. E. A., 1999, "An experimental and numerical study of turbulent swirling flow in gas cyclones," Chem. Eng. Sci., **54**, pp. 2055–2065.
[12] Peng, W., Hoffmann, A. C., Dries, H. W. A., Regelink, M. A., and Stein, L. E., 2005, "Experimental Study of the Vortex End in Centrifugal Separators: The Nature of the Vortex End," Chem. Eng. Sci., **60**, pp. 6919–6928.
[13] Biffin, M., Syred, N., and Sage, P., 1984, "Enhanced Collection Efficiency for Cyclone Dust Separators," Chem. Eng. Res. Des., **62**(4), pp. 261–265.
[14] Yazdabadi, P. A., Griffiths, A. J., and Syred, N., 1994, "Characterization of the PVC Phenomena in the Exhaust of a Cyclone Dust Separator," Exp. Fluids, **17**, pp. 84–95.
[15] Schildmacher, K. U., and Koch, R., 2005, "Experimental Investigation of the Interaction of Unsteady Flow With Combustion," ASME J. Eng. Gas Turbines Power, **127**(2), pp. 295–300.
[16] Czarny, O., Iacovides, H., and Launder, B. E., 2002, "Precessing Vortex Structures in Turbulent Flow Within Rotor-Stator Disc Cavities," Flow, Turbul. Combust., **69**, pp. 51–61.
[17] Wang, Z. J., Zhou, Y., Huang, J. F., and Xu, Y. L., 2005, "Fluid Dynamics Around an Inclined Cylinder With Running Water Rivulets," J. Fluids Struct., **21**, pp. 49–64.
[18] Hu, J. C., Zhou, Y., and Dalton, C., 2006, "Effects of the Corner Radius on the Near Wake of a Square Prism," Exp. Fluids, **40**, pp. 106–118.
[19] Solero, G., and Coghe, A., 2002, "Experimental Fluid Dynamic Characterization of a Cyclone Chamber," Exp. Therm. Fluid Sci., **27** pp. 87–96.
[20] Hoffmann, A. C., and Stein, L. E., 2002, *Gas Cyclones and Swirl Tubes, Principles, Design and Operation*, Springer, New York, p. 38.
[21] Peng, W., Boot, P. J. A. J., Hoffmann, A. C., Dries, H. W. A., Kater, J., and Ekker, A., 2001, "Flow in the Inlet Region in Tangential Inlet Cyclones," Ind. Eng. Chem. Res., **40**, pp. 5649–5655.
[22] Chao, Y. C., Leu, J. H., Hung, Y. F., and Lin, C. K., 1991, "Downstream Boundary Effects on the Spectral Characteristics of a Swirling Flowfield," Exp. Fluids, **10**, pp. 341–348.
[23] Derksen, J. J., 2003, "Separation Performance Predictions of a Stairmand High-Efficiency Cyclone," AIChE J., **49**, pp. 1359–1371.
[24] Hoekstra, A. J., 2000, "Gas Flow Field and Collection Efficiency of Cyclone Separators," Ph.D. thesis, Delft University of Technology.
[25] Zhou, Y., and Antonia, R. A., 1995, "Memory Effects in Turbulent Plane Wakes," Exp. Fluids, **19**, pp. 112–120.
[26] Wang, Z. J., and Zhou, Y., 2005, "Vortex Interactions in a Two Side-by-Side Cylinder Near-Wake," Int. J. Heat Fluid Flow, **26**, pp. 362–377.
[27] Wang, Z. J., Zhou, Y., Huang, J. F., and Xu, Y. L., 2005, "Fluid Dynamics Around an Inclined Cylinder With Running Water Rivulets," J. Fluids Struct., **21**, pp. 49–64.

Downloaded 03 Jun 2010 to 171.66.16.156. Redistribution subject to ASME license or copyright; see http://www.asme.org/terms/Terms_Use.cfm

Attainment of Flowrate Uniformity in the Channels That Link a Distribution Manifold to a Collection Manifold

Jimmy C. K. Tong

Ephraim M. Sparrow

Laboratory for Heat Transfer
and Fluid Flow Practice,
Department of Mechanical Engineering,
University of Minnesota,
Minneapolis, MN 55455

John P. Abraham

Laboratory for Heat Transfer
and Fluid Flow Practice,
School of Engineering,
University of St. Thomas,
St. Paul, MN 55105

A logic-based systematic method of designing manifold systems to achieve flowrate uniformity among the channels that interconnect a distribution manifold and a collection manifold has been developed, implemented, and illustrated by case studies. The method is based on tailoring the flow resistance of the individual channels to achieve equal pressure drops for all the channels. The tailoring of the flow resistance is accomplished by the use of gate-valve-like obstructions. The adjustment of the valve-like obstructions is determined here by means of numerical simulations. Although the method is iterative, it may converge in one cycle of the iterations. Progress toward the goal of per channel uniformity can be accelerated by tuning a multiplicative constant. The only departure of the method from being fully automatic is the selection of the aforementioned multiplicative constant. The method is described in detail in a step-by-step manner. These steps are illustrated both generically and specifically for four case studies. As an example, in one of the case studies, an original flow imbalance of over 100% in an untailored manifold system was reduced to a flow imbalance of less than 10% in one cycle of the method.
[DOI: 10.1115/1.2754319]

1 Introduction

Manifolds are among the most commonly encountered fluid-flow devices. The applications in which manifolds play a major role extend from long-standing situations such as municipal water distribution systems and automobile engines to very recent, high-technology devices such as microchannel heat sinks and critical biological systems such as blood circulation in the human body. The quantitative history of manifold design may be traced back to the 1950s. For the next several decades thereafter, and to a lesser extent up to the present era, one-dimensional models have been used extensively for the design of manifolds [1–10]. The use of a one-dimensional approach to model a situation that is intrinsically three dimensional requires many simplifying assumptions. In more recent times, numerical simulation has been used for manifold design. References [11–17] constitute a representative sample of the literature. In general, the use of numerical simulation for manifold design has been restricted to specific applications.

Manifolds may be classified into two categories. One of these categories is *distribution manifolds*, where there is a single inlet and multiple exits. The other category is *collection manifolds*, where there are multiple inlets and a single exit. A major goal of manifold design is the attainment of flow uniformity at the multiple exits of a distribution manifold. In systems consisting of both a distribution manifold and a collection manifold, the design goal is to achieve an identical rate of flow in each of the channels that links the exits of the distribution manifold to the inlets of the collection manifold.

To the best of the author's knowledge, presently there is no general method to achieve the goal of per channel flowrate uniformity that has been identified in the preceding paragraph. The focus of this paper is to develop such a methodology and to test its capability. The method departs from being fully automatic only in that there is some flexibility in the choice of a parameter which controls the rate convergence to the final solution. However, convergence appears to be unconditional, and only the rate of convergence is at issue. The implementation of the method can be based either on numerical simulations or baseline experiments. Here, the implementation was performed by means of numerical simulations because that approach is believed to be more cost effective and less time consuming. The efficacy of the method has been definitively proven for laminar flow. In principle, the method can be extended to turbulent flow pending the development of more reliable turbulence models.

2 Model Problem

The proposed method for the design of manifold systems with equal flowrates in the interconnecting channels will be developed using a model problem that is illustrated in Fig. 1. As seen in the figure, the model problem consists of a system comprised of ten parallel channels that interconnect rectangular distribution and collection manifolds. The system is assumed to be two dimensional for computational convenience, but this simplification in no way prejudices the development of the proposed method of manifold design. Although various intuition-based geometrical modifications might be considered for the possible attainment of the same mass flow in each channel, such approaches are highly specific to individual cases and will not be considered here.

3 Development of the Design Method

From prior experience with manifold design, it may be expected that in the geometry pictured in Fig. 1, there will be a nonuniform mass flow distribution such that the smallest mass flowrate will occur in the channel closest to the inlet and the highest flowrate will be encountered in the channel farthest from the inlet. Correspondingly, the end-to-end pressure drops in the respective channels will also be nonuniform. Let the respective channels be numbered such that channel 1 is the first channel of the system and channel 10 is the last channel. Furthermore, let the pressure drop in each of the channels be denoted by

Contributed by the Fluids Engineering Division of ASME for publication in the JOURNAL OF FLUIDS ENGINEERING. Manuscript received June 13, 2006; final manuscript received March 28, 2007. Review conducted by Ali Beskok.

 Copyright © 2007 by ASME

Downloaded 03 Jun 2010 to 171.66.16.156. Redistribution subject to ASME license or copyright; see http://www.asme.org/terms/Terms_Use.cfm

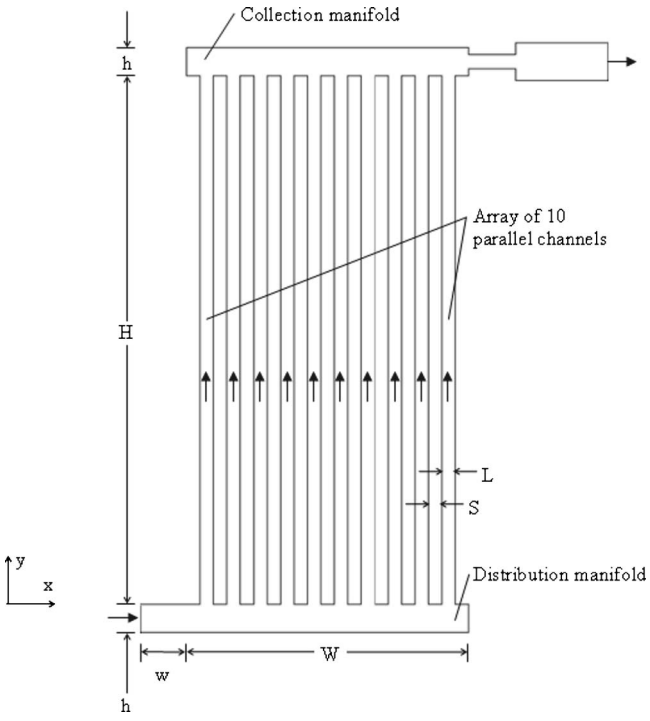

Fig. 1 A schematic diagram of a generic manifold system

$\Delta p_1, \Delta p_2, \ldots, \Delta p_{10}$, respectively. Then, with the use of Δp_1 as a reference pressure drop, the differences in the successive pressure drops can be written as

$$\Delta^2 p_n = \Delta p_n - \Delta p_1, \quad n \geq 2 \tag{1}$$

In general, the magnitude of $\Delta^2 p_n$ increases with increasing values of n. Clearly, to obtain the same per channel flowrate, it is necessary to adjust the respective values of Δp_n so as to achieve values of $\Delta^2 p_n$ that are approximately zero for all n.

In practice, a viable approach to the adjustment of Δp_n is to install valves in each of the channels. With this idea as a guideline, it is envisioned that a valve is installed at the downstream end of each one of the flow passages. The envisioned valves are assumed to be gate valves so that any valve setting corresponds to a simple partial blockage of the flow cross section. Figure 2 illustrates the concept in a schematic manner. The figure suggests valve openings that decrease monotonically from channel 2 to channel 10. Note that channel 1 is not equipped with a valve because it is generally the most flow-starved of all the channels, and an installed valve would lead to further starvation.

The method for determining the valve-adjustment protocol that leads to per-channel flow uniformity makes use of a module of information based on the fluid flow and pressure drop properties of a single flow channel. This module of information, once obtained, is generalized for application to all of the channels in the array. The physical model of the single channel selected as the module is illustrated in Fig. 3. Physical walls are indicated by the solid lines in the figure, while the dashed lines correspond to flow cross sections.

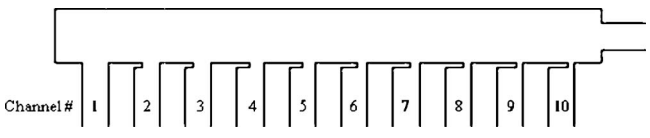

Fig. 2 A schematic diagram showing simulated valves at the exits of the interconnecting channels

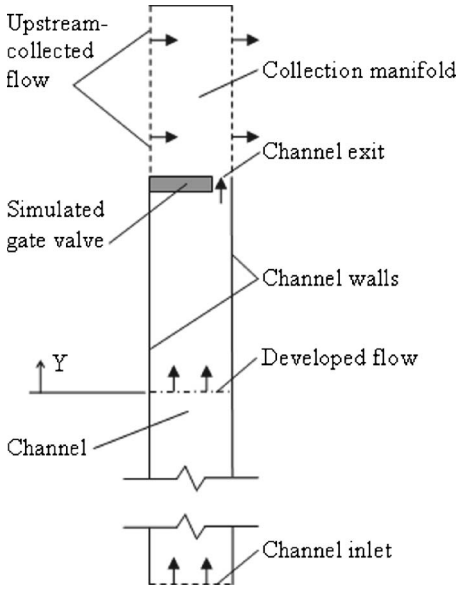

Fig. 3 The physical model of a typical channel

The exit of the channel is partially blocked to model a partially open gate valve. The space above the simulated gate valve is a portion of the collection manifold. That space is bounded at the left by a dashed line through which flow is passing. As indicated in Fig. 3, that flow is the accumulation of all of the fluid received by the collection manifold from upstream-situated channels. The right-hand boundary of that space is an outflow boundary.

In analyzing the fluid flow and pressure drop in the typical channel, it is convenient to assume that the desired condition of equal flowrates in each of the ten channels has been achieved. This assumption will automatically become reality once the goal of the method is attained. As a consequence of this assumption, the rate of fluid flow shown entering the inlet of the typical channel is one-tenth of the total flowrate of the system. At some distance downstream of the inlet of the typical channel, the flow becomes fully developed as indicated by the dot-dash line.

The rate of fluid flow entering the left-hand face of the collection manifold situated above the typical channel is equal to $(n-1)/10$ of the total flowrate of the system, where n is the number assigned to the typical channel.

3.1 Implementation of the Method. The implementation of the method is most conveniently described as a step-by-step procedure carried out for a given system flowrate:

1. For a manifold system of interest such as that of Fig. 1, determine the individual channel pressure drops Δp_n corresponding to the absence of the adjustable valves. The determination may be performed numerically as detailed later. Then, evaluate $\Delta^2 p_n$ according to Eq. (1);
2. For each channel n ($n \geq 2$), use the physical model defined by Fig. 3 to determine the valve-induced pressure drops $\Delta p_{\text{valve},n}$ for a range of valve openings. These pressure drops are obtained here by numerical simulation using the model that was described in connection with Fig. 3. The generic results of this determination are illustrated in Fig. 4, where $\Delta p_{\text{valve},n}$ is plotted as a function of the percentage opening of the valve;
3. The values of $\Delta^2 p_n$ from step 1 for each $n \geq 2$ may be plotted as horizontal lines in Fig. 4. Each such horizontal line for a specific n, if plotted, would intersect with a curve labeled with the same value of n. These intersections may be used as the valve settings for the respective channels;
4. To accelerate and ensure the attainment of the desired per

Downloaded 03 Jun 2010 to 171.66.16.156. Redistribution subject to ASME license or copyright; see http://www.asme.org/terms/Terms_Use.cfm

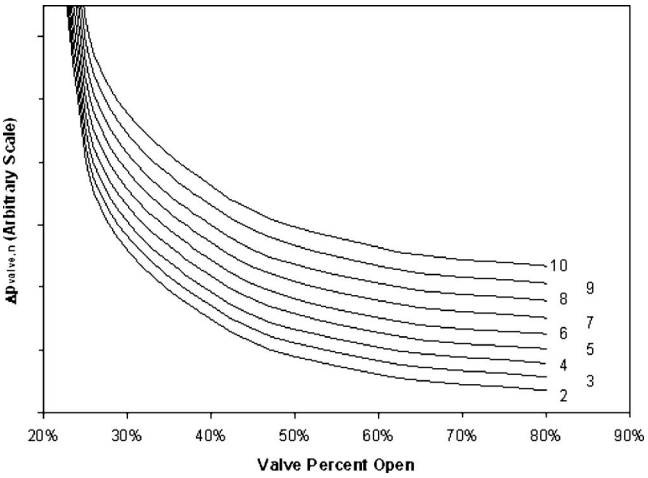

Fig. 4 Generic presentation of pressure drops of the simulated valves for the individual channels having a common per channel flowrate

channel flow uniformity, multiply each $\Delta^2 p_n$ from step 1 by a constant factor C, greater than one, that is the same for each n, and rename the thus multiplied values as $C\Delta^2 p_n$. Plot these values of $C\Delta^2 p_n$ as horizontal lines in Fig. 4, which results in Fig. 5. The horizontal line for a specific n should intersect the curve labeled with the same n. These intersections will be used as the valve settings for the next evaluation of the Δp_n. The process of choosing the constant multiplying factor will be deferred until later;

5. Let the system now be defined by Fig. 1, in which there are valves installed in accordance with the settings determined in step 4. The fluid flow and the pressure drops for that system are then solved for numerically. That solution may be identified as the first upgrade of the original solution for the unvalved system. To identify that this is the first upgrade, a superscript 1 will be appended to all relevant quantities;
6. For this first upgrade, calculate the mass flowrates passing through the individual channels. Next, compute the mean and standard deviation of these flowrate values. If the standard deviation divided by the mean is less than a preselected value (for example, 10%), the method can be regarded as having provided a satisfactory end result;

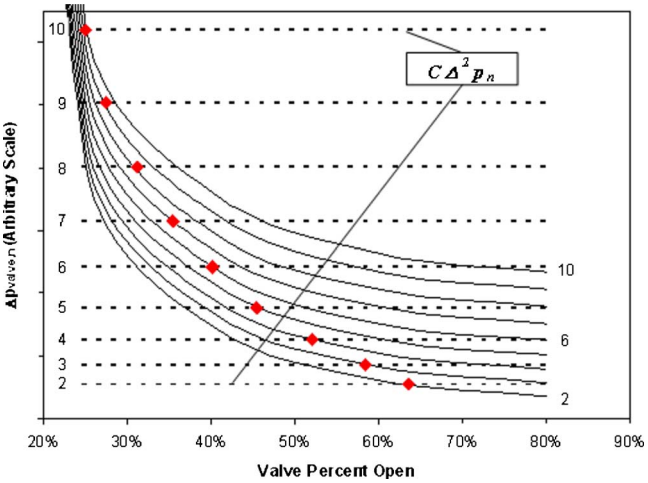

Fig. 5 Generic presentation of pressure drops of the simulated valves (curves) and the relative per channel pressure drops (horizontal straight lines)

7. If the value of the standard deviation divided by the mean is greater than the preselected value, another iteration of the type described in the foregoing is necessary;
8. To begin the next iteration, extract the values of $(\Delta p_n)^1$ from the first upgrade solution and evaluate $(\Delta^2 p_n)^1$ in accordance with Eq. (1);
9. Use the plot of $\Delta p_{\text{valve},n}$ versus valve opening percentage, already presented in Fig. 4, again without modification;
10. Multiply each value of $(\Delta^2 p_n)^1$ from step 8 by a common constant C^1 to obtain $C^1(\Delta^2 p_n)^1$. Then, for each n, plot the value of $C^1(\Delta^2 p_n)^1$ as a horizontal line in Fig. 4 and note the intersection of each horizontal line with the same number curve. These intersections define the new valve opening settings for the second upgrade; and
11. Continue as indicated in step 5 until the ratio of the standard deviation to the mean for the distribution of the per channel mass flowrates is less than the preselected value.

4 Numerical Solutions for Use in the Design Method

4.1 Governing Equations. In the design method that was discussed in the preceding section, numerical solutions were indicated as the preferred means of implementation. The details of the numerical simulations will be described here. To begin, it is appropriate to specify the flow regime, whether laminar or turbulent, and to write the governing conservation laws corresponding to the selected regime. The present analysis will be performed for steady, two-dimensional, laminar, constant-property flow, for which the equations representing conservation of mass and momentum (Navier–Stokes equations) are as follows:
mass conservation

$$\frac{\partial u}{\partial x} + \frac{\partial v}{\partial y} = 0 \tag{2}$$

x-direction momentum

$$\rho\left(u\frac{\partial u}{\partial x} + v\frac{\partial u}{\partial y}\right) = -\frac{\partial p}{\partial x} + \mu\left(\frac{\partial^2 u}{\partial x^2} + \frac{\partial^2 u}{\partial y^2}\right) \tag{3}$$

y-direction momentum

$$\rho\left(u\frac{\partial v}{\partial x} + v\frac{\partial v}{\partial y}\right) = -\frac{\partial p}{\partial y} + \mu\left(\frac{\partial^2 v}{\partial x^2} + \frac{\partial^2 v}{\partial y^2}\right) \tag{4}$$

4.2 The Solution Domain and Boundary Conditions. Next, the solution domain within which these equations are to be solved has to be specified. That specification is conveniently described by making reference to Fig. 1, which is now to be viewed as including valves situated at the downstream ends of the flow channels. The *inflow boundary* of the domain is indicated by the dashed line at the inlet of the system. Similarly, the *outflow boundary* is identified by a dashed line at the outlet of the system. The internal boundaries of the solution domain are the walls of the manifolds and of the interconnecting channels.

At the inflow boundary, it is assumed that there is a uniform velocity distribution whose magnitude corresponds to the desired flowrate. At the outflow boundary, the streamwise second derivatives of the velocities are set equal to zero and the average pressure is specified. This treatment of the outflow boundary is intended to impose minimal constraints on the flow. At the solid walls that bound the solution domain, the velocity components u and v are zero.

4.3 Discretization and Details of the Numerical Algorithm. The next step is to discretize the solution domain by subdividing it into a large number of very small elements. The accuracy of the numerical solution depends critically on the number of such elements and on their deployment. It is absolutely necessary to use a very dense distribution of elements in regions of high gradients. In particular, for the systems considered here, very high velocity gra-

Downloaded 03 Jun 2010 to 171.66.16.156. Redistribution subject to ASME license or copyright; see http://www.asme.org/terms/Terms_Use.cfm

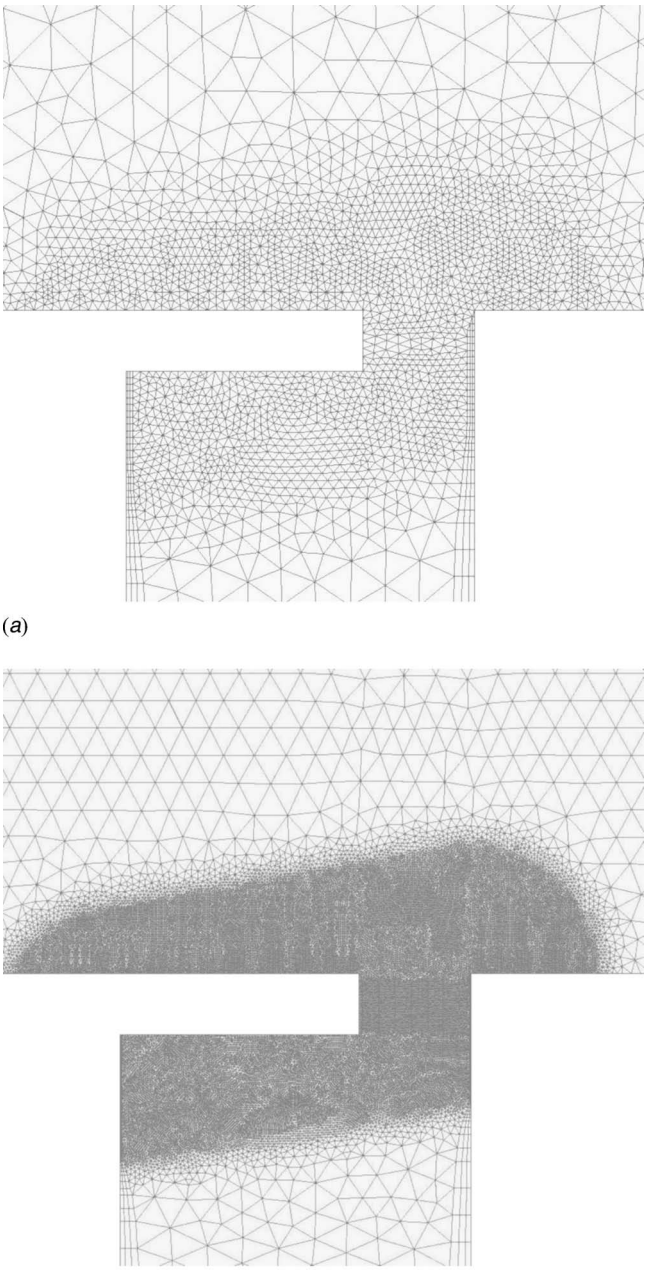

(*a*)

(*b*)

Fig. 6 Discretization of the solution domain in the neighborhood of a valve: (*a*) coarse mesh; and (*b*) fine mesh

dients occur adjacent to the valves. To illustrate the painstaking approach that was used to resolve these gradients, Figs. 6(*a*) and 6(*b*) have been prepared. The (*a*) part of the figure shows what would normally be considered as a sufficiently fine mesh. To ensure the accuracy of the results, the actual mesh that was used for the numerical solutions is pictured in the (*b*) part of Fig. 6.

A further and more quantitative measure of the accuracy of the solutions is obtained from a mesh-independence study. Three different cases were run to comprise this study, with each case corresponding to a different flowrate. In each case, one solution was obtained for a mesh consisting of approximately 150,000 nodes, and a second solution was carried out for a mesh of approximately 1,200,000 nodes. In two of the three cases, the ratio of the standard deviation to the mean of the per channel flowrates was unchanged for the two meshes. In the third case, the ratio changed by 2%. These results strongly indicate mesh independence. Subsequent to the mesh independence study, all solutions were run with meshes of approximately 1,200,000 nodes.

The calculations were carried out using CFX 9.0, a commercial finite-volume-based CFD program. The continuity and momentum equations are conserved over each element in the mesh; and overall conservation throughout the entire domain is thereby guaranteed. A false-transient time-stepping approach was employed to enable convergence to the steady-state solution. While the fully implicit, backward-Euler, time-stepping algorithm exhibits first-order accuracy in time, its presence does not affect the accuracy of the final, converged solution.

Coupling of the velocity-pressure equations was achieved on a nonstaggered, collocated grid using the techniques developed by Rhie and Chow [18] and Majumdar [19]. The inclusion of pressure-smoothing terms in the mass conservation equation suppresses oscillations which can occur when both the velocity and pressure are evaluated at coincident locations.

The advection term in the momentum equations was evaluated by using the upwind values of the momentum flux, supplemented with an advection-correction term. The correction term reduces the occurrence of numerical diffusion and is of second-order accuracy. Details of the advection treatment can be found in Ref. [20].

4.4 Calculation of Valve-Induced Pressure Losses. Numerical solutions were not only performed for the overall system (Fig. 1 with valves in place), but also for the typical channel module that is pictured in Fig. 3. The governing equations for that case are those of Eqs. (2)–(4). The specific goal of the numerical solutions for the typical module is to determine the valve-induced pressure drops $\Delta p_{\text{valve},n}$.

The solution domain for the typical channel module was selected specifically to facilitate the determination of $\Delta p_{\text{valve},n}$. In Fig. 3, the solution domain is shown bounded from below by the dot-dash line where fully developed flow prevailed in the channel. That line was situated five channel widths upstream of the channel exit. This location was identified from preliminary solutions. The upper boundary of the domain was taken to be the outer wall of the portion of the collection manifold situated above the typical channel.

The right-hand boundary of the solution domain consists of the right wall of the channel and its continuation, shown dashed in Fig. 3, which extends upward through the collection manifold. The left-hand boundary includes the left wall of the channel, the perimeter of the valve, and the inlet face of the portion of the collection manifold situated above the typical module.

Next, the boundary conditions at the surfaces of the solution domain must be specified. At all solid surfaces, $u=v=0$. At the inlet boundary of the domain, the parabolic velocity profile for fully developed laminar flow in a parallel-plate channel is imposed. The inlet face of the collection manifold is given a uniform velocity with a value corresponding to a flowrate equal to $(n-1)/10$ of the total flowrate of the system. At the outlet face of the collection manifold, the streamwise second derivatives of the velocities are set equal to zero and the average pressure is specified.

The procedure for determining the numerical values of $\Delta p_{\text{valve},n}$ is conveniently described by making reference to Fig. 7, which is a generic presentation and not related to any particular case. The figure is a graph in which the pressures at the left-hand and right-hand walls of the typical flow channel are plotted as a function of a distance Y/L from the inlet of the solution domain. The Y coordinate is illustrated in Fig. 3. It is seen from Fig. 7 that the pressures at respective channel walls are identical except in the near neighborhood of the valve. In that region, the pressure at the right-hand wall experiences a very sharp decrease as the flow contracts and accelerates during its passage through the valve opening. The valve-related pressure drop is defined in the figure as the difference between the pressures at the left- and right-hand

Downloaded 03 Jun 2010 to 171.66.16.156. Redistribution subject to ASME license or copyright; see http://www.asme.org/terms/Terms_Use.cfm

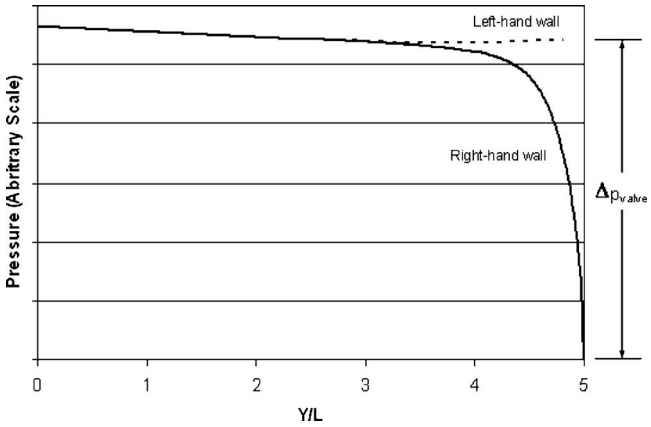

Fig. 7 Generic presentation of the method of obtaining Δp_{valve}

walls at the valve exit.

The value pressure drop is caused by a combination of phenomena which occur both upstream and downstream of the valve location. As mentioned earlier, the acceleration of flow passing through the restricted valve area results in a Bernoulli-type pressure decrease. This pressure decrease, while reversible in principle, is a pressure loss in practice, since virtually none of the dynamic head is recovered downstream of the valve. Rather, it is lost in the viscous mixing which occurs in the collection plenum.

In addition to pressure losses mentioned in the preceding paragraph, there are additional pressure losses caused by the turning of fluid as it passes into the collection plenum and out through the outflow boundary. The turning radius is affected by the strength of the upstream-collected flow shown in Fig. 3. Inasmuch as the downstream channels are subject to stronger plenum flows, they are expected to exhibit more severe turning (and consequently greater pressure losses) than are the upstream channels. The higher downstream valve-related pressure losses are evident in Fig. 4 by the vertical segregation of the nine curves.

5 Determination of the Multiplicative Constant

In the step-by-step outline (Sec. 3.1) of the method for obtaining per channel flow uniformity, a constant C was introduced in step 4 in order to accelerate and ensure the attainment of the method's goal. A formal lower bound on the value of C, as explained in step 3, is $C=1$. An operational lower bound greater than 1 may exist and can be determined by revisiting step 3. Suppose, in executing step 3, it is found that one or more of the horizontal lines do not intersect the corresponding curves with the same values of n as the lines. If so, all the $\Delta^2 p_n$ can be multiplied by a constant whose magnitude is chosen to enable all of the horizontal lines to intersect with their respective n-numbered curves.

To find an upper bound for C, a conservative approach may be suggested based on the authors' experience with the method. First, a value of $C=1.5$ is used as the multiplying factor, giving rise to a figure similar to Fig. 5. By making use of the intersections displayed in such a figure, step 5 is executed. Then, the pressure drops $(\Delta p_n)^1$ are extracted and the corresponding values of $(\Delta^2 p_n)^1$ calculated. If the magnitudes of $(\Delta^2 p_n)^1$ increase monotonically with n, then the method set forth in steps 6,7,… can be continued. For the continuation, a value of C^1 greater than 1.5 should be used. If, on the other hand, the magnitudes of $(\Delta^2 p_n)^1$ do *not* increase monotonically with n, then a value of C less than 1.5 must be used.

6 Applications of the Method

The method will now be demonstrated numerically as a case study. The geometry of the system selected for the case study is that of Fig. 1, with the dimensions $S=L$, $h=4L$, $w=3.5L$, $H=39L$, $W=21L$, and $L=1.8$ cm. A final specification of the system is the per channel Reynolds number based on a uniform distribution of the total flowrate among the individual channels. If Q_{total} is the total volumetric flowrate per unit depth, then Q_{total}/n is the uniformly prorated per channel flowrate per unit depth, $Q_{channel}$. Then

$$\mathrm{Re}_{channel} = \frac{2\rho Q_{channel}}{\mu} \tag{5}$$

For the case study, $\mathrm{Re}_{channel}=1000$.

To start the design process, step 1 of Sec. 3.1 is executed. The pressure drops and differences that result from the numerical solution for the just-specified geometry of the system are listed in Table 1. As can be seen from the table, the per channel pressure drops increase substantially from the first to the last channel. This variation indicates a correspondingly large change in the per channel flowrates.

To proceed, the numerical solutions specified in step 2 are performed. The solutions yield the valve-related pressure drops $\Delta p_{valve,n}$. These results are plotted as the downsloping curves in Fig. 8. According to step 3, the values of $\Delta^2 p_n$ that are listed in Table 1 may be plotted as horizontal lines in Fig. 8. However, for maximum efficiency, step 3 was skipped. To execute step 4, it is necessary to select a constant factor C as a multiplier of the values of the $\Delta^2 p_n$ of Table 1. A conservative trial $C=1.5$ advanced the method but fell short of the specified goal of per channel uniformity of 10%. A bold leap to $C^1=5$ was then made. The $\Delta^2 p_n$ values of Table 1 were multiplied by five and plotted as the horizontal lines in Fig. 8.

Table 1 Pressure drops and pressure differences for the first case study

Channel n	Δp_n (Pa)	$\Delta^2 p_n$ (Pa)
1	0.086	
2	0.208	0.122
3	0.308	0.222
4	0.409	0.324
5	0.500	0.414
6	0.786	0.701
7	0.907	0.822
8	1.081	0.996
9	1.552	1.466
10	2.669	2.583

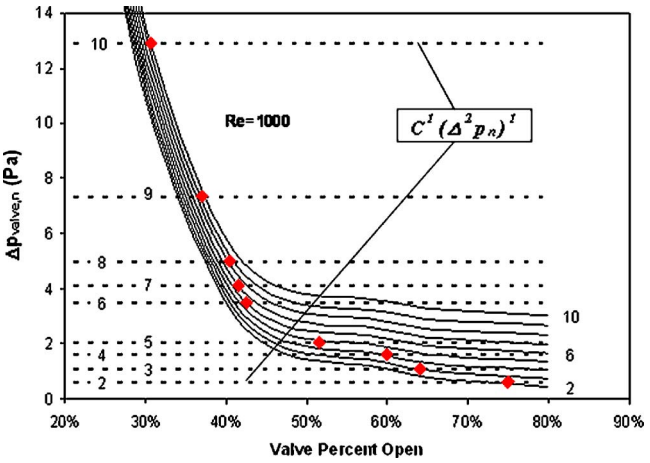

Fig. 8 Valve-related pressure drops (curves) and relative per channel pressure drops (horizontal straight lines) for Case Study 1

Downloaded 03 Jun 2010 to 171.66.16.156. Redistribution subject to ASME license or copyright; see http://www.asme.org/terms/Terms_Use.cfm

Table 2 Summary of results for Case Studies 2, 3, and 4

Case study	$Re_{channel}$	C	Uniformity	
			Original (%)	Final (%)
2	70	1.00	43	10
3	220	1.75	72	5
4	430	1.75	102	9

The intersections of the corresponding curve and horizontal line for each n were noted and then used as the valve settings. For the system geometry defined by Fig. 1 with these valve settings in place, a numerical solution was obtained. The per channel flowrates were determined from the solution and the mean and standard deviation calculated. These results yielded a ratio of the standard deviation to the mean of 8%. This outcome was deemed satisfactory relative to a preselected criterion of 10%. Since the ratio of the standard deviation to the mean for the original unvalved system was 75%, the final valved system represents a major improvement.

The method was used for other cases, the results of which are summarized in Table 2. The table strongly confirms the viability of the design method, especially in Case Study 3 where the original uniformity metric is 102%. The only geometrical difference between Case Studies 2, 3, and 4 and Case Study 1 is that for the former $h=2.1L$, whereas for the latter it equaled $4.2L$. For the cases studied, a satisfactory uniformity within the specified target of 10% was achieved with no more than three iterations.

It is relevant to provide guidance for the choice of the constant factor C. A lower bound for C can be determined by noting the condition under which the horizontal lines, whose level depends on the value of C, do not intersect all of the curves. A guide for the upper bound is related to the allowable pressure drop for the system. It is clear from Fig. 5 that the larger the selected value of C, the smaller the valve openings, and the higher the overall pressure drop. The specification of the maximum overall pressure drop therefore provides the upper bound.

7 Illustrative Flow Patterns

Insights into the patterns of fluid flow in the system being studied may be obtained via observation of vector diagrams extracted from the numerical solutions. Figure 9 displays the flow pattern in the neighborhood of a valve situated at the downstream end of a flow channel. The valve is about 29% open. As seen in the figure, the flow turns sharply in the neighborhood of the valve inlet and converges in order to pass through the opening. The flow emerges from the valve opening as a jet that discharges into the collection manifold. The upward momentum of the jet carries it across the collection manifold. The inability of the exiting jet to follow the contour of the wall of the collection manifold gives rise to a recirculating flow adjacent to the wall of the manifold. Clearly, the flow in the collection manifold is highly complex due to these processes.

Next, attention may be turned to the flow pattern in the neighborhood of the inlet of a typical flow channel. A vector diagram displaying that flow pattern is presented in Fig. 10. The main feature in evidence in this figure is the recirculation zone situated adjacent to the left-hand wall of the channel near the inlet. This recirculation zone is caused by the flow's inability to turn sharply from its horizontal path in the distribution manifold to its vertical upward path in the channel. As a consequence, the flow entering the channel hugs the right-hand wall of the channel while, at the same time, there is a downflow hugging the left-hand wall.

The flow separation and consequent recirculation illustrated in Figs. 9 and 10 are major contributors to the pressure drop of the system.

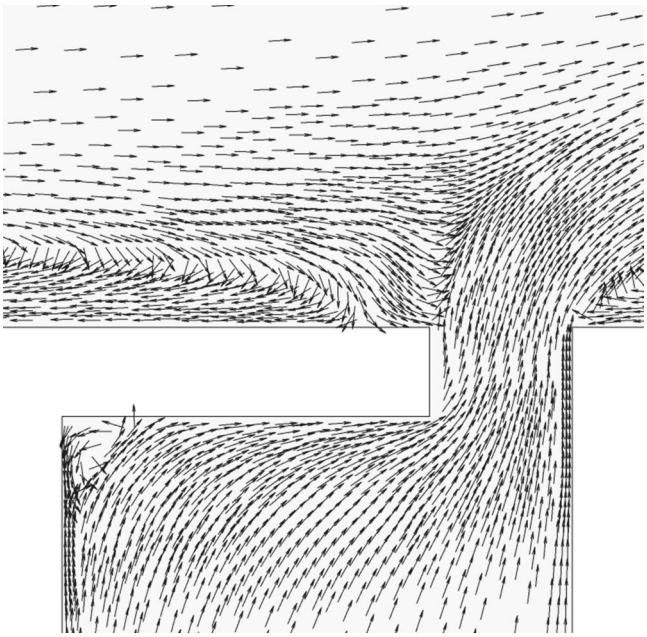

Fig. 9 Pattern of fluid flow in the neighborhood of a valve at the exit of a channel

8 Concluding Remarks

The goal of this investigation has been to develop, implement, and illustrate a method for designing manifold systems so that the flow in the channels linking a distribution manifold to a collection manifold is the same in each channel. In general, without using remedial measures, there will be a substantial variation in the flowrates carried by the respective channels.

The approach used here is based on the tailoring of the flow resistance in the individual channels so as to create the same end-to-end pressure drop in each. The tailoring is performed systematically in a stepwise manner that is described in detail in Sec. 3.1 of the paper. As implemented here, the method is consummated by

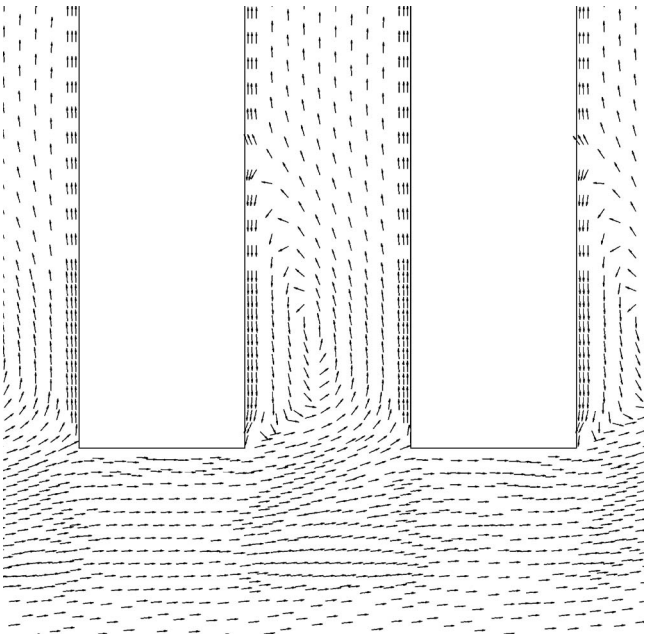

Fig. 10 Pattern of fluid flow in the neighborhood of the inlet of a channel

Downloaded 03 Jun 2010 to 171.66.16.156. Redistribution subject to ASME license or copyright; see http://www.asme.org/terms/Terms_Use.cfm

the use of numerical solutions for the manifold system in question. Alternatively, an experimental approach can be used, but the numerical-based procedure is believed to be much more cost effective and less time-consuming.

The systematic nature of the method attempts to supersede intuition-based approaches that rely on the experience of the designer. The fact that the new method is semi-automatic facilitates its use.

The method was used here to obtain uniformity in the per channel flowrates for four case studies. One of these case studies was described in detail in order to illustrate all the essential steps. For example, in one of the case studies, an original flow imbalance, as quantified by the ratio of the standard deviation to the mean of the per channel flowrates of 102%, was reduced to an acceptable value of 9% in one cycle of the procedure.

Illustrative flow patterns are conveyed showing that flow separation and recirculation are common features in manifold systems. These processes occur because the fluid is unable to pass smoothly from the distribution manifold to the interconnecting channels and from the interconnecting channels to the collection manifold.

Acknowledgment

The support from H. Birali Runesha and the Supercomputing Institute for Digital Simulation & Advanced Computation at the University of Minnesota is gratefully acknowledged.

References

[1] Spengos, A. C., and Kaiser, R. B., 1963, "Tapered Manifold Flow Spreader," Tappi J., **46**, pp. 195–200.
[2] Leydorf, Jr., G. F.,, Minty, R. G., and Fingeroot, M., 1972, "Design Refinement of Induction and Exhaust Systems Using Steady-State Flow Bench Techniques," SAE Paper No. 720214, p. 23.
[3] Bajura, R. A., and Jones, E. H., 1976, "Flow Distribution Manifolds," ASME J. Fluids Eng., **98**, pp. 654–666.
[4] Furzer, I. A., 1980, "Steady State Flow Distributions in a Plate Column Fitted with a Manifold," Chem. Eng. Sci., **35**, pp. 1291–1298.
[5] Hsu, C., 1985, "How to Achieve Balanced Cooling with Internal Manifolding," *Proceedings Annual Technical Conference*, Washington, DC, April 29–May 2, Society of Plastics Engineers, pp. 759–760.
[6] Riggs, J. B., 1987, "Development of Algebraic Design Equations for Dividing, Combining, Parallel, and Reverse Flow Manifolds," Ind. Eng. Chem. Res., **26**, pp. 129–133.
[7] Jones, G. F., and Lior, N., 1994, "Flow Distribution in Manifolded Solar Collectors with Negligible Buoyancy Effects," Sol. Energy, **52**, pp. 289–300.
[8] Chen, C., Jen, P., and Lai, F. S., 1997, "Optimization of the Coathanger Manifold via Computer Simulation and an Orthogonal Array Method," Polym. Eng. Sci., **37**, pp. 188–196.
[9] Pan, J. P., Liu, T. J., and Wu, P. Y., 1999, "Theoretical Analysis on Extrusion Die Flow of Electronic Packaging Materials," AIChE J., **45**, pp. 424–431.
[10] Argyropoulos, P., Scott, K., and Taama, W. M., 2000, "Hydrodynamic Modelling of Direct Methanol Liquid Feed Fuel Cell Stacks," J. Appl. Electrochem., **30**, pp. 899–913.
[11] Childs, E. P., 1987, "Flow Maldistribution in Disc-Type Power Transformer Windings," ASME, Heat Transfer Division, **75**, pp. 137–143.
[12] Poh, S. T., and Ng, E. Y. K., 1998, "Heat Transfer and Flow Issues in Manifold Microchannel Heat Sinks: A CFD Approach," *Proceedings of 2nd Electronics Packaging Technology Conference*, Singapore, December 8–10, pp. 246–250.
[13] Ng, E. Y. K., and Poh, S. T., 1999, "Investigative Study of Manifold Microchannel Heat Sinks for Electronic Cooling Design," J. Electron. Manuf., **9**, pp. 155–166.
[14] Commenge, J. M., Falk, L., Corriou, J. P., and Matlosz, M., 2002, "Optimal Design for Flow Uniformity in Microchannel Reactors," AIChE J., **48**, pp. 345–358.
[15] Karki, K. C., Radmehr, A., and Patankar, S. V., 2003, "Use of Computational Fluid Dynamics for Calculating Flow Rates Through Perforated Tiles in Raised-Floor Data Centers," HVAC&R Res., **9**, pp. 153–156.
[16] Ryu, J. H., Choi, D. H., and Kim, S. J., 2003, "Three-Dimensional Numerical Optimization of a Manifold Microchannel Heat Sink," Int. J. Heat Mass Transfer, **46**, pp. 1553–1562.
[17] Tonomura, O., Tanaka, S., Noda, M., Kano, M., Hasebe, S., and Hashimoto, I., 2004, "CFD-Based Optimal Design of Manifold in Plate-Fin Microdevices," Chem. Eng. J., **101**, pp. 397–402.
[18] Rhie, C. M., and Chow, W. L., 1982, "A Numerical Study of the Turbulent Flow Past an Isolated Airfoil with Trailing Edge Separation, AIAA Paper No. 82-0998.
[19] Majumdar, S., 1988, "Role of Underrelaxation in Momentum Interpolation for Calculation of Flow with Nonstaggered Grids," Numer. Heat Transfer, **13**, pp. 125–132.
[20] Barth, T. J., and Jesperson, D. C., 1989, "The Design and Applications of Upwind Schemes on Unstructured Meshes," AIAA Paper No. 89-0366.

Downloaded 03 Jun 2010 to 171.66.16.156. Redistribution subject to ASME license or copyright; see http://www.asme.org/terms/Terms_Use.cfm

CFD Analysis of Compressible Flow Across a Complex Geometry Venturi

Diego A. Arias
Solar Energy Laboratory,
Department of Mechanical Engineering,
University of Wisconsin-Madison,
Madison, Wisconsin, 53706
e-mail: daarias@engr.wisc.edu

Timothy A. Shedd[1]
Multiphase Flow Visualization and Analysis Laboratory,
Department of Mechanical Engineering,
University of Wisconsin-Madison,
Madison, Wisconsin, 53706
e-mail: shedd@engr.wisc.edu

A commercial computational fluid dynamics (CFD) package was used to develop a three-dimensional, fully turbulent model of the compressible flow across a complex-geometry venturi, such as those typically found in small engine carburetors. The results of the CFD simulations were used to understand the effect of the different obstacles in the flow on the overall discharge coefficient and the static pressure at the tip of the fuel tube. It was found that the obstacles located at the converging nozzle of the venturi do not cause significant pressure losses, while those obstacles that create wakes in the flow, such as the fuel tube and throttle plate, are responsible for most of the pressure losses. This result indicated that an overall discharge coefficient can be used to correct the mass flow rate, while a localized correction factor can be determined from three-dimensional CFD simulations in order to estimate the static pressure at locations of interest within complex venturis. [DOI: 10.1115/1.2754321]

1 Introduction

At the time of publication, over 35 million small engines are sold every year in the United States and their emissions comprise a significant percentage of total pollutants in the U.S. and worldwide. As demonstrated by the automotive industry, significant reductions in emissions are technologically possible, particularly with the use of electronic fuel injection. However, due primarily to cost constraints, small engine manufacturers rely on small, inexpensive carburetors to generate the fuel mixture for their engines. Thus, a better understanding of carburetor performance and modeling could lead to better fuel mixture control and lower emissions from small engines.

The equations used to represent the flow across a carburetor venturi are typically based on isentropic compressible flow relations. The deviation from this ideal flow is corrected with a discharge coefficient. This discharge coefficient is influenced by many factors, including geometry, mass flow rate, and fluid properties [1]. A real carburetor venturi has details in its geometry that create disturbances in the flow and may cause pressure losses that cause deviations from an ideal isentropic flow. Examples of these carburetor parts are the choke plate, throttle plate, fuel tube, side passages to secondary systems, and, sometimes, an additional concentric fuel tube in the venturi throat. Some details of typical carburetors used in small engines are shown in Fig. 1. The pressure losses created by these elements reduce the mass flow rate that could be driven through the venturi for a given pressure difference between the inlet of the venturi and the intake manifold.

In the present study, the inlet obstacles, fuel tube, and throttle plate were modeled with FLUENT [2] in order to gain a better understanding of the flow in complex venturis. The results of this study can be used to aid in the design of devices employing venturis, such as jet pumps, ejectors, venturi scrubbers, and industrial mixers.

2 Background on Prediction of Airflow in Carburetor Venturis

2.1 Zero- and One-Dimensional Studies. The simplest model of airflow in a carburetor venturi is based on the equations for compressible flow of an ideal gas through a converging isentropic nozzle. The air mass flow rate $\dot{m}_a$ is given by

$$\dot{m}_a = C_{d,t} A_t \sqrt{2\rho_{a0}(P_{v,0} - P_{v,t})}\Phi \tag{1}$$

$$\Phi = \left(\frac{[\gamma/(\gamma-1)][(P_{v,0}/P_{v,t})^{2/\gamma} - (P_{v,0}/P_{v,t})^{(\gamma+1)/\gamma}]}{1 - P_{v,0}/P_{v,t}} \right)^{1/2} \tag{2}$$

where C_D is the discharge coefficient based on the throat area A_t, ρ_{a0} is the air density at total inlet conditions, $P_{v,0}$ is the isentropic stagnation pressure at the inlet of the venturi, and $P_{v,t}$ is the static pressure at the venturi throat [1]. Φ accounts for the compressibility effects, where γ is the ratio of specific heats. These expressions can be used for real gases by using the compressibility factor Z in the denominator of Eq. (1), as used by Cornelius and Srinivas [3].

Equations (1) and (2) may be regarded as a steady-state one-dimensional model of compressible flow across a variable area duct. For a given flow rate, they can be used to predict the static pressure as a function of the local duct area, assuming that all the properties of the flow are uniform across the cross-sectional area. As it will be shown later, this may not be true for the flow in the carburetor throat due to acceleration, as well as the presence of different obstacles, such as the fuel tube.

Aside from the intake valves, the throttle plate is the largest restriction that the air encounters in its way through the engine intake system. Harrington and Bolt [4] applied Eqs. (1) and (2) to the throttle plate and calculated the discharge coefficient based on the open cross-sectional area for the actual throttle plate angle. Based on the analysis of the different elements in the throttle plate (shaft and plate), Harrington and Bolt [4] derived an expression for the projected cross-sectional area available for the air to flow through

$$\frac{4A_{th}}{\pi D^2} = \left(1 - \frac{\cos(\psi)}{\cos\psi_0}\right) + \frac{2}{\pi}\left[\frac{a}{\cos\psi}(\cos^2\psi - a^2\cos^2\psi_0)^{1/2} - \frac{\cos\psi}{\cos\psi_0}\sin^{-1}\left(\frac{a\cos\psi_0}{\cos\psi}\right) - a(1-a^2)^{1/2} + \sin^{-1}a\right] \tag{3}$$

where $a = d/D$, d is the throttle shaft diameter, D is the throttle bore diameter, ψ is the throttle plate angle, and ψ_0 is the minimum angle when the throttle is closed. An example of this function is shown in Fig. 2. A minimum area is available due to small leaks and reaches a maximum due to the blockage created by the

[1]Corresponding author.

Contributed by the Fluids Engineering Division of ASME for publication in the JOURNAL OF FLUIDS ENGINEERING. Manuscript received July 22, 2006; final manuscript received April 10, 2007. Review conducted by Ye Zhou.

 Copyright © 2007 by ASME

Downloaded 03 Jun 2010 to 171.66.16.156. Redistribution subject to ASME license or copyright; see http://www.asme.org/terms/Terms_Use.cfm

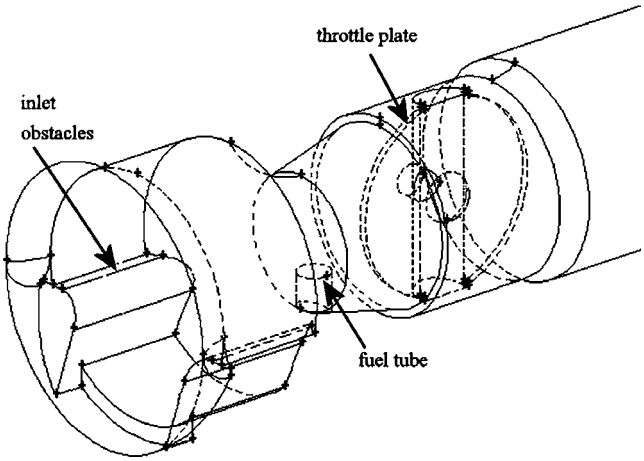

Fig. 1 Details of carburetor parts inside the venturi

throttle plate shaft.

Although the steady flow assumption may seem too restrictive for the application of this analysis in small utility engines, it was used by Harrington and Bolt [4] to predict the airflow through the intake system of an eight-cylinder engine. In this case, the airflow was nearly constant; thus, the steady flow assumption was valid. From these results [4], it is possible to deduce the following:

- For a given throttle plate angle, the mass flow rate increases for a decreasing manifold pressure. The flow behaves linearly when the pressure difference is small (high manifold pressure), but the lines curve at higher pressure difference indicating the compressibility effects.
- The flow chokes when the intake manifold is lowered to around the critical pressure $P/P_0=0.528$.
- At large throttle angles, the flow does not reach choked conditions, even at the highest engine speeds.
- For small throttle plate angles, the flow will be choked most of the time.

As indicated in Eq. (1), the actual mass flow rate is corrected with a discharge coefficient, which must be determined experimentally. Pursifull et al. [5] found that the discharge coefficient is a strong function of throttle plate angle and a weak function of intake manifold pressure. The discharge coefficient varies at small pressure differences but reaches an almost constant value for lower intake manifold pressures. This result is widely used in engine testing and simulation: the discharge coefficient is determined experimentally on a steady flow bench at a given pressure difference; the results are then used for all other pressure differences.

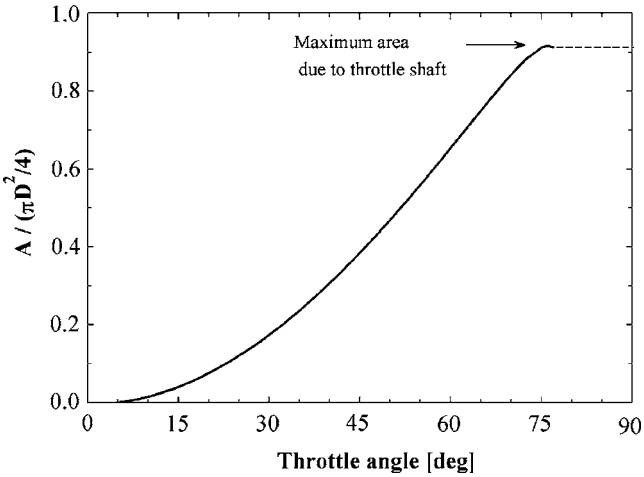

Fig. 2 Projected open area for airflow across throttle plate: closed=0 deg, open=90 deg

The natural extension to the theoretical model of airflow rate in the intake system is to use a quasi-steady-state approximation. With this assumption, the compressible nozzle model may be applied to the pulsating flow in a single- or two-cylinder engine. Woods and Goh [6] studied the compressible flow across a throttle plate under steady and unsteady conditions. They measured the airflow in the intake system of a single-cylinder engine and found that the prediction of the flow by using a quasi-steady-state assumption for the discharge coefficients produced good results for the engine operating at 530 rpm and 1000 rpm.

However, only the simultaneous solution of instantaneous mass, momentum, and energy equations for compressible flows can capture the dynamic effects of the flow inside of intake manifolds [7]. The solution of the instantaneous one-dimensional flow equations has been generally performed with two methods: the method of characteristics (e.g., [8,9]) and the finite difference method (e.g., [10]). Both these methods can predict the pressure and velocity fields for motored engines with good agreement with experiments. The solution to the one-dimensional flow equations has been implemented in several commercial packages, such as GT-Power [11], Ricardo-Wave [12], and AVL-Boost [13]. These packages are based on the assumptions of one-dimensional flow, ideal gas behavior, quasi-steady boundary conditions, no interaction between air and fuel, and that heat transfer, friction, and discharge coefficients are valid for both steady and unsteady flow [1].

2.2 CFD Studies. Although the one-dimensional methods address many important questions in relation to the transient gas dynamics, they do not provide detailed information about the flow field in specific parts of the system [14]. This kind of information may be obtained by using computational fluid dynamics (CFD). However, the use of CFD for the analysis of the flow across the complex geometries in the carburetor venturi has been very limited.

Tekriwal [15] performed a CFD analysis of venturis used as flow measurement devices. FLUENT was used to model the flow with an axisymmetric geometry; two turbulence models were compared in the simulations: Renormalized Group (RNG) k-ϵ model and Reynolds stress model (RSM). It was found that

- Both models predicted the pressure drop at the venturi throat with very good agreement with experimental results, but the overall pressure drop (from the inlet to the end of the diffuser) was better predicted by the RSM model. It was argued that this difference was caused by the assumption used in the k-ϵ model of isotropic turbulence in all of the Reynolds stresses. The use of the RSM model provided a better accuracy at the cost of more computations.
- Inlet turbulence intensity up to 10% had no effect on the pressure change through the venturi.
- The effect of air viscosity on the pressure drop is negligible for the conditions tested.

Examples of other studies that have used CFD for the characterization of airflow across venturi nozzles without obstacles and under subsonic conditions are those performed by Guessous [16] and Sera et al. [17]. CFD has also been used for choked conditions, such as the study by von Lavante et al. [18].

Sanatian and Moss [14] used a standard k-ϵ turbulence model to study the steady three-dimensional flow across a throttle valve in the intake system of a two-cylinder engine. The studies were conducted for two throttle-plate angles (30 deg and 50 deg). The results were given in terms of the mean velocity and turbulence intensity profiles along the intake pipe that houses the throttle valve. Comparisons to visualization experiments of stream lines

Downloaded 03 Jun 2010 to 171.66.16.156. Redistribution subject to ASME license or copyright; see http://www.asme.org/terms/Terms_Use.cfm

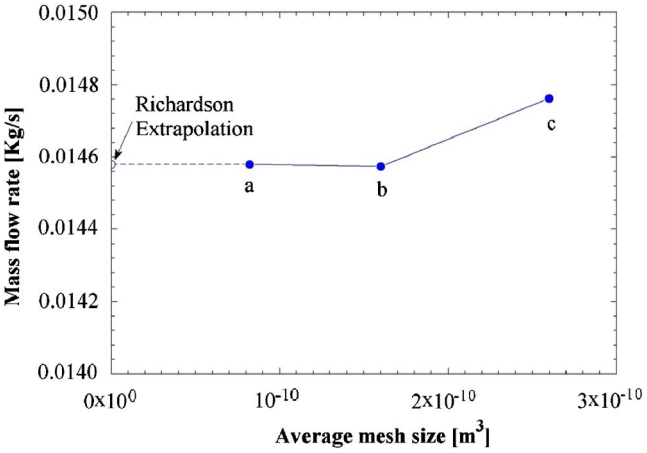

Fig. 3 Mesh size sensitivity of the mass flow rate

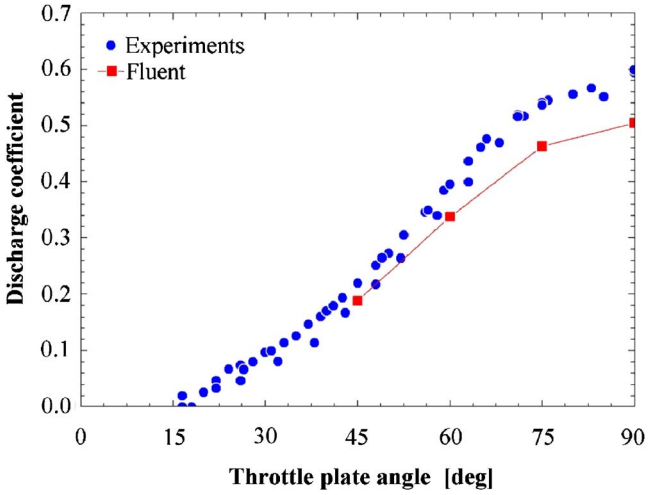

Fig. 4 Comparison of discharge coefficient for a Briggs & Stratton carburetor as function of throttle plate angle

and limited hot-wire anemometer measurements showed that the simulations could give an good indication of the flow fields in this geometry.

A more complete three-dimensional analysis of the flow across a throttle valve was performed by Alsemgeest et al. [19]. They used a standard k-ϵ model to study the unsteady compressible flow across a throttle valve under constant boundary conditions. They found that the obstruction created by the throttle plate produced vortex shedding behind it at a frequency of 200–600 Hz.

The only known work that has used CFD for the characterization of the flow across the carburetor was done by Wu et al. [20]. However, the carburetor was represented as a two-dimensional channel, where the fuel tube was a large obstacle in the flow field. The only results shown in this work were the static pressure drop along the axis of the carburetor.

3 Three-Dimensional CFD Study

3.1 General Characteristics of the Numerical Model. A three-dimensional model of a carburetor venturi was generated in GAMBIT and used in FLUENT to study the effect of different venturi parts on the flow field. The geometry was discretized with an unstructured tetrahedral mesh, with a refined mesh near the venturi throat. The RNG k-ϵ turbulence model was used, with standard wall functions for near-wall treatment. The discretization scheme used was second order in space. The pressure-velocity coupling was performed with the SIMPLE algorithm.

The convergence criteria were set to a maximum residual equal to 1×10^{-6} for the energy equation and to 1×10^{-4} for the other equations. The convergence of the solution with respect to mesh size was assessed by running the simulations with three meshes of different size. The result for an infinitely small mesh was approximated using the Richardson extrapolation [21,22]. Figure 3 shows the effect of mesh size on the mass flow rate, at a representative flow condition in the venturi without obstacles. According to Fig. 3, the intermediate mesh size was selected for the following simulations because it ensured a mesh independent solution.

The inlet boundary condition was defined with the isentropic stagnation pressure and temperature, and the outlet boundary condition was defined with the outlet static pressure. An ideal gas model was used in order to take into account the compressibility of the airflow.

3.2 Comparison to Experimental Results. Carburetor venturis are typically tested on steady-state flow benches, and the experimental discharge coefficient is found as a function of the throttle plate angle. On the steady-state flow bench, the inlet of the carburetor is open to the laboratory conditions and the outlet is connected to a low-pressure plenum, created by the low-pressure side of a blower. Once the throttle plate is set to a known position, the pressure in the outlet plenum is adjusted until a recommended static vacuum pressure is achieved. The volumetric airflow rate at these conditions is recorded. Figure 4 shows the measured discharge coefficient of a Briggs & Stratton carburetor as function of throttle plate angle.

In order to validate the simulations with experimental data, a Briggs & Stratton carburetor venturi was modeled in FLUENT. The carburetor venturi had an inlet diameter of 25 mm, a throat diameter of 12 mm and exit diameter of 20 mm. This venturi had inlet obstacles, a fuel tube, and a throttle plate. The inlet boundary conditions in FLUENT were set to the laboratory conditions (T_0 =293 K and P_0=1 atm) and the outlet boundary condition to the outlet pressure in the low-pressure plenum in the flow bench (P_{out}=94.5 KPa, or a static pressure difference of −28 in H_2O). Four throttle plate angles were simulated: 90 deg (wide open throttle), 75 deg, 60 deg, and 45 deg. Figure 4 compares the discharge coefficient calculated from the simulations to the experimental results. It was found that the FLUENT-calculated discharge coefficient was within 10% of the experimental value and closely followed the trends of the experimental results. The smaller values of C_D predicted by FLUENT indicated that the numerical model overpredicted the pressure losses.

The good agreement with experimental results over the range of throttle plate angle indicates that the characteristics of the simulations are appropriate to capture the flow conditions in the carburetor venturi with all of the inner parts. This was an encouraging result, as the range of throttle plate angles created complex details in the geometry, such as small passages when it is in a more closed position.

The CFD results were used for assessing the details of the flow, the values of the discharge coefficients, and localized values of the flow variables; specifically, the static pressure at the tip of the fuel tube. The following sections present a systematic study of the effect of different carburetor parts. First, the Briggs & Stratton carburetor venturi was modeled without obstacles. Second, the inlet obstacles were added, and then the fuel tube was added to the geometry. Finally, the effect of throttle plate angle was studied.

3.3 Venturi Without Obstacles. Figures 5(a) and 5(b) show the static pressure and Mach number for the compressible airflow across the carburetor venturi without obstacles in the flow. Figure 5 shows that the static pressure is almost uniform in the radial direction, with an exception occurring at the venturi throat, where the static pressure changes next to the wall. The velocity increases at the converging nozzle and then separates from the wall at the

Downloaded 03 Jun 2010 to 171.66.16.156. Redistribution subject to ASME license or copyright; see http://www.asme.org/terms/Terms_Use.cfm

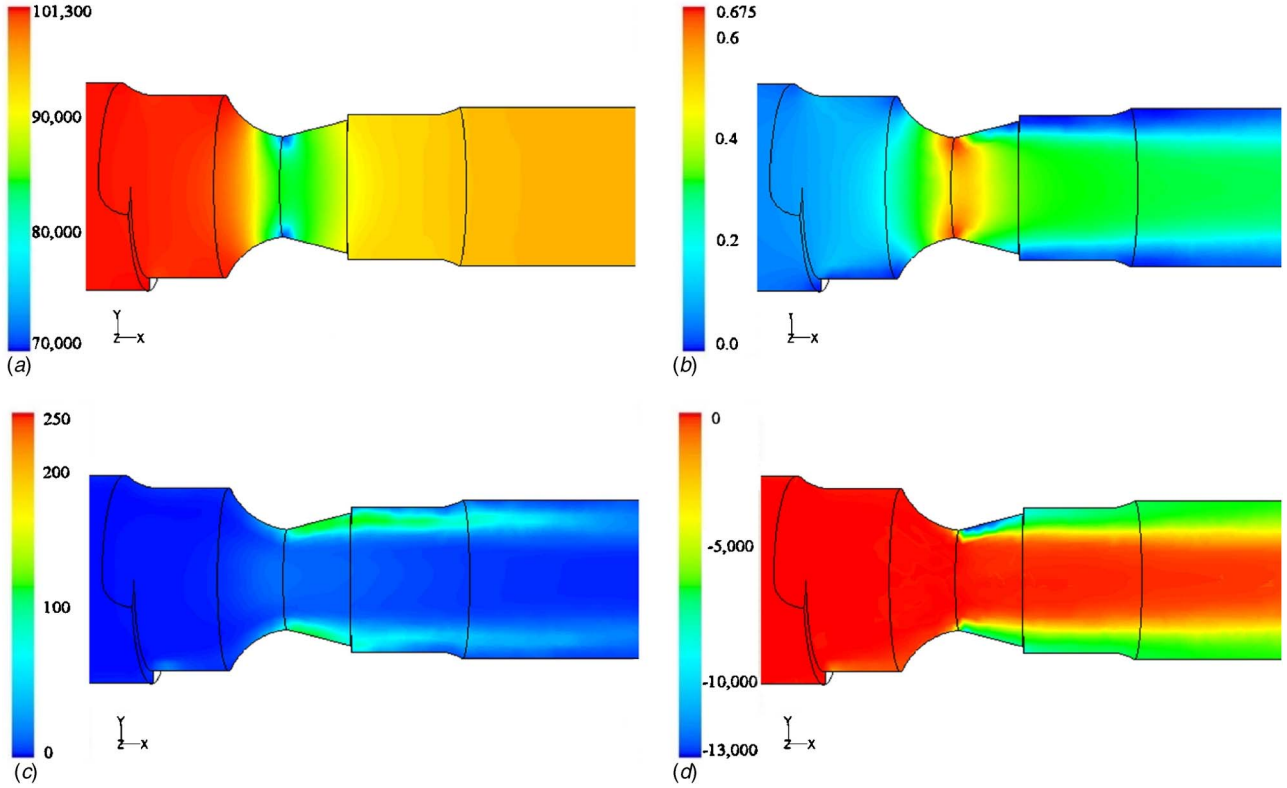

Fig. 5 Steady airflow across carburetor venturi without obstacles: (*a*) static pressure (in Pascal), (*b*) Mach number, (*c*) turbulent kinetic energy (in meters squared per seconds squared), and (*d*) gage total pressure (in Pascal)

diffuser in the region of adverse pressure gradient. The velocity field then resembles a free jet entering a constant pressure reservoir, although in this case the jet interacts with the surrounding wall.

The turbulent kinetic energy is shown in Fig. 5(*c*). It shows that the regions of high turbulence are those next to the walls of the diffuser and that they extend downstream of the carburetor venturi. This result is similar to the turbulence intensity in a free jet, where the highest turbulence region occurs in the region of velocity transition from the high-velocity zone to the quiescent air [23]. The final effect is the reduction of isentropic stagnation pressure at the outlet of the venturi, shown in Fig. 5(*d*). This result indicates that, in a venturi without inlet obstacles, the converging nozzle does not cause noticeable losses; it is the separation at the diffuser and the turbulence at the free shear zone of the jet that causes the pressure losses.

3.4 Effect of Inlet Obstacles. It was found that the presence of the inlet obstacles did not create a noticeable effect on the flow field, as shown in Fig. 6. As these obstacles are located in the converging zone of the venturi, the favorable pressure gradient keeps the velocity profile attached to the walls. The inlet obstacles affect the convergent flow but do not cause any wake or free shear region. In the same manner as in the venturi without obstacles, the high turbulence zones and pressure losses are located in the separation regions of the diffuser at the free shear region downstream of the venturi throat.

3.5 Effect of Fuel Tube. The presence of the fuel tube resulted in a strong change in the flow field in the carburetor venturi. Figure 7 shows the effect of a fuel tube with length equal to 3 mm and diameter equal to 3 mm. The length was equivalent to 1/4 of the throat diameter. The presence of the fuel tube produced a reduced cross-sectional throat area and a large wake zone behind it. This wake completely changes the nature of the pressure losses and effective area for the flow downstream of the venturi throat.

The static pressure shows a similar behavior to the previous cases: uniform pressure in the cross section everywhere but in the venturi throat. At this location, there is a different static pressure in the radial direction. In addition, the sharp leading edge of the fuel tube creates a separation region, which results in a lower pressure at the tip of the fuel tube. Downstream of the fuel tube, the static pressure is almost uniform in the radial and axial directions.

The velocity field shows the wake region created by the fuel tube. The final effect of the fuel tube on the airflow is to reduce the effective area used by the flow behind the venturi. The size of the wake region is increased with the length of the fuel tube. The wake region increased when the fuel tube was modeled with a length equal to 1/2 of the throat diameter. This wake zone may be responsible for fuel puddling after the carburetor: once a fuel droplet is captured in this region, there is no momentum to drive it downstream of the carburetor.

The turbulent kinetic energy field indicates that the nature of the pressure losses are quite different when the fuel tube is present in the carburetor. The wake zone has the region of highest turbulence intensity; the turbulence intensity next to the walls of the diffuser is almost negligible in comparison. The effect of turbulence is seen in the total pressure: the wake zone is also the region where the isentropic stagnation pressure is reduced most significantly.

Because the analysis was performed with the same pressure difference for all of the venturi geometries, the effect of the fuel tube is a reduced mass flow rate of air. If the analysis were performed at constant mass flow rate, the mass conservation in the reduced area would have produced a higher velocity and lower static pressure.

These images allow for a better understanding of the complex interaction between the fuel tube and the airflow: in current car-

Downloaded 03 Jun 2010 to 171.66.16.156. Redistribution subject to ASME license or copyright; see http://www.asme.org/terms/Terms_Use.cfm

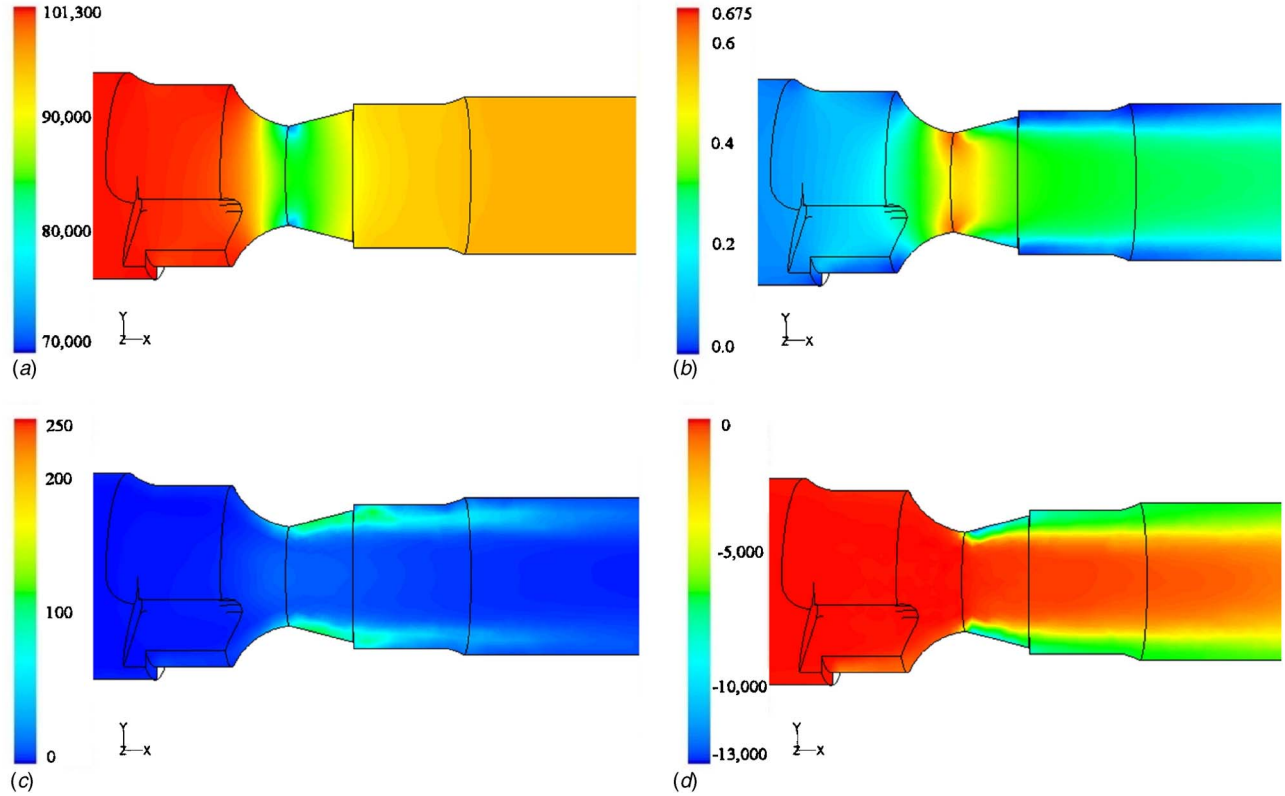

Fig. 6 Steady airflow across carburetor venturi with inlet obstacles: (*a*) static pressure (in Pascal), (*b*) Mach number, (*c*) turbulent kinetic energy (in meters squared per seconds squared), and (*d*) Gage total pressure (in Pascal)

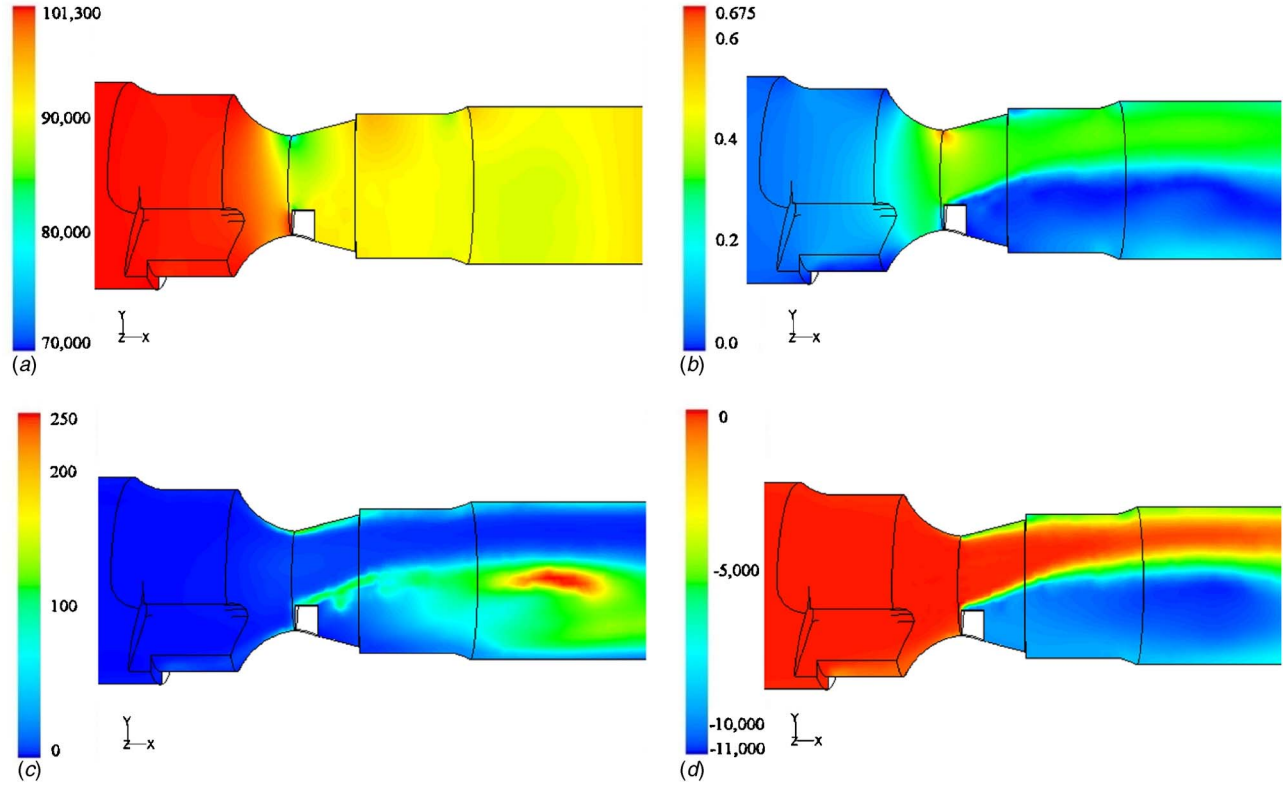

Fig. 7 Steady airflow across carburetor venturi with inlet obstacles and fuel tube: (*a*) static pressure (in Pascal), (*b*) Mach number, (*c*) turbulent kinetic energy (in meters squared per seconds squared), and (*d*) gage total pressure (in Pascal)

Downloaded 03 Jun 2010 to 171.66.16.156. Redistribution subject to ASME license or copyright; see http://www.asme.org/terms/Terms_Use.cfm

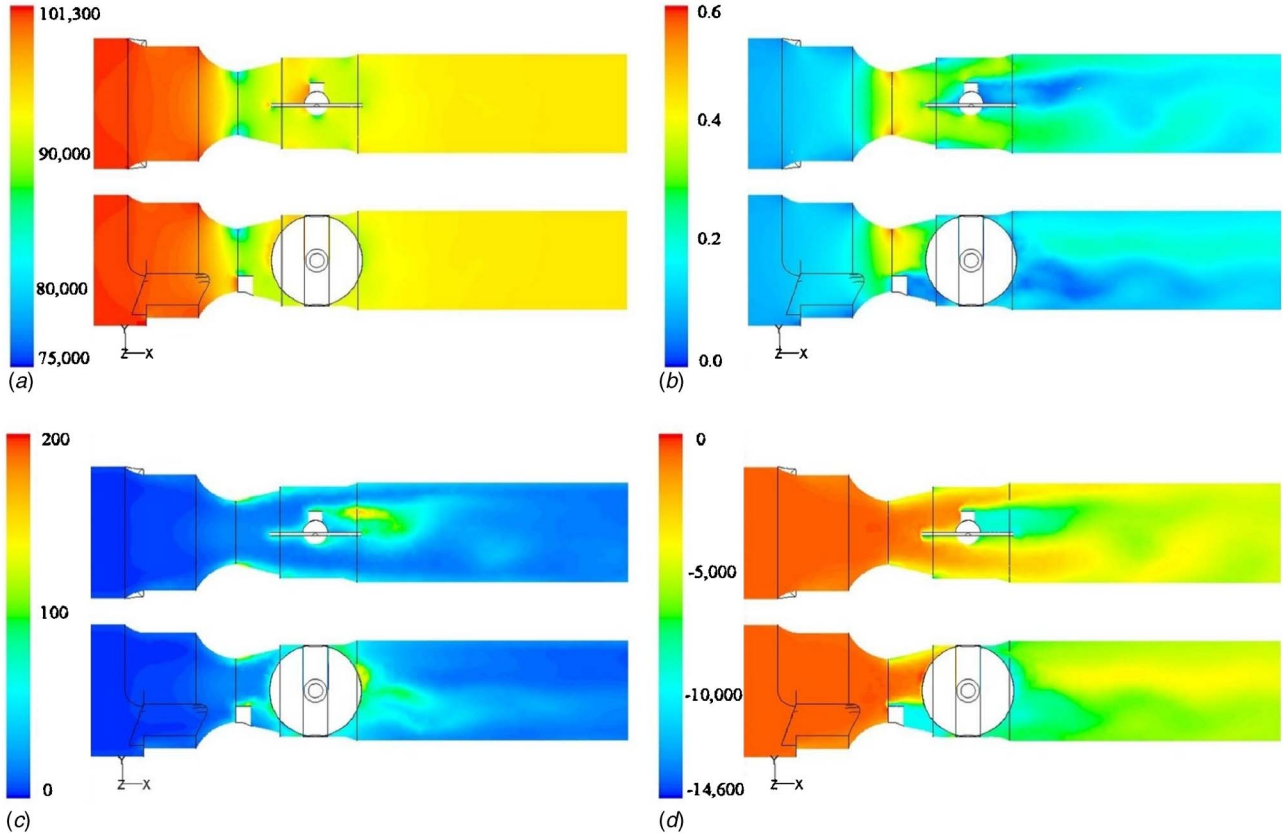

Fig. 8 Steady airflow across carburetor venturi with fuel tube, inlet obstacles, and throttle plate at 90 deg: (*a*) static pressure (in Pascal), (*b*) Mach number, (*c*) turbulent kinetic energy (in meters squared per seconds squared), and (*d*) gage total pressure (in Pascal)

buretor designs, a fuel tube extending into the venturi throat, beyond the throat wall, is necessary. It brings the fuel flow near the centerline of the venturi, which is intended to help generate an even distribution of the fuel droplets in the flow field. A fuel tube that does not extend beyond the wall would not prevent the fuel flow from staying next to the wall. But the fuel tube itself also completely disturbs the airflow, increasing the pressure losses and, therefore, decreasing the mass flow rate at a given pressure drop.

3.6 Effect of Throttle Plate at Wide Open Angle. Besides the intake valves, the throttle plate is the largest restriction to the airflow in the intake manifold. The carburetor venturi was next simulated with the inlet obstacles, fuel tube, and throttle plate. The throttle plate was modeled as close as possible to the physical model: it was composed of the axis rod, plate, and screw.

Figure 8 shows that, even when it is aligned with the flow, the presence of the throttle plate causes a large effect on the flow field, increasing the wake zone and producing asymmetric features in the flow.

The static pressure field does not change significantly from the previous cases; additional stagnation points are created by the leading edge of the throttle plate, shaft, and screw. However, the velocity field is greatly influenced by the throttle plate: the high-speed stream created by the fuel tube now encounters a large obstacle just downstream. The wakes created by the fuel tube and the throttle plate interact between them, producing a vortex shedding seen in both planes of Fig. 8.

The flow field shows that, even at wide-open conditions, the screw creates an asymmetry in the flow. The highest velocity on the right side of the throttle plate (seen on the top view) shows that this side of the flow would experience a higher airflow and, it may be inferred, more fuel droplets.

The turbulent kinetic energy indicates that the throttle plate, shaft, and screw are responsible for the largest turbulence regions in the flow. This turbulence results in a reduced isentropic stagnation pressure.

3.7 Effect of Throttle Plate at Different Angles. The effect of throttle plate angle on the flow field in the carburetor venturi is a strong function of the angle at which it operates. As the throttle plate closes, the mass flow rate is reduced for the given pressure difference across the entire carburetor. Figures 9 and 10 show the throttle plate at 75 deg and 60 deg, respectively. In these two cases, there are increased pressure losses and increased asymmetry in the flow. A conclusion from this asymmetry would be an increased tendency for droplets to impact the throttle plate and one side of the intake manifold.

When the throttle plate angle is further closed to 45 deg, the flow is different from the previous cases (Fig. 11). The mass flow rate has decreased significantly, and the flow fields resembled those in an orifice: the static pressure is uniform everywhere upstream of the throttle plate (even at the venturi throat), it decreases suddenly next to the reduced area created by the plate, and then is uniform downstream of the plate. The velocity field shows the same characteristics of an orifice: small magnitude everywhere but in the region next to the reduced area opening.

This is a case where it is very likely that the main fuel system of the carburetor is not active; the airflow does not create a pressure at the venturi throat that is low enough as to drive fuel flow from the fuel tube. Under these conditions, the idle system could be activated. An interesting feature of these plots is that the asymmetry of the flow would make it different if the idle ports are located in one side of the carburetor or the other. This asymmetry could also be a large player in the uneven fuel distribution in the intake manifold.

Downloaded 03 Jun 2010 to 171.66.16.156. Redistribution subject to ASME license or copyright; see http://www.asme.org/terms/Terms_Use.cfm

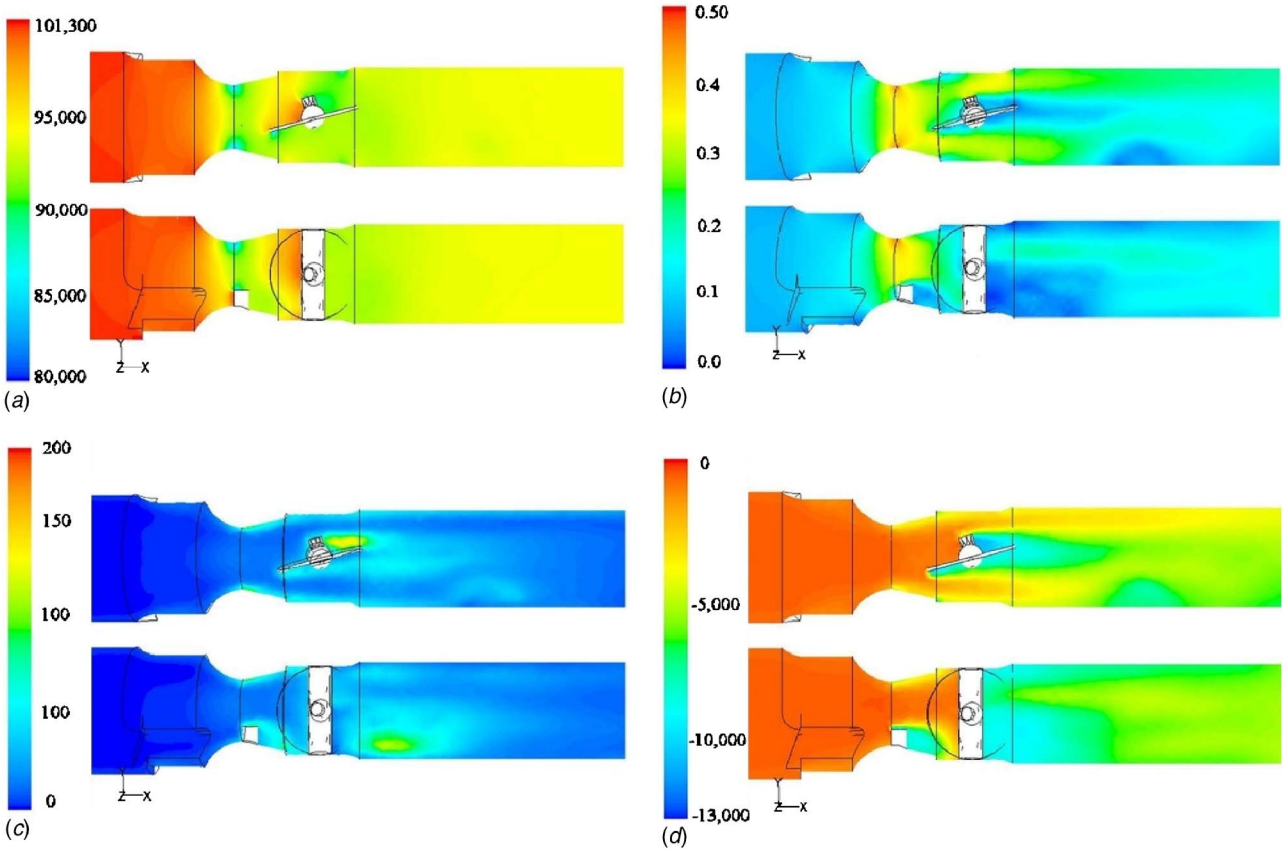

Fig. 9 Steady airflow across carburetor venturi with fuel tube, inlet obstacles, and throttle plate at 75 deg: (*a*) static pressure (in Pascal), (*b*) Mach number, (c) turbulent kinetic energy (in meters squared per seconds squared), and (*d*) gage total pressure (in Pascal)

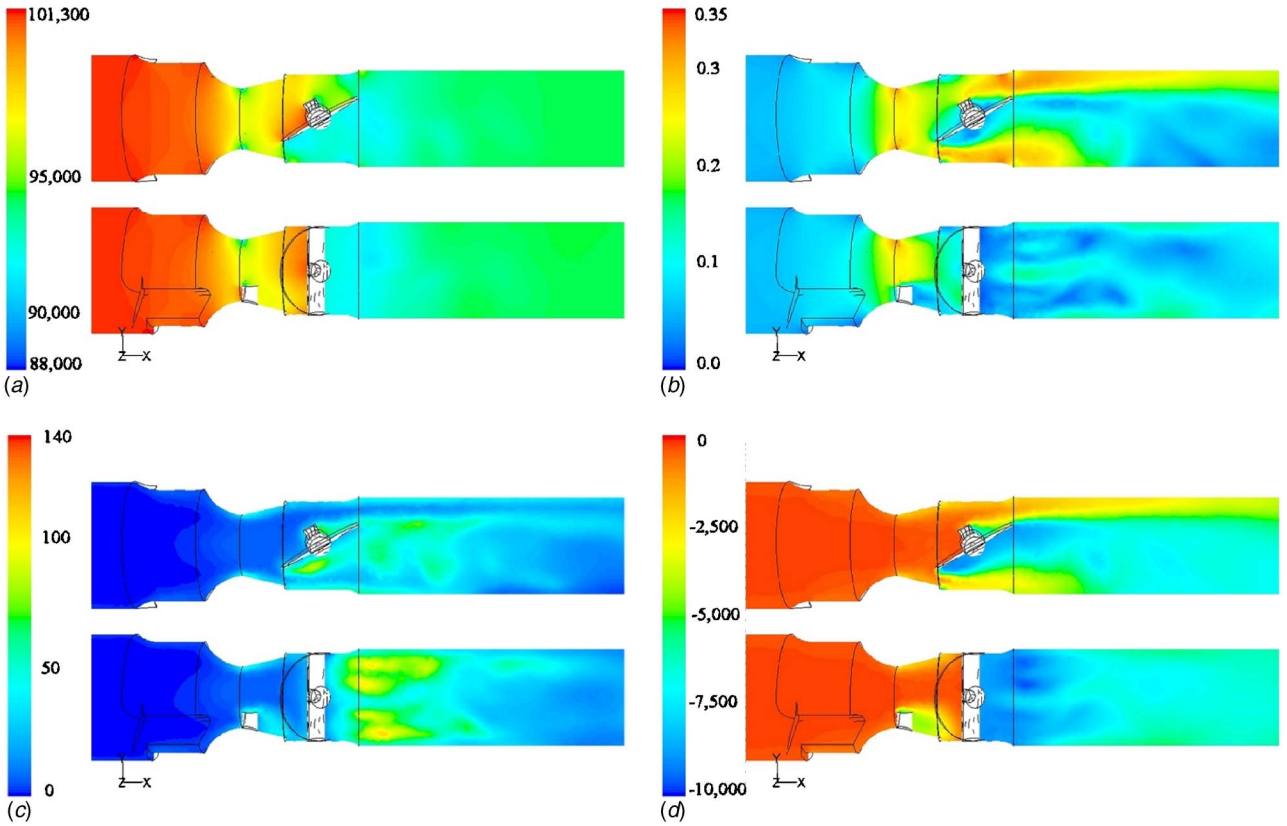

Fig. 10 Steady airflow across carburetor venturi with fuel tube, inlet obstacles, and throttle plate at 60 deg: (*a*) static pressure (in Pascal), (*b*) Mach number, (*c*) turbulent kinetic energy (*d*) gage total pressure (in Pascal)

Downloaded 03 Jun 2010 to 171.66.16.156. Redistribution subject to ASME license or copyright; see http://www.asme.org/terms/Terms_Use.cfm

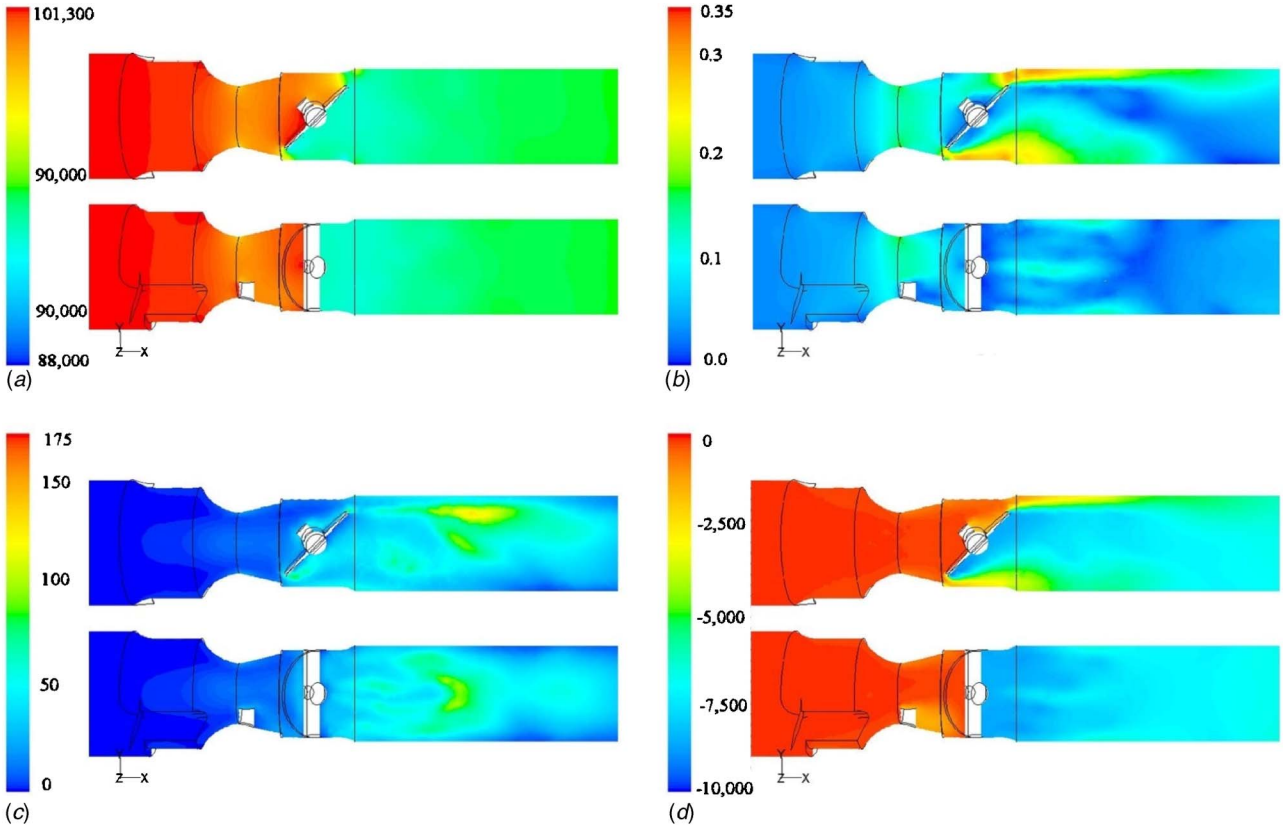

Fig. 11 Steady airflow across carburetor venturi with fuel tube, inlet obstacles, and throttle plate at 45 deg: (*a*) static pressure (in Pascal), (*b*) Mach number, (*c*) turbulent kinetic energy (*d*) gage total pressure (in Pascal)

4 Discussion

4.1 Calculation of the Overall Discharge Coefficient. In addition to the qualitative analysis of the flow fields in the different carburetor venturi configurations, a quantitative comparison was performed by calculating the discharge coefficient from Eqs. (1) and (2). These equations may be regarded as a one-dimensional model of the steady-state compressible flow across a variable-area duct. In an ideal isentropic flow, for a given mass flow rate and inlet conditions, T_0 and P_0, the information about the local area A is enough to solve for the local static pressure. This is the classical behavior of an isentropic converging-diverging nozzle, shown in Fig. 12(*a*) as dotted lines; the total pressure remains constant and the static pressure depends on the local velocity. As the venturi studied has an outlet of different diameter than the inlet, the static pressures are different. The real flow in this venturi is shown as solid lines: friction losses reduce the total pressure as well as the static pressure.

When the different obstacles are considered in the flow, the one-dimensional model may seem too simplistic for all the information seen with the CFD analysis. Figure 12(*b*) shows a one-dimensional representation of the total and static pressure behavior in the carburetor venturi with inlet obstacles, fuel tube, and throttle plate. The total pressure shows a larger decrease after the fuel tube and throttle plate, and it shows a segregation of the flow, i.e., there are regions of different values of total pressure. Finally, the flow reconverges to a one-dimensional model. The same trends are seen in the static pressure. Table 1 shows a summary of the different geometries used in this study and presents the FLUENT results in terms of mass flow rate $\dot{m}$, the overall discharge coefficient C_D, and the localized discharge coefficient calculated at the fuel tube $C_{D,ft}$.

The results of the overall discharge coefficient as a function of

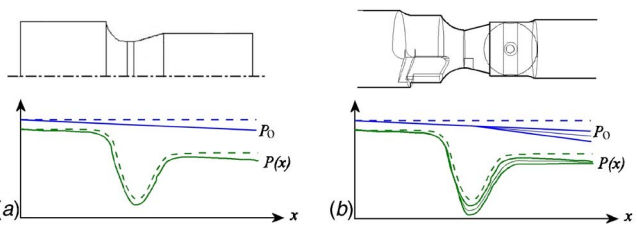

Fig. 12 One-dimensional model of carburetor venturi: (*a*) clear venturi and (*b*) carburetor venturi

Table 1 Effect of carburetor parts on the discharge coefficient

Case	Fuel tube (mm)	Inlet obstacle	Throttle plate (deg)	$\dot{m}$ (kg/s)	C_D	$C_{D,ft}$
1	-	-	-	0.0222	0.630	1.14
2	3 ($1/4D_{throat}$)	-	-	0.0177	0.503	1.03
3	6 ($1/2D_{throat}$)	-	-	0.0169	0.481	1.02
4	-	✓	-	0.0217	0.617	1.08
5	3 ($1/4D_{throat}$)	✓	-	0.0177	0.503	1.05
6	6 ($1/2D_{throat}$)	✓	-	0.0164	0.468	1.03
7	-	-	✓(90)	0.0200	0.569	1.09
8	3 ($1/4D_{throat}$)	-	✓(90)	0.0179	0.509	0.99
9	6 ($1/2D_{throat}$)	-	✓(90)	0.0167	0.474	1.06
10	-	✓	✓(90)	0.0192	0.547	1.09
11	3 ($1/4D_{throat}$)	✓	✓(90)	0.0178	0.505	1.00
12	6 ($1/2D_{throat}$)	✓	✓(90)	0.0166	0.473	1.00
13	3 ($1/4D_{throat}$)	✓	✓(75)	0.0163	0.463	0.98
14	3 ($1/4D_{throat}$)	✓	✓(60)	0.0119	0.339	0.97
15	6 ($1/2D_{throat}$)	✓	✓(45)	0.0066	0.189	0.96

Downloaded 03 Jun 2010 to 171.66.16.156. Redistribution subject to ASME license or copyright; see http://www.asme.org/terms/Terms_Use.cfm

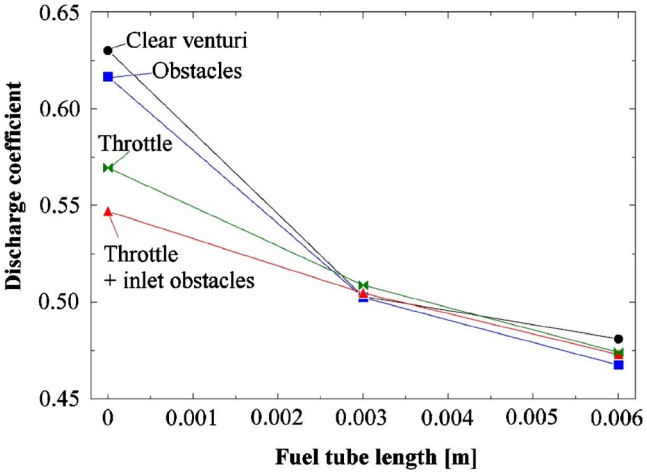

Fig. 13 Effect of carburetor parts on the discharge coefficient of the carburetor venturi

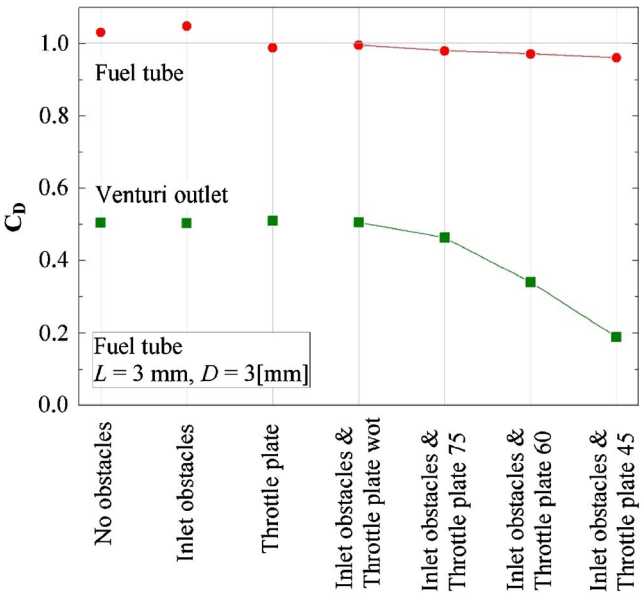

Fig. 14 Discharge coefficients

fuel tube length are plotted in Fig. 13. The results of those cases in which the inlet obstacles are present, but there is no fuel tube (fuel tube length equal to zero) show that the inlet obstacles reduce the discharge coefficient a small amount. The throttle plate, when it is wide open, is responsible for a larger decrease in the discharge coefficient. The largest effect on the discharge coefficient is created by the fuel tube. In addition, when the fuel tube is 3 mm long, the discharge coefficient is the same for all of the different geometries. Furthermore, when the length of the fuel tube length is doubled, the discharge coefficient is further reduced and gives the same value among the different geometries.

This quantitative assessment of the discharge coefficient is in agreement with the qualitative description of the flow inside the carburetor venturi. The pressure losses in the venturi without obstacles are due to the free shear generated at the jet leaving the venturi throat. The presence of the intake obstacles create a very small effect on the discharge coefficient because they affect the flow in the region of favorable pressure gradient. The fuel tube and throttle plate are the most important elements affecting the flow: the wake created by these elements is responsible for the generated turbulence and the corresponding pressure losses.

4.2 Calculation of a Localized Discharge Coefficient. In addition to getting the information about the overall discharge coefficient to correct the mass flow rate across the carburetor venturi given a pressure drop, it is possible to calculate a local discharge coefficient that may be used to get the static pressure at a particular location in the carburetor venturi. For example, it is of great interest to use the information from the CFD simulations to set the appropriate boundary condition at the tip of the fuel tube in a fuel flow network. The discharge coefficient at the tip of the fuel tube $C_{D,ft}$ was calculated using the average static pressure at the tip of the fuel tube and the mass flow rate. This discharge coefficient was calculated based on the actual cross-sectional area at the venturi throat A_{vt}. The last column in Table 1 shows the results for all of the different geometries studied. It can be seen that $C_{D,ft} \approx 1$. This result indicates that the assumption of isentropic flow is valid for the converging side of the carburetor venturi.

Figure 14 shows the overall discharge coefficient for the different geometries that had a fuel tube 3 mm long. It shows the strong relationship between the overall discharge coefficient and the throttle plate angle. However, the discharge coefficient calculated for correcting the static pressure at the tip of the fuel tube remains almost constant and equal to 1, even in these cases. Therefore, the information required to model the actual static pressure in the tip of the fuel tube is only the actual cross-sectional area at the venturi throat. Once the mass flow rate is corrected using the overall C_D, Eqs. (1) and (2) can be used with the actual throat area and $C_{D,ft} \approx 1$ to calculate the static pressure on top of the fuel tube.

5 Conclusions

The key findings of this study can be summarized as follows:

- Obstacles located in the converging zone of the venturi do not create a noticeable effect on the flow field because the favorable pressure gradient prevents separation and wall shear stress does not significantly determine the flow in the nozzle.
- The pressure loss in a venturi without objects in the throat or expansion zone is due primarily to the separation of flow from the wall during the expansion. The dissipation of flow energy in the free shear zone of the resulting turbulent jet causes the reduction in total pressure.
- Obstacles in the throat and diffuser, such as the fuel tube and throttle plate, create wakes and are responsible for most of the pressure losses in a venturi with complex geometries.
- Significantly, once the mass flow rate is corrected using an overall discharge coefficient, the knowledge of the actual cross-sectional area at the venturi throat is enough to calculate the static pressure at the tip of the fuel tube.

The results of these simulations indicate that CFD simulations can be used to understand the nature of the flow field in venturis of complex geometry and to find quantitative information that can be used as boundary conditions for additional systems coupled to the venturi. Future work should focus on the analysis of the static pressure at different inlet obstacles, as well as next to the throttle plate, in order to improve on the design of flow systems incorporating complex venturis.

Acknowledgment

The authors would like to acknowledge the support provided by the Wisconsin Small Engine Consortium.

Nomenclature

A = cross sectional area (m^2)
C_D = discharge coefficient
D = diameter (m)
f = friction factor

Downloaded 03 Jun 2010 to 171.66.16.156. Redistribution subject to ASME license or copyright; see http://www.asme.org/terms/Terms_Use.cfm

g = gravitational constant (m/s^2)
h = height (m)
k = parameter for sensitivity analysis
k_m = pressure loss coefficient
L = pipe length (m)
$\dot{m}$ = mass flow rate (kg/s)
P = pressure (N/m^2)
v = average velocity (m/s)

References

[1] Heywood, J., 1988, *Internal Combustion Engine Fundamentals*, McGraw-Hill, New York.
[2] Fluent, 1999, *FLUENT 6.2 User's Guide*, Fluent, Inc., Lebanon, NH.
[3] Cornelius, K. C., and Srinivas, K., 2004, "Isentropic Compressible Flow for Non-Ideal Gas Models for a Venturi," ASME J. Fluids Eng., **126**(2), pp. 238–244.
[4] Harrington, D. L., and Bolt, J. A., 1970, "Analysis and Digital Simulation of Carburetor Metering," SAE Technical Report No. 700082.
[5] Pursifull, R., Kotwicki, A. J., and Hong, S., 2000, "Throttle Flow Characterization," SAE Technical Report No. 2000-01-0571.
[6] Woods, W. A., and Goh, G. K., 1979, "Compressible Flow Through a Butterfly Throttle Valve in a Pipe," Proc. Inst. Mech. Eng., **193**, pp. 237–244.
[7] Winterbone, D. E., and Pearson, R. J., 1999, *Design Techniques for Engine Manifolds*, SAE International, Warrendale, PA.
[8] Benson, R. S., Baruah, P. C., and Sierens, R., 1974, "Steady and Non-Steady Flow in a Simple Carburettor," Proc. Inst. Mech. Eng., **188**(53), pp. 537–548.
[9] Zhu, Y., and Reitz, R. D., 1999, "A 1-D Gas Dynamics Code for Subsonic and Supersonic Flows Applied to Predict EGR Levels in a Heavy-Duty Diesel Engine," Int. J. Veh. Des., **22**(3), pp. 227–252.
[10] Bajema, D. L., and Gatecliff, G. L., 1978, "Prediction and Measurement of Fluid Flow in Single Cylinder Engine Carburetors," SAE Technical Report No. 780285.
[11] Gamma Technologies, 2001, *GT-Power: User's Manual and Tutorial*, Gamma Technologies, Westmont, IL.
[12] Ricardo Software, 2006, Wave, http://www.ricardo.com/wave
[13] AVL, 2006, Boost, http://www.avl.com
[14] Sanatian, R., and Moss, J. B., 1989, "Computer Simulation of Induction Flows in Spark Ignition Engines," *Proc. of the International Centre for Heat and Mass Transfer*, Hemisphere Publ. Corp, Dubrovnik, Croatia, pp. 275–289.
[15] Tekriwal, P. K., 1996, "Pressure Drop Calculations and Measurements in Converging-Diverging Nozzles," Technical Information Series 96CRD157, GE Research & Development Center.
[16] Guessous, L., 2003, "Theaching CFD: Combining Experiments and Practical Projects With Numerical Simulations," *Proceedings of the ASME FEDSM'03*, ASME, New York, pp. 999–1004.
[17] Sera, M. A., Bakar, R. A., and Leong, S. K., 2003, "CNG Engine Performance Improvement Strategy Through Advanced Intake System," SAE Technical Report No. 2003-01-1937.
[18] von Lavante, E., Zachcial, A., Nath, B., and Dietrich, H., 2000, "Numerical and Experimental Investigation of Unsteady Effects in Critical Venturi Nozzles," Flow Meas. Instrum., **11**(4), pp. 257–264.
[19] Alsemgeest, R., Shaw, C. T., Richardson, S. H., and S., P., 2000, "Modeling the Time-Dependent Flow Through a Throttle Valve," SAE Technical Report No. 2000-01-0659.
[20] Wu, B., Feng, Y., and Liu, J., 1997, "Numerical Simulation of Gas-Liquid Two-Phase Flow in Motorcycle Carburetor," *Proceedings of the International Symposium on Multiphase Flow*, ISMF, Beijing, China, pp. 271–275.
[21] Roache, P. J., 1994, "Perspective: A Method for Uniform Reporting of Grid Refinement Studies," ASME J. Fluids Eng., **116**(3), pp. 405–413.
[22] Celik, I., and Karatekin, O., 1997, "Numerical Experiments on Application of Richardson Extrapolation With Nonuniform Grids," ASME J. Fluids Eng., **119**(3), pp. 584–590.
[23] Hinze, J. O., 1975, *Turbulence*, McGraw-Hill, New York.

Downloaded 03 Jun 2010 to 171.66.16.156. Redistribution subject to ASME license or copyright; see http://www.asme.org/terms/Terms_Use.cfm

An Experimental Investigation of the Separation Points on a Circular Rotating Cylinder in Cross Flow

L. Labraga
G. Kahissim
L. Keirsbulck
F. Beaubert

Laboratoire de Mécanique des Fluides
et d'Energétique,
Université de Valenciennes,
59304 Valenciennes, France

The flow past a rotating cylinder placed within a uniform stream is investigated at Reynolds numbers ranging from 8500 to 17,000 to 34,000. The dimensionless rotation rate α (ratio of the cylinder peripheral speed to the free-stream velocity) varies from 0 to 7. The experimental investigation is based on laser-Doppler anemometry measurements and particle-image velocimetry (PIV) within a water channel. The analysis of the experimental results mainly concerns the location of the separation points as defined by various criteria. It is found that the criterion suggested by Moore, Rott and Sears (MRS) is met in the case of the downstream-moving walls. Moreover, this study shows that sufficient information was obtained to confirm that the MRS criterion is still valid even in the case of the upstream-moving walls. This is confirmed by the behavior of the vertical velocity component educed from the averaged two-dimensional flow field obtained by PIV measurements. [DOI: 10.1115/1.2746894]

Introduction

In addition to its academic interest, the flow around a rotating cylinder also has applications in flow control. Tokumaru and Dimotakis [1] showed that the addition of forced rotary oscillations to the steady rotation of the cylinder not only helped increase the lift coefficient but also produced significant reduction in drag on the cylinder. The rotation of the cylinder, spinning at a constant rate in a viscous uniform flow, is expected to modify the flow field and vortex shedding, with significant consequences as regards the wake modification, the flow-induced vibration, and the lift force. Modi et al. [2] showed that a rotating cylinder placed at appropriate locations in the flow may be used to control flow past airfoils, resulting in a significant increase in the lift. One of the characteristic features of such flows is the separation phenomenon. It should be mentioned that separation is defined here as the phenomenon of large-scale breaking away of fluid from the wall, which marks the boundary-layer approximation breakdown and the wake initiation. The location of actual separation has a drastic effect on control forces generated by aerodynamic surfaces, loads carried by aerodynamic structures, and control phenomena such as stall flutter of an airfoil or the rotating stall of current flow compressors.

It has long been recognized that the standard criterion for flow separation $\partial u_\theta/\partial r=0$ at the wall is inadequate for cases other than steady flows over fixed walls (where u_θ is a tangential velocity and (r,θ) are the polar coordinates taken with the origin at the center of the cylinder, see Fig. 1). For the case of steady flows over moving walls, Moore [3], Rott [4], and Sears [5] proposed a more appropriate criterion: $\partial u_\theta/\partial r=0$ and $u_\theta=0$. This criterion is called the "MRS criterion," according to those authors. The present study was treated separately for the cases of the wall in downstream and upstream motions. In the former case, it was found that vanishing shear occurred at some distance and that separation was characterized by a separated region embedded in the flow. In this instance, separation would not occur at the wall but at a finite height above the wall, and there would be a boundary-layer flow beneath the wake region. In the case of the upstream-moving wall, it was hypothesized that a probable profile at separation was one that flattened against the axis over a relatively large height with a singularity at the foot, i.e., one in which the velocity abruptly changed from zero near the wall to the wall velocity at the wall. Ludwig [6], using hot-wire anemometers, measured the velocity profiles of steady separation on a rotating cylinder for various low α, where α is the ratio of the peripheral velocity to free-stream velocity. He obtained velocity profiles corresponding to those expected by the MRS model. Ludwig [6] found that the position of laminar separation on the downstream-moving wall of the cylinder is linearly dependent on the velocity ratio α.

Koromilas and Telionis [7] obtained streamlines around a rotating cylinder by flow visualization, quite similar near a separation point to those suggested by the MRS model both for the case of upstream- and downstream-moving walls. Tsahalis and Telionis [8] and Telionis and Werle [9] numerically studied the problem of steady separating flows over a downstream-moving wall. In these references, it was shown that a separation singularity appears at the MRS point instead of at the point of zero skin friction. Peller [10] confirmed the location of the separation points on downstream-moving walls by the MRS criterion by using laser-Doppler velocimetry, and he showed that the position of the separation point on the downstream-moving wall of the cylinder is linearly dependent on the velocity ratio α, as predicted by Ludwig [6]. Recently, Labraga et al. [11] showed that the displacement of the separation points on the downstream-moving wall of the cylinder is linearly dependent on α, for $\alpha \leqslant 1.5$, and that the Reynolds number has but little influence on the location of the downstream separation point.

For the case of upstream-moving walls, the peripheral velocity component is negative near the wall and positive in the upper part of the boundary layer; therefore, special techniques are required in order to obtain a numerical solution. Ludwig [6] noticed that for an upstream-moving wall, the boundary layer starts to thicken rapidly at a considerable distance upstream of the separation, leading to a difficult experimental separation point determination. The numerical study of Chew et al. [12] demonstrates that both the separation points move along the anticlockwise rotational direction with increasing α and that the separation point motion rate on

Contributed by the Fluids Engineering Division of ASME for publication in the JOURNAL OF FLUIDS ENGINEERING. Manuscript received June 30, 2005; final manuscript received March 5, 2007. Review conducted by Joseph Katz.

 Copyright © 2007 by ASME

Downloaded 03 Jun 2010 to 171.66.16.156. Redistribution subject to ASME license or copyright; see http://www.asme.org/terms/Terms_Use.cfm

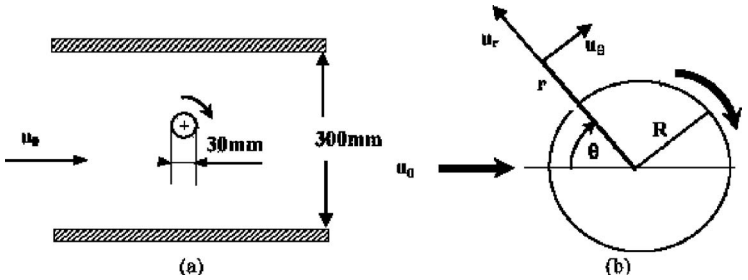

Fig. 1 Sketch of the cylinder in (*a*) the test section (*b*) and the coordinate system

the lower side of the cylinder is higher. Inoue [13] numerically studied steady laminar boundary-layer flows over moving walls, with special regard to the MRS criterion for flow separation. He found that the MRS criterion is not met in the case of upstream-moving walls. He maintained that the MRS criterion is not met in the case of upstream-moving walls, although it is met in the case of downstream-moving walls. Peller [10] found that the MRS criterion for the flow behavior around the upstream-moving wall of the cylinder could not be confirmed. He concluded that the estimation of the separation point location could be achieved only by a simultaneous observation of the velocity profiles, the rms values of the fluctuating velocity, and, above all, the boundary-layer thickness.

Tsahalis [14] numerically investigated the laminar boundary layer and separation for a steady inviscid flow. He found that the MRS separation criterion, in the case of a steady flow over an upstream-moving wall, is valid and in agreement with Ludwig's [6] experimental results. The variation of the Strouhal number for vortex shedding, with rotational rate, is another point of disagreement among the various results found in literature. The results of Chew et al. [12] and Diaz et al. [15] show that the Strouhal number increases with α. However, Hu et al. [16] and Kang et al. [17] reported that the Strouhal number steadily decreases with α. The vorticity field is closely linked to vortex shedding. Therefore, some authors also investigated the changes in the surface vorticity distribution at different cylinder spin rates. Kang et al. [17] found that while vortex shedding exists, the vorticity contours away from the cylinder surface are similar in overall shape, which indicates that the rotational effect is confined to the flow in the vicinity of the cylinder surface. They showed that for $\alpha \geqslant 1$, the negative isovorticity lines in front of the cylinder make up an acute curved tail that grows around the cylinder in the rotational direction with increasing α.

This paper shows that accurate experimental techniques capable of locating both the upper and lower separation points and of finding out the effects of the rotation of the cylinder on vortex shedding are much needed. The present study contributes to a better knowledge of the location of the separation points on the upstream-moving wall. Indeed, results found by previous researchers on this topic are still a matter of controversy. Moreover, this paper sheds some light onto the underlying mechanism of vortex shedding around a rotating cylinder at high Reynolds numbers and rotational rates. One of the aims of this study is to confirm the MRS criterion on the downstream-moving wall and to estimate the location of the separation point on the upstream-moving wall on a rotating cylinder placed in a uniform stream. This was made possible by the local and high-resolution measurements provided by the laser-Doppler anemometry (LDA) system and by a fine analysis of the flow field measured with the particle-image velocimetry (PIV) technique. The location of the separation point was investigated by a combined inspection of the radial and the tangential velocity profiles. This study examines the influence both of the rotational rate and of the Reynolds number on the flow field.

Experimental Apparatus and Procedure

Measurements were performed in a 300×300 mm^2 water channel. The free-stream turbulence intensity was less than 2%. The 30 mm diameter rotatable cylinder is mounted horizontally in the center of the test section and spans over its overall height. The cylinder was supported by bearings attached to the channel walls, with one end of the cylinder protruding through the tunnel wall and connected to a dc motor via a belt so that it could be rotated gradually up to 1200 rpm. A schematic view of the cylinder in the test section and the coordinate system are shown in Fig. 1.

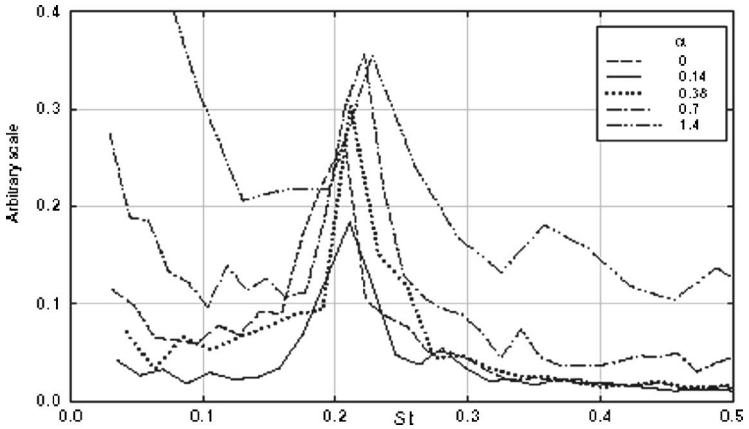

Fig. 2 Power spectra of the tangential velocity fluctuations for different α

Downloaded 03 Jun 2010 to 171.66.16.156. Redistribution subject to ASME license or copyright; see http://www.asme.org/terms/Terms_Use.cfm

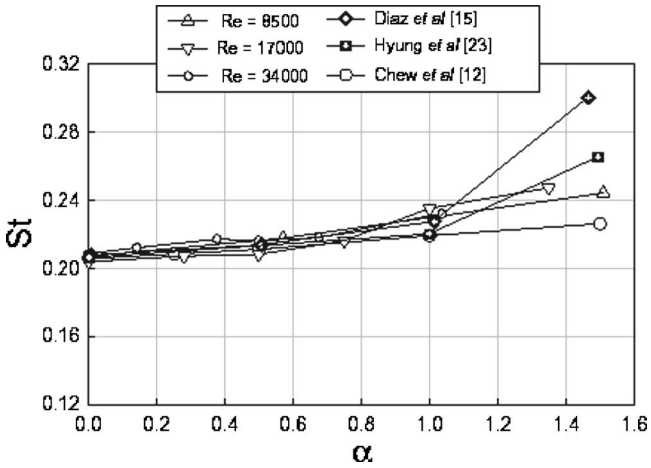

Fig. 3 Variation of the Strouhal number with α

The adjustable cylinder rotational speed was controlled using a stroboscope to within 1%. The free-stream velocities must be corrected for blockage effects. The velocities are corrected using a correction factor for blockage (C_b) according to the formula $U_c = U_0 C_b$. The correction factor for blockage is estimated from the experimental study of Oosthuizen and Madan et al. [18], who used the following formula $U_c/U_0 = [1+1.18(D/B)^2]^3$, where D is the cylinder diameter and B the tunnel width. In the present study, the correction factor for blockage C_b is estimated around 3.58%. The good agreement with results obtained from experiments conducted under different conditions (Morgan [19]) indicates that the blockage ratio ($D/B=0.1$) used in our test only minimally affects the boundary-layer development around the cylinder. Three-dimensional (3D) effects were not observed around the cylinder principally due to the low Reynolds number used. Corresponding measurements of local velocities showed that, especially in the middle part of the cylinder, two-dimensional (2D) flow conditions could be simulated with sufficient accuracy. The 2D flow assumption is therefore applicable to a reasonable degree of accuracy, at least for most of the cylinder central portion.

The tangential velocity was measured by using a laser Doppler anemometer. A standard 4 W argon-ion laser was connected to a multicolored beam separator, which split up the incoming light into two beams. A Bragg cell dynamically shifts the frequency, leading to an offset in the measured Doppler shift. Thus, both the value and the direction for the velocity component may be accurately determined. Couplers directed each beam to the laser probe via a fiber optic cable. The flow was seeded with Iriodin particles suitable for measurements in liquids. They have a narrow particle size distribution with a mean of 1.5 μm diameter. The laser probe operating in the backscatter mode contained receiving optics that directed the reflected light of particles to the photomultipliers in the receiver. A 120 mm focal length lens was used, resulting in an effective measuring $0.05\times0.05\times0.32$ mm^3 volume. Analog Doppler bursts were then sent to the digital burst correlator TSI-IFA 750. Digitized data were transferred via a direct memory access cable to a personal computer. The velocity data were resampled at equidistant time intervals by using a first order interpolation in order to reduce bias in spectral estimates from randomly sampled

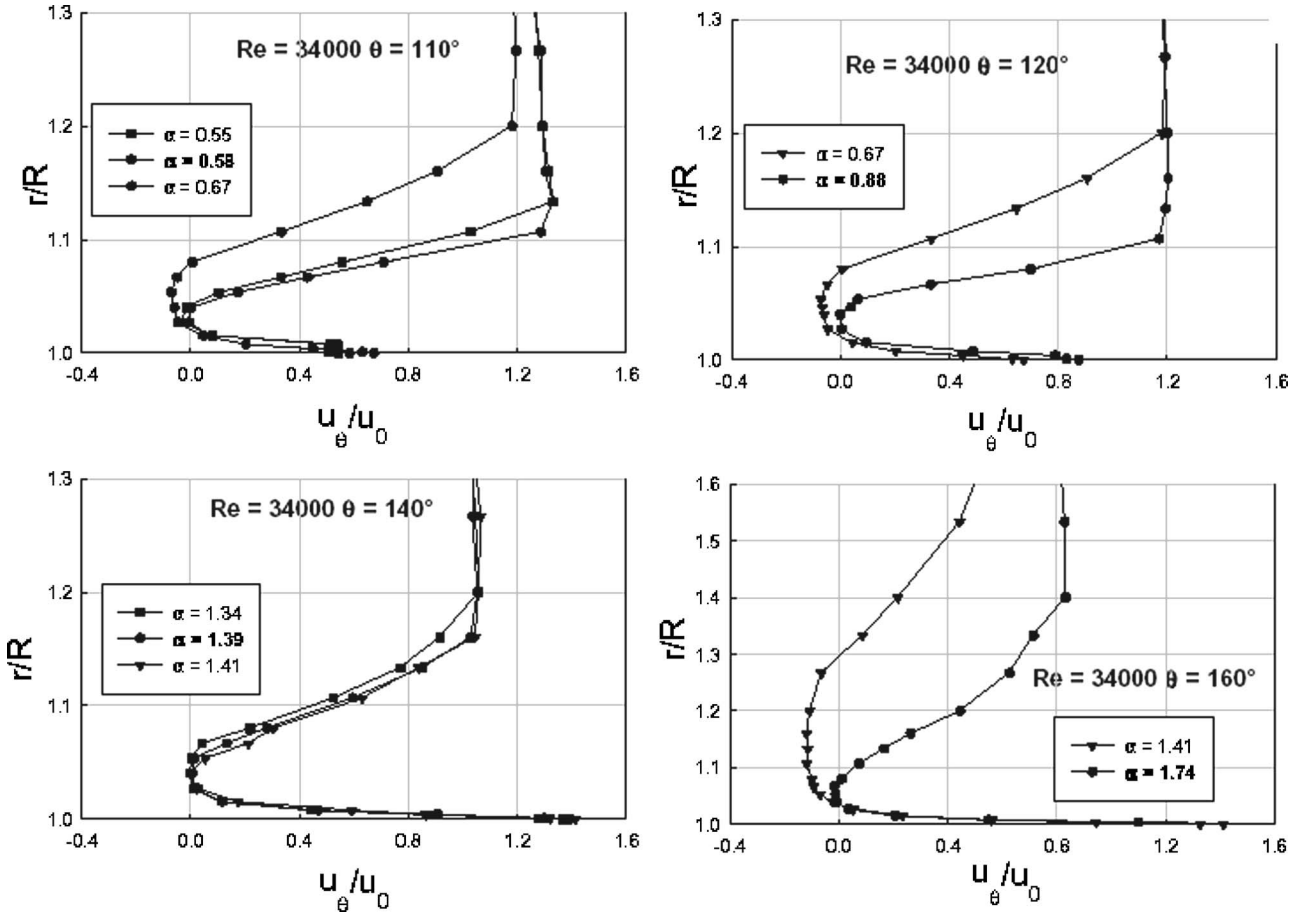

Fig. 4 Measured velocity profiles by LDA around the separation point for a downstream-moving wall at Re=34,000 (uncertainty in u_θ/u_0: ±2%)

Downloaded 03 Jun 2010 to 171.66.16.156. Redistribution subject to ASME license or copyright; see http://www.asme.org/terms/Terms_Use.cfm

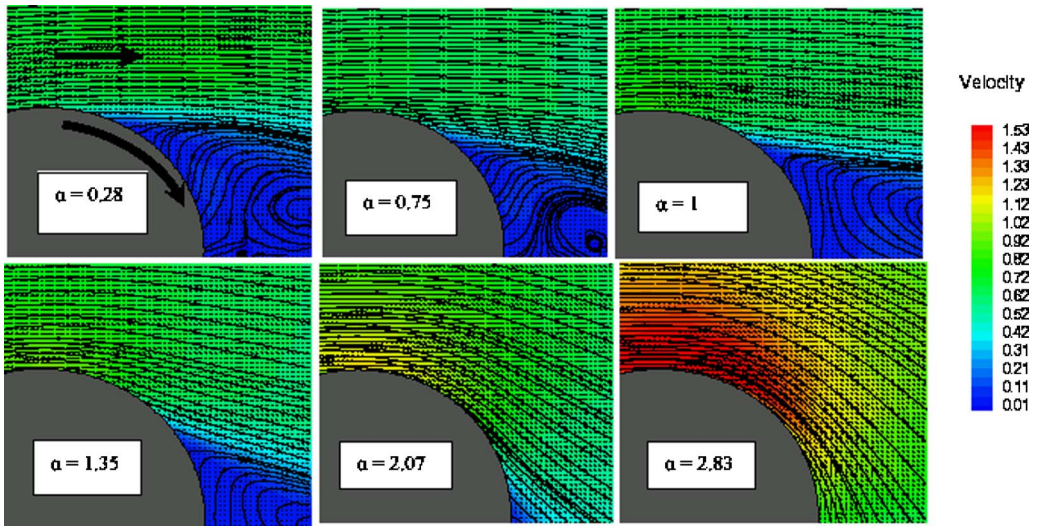

Fig. 5 Mean flow field (downstream-moving wall) for Re=17,000 (velocity (m/s))

data. The mean velocity was determined by averaging 50,000 data points particularly for the spectral analysis. The random sampling rate varied from 200 s^{-1} near the wall to about 3000 s^{-1} at a distance far from the wall for Re=17,000.

A three-axis traversing device was used to position the LDA probe with 0.01 mm increments for each axis. The uncertainty in the data on the LDA was calculated using estimates of bias and precision errors in the experiments. The bias estimates were based on the geometrical position of points, refraction window index, seeding etc. The total bias and precision were combined to give an estimate of the total uncertainty of the tangential velocity component of ±0.02 m/s for the highest Reynolds number.

The PIV, a quantitative flow visualization technique, was used to determine the instantaneous velocity flow fields by recording and processing the multiple exposed particle-image pattern of small traces suspended within the fluid. The flow was seeded by the same Iriodin particles used for LDA measurements. The PIV image is first obtained by illuminating the seeded flow field with a thin laser sheet. The light scattered by the seed particles generates a particle-image pattern. This pattern is recorded using a digital charge-coupled device (CCD) video technique. The local fluid velocity is then obtained using digital signal processing techniques. The PIV system is based on a TSI PowerView system, including a 200 mJ dual yttrium aluminum garnet (YAG) laser (Spectra Physics), a light arm, a PIVCAM 10-30 high-resolution cross correlation camera (1000×1000 resolution), and a SYNCHRONIZER and "INSIGHT" windows NT-based software for acquisition, processing, and postprocessing.

Experimental Uncertainties

PIV Accuracy. Prasad et al. [20] showed that when particle images are well resolved during digitization (i.e., the ratio of particle-image diameter d_{par} to the size of a CCD pixel on the photograph d_{par} is $d_{par}/d_{pix}>3-4$), the uncertainty of the measurements is roughly one-tenth to one-twentieth of the particle-image diameter. By zooming in the PIV image using the PHOTOSHOP software, the number of pixels for each particle image appearing in the PIV image can be counted. Thus, about three pixels on average for each particle image were yielded for the present measurement. This indicates that the particle images were adequately resolved for the present experiment. During the experiment, we judged the PIV image to be adequate based on a particle displacement of about eight pixels (corresponding to 0.25% of interrogation window) on average by inspecting the same particle in the double images. Normalizing the uncertainty of measure-

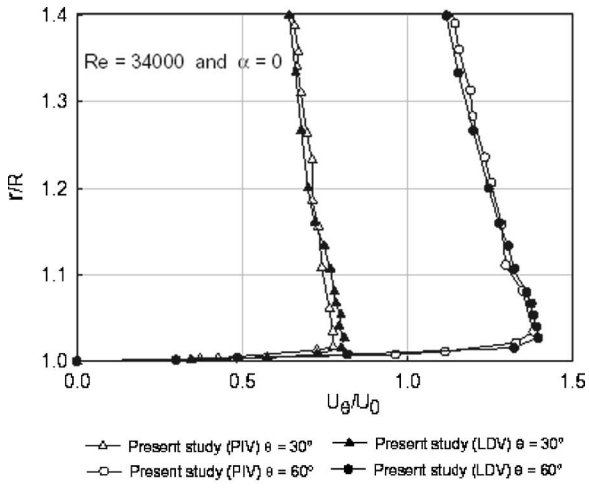

(*a*)

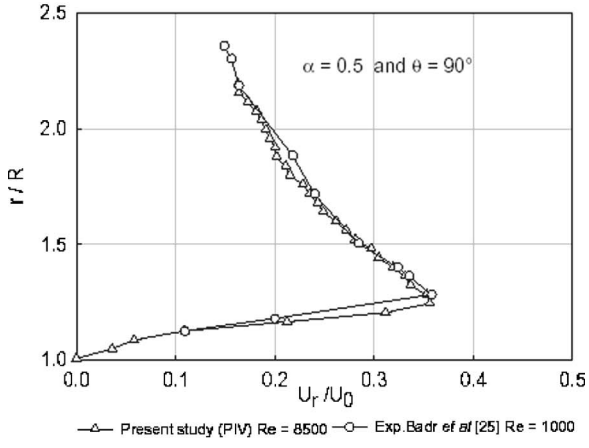

(*b*)

Fig. 6 (*a*) Tangential velocity for α=0, θ=30°, and θ=60° (uncertainty in u_θ/u_0 estimated at about ±2%). (*b*) Radial velocity for α=0.5 at θ=90° (uncertainty in u_r/u_0 estimated at about ±2%).

Downloaded 03 Jun 2010 to 171.66.16.156. Redistribution subject to ASME license or copyright; see http://www.asme.org/terms/Terms_Use.cfm

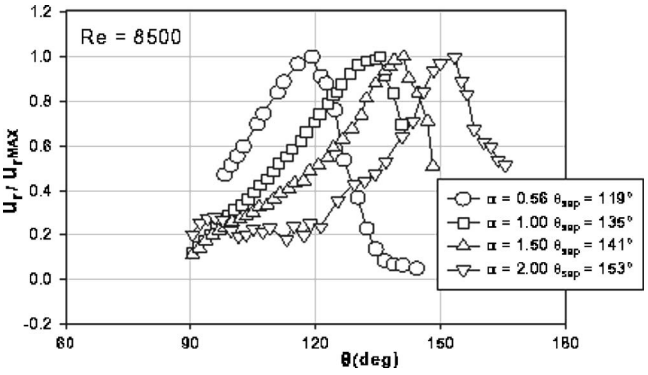

Fig. 7 Radial velocity component nondimensionalized with respect to the maximum value

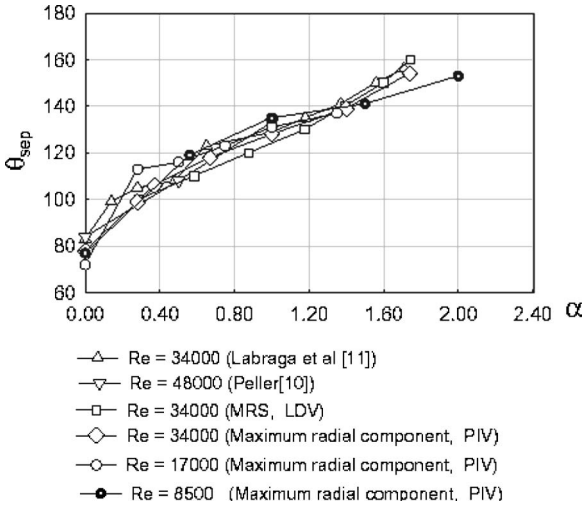

Fig. 8 Evolution of the separation point with α for different Re

ment with this mean displacement of particles yields a relative error of less than 1.2% (Adrian et al. [21]).

Results

Strouhal Number. The power spectra of the velocity fluctuations at $\theta=300°$ and at a distance from the wall of about 10 mm are computed for different α values. The shedding frequency f is displayed in Fig. 2 as a dimensionless parameter, the Strouhal number $St=fd/u_0$.

The variation of St with α is given in Fig. 3.

The uncertainties in St and α are, respectively, ±5% and ±1%. For $\alpha=0$, St is in good agreement with the well-known St ≈ 0.21 value. As the cylinder rotational rate increases, Fig. 3 shows that the dominant shedding frequency is shifted to higher values. However, it should be emphasized that no clearly definable St exists when $\alpha>1.5$. This reflects the fact that the wake becomes diffuse and randomized, and a pronounced frequency peak is not discernible in the power spectra. All the earlier experimental studies report a similar trend. For the case of an impulsively translating and rotating cylinder, Coutanceau and Menard [22] noted that as α increases, the shedding of the eddies behind the cylinder tends to accelerate. However, for $\alpha>2$, the frequency peak itself becomes less distinctly identifiable. Results of Diaz et al. [15] for Re=9000, of Hyung et al. [23] for Re=900, and of Chew et al. for Re=1000 are reported in Fig. 3 and show an increase in the Strouhal number with the rotational rate. Diaz et al. [15] found that for α greater than 1.0, a specific Strouhal number cannot be defined since the shedding process then becomes rapidly more random and no definite shedding frequency can be inferred from the autospectral results.

The present results are in good agreement with those numerically found by Chew et al. [12], who found that the Strouhal number increases with increasing α up to $\alpha=2$. They argued that the increase in St with increasing α can be explained by the closer interaction between the two separated shear layers. The closer interaction of the two shear layers results in early roll-up and shedding of vortices. However, except for the results of Chew et al. [12], the computational studies show a decrease or a weak dependence in the Strouhal number with increasing α. Mittal and Kumar [24] studied the effect of the cylinder rotation on vortex shedding via 2D computations based on a stabilized finite element method (FEM) used to solve the Navier-Stokes equations in the primitive variable formulation for Re=200 and found that for $\alpha<1.9$, the Strouhal number decreases as α increases. It appears that the experiments and computations show an opposite trend in the behavior of the Strouhal number as a function of α. Mittal and Kumar [24] suggested that this difference may be related to the interaction between the vortex-shedding and centrifugal instabilities that might exist for such flows. They added that it would be interesting to carry out 3D computations for this flow.

Separation on the Downstream-Moving Wall. Typical boundary-layer profiles obtained on the downstream-moving wall for Re=34,000 are shown in Fig. 4. A characteristic feature of the flow around a rotating cylinder is the asymmetric shape of the

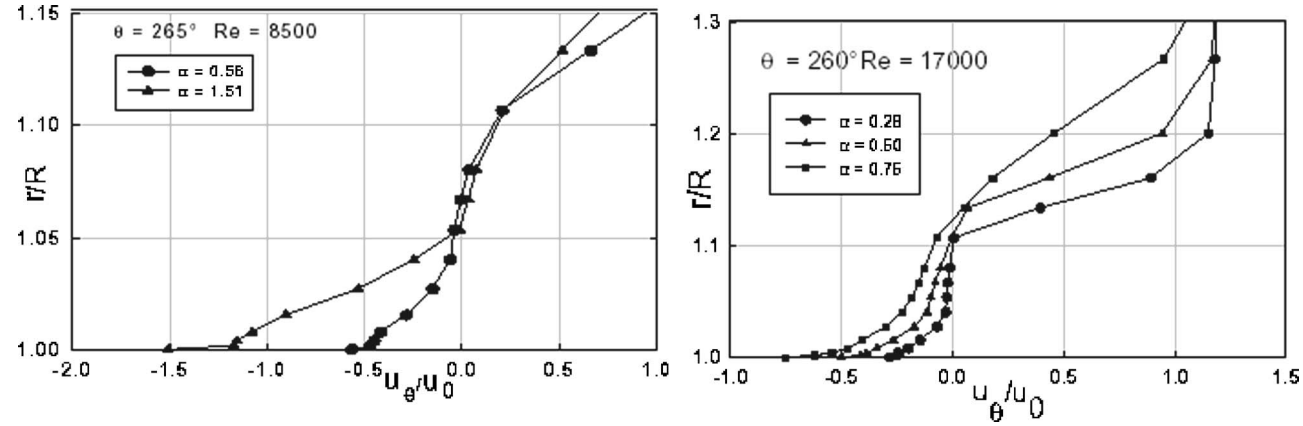

Fig. 9 LDA measurements of velocity profiles around the separation point for an upstream-moving wall (uncertainty in u_θ/u_0: ±2%)

Downloaded 03 Jun 2010 to 171.66.16.156. Redistribution subject to ASME license or copyright; see http://www.asme.org/terms/Terms_Use.cfm

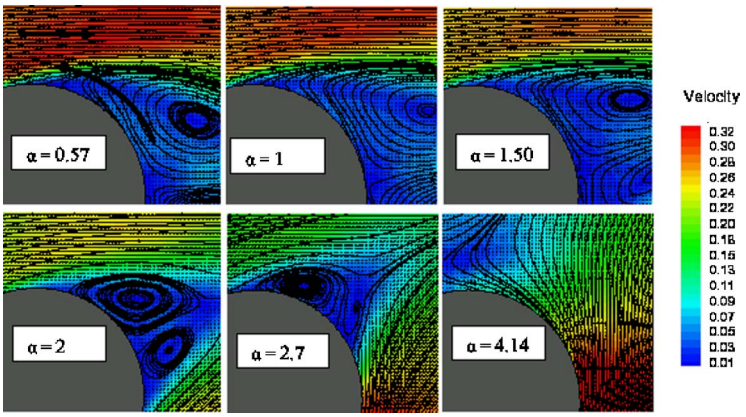

Fig. 10 Patterns of mean streamlines and mean flow for the upstream-moving wall for Re=8500 (velocity (m/s))

velocity profiles that vary according to the values of α. It is seen in Fig. 4 that the position of the separation points on the downstream-moving wall is well defined by the MRS criterion and that it is shifted downstream as α increases. In other words, the separation is delayed (moved downstream) when the wall moves in the direction of the flow. It is shown that the MRS criterion is met at a dimensionless distance from the wall between 0.03 and 0.07 and for θ between 110° and 160°. The same trend, hereby unreported, was observed for Re=8500. Figure 4 shows that the correct location of the separation point was made possible by numerous tests near separation, involving a large range of the cylinder velocity speeds and very small increments in the radial component, for a given angular position.

Figure 5 shows an example of a mean flow field around the rotating cylinder obtained by the PIV technique for Re=17,000 and different values of α. The mean flow field is the time average over up to 500 instantaneous vector maps. Experimental PIV measurements have been carried out on a 32×32 mm^2 field with 32×32 pixel interrogation cell, corresponding to about 1 mm^2 spatial resolution. This figure shows a region where the velocity is large and a region where the velocity takes low values. The velocity decreases and increases on the lower and the upper sides of the cylinder, respectively, because of the clockwise cylinder rotation. On the other hand, the velocities of the fluid relative to the wall increase with increasing α on the lower side of the cylinder, whereas the opposite applies to the upper side. When α is sufficiently high, it is clearly seen that the fluid in a region near the surface is drawn by the cylinder rotation. As α increases, this region becomes larger, and the relative velocities of the fluid near the surface of the wall decrease with increasing α both on the upper and the lower cylinder sides.

Figure 5 qualitatively shows the variation of the mean positions of the separation points. For $\alpha=2.83$, closed streamlines appear in the second quadrant where the separation point completely vanishes. The previous map gives a qualitative behavior of the flow field. It seems interesting to educe the radial velocity component from the PIV results and to examine its distribution. Indeed, Ludwig [6] suggested that "the only reliable experimental indication of separated flow when the wall is moving upstream appears to be in the behavior of the vertical velocity component in the boundary layer." If this criterion is expected to be valid for an upstream-moving wall, a fortiori, it should be valid when the wall moves downstream.

To prove the validity of the present experimental results obtained by the PIV data, some of them are compared with those found by LDA. Figure 6(*a*) shows a good agreement between PIV and LDA data for the tangential velocity component. The radial velocity component of the present study is in good agreement with that found by Badr et al. [25] for $\alpha=0.5$ and $\theta=90°$ (see Fig. 6(*b*)).

The radial velocity component u_r, nondimensionalized with respect to the maximum value, was plotted on Fig. 7 at a fixed distance from the wall as a function of the angular position for different values of α and for Re=8500.

For Re=17,000 and 34,000, the distribution of the radial component exhibits the same trend, with a maximum value reached when the MRS criterion is met. The radial velocity component behavior may be used as a criterion for separation on the upstream-moving wall.

The locations of the separation point are summarized in Fig. 8 as a function of α for different Reynolds numbers. Included in this figure are the results experimentally found by Peller [10] and Labraga et al. [11]. A good agreement between the present results and those of Labraga et al. [11] is observed for $\alpha>1.2$. The experimental results of Peller [10] agree well for a range of α between 0 and 0.5.

Separation on the Upstream-Moving Wall. In Fig. 9, measured velocity profiles at the upstream-moving wall are plotted for Re=8500 and Re=17,000 for different α values. As mentioned above, it is difficult to determine the separation point with the MRS criterion for this case. However, this study shows that the MRS criterion is approximately met for ($\theta=260°$, $\alpha\approx0.3$) and ($\theta=265°$, $\alpha\approx0.6$), respectively, for Re=17,000 and Re=8500.

The point where both the shear and the velocity simultaneously vanish occurs at about 1 mm from the cylinder surface, consistent

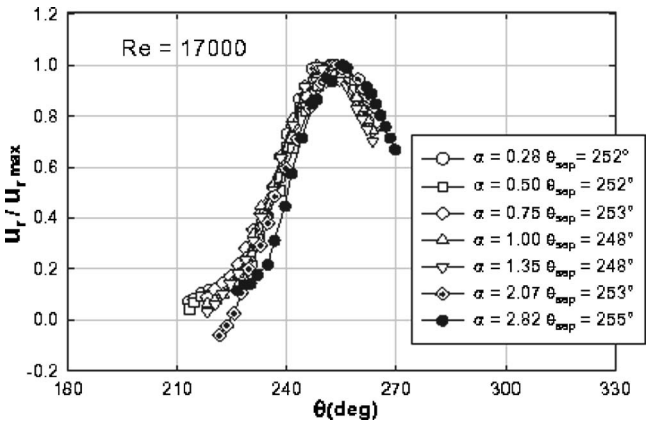

Fig. 11 Radial velocity component nondimensionalized with respect to the maximum value for Re=17,000

Downloaded 03 Jun 2010 to 171.66.16.156. Redistribution subject to ASME license or copyright; see http://www.asme.org/terms/Terms_Use.cfm

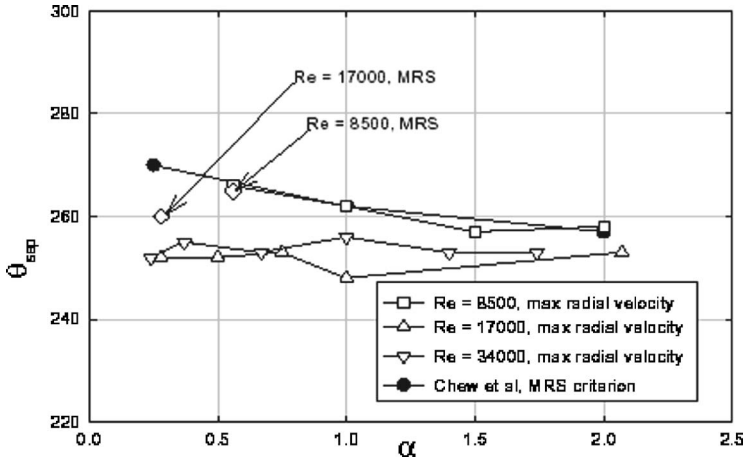

Fig. 12 Position of the separation points on the upstream-moving wall

with the separation on the upstream-moving wall plotted in Fig. 9. An inspection of the separation velocity profiles in Fig. 9 shows that the boundary layer is about 3.5 mm. The vanishing point occurs at approximately 30% of the boundary-layer thickness, being in good agreement with Ludwig's [6] study. Results found by Peller [10] reveal no realistic flow profile with the relationship $u_\theta=0$ and $\partial u_\theta/\partial r=0$. Peller [10] concluded that the separation point could not be determined with this model. Indeed, he used only four values of α between 0 and 2. The fact that the MRS criterion was not met with its data is likely to be due to the lack of α values within this range.

The overall features of the flow field on the upstream-moving wall obtained by the PIV technique is shown in Fig. 10. It is seen that both the separation points move along the anticlockwise direction of rotation with increasing α, with the motion rate of the separation point on the lower side of the cylinder being higher, yielding a narrowing of the wake clearly revealed in this figure.

When the cylinder rotates at low rotational speeds, two vortices are alternately shed on each side of the cylinder, but the vortex-shedding configuration varies according to α. As α increases, the vortex on the upper side of the wake becomes stronger, while that of the lower side becomes weaker. Computational results from Badr et al. [25] and Chew et al. [12] show from the patterns of the instantaneous streamlines for $\alpha=0.5$ at different times the existence of the first vortex and a bulging of streamlines near the right lower side of the cylinder at the beginning of the impulsively started motion. The first vortex grows gradually in the upper wake, while the bulge leads to the formation of the second vortex. This observation is in full agreement with our experimental results. According to the potential flow theory, closed streamlines surrounding the cylinder exist only when $\alpha>2$, where the stagnation point is separated from the cylinder. The same phenomena can be observed in the viscous flow but for different conditions. The present study is in good agreement with that of Labraga et al. [11], who showed that for $\alpha>4$, points of zero shear stress on the rotating cylinder vanish, consistent with the previous arguments that the cylinder is surrounded by a set of closed streamlines. Quantitative information was extracted from the PIV flow field in order to determine the radial velocity component in the same manner as that of the downstream moving wall.

The most striking point arising from Fig. 11 is that the position of the upstream separation point is much less sensitive to the rotational rates than that of the downstream-moving wall. The difference between the minimum and the maximum angular positions is $\Delta\theta=7°$ for Re=8500 and for Re=17,000 and $\Delta\theta=4°$ for Re=34,000. The mean angular position is about 255° for the Reynolds numbers of the present study. The present results are consistent with those found by Ludwig [6]. He found that for α

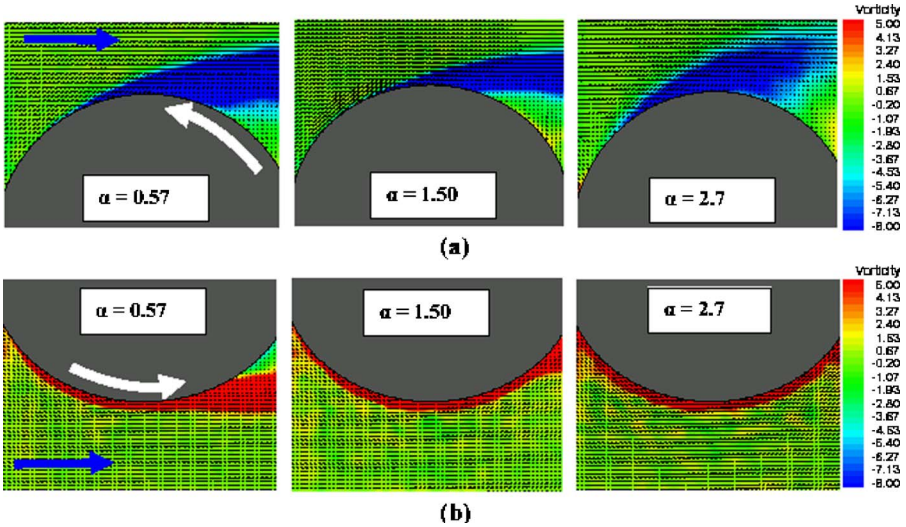

Fig. 13 The vorticity field for Re=8500, (*a*) downstream-moving wall region and (*b*) upstream-moving wall region

Downloaded 03 Jun 2010 to 171.66.16.156. Redistribution subject to ASME license or copyright; see http://www.asme.org/terms/Terms_Use.cfm

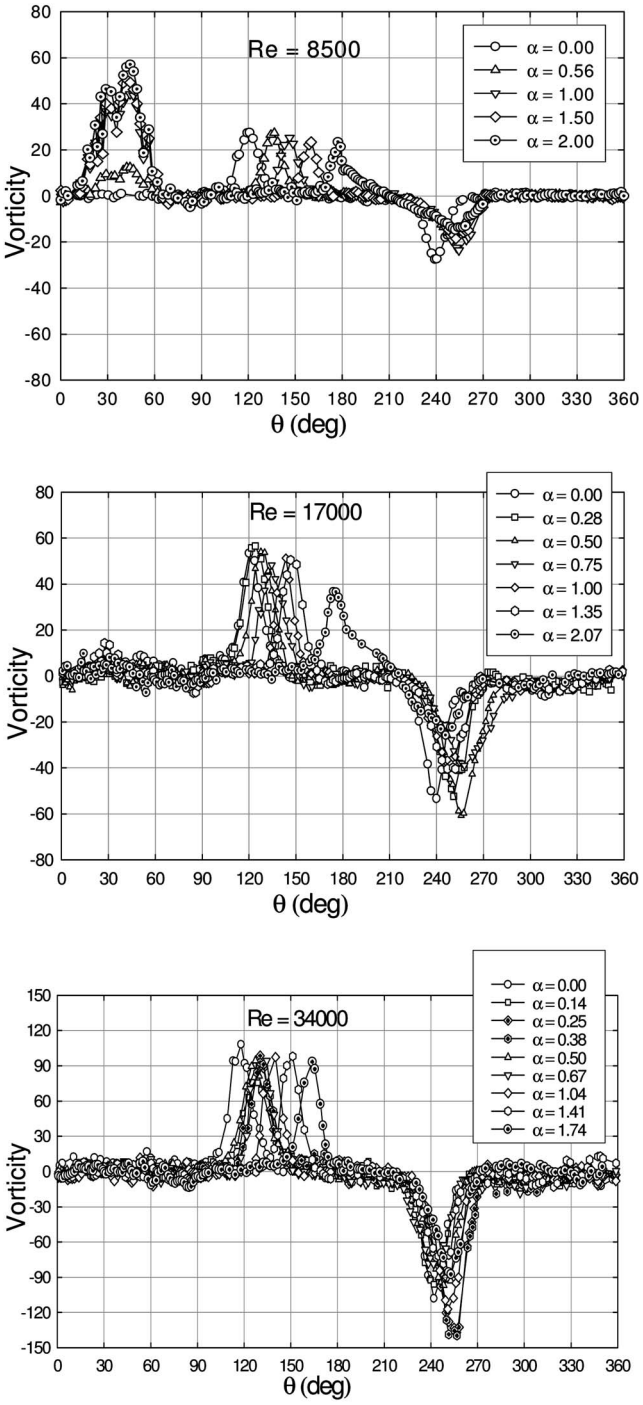

Fig. 14 Variation of mean vorticity (≈4 mm from the surface of the cylinder) at different Reynolds numbers and for various α

$=0.12$, the vertical velocity reaches a peak value for $\theta=250°$. The measurements made at this rotation rate are, according to Ludwig [6], probably not very accurate because of the extremely low velocities and the nearness to the wall at which these velocities were observed. For $\alpha=0.58$, 0.88, and 1.18, he found that the radial velocity is maximum for about $\theta=260°$; beyond this angular position, the flow becomes turbulent.

The locations of the separation points on the upstream-moving wall cylinder are summarized in Fig. 12 as a function of the rotational rate for different Reynolds numbers. Included in this figure are the results of Chew et al. [12], who determined the position of the separation points by the MRS condition and found that the upstream separation point occurs at $\theta\approx262°$ and $\theta\approx257°$, respectively, for $\alpha=1$ and $\alpha=2$.

The results of this work are in good agreement with those found by Chew et al. [12] for Re=17,000 and Re=34,000.

The Vorticity Field Distribution. Figure 13 shows the vorticity field at the upper and lower sides of the rotating cylinder. At low α values, the positive isovorticity field at the downstream-moving wall region is similar to a "plume" that takes place at about $\theta=120°$ and moves in the direction of the rotation as α increases. The positive vorticity peak disappears from this area for $\alpha>2$. At the upper side of the cylinder, a clockwise rotating vortex is shed. However, the negative vorticity forms a quasistationary "tail" at $\theta\approx260°$ and widens in this region as α increases. It seems interesting to analyze locally the vorticity distribution by extracting the results from the PIV data.

Figure 14 shows the mean vorticity profiles at a fixed distance of about 4 mm from the cylinder surface for different Reynolds numbers and rotational rates. As expected, for $\alpha=0$, the mean vorticity exhibits a positive peak value at $\theta\approx120°$ and a negative one at $\theta\approx240°$. Kang et al. [17] found the peaks at $\theta\approx130°$ and $\theta\approx230°$ for Re=100, consistent with the results of Mittal and Kumar [24]. As α increases, the distributions of the vorticity display the same trend for the Reynolds numbers of the present study, with a shifting of the peak of the positive vorticity in the direction of the rotation, consistent with the position of the separation point at the downstream-moving wall.

As the Reynolds number increases, the amplitude of the positive and negative peaks increases. For $\alpha>2.5$, not shown here, the peaks are no longer discernible, which is consistent with vortex shedding. The negative vorticity peak value occurred roughly at the same angular location, thus confirming the radial velocity distribution and the separation point behavior in this region which are consistent with the results of Mittal and Kumar [24]. For Re =8500, a positive peak is observed at $\theta\approx30°$. Mittal and Kumar [24] found that new peaks initiate for $\alpha=1$ at the front stagnation point of the cylinder and that an overall peak is located at $\theta\approx340°$ for $\alpha=2$. The present results disagree with those of Mittal and Kumar [24] and those of Kang et al. [17]. A possible explanation for this disagreement may be attributed to the fact that the vorticity of the present study is taken at a distance from the cylinder surface larger than that used in the theoretical results found at low Reynolds numbers.

Conclusion

The results of our investigations can be summarized as follows.

(i) The dominant vortex shedding frequency shifts to a higher value, as α increases up to a critical value for which the peak frequency becomes less distinctly identifiable.
(ii) The position of the separation points on the downstream-moving wall is well defined by the MRS criterion and moves downstream when the wall moves in the direction of the flow.
(iii) The separation criterion on the upstream-moving wall was found to be the same as that for a downstream-moving wall. The radial velocity behavior proves to be a satisfactory criterion to determine the location of both the separation points on the downstream and the upstream-moving walls.
(iv) This paper shows that the position of the separation point on the upstream-moving wall is less sensitive to the rotational rate.

Nomenclature

D = cylinder diameter
f = vortex-shedding frequency
R = cylinder radius

Downloaded 03 Jun 2010 to 171.66.16.156. Redistribution subject to ASME license or copyright; see http://www.asme.org/terms/Terms_Use.cfm

Re = free-stream Reynolds number=$u_0 D/\nu$
St = Strouhal number: fD/u_0
u_p = peripheral velocity
u_0 = free-stream velocity
$\alpha = u_P/u_0$ = ratio between the peripheral speed of the cylinder and the free-stream velocity
u_r = radial velocity
u_θ = tangential velocity
θ = angular position measured from the cylinder leading edge
ν = kinematic viscosity

References

[1] Tokumaru, P. T., and Dimotakis, P. E., 1991, "Rotary Oscillation Control of Cylinder Wake," J. Fluid Mech., **224**, pp. 77–90.
[2] Modi, V. P, Mokhtarian, F., and Fernando, M. S. U. K., 1991, "Moving Surface Boundary Layer Control as Applied to Two-Dimensional Airfoils," J. Aircr., **28**, pp. 104–112.
[3] Moore, F. K., 1958, "On the Separation of the Unsteady Laminar Boundary Layers," *Boundary Layer Research*, H. G. Görtler, ed., Springer, Berlin, pp. 296–310.
[4] Rott, N., 1956, "Unsteady Viscous Flow in the Vicinity of a Stagnation Point," Q. Appl. Math., **13**, pp. 444–451.
[5] Sears, W. R., 1956, "Some Recent Development in Airfoil Theory," J. Aeronaut. Sci., **23**, pp. 490–499.
[6] Ludwig, G. R., 1964, "An Experimental Investigation of Laminar Separation From a Moving Wall," AIAA Paper No. 64-6, Aerosp. Sci. Meeting, New York, January 20–22.
[7] Koromilas, C. A., and Telionis, D. P., 1980, "Unsteady Laminar Separation: An Experimental Study," J. Fluid Mech., **97**, pp. 347–384.
[8] Tsahalis, D. T., and Telionis, D. P., 1973, "The Effect of Blowing on Laminar Separation," J. Appl. Mech., **40**, pp. 1133–1134.
[9] Telionis, D. P., and Werle, M. J., 1973, "Boundary Layer Separation From Downstream Moving Boundaries," J. Appl. Mech., **40**, pp. 369–374.
[10] Peller, H., 1986, "Thermofluiddynamic Experiments With a Heated and Rotating Circular Cylinder in Cross Flow," Exp. Fluids, **4**, pp. 223–231.
[11] Labraga, L., Bourabaa, N., and Berkah, T., 2002, "Wall Shear Stress From a Rotating Cylinder in Cross Flow Using the Electrochemical Technique," Exp. Fluids, **33**, pp. 488–496.
[12] Chew, Y. T., Cheng, M., and Luo, S. C., 1995, "A Numerical Study of Flow Past a Rotating Circular Cylinder Using a Hybrid Vortex Scheme," J. Fluid Mech., **299**, pp. 35–71.
[13] Inoue, O., 1981, "MRS Criterion for Flow Separation Over Moving Walls," AIAA J., **19**(9), pp. 1108–1111.
[14] Tsahalis, D. T, 1977, "Laminar Boundary-Layer Separation From an Upstream-Moving Wall," AIAA J., **15**(4), pp. 561–566.
[15] Diaz, F., Gavaldà, J., Kawall, J. G., Keffer, J. F., and Girald, F., 1983, "Vortex Shedding From a Spinning Cylinder," Phys. Fluids, **26**(12), pp. 3454–3460.
[16] Hu, G., Sun, D., Yin, X., and Tong, B., 1996, "Hopf Bifurcation in Wakes Behind a Rotating and Translating Circular Cylinder," Phys. Fluids, **8**(7), pp. 1972–1974.
[17] Kang, S., Choi, H., and Lee, S., 1999, "Laminar Flow Past a Rotating Circular Cylinder," Phys. Fluids, **11**(11), pp. 3312–3321.
[18] Oosthuizen, P. H., and Madan, S., 1970, "Combined Convective Heat Transfer From Horizontal Cylinders in Air," ASME J. Heat Transfer **83**, pp. 194–196.
[19] Morgan, V. T., 1975, "The Overall Convective Heat Transfer From Smooth Circular Cylinders" Adv. Heat Transfer, **11**, pp. 199–264.
[20] Prasad, A. K., Adrian, R. J., Landreth, C. C., and Offutt, P. W., 1992, "Effect of Resolution on the Speed and Accuracy of Particle Image Velocimetry Interrogation" Exp. Fluids, **13**, pp. 105–116.
[21] Adrian, R. J., Meinhart, C. D., and Tomkins, C. D., 2000, "Vortex Organization in the Outer Region of the Turbulent Boundary Layer," J. Fluid Mech., **422**, pp. 1–54.
[22] Coutanceau, M., and Menard, C., 1985, "Influence of Rotation on the Near-Wake Development Behind an Impulsively Started Circular Cylinder," J. Fluid Mech., **158**, pp. 399–446.
[23] Sung, H. J., Chun, C. K., and Hyun, J. M., 1995, "Experimental Study of Uniform-Shear Flow Past a Rotating Cylinder," ASME J. Fluids Eng., **117**, pp. 62—67.
[24] Mittal, S., and Kumar, B., 2003, "Flow Past Rotating Cylinder," J. Fluid Mech., **476**, pp. 303–334.
[25] Badr, H. M., Coutanceau, M., Dennis, S. C. R., and Menard, C., 1990, "Unsteady Flow Past a Rotating Circular Cylinder at Reynolds Numbers 10^3 and 10^4," J. Fluid Mech., **220**, pp. 459–484.

Downloaded 03 Jun 2010 to 171.66.16.156. Redistribution subject to ASME license or copyright; see http://www.asme.org/terms/Terms_Use.cfm

Robust Implicit Multigrid Reynolds-Stress Model Computation of 3D Turbomachinery Flows

G. A. Gerolymos
e-mail: geg@ccr.jussieu.fr

I. Vallet
e-mail: vallet@ccr.jussieu.fr

Institut d'Alembert,
Université Pierre-et-Marie-Curie,
75005 Paris, France

The purpose of this paper is to present a numerical methodology for the computation of complex 3D turbomachinery flows using advanced multiequation turbulence closures, including full seven-equation Reynolds-stress transport models. The flow equations are discretized on structured multiblock grids, using an upwind biased ($O[\Delta x_{\mathrm{H}}^3]$ MUSCL reconstruction) finite-volume scheme. Time integration uses a local dual-time-stepping implicit procedure, with internal subiterations. Computational efficiency is achieved by a specific approximate factorization of the implicit subiterations, designed to minimize the computational cost of the turbulence transport equations. Convergence is still accelerated using a mean-flow-multigrid full-approximation-scheme method, where multigrid is applied only on the mean-flow variables. Speed-ups of a factor 3 are obtained using three levels of multigrid (fine plus two coarser grids). Computational examples are presented using two Reynolds-stress models, and also a baseline $k-\varepsilon$ model, for various turbomachinery configurations, and compared to available experimental measurements.
[DOI: 10.1115/1.2754320]

1 Introduction

Turbomachinery flows are a major challenge for turbulence modeling because they are dominated by many complex flow phenomena: (i) 3D secondary effects have a major influence, both for compressors [1] and turbines [2] especially with the decreasing aspect ratio tendency of modern designs [3]; (ii) large 3D separation regions are observed in compressors [4]; (iii) transitional phenomena are important in the strongly accelerated flows observed in turbines [5,6]; and (iv) flow unsteadiness [7] and freestream turbulence effects [8] have a strong effect, especially off design.

To address such complex flows, it is necessary to include more physics in turbulence models, and in particular, the effects of anisotropy [9]. With the exception of transition modeling (which requires specific approaches [10]), Reynolds-stress models (RSMs) can offer a definite advantage over more standard two-equation closures, especially for complex 3D separated flows [11]. Furthermore, it was quite early recognized [[12], p. 469] that only such advanced transport-equation anisotropy-resolving closures can predict the effects of freestream turbulence on the flow. The increasing number of 3D compressible flow computations using RSMs [13,14] suggests that the numerical stability issues that have hindered the widespread application of these closures in the past can be treated efficiently [15,16].

There exist several efficient and robust multistage turbomachinery CFD solvers, mainly using two-equation closures [17–21]. These solvers handle flows in a complex multistage environment [22], including modeling of complex technological effects [23].

There are, however, very few applications of RSM closures to 3D turbomachinery flows. Gerolymos et al. [24] have evaluated the performance of a wall-normal-free RSM [11,25] for compressor and turbine configurations, using an implicit upwind solver. This method was latter enhanced by a local dual time-stepping technique [15] to avoid limit-cycle oscillations in flows with large separation. Rautaheimo et al. [26] have used an implicit upwind solver, with mean-flow-multigrid acceleration to compute the flow in a low-speed centrifugal compressor rotor [27], using a hybrid RSM, blending the quadratic Speziale–Sarkar–Gatski high-turbulence-Reynolds-number model [28] with the quasilinear Shima low-turbulence-Reynolds-number model [29]. More recently, Borello et al. [30] used the elliptic blending model of Manceau and Hanjalic [31], to compute flows around 2D cascades [30], and within tip-clearance gaps [32].

The purpose of this paper is to present an efficient and robust numerical methodology for the computation of complex turbomachinery flows using seven-equation turbulence closures (which is of course equally applicable to lower level two-equation and one-equation closures). The wall-normal-free Reynolds-stress model is implemented numerically using a finite volume upwind-biased implicit multigrid solver on multiblock structured grids. Robustness is achieved through the explicit application of Reynolds-stress realizability constraints and computational efficiency through the use of specifically designed approximate Jacobians for the implicit solver. Computational efficiency is further enhanced by the application of multigrid acceleration (applied only on the mean-flow variables, turbulence variables being simply injected onto coarser grids), obtaining a factor-3 speed-up. Computational results are presented for two axial-flow compressor configurations.

2 Flow Model

The flow is modeled by the 3D compressible Favre–Reynolds-averaged Navier–Stokes equations, with a seven-equation Reynolds-stress turbulence closure [11,25]. The 12 transport equations are written symbolically, in a Cartesian reference frame rotating with constant (time-independent) rotational velocity $\vec{\Omega}=\Omega_i\vec{e}_i\equiv\Omega\vec{e}_x$, as

$$\frac{\partial \underline{w}}{\partial t}+\frac{\partial \underline{F}_\ell}{\partial x_\ell}+\underline{S}\equiv\frac{\partial \underline{w}}{\partial t}+\frac{\partial \underline{F}_x}{\partial x}+\frac{\partial \underline{F}_y}{\partial y}+\frac{\partial \underline{F}_z}{\partial z}+\underline{S}=0 \qquad (1)$$

where t is the time, x_ℓ (x,y,z) are the Cartesian space coordinates in the relative frame of reference, and $\underline{w}\in\mathbb{R}^{12}$ is the vector of

Contributed by the Fluids Engineering Division of ASME for publication in the JOURNAL OF FLUIDS ENGINEERING. Manuscript received June 16, 2006; final manuscript received March 31, 2007. Review conducted by Paul Durbin. Paper presented at the ASME Turbo Expo 2006: Land, Sea and Air (GT2006), May 8–11, 2006, Barcelona, Spain.

 Copyright © 2007 by ASME

Downloaded 03 Jun 2010 to 171.66.16.156. Redistribution subject to ASME license or copyright; see http://www.asme.org/terms/Terms_Use.cfm

unknowns, which is split in a vector of mean-flow variables $\underline{w}_{\mathrm{MF}} \in \mathbb{R}^5$, and a vector of turbulence variables (Reynolds stresses and dissipation rate) $\underline{w}_{\mathrm{RSM}} \in \mathbb{R}^7$

$$\underline{w} = [\underline{w}_{\mathrm{MF}}^{\mathrm{T}}, \underline{w}_{\mathrm{RSM}}^{\mathrm{T}}]^{\mathrm{T}};$$

$$\underline{w}_{\mathrm{MF}} = \left[\bar{\rho}, \bar{\rho}\tilde{W}_x, \bar{\rho}\tilde{W}_y, \bar{\rho}\tilde{W}_z, \bar{\rho}\left(\breve{h}_{t_{\mathrm{W}}} - \frac{1}{2}\Omega^2 R^2\right) - \bar{p}\right]^{\mathrm{T}} \tag{2}$$

$$\underline{w}_{\mathrm{RSM}} = [\widetilde{\bar{\rho}w_x''w_x''}, \widetilde{\bar{\rho}w_x''w_y''}, \widetilde{\bar{\rho}w_y''w_y''}, \widetilde{\bar{\rho}w_y''w_z''}, \widetilde{\bar{\rho}w_z''w_z''}, \widetilde{\bar{\rho}w_z''w_x''}, \bar{\rho}\varepsilon^*]^{\mathrm{T}}$$

where R is the radius (distance from the axis of rotation: $R^2=[x_i - |\Omega|^{-2}x_j\Omega_j\Omega_i][x_i - |\Omega|^{-2}x_k\Omega_k\Omega_i] \equiv y^2+z^2$), W_i are the relative velocity components, ρ is the density, p the pressure, $-\widetilde{\bar{\rho}w_i''w_j''}$ are the Reynolds stresses, and ε^* is the modified [33] dissipation rate ($\varepsilon^* = \varepsilon - 2\breve{\nu}[\mathrm{grad}(\sqrt{\mathrm{k}})]^2$), ε is the dissipation rate, $k=(1/2)\widetilde{w_i''w_i''}$ is the turbulence kinetic energy, and ν is the kinematic viscosity. The symbol $(\tilde{\cdot})$ denotes Favre-averaging, $(\bar{\cdot})$ denotes nonweighted averaging, $(\cdot'')$ are Favre fluctuations, $(\cdot')$ are nonweighted fluctuations, and $\breve{h}_{t_{\mathrm{W}}} = \tilde{h} + 1/2\tilde{W}_i\tilde{W}_i$ is the total enthalpy of the relative mean flow (h is the specific enthalpy). The symbol $(\breve{\cdot})$ is used to denote a function of average quantities that is neither a Favre average nor a nonweighted average. The fluxes $\underline{F}_\ell \in \mathbb{R}^{12}$ ($\underline{F}_x$, $\underline{F}_y$, $\underline{F}_z$ (Eq. (1)) are the combined convective ($\underline{F}_\ell^{\mathrm{C}}$) and diffusive (viscous, $\underline{F}_\ell^{\mathrm{V}}$) fluxes

$$\underline{F}_\ell = \underline{F}_\ell^{\mathrm{C}} + \underline{F}_\ell^{\mathrm{V}} = \begin{bmatrix} \bar{\rho}\tilde{W}_\ell \\ \bar{\rho}\tilde{W}_\ell\tilde{W}_x + \bar{p}\,\delta_{x\ell} \\ \bar{\rho}\tilde{W}_\ell\tilde{W}_y + \bar{p}\,\delta_{y\ell} \\ \bar{\rho}\tilde{W}_\ell\tilde{W}_z + \bar{p}\,\delta_{z\ell} \\ \bar{\rho}\tilde{W}_\ell\left(\breve{h}_{t_{\mathrm{W}}} - \frac{1}{2}\Omega^2R^2\right) \\ \bar{\rho}\tilde{W}_\ell\widetilde{w_x''w_x''} \\ \bar{\rho}\tilde{W}_\ell\widetilde{w_x''w_y''} \\ \bar{\rho}\tilde{W}_\ell\widetilde{w_y''w_y''} \\ \bar{\rho}\tilde{W}_\ell\widetilde{w_y''w_z''} \\ \bar{\rho}\tilde{W}_\ell\widetilde{w_z''w_z''} \\ \bar{\rho}\tilde{W}_\ell\widetilde{w_z''w_x''} \\ \bar{\rho}\tilde{W}_\ell\varepsilon^* \end{bmatrix} + \begin{bmatrix} 0 \\ \widetilde{\bar{\rho}w_\ell''w_x''} - \bar{\tau}_{\ell x} \\ \widetilde{\bar{\rho}w_\ell''w_y''} - \bar{\tau}_{\ell y} \\ \widetilde{\bar{\rho}w_\ell''w_z''} - \bar{\tau}_{\ell z} \\ \tilde{W}_i(\widetilde{\bar{\rho}w_i''w_\ell''} - \bar{\tau}_{i\ell}) + (\bar{q}_\ell + \widetilde{\bar{\rho}h''w_\ell''}) \\ -\mathcal{D}_{xx\ell} \\ -\mathcal{D}_{xy\ell} \\ -\mathcal{D}_{yy\ell} \\ -\mathcal{D}_{yz\ell} \\ -\mathcal{D}_{zz\ell} \\ -\mathcal{D}_{zx\ell} \\ -\mathcal{D}_{\varepsilon_\ell} \end{bmatrix} \tag{3}$$

where τ_{ij} are the viscous stresses, q_i are the molecular heat fluxes, $\widetilde{\bar{\rho}h''w_i''}$ are the turbulent heat fluxes, $\mathcal{D}_{ijk}$ are the turbulence-diffusion flux terms, and $\mathcal{D}_{\varepsilon_i}$ denotes the ε diffusion flux. The source-terms vector $\underline{S} \in \mathbb{R}^{12}$

$$\underline{S} = -[0, \bar{\rho}f_{\mathfrak{v}_x}, \bar{\rho}f_{\mathfrak{v}_y}, \bar{\rho}f_{\mathfrak{v}_z}, S_{\breve{h}_t}, S_{w_xw_x}, S_{w_xw_y}, S_{w_yw_y}, S_{w_yw_z}, S_{w_zw_z}, S_{w_zw_x}, S_\varepsilon]^{\mathrm{T}} \tag{4}$$

contains the centrifugal and Coriolis acceleration terms ($f_{\mathfrak{v}_i} = -2\epsilon_{ij\ell}\Omega_j\tilde{W}_\ell - \partial[-(1/2)\Omega^2R^2]/\partial x_i$), the source terms of the turbulence model ($S_{w_iw_j}$ and S_ε), and the energy-equation source term $S_{\breve{h}_t}$ [25], which contains terms from the turbulence-kinetic-energy transport equation. The terms $\mathcal{D}_{ij\ell}$, $\mathcal{D}_{\varepsilon_\ell}$, $S_{\breve{h}_t}$, $S_{w_iw_j}$, S_ε, and $\widetilde{h''u_\ell''}$ depend on the particular closure used. Full details on the development of the Reynolds-stress models used have been presented elsewhere [11,25,34]. These closures are wall-normal free (WNF), i.e., completely independent of wall-topology parameters, such as the distance-from-the-wall or the normal-to-the-wall direction, using instead a modeled unit vector pointing in the turbulence-inhomogeneity direction, which, as well as the coefficients of the inhomogeneous terms, is a function of the gradients of local turbulence quantities [11]. In the computational examples reported in the present paper, three variants of the same family of quasilinear return-to-isotropy isotropization-of-production WNF RSMs [11] were used, the Gerolymos-Vallet (GV) RSM [25], the WNF Launder-Shima-Sharma (LSS) RSM [11], and the Sauret-Vallet (SV) RSM [34].

The working medium thermodynamics are approximated by a thermodynamically and calorically perfect gas ($\bar{p} = \bar{\rho}R_g\tilde{T}$ and $c_p = \gamma R_g/[\gamma - 1]$). All computations were run for air ($R_g = 287.04\ \mathrm{m^2\,s^{-2}\,K^{-1}}$, $\gamma = 1.4$) and used a Sutherland-law dependence for viscosity and a corrected Sutherland law for heat conductivity ([25] p. 192, Eqs. (5)).

3 Numerical Method

The numerical scheme is based on analogous work by the authors in nonrotating frames of Refs. [15,16] and is summarized below, insisting on the differences due to rotation and on the specifics to turbomachinery boundary conditions.

3.1 Multiblock Mesh Structure. The flow equations are discretized in structured multidomain multiblock grids to compute flow through tip-clearance gaps [35], but also for multistage computations [36]. The flow equations are solved using conservative variables in a rotating Cartesian frame of reference $\underline{w} = [\underline{w}_{\mathrm{MF}}^{\mathrm{T}}, \underline{w}_{\mathrm{RSM}}^{\mathrm{T}}]^{\mathrm{T}}$ (Eqs. (2)), but the multiblock data management is based on primitive variables in the absolute cylindrical frame of reference

$$\underline{v} = [\underline{v}_{\mathrm{MF}}^{\mathrm{T}}, \underline{v}_{\mathrm{RSM}}^{\mathrm{T}}]^{\mathrm{T}};$$

$$\underline{v}_{\mathrm{MF}} = [\bar{\rho}, \tilde{W}_x, \tilde{W}_R, \tilde{W}_\theta, \bar{p}]^{\mathrm{T}}$$

$$\underline{v}_{\mathrm{RSM}} = [\widetilde{w_x''w_x''}, \widetilde{w_x''w_R''}, \widetilde{w_R''w_R''}, \widetilde{w_R''w_\theta''}, \widetilde{w_\theta''w_\theta''}, \widetilde{w_\theta''w_x''}, \varepsilon^*]^{\mathrm{T}} \tag{5}$$

3.2 Space Discretization. For each grid subdomain, the mean-flow and turbulence-transport equations (Eqs. (1)–(4)) are discretized on a structured grid using a finite-volume technique, with vertex-storage, resulting to the semi-discrete scheme [15,16]

$$\frac{d\underline{w}_{i,j,k}}{dt} + \underline{\mathcal{L}}_{i,j,k} \equiv \frac{d\underline{w}_{i,j,k}}{dt} + \frac{1}{\mathcal{V}_{i,j,k}}\begin{bmatrix} +{}^{\xi}\mathcal{S}_{i+(1/2),j,k}\,{}^{\xi}\underline{F}^{\mathrm{N}}_{i+(1/2),j,k} - {}^{\xi}\mathcal{S}_{i-(1/2),j,k}\,{}^{\xi}\underline{F}^{\mathrm{N}}_{i-(1/2),j,k} \\ +{}^{\eta}\mathcal{S}_{i,j+(1/2),k}\,{}^{\eta}\underline{F}^{\mathrm{N}}_{i,j+(1/2),k} - {}^{\eta}\mathcal{S}_{i,j-(1/2),k}\,{}^{\eta}\underline{F}^{\mathrm{N}}_{i,j-(1/2),k} \\ +{}^{\zeta}\mathcal{S}_{i,j,k+(1/2)}\,{}^{\zeta}\underline{F}^{\mathrm{N}}_{i,j,k+(1/2)} - {}^{\zeta}\mathcal{S}_{i,j,k-(1/2)}\,{}^{\zeta}\underline{F}^{\mathrm{N}}_{i,j,k-(1/2)} \end{bmatrix}$$

Downloaded 03 Jun 2010 to 171.66.16.156. Redistribution subject to ASME license or copyright; see http://www.asme.org/terms/Terms_Use.cfm

$$+\underline{S}_{i,j,k} \cong 0 \tag{6}$$

where $\mathcal{V}_{i,j,k}$ is the control-volume, delimited by the surfaces $\mathcal{S}$, with unit-normals $\vec{n}$ in the positive grid-direction (ξ, η, ζ, respectively i, j, k), and $\underline{F}^{\mathrm{N}}=\underline{F}^{+}(\underline{w}^{-};n_x,n_y,n_z)+\underline{F}^{-}(\underline{w}^{+};n_x,n_y,n_z)+\underline{F}^{\mathrm{V}}_{\ell}n_{\ell}$ are the numerical fluxes. The convective fluxes $\underline{F}^{\pm}$ are computed using van Leer flux-vector-splitting [37]

$$\underline{F}^{\pm}(\underline{w})=\begin{cases}\underline{0}; & \pm\breve{M}_{\mathrm{W}_n}<-1\\ \begin{bmatrix}1\\ n_x\frac{\breve{a}}{\gamma}(-\breve{M}_{\mathrm{W}_n}\pm 2)+\tilde{W}_x\\ n_y\frac{\breve{a}}{\gamma}(-\breve{M}_{\mathrm{W}_n}\pm 2)+\tilde{W}_y\\ n_z\frac{\breve{a}}{\gamma}(-\breve{M}_{\mathrm{W}_n}\pm 2)+\tilde{W}_z\\ \frac{-(\gamma-1)\breve{M}^2_{\mathrm{W}_n}\pm 2(\gamma-1)\breve{M}_{\mathrm{W}_n}+2}{\gamma^2-1}\breve{a}^2+\frac{\tilde{W}^2}{2}-\frac{\Omega^2R^2}{2}\\ \widetilde{w''_xw''_x}\\ \widetilde{w''_xw''_y}\\ \widetilde{w''_yw''_y}\\ \widetilde{w''_yw''_z}\\ \widetilde{w''_zw''_z}\\ \widetilde{w''_zw''_x}\\ \varepsilon^*\end{bmatrix}; & |\breve{M}_{\mathrm{W}_n}|\leqslant 1\\ \pm\bar{\rho}\breve{a}\frac{(\breve{M}_{\mathrm{W}_n}\pm 1)^2}{4}\begin{bmatrix}\\ \\ \\ \\ \\ \\ \\ \\ \\ \end{bmatrix}; & \\ \underline{F}^{\mathrm{C}}_{\ell}; & \pm\breve{M}_{\mathrm{W}_n}>1\end{cases} \tag{7}$$

where $\breve{M}_{\mathrm{W}_n}(\underline{w};n_x,n_y,n_z)=\tilde{W}_{\ell}(\underline{w})n_{\ell}\breve{a}^{-1}(\underline{w})=\tilde{W}_n\breve{a}^{-1}$ and $\breve{a}(\underline{w})=\sqrt{\gamma R_g\tilde{T}(\underline{w})}$. The MUSCL variables $\underline{w}^{\mp}$ are computed using $O(\Delta x_H^3)$ extrapolation with limiters [37]. The viscous fluxes $\underline{F}^{\mathrm{V}}$ are discretized using an $O(\Delta x_H^2)$ centered scheme [15].

Defining $N_{ijk}=N_i\times N_j\times N_k$ the number of points of a grid subdomain n_{D}, $\mathfrak{w}=[\underline{w}^{\mathrm{T}}_{1,1,1},\underline{w}^{\mathrm{T}}_{1,1,2},\ldots,\underline{w}^{\mathrm{T}}_{N_i,N_j,N_k}]^{\mathrm{T}}\in\mathbb{R}^{12N_{ijk}}$ the global vector of unknowns, $\mathcal{L}=[\underline{\mathcal{L}}^{\mathrm{T}}_{1,1,1},\underline{\mathcal{L}}^{\mathrm{T}}_{1,1,2},\ldots,\underline{\mathcal{L}}^{\mathrm{T}}_{N_i,N_j,N_k}]^{\mathrm{T}}\in\mathbb{R}^{12N_{ijk}}$ the global vector of the spaceoperators (Eq. (6)), and $\Delta\mathfrak{t}=\mathrm{diag}[(\Delta t_{1,1,1})\underline{\underline{I}}_{12},(\Delta t_{1,1,2})\underline{\underline{I}}_{12},\ldots,(\Delta t_{N_i,N_j,N_k})\underline{\underline{I}}_{12}]$ the diagonal matrix of local time steps $\Delta t_{i,j,k}$ ($\underline{\underline{I}}_{12}$ denotes the 12×12 identity matrix), an implicit $O(\Delta t)$ backward-Euler discretization of the equations results, at each iteration $n\equiv n_{\mathrm{it}}$, to the nonlinear system [15,16]

$$\mathfrak{R}({}^{n+1}\mathfrak{w},{}^{n}\mathfrak{w},\Delta\mathfrak{t})\equiv\frac{{}^{n+1}\mathfrak{w}-{}^{n}\mathfrak{w}}{\Delta\mathfrak{t}}+\mathfrak{L}({}^{n+1}\mathfrak{w})\cong 0;\quad\forall\, n_{\mathrm{D}} \tag{8}$$

where $\mathfrak{R}\in\mathbb{R}^{12N_{ijk}}$ is the residual, and $1/\Delta\mathfrak{t}\equiv\Delta\mathfrak{t}^{-1}$. This system of $12N_{ijk}$ nonlinear equations must be solved at every iteration n_{it}, for each grid subdomain n_{D}. The subscript n_{D} could have been added to $\mathfrak{R}$, $\mathfrak{w}$, $\mathfrak{L}$, $\Delta\mathfrak{t}$,..., but was omitted to simplify notation.

3.3 LDTS Implicit Iterative Solution. This nonlinear system can be solved using a local dual time-stepping (LDTS) procedure [15,16], by introducing an additional subiterative pseudotime step Δt^* with implicit subiterations ($m_{\mathrm{it}}=1,\ldots,M_{\mathrm{it}}(n_{\mathrm{it}})$)

$$\frac{{}^{m+1,n+1}\mathfrak{w}-{}^{m,n+1}\mathfrak{w}}{\Delta\mathfrak{t}^*}+\mathfrak{R}({}^{m+1,n+1}\mathfrak{w},{}^{n}\mathfrak{w},\Delta\mathfrak{t})\cong 0;\quad\forall\, n_{\mathrm{D}} \tag{9}$$

where we have used for simplicity the iteration counters $n\equiv n_{\mathrm{it}}$ and $m\equiv m_{\mathrm{it}}$. After some algebra [15,16], which will not be repeated here, the LDTS iteration can be written, symbolically,

$$\forall n\equiv n_{\mathrm{it}}\in[1,N_{\mathrm{it}}];\quad\{\forall m\equiv m_{\mathrm{it}}=1,\ldots:[r_{\mathrm{MF}}\geqslant r_{\mathrm{OBJ}}]\};$$

$$\forall n_{\mathrm{D}}\in[1,N_{\mathrm{D}}]$$

$$\begin{aligned}{}^{m+1,n+1}\mathfrak{w}&=\mathbf{RBR}\Bigg\{{}^{m,n+1}\mathfrak{w}-\left[\mathfrak{I}+\Delta\mathfrak{t}^{**}\frac{\partial\mathfrak{L}^{\mathrm{J}}}{\partial\mathfrak{w}}({}^{m,n+1}\mathfrak{w})\right]^{-1}_{\mathrm{approx}}\\&\quad\times\Delta\mathfrak{t}^{**}[\mathfrak{R}({}^{m,n+1}\mathfrak{w},{}^{n}\mathfrak{w},\Delta\mathfrak{t})+\mathfrak{F}]\Bigg\}\\&\equiv{}^{m}\mathbf{S}({}^{m,n+1}\mathfrak{w},{}^{n}\mathfrak{w},\Delta\mathfrak{t},\Delta\mathfrak{t}^*,\mathfrak{F})\end{aligned} \tag{10}$$

where $\Delta\mathfrak{t}^{**}=[\mathfrak{I}+\Delta\mathfrak{t}^{-1}\Delta\mathfrak{t}^*]^{-1}\Delta\mathfrak{t}^*$, and N_{D} is the number of grid subdomains. The operator $\mathbf{B}(\mathfrak{w})$ represents the explicit application of boundary-conditions (cf. Sec. 3.7). The operator $\mathbf{R}(\mathfrak{w})$ represents the explicit application (cf. Sec. 3.6) of Reynolds-stress realizability constraints [16], to conform with Reynolds-stress realizability [38]. The term $\mathfrak{F}\in\mathbb{R}^{12N_{ijk}}$ is a forcing source term, which serves only in the multigrid iteration [39] and which is equal to zero for the monogrid scheme ($\mathfrak{F}=0$). The LDTS iteration (Eqs. (10)) can be written more concisely using a global full-iteration operator $\mathbf{N}(\mathfrak{w},\mathrm{CFL},\mathrm{CFL}^*,\mathfrak{F};r_{\mathrm{OBJ}})$

Downloaded 03 Jun 2010 to 171.66.16.156. Redistribution subject to ASME license or copyright; see http://www.asme.org/terms/Terms_Use.cfm

$$\forall n \equiv n_{\mathrm{it}} \in [1, N_{\mathrm{it}}]; \quad {}^{n+1}\mathfrak{w} = \mathbf{N}({}^{n}\mathfrak{w}, \mathrm{CFL}, \mathrm{CFL}^{*}, \mathfrak{F}; r_{\mathrm{obj}}) \quad (11)$$

where Courant-Friedricks-Levy (CFL) and CFL^{*} are the CFL numbers used to evaluate Δt and Δt^{*} (cf. Sec. 3.5). The number of subiterations $M_{\mathrm{it}}(n_{\mathrm{it}})$ is dynamically fixed (Eqs. (10)) to satisfy the convergence criterion $r_{\mathrm{MF}} \leqslant r_{\mathrm{OBJ}}$ (cf. Sec. 3.5). The Jacobian matrix $\partial \mathfrak{L}^{\mathrm{J}} / \partial \mathfrak{w}$ (Eqs. (10)) is an approximation to the exact Jacobian $\partial \mathfrak{L} / \partial \mathfrak{w}$, chosen so as to minimize implicit work for the turbulence-variables ([15], pp. 766–767, Eqs. (18)–(27)). The subscript approx indicates that the matrix inversion (linear system solution) at each subiteration is approximate. In the present work, it is obtained using approximate factorization [40] allowing sweeps in each grid direction (alternating direction implicit approximate factorization (ADI-AF)) ([15], pp. 766–767, Eqs. (18)–(27)). To ensure stability at high time steps ($\Delta \mathrm{t}^{*}$), implicit boundary conditions are applied following the method of characteristics approach of Chakravarthy [41], which implies appropriate modifications of the Jacobians $\partial \mathfrak{L}^{\mathrm{J}} / \partial \mathfrak{w}$ to conform with boundary conditions. Of course, because of the approximate factorization procedure, the implicit boundary conditions cannot relate different points on the boundary surface, one with another, as is necessary in the case of exact nonreflecting boundary conditions (NRBCs) [42], or in the case of conditions involving surface integrals (mixing planes, throttle outflow condition, etc.). The same problem appears at the interfaces between subdomains, since the linear system is solved by ADI-AF separately in each domain (with no-change implicit boundary conditions for the outer phantom nodes; cf. Sec 3.7). In these cases simple approximate implicit boundary conditions are used (no-change, extrapolation, constant pressure, reservoir, …), and the appropriate exact boundary conditions are applied explicitly (cf. Sec. 3.7).

3.4 Quasi-Newton Implicit Iterative Solution. A quasi-Newton iterative procedure is obtained in the limit $\Delta t \to \infty$, so that the unsteady term in the nonlinear system (Eqs. (8)) disappears, giving $\mathfrak{L}({}^{n+1}\mathfrak{w}) \cong 0$. The corresponding quasi-Newton iterative procedure, after linearization, reads [16]

$$\forall n \equiv n_{\mathrm{it}} \in [1, N_{\mathrm{it}}]; \quad \{\forall m \equiv m_{\mathrm{it}} = 1, \ldots : [r_{\mathrm{MF}} \geqslant r_{\mathrm{OBJ}}]\};$$

$$\forall n_{\mathrm{D}} \in [1, N_{\mathrm{D}}]$$

$$\begin{aligned} {}^{m+1,n+1}\mathfrak{w} &= \mathbf{RBR}\left\{ {}^{m,n+1}\mathfrak{w} - \left[\mathfrak{I} + \Delta \mathrm{t}^{*} \frac{\partial \mathfrak{L}^{\mathrm{J}}}{\partial \mathfrak{w}}({}^{m,n+1}\mathfrak{w}) \right]^{-1}_{\mathrm{approx}} \right. \\ &\quad \left. \times \Delta \mathrm{t}^{*} [\mathfrak{L}({}^{m,n+1}\mathfrak{w}) + \mathfrak{F}] \right\} \\ &\equiv {}^{m}\mathbf{S}_{\mathrm{QN}}({}^{m,n+1}\mathfrak{w}, \Delta \mathrm{t}^{*}, \mathfrak{F}) \end{aligned} \quad (12)$$

3.5 Iteration Strategies and Convergence Monitoring. The local time step is based on a combined convective (Courant) and viscous (von Neumann) criterion [15]

$$\Delta t_{i,j,k} = \min\left\{ \mathrm{CFL} \frac{\ell_g}{\tilde{W} + \breve{a}\sqrt{1 + (5/6)(\gamma - 1) M_{\mathrm{T}}^{2}}}, \mathrm{VNN} \frac{\ell_g^{2}}{2 \nu_{eq}} \right\} \quad (13)$$

$$\nu_{eq} = \max\left\{ \frac{4}{3}(\breve{\nu} + \nu_{\mathrm{T}}), \frac{\gamma - 1}{\bar{\rho} R_g}(\breve{\kappa} + \kappa_{\mathrm{T}}) \right\} \quad (14)$$

where ℓ_g is the grid cell size, $\tilde{W}$ is the relative flow velocity, $\breve{a}$ is the sound velocity, ν_{eq} is the equivalent diffusivity, $\breve{\nu}$ is the molecular kinematic viscosity, $\breve{\kappa}$ is the molecular heat conductivity, $M_{\mathrm{T}} = \sqrt{2\mathrm{k}\breve{a}^{-2}}$ is the turbulence Mach number, ν_{T} is the eddy viscosity, and κ_{T} is the eddy conductivity (equations for these quantities are given in [15]). This relation (Eq. (13)) is used both for the physical time step ($\Delta t_{i,j,k}$, CFL, von Neumann (VNN)) and for the dual pseudo-time step ($\Delta t^{*}_{i,j,k}$, CFL^{*}, VNN^{*}). In all of the computations presented here, the relations VNN=CFL and $\mathrm{VNN}^{*} = \mathrm{CFL}^{*}$ were assumed.

The relative variation of the mean flow e_{MF} and of the turbulence variables e_{RSM} are monitored by the following error–L_2 pseudonorms:

$$e_{\mathrm{MF}}[\mathfrak{v}_{\mathrm{MF}}, \Delta \mathfrak{v}_{\mathrm{MF}}] = \log_{10} \sqrt{\frac{1}{5}\left\{ \frac{\sum [\Delta \bar{\rho}]^2}{\sum [\bar{\rho}]^2} + \frac{\sum [\Delta(\tilde{W}_i)\Delta(\tilde{W}_i)]}{\sum [\tilde{W}_i \tilde{W}_i]} + \frac{\sum [\Delta(\bar{p})]^2}{\sum [\bar{p}]^2} \right\}} \quad (15)$$

$$e_{\mathrm{RSM}}[\mathfrak{v}_{\mathrm{RSM}}, \Delta \mathfrak{v}_{\mathrm{RSM}}] = \log_{10} \sqrt{\frac{1}{7}\left\{ \frac{\sum [\Delta(\widetilde{w_i'' w_j''})\Delta(\widetilde{w_i'' w_j''})]}{\sum [(\widetilde{w_i'' w_j''})(\widetilde{w_i'' w_j''})]} + \frac{\sum [\Delta \varepsilon^{*}]^2}{\sum [\varepsilon^{*}]^2} \right\}} \quad (16)$$

where Σ implies summation over all of the grid nodes N_{P} (and over all of the subdomains N_{D}), and the summation convention for the cylindrical coordinates indices $i,j = x, R, \theta$ is used. In the present turbomachinery solver, e_{MF} is defined as the relative variation of the primitive mean-flow variables, contrary to previous work [15,16] where conservative variable variations were used. This quantity (e_{MF}) approximately defines the number of digits to which the computation of the mean-flow variables is converged. It is used to define the subiterative convergence of the increment by the error reduction between subiterations $[m, n+1]$ and $[m+1, n+1]$ (Eqs. (12))

$$r_{\mathrm{MF}}(m+1, n+1) = \log_{10}\left\{ \frac{10^{[e_{\mathrm{MF}}(m+1,n+1)]} - 10^{[e_{\mathrm{MF}}(m,n+1)]}}{10^{[e_{\mathrm{MF}}(m,n+1)]}} \right\} \quad (17)$$

$$e_{\mathrm{MF}}(m+1, n+1) \equiv e_{\mathrm{MF}}[{}^{n}\mathfrak{v}_{\mathrm{MF}}, {}^{m+1,n+1}\mathfrak{v}_{\mathrm{MF}} - {}^{n}\mathfrak{v}_{\mathrm{MF}}] \quad (18)$$

The reduction (r_{MF}) approximately indicates the number of digits to which the increment is converged during the subiterations. The error reduction for the turbulence variables $\mathfrak{v}_{\mathrm{RSM}}$, r_{RSM}, is defined in exactly the same way ([15], p. 768, Eqs. (32)–(33)).

The parameters controlling the numerical scheme (time integration) are the CFL numbers [15], CFL for the physical time step Δt, and CFL^{*} for the dual pseudo-time step (assuming [15,16] that $\mathrm{VNN}^{*} = \mathrm{CFL}^{*}$, and VNN=CFL), and the convergence criterion r_{OBJ} used to dynamically fix the number of subiterations (Eqs. (12)). The time-integration scheme is therefore defined by the triplet $[\mathrm{CFL}, \mathrm{CFL}^{*}, r_{\mathrm{OBJ}}]$. The quasi-Newton-integration scheme ($\mathrm{CFL} \to \infty$) is therefore defined by $[\mathrm{CFL}, \mathrm{CFL}^{*}, r_{\mathrm{OBJ}}] = [\infty, \mathrm{CFL}^{*}, r_{\mathrm{OBJ}}]$ or equivalently the couple $\mathrm{QN}[\mathrm{CFL}^{*}, r_{\mathrm{MF}}]$.

3.6 Heuristic Stabilization by Explicit Application of Realizability Constraints. During the iterations, Reynolds stresses may not satisfy the realizability constraints introduced by Schumann [38]. Such anomalous behavior is systematically checked for at every subiteration. If the realizability constraints are not satisfied for a given grid point n_{P}, then all turbulence variables are set to 0 at this grid point

Downloaded 03 Jun 2010 to 171.66.16.156. Redistribution subject to ASME license or copyright; see http://www.asme.org/terms/Terms_Use.cfm

$$\text{if}\left\{\begin{array}{l}\widetilde{w_x''^2}<0\vee\\ \widetilde{w_R''^2}<0\vee\\ \widetilde{w_\theta''^2}<0\vee\\ (\widetilde{w_x''w_R''})^2-\widetilde{w_x''^2}\widetilde{w_R''^2}>0\vee\\ (\widetilde{w_R''w_\theta''})^2-\widetilde{w_R''^2}\widetilde{w_\theta''^2}>0\vee\\ (\widetilde{w_\theta''w_x''})^2-\widetilde{w_\theta''^2}\widetilde{w_x''^2}>0\vee\\ \det[\widetilde{w_i''w_j''}]<0\vee\\ \varepsilon^*<0\vee\\ \ell_T^*=k^{(3/2)}\varepsilon^{*-1}>\ell_{T_{max}}\end{array}\right\}:\underline{v}_{RSM}\leftarrow\underline{0};\quad\forall\, n_P=1,\ldots,N_P \tag{19}$$

where $\ell_{T_{max}}$ is a maximum admissible length scale (automatically computed as the maximum half height of the flow path). These simple realizability and boundedness fixes (which are completely explicit and, as a consequence, easy to implement) efficiently stabilize the computations for a large number of applications studied by the authors [11,15,16,24,25,34]. The explicit realizability constraints (Eqs. (19)) will be represented by the operator $\mathbf{R}(\mathfrak{w})$.

When running the two-equation model [35,36], the complete realizability conditions for the Reynolds stresses are relaxed, since the Launder–Sharma [33] $k-\varepsilon$ model does not necessarily return realizable Reynolds stresses. In this case, simple positivity and boundedness constraints are used [16].

3.7 Interface and Boundary Conditions

3.7.1 Wall and Interface Conditions. At solid walls (hub, casing, and blades), a standard adiabatic no-slip wall condition is applied [35]. At interfaces between grid domains, such as periodicity boundaries, H–O interfaces, or interfaces between the TC–OZ–O grids used to compute flow through tip-clearance gaps [35], information is exchanged using $N_{PH}=2^{L_{GRD}}$ phantom nodes (L_{GRD} is the number of grids in the multigrid sequence [16], Fig. 4, cf. Sec. 3.8), which are updated at each subiteration from corresponding grid nodes. At the interface itself, a simple average is applied between values obtained from the computation in each domain.

3.7.2 Mixing-Plane Conditions. Multistage steady computations are based on a mixing-plane (MP) approach, at the interface between neighboring blade rows [36]. Note that MPs are, in general, nonconical surfaces of revolution and not planes. At these interfaces, $N_{PH}=2^{L_{GRD}}$ phantom nodes are also used. These phantom nodes are updated at each subiteration using meridional averages at the corresponding locations in the grid of the neighboring blade row. At the meridional interface itself, values are interchanged at each iteration. The mixing-plane phantoms methodology is presented in detail in [36]. In the present work, two different averaging procedures were used and compared, as follows:

1. *basicMPs:* area averaging of $[\bar{\rho},\bar{\rho}\widetilde{V}_i,\bar{p},\widetilde{w_i''w_j''},\varepsilon^*]$ [17]
2. *mxoutMPs:* mixed-out or stream-thrust-flux averages [43], which correspond to area averaging of $[\bar{\rho}\widetilde{V}_n,\ \bar{\rho}\widetilde{V}_i\widetilde{V}_n+\bar{p}n_i,\ \bar{\rho}\breve{h}_t\widetilde{V}_n,\ \widetilde{w_i''w_j''},\ \varepsilon^*]$, where $[n_x,n_R,n_\theta]^T$ is the unit-normal vector at the mixing-surface, and $\widetilde{V}_n=\widetilde{V}_in_i$ (the corresponding mixed-out averages are computed analytically from the above pitchwise integrals [44]). In general, important differences between these two averaging procedures are expected in presence of backflow regions at the MP.

3.7.3 Inflow/Outflow Conditions. At the inflow/outflow boundaries, it is important to apply the correct meridional averages at each spanwise station, while ensuring minimum reflexion at the boundaries. The basic idea is to describe the flowfield at the inflow or outflow boundaries as θ-Fourier series at each spanwise grid surface [45,46]

$$\underline{v}(\theta;x,R)=\sum_{n_\theta=-\infty}^{+\infty}\underline{\hat{v}}(n_\theta;x,R)e^{i n_\theta\theta};\quad \underline{\hat{v}}\in\mathbb{C} \tag{20}$$

Then, the boundary conditions are treated separately in two parts:

1. Classical reflecting boundary conditions (reservoir inflow, outflow pressure, outflow massflow, or outflow throttle conditions [35]) are applied for the meridional field ($n_\theta=0$); this is necessary to correctly apply the mean (in the sense of meridional averages) operating conditions.
2. The inhomogeneities ($n_\theta\neq 0$) are treated using the steady nonreflecting boundary conditions (NRBCs), developed by Giles [42], on the corresponding harmonics; it should be noted that the exact conditions are applied on the harmonics, without using local approximations, as suggested in the original paper by Giles [42], because these were found unsatisfactory in several cases. Of course, these quasi-3D NRBCs, applied separately on each spanwise grid surface, are only approximately nonreflecting in 3D.

For all of the computations presented in the present paper, a throttle condition [35] was applied at outflow, aiming at fixing

$$\Upsilon_o=\frac{\hat{p}_o}{\dot{m}_o}=\Upsilon_{OBJ} \tag{21}$$

where $\hat{p}_o$ is the mass-averaged outflow static pressure, and $\dot{m}_o$ the massflow at the outflow boundary (note that here $\hat{p}$ is used to define Υ, whereas in [35] the static pressure at the casing was used). This condition is used to dynamically fix, at each subiteration, the static pressure at the casing. A radial-equilibrium condition is then used to define the outflow-pressure profile ([35], p. 1772, Eq. (5)).

3.8 Mean-Flow-Multigrid Acceleration

3.8.1 Mean-Flow Multigrid. Multigrid is applied only on mean-flow variables, whereas turbulence variables are simply injected on coarser grids, and are only updated on the fine grid (no multigrid residuals for the turbulence variables). The prolongation and restriction operators are based on a characteristic multigrid [47], which conserves the upwind bias of the space discretization. The multigrid approach used is a standard FAS (full approximation scheme) method, based on a sawtooth cycle with appropriate multigrid forcing terms [39], with the following characteristics:

1. The restriction (transfer) operator from the fine to the coarse grid, for the variables, $\mathbf{T}^{2h}_{\mathfrak{w};h}$, is a simple injection operator.
2. The restriction (transfer) operator from the fine to the coarse grid, for the residuals, $\mathbf{T}^{2h}_{\mathfrak{R};h}$, is a weighted operator based on the direction of propagation of information along characteristics [47].
3. The prolongation (interpolation) operator, which is applied only to $\mathfrak{w}_{MF}$, is a simple geometric interpolation operator [47].
4. The coarse grid scheme is applied only on $\mathfrak{w}_{MF}$, with frozen turbulence.

The multigrid method equations are identical (with the appropriate definition of the operator $\mathbf{N}$ (Eq. (11)), and analogous definition of the full-iteration mean-flow operator $\mathbf{N}_{MF}$ ([16], p. 1891, Eqs. (22)) to those used by the authors for nonrotating-frame applications [16] and will not be reproduced here. The details concerning the restriction and interpolation operators, on structured grids, are given in [16] (pp. 1891–1892, Eqs. (23)–(30)), and the multigrid algorithm in [16] (p. 1892, Eqs. (31)–(36)). All of the

Downloaded 03 Jun 2010 to 171.66.16.156. Redistribution subject to ASME license or copyright; see http://www.asme.org/terms/Terms_Use.cfm

Table 1 Summary of computational grids used for the NASA_37 rotor [3,48,49]

	UH[a]	O[b]	DH[a]	TC[b]	OZ[b]	points[c]	$n^+_{w_B}$ [d]	$n^+_{w_{FP}}$ [e]
grid_B	$49\times41\times65$	$201\times45\times65$	$81\times61\times65$	$201\times11\times21$	$201\times21\times31$	1149421	<0.3	<1.5
grid_C	$49\times41\times101$	$201\times53\times101$	$81\times61\times101$	$201\times17\times31$	$201\times21\times41$	1955587	<0.3	<1.0
grid_D	$49\times41\times161$	$201\times53\times161$	$81\times61\times161$	$201\times17\times41$	$201\times21\times61$	3067042	<0.3	<0.5
grid_D_3	$49\times41\times161$	$201\times53\times161$	$81\times65\times161$	$201\times21\times41$	$201\times33\times61$	3191968	<0.3	<0.5
grid_E_3	$81\times65\times201$	$321\times69\times201$	$161\times97\times201$	$321\times21\times49$	$321\times41\times69$	9242760	<0.3	<0.5

[a]Axial × tangential × radial.
[b]Around the blade × away from blade × radial.
[c]Without O-grid points overlapped by the OZ-grid (grid topology [35], defined in Sec. 4.2.1).
[d]$n^+_{w_B}$ is nondimensional wall units [33] distance of the first grid point away from the blade surface.
[e]$n^+_{w_{FP}}$ is nondimensional wall units [33] distance of the first grid point away from the flow-path walls.

multigrid computations presented in the present work use three levels of multigrid ($L_{GRD}=3$; fine and two coarser grids).

3.8.2 Boundary Conditions Multigrid Forcing Terms. The use of a Y_{OBJ} outflow boundary condition within a multigrid computation requires caution in the estimation of the computed value of Y on coarser grids. Indeed, for a given flowfield, the evaluation of mass-flow and mass-averaged static pressure by integration on different grids, will not return grid-independent results. To avoid oscillations when going from one grid to another, a forcing term was used, quite analogous to the forcing terms of the multigrid procedure [16]. The same forcing-term method was used for the exchange of information through mixing planes.

4 Results

4.1 Configurations Studied. The performance of the present computational methodology was evaluated on two different configurations: (i) the NASA_37 compressor rotor [3,48,49] and (ii) the multistage ($3\frac{1}{2}$-stage) compressor CREATE_1 [50–52].

4.2 NASA_37 Axial Compressor Rotor. The NASA_37 transonic rotor [3,48,49] is a well-known turbomachinery test case. Experimental data for the NASA_37 transonic rotor were obtained at various measurement planes, using both LDA (Laser Doppler anemometry) and classical rake measurements of p_{t_M} and T_{t_M} (the averaging procedure $(\cdot)_M$ is described in Davis et al. [48]). This rotor has 36 blades, nominal speed 17188.7 rpm, and maximum mass flow at nominal speed $\dot{m}_{CH}=20.93\pm0.14$ kg s^{-1}. The nominal tip-clearance gap is 0.356 mm [49].

4.2.1 Grid-Convergence Study. To assess the computational grid influence on the results, computations were run on four different grids (Table 1): grid_B (1.2×10^6 points), grid_C (2×10^6 points), grid_D_3 (3.2×10^6 points), and grid_E_3 (9.3×10^6 points). Grids D_3 and E_3 are designed to allow for two coarser grids in the multigrid sequencing procedure ($L_{GRD}=3$).

The structure of the grids used in the present work consists of five domains [35]. The space outside the tip-clearance gap is discretized using an H–O–H grid, consisting of three domains: the upstream UH-grid, the O-grid around the blade, which is generated biharmonically ([35], p. 1771, Fig. 1), and the downstream DH-grid. The tip-clearance gap is discretized using an O-grid (TC-grid), also generated biharmonically [35]. The TC-grid is stretched both near the flow-path wall and at the blade tip, in order to describe correctly the boundary layers ([35], p. 1772, Fig. 2). A jetlike structure emanates from the tip-clearance gap, on the suction side of the blade and mixes with the main flow, creating a mixing zone, which persists far away from the blade. To accurately compute this part of the flow field, an O-grid (OZ-grid) was patched within the O-grid of the blade ([35], p. 1772, Fig. 2). This grid is stretched both at the flow-path wall and at the blade tip, thus accurately describing the mixing of the leakage flow with the passage flow. The blade O-grid is thus stretched only near the casing and the hub, independently of the tip-clearance gap. All stretchings of the grid near the solid walls are geometric ($(1/2)N_j$ points stretched with ratio r_j away from the blade surface, and $(1/3)N_k$ points stretched with ratio r_k away from the casing and hub surfaces). Details of the grid-generation procedure are given in [35] and Refs. therein.

Computational results using the SV–RSM [34] show reasonable agreement of the compressor characteristic predicted using the various grids (Fig. 1). Comparison of pitchwise-averaged total pressure p_{t_M}, total temperature T_{t_M}, and absolute flow angle $\alpha_{x\theta_M}$ (computed neglecting $\tilde{V}_R$, consistently with measurements), at station 4, and isentropic efficiency η_{is_M} at station 4 (Fig. 1), for the operating point at $\dot{m}=20.12$ kg s^{-1}, shows satisfactory agreement between the various grids and with experimental measurements.

In general, results obtained with grid_D_3 and the much finer grid_E_3 are in quite good agreement, indicating that grid_D_3 is reasonably near grid convergence. There is, however, a slight improvement using grid_E_3 near the casing both for T_{t_M} and $\alpha_{x\theta_M}$. The most important differences between the computations using the various grids and with measurements are observed in the p_{t_M} profile. There is still a slight difference between grid_D_3 and grid_E_3, in the p_{t_M} profile for $\varsigma<0.5$, but comparison to grid_C indicates that grid convergence is being approached. It is generally accepted that the deficit in p_{t_M} at $\varsigma=10\%$ is associated with hub leakage through the gap between the stationary and rotating parts of the hub upstream of the rotor [53], which was not modeled in the present computations. Note that results are sensitive to the particular treatment of the tip clearance and to the spanwise and pitchwise extent of the OZ patched buffer grid, where the formation of the tip vortices and their initial interaction with the main throughflow is computed (Table 1). Note also that the two coarser grids (B and C, Table 1) fail to correctly transport the peak of p_{t_M} near the hub, from the rotor outlet (although not plotted here, spanwise distributions of p_{t_M} at station 3, located near the rotor trailing edge, with all of the four grids, are in very good agreement near the hub) to station 4, further downstream (Fig. 1). This is related to insufficient spanwise/pitchwise grid resolution, in connection with the rather dissipative (but very robust) van Leer flux-vector splitting [37]. Results with the two coarser grids might be nearer grid convergence if a more accurate contact-discontinuity-resolving approximate Riemann solver were used [54].

4.2.2 Subiterative Convergence and Multigrid Acceleration. A typical behavior of the convergence of the computations is illustrated by considering grid_E_3 (Table 1) multigrid ($L_{GRD}=3$) computations with a throttle outflow boundary condition ($Y_{OBJ}=6250$ Pa s kg^{-1}) giving at convergence $\dot{m}=20.15$ kg s^{-1}, and a subiteration strategy $[CFL, CFL^*, r_{OBJ}]=[150, 15, -2]$ (Fig. 2). The evolution of mass flow at rotor inflow $\dot{m}_i$ and outflow $\dot{m}_o$ indicates (Fig. 2) that convergence of the computations is

Downloaded 03 Jun 2010 to 171.66.16.156. Redistribution subject to ASME license or copyright; see http://www.asme.org/terms/Terms_Use.cfm

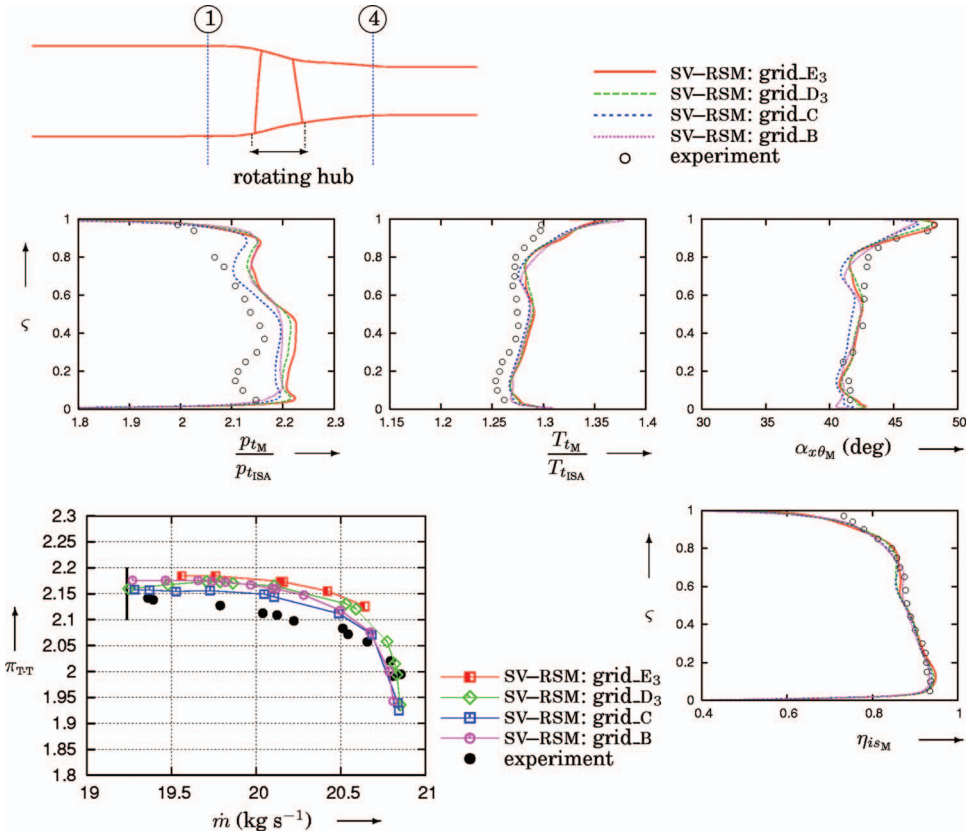

Fig. 1 Grid-convergence study of computations with the SV–RSM [34] of the NASA_37 rotor [3,48,49], using progressively finer grids (1.15×10^6 points grid_B, 1.96×10^6 points grid_C, 3.19×10^6 points grid_D_3, and 9.24×10^6 points grid_E_3 (Table 1)): Operating map of total-pressure ratio $\pi_{T\text{-}T}$ between stations 1 and 4 versus mass flow $\dot{m}$, and distributions of pitchwise-averaged total pressure p_{t_M}, total temperature T_{t_M}, and absolute-flow angle $\alpha_{x\theta_M}$, at station 4, and isentropic efficiency between stations 1 and 4 η_{is_M} versus span ς ($\dot{m}=20.12$ kg s^{-1}; $T_{u_i}=3\%$; $\ell_{T_i}=5$ mm; $\delta_{TC}=0.356$ mm)

achieved, for this very fine 9.24×10^6 points grid_E_3 (Table 1), in nearly 90 CPU–h (with a 2 Gflops sustained performance). It is interesting to consider the convergence of the errors pseudonorms for the mean flow (e_{MF}; Eq. (15)) and for the turbulence variables (e_{RSM}; Eq. (16)), as a function of both the number of iterations n_{it} and of CPU time (Fig. 2). The present sample results (Fig. 2) illustrate the generally observed similarity in the convergence of e_{RSM} and e_{MF} (it is for this reason, and also because e_{RSM} is irrelevant on the coarser grids where $\mathfrak{w}_{RSM}$ is frozen, that r_{MF} was used to determine the dynamically fixed number of subiterations). Each iteration (n_{it}) corresponds to a full multigrid sawtooth cycle [39], and the computational time per iteration is variable because the number of subiterations $M_{it}(n_{it},\ell_{GRD})$ is dynamically adjusted at every iteration and on each grid of the multigrid sequence ($\ell_{GDQ}=1,2,3$; 1 corresponding to the fine grid, and 3 to the coarsest multigrid level), to obtain $r_{MF}(n_{it},\ell_{GRD})\leq r_{OBJ}$ (in the present computations $r_{OBJ}=-2$; Fig.2). The number of subiterations $M_{it}(n_{it},\ell_{GRD})$ varies from $M_{it}\in[35,45]$ at the early stages of the iterations to $M_{it}\in[10,15]$ at convergence (Fig. 2). Because of this large variation of $M_{it}(n_{it},\ell_{GRD})$ the computational cost per iteration may vary by a factor of 3–4. Practical experience with the method [15,16] suggests that using an increment-convergence tolerance to dynamically adjust the number of subiterations greatly enhances robustness and convergence behavior. As noted in [15], computational stability loss, induced by the approximate Jacobians and the approximate solution of the linear system (Eqs. (10)), is compensated by using a sufficient number of subiterations (sufficiently high $|r_{OBJ}|$).

The performance of the multigrid acceleration is evaluated by comparing the convergence of monogrid ($L_{GRD}=1$) and multigrid ($L_{GRD}=3$) computations using two wall-normal-free RSMs (SV–RSM [34] and WNF–LSS–RSM [11]) and the Launder–Sharma $k-\varepsilon$ two-equation model [33], on the 3.2×10^6 points grid_D_3 (Fig. 3). Mass flow at rotor inlet $\dot{m}_i$, mass-averaged total pressure at rotor outlet $\hat{p}_{t_o}$, and entropy at rotor outlet $\hat{s}_o-s_{ISA}$ (ISA=International Standard Atmosphere) are normalized by their respective values at convergence of the computations, so that convergence is achieved when the plotted curves reach a value of 1 note the dilated plot scale, ranging from [±0.2%] to [±0.5%], (depending on the observed quantity (Fig. 3). Examination of the convergence of these quantities as a function of CPU time (2 Gflops sustained performance) indicates that a speed-up of 3 is achieved by the multigrid acceleration, independently of the turbulence model used; (Fig. 3), corroborating analogous conclusions from the application of the present computational methodology to various nonturbomachinery configurations [16].

It is interesting to note that although there is some noise in the monogrid computations (Fig. 3) because of the aggressive quasi-Newton iteration strategy used QN[CFL*,r_{OBJ}]=[10,−2] (less aggressive and slower to converge, LDTS iteration strategies, e.g., [CFL,CFL*,r_{OBJ}]=[150,15,−2] suppress this noise). The multigrid acceleration procedure effectively filters out this noise, even with the aggressive QN[10,-2] strategy (Fig. 3). Comparing the

Downloaded 03 Jun 2010 to 171.66.16.156. Redistribution subject to ASME license or copyright; see http://www.asme.org/terms/Terms_Use.cfm

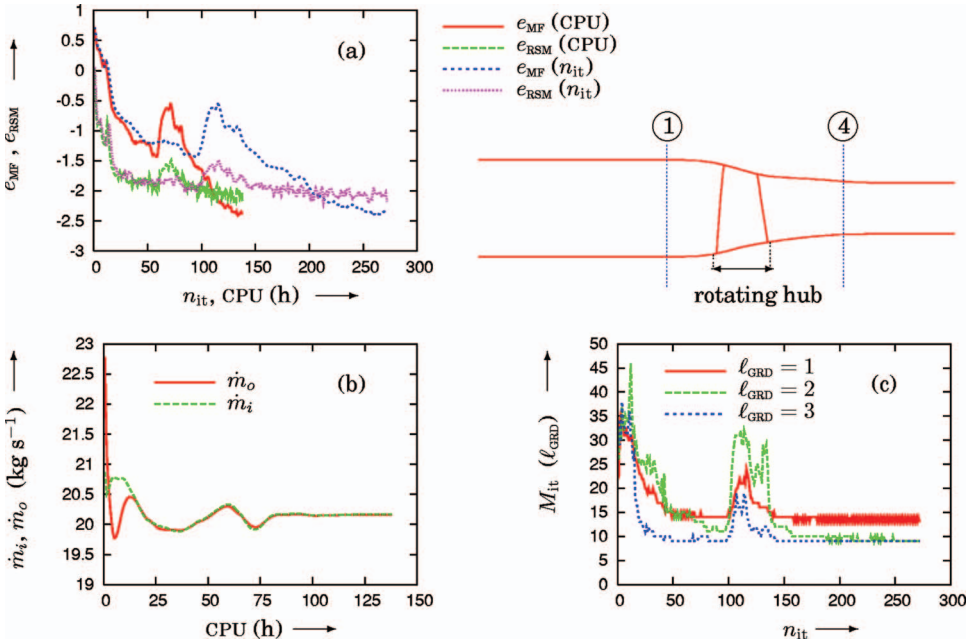

Fig. 2 Convergence (*a*) of the error pseudonorms for the mean flow (e_{MF}, Eq. (15)) and for the turbulence variables (e_{RSM}; Eq. (16)), as a function of both the number of iterations n_{it} and of CPU time (2 Gflops sustained performance), (*b*) of mass flow at rotor inflow $\dot{m}_i$ and outflow $\dot{m}_o$ versus CPU, and (*c*) of the number of subiterations $M_{it}(n_{it}, \ell_{GRD})$ required for an error reduction of $r_{MF} \leq r_{OBJ} = -2$ on each grid, for multigrid ($L_{GRD}=3$; [CFL, CFL*, r_{OBJ}]=[150, 15, −2]) computations of the NASA_37 rotor [3,48,49] using the SV–RSM [34] ($\Upsilon_{OBJ}=6250$ Pa s kg^{-1}; $\dot{m}=20.12$ kg s^{-1}; $T_{u_i}=3\%$; $\ell_{T_i}=5$ mm; $\delta_{TC}=0.356$ mm; 9.24×10^6 points grid_E_3; Table 1)

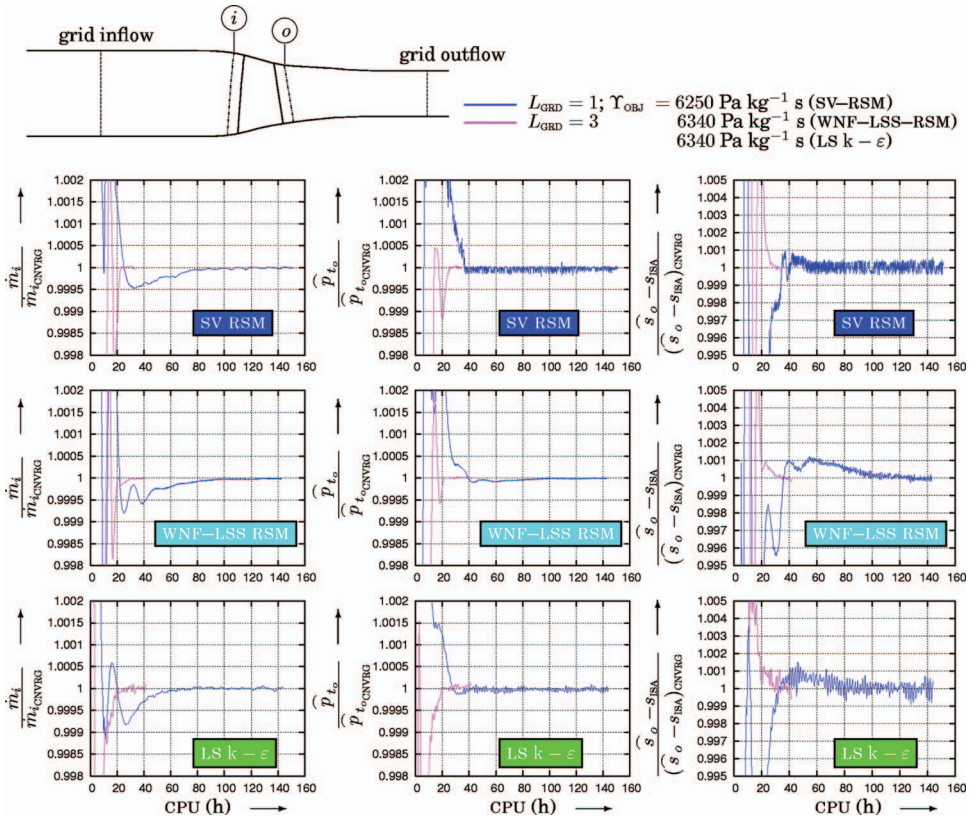

Fig. 3 Convergence as a function of CPU-time (2 Gflops sustained performance) of mass flow at rotor inlet $\dot{m}_i$, mass-averaged total pressure at rotor outlet $\hat{p}_{t_o}$, and entropy at rotor outlet $\hat{s}_o - s_{ISA}$, for monogrid ($L_{GRD}=1$) and multigrid ($L_{GRD}=3$) computations of the NASA_37 rotor [3,48,49], using two wall-normal-free RSMs (SV–RSM [34] and WNF–LSS–RSM [11]) and the Launder-Sharma $k-\varepsilon$ two-equation model [33], using appropriate Υ_{OBJ} throttle boundary conditions ($\dot{m}=20.12$ kg s^{-1}; $T_{u_i}=3\%$; $\ell_{T_i}=5$ mm; $\delta_{TC}=0.356$ mm; 3.2×10^6 points grid_D_3; $QN[CFL^*, r_{OBJ}]=[10, -2]$)

Downloaded 03 Jun 2010 to 171.66.16.156. Redistribution subject to ASME license or copyright; see http://www.asme.org/terms/Terms_Use.cfm

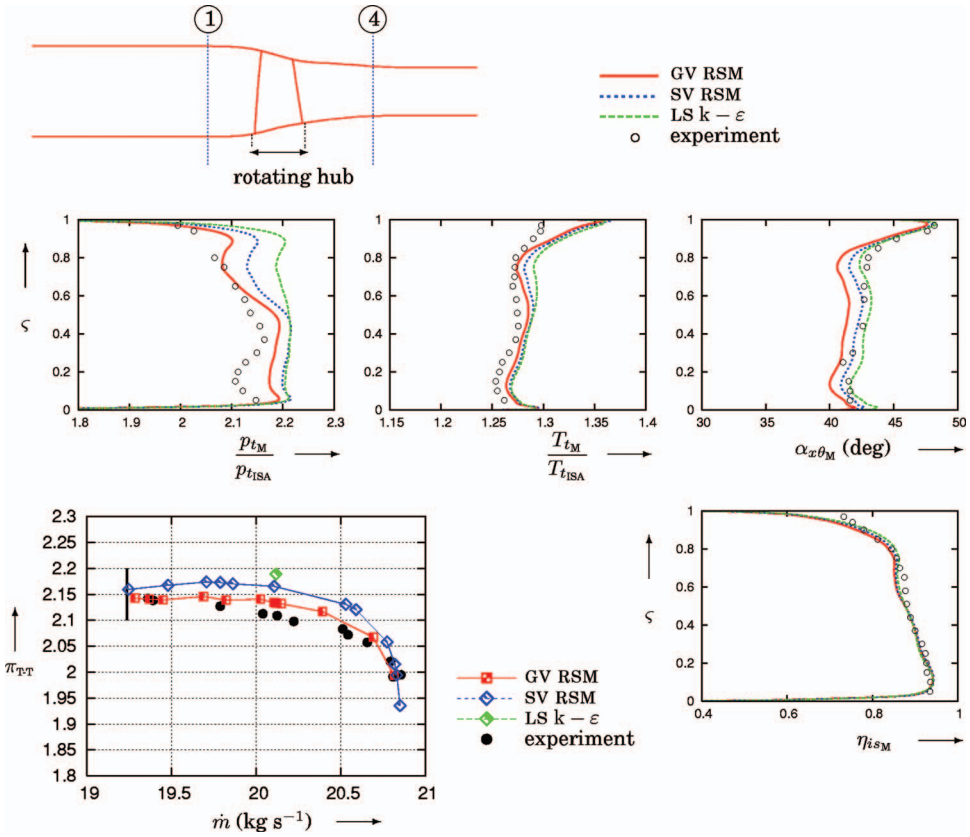

Fig. 4 Comparison of computed and measured operating map of total-pressure ratio $\pi_{T\text{-}T}$ between stations 1 and 4 versus mass flow $\dot{m}$, and spanwise (ς) distributions of pitchwise-averaged absolute-flow angle $\alpha_{x\theta_M}$, total pressure p_{t_M} and total temperature T_{t_M} at station 4, and isentropic efficiency between stations 1 and 4 η_{is_M}, of the NASA_37 rotor [3,48,49], using two wall-normal-free RSMs (GV–RSM [25] and SV–RSM [34]) and the Launder–Sharma $k-\varepsilon$ two-equation model [33] ($\dot{m}$=20.12 kg s^{-1}; T_{u_i}=3%; ℓ_{T_i}=5 mm; δ_{TC}=0.356 mm; 3.2×10^6 points grid_D_3)

CPU time to convergence with the various turbulence models (Fig. 3) indicates that the RSM closures require practically the same time as the lower-level two-equation $k-\varepsilon$ model, substantiating both the efficiency of the numerical method (essentially LDTS with dynamically fixed number of subiterations, combined with carefully designed approximate Jacobians [15,16]) and the robustness of the proposed RSMs.

4.2.3 Comparison of Turbulence Models. Computational results obtained with two wall-normal-free RSMs (GV–RSM [25] and SV–RSM [34]) and with the Launder–Sharma $k-\varepsilon$ two-equation model [33], are compared to experimental measurements (Fig. 4) on grid_D_3, which was shown to be reasonably grid converged (cf. Sec. 4.2.1, Fig. 1). Comparison of computed and measured compressor operating map (Fig. 4) shows noticeable differences among the three models. The GV–RSM [25] gives the best prediction of the compressor characteristic, compared to measurements (Fig. 4). The SV–RSM [34] systematically predicts higher values for the pressure ratio $\pi_{T\text{-}T}$, for the entire mass-flow range (Fig. 4), and the Launder–Sharma $k-\varepsilon$ two-equation model [33] even higher (Fig. 4). Detailed comparisons of spanwise distributions of $\alpha_{x\theta_M}$, T_{t_M}, and η_{is_M}, show quite close agreement among all three models and with measurements (Fig. 4). The $\alpha_{x\theta_{xM}}$ predictions with all three models are within the experimental measurements uncertainty of ±1 deg [55]. Concerning T_{t_M} the difference between computations and measurements for $\varsigma \in [0,0.9]$ is ~3 K (which is larger than the experimental uncertainty of ±0.6 K [55]), the GV–RSM [25] being closer to the experimental values, although all three models predict too high T_{t_M} values near the casing ($\varsigma > 0.9$) and, as a consequence, too low η_{is_M} values (Fig. 4). The main differences between predictions with the three models, and the most significant discrepancies with measurements, are observed in the spanwise distributions of p_{t_M} (Fig. 4). The Launder–Sharma $k-\varepsilon$ two-equation linear model [33] predicts an almost uniform p_{t_M} profile (with the exception of the hub and casing boundary layers), in disagreement with measurements (Fig. 4). The two RSM models correctly predict the p_{t_M} slope for the upper part of the span ($\varsigma > 0.4$), the GV–RSM [25] being quite close to the experimental values. For the lower part of the span ($\varsigma < 0.4$), the GV–RSM [25] gives the best overall prediction, while the SV–RSM [34] results are very close to those obtained with the Launder–Sharma $k-\varepsilon$ [33]. As noted earlier, the lower part of the span ($\varsigma \leq 0.3$) is influenced by mass flow through the gap between the stationary and rotating parts of the hub [53], which was not modeled in the present computations.

The main difference between the two RSMs used is the functional dependence of the coefficient of the isotropization-of-production model for the rapid part of the redistribution tensor ϕ_{ij} on the Lumley flatness parameter A [11,34]. Both RSMs use the same ε-equation, and give very similar results for simple shear flows, but the GV–RSM [25] coefficient was optimized to correctly predict separated flows, the SV–RSM [34] underpredicting separation.

4.3 Multistage Axial Compressor. Computations are also

Downloaded 03 Jun 2010 to 171.66.16.156. Redistribution subject to ASME license or copyright; see http://www.asme.org/terms/Terms_Use.cfm

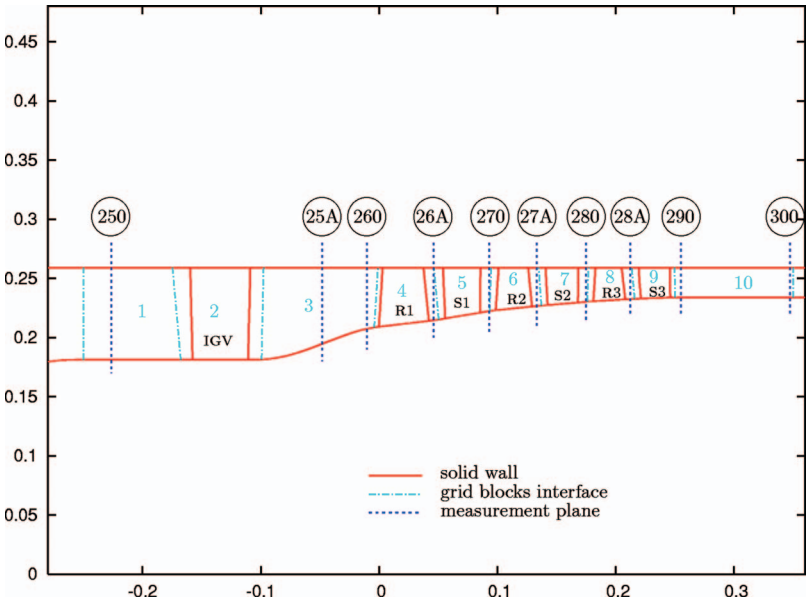

Fig. 5 Meridional view of the CREATE_1 $3\frac{1}{2}$ stage compressor [50–52], showing measurement planes and interfaces between grid blocks ($\ell_{BR}=1,\ldots,10$)

presented for the multistage ($3\frac{1}{2}$-stage) axial-flow compressor CREATE_1 [50–52], which is representative of the rear block of HP compressors [52]. Experimental data were obtained at various measurement planes (Fig. 5), using both LDA (laser Doppler anemometry) and classical probe measurements [50–52]. This configuration is included to illustrate the capacity of the multigrid procedure to accelerate the convergence of the computations in a multistage environment (Figs. 5 and 6). Computations were run at design speed ($N_{DSGN}=11{,}543$ rpm), on the 11×10^6 points grid_C_3 (Table 2), designed to allow for two coarser grids in the multigrid sequencing procedure ($L_{GRD}=3$).

The computational domain is separated in blocks and subdomains. The CREATE_1 $3\frac{1}{2}$-stage compressor (Fig. 5) is made up of $N_{BR}=7$ blade-rows ($n_{BR}=1,\ldots,N_{BR}$). The computational grid (Figs. 5 and 6) is made up of $L_{BR}=N_{BR}+3=10$ blocks: an upstream UH-grid ($\ell_{BR}=1$), seven O-grids corresponding to the seven blade rows ($\ell_{BR}=2,4,\ldots,N_{BR}+2$), a downstream DH-grid ($\ell_{BR}=L_{BR}=10$), and an intermediate IH-grid ($\ell_{BR}=3$) between the IGV and R1 (Figs. 5 and 6).

Several blocks are resolved using a single subdomain with a structured grid (UH-grid, IH-grid, DH-grid, O-grids around the stators). The three rotors (R1, R2, R3) have tip clearances at the casing, and the IGV is cantilevered with a tip clearance at the hub (Fig. 5). These blocks are meshed using three subdomains, as for the NASA_37 rotor (O-grid, TC-grid, and OZ-grid; cf. Sec. 4.2.1). The 3D grid is generated in each block using a biharmonic mesh-generation methodology [35,36].

This 11×10^6 point grid_C_3 (Table 2) is rather coarse, compared to the grids used for the NASA_37 rotor (cf. Sec. 4.2.1), since it is similar to the NASA_37 C (Table 1). The grid-convergence study for the NASA_37 rotor (Sec. 4.2.1) indicates that reasonable results can be expected using this grid (Fig. 1).

Results were obtained with the SV–RSM [34] and with the Launder–Sharma $k-\varepsilon$ two-equation model [33], using multigrid ($L_{GRD}=3$) computations on grid_C_3 (Table 2) with an aggressive QN[CFL*,r_{OBJ}]=[20,−2] subiteration strategy (Fig. 7). For the

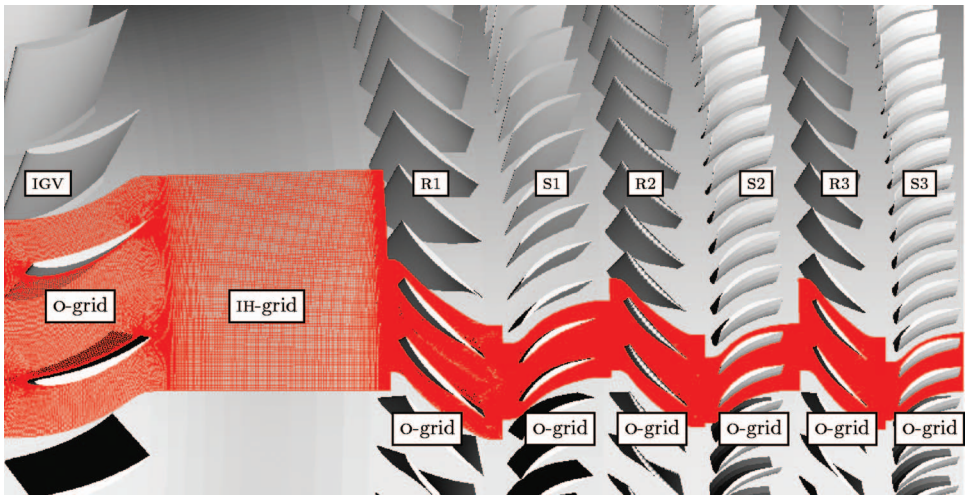

Fig. 6 View of the computational grid at midspan of the CREATE_1 $3\frac{1}{2}$ stage compressor [50–52] (11×10^6 points grid_C_3)

Downloaded 03 Jun 2010 to 171.66.16.156. Redistribution subject to ASME license or copyright; see http://www.asme.org/terms/Terms_Use.cfm

Table 2 Computational grid for the CREATE_1 $3\frac{1}{2}$ stage compressor [50–52] (11,049,714 points grid_C_3; without O-grid points overlapped by the OZ-grid)

ℓ_{BR}	n_{BR}	n_D	N_B	N_i	N_j	N_k	r_j	r_k	N_{ijk}
1	1	1 (UH)	32	41	41	101		1.265	169781
2	1	2 (O)	32	201	53	101	1.35	1.265	1075953
		3 (TC)		201	21	33		1.430	139293
		4 (OZ)		201	33	49			325017
3	1	5 (IH)	32	121	41	101		1.265	501061
4	2	6 (O)	64	201	53	101	1.35	1.265	1075953
		7 (TC)		201	21	33		1.430	139293
		8 (OZ)		201	33	49			325017
5	3	9 (O)	96	201	53	101	1.35	1.265	1075953
6	4	10 (O)	80	201	53	101	1.35	1.265	1075953
		11 (TC)		201	21	33		1.430	139293
		12 (OZ)		201	33	49			325017
7	5	13 (O)	112	201	53	101	1.35	1.265	1075953
8	6	14 (O)	80	201	53	101	1.35	1.265	1075953
		15 (TC)		201	21	33		1.265	139293
		16 (OZ)		201	33	49			325017
9	7	17 (O)	128	201	53	101	1.35	1.265	1075953
10	7	18 (DH)	128	301	57	101		1.265	1732857

Notes: cf. Nomenclature of Table 1.
Grid topology [35] defined in Secs. 4.3 and 4.2.1.
r_j, r_k: geometric progression ratios j-wise and k-wise.
ℓ_{BR}: grid-block index.
n_D: grid-domain index.
n_{BR}: blade-row.
N_B: number of blades.

$\dot{m}=0.96\dot{m}_{CH}$ ($\dot{m}_{CH}$ is the chocking mass flow at design speed) operating point (Fig. 7), SV–RSM [34] computations were run using two different mixing-plane averages (BASIC and MXOUT MPs; cf. Sec. 3.7.2), to evaluate the relative importance of the turbulence closure and of the MP model on the results.

4.3.1 Multigrid Acceleration. To evaluate the efficiency of multigrid acceleration, monogrid ($L_{GRD}=1$) computations were also run (Fig. 8), using the SV–RSM [34], with the same subiteration strategy, and with a throttle outflow boundary condition ($\Upsilon_{OBJ}=23{,}150$ Pa kg^{-1}) giving at convergence $\dot{m}=0.96\dot{m}_{CH}$.

Mass flow at the compressor inlet $\dot{m}_i$, mass-averaged total pressure at the compressor outlet $\hat{p}_{t_o}$, and entropy at the compressor outlet $\hat{s}_o-s_{ISA}$ are normalized by their respective values at convergence of the computations, so that convergence is achieved when the plotted curves reach a value of 1 (note the dilated plot scale, ranging from [±2%] to [±4%], depending on the observed quantity (Fig. 8)). Examination of the convergence of these quantities as a function of CPU time (2 Gflops sustained performance) indicates that a speed-up of 3 is achieved by the multigrid acceleration (Fig. 8), as was the case for the NASA_37 rotor (Fig. 3). The monogrid computations contain a lot of noise (Fig. 8) because of the aggressive quasi-Newton iteration strategy used QN[CFL*,r_{OBJ}]=[20,−2]. The multigrid acceleration procedure effectively filters out this noise (Fig. 8).

4.3.2 Comparison to Measurements. Comparison of computed

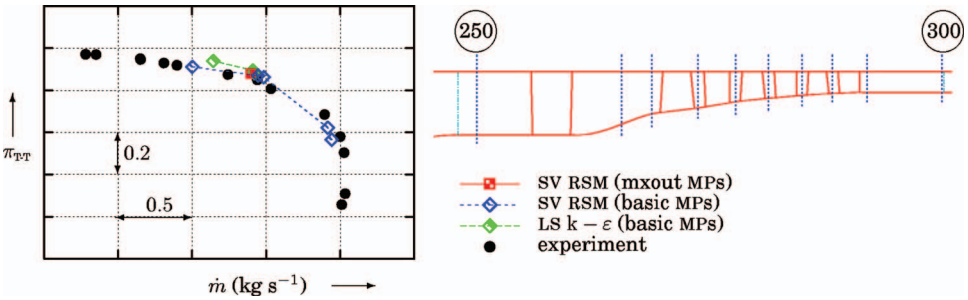

Fig. 7 Experimental and computed, using the SV–RSM [34] (both with basic and mxout MPs; cf. Sec. 3.7.2) and the Launder-Sharma k−ε two-equation model [33], performance map (total-pressure-ratio $\pi_{T\text{-}T}$ between planes 300 and 250 versus massflow $\dot{m}$) of the CREATE_1 $3\frac{1}{2}$ stage compressor [50–52] (T_{u_i}=2%; ℓ_{T_i}=10 mm; δ_{TC}=0.3 mm, 0.53 mm, 0.57 mm, 0.52 mm (IGV, R1, R2, R3); QN[CFL*,r_{OBJ}]=[20,−2]; L_{GRD}=3; 11×10^6 points grid_C_3; Table 2)

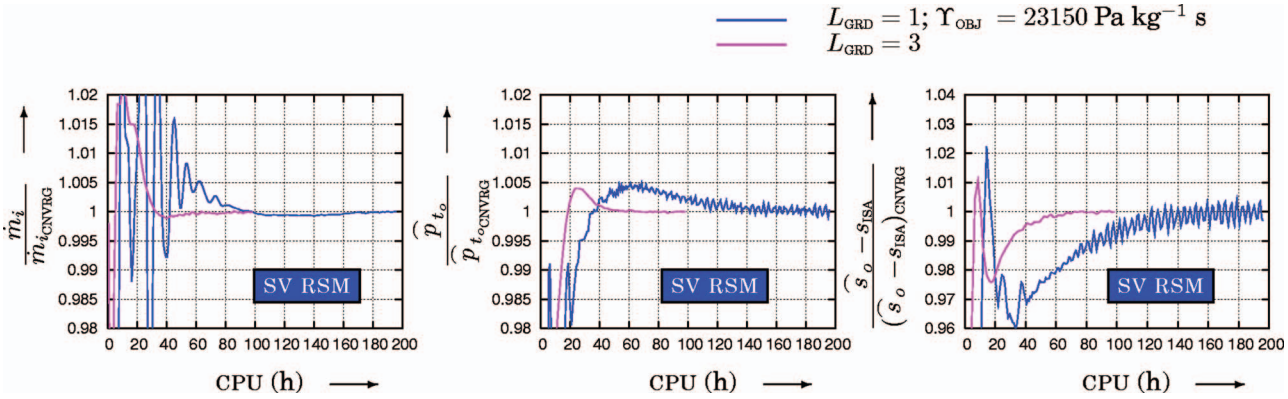

Fig. 8 Convergence as a function of CPU time (2 Gflops sustained performance) of mass flow at compressor inlet $\dot{m}_i$, mass-averaged total pressure at compressor outlet $\hat{p}_{t_o}$, and entropy at compressor outlet $\hat{s}_o-s_{ISA}$, for monogrid (L_{GRD}=1) and multigrid (L_{GRD}=3) computations, using the SV–RSM [34] with basic MPs (cf. Sec. 3.7.2), of the CREATE_1 $3\frac{1}{2}$ stage compressor [50–52] ($\dot{m}=0.96\dot{m}_{CH}$, Υ_{OBJ}=23,150 Pa s kg^{-1}; T_{u_i}=2%; ℓ_{T_i}=10 mm; δ_{TC}=0.3 mm, 0.53 mm, 0.57 mm, 0.52 mm (IGV, R1, R2, R3); QN[CFL*,r_{OBJ}]=[20,−2]; 11×10^6 points grid_C_3; Table 2)

Downloaded 03 Jun 2010 to 171.66.16.156. Redistribution subject to ASME license or copyright; see http://www.asme.org/terms/Terms_Use.cfm

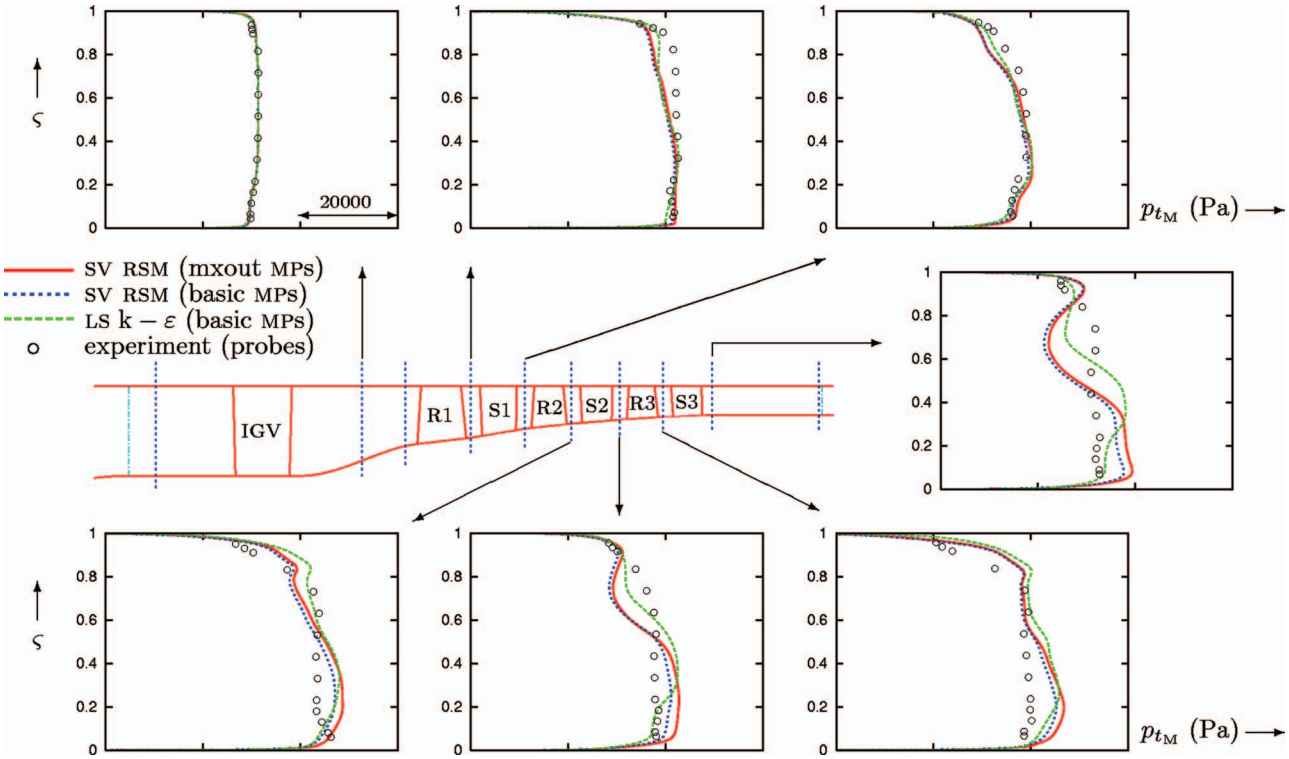

Fig. 9 Comparison of computed and measured spanwise (ς) distributions of pitchwise-averaged total pressure p_{t_M} for the CREATE_1 $3\frac{1}{2}$ stage compressor [50–52], using the SV–RSM [34] (both with BASIC and MXOUT MPS; cf. Sec. 3.7.2) and the Launder–Sharma $k-\varepsilon$ two-equation model [33] ($\dot{m}=0.96\dot{m}_{CH}$, $\Upsilon_{OBJ}=23{,}150$ Pa s kg^{-1}; $T_{u_i}=2\%$; $\ell_{T_i}=10$ mm; $\delta_{TC}=0.3$ mm, 0.53 mm, 0.57 mm, 0.52 mm (IGV, R1, R2, R3); $L_{GRD}=3$; QN[CFL*, r_{OBJ}]=[20, −2]; 11×10^6 points grid_C$_3$; Table 2)

(using the two turbulence closures and the two MP models) and measured compressor performance map (total pressure ratio $\pi_{T\text{-}T}$ between planes 300 and 250 [Fig. 5] versus mass flow $\dot{m}$) shows satisfactory agreement (Fig. 7). For the $\dot{m}=0.96\dot{m}_{CH}$ operating point, for which detailed comparisons are presented in the following, all three approaches give very similar results, in close agreement with experiment (Fig. 7).

LDA measurements for V_x and V_θ were acquired [50,51] at planes (Fig. 5) 26A (R1|S1), 27A (R2|S2), 280 (S2|R3), and 28A (R3|S3), and were used to compute pitchwise-averaged experimental values for β_M, α_M, and V_{x_M} [52]. Probe measurements were acquired [50,51] at planes (Fig. 5) 25A, 26A, 270, 27A, 280, 28A, and 290, and were used to compute pitchwise-averaged experimental values for p_{t_M}, T_{t_M}, and α_M [52]. Comparison of computed (using the three turbulence closures) and measured spanwise distributions of pitchwise-averaged total pressure p_{t_M}(Fig. 9), pitchwise-averaged absolute-flow angle α_M (Fig. 10), pitchwise-averaged total temperature T_{t_M} (Fig. 11), pitchwise-averaged relative-flow angle β_M (Fig. 12), and pitchwise-averaged axial velocity V_{x_M} (Fig. 13), show satisfactory overall agreement.

Comparison of computed spanwise distributions of β_M with LDA measurements shows quite satisfactory agreement, for all of the 3 approaches used (Fig. 12). There are some discrepancies ($\sim$5 deg for $\varsigma\in[0.75,0.95]$ at the S2|R3 interface). The SV–RSM [34] computations with BASIC or MXOUT MPS give quasi-identical results (Fig. 12).

Comparison of computed spanwise distributions of V_{x_M} to LDA measurements shows satisfactory agreement (Fig. 13), with the exception of the near-casing region ($\varsigma>0.7$). The SV–RSM [34] computations with basic or mxout MPs give quasi-identical results (Fig. 13).

Comparison of computed spanwise distributions of α_M to both LDA and probe measurements indicates quite good agreement with LDA measurements, at the rotor-exit planes (Fig. 10). There are significant differences between the LDA and the probe measurements at the rotor-exit planes (Fig. 10), for ($\varsigma<0.5$). The very good agreement of the computations with the LDA measurements, together with the intrusive character of the probe measurements, suggest that the LDA measurements should be considered more reliable. Again, the SV–RSM [34] computations with BASIC or MXOUT MPs give quasi-identical results (Fig. 10).

Comparison of computed spanwise distributions of p_{t_M} to probe measurements shows good agreement (Fig. 9), except at the S2|R3 interface and at the S3 exit. The SV–RSM [34] computations with BASIC or MXOUT MPs are again in close agreement one with another, despite some larger discrepancies compared to β_M, α_M, and V_{x_M}.

The spanwise distributions of T_{t_M} exhibit the larger differences between the two MP averaging procedures (Fig. 11) The MXOUT MPs systematically predict higher values of T_{t_M} and, ultimately, give the best prediction at the compressor exit (Fig. 11).

Overall (Figs. 7 and 9–13), the SV–RSM [34] with MXOUT MPs, gives consistently the best results. It is however difficult to draw definitive conclusions from these comparisons because, for the operating point studied in the present work, for which no extended separation is observed, the linear two-equation Launder–Sharma k-ε model [33] performs quite satisfactorily, but also because the deterministic stresses [56] due to the rotor/stator interactions were not modeled.

4.4 A Note on Modeling. As noted earlier, it is beyond the scope of this paper to evaluate different turbulence closures or mixing-plane averages. To do this grid-converged computations of many configurations, including all important technological details (such as hub-leakage flows, cf. Sec. 4.2) and systematic comparison to measurements, are necessary. From the results obtained in

Downloaded 03 Jun 2010 to 171.66.16.156. Redistribution subject to ASME license or copyright; see http://www.asme.org/terms/Terms_Use.cfm

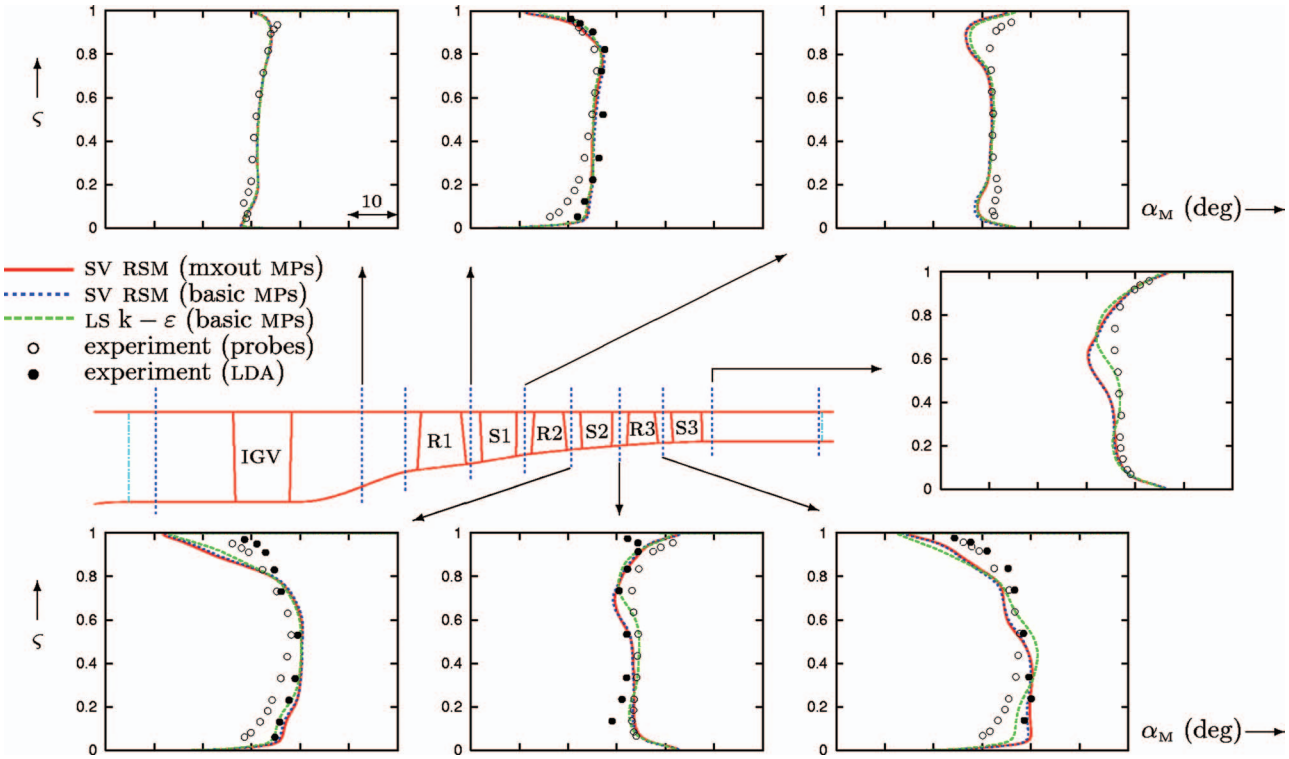

Fig. 10 Comparison of computed and measured spanwise (ς) distributions of pitchwise-averaged absolute-flow angle α_M for the CREATE_1 $3\frac{1}{2}$ stage compressor [50,52], using the SV–RSM [34] (both with BASIC and MXOUT MPs; cf. Sec. 3.7.2) and the Launder-Sharma $k-\varepsilon$ two-equation model [33] ($\dot{m}=0.96\dot{m}_{CH}$, $\Upsilon_{OBJ}=23{,}150$ Pa s kg^{-1}; $T_{u_i}=2\%$; $\ell_{T_i}=10$ mm; $\delta_{TC}=0.3$ mm, 0.53 mm, 0.57 mm, 0.52 mm (IGV, R1, R2, R3); $L_{GRD}=3$; QN[CFL*, r_{OBJ}]=[20, −2]; 11×10^6 points grid_C$_3$; Table 2)

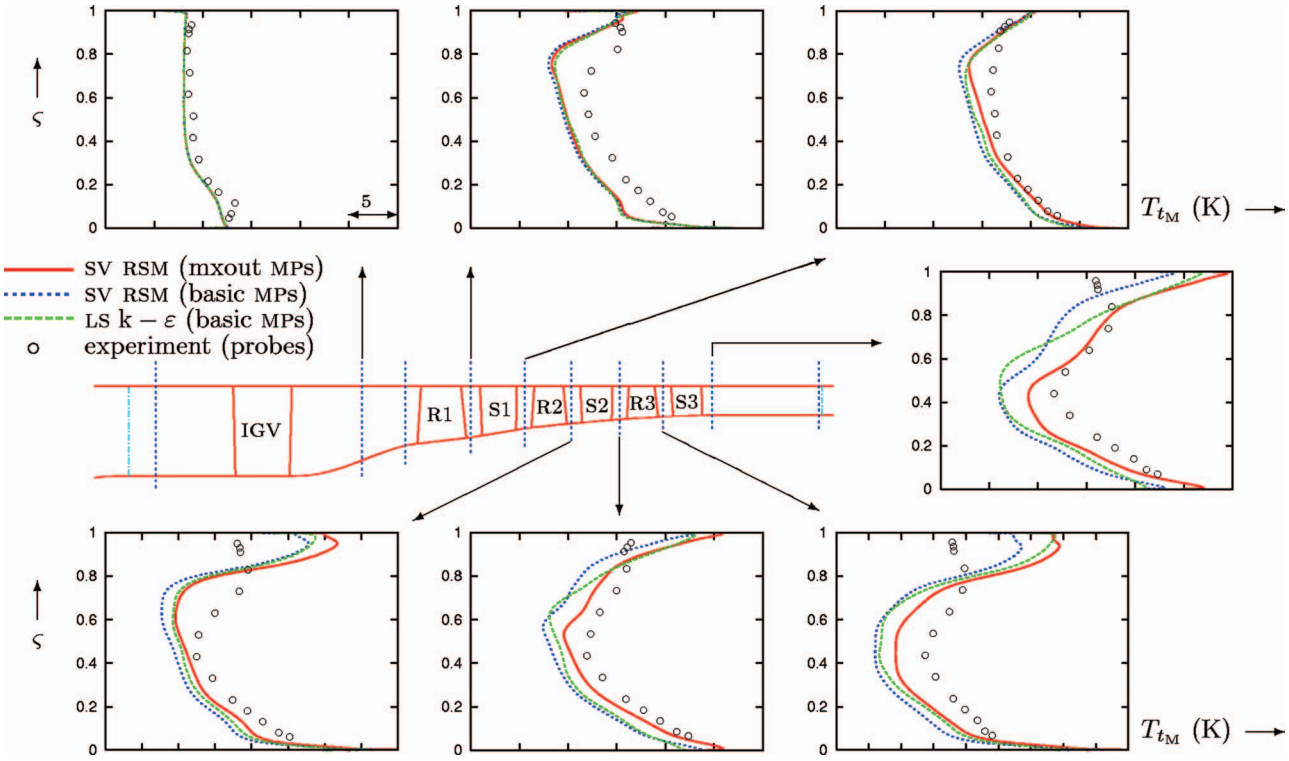

Fig. 11 Comparison of computed and measured spanwise (ς) distributions of pitchwise-averaged total temperature T_{t_M} for the CREATE_1 $3\frac{1}{2}$ stage compressor [50,52], using the SV–RSM [34] (both with BASIC and MXOUT MPs; cf. Sec. 3.7.2) and the Launder–Sharma $k-\varepsilon$ two-equation model [33] ($\dot{m}=0.96\dot{m}_{CH}$, $\Upsilon_{OBJ}=23{,}150$ Pa s kg^{-1}; $T_{u_i}=2\%$; $\ell_{T_i}=10$ mm; $\delta_{TC}=0.3$ mm, 0.53 mm, 0.57 mm, 0.52 mm (IGV, R1, R2, R3); $L_{GRD}=3$; QN[CFL*, r_{OBJ}]=[20, −2]; 11×10^6 points grid_C$_3$; Table 2)

Downloaded 03 Jun 2010 to 171.66.16.156. Redistribution subject to ASME license or copyright; see http://www.asme.org/terms/Terms_Use.cfm

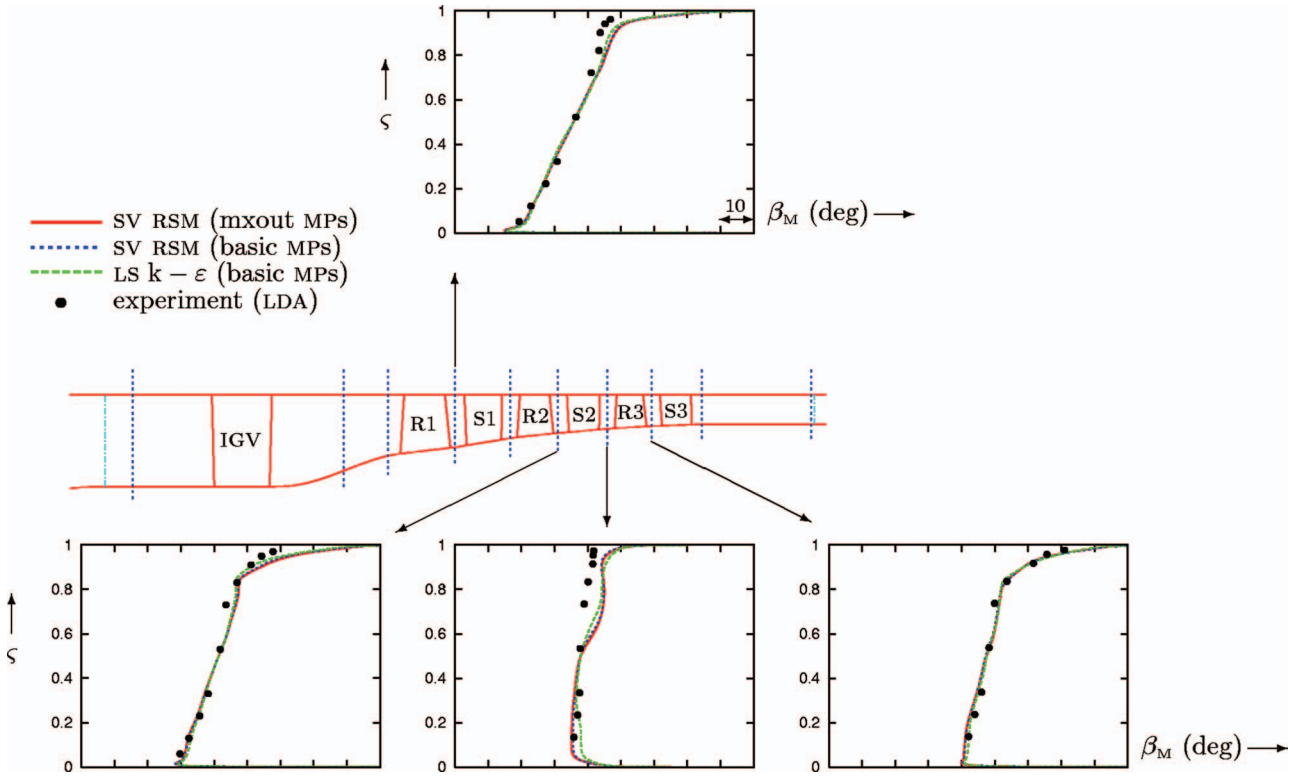

Fig. 12 Comparison of computed and measured spanwise (ς) distributions of pitchwise-averaged relative-flow-angle β_M for the CREATE_1 $3\frac{1}{2}$ stage compressor [50,52], using the SV–RSM [34] (both with BASIC and MXOUT MPs; cf. Sec. 3.7.2) and the Launder–Sharma $k-\varepsilon$ two-equation model [33] ($\dot{m}=0.96\dot{m}_{CH}$, $Y_{OBJ}=23{,}150$ Pa s kg^{-1}; $T_{u_i}=2\%$; $\ell_{T_i}=10$ mm; $\delta_{TC}=0.3$ mm, 0.53 mm, 0.57 mm, 0.52 mm (IGV, R1, R2, R3); $L_{GRD}=3$; QN[CFL*, r_{OBJ}]=[20, −2]; 11×10^6 points grid_C$_3$; Table 2)

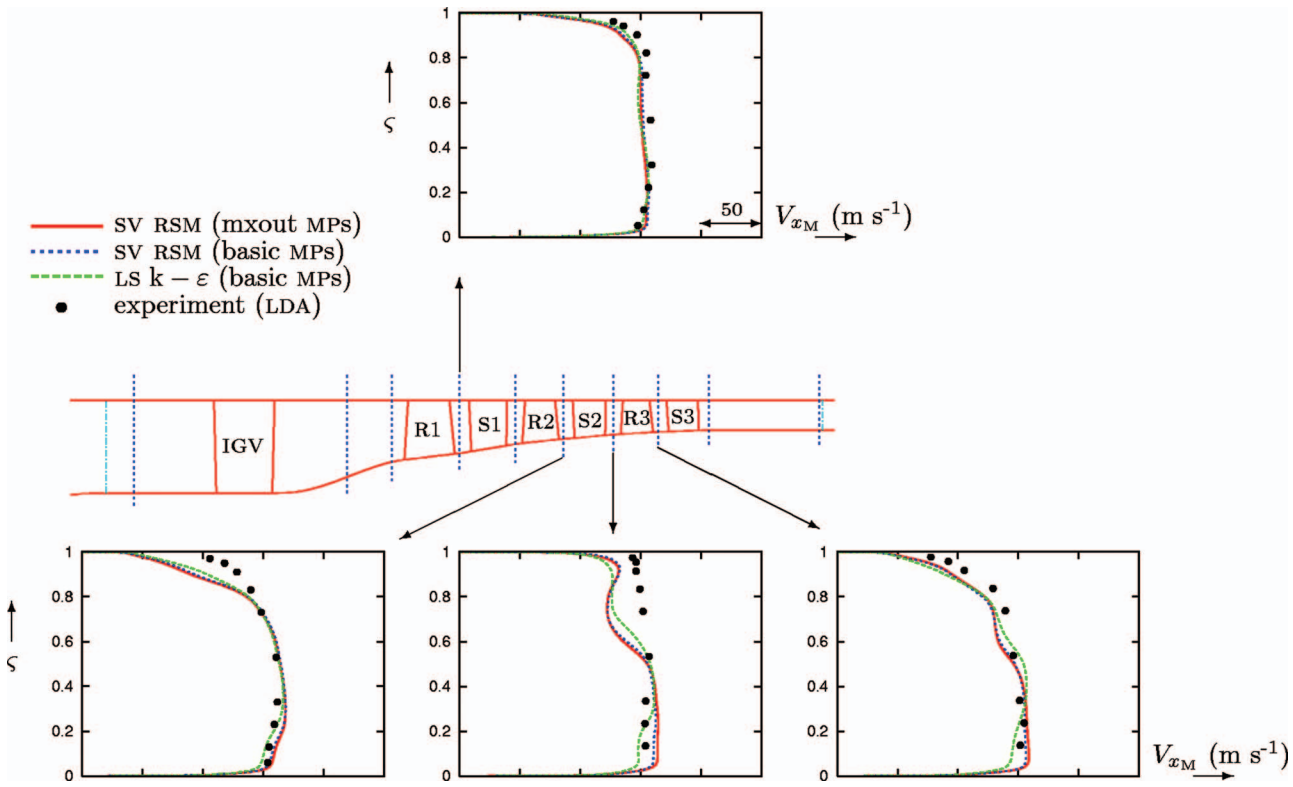

Fig. 13 Comparison of computed and measured spanwise (ς) distributions of pitchwise-averaged axial-velocity V_{x_M} for the CREATE_1 $3\frac{1}{2}$ stage compressor [50–52], using the SV–RSM [34] (both with BASIC and MXOUT MPs; cf. Sec. 3.7.2) and the Launder–Sharma $k-\varepsilon$ two-equation model [33] ($\dot{m}=0.96\dot{m}_{CH}$, $Y_{OBJ}=23{,}150$ Pa s kg^{-1}; $T_{u_i}=2\%$; $\ell_{T_i}=10$ mm; $\delta_{TC}=0.3$ mm, 0.53 mm, 0.57 mm, 0.52 mm (IGV, R1, R2, R3); $L_{GRD}=3$; QN[CFL*, r_{OBJ}]=[20, −2]; 11×10^6 points grid_C$_3$; Table 2)

Downloaded 03 Jun 2010 to 171.66.16.156. Redistribution subject to ASME license or copyright; see http://www.asme.org/terms/Terms_Use.cfm

the present paper, it appears that RSMs can improve the prediction of flows dominated by large separation (e.g., NASA_37 rotor). For flows that are not dominated by large separation (e.g., CREATE compressor), results obtained using a linear k-ε closure are reasonably good; thus, the improvement is marginal. These conclusions are corroborated by many previous studies on nonturbomachinery flows [11,34]. Current work on turbulence modeling by many researchers [9,57,58] focuses on the development of continuous RANS-to-DNS (VLES) approaches, based on anisotropic multiequation models for the unresolved stresses. The extension of wall-normal-free RSMs from RSM–RANS to RSM–VLES approaches, seems a promising area of future research [58].

5 Conclusions and Perspectives

In the present work, an efficient and robust implicit multigrid Navier–Stokes solver with seven-equation RSM closures was developed and validated by computing a transonic compressor rotor and a $3\frac{1}{2}$ stage compressor. The Reynolds-stress model (RSM) closures used are based on robust quasilinear models for redistribution, and on a wall-normal-free (WNF) formulation, completely independent of wall distances.

The numerical method is based on a subiterative LDTS iteration procedure, where the number of subiterations is dynamically determined to achieve a prescribed tolerance of increment convergence. This basic solver is augmented by multigrid applied on mean flow variables only, which consistently speeds up the computations by a factor ~ 3, independently of the turbulence model used (RSM or k-ε). It should be noted that for the complex flows and for the stretched and strongly curved computational grids used, this speed-up is quite satisfactory [59]. The numerical method, combined with the robust quasilinear WNF RSMs, is particularly efficient, the time to convergence with RSM closures being approximately the same as that of the k-ε closure, despite the larger number of turbulence-transport equations (seven instead of two). This is attributed both to some specific ingredients of the numerical method (explicit-application of realizability constraints, carefully designed approximate Jacobians for the implicit subiterations, LDTS), and to the physical representativity of the RSM closure for the strongly anisotropic flows encountered in turbomachinery, compared to the lower-level k-ε closures.

The numerical efficiency of the monogrid method could be improved by (i) the use of a nonfactored linear-system solver (GMRES), which should improve computational speed, and (ii) by the replacement of the van Leer flux-vector splitting [54] by a contact-discontinuity-resolving approximate Riemann solver (e.g., of the Harten Lax van-Leer with restored contact discontinuity (HLLC) family [54]), which should allow equivalent resolution on coarser grids. Concerning the multigrid strategy used (mean-flow multigrid), it is well known [60] that convergence can be accelerated by developing a fully coupled multigrid algorithm, including the turbulent variables.

Acknowledgment

The computations presented in this work were run at the Institut pour le Développement des Resources en Informatique Scientifique (IDRIS), where computer resources were made available by the Comité Scientifique. The numerical methodology described in the present paper was implemented in the *turbo_3D@RSM_3D* software developed by the authors. The authors are grateful to SNECMA (*Safran* Group) for permission to publish results for the CREATE compressor, and particularly to A. Touyeras and M.Vilain who provided the experimental data to the authors.

References

[1] Hah, C., and Krain, H., 1990, "Secondary Flows and Vortex Motion in a High-Efficiency Backswept Impeller at Design and Off-Design Conditions," ASME J. Turbomach., **112**(1), pp. 7–13.

[2] Sieverding, C. H., 1985. "Recent Progress in the Understanding of Basic Aspects of Secondary Flows in Turbine Blade Passages," ASME J. Eng. Gas Turbines Power, **107**, pp. 248–257.

[3] Reid, L., and Moore, R. D., 1978. "Design and Overall Performance of 4 Highly Loaded, High-Speed Inlet Stages for an Advanced High-Pressure-Ratio Core Compressor," Tech. Paper No. TP–1337, NASA, Lewis Research Center, Cleveland, Oct.

[4] Hah, C., and Loellbach, J., 1999. "Development of Hub Corner Stall and Its Influence on the Performance of Axial Compressor Blade Rows," ASME J. Turbomach., **121**(1), pp. 67–77.

[5] Volino, R. J., 2002. "Separated Flow Transition Under Simulated Low-Pressure Turbine Airfoil Conditions—Part 1: Mean-Flow and Turbulence Statistics," ASME J. Turbomach., **124**, pp. 645–655.

[6] Volino, R. J., 2002. "Separated Flow Transition Under Simulated Low-Pressure Turbine Airfoil Conditions—Part 2: Turbulence Spectra," ASME J. Turbomach., **124**, pp. 656–664.

[7] Copenhaver, W. W., Puterbaugh, S. L., and Hah, C., 1997. "Unsteady Flow and Shock Motion in a Transonic Compressor Rotor," J. Propul. Power, **13**(1), pp. 17–23.

[8] Volino, R. J., 1998. "A New Model for Freestream Turbulence Effects on Boundary Layers," ASME J. Turbomach., **120**, pp. 613–620.

[9] Speziale, C. G., 1998. "Turbulence Modeling for Time-Dependent RANS and VLES: A review," AIAA J., **36**(2), pp. 173–184.

[10] Walters, D. K., and Leylek, J. H., 2004, "A New Model for Boundary-Layer Transition Using a Single-Point RANS Approach," ASME J. Turbomach., **126**(1), pp. 193–202.

[11] Gerolymos, G. A. Sauret, E., and Vallet, I., 2004, "Contribution to the Single-Point-Closure Reynolds-Stress Modeling of Inhomogeneous Flow," Theor. Comput. Fluid Dyn., **17**(5–6), pp. 407–431.

[12] Scholz, N., ed., 1977, *Aerodynamics of Cascades*, AGARD, Neuilly-sur-Seine, No. AGARD–AG–220 in AGARDograph. (translated and revised by A. Klein from the original german *Aerodynamik der Schaufelgitter*).

[13] Chenault, C. F. Beran, P. S., and Bowersox, R. D. W., 1999, "Numerical Investigation of Supersonic Injection Using a Reynolds-Stress Turbulence Model," AIAA J., **37**(10), pp. 1257–1269.

[14] Batten, P. Craft, T. J. Leschziner, M. A., and Loyau, H., 1999, "Reynolds-Stress-Transport Modeling for Compressible Aerodynamics Applications," AIAA J., **37**(7), pp. 785–797.

[15] Chassaing, J. C. Gerolymos, G. A., and Vallet, I., 2003, "Efficient and Robust Reynolds-Stress Model Computation of 3-D Compressible Flows," AIAA J., **41**(5), pp. 763–773.

[16] Gerolymos, G. A., and Vallet, I., 2005, "Mean-Flow-Multigrid for Implicit Reynolds-Stress-Model Computations," AIAA J., **43**(9), pp. 1887–1898.

[17] Dawes, W. N., 1992, "Toward Improved Throughflow Capability: The Use of 3-D Viscous Flow Solvers in a Multistage Environment," ASME J. Turbomach., **114**, pp. 8–17.

[18] Turner, M. G., and Jennions, I. K., 1993, "An Investigation of Turbulence Modeling in Transonic Fans Including a Novel Implementation of an Implicit $k-\varepsilon$ Turbulence Model," ASME J. Turbomach., **115**(2), pp. 249–260.

[19] Jennions, I. K., and Turner, M. G., 1993, "3-D Navier-Stokes Computations of Transonic Fan Flow Using an Explicit Flow Solver and an Implicit $k-\varepsilon$ Turbulence Model," ASME J. Turbomach., **115**(2), pp. 261–272.

[20] Rhie, C. M. Gleixner, A. J. Spear, D. A. Fischberg, C. J., and Zacharias, R. M., 1998, "Development and Application of a Multistage Navier-Stokes Solver—Part I: Multistage Modeling Using Bodyforces and Deterministic Stresses," ASME J. Turbomach., **120**, pp. 205–214.

[21] LeJambre, C. R. Zacharias, R. M. Biederman, B. P. Gleixner, A. J., and Yetka, C. J., 1998, "Development and Application of a Multistage Navier-Stokes Solver—Part II: Application to a High-Pressure Compressor Design," ASME J. Turbomach., **120**, pp. 215–223.

[22] Adamczyk, J. J., 2000, "Aerodynamic Analysis of Multistage Turbomachinery Flows in Support of Aerodynamic Design," ASME J. Turbomach., **122**, pp. 189–217.

[23] Gier, J. Stubert, B. Brouillet, B., and de Vito, L., 2005, "Interaction of Shroud Leakage Flow and Main Flow in a 3-Stage LP Turbine," ASME J. Turbomach., **127**(4), pp. 649–658.

[24] Gerolymos, G. A. Neubauer, J. Sharma, V. C., and Vallet, I., 2002, "Improved Prediction of Turbomachinery Flows Using Near-Wall Reynolds-Stress Model," ASME J. Turbomach., **124**(1), pp. 86–99.

[25] Gerolymos, G. A., and Vallet, I., 2002, "Wall-Normal-Free Reynolds-Stress Model for Rotating Flows Applied to Turbomachinery," AIAA J., **40**(2), pp. 199–208.

[26] Rautaheimo, P. P. Salminen, E. J., and Sikonen, T. L., 2003, "Numerical Simulation of the Flow in the NASA Low-Speed Centrifugal Compressor," Int. J. Turbo Jet Engines, **20**, pp. 155–170.

[27] Chriss, R. M. Hathaway, M. D., and Wood, J. R., 1996, "Experimental and Computational Results From the NASA Lewis Low-Speed Centrifugal Impeller at Design and Part-Flow Conditions," ASME J. Turbomach., **118**(1), pp. 55–65.

[28] Speziale, C. G. Sarkar, S., and Gatski, T. B., 1991, "Modelling the Pressure-Strain Correlation of Turbulence: An Invariant Dynamical Systems Approach," J. Fluid Mech., **227**, pp. 245–272.

[29] Shima, N., 1988, "A Reynolds-Stress Model for Near-Wall and Low-Reynolds-Number Regions," ASME J. Fluids Eng., **110**, pp. 38–44.

[30] Borello, D. Hanjalić, K., and Rispoli, F., 2005, "Prediction of Cascade Flows With Innovative Second-Moment Closures," ASME J. Fluids Eng., **127**, pp. 1059–1070.

[31] Manceau, R., and Hanjalić, K., 2002, "Elliptic Blending Model: A New Near-Wall Reynolds-Stress Turbulence Closure," Phys. Fluids, **14**(2), pp. 744–754.

Downloaded 03 Jun 2010 to 171.66.16.156. Redistribution subject to ASME license or copyright; see http://www.asme.org/terms/Terms_Use.cfm

[32] Borello, D. Rispoli, F., and Hanjalić, K., 2006, "Prediction of Tip-Leakage Flow in Axial Flow Compressor With Second Moment Closure," June, ASME Paper No. GT–2006–90535.
[33] Patel, V. G. Rodi, W., and Scheuerer, G., 1985, "Turbulence Models for Near-Wall and Low-Reynolds-Number Flows: A Review," AIAA J., **23**, pp. 1308–1319.
[34] Sauret, E., and Vallet, I., 2007, "Near-Wall Turbulent Pressure Diffusion Modelling and Influence in 3-D Secondary Flows," ASME J. Fluids Eng., **129**(5), pp. 634–642.
[35] Gerolymos, G. A. Tsanga, G., and Vallet, I., 1998, "Near-Wall $k-\varepsilon$ Computation of 3-D Transonic Turbomachinery Flows With Tip-Clearance," AIAA J., **36**(10), pp. 1769–1777.
[36] Gerolymos, G. A., and Hanisch, C., 1999, "Multistage 3-D Navier-Stokes Computation of Off-Design Operation of a 4-Stage Turbine," Proc. Inst. Mech. Eng., Part A, **213**, pp. 243–261.
[37] Anderson, W. K. Thomas, J. L., and Van Leer, B., 1986, "Comparison of Finite-Volume Flux-Vector-Splittings for the Euler Equations," AIAA J., **24**(9), pp. 1453–1460.
[38] Schumann, U., 1977, "Realizability of Reynolds-Stress Turbulence Models," Phys. Fluids, **20**, pp. 721–725.
[39] Jameson, A., 1983, "Solution of the Euler Equations for 2-D Transonic Flow by a Multigrid Method," Appl. Math. Comput., **13**, pp. 327–355.
[40] Mottura, L. Vigevano, L., and Zaccanti, M., 2000, "Factorized Implicit Upwind Methods Applied to Inviscid Flows at High Mach Number," AIAA J., **38**(10), pp. 1846–1852.
[41] Chakravarthy, S. R., 1983, "Euler Equations—Implicit Schemes and Boundary Conditions," AIAA J., **21**(5), pp. 699–706.
[42] Giles, M. B., 1990, "Nonreflecting Boundary Conditions for Euler Equation Calculations," AIAA J., **28**(12), pp. 2050–2058.
[43] Goyal, R. K., and Dawes, W. N., 1993, "A Comparison of the Measured and Predicted Flowfield in a Modern Fan-Bypass Configuration," ASME J. Turbomach., **115**, pp. 273–282.
[44] Chima, R. V., 1998, "Calculation of Tip Clearance Effects in a Transonic Compressor Rotor," ASME J. Turbomach., **120**(1), pp. 131–140.
[45] Saxer, A. P., and Giles, M. B., 1994, "Predictions of 3-D Steady and Unsteady Inviscid Transonic Stator/Rotor Interaction With Inlet Radial Temperature Nonuniformity," ASME J. Turbomach., **116**, pp. 347–357.
[46] Gerolymos, G. A., Neubauer, J., and Michon, G. J., 2002, "Analysis and Application of Chorochronic Periodicity for Turbomachinery Rotor/Stator Interaction Computations," J. Propul. Power, **18**(2), pp. 1139–1152.
[47] Leclercq, M. P., and Stoufflet, P. L., 1993, "Characteristic Multigrid Method Application to Solve the Euler Equations With Unstructured and Unnested Grids," J. Comput. Phys., **104**, pp. 329–346.
[48] Davis, R. L., Delaney, R. A., Denton, J. D., Giles, M. B., Strazisar, A. J., and Wisler, D. C., 1993, "CFD Code Assessment in Turbomachinery—Author's Information Package," ASME Turbomachinery Committee, ASME–IGTI, Atlanta.
[49] Strazisar, A. J., 1994, "Data Report and Data Diskette for NASA Transonic Compressor Rotor 37," NASA, Lewis Research Center, Cleveland, Nov.
[50] Arnaud, D., Ottavy, X., and Vouillarmet, A., 2004, "Experimental Investigation of the Rotor/Stator Interactions Within a High-Speed Multistage Axial Compressor—Part 1: Experimental Facilities and Results," ASME Paper No. 2004–GT–53764.
[51] Arnaud, D., Ottavy, X., and Vouillarmet, A., 2004, "Experimental Investigation of the Rotor/Stator Interactions Within a High-Speed Multistage Axial Compressor—Part 2: Modal Analysis of the Interactions," ASME Paper No. 2004–GT–53778.
[52] Touyeras, A., and Villain, M., 2004, "Aerodynamic Design and Test Result Analysis of a 3-Stage Research Compressor," June, ASME Paper No. GT2004–53940.
[53] Shabbir, A., Celestina, M. L., Adamczyk, J. J., and Strazisar, A. J., 1997, "The Effect of Hub Leakage on 2 High Speed Axial Flow Compressor Rotors," June, ASME Paper No. 97–GT–346.
[54] Toro, E. F., 1997, *Riemann Solvers and Numerical Methods for Fluid Dynamics*, Springer-Verlag, Berlin.
[55] Suder, K. L., 1998, "Blockage Development in a Transonic Axial Compressor Rotor," ASME J. Turbomach., **120**, pp. 465–476.
[56] van de Wall, A. G., Kadambi, J. R., and Adamczyk, J. J., 2000, "A Transport Model for the Deterministic Stresses Associated With Turbomachinery Blade-Row Interactions," ASME J. Turbomach., **122**(4), pp. 593–603.
[57] Hanjalić, K., 2005, "Will RANS Survive LES? A View of Perspectives," ASME J. Fluids Eng., **127**, Sept., pp. 831–839.
[58] Chaouat, B., and Schiestel, R., 2005, "A New Partially Integrated Transport Model for Subgrid-Scale Stresses and Dissipation Rates for Turbulent Developing Flows," Phys. Fluids, **17**(6), pp. 065106-1–19.
[59] Cornelius, C., Volgmann, W., and Stoff, H., 1999, "Calculation of 3-D Turbulent Flow With a Finite Volume Multigrid Method," Int. J. Numer. Methods Fluids, **31**, pp. 703–720.
[60] Lien, F. S., and Leschziner, M. A., 2003, "Multigrid Convergence Acceleration for Complex Flow Including Turbulence," *Multigrid Methods III*, Hackbusch, W., and Trottenberg, U., eds., International Series on Numerical Mathematics, No. 98, Birkhäuser, pp. 277–288.

Downloaded 03 Jun 2010 to 171.66.16.156. Redistribution subject to ASME license or copyright; see http://www.asme.org/terms/Terms_Use.cfm

Hydraulic Turbine Diffuser Shape Optimization by Multiple Surrogate Model Approximations of Pareto Fronts

B. Daniel Marjavaara
e-mail: dama@ltu.se

T. Staffan Lundström

Division of Fluid Mechanics,
Luleå University of Technology,
SE-97187 Luleå, Sweden

Tushar Goel

Yolanda Mack

Department of Mechanical and Aerospace Engineering,
University of Florida,
Gainesville, FL 32611

Wei Shyy
Department of Aerospace Engineering,
University of Michigan,
3064 FXB, 1320 Beal Avenue,
Ann Arbor, MI 48109

A multiple surrogate-based optimization strategy in conjunction with an evolutionary algorithm has been employed to optimize the shape of a simplified hydraulic turbine diffuser utilizing three-dimensional Reynolds-averaged Navier–Stokes computational fluid dynamics solutions. Specifically, the diffuser performance is optimized by changing five geometric design variables to maximize the average pressure recovery factor for two inlet boundary conditions with different swirl, corresponding to different operating modes of the hydraulic turbine. Polynomial response surfaces and radial basis neural networks are used as surrogates, while a hybrid formulation of the NSGA-IIa evolutionary algorithm and a ϵ-constraint strategy is applied to construct the Pareto front from the two surrogates. The proposed optimization framework drastically reduces the computational load of the problem, compared to solely utilizing an evolutionary algorithm. For the present problem, the radial basis neural networks are more accurate near the Pareto front while the response surface performs better in regions away from it. By using a local resampling updating scheme the fidelity of both surrogates is improved, especially near the Pareto front. The optimal design yields larger wall angles, nonaxisymmetrical shapes, and delay in wall separation, resulting in 14.4% and 8.9% improvement, respectively, for the two inlet boundary conditions. [DOI: 10.1115/1.2754324]

Keywords: surrogate model approximations, response surface methodology, neural networks, Pareto fronts, evolutionary algorithms, diffuser

Introduction

Hydraulic turbine diffusers, or so-called draft tubes, are an important part of low and medium headed hydropower plants. They recover kinetic energy into the head to improve the hydraulic system's overall efficiency. The designs of these diffusers have traditionally been based on simplified analytical methods, and reduced and full scale experiments. In the last decades, however, the usage of computational fluid dynamics (CFD) has dramatically increased. Such computations are challenging and time consuming, caused by complex flow features including turbulence, swirl, separation, and secondary flow. The majority of the work reported to date has been focused on the accuracy and reliability of the CFD simulations [1–3]. At the same time it is evident that the primary concern in the industry is not to analyze and understand the flow; it is instead to improve the design capability for the system. In this context a surrogate model-based optimization strategy has been shown to be an effective tool for estimating the responses of computationally expensive problems as exemplified in other applications involving structural design and fluid design optimization [4–9], as well as in diffuser shape optimization [10–13]. The surrogate models provide global approximation of the system response, and by using these models instead of complex CFD simulations in the optimization phase, the total computational time in the design process can be reduced. Furthermore, better insight into the design space characteristics, such as the interplay between design variables and quantitatively ranked sensitivity of the design objective with respect to the individual design variables [9], can be gained. However, the outcome of such a procedure is highly affected by the effectiveness of the surrogate models. Examples of common surrogate models are polynomial response surfaces, neural networks, and Kriging approximations [4–14]. The selection of a suitable surrogate model is naturally problem dependent, and it is therefore preferable to evaluate several models in the optimization phase in order to chose the best one [5,15,16]. Another important issue is how to search for the optimal solution of the surrogate model approximation, especially for multi-objective optimization problems. Multi-objective optimization problems usually have several optimal solutions known as Pareto optimal solutions, and there exist a number of approaches to find these solutions, like weighted sum strategy, ϵ-constraint strategy, and desirability functions [4,17,18]. Furthermore, one can employ evolutionary algorithms (EAs) [19–21] to probe the solution space characteristics. On the other hand, the EAs require a large number of function evaluations and are generally not suitable for expensive problems such as CFD-based shape optimization. However, with the aid of surrogate model approximations, these algorithms have recently been successfully implemented for computationally costly problems [22,23].

In the present work, a multi-objective evolutionary algorithm in conjunction with multiple surrogate model approximations will be used to optimize the shape of a 3D hydraulic turbulent diffuser. The diffuser in focus is an extension of the cone part of the ERCOFTAC Turbine-99 Workshop draft tube [3], where optimal solutions are sought for two competing inlet boundary conditions. In prior work on turbulent diffuser shape optimization, competing inlet boundary conditions have not been studied in detail [10–13,24–28]. This issue is very important and challenging because the shape of the draft tube (and thus the performance of the turbine) needs to be designed by considering the multiple operational modes at which a turbine operates. Hence, the chosen multi-objective diffuser shape optimization problem will be scrutinized

Contributed by the Fluids Engineering Division of ASME for publication in the JOURNAL OF FLUIDS ENGINEERING. Manuscript received August 8, 2006; final manuscript received April 4, 2007. Review conducted by Yu-Tai Lee.

 Copyright © 2007 by ASME

Downloaded 03 Jun 2010 to 171.66.16.156. Redistribution subject to ASME license or copyright; see http://www.asme.org/terms/Terms_Use.cfm

in detail using a hybrid formulation of the archiving elitist nondominating sorting genetic algorithm (NSGA-IIa) in conjunction with a local search method (ϵ-constraint strategy) by Goel et al. [23,29–32] on a five design variable case. Surrogate models will be applied based on response surface methodology and radial basis neural networks [6,14]. The objective function is defined for simultaneous optimization of the pressure recovery factor for the two competing operational modes of the diffuser, as mentioned earlier. Major topics to be addressed are the interactions and tradeoffs between competing objectives and the fidelity of multiple surrogate models.

In this paper we will first describe the diffuser geometry, the multi-objective optimization problem definition, and the main components of the optimization techniques. Then, we will present the results based on the CFD analyses and discuss the outcome and implications of the design optimization process.

Geometric and Problem Definition

Hydraulic turbine diffusers convert dynamic pressure into static pressure by a gradual increase in the cross-sectional area. Their performance is highly influenced by the wall shape and the cross-sectional area ratio in combination with the velocity distribution at the inlet. A typical measure of its efficiency is the average pressure recovery factor C_p defined as

$$C_p = \frac{\frac{1}{A_{\text{out}}}\int_{A_{\text{out}}} p\, dA - \frac{1}{A_{\text{in}}}\int_{A_{\text{in}}} p\, dA}{\frac{1}{2}\rho\left(\frac{Q_{\text{in}}}{A_{\text{in}}}\right)^2} \tag{1}$$

where A is the area; p is the static pressure; Q is the flow rate; ρ is the density, and the subscripts in and out correspond to the inlet and outlet, respectively.

The geometry in consideration is a 3D extension of the inlet cone part of the ERCOFTAC Turbine-99 Workshop draft tube [3], since most of the pressure recovery is obtained in this portion of the flow domain. Both the original Turbine-99 geometry and the simplified geometry adopted in the present work are presented in Fig. 1. The simplified geometry is used to reduce the computational load of the problem so that an optimization framework can be established and general findings can be investigated. It is, however, important to notice that the exclusion of the elbow, or bend, will have a huge impact on the flow field in the diffuser, especially regarding secondary and recirculation flow patterns, and the optimal shape of the simplified geometry obviously cannot be directly transformed to the curved diffuser. Five cross sections, including the inlet and outlet, are used to define the shape of the simplified diffuser, as shown in Fig. 2. Cross sections 1 and 2 are elliptical, while cross section 3 and the outlet are rectangular, so the diffuser geometry includes nonaxisymmetric shapes and matches the Turbine-99 draft tube exit area. Note also that the inlet profile follows the Turbine-99 draft tube inlet. The four elliptical parameters a_1, b_1, a_2, and b_2, together with the distance l_2 to cross section 2, are used as design variables (i.e., five total design variables). The distance l_1 to cross section 1 is fixed at 178.8 mm. All of these parameters are allowed to vary by about ±24% compared to the original design variables such that the area of cross section 1 is always smaller than the area of cross section 2.

The performance of the diffuser in terms of the pressure recovery factor will be optimized for two competing inlet boundary conditions, denoted as the T mode and R mode, respectively [3]. The T mode is based on measurements from the top point of the propeller curve of the turbine, while the R mode represents measurements from the right leg of the same curve as depicted in Fig. 3. The modes differ mainly in the amount of swirl present. Boundary conditions regarding the axial and the tangential velocity profiles will follow experimental measurements, and quantities needed by the turbulence model and the radial velocity profile are taken from Ref. [3].

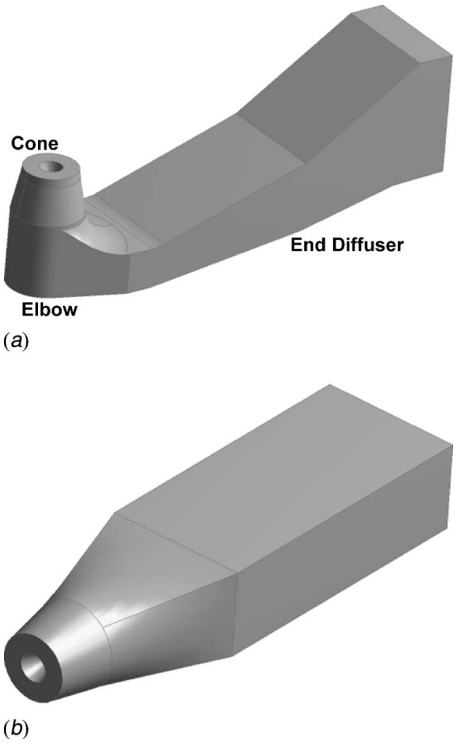

Fig. 1 Three-dimensional models of the diffuser geometries in focus: (*a*) ERCOFTAC Turbine-99 Workshop draft tube; and (*b*) simplified diffuser geometry

Under these conditions, the final multi-objective optimization problem can be formulated as

$$\begin{aligned} &\text{Maximize:} \quad \mathbf{f} = (C_p(T \text{ mode}), C_p(R \text{ mode}))^T \\ &\text{Subject to:} \quad \mathbf{g} = (a_2 - a_1, b_2 - b_1)^T \geq 0 \\ &236.46 \text{ mm} \leq a_1 \leq 309.01 \text{ mm} \\ &236.46 \text{ mm} \leq b_1 \leq 309.01 \text{ mm} \end{aligned} \tag{2}$$

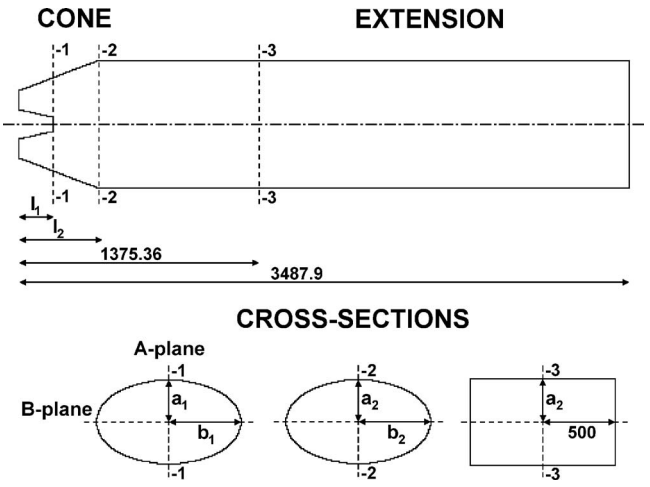

Fig. 2 Two-dimensional sketch of the diffuser geometry and its design variables. The dimensions are in millimeters.

Downloaded 03 Jun 2010 to 171.66.16.156. Redistribution subject to ASME license or copyright; see http://www.asme.org/terms/Terms_Use.cfm

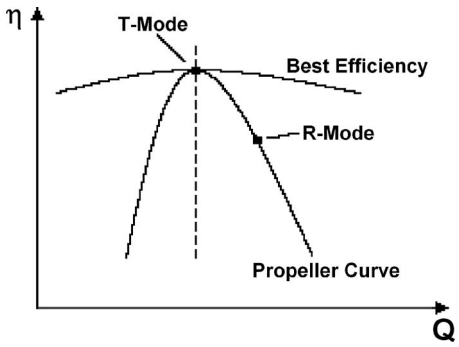

Fig. 3 Sketch of the propeller curve and the operational modes

$$236.46 \text{ mm} \leq a_2 \leq 381.56 \text{ mm}$$

$$236.46 \text{ mm} \leq b_2 \leq 381.56 \text{ mm}$$

$$278.46 \text{ mm} \leq l_2 \leq 429.80 \text{ mm}$$

where **f** contains the two objective functions and **g** contains the geometrical inequality constraints, while the remaining side constraints are the design variable bounds.

Optimization Approach

Surrogate-based optimization analysis can be seen as an approximation problem for which one aims at determining the true relationship between the design variables, $\mathbf{x}=(x_1,\ldots,x_N)$, and the calculated response y_i from a prescribed set of data points, i.e., to find $y_i=g(\mathbf{x})$. By this approach, the original computer model y can be replaced with the surrogate model $\hat{y}_i=h(\mathbf{x})$ in the optimizations process to provide a faster and potentially more effective tool to explore the design and solution space. The key steps in the approach, i.e., experimental design, computer analysis, surrogate model construction, and design exploration, will be highlighted in the following subsections.

Experimental Design. The first step in the surrogate-based optimization process is the selection of n data or design points for the surrogate model approximation. This is a crucial step since the predictive capability of the surrogate model used is strongly dependent on the distribution of these points. Usually a design of experiments (DOE) or a design and analysis of computer experiment (DACE) strategy is adopted in order to select the data points and to improve the fidelity of the surrogate approximation [7,8]. The DOEs are developed for physical experiments (especially polynomial response surfaces) while the DACEs are designed for computer analysis. It has also been shown by Giunta [33] that using a DOE design strategy is superior to a random selection strategy. Some examples of standard DOE strategies that can be found in the literature are central composite design (CCD), face-centered composite design (FCCD), and Box–Behnken design (BBD) [14]. In addition there also exist a number of computer-generated DOE strategies based on different optimal criterion like *A*-optimal, *D*-optimal, *G*-optimal, and *I*-optimal also referred to as *Q*-optimal [14], which might be preferable before standard DOE strategies in problems with constrained design spaces or when the total number of design points wants to be reduced. Examples of standard DACE strategies, on the other hand, are Latin-hypercube, orthogonal arrays, and minimax and maximin designs, to name a few [7,8]. The choice of a suitable experimental design strategy, however, is also problem dependent, exemplified by the fact that the often used FCCD design method is only effective as long as the number of design variables is modest [14].

Here, 34 initial data points were selected (including both the central point and original design point) according to the *I*-optimal DOE strategy [14], as is listed in Table 1 since many of the tested standard DOE and DACE designs strategies yielded to many unfeasible data points in the design plan. The actual data points were generated with the commercial software JMP 5.0.1A [34] using coded (scaled) design variables that satisfied the noncoded constraints. In this case, a computer based DOE strategy was preferred instead of one of the standard strategies in order to satisfy the constraints and to keep the total number of data points relatively small. The *I*-optimal criterion was finally chosen based on a comparison with the *D*-optimal criterion since the former gave the smallest average prediction variance profile with the same amount of data points in the design plan. The data points chosen using *I*-optimal criterion are found by minimizing the following equation

$$I = \text{tr}[(\mathbf{X}^T\mathbf{X})^{-1}\mathbf{M}] \tag{3}$$

where **X** is the model design matrix and **M** is the moment matrix.

CFD Analysis. The second step in a surrogate-based optimization process is the evaluation of the objective functions for each data point in the experimental design plan. In this case, the objective functions (i.e., C_p for the *T* and *R* modes) were obtained by solving the 3D flow field for each diffuser design and inlet boundary condition using the commercial CFD code CFX-5.7.1 from ANSYS [35]. To obtain a closed form of the solved Reynolds-averaged Navier–Stokes (RANS) equations, the standard k-ϵ turbulence model with scalable wall functions was used. For the numerical discretization of the continuity and momentum equations, a second-order upwind scheme was applied for the advection term, while a first-order upwind scheme was employed for the turbulent equations to ensure positive physical quantities and numerical stability. A consistent second-order accurate scheme, the high resolution scheme, was tested for the turbulent equations, but the impact on the turbulence models was negligible [36]. The derivatives for the pressure gradient term and diffusion term were obtained with shape functions. At the outlet of the fluid domain, a zero-average static pressure condition was applied. The walls were considered smooth, while the inlet boundary conditions were altered between the *T* mode and *R* mode as described in the previous section. Overall, the numerical setup selected can satisfactorily predict the main flow field patterns in a draft tube diffuser [3,36].

For each diffuser geometry, structured computational grids were generated using the commercial grid generator ICEM CFD 5.1 [37]. In order to minimize the variation in grid quality, the same topology and mesh parameters were used for all grid systems. The grid systems used are nonuniform, with clustering near the walls, the inlet, and in the wake region downstream of the runner. Grid layouts of different sizes were also evaluated in order to determine the one that provided the best balance in terms of accuracy, convergence, and execution time. The selected grid consisted of 708k nodes.

Surrogate Model Construction. The third step in a surrogate-based optimization process is the surrogate model approximation. Using response surface methodology, a polynomial is fitted to the evaluated data points according to the experimental design plan so that it reflects the global behavior of the objective function over the design space. Frequently, quadratic polynomials are employed due to their cost effectiveness. For example, a quadratic response surface (RS) model can be written as

$$\hat{y} = b_0 + \sum_{i=1}^{n} b_i x_i + \sum_{i=1}^{n} b_{ii} x_i^2 + \sum \sum_{i<j=2}^{n} b_{ij} x_i x_j \tag{4}$$

where $\hat{y}$ is the system response; x_i are the design variables; and b_i are the regression coefficients to be determined. The error ε_i between the approximated response $\hat{y}_i$ and true response y_i at each data point can be expressed as

Downloaded 03 Jun 2010 to 171.66.16.156. Redistribution subject to ASME license or copyright; see http://www.asme.org/terms/Terms_Use.cfm

Table 1 CFD data for the *I*-optimal designs and validated Pareto optimal solutions.

Geo	a_1 (mm)	b_1 (mm)	a_2 (mm)	b_2 (mm)	l_2 (mm)	C_p T mode	C_p R mode
34 I-optimal data points							
1*	269.07	269.07	309.01	309.01	397.8	0.71	0.75
2	236.46	236.46	236.46	381.56	429.80	0.51	0.60
3	236.46	236.46	294.50	236.46	429.80	0.41	0.48
4	236.46	236.46	294.50	309.01	278.46	0.33	0.43
5	236.46	236.46	367.05	381.56	323.86	0.31	0.42
6	236.46	236.46	381.56	236.46	278.46	0.27	0.37
7	236.46	236.46	381.56	309.01	429.80	0.47	0.56
8	236.46	265.48	236.46	265.48	278.46	0.54	0.57
9	236.46	272.74	309.01	338.03	369.26	0.60	0.69
10	236.46	277.64	323.52	277.64	354.13	0.60	0.69
11	236.46	301.76	381.56	381.56	429.80	0.56	0.55
12	236.46	309.01	236.46	309.01	399.53	0.52	0.53
13	236.46	309.01	371.40	309.01	278.46	0.35	0.36
14	239.65	309.01	252.41	381.56	278.46	0.63	0.57
15	258.22	279.30	332.23	279.30	354.13	0.69	0.74
16	266.47	272.51	266.47	272.51	429.80	0.56	0.58
17	267.86	236.46	267.86	309.01	354.13	0.59	0.66
18	270.29	287.25	304.11	381.56	429.80	0.76	0.76
19	271.28	272.74	271.28	348.91	354.13	0.73	0.75
20	272.74	272.74	309.01	309.01	354.13	0.73	0.76
21	272.74	272.74	381.56	359.80	278.46	0.60	0.71
22	272.74	284.00	327.15	284.00	278.46	0.74	0.74
23	272.74	307.89	381.56	307.89	429.80	0.63	0.62
24	272.74	309.01	316.26	309.01	339.00	0.66	0.60
25	279.99	254.51	381.56	254.51	369.26	0.69	0.75
26	287.25	236.46	371.40	381.56	429.80	0.62	0.65
27	300.00	236.46	307.06	236.46	323.86	0.59	0.57
28	309.01	236.46	309.01	381.56	278.46	0.41	0.35
29	309.01	236.46	381.56	309.01	278.46	0.52	0.52
30	309.01	243.72	309.01	323.52	429.80	0.64	0.59
31	309.01	275.60	381.56	275.60	414.67	0.68	0.59
32	309.01	288.92	309.01	288.92	278.46	0.61	0.60
33	309.01	296.36	309.01	296.36	429.80	0.57	0.58
34	309.01	309.01	381.56	381.56	354.13	0.56	0.56
15 Pareto optimal solutions obtained based on the 34-case design plan (Geo 1-34)							
35[a]	270.74	271.63	332.15	357.48	400.42	0.71	0.80
36[a]	272.18	274.27	329.19	373.96	417.54	0.72	0.80
37[a]	273.13	275.34	330.09	381.56	429.80	0.72	0.80
38[b]	273.89	267.19	380.78	272.39	344.43	0.70	0.78
39[b]	272.72	275.12	319.61	373.84	423.72	0.73	0.80
40[b]	278.02	277.13	338.64	362.19	423.47	0.74	0.79
41[c]	278.78	266.81	381.56	332.91	425.48	0.71	0.80
42[c]	280.81	268.68	380.49	333.63	429.80	0.72	0.80
43[c]	277.29	273.73	344.45	353.16	429.80	0.73	0.79
44[d]	275.70	267.25	373.86	292.21	339.24	0.70	0.79
45[d]	275.13	276.12	331.33	367.87	410.23	0.73	0.80
46[d]	282.41	278.19	349.40	358.82	411.24	0.76	0.78
47[e]	276.10	273.16	361.75	372.31	404.83	0.72	0.82
48[e]	275.30	274.80	338.50	373.54	411.03	0.73	0.81
49[e]	273.49	278.58	307.31	381.56	406.79	0.75	0.79
15 Pareto optimal solutions obtained based on the 34-case design plan (Geo 1-49)							
50[a]	272.86	270.39	346.30	350.90	398.02	0.71	0.80
51[a]	274.19	273.77	331.20	355.37	396.25	0.72	0.80
52[a]	270.76	281.42	294.48	381.56	387.75	0.76	0.78
53[b]	272.09	267.69	366.31	344.93	410.13	0.70	0.79
54[b]	279.60	269.03	371.75	325.27	384.28	0.72	0.80
55[b]	268.91	300.35	284.62	381.56	405.08	0.72	0.66
56[c]	278.24	267.55	381.56	338.91	419.91	0.71	0.81
57[c]	278.70	269.29	381.56	339.94	429.23	0.71	0.81
58[c]	283.56	285.29	283.56	285.29	278.46	0.66	0.66
59[d]	271.86	267.23	374.25	337.37	397.46	0.70	0.79
60[d]	280.70	268.35	374.26	313.88	369.91	0.81	0.80
61[d]	289.22	271.84	363.37	306.03	352.68	0.77	0.77
62[e]	274.28	270.42	350.03	350.03	396.26	0.71	0.81
63[e]	274.29	274.10	326.98	356.67	393.91	0.75	0.76
64[e]	269.37	281.57	270.15	381.56	373.42	0.75	0.76

*Original geometry.
[a]Full quadratic RS model.
[b]Ordinary RBNN model.
[c]Full quadratic RS model excluding outliers.
[d]RBNN model excluding outliers.
[e]Reduced quadratic RS model.

Downloaded 03 Jun 2010 to 171.66.16.156. Redistribution subject to ASME license or copyright; see http://www.asme.org/terms/Terms_Use.cfm

$$y_i = \hat{y}_i + \varepsilon_i, \quad i = 1,2, \ldots, n \tag{5}$$

The error term in Eq. (5) represents random noise errors and modeling errors. The former type originates from background noise and/or measurement/numerical errors which are absent in deterministic computer models, while the latter is plainly an outcome of the insufficient flexibility of the approximation of the chosen polynomial. Equations (4) and (5) can now be combined to yield the following expression

$$\mathbf{y} = \mathbf{X}\boldsymbol{\beta} + \boldsymbol{\varepsilon} \tag{6}$$

where $\mathbf{y}$ is the response vector; $\mathbf{X}$ is again the model design matrix; $\boldsymbol{\beta}$ is the regression coefficient vector; and $\boldsymbol{\varepsilon}$ is the error vector. The regression coefficient vector $\boldsymbol{\beta}$ in Eq. (6) are usually determined by the method of least squares, i.e., minimizing the sum of the square of the errors SS_E

$$\mathrm{SS}_E = \sum_{i=1}^{n} \varepsilon_i^2 = \boldsymbol{\varepsilon}^T\boldsymbol{\varepsilon} = (\mathbf{y} - \mathbf{X}\boldsymbol{\beta})^T(\mathbf{y} - \mathbf{X}\boldsymbol{\beta}) \tag{7}$$

giving the least square estimator $\mathbf{b}$ of the regression coefficients $\boldsymbol{\beta}$ as

$$\mathbf{b} = (\mathbf{X}^T\mathbf{X})^{-1}\mathbf{X}^T\mathbf{y} \tag{8}$$

The final RS model can then be expressed as

$$\hat{y}(\mathbf{x}) = \mathbf{x}^T\mathbf{b} \tag{9}$$

which can be used to predict an approximated response $\hat{y}$ for an arbitrary data point $\mathbf{x}$.

The fidelity of the RS model can be judged by comparing a number of quality statistics. The two most commonly used, the coefficient of multiple regression, R^2, and its adjusted form, R_a^2, are defined as

$$R^2 = 1 - \frac{\mathrm{SS}_E}{\mathrm{SS}_T} \tag{10}$$

$$R_a^2 = 1 - \frac{\mathrm{SS}_E/(n-r)}{\mathrm{SS}_T/(n-1)} = 1 - \left(\frac{n-1}{n-r}\right)(1-R^2) \tag{11}$$

where

$$\mathrm{SS}_E = \sum_{i=1}^{n} (y_i - \hat{y}_i)^2 \tag{12}$$

$$\mathrm{SS}_T = \sum_{i=1}^{n} y_i^2 - \frac{1}{n}\left(\sum_{i=1}^{n} y_i\right)^2 \tag{13}$$

and r is the number of regression coefficients. These two measures determine the proportion of the variation around the mean in the response which can be captured by the RS model. The R_a^2 value also takes into account the degrees of freedom and is therefore generally more trustworthy. Based on Eqs. (10) and (11), it can be concluded that the range of these two quantities is between [0, 1], where a value close to one corresponds to a good fit. Two other relevant quality measures are the root mean square (RMS) error σ and its adjusted counterpart σ_a each defined as

$$\sigma = \sqrt{\frac{\mathrm{SS}_E}{n}} \tag{14}$$

$$\sigma_a = \sqrt{\frac{\mathrm{SS}_E}{n-r}} \tag{15}$$

are estimations of the standard error of the RS model. To check the significance of each regression coefficient β_i (i.e., H_0: $\beta_i = 0$, $H1$: $\beta_i \neq 0$), the t_0 test statistic is commonly used. It rejects the null hypothesis (H_0) if

$$|t_0| = \left|\frac{b_i}{\sigma_a^2 C_{ii}}\right| > t_{\alpha/2,n-p} \tag{16}$$

where C_{ii} is the diagonal element to $(\mathbf{X}^T\mathbf{X})^{-1}$ corresponding to β_i, and is the significance level. Note that this is only a partial test because the regression coefficient β_i depends on all variables in the model.

In radial basis neural networks (RBNN) the approximation $\hat{y}_i$ of the true response y_i is obtained by employing neurons (perceptrons) in a two-layer network. The first hidden layer consists of radial basis neurons, while the second output layer consists of linear neurons. The RBNN networks differ from standard backpropagation neural networks in the use of radial basis neurons, in which the transfer function is formed differently. For radial basis neurons, the transfer function is given as a bias scaled vector distance between the weights and the inputs, while in standard neurons (as linear and sigmoid neurons) it is given by the sum of the weighted input and a bias. The transfer function, a, represented by the radial basis function can be expressed as follows for each neuron

$$a = e^{-(\|\mathbf{w} - \mathbf{x}\|b)^2} \tag{17}$$

and in the output linear layer by the linear function

$$a = \mathbf{w}^T\mathbf{x} + b \tag{18}$$

where b is the bias; $\mathbf{w}$ is the neuron weight vector; and $\mathbf{x}$ is the design variable (input) vector. The RBNN networks are therefore also trained or fitted differently than standard backpropagation networks which normally use a gradient descent algorithm. In principle, each neuron in the hidden radial basis layer is assigned a weight $\mathbf{w}$ equal to one of the data points $\mathbf{x}$ in the experimental design plan. Therefore, each neuron acts as a detector for a given input. The bias for each neuron is set to 0.8326/*spread*, where *spread* is a user defined constant and determines the radius of influence of each neuron. Large values of *spread* can result in flat networks since many neurons will have high response to a given input, while small values of *spread* can result in many neurons with poor response to a given input. Hence, the best value of the *spread* constant can be found by comparing the RMS error σ in Eq. (14) for different *spread* constants. The bias b and the neuron weights $\mathbf{w}$ of the output linear layer is in turn found explicitly by simulating the output of the hidden radial basis layer and combining it with knowledge of the target output.

In general, the RBNN model is generated by adding neurons one by one to the hidden radial basis layer until the network error falls beneath a predetermined error *goal* or when the maximum number of neurons has been reached. At each iteration, the weights of the added neuron are set to the input vector $\mathbf{x}$ that lowers the network error at most. This procedure is usually done recursively. First the network is exposed to the training data and then it is tested with the validation data for a large range of *goal* and *spread* constants. The values of *goal* and *spread* that produce the smallest error according to Eq. (14) in the validation data, i.e., σ_v, are then finally selected before the range of *goal* and *spread* are reduced and some new values are identified. This cross validation continues until the *goal* and *spread* combination that minimizes the error in the validation data is found. A special RBNN network design, with zero network error on the training vectors, can be created by adding as many radial basis neurons as there are input vectors.

The advantage of radial basis networks as compared to standard backpropagation networks is that they often can be constructed much faster. However, with many neurons employed, the RBNN can "overfit" the training data while potentially deteriorating the overall accuracy. In this study the RS and the RBNN were implemented in MATLAB 7.0.1 using coded design variables [38].

A frequently used method to improve the quality of the surrogate models is to detect and eliminate outliers. Outliers are individual data points that do not follow the overall trends seen in

Downloaded 03 Jun 2010 to 171.66.16.156. Redistribution subject to ASME license or copyright; see http://www.asme.org/terms/Terms_Use.cfm

other data points. In this work a method analogous to the iterative reweighted least square (IRLS) approach suggested by Beaton and Tuckey [39] was applied to both surrogate models. In principle, the method assigns low weights to outliers and by refitting the surrogate model with these weights the effects of the outliners can be suppressed. This process is repeated until convergence. The weight w_i that is given to a data point in this case is

$$w_i = \begin{cases} \left[1 - \left(\frac{|e_i/\sigma|}{B}\right)^2\right]^2, & \text{if } |e_i/\sigma| \le B \\ 0, & \text{otherwise} \end{cases} \tag{19}$$

where B is a tuning parameter usually having a value between 1 and 3; and e_i is the residual. In, this case a value of 1.9 was chosen for B.

Design Exploration. The final step in the surrogate-based optimization analysis is the design exploration where the optimal design variables are sought. In general there exists two broad classes of optimization tools: gradient-based and nongradient-based algorithms. Optimization frameworks based on gradient-based algorithms have drawn the most attention in the past years [4–13]. They are suitable when the objective function is smooth and the optimums are clearly identifiable. However, for multiple-objective optimization problems or noisy and complex objective functions, EAs are usually more effective because they not only present multiple scenarios to allow for more informed analyses and tradeoffs, but they also enable one to examine the characteristics of the entire design space so that the impact of individual design variables on the system response can be better assessed. In this study, in order to assess the interplay of the multiple objectives, the Pareto optimal solutions were found by using a hybrid formulation of the archiving elitist NSGA-IIa and a local search method (ε-constraint strategy) developed by Goel et al. [23]. Here, the real coded version of the algorithm was used. "Real coded" means that the crossover and mutation operator is conducted over real rather than binary space, and archiving the Pareto optimal solutions is dynamic rather than static. The ε-constraint strategy was chosen as the local search method since it has been shown that it can improve the Pareto optimal solutions further [23]. The algorithm was implemented in MATLAB 7.0.1 [38], and is described as follows:

1. Randomly initialize a parent population of size *pop*;
2. Compute objectives and constraints for each individual in the parent population;
3. Rank the parent population based on feasible designs, nondomination criteria and crowding distance;
4. Copy possible elite individuals in the parent population to the elite archive;
5. For each generation, *gen*
   - Generate a child population of size *pop* from the parent population based on the parents' individual rankings using the genetic operators: selection, crossover, and mutation;
   - Compute objectives and constraints for each individual in the child population;
   - Combine the two populations, child and parent, and rank them based on feasible designs, nondomination criteria, and crowding distance;
   - Select a new parent population of size *pop* from the combined populations based on their individual ranking;
   - Update the elite archive by copying the new elite individuals in the combined population to the archive, then delete possible duplicates and remove nonelitists based on nondomination criteria in the archive; and
6. Improve and avoid Pareto drifts in the elite archive by using a local search method on each individual in the archive, then remove nonelitists based on nondomination criteria.

The selection, crossover, and mutation operators in the above algorithm were set to two-crowded binary tournament selection operator, simulated binary crossover (SBX) operator, and polynomial mutation operator, respectively. In the two-crowded binary tournament selection operator, the best one of two randomly selected individuals in the parent population is chosen as a parent. This tournament process is repeated until the mating pool is full, with at most two copies of each parent in the mating pool. The SBX operator is next used to mix the genetic information between two parents (P_i) in the mating pool in order to create one child (C_i) near each of the parents with a high crossover probability ρ_X

$$\begin{aligned} C_1 &= 0.5[(1+\beta_X)P_1 + (1-\beta_X)P_2] \\ C_2 &= 0.5[(1-\beta_X)P_1 + (1+\beta_X)P_2] \end{aligned} \tag{20}$$

where

$$\beta_X = \begin{cases} (2u)^{\frac{1}{\eta_x+1}}, & \text{if } u < 0.5 \\ (1/2(1-u))^{\frac{1}{\eta_x+1}}, & \text{otherwise} \end{cases}$$

and η_X is the crossover distribution parameter and u is a random number between [0, 1]. The polynomial mutation operator is finally adopted to create a random change in a child with a certain mutation probability ρ_M

$$C = P + (P^{\mathrm{UP}} - P^{\mathrm{LOW}})\delta_M$$

where

$$\delta_M = \begin{cases} (2u)^{\frac{1}{\eta_M+1}}, & \text{if } u < 0.5 \\ 1 - (2(1-u))^{\frac{1}{\eta_M+1}}, & \text{otherwise} \end{cases} \tag{21}$$

and η_M is the mutation distribution parameter, and P^{UP} and P^{LOW} are the bounds.

Results and Discussion

The CFD solutions for the construction and validation of the surrogate models were obtained for a total of 64 geometries shown in Table 1. The first 34 geometries correspond to the computer generated *I*-optimal designs while the rest represent the CFD validated Pareto optimal solutions. Of these latter points, the first 15 are Pareto optimal solutions based on the original 34-case design plan containing the *I*-optimal designs, while the remaining ones are based on an enhanced 49-case design plan. The latter design plan was constructed by adding the first 15 CFD validated designs points to the original design plan in order to improve the accuracy of the surrogate models, i.e., a local resampling updating scheme. Having two inlet boundary conditions for each design point, the total number of performed CFD simulations boils down to 128 (64×2). Each of these CFD simulations was assumed converged when all the RMS residuals had dropped to about 10^{-6} (four orders of magnitude), which is sufficient for most industrial applications according to Ref. [35]. The average y_+ values for each calculation at near wall nodes was about 42 for the diffuser wall, and about 52 for the runner wall, which are sufficient based on established practices [35]. The run time for one simulation was approximately 8 CPU h on a dual Intel Xeon 2.4 GHz 32-bit processor and with 2 GB ram available. Once the Pareto fronts were constructed, the CFD validated Pareto optimal solutions were selected from sets containing 255–434 solutions for the 34-case design plan and 333–656 solutions for the 49-case design plan, depending on the surrogate model approximation. The input parameters for the hybrid NSGA-IIa algorithm for the construction of the Pareto fronts were chosen based on an extensive parametric study, and were set to the following values:

- Population size, *pop* 100;
- Generations, *gen* 250;
- Crossover probability, ρ_X 1.0;
- Crossover distribution parameter, η_X 5.0;

Downloaded 03 Jun 2010 to 171.66.16.156. Redistribution subject to ASME license or copyright; see http://www.asme.org/terms/Terms_Use.cfm

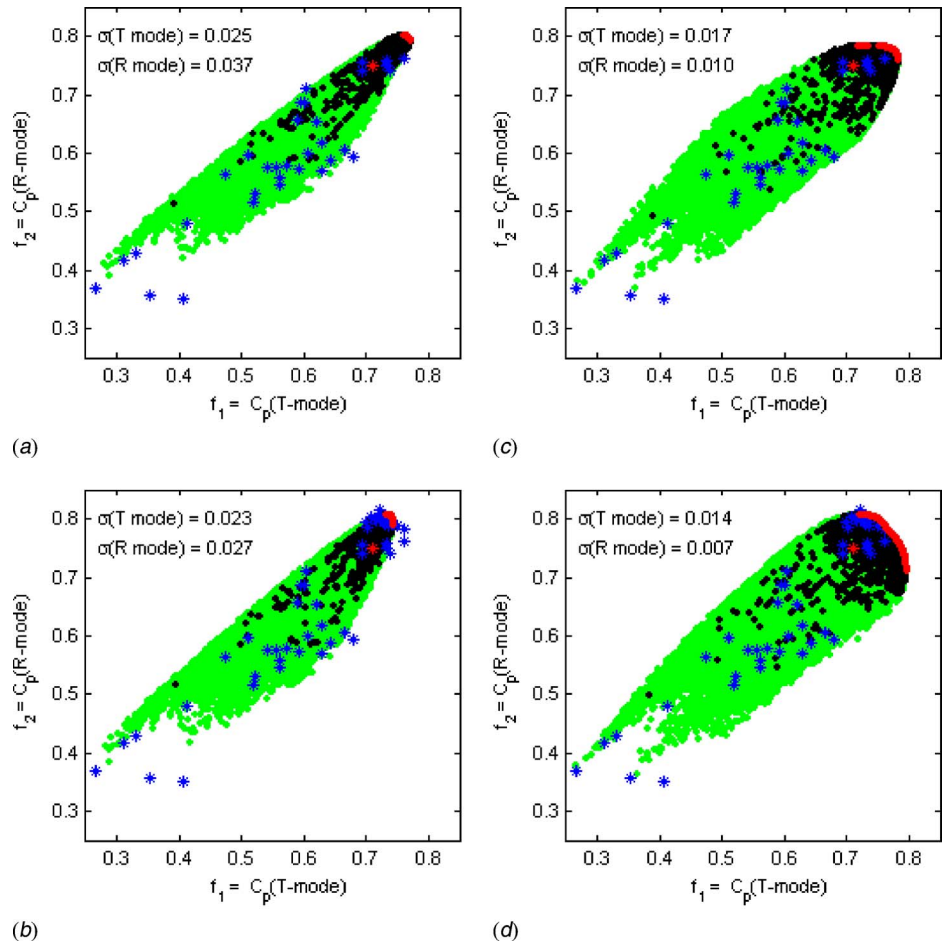

Fig. 4 Solution space (green dots), Pareto front (red dots), CFD calculated designs (blue and red stars), and the hybrid NSGA-IIa evaluated designs (black dots) for the constructed surrogate models: (*a*) full quadratic RS model based on the 34-case design plan; (*b*) full quadratic RS model based on the 49-case design plan; (*c*) RBNN model based on the 34-case design plan; and (*d*) RBNN model based on the 49-case design plan

- Mutation probability, ρ_M 0.2; and
- Mutation distribution parameter, η_M 20.0.

The total number of evaluated functions, for each surrogate model and both objectives in the hybrid NSGA-IIa algorithm was therefore 50,000 ($100\times250\times2$), as seen in Fig. 4 (black dots).

Optimization Analysis. Only quadratic polynomials were considered in this study for the construction of the RS models, since the number of data points needed grows rapidly as the order of the polynomial increases. Specifically, three RS models were constructed for each objective and each design plan, as summarized in Tables 2 and 3. These include: (a) the full quadratic RS model; (b) the reduced quadratic RS model omitting regression coefficients with a *t*-ratio less than 1.0; and (c) the full quadratic RS model excluding outliers with a weight less than 0.1, respectively. The full quadratic RS models based on the 34-case design plan was, however, of poor accuracy as seen in Table 2 by its low R_a^2 and high σ_a values for both the *T* and *R* modes (R_a^2=0.91 and 0.82, respectively, σ_a=0.038 and 0.051). Comparable results were also obtained for both objectives using the reduced quadratic RS

Table 2 Fidelity of the quadratic RS models based on the original 34-case design plan

	Full quadratic RS[a] model		Reduced quadratic[b] RS model		Full quadratic RS[c] model excl. outliers	
C_p	*T* mode	*R* mode	*T* mode	*R* mode	*T* mode	*R* mode
Mean	0.57	0.60	0.57	0.60	0.58	0.59
σ_a	0.038	0.051	0.038	0.049	0.023	0.027
σ	0.025	0.037	0.024	0.031	0.012	0.014
# of obs.	34	34	34	34	29	29
R^2	0.96	0.93	0.96	0.90	0.99	0.99
R_a^2	0.91	0.82	0.91	0.83	0.96	0.95

[a]Full quadratic RS model (see Eq. (4) and Table 4).
[b]Omitting regression coefficients with *t*-ratio less than 1.0 (see Table 4).
[c]Excluding outliers with a weight less than 0.1 (*T* mode: {Geo 4, 13, 16, 22 and 30} and *R* mode: {Geo 10, 16, 21, 31 and 33}).

Downloaded 03 Jun 2010 to 171.66.16.156. Redistribution subject to ASME license or copyright; see http://www.asme.org/terms/Terms_Use.cfm

Table 3 Fidelity of the quadratic RS models based on the enhanced 49-case design plan

	Full quadratic RS[a] model		Reduced quadratic[b] RS model		Full quadratic RS[c] model excl. outliers	
C_p	T mode	R mode	T mode	R mode	T mode	R mode
Mean	0.62	0.66	0.62	0.66	0.62	0.66
σ_a	0.030	0.035	0.030	0.035	0.016	0.018
σ	0.023	0.027	0.023	0.027	0.011	0.013
# of obs.	49	49	49	49	42	44
R^2	0.97	0.96	0.97	0.96	0.99	0.99
R_a^2	0.95	0.93	0.95	0.94	0.99	0.98

[a]Full quadratic RS model (see Eq. (4) and Table 5).
[b]Omitting regression coefficients with t-ratio less than 1.0 (see Table 5).
[c]Excluding outliers with a weight less than 0.1 (T mode: {Geo 10, 13, 16, 21, 22, 30, and 32} and R mode: {Geo 10, 16, 21, 31, and 33}).

model (R_a^2=0.91 and 0.83, respectively, σ_a=0.038 and 0.049), as seen Tables 2 and 4. By excluding outliers, however, the fidelity of the RS models become enhanced in both objectives (R_a^2=0.96 and 0.95, respectively, σ_a=0.023 and 0.027), as seen in Table 2. A note of caution regarding the so-called outliers should be made. As investigated by Mack [16] and Goel [40], the outliers may suggest unusual but desirable points from the viewpoint of design optimization. Therefore, in the present approach a local resampling updating scheme was employed, meaning that once the Pareto front had been constructed, additional cases along the Pareto front were added to the original design plan to enhance the fidelity of the surrogate models in the critical region. Specifically, three data points on the Pareto front were selected using a weighted sum approach with weights (1,0), (0.5,0.5), and (0,1) from each of the three fitted quadratic RS models in Table 2 and from the two constructed RBNN models in Table 6 (explained later) that were then added to the 34-case design plan. By this approach, the accuracy of the three quadratic RS models, now being based on the enhanced 49-case design plan, becomes more satisfactory (R_a^2=0.95 and 0.93 respectively, σ_a=0.030 and 0.035 for the full quadratic RS model), as shown in Tables 3 and 5. Furthermore, the fidelity of all three quadratic RS models, shown in Tables 2 and 3, is somewhat higher for the T mode than for the R mode.

For the construction of the RBNN models, two models were tested for each objective and each design plan, as shown in Tables 6 and 7. These two are the (b) ordinary RBNN model and the (c) RBNN model excluding outliers with a weight less than 0.1. In both models, about 20% of the data points in each design plan (seven and ten, respectively) were randomly selected as the validation set as seen in Tables 6 and 7. As in the quadratic RS models, the fidelity of the RBNN models for both objectives becomes enhanced by excluding outliers. They are also enhanced by using the 49-case design plan as shown by the decrease in σ_v and σ between the RBNN models in Tables 6 and 7. It is also noticed that the improvement in σ_v is related to the number of validation points being dismissed as outliers. For example, the ordinary

Table 4 Regression coefficients and *t*-ratios of the full and reduced quadratic RS models based on the 34-case design plan

	Full quadratic RS model[a]				Reduced quadratic RS model[b]			
Term	T mode	t ratio	R mode	t ratio	T mode	t ratio	R mode	t ratio
Inter.	0.737	48.2	0.778	38.5	0.737	48.6	0.773	40.5
a_1	0.035	2.7	−0.005	−0.3	0.042	4.2	0	0
b_1	0.019	1.5	−0.011	−0.7	0.015	1.3	0	0
a_2	0.015	0.9	0.026	1.1	0	0	0.015	0.9
b_2	0.033	2.1	0.042	2.0	0.033	2.1	0.029	1.8
l_2	0.015	1.5	0.013	1.0	0.014	1.4	0.012	1.0
$b_1^* a_1$	−0.023	−2.0	0.007	0.4	−0.024	−2.2	0	0
$a_2^* a_1$	0.059	3.1	0.059	2.3	0.045	3.5	0.048	2.6
$b_2^* a_1$	−0.021	−1.5	−0.017	−0.9	−0.019	−1.4	0	0
$l_2^* a_1$	−0.021	−2.0	−0.023	−1.7	−0.020	−1.9	−0.022	−1.7
$a_2^* b_1$	−0.012	−0.9	−0.017	−1.0	0	0	0	0
$b_2^* b_1$	0.040	2.4	0.043	1.9	0.042	2.5	0.030	1.6
$l_2^* b_1$	−0.034	−3.1	−0.033	−2.3	−0.034	−3.2	−0.036	−2.6
$b_2^* a_2$	−0.035	−2.2	−0.020	−0.9	−0.035	−2.3	0	0
$l_2^* a_2$	0.044	3.5	0.022	1.3	0.045	3.7	0.019	1.2
$l_2^* b_2$	0.043	3.2	0.046	2.6	0.040	3.1	0.047	2.8
a_1^2	−0.102	−6.3	−0.112	−5.2	−0.101	−6.2	−0.109	−5.3
b_1^2	−0.101	−5.7	−0.124	−5.3	−0.103	−5.9	−0.121	−5.5
a_2^2	−0.043	−1.8	−0.035	−1.1	−0.026	−1.5	−0.022	−0.9
b_2^2	−0.030	−1.4	−0.047	−1.7	−0.031	−1.5	−0.035	−1.5
l_2^2	−0.031	−1.9	−0.043	−2.0	−0.034	−2.1	−0.048	−2.3

[a]Full quadratic RS model (see Eq. (4)).
[b]Omitting regression coefficients with t ratio less than 1.0.

Downloaded 03 Jun 2010 to 171.66.16.156. Redistribution subject to ASME license or copyright; see http://www.asme.org/terms/Terms_Use.cfm

Table 5 Regression coefficients and *t* ratios of the full and reduced quadratic RS models based on the 49-case design plan

	Full quadratic RS model[a]				Reduced quadratic RS model[b]			
Term	*T* mode	*t* ratio	*R* mode	*t* ratio	*T* mode	*t* ratio	*R* mode	*t* ratio
Inter.	0.728	70.8	0.784	64.8	0.728	72.4	0.783	66.5
a_1	0.039	3.9	−0.005	−0.4	0.042	5.5	0	0
b_1	0.023	2.4	−0.013	−1.1	0.019	2.2	−0.014	−1.3
a_2	0.008	0.6	0.028	1.8	0	0	0.024	2.0
b_2	0.024	2.1	0.042	3.1	0.025	2.2	0.042	3.2
l_2	0.011	1.6	0.013	1.5	0.011	1.5	0.013	1.6
$b_1^* a_1$	−0.023	−2.5	0.006	0.6	−0.024	−2.8	0	0
$a_2^* a_1$	0.052	3.5	0.059	3.4	0.045	4.4	0.053	4.1
$b_2^* a_1$	−0.023	−2.1	−0.016	−1.3	−0.021	−2.0	−0.015	−1.2
$l_2^* a_1$	−0.022	−2.6	−0.024	−2.4	−0.021	−2.5	−0.023	−2.4
$a_2^* b_1$	−0.010	−1.0	−0.017	−1.4	0	0	−0.016	−1.4
$b_2^* b_1$	0.035	2.7	0.043	2.8	0.037	2.8	0.044	2.9
$l_2^* b_1$	−0.035	−4.1	−0.034	−3.3	−0.035	−4.1	−0.035	−3.5
$b_2^* a_2$	−0.035	−2.9	−0.022	−1.5	−0.036	−3.0	−0.022	−1.5
$l_2^* a_2$	0.042	4.4	0.023	2.0	0.043	4.5	0.022	2.0
$l_2^* b_2$	0.037	3.8	0.047	4.0	0.036	3.7	0.047	4.1
a_1^2	−0.095	−7.7	−0.116	−8.0	−0.095	−7.8	−0.113	−8.1
b_1^2	−0.092	−7.1	−0.129	−8.5	−0.094	−7.5	−0.131	−8.9
a_2^2	−0.034	−2.0	−0.030	−1.5	−0.025	−2.3	−0.024	−1.5
b_2^2	−0.028	−1.8	−0.048	−2.6	−0.028	−1.8	−0.047	−2.6
l_2^2	−0.038	−3.2	−0.046	−3.3	−0.039	−3.4	−0.048	−3.6

[a]Full quadratic RS model (see Eq. (4)).
[b]Omitting regression coefficients with *t* ratio less than 1.0.

RBNN model for the *T* mode, based on the 34-case design plan, is improved (σ_v decreased from to 0.035 to 0.002) due to the fact that all outliers actually corresponded to validation data points, as shown in Table 6. In general, however, the size and deviation in σ, σ_v, # of neurons, spread, and goal in Tables 6 and 7 between the different RBNN models, indicate that the prediction capabilities of the RBNN models are adequate. Moreover, the fidelity of the two RBNN models is generally higher for the *R* mode than for the *T* mode, in contrast to the quadratic RS models, as seen in Tables 5 and 6.

As indicated in Tables 2, 3, 6, and 7, the σ values are generally lower for the RBNN models as compared to those for the quadratic RS models. Hence, in the present case, the RBNN models are considered better than the quadratic RSM models. Examining the Pareto fronts in Fig. 4, where the solution space (green dots) of the two competing objectives is plotted for alternative surrogate models and design plans, it is also observed that the predictive capabilities near the Pareto front are better for the RBNN models. In fact, the fidelity of the quadratic RS models in this region is poor, since the shape of the Pareto front (red dots) is not in agreement with the CFD data for any of the design plans (blue and red stars). Instead, the shape of the Pareto front, for both design plans, seems to converge into a single optimum solution, due to the sharp-edged solution spaces. In addition, the variation in the Pareto front shape (and solution space) as a function of the design plan (number of data points) is small, due to the properties of the fitted quadratic polynomials. Reducing the design space near the Pareto front or using higher order polynomials would probably give larger variations and better agreements. The RBNN models on the other hand generally have a more blunted solution space, and the shape of the Pareto front corresponds better to the CFD data in this region, as shown in Fig. 4. It is also observed that the variation in the Pareto front shape as the number of data points increases is larger for the RBNN models. In particular, the Pareto front based on the enhanced 49-case design plan is the preferred surrogate model and seems to match the CFD data, except for high C_p values in the *T* mode and low C_p values in the *R* mode, as seen in Figs. 4 and 5. The fidelity of the Pareto front based on the original 34-case design plan, however, is poorer and comparable

Table 6 Fidelity of the RBNN models based on the original 34-case design plan

	Ordinary RBNN[b] model		RBNN model excl.[c] outliers	
C_p	*T* mode	*R* mode	*T* mode	*R* mode
Mean	0.57	0.60	0.56	0.60
σ_v	0.035	0.018	0.002	0.009
σ	0.017	0.010	0.001	0.005
# of neurons	23	24	25	25
# of val points[a]	7	7	7	7
spread	0.001	0.001	0.001	0.001
goal	1.9	1.8	1.7	1.7

[a]Validation points randomly selected ({Geo 7, 16, 15, 27, 30, 32, and 34}).
[b]Ordinary RBNN model.
[c]Excluding outliers with a weight less than 0.1 (*T* mode: {Geo 7, 16, 27, 30, 32, and 34} and *R* mode: {Geo 16, 24, 27, and 32}).

Table 7 Fidelity of the RBNN models based on the enhanced 49-case design plan

	Ordinary RBNN[b] model		RBNN model excl.[c] outliers	
C_p	*T* mode	*R* mode	*T* mode	*R* mode
Mean	0.62	0.66	0.62	0.66
σ_v	0.030	0.012	0.008	0.007
σ	0.014	0.007	0.005	0.004
# of neurons	29	28	29	27
# of val points[a]	10	10	10	10
spread	0.001	0.001	0.001	0.001
goal	1.8	1.9	1.6	2.0

[a]Validation points randomly selected ({Geo 15, 27, 30, 32, 35, 40, 41, 44, 45, and 47}).
[b]Ordinary RBNN model.
[c]Excluding outliers with a weight less than 0.1 (*T* mode: {Geo 27, 30, 32, and 45} and *R* mode: {Geo 9, 27, 32 and 48}).

Downloaded 03 Jun 2010 to 171.66.16.156. Redistribution subject to ASME license or copyright; see http://www.asme.org/terms/Terms_Use.cfm

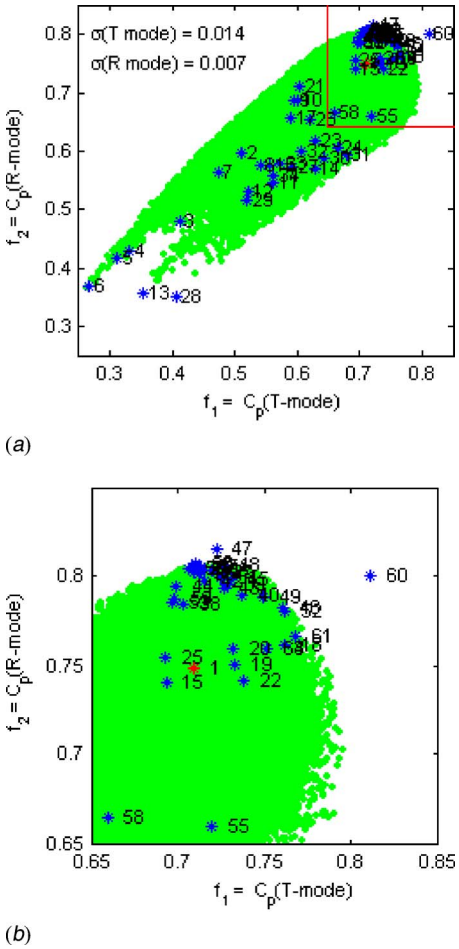

Fig. 5 Solution space (green dots) for the RBNN model based on the enhanced 49-case design plan, and all calculated CFD data points (blue and red stars): (*a*) whole solution space; (*b*) zoomed solution space

to the ones estimated by the quadratic RS models. In fact, it also tends to converge to a single optimum solution, as seen in Fig. 4. Furthermore, it can be assessed that the quadratic RS models is, to some extent, more accurate away from the Pareto front than the RBNN models. In addition, it is also observed that all of the selected and CFD validated Pareto optimal solutions except one (Geo 58) actually improve at least one of the two objectives as compared to the original design (Geo 1) as seen in Fig. 5 and in the C_p values of Table 1. This solution was obtained with the full quadratic RS model omitting outliers, and the shape of its diffuser geometry is quite different from the rest of the validated geometries, as seen in Table 1. However, the overall best CFD validated design point (Geo 60) seems not to be located on the Pareto front; instead it is an outlier that appears to be a single optimum point, as shown in Fig. 5. This source of the outcome needs to be further evaluated from the computational and surrogate modeling, and fluid dynamics viewpoints.

In geometrical terms the optimization result shows that the diffuser wall angle can be larger, and that a nonaxi-symmetrical cross-sectional shape is preferable in comparison to an axi-symmetrical one to gain the best performance due to the rectangular outlet area (see geometries in Table 1). How much the wall angle can increase depends on the choice of the tradeoffs between the competing objectives. The maximum improvement of the pressure recovery is 14.4% for the *T* mode and 8.9% for the *R* mode, and is obtained for Geo 60 and Geo 47, respectively. However, the overall most favorable design is Geo 60, for which the wall angle increases with approximately 3.5 deg at the *B* plane (see Fig. 2 for plane definition).

Flow Analysis. The calculated steady flow field typically exhibits a stagnation or recirculation bubble downstream from the runner. In some cases there is separated flow near the walls, as shown in Fig. 6 for designs representing the original (Geo 1), overall best (Geo 60), and worst (Geo 6) geometry. The size of the stagnation bubble and the wall separated zones is highly geometrically dependent, and generally the optimal shape occurs with a relatively small stagnation bubble and with flows in the onset of wall separation. These observations also follow earlier investigations in this area as seen in Refs. [24–27]. Comparing the overall best (Geo 60) and original (Geo 1) geometry in Fig. 6, it is noticed that the stagnation bubbles between the geometries are of comparable sizes for each operational mode. However, the larger wall angles of the former geometry, without any wall separation, allow the flow to operate with a larger inlet to outlet area ratio, which leads to improvement in the diffuser performance (pressure recovery factor). This efficiency improvement is also more pronounced for the *T* mode, mainly due to its somewhat larger difference in the size of the stagnation bubble as compared to the *R* mode, which has a higher swirl factor. In general, the flow field characteristics can be divided into three major groups based on the sizes and locations of the separated zones as illustrated in Fig. 7. Group *A* corresponds to diffuser geometries with "bad" performance, where strongly separated flow regions appear near the walls, and/or there is a large stagnation bubble downstream from the runner. Group *C* contains diffuser geometries with "good" performance, where the flow is largely attached with a small stagnation bubble. Finally, the geometric characteristics of Group *B* are located between Groups *A* and *C*.

Conclusion

The present study reports our efforts in the shape optimization of a simplified 3D hydraulic diffuser by maximizing the pressure recovery for two competing inlet velocity profiles. Such real-world design problems can be effectively addressed by using multiple surrogate models. In particular, RBNN and polynomial RS models can be fruitfully employed to offer contrast. The accuracy of the global surrogate model can be improved by judiciously adding data points once the Pareto optimal solutions are created. By excluding outliers and uncertain regression coefficients for the RS model in a reasonable manner, the accuracy of the surrogates can be improved even further. Furthermore, it is demonstrated that by using global surrogate approximations in conjunction with an evolutionary algorithm, a Pareto front can be constructed on a computationally limited budget as compared to using an evolutionary algorithm. In the present design problem, the fidelity of the Pareto front improves as the number of data points increases, and the RBNN model performs better than the quadratic RS model. The optimization resulted in optimal 3D hydraulic diffuser designs with very small separation regions. An interesting result is that the corresponding geometries are not axi-symmetric, thus giving ideas of innovative designs in the future. However, it is important to notice that these optimal designs cannot directly be applicable to the original geometry, due to the present geometry simplification, (see Fig. 1).

In summary, the proposed methodology is found to be very promising when solving complex multi-objective and computationally expensive design problems. In particular, it helps to visualize and assess tradeoffs among different design objectives, offering a systematic and efficient framework to address the design optimization issues in fluid machinery.

Downloaded 03 Jun 2010 to 171.66.16.156. Redistribution subject to ASME license or copyright; see http://www.asme.org/terms/Terms_Use.cfm

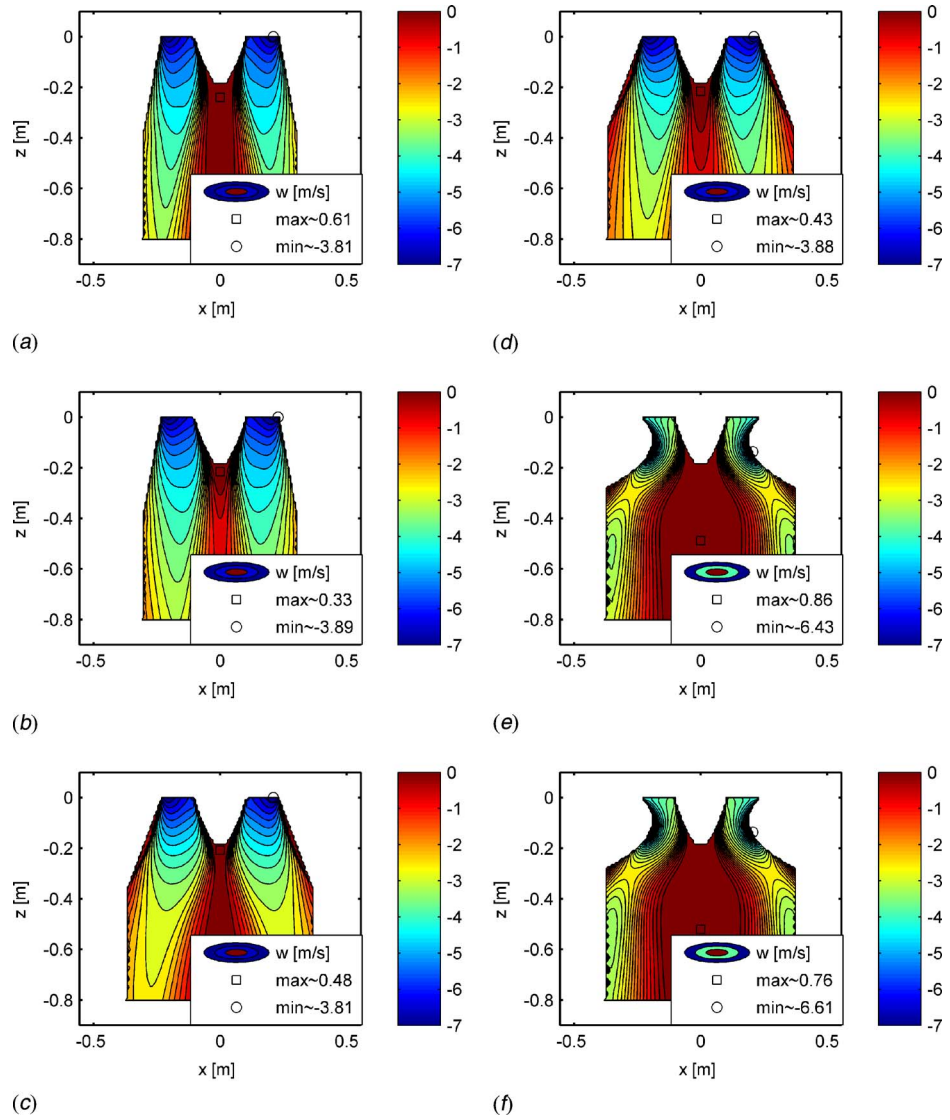

Fig. 6 CFD calculated axial velocity fields at the *A* plane for two diffuser geometries: (*a*) Geo 1, *T* mode; (*b*) Geo 1, *R* mode; (*c*) Geo 60, *T* mode; (*d*) Geo 60, *R* mode; (*e*) Geo 6, *T* mode; and (*f*) Geo 6, *R* mode

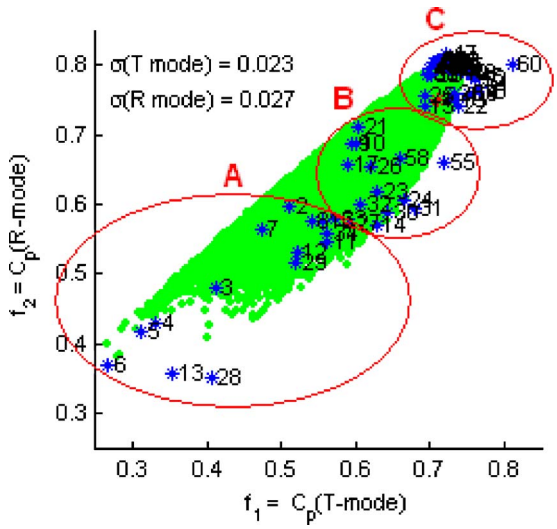

Fig. 7 Flow characteristics in the solution space (green dots). The solution space is from the full quadratic RS model based on the enhanced 49-case design plan.

Acknowledgments

The authors gratefully acknowledge the valuable support provided by Vattenfall Research and Development, Vattenfall Vattenkraft AB, the Swedish Agency for Innovation Systems (VINNOVA), and the participating industries in the Polhem Laboratory that made this collaboration between the authors possible.

Nomenclature

Symbols

a = transfer function in neural networks
a_i = minor ellipse axis
A_i = area
b = bias in neural networks transfer functions
b_i = major ellipse axis, or estimated regression coefficients in polynomial response surfaces
B = tuning parameter in iterative reweighted least square method
C_i = child in crossover and mutation operators
C_{ii} = diagonal element of $(\mathbf{X}^T\mathbf{X})^{-1}$ in t_0 test statistic
C_p = average pressure recovery factor

Downloaded 03 Jun 2010 to 171.66.16.156. Redistribution subject to ASME license or copyright; see http://www.asme.org/terms/Terms_Use.cfm

e_i = residual of true and approximated response
gen = number of generations used in the evolutionary algorithm
$goal$ = goal constant in radial basis neural networks
H_0 = null hypothesis
I = I-optimal criterion in DOE design
l_i = length
n = number of design points
N = number of design variables
p = static pressure
P_i = parent in crossover and mutation operators
pop = population size used in the evolutionary algorithm
Q_i = volume flow rate
r = number of regression coefficients in polynomial response surfaces
R^2 = coefficient of multiple regression in polynomial response surfaces
R_a^2 = adjusted coefficient of multiple regression in polynomial response surfaces
$spread$ = spread constant in radial basis neural networks
SS_E = error sum of square in polynomial response surfaces
SS_T = total sum of squares in polynomial response surfaces
t_0 = test statistic in polynomial response surfaces
u = random variable
x_i = design variable
y_i = response
$\hat{y}_i$ = surrogate model response
β_i = regression coefficients in polynomial response surfaces
ε_i = error
η_M = mutation probability
η_X = crossover probability
ρ = density
ρ_M = mutation operator distribution parameter
ρ_X = crossover operator distribution parameter
σ = root mean square error
σ_a = adjusted root mean square error
σ_v = root mean square error of validation data points
$\mathbf{b}$ = estimated regression coefficient vector in polynomial response surfaces
$\mathbf{f}$ = objective function
$\mathbf{g}$ = inequality constraint function
$\mathbf{M}$ = moment matrix in DOE designs
$\mathbf{x}$ = design variable vector
$\mathbf{X}$ = moment design matrix
$\mathbf{y}$ = response vector
$\mathbf{w}$ = weight vector in neural networks
$\boldsymbol{\beta}$ = regression coefficient vector in polynomial response surfaces
$\boldsymbol{\varepsilon}$ = error vector

Subscripts

1 = cross section, or parent/child 1
2 = cross section, or parent/child 2
in = inlet
out = outlet
UP = upper bound
LOW = lower bound

References

[1] Avellan, F., 2000, "Flow Investigation in a Francis Draft Tube: The FLINDT Project," *Proceedings of 20th IAHR Symposium on Hydraulic Machinery and Systems*, Charlotte, NC, August 6–9.

[2] Ruprecht, A., Helmrich, T., Aschenbrenner, T., and Scherer, T., 2002, "Simulation of Vortex Rope in a Turbine Draft Tube," *Proceedings of 22nd IAHR Symposium on Hydraulic Machinery and Systems*, Lausanne, Switzerland, August 9–12.

[3] Turbine-99, 2006, "The IAHR Workshops on Draft Tube Flow," http://www.turbine-99.org, August 2006.

[4] Shyy, W., Papila, N., Tucker, P. K., Vaidyanathan, R., and Griffin, L., 2000, "Global Design Optimization for Fluid Machinery Applications," *Proceedings of 2nd International Symposium on Fluid Machinery and Fluid Engineering*, Beijing, China, October 22–25, pp. 1–10.

[5] Jin, R., Chen, W., and Simpson, T. W., 2001, "Comparative Studies of Metamodeling Techniques Under Multiple Modeling Criteria," Optim. Eng., **23**(1), pp. 1–13.

[6] Shyy, W., Papila, N., Vaidyanathan, R., and Tucker, P. K., 2001, "Global Design Optimization for Aerodynamics and Rocket Propulsion Components," Prog. Aerosp. Sci., **37**, pp. 59–118.

[7] Simpson, T. W., Peplinski, J. D., Koch, P. N., and Allen, J. K., 2001, "Metamodels for Computer-Based Engineering Design: Survey and Recommendations," Eng. Comput., **17**(2), pp. 129–150.

[8] Simpson, T. W., Booker, A. J., Ghosh, D., Giunta, A. A., Koch, P. N., and Yang, R.-J., 2004, "Approximation Methods in Multidisciplinary Analysis and Optimization: A Panel Discussion," Optim. Eng., **27**(5), pp. 302–313.

[9] Queipo, N. V., Haftka, R. T., Shyy, W., Goel, T., Vaidyanathan, R., and Tucker, P. K., 2005, "Surrogate-Based Analysis and Optimization," Prog. Aerosp. Sci., **41**(1), pp. 1–28.

[10] Madsen, J. I., Shyy, W., and Haftka, R. T., 2000, "Response Surface Techniques for Diffuser Shape Optimization," AIAA J., **38**(9), pp. 1512–1518.

[11] Eisinger, R., and Ruprecht, A., 2001, "Automatic Shape Optimization of Hydro Turbine Components Based on CFD," TASK Q., **6**(1), pp. 101–111.

[12] Marjavaara, B. D., and Lundström, T. S., 2003, "Automatic Shape Optimization of a Hydropower Draft Tube," *Proceedings of 4th ASME_JSME Joint Fluids Engineering Conference*, Honolulu, HI, July 6–11, 1(C), pp. 1819–1824.

[13] Marjavaara, B. D., and Lundström, T. S., 2006, "Redesign of a Sharp Heel Draft Tube by a Validated CFD-Optimization," Int. J. Numer. Methods Fluids, **50**(8), pp. 911–924.

[14] Myers, R. H., and Montgomery, D. C., 2002, *Response Surface Methodology: Process and Product Optimization Using Designed Experiments*," Wiley, New York, NY.

[15] Alexandrow, N., Lewis, R., Gumbert, C., Green, L., and Newmann, P., 2000, "Optimization With Variable Fidelity Models Applied to Wing Design," *Proceedings of the 38th AIAA Aerospace Sciencis Meeting and Exhibit*, Reno, NV, January 10–13, 2000-0841.

[16] Mack, Y., Goel, T., Shyy, W., Haftka, R. T., and Queipo, N. V., 2005, "Multiple Surrogates for the Shape Optimization of Bluff Body-Facilitated Mixing," *Proceedings of the 43rd AIAA Aerospace Sciencis Meeting and Exhibit*, Reno, NV, January 10–13, 2005-0333.

[17] Chankong, V., and Haimes, Y. Y., 1983, *Multiobjective Decision Making Theory and Methodology*, Elsevier Science, New York, NY.

[18] Sen, P., and Yang, J-B., 1998, *Multiple Criteria Decision Support in Engineering Design*, Springer Verlag, London, UK.

[19] Hämäläinen, J. P., Mäkinen, R. A. E., Tarvainen, P., and Toivanen, J., 2000, "Evolutionary Shape Optimization in CFD With Industrial Applications," *Proceedings of ECCOMAS 2000 Conference*, Barcelona, Spain, September 11–14.

[20] Deb, K., 2001, *Multi-Objective Optimization Using Evolutionary Algorithms*, Wiley Ltd, Chichester, UK.

[21] Obayashi, S., Sasaki, D., Sendai, A., and Oyama, A., 2003, "Finding Tradeoffs by Using Multi-objective Optimization Algorithms," *Proceedings EUROGEN'03*, Barcelona, Spain, September 15–17.

[22] Ong, Y. S., Nair, P. B., and Keane, A. J., 2003, "Evolutionary Optimization of Computationally Expensive Problems via Surrogate Modeling," AIAA J., **41**(4), pp. 687–696.

[23] Goel, T., Vaidyanathan, R., Haftka, R. T., Queipo, N. V., Shyy, W., and Tucker, P. K., 2004, "Response Surface Approximation of Pareto Optimal Front in Multi-objective Optimization," Comput. Methods Appl. Mech. Eng., in press.

[24] Gibson, A. H., 1911, "On the Resistance to Flow of Water Through Pipes or Passages Having Divergent Boundaries," Trans. - R. Soc. Edinbrgh, **48**(5), pp. 97–115.

[25] Kline, S. J., Abbott, D. E., and Fox, R. W., 1959, "Optimum Design of Straight Walled Diffuser," J. Basic Eng., **81**, pp. 321–329.

[26] McDonald, A. T., Fox, R. W., and van Dewoestine, R. V., 1971, "Effects of Swirling Flow on Pressure Recovery in Conical Diffusers," AIAA J., **9**, pp. 2014–2018.

[27] Moses, H. L., 1986, *Diffuser Performance for Draft Tube Applications*, ASCE, New York, NY, pp. 1218–1227.

[28] Vu, T. C., 1989, "A Design Parameter Study of Turbine Draft Tube by Viscous Flow Analysis," *Proceedings of the International Conference on Hydropower (Waterpower '89)*, Niagara Falls, NY, August 23–25.

[29] Deb, K., Agrawal, S., Pratap, A., and Meyarivan, T., 2000, "A Fast and Elitist Multi-objective Genetic Algorithm for Multi-objective Optimization: NSGA-II," *Proceedings of the Parallel Problem Solving from Nature VI Conference*, Paris, France, September 18–20, pp. 849–858.

[30] Deb, K., and Goel, T., 2000, "Multi-Objective Evolutionary Algorithms for Engineering Shape Design," *Evolutionary Optimization*, R. Sarker, M. Mohammadin, and X. Yao, eds., Kluwer, Dordrecht, The Netherlands, pp. 147–176.

[31] Deb, K., and Goel, T., 2001, "A Hybrid Multi-objective Evolutionary Approach to Engineering Shape Design," *Proceedings of Evolutionary Multi-*

Downloaded 03 Jun 2010 to 171.66.16.156. Redistribution subject to ASME license or copyright; see http://www.asme.org/terms/Terms_Use.cfm

criterion Optimization Conference, Zurich, Switzerland, March 7–9, pp. 385–399.
[32] Deb, K., and Goel, T., 2002, "Hybrid Methods for Multi-Objective Evolutionary Algorithms," *Proceedings of the 4th Asia-Pacific Conference on Simulated Evolution and Learning Computational Intelligence for the E-age, SEAL'02*, Singapore, November 18–22, pp. 188–192.
[33] Giunta, A. A., Dudley, J. M., Narducci, R., Grossman, B., Haftka, R., Mason, W. H., and Watson, L. T., 1994, "Noisy Response and Smooth Approximation in HSCT Design," *Proceedings of 5th AIAA/USAF/NASA/ISSMO Symposium on Multidisciplinary Analysis and Optimization*, Panama City, FL, September 7–9.
[34] JMP, 2002, *The Statistical Discovery SoftwareTM*, Release 5.0.1a, SAS Institute, Inc., Cary, NC.
[35] CFX, 2004, *CFX-5*, Version 5.7.1, ANSYS Europe Ltd., Riseley, UK.
[36] Marjavaara, B. D., Kamakoti, R., Lundström, T. S., Thakur, S., Wright, J., and Shyy, W., 2005, "Steady and Unsteady CFD Simulations of the Turbine-99 Draft Tube Using CFX-5 and STREAM," *Proceedings of 3rd IAHR/ERCOFTAC Workshop on Draft Tube Flow*, Porjus, Sweden, December 8–9.
[37] ICEM CFD, 2004, *ICEM CFD*, Version 5.1, ANSYS, Inc., Canonsburg, PA.
[38] MATLAB, 2004, *The Language of Technical Computing*, Version 7.0.1, The MathWorks, Inc., Natick, MA.
[39] Beaton, A. E., and Tuckey, J. W., 1974, "The Fitting of Power Series, Meaning Polynomials, Illustrated on Spectroscopic Data," Technometrics, **16**(2), pp. 147–185.
[40] Goel, T., Mack, Y., Shyy, W., Haftka, R. T., and Queipo, N. V., 2005, "Numerical and Surrogate Model Uncertainty Assessment for Bluff Body Facilitated Mixing," *Proceedings of the 43rd AIAA Aerospace Sciencis Meeting and Exhibit*, Reno, NV, January 10–13, 2005-0125.

Downloaded 03 Jun 2010 to 171.66.16.156. Redistribution subject to ASME license or copyright; see http://www.asme.org/terms/Terms_Use.cfm

Journal of Fluids Engineering

Technical Brief

Numerical Evaluation of Contemporary Low-Speed Wind Tunnel Contraction Designs

Con J. Doolan
School of Mechanical Engineering,
The University of Adelaide,
Adelaide, SA 5005, Australia

A potential flow and viscous flow solver have been coupled to produce a robust computational tool useful for the design of low-speed wind tunnel contractions. After validation against published numerical and experimental wind tunnel data, the method is used to evaluate recently proposed contraction shapes from the literature. The results show that, on balance, a fifth-order polynomial provides a good design solution. Newly proposed shapes will either improve available flow area at the expense of contraction outlet flow uniformity or vice versa. [DOI: 10.1115/1.2771578]

1 Introduction

When designing a new wind tunnel contraction section, the engineer must choose a shape that simultaneously reduces overall wind tunnel losses and provides a high quality test flow at the working section. A contraction should be designed to prevent flow separation along its walls and also to minimize exit plane boundary layer thickness and flow nonuniformity. A popular and successful choice for wind tunnel contraction shapes has been the fifth-order polynomial originally identified by Bell and Mehta [1]. Recently, Brassard and Ferchichi [2] have proposed a modification to Bell and Mehta's fifth-order polynomial that allows the designer to model any shape, particularly those that were previously described as the qualitative "by-eye" technique, which some designers prefer [2,3]. While Brassard and Ferchichi have provided an excellent method to describe these shapes, a quantitative evaluation of their performance was not presented.

A potential flow solver and a laminar viscous solver have been coupled to produce a method of calculating the performance of two-dimensional wind tunnel contractions. This method was used to evaluate the performance of recently proposed wind tunnel contraction shapes of Brassard and Ferchichi. In addition, shapes used by the Royal Institute of Technology, Sweden [4] and the University of Tasmania, Australia [5] were also evaluated as part of the study. It is the intention that the results presented here will assist engineers in the design of future wind tunnel components.

Contributed by the Fluids Engineering Division of ASME for publication in the JOURNAL OF FLUIDS ENGINEERING. Manuscript received November 28, 2006; final manuscript received May 31, 2007. Review conducted by Paul Durbin.

2 Numerical Method

While accurate and common, the solution of a three-dimensional viscous flow field using a Reynolds averaged approach is still a time consuming task on a desk-top personal computer, especially if multiple design options are to be simultaneously compared. Here, a classical approach is taken where a three-dimensional potential flow solver is used to compute the inviscid flow within the contraction. This solution is then used as a boundary condition to a laminar viscous flow solver to compute boundary layer properties along the contraction. The combination of potential and viscous flow solvers provides enough accurate information to make rational decisions regarding the design of contraction sections.

2.1 Potential Flow Solver. Three-dimensional potential flow solutions were performed using the OPENFOAM [6] computational fluid dynamics software package. OPENFOAM was used with a structured three-dimensional mesh to describe the interior flow domain. The governing equations of the solution method describe an incompressible, irrotational fluid

$$\nabla \cdot \mathbf{U} = 0 \tag{1}$$

$$\nabla^2 p = 0 \tag{2}$$

where $\mathbf{U}$ is the fluid velocity vector; and p is the pressure. A second-order accurate, finite-volume discretization method (semi-implicit method for pressure linked equations, SIMPLE) was used to solve the governing equations. The solution was considered converged when the solution tolerance reached a level below 10^{-6}.

In all cases, a two-dimensional contraction was analyzed where the contraction height varies only along its length, implying flat, straight side walls. Figure 1 shows a side view of a two-dimensional contraction that describes the flow domain. The contraction has depth, as indicated by the coordinate system centered at the inlet on the center line of the contraction. Actually, only a quarter of the contraction was modeled, with symmetry boundary conditions used to simplify the flow domain (i.e., the normal derivatives of the flow quantities were set to zero). A constant non-dimensional velocity boundary condition ($U_{\text{inlet}}=1$) was set at the contraction inlet (left side of the flow domain). To convert the velocity computed by the solver to the desired velocity, the entire solution was multiplied by the desired inlet velocity.

A constant pressure outlet condition was specified for the right boundary ($p=0$). The normal derivative of flow variables not specified at the inlet and outlet was set to zero. As this was an inviscid solution, walls were modeled as symmetry boundary conditions.

The flow domain was split into two parts: The contraction section, which had length L, and an extension section that had the same cross-sectional area as the contraction exit plane over its length. For all results presented in this paper, the extension length is half the length of the contraction ($0.5L$).

2.2 Viscous Flow Solver. The potential flow solver produces a velocity distribution throughout the flow domain. The velocity

 Copyright © 2007 by ASME

Downloaded 03 Jun 2010 to 171.66.16.156. Redistribution subject to ASME license or copyright; see http://www.asme.org/terms/Terms_Use.cfm

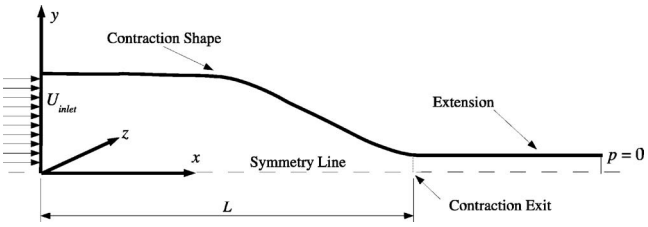

Fig. 1 Flow domain

distribution at the walls is used with Thwaites' method to generate laminar boundary layer solutions at critical locations on the surface. Full details of Thwaites' method can be found in Cebeci and Bradshaw [7]. For the present paper, it is sufficient to state that the method uses the velocity distribution of the potential solver to estimate the laminar momentum thickness (θ). Semi-empirical relations are then used to evaluate other boundary layer parameters, such as skin friction coefficient (c_f).

The assumption of a laminar boundary layer was assumed to be valid based on the original arguments of Bell and Mehta [1], who use a similar method to the one used here for contraction performance calculations. First, it was assumed that the boundary layer originates from stagnation conditions at the beginning of the contraction and there appears to be sufficient evidence to show that this is a reasonable assumption [1]. Second, it can be argued that the boundary layer will experience a strong favorable pressure gradient over most of the contraction length, thereby providing conditions suitable for relaminarization. In any case, for the contractions studied here, the exit plane Reynolds number based on momentum thickness was small enough ($\mathrm{Re}_{\theta,\mathrm{exit}} < 700$) for laminar flow assumptions to be reasonable. The criteria for separation were taken to be when $c_f \leqslant 0$.

2.3 Validation Study

2.3.1 Mesh Resolution. A study was performed based on the geometry of the small wind tunnel contraction described in the next section. In this case, the mesh density was progressively increased until the computed result stabilized to an acceptable level. Table 1 shows a summary of the mesh resolution study where the flow results were taken at the contraction exit plane. It was found that the $150 \times 20 \times 20$ (cells in the $x \times y \times z$ directions) mesh was of sufficient accuracy for our investigation. The exit plane uniformity was calculated by sampling the velocity at 100 equispaced points across the contraction exit plane and taking 1 SD of these data.

2.3.2 Comparison With Published Data. The numerical method was validated by comparing the boundary layer momentum thickness, skin friction coefficient, and exit plane uniformity for a small wind tunnel contraction against the experimental and numerical results of Bell and Mehta [1]. These results were obtained for a wind tunnel using a two-dimensional contraction with contraction ratio (CR)=7.61, length L=2.44 m, and outlet height H_0=0.18 m, and a shape defined by a fifth-order polynomial. The contraction shape used to simulate the experiments was defined by the following fifth-order polynomial [1]

Table 1 Grid resolution study results, Bell and Mehta fifth-order polynomial, 15 m/s

Grid	θ (mm)	c_f	Exit plane uniformity
$150 \times 20 \times 20$	0.44024	0.00107	0.004
$300 \times 40 \times 40$	0.44185	0.00102	0.004

Table 2 Validation study results 9 m/s

	θ (mm)	c_f	Exit plane nonuniformity
Experiment	0.615	0.00262	—
Bell and Mehta prediction	0.621	0.00091	0.004
Current prediction	0.662	0.00113	0.004

$$h = [-10\xi^3 + 15\xi^4 - 6\xi^5]\left(1 - \frac{H_o}{H_i}\right) + 1 \tag{3}$$

where $h = y/H_i$ is the contraction height (y) normalized by the contraction inlet height (H_i); H_o is the contraction outlet height; and $\xi = x/L$.

Boundary layer calculations using the current method were compared with published experimental and numerical data obtained at a distance approximately 150 mm downstream of the contraction exit; however, the exact location was not clear from the available reports. Bell and Mehta used a three-dimensional inviscid panel method with Thwaites' method to calculate boundary layer properties along the contraction. Exit plane nonuniformity was compared with the Bell and Mehta potential flow predictions at the contraction exit plane. Experimental skin friction coefficient was inferred by Bell and Mehta [1] using laminar boundary layer theory and measured boundary layer thickness. Results comparing Bell and Mehta's experimental and numerical results with results obtained using the current method are shown in Tables 2 and 3 for nominal outlet flow velocities of 9 m/s and 15 m/s, respectively.

Pressure and boundary layer calculations were made for three paths along the interior surface of the contraction. These were along the corner joining the top and side of the contraction, along the center of the top (curved) surface, and along the center of the side (flat) surface. The results show that the most difficult pressure distribution for the boundary layer to negotiate and remain attached was the one for the top surface. Hence, all boundary layer calculations presented hereafter were performed using the velocity field calculated for the top surface.

Comparisons between the current prediction method and experiment are reasonable, with the largest error in momentum thickness observed for the 9 m/s case. The results obtained in this study are of the same accuracy as the previous Bell and Mehta study who compared a range of wind tunnel data with a coupled potential-viscous model and found differences on the order of 1–11%. Skin friction simulations using the current method are closer to the experiment than the Bell and Mehta predictions.

There was insufficient information in Bell and Mehta's report to perform further comparisons against experimental data. Further, the exact downstream location where the experimental data were obtained was not precisely indicated. The report states that the measurements were taken *typically* less than 150 mm downstream of the contraction exit. This may explain the increased boundary layer thickness predicted using the current method for the 9 m/s case. The current prediction shows that the boundary layer thickness varies from 0.568 mm to 0.662 mm over the 150 mm downstream of the contraction exit. It is therefore possible that the current method is more accurate than the comparisons listed here suggest.

Table 3 Validation study results 15 m/s

	θ (mm)	c_f	Exit plane nonuniformity
Experiment	0.508	0.00181	—
Bell and Mehta prediction	0.483	0.00072	0.004
Current prediction	0.513	0.00087	0.004

Downloaded 03 Jun 2010 to 171.66.16.156. Redistribution subject to ASME license or copyright; see http://www.asme.org/terms/Terms_Use.cfm

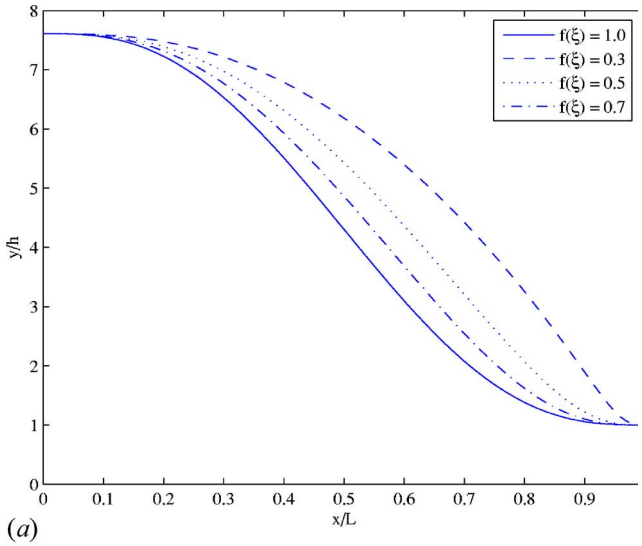

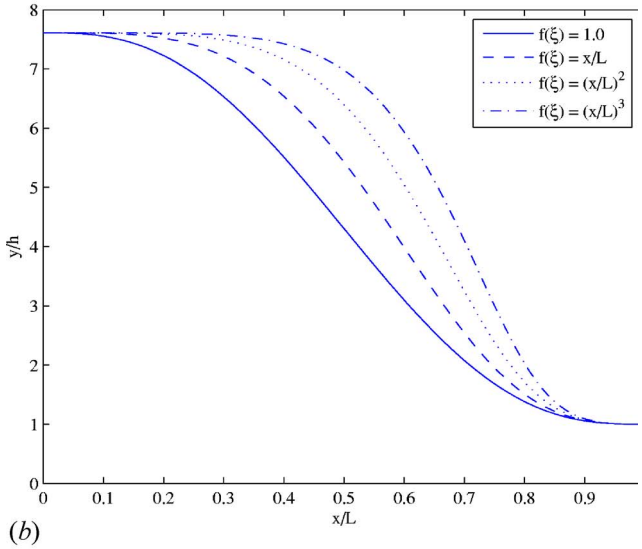

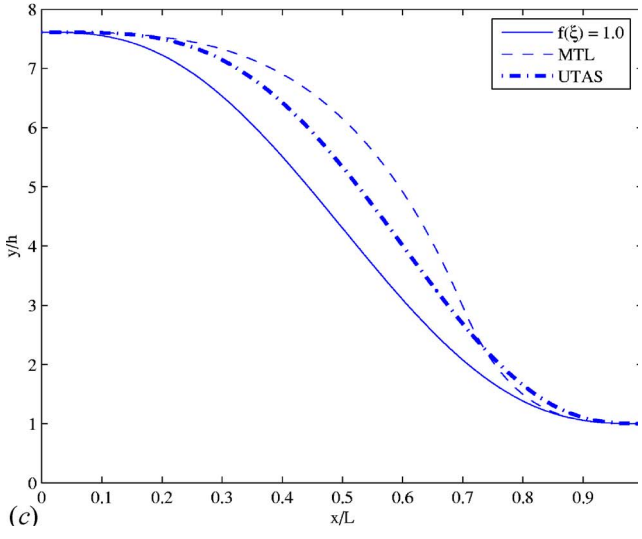

Fig. 2 Contemporary contraction shapes investigated in this study: (*a*) Modified fifth-order polynomial with $f(\xi)=0.3-1.0$; (*b*) modified fifth-order polynomial with $f(\xi)=1.0$, $f(\xi)=x/L$, $f(\xi)=(x/L)^2$, $f(\xi)=(x/L)^3$; and (*c*) fifth-order polynomial ($f(\xi)=1.0$), MTL, and UTAS

Table 4 Comparison of contraction shapes, 9 m/s

Contraction shape	Separation	Re_θ	Exit plane uniformity
Fifth-order polynomial $f(\xi)=1.0$	No	344.49	0.004
Fifth-order polynomial $f(\xi)=0.3$	Yes	—	—
Fifth-order polynomial $f(\xi)=0.5$	No	277.15	0.017
Fifth-order polynomial $f(\xi)=0.7$	No	309.21	0.007
Fifth-order polynomial $f(\xi)=x/L$	No	332.18	0.004
Fifth-order polynomial $f(\xi)=(x/L)^2$	Yes	—	—
Fifth-order polynomial $f(\xi)=(x/L)^3$	Yes	—	—
MTL	No	354.29	0.004
UTAS	No	309.46	0.008

3 Performance of Contemporary Contraction Shapes

3.1 Contraction Shapes. The contraction shapes suggested by Brassard and Ferchichi [2] are a family of curves based on modifications to Bell and Mehta's fifth-order polynomial. Brassard and Ferchichi's transformation can be described by considering Eq. (3) and defining the core polynomial as

$$\eta = 10\xi^3 - 15\xi^4 + 6\xi^5 \tag{4}$$

then using η in the following

$$h = \left\{ -\eta\left[1 - \left(\frac{H_o}{H_i}\right)^{1/f(\xi)}\right] + 1 \right\}^{f(\xi)} \tag{5}$$

where $f(\xi)$ is an arbitrary, continuous function of ξ defined for $0 \leqslant \xi \leqslant 1$ and normalized such that $0 \leqslant f(\xi) \leqslant 1$.

In the current investigation, shapes where $f(\xi)$ is constant ($f(\xi)=0.3-1.0$), linear ($f(\xi)=\xi=x/L$), quadratic ($f(\xi)=\xi^2=(x/L)^2$), and cubic ($f(\xi)=\xi^3=(x/L)^3$) were investigated. When $f(\xi)=1$, the Brassard and Ferchichi transformation reduces to the original Bell and Mehta fifth-order polynomial, which is used as a base-line comparison case.

Two additional wind tunnel contraction shapes were also compared in the current study. The first was developed at the Royal Institute of Technology, Sweden (MTL) [4] and is described using the following polynomials

$$g = A\{\sinh(B\xi) - B\xi\} \quad \xi \leqslant 0.7 \tag{6}$$

$$g = 1.0 - C[\sinh\{D(1-\xi)\} - D\{1-\xi\}] \quad \xi > 0.7 \tag{7}$$

$$H = H_o[\sqrt{\mathrm{CR}}\{1 - g(\xi)\} + \tfrac{1}{2}g(\xi)] \tag{8}$$

where $A=0.205819$, $B=3.52918$, $C=0.08819$, and $D=8.23523$.

The second shape considered in the current study was developed by the University of Tasmania, Australia (UTAS) [5]. This is a sixth-order polynomial described by

$$y = ax^6 + bx^5 + cx^4 + dx^3 + ex^2 + fx + g \tag{9}$$

where $a=0.0041$, $b=0.1651$, $c=-0.2518$, $d=1.9054\times10^{-15}$, $e=f=0$, and $g=H_o\times\mathrm{CR}$.

A summary of all contraction shapes is graphically presented in Fig. 2.

3.2 Results. The coupled potential-viscous flow solver was used to simulate the flow within each of the contraction shapes described above. The length (L), inlet height (H_i), and contraction ratio (CR) were maintained at the values used for the experimental validation. Boundary layer properties were calculated along the top surface of the contraction and values at 150 mm from the exit plane are used for comparison purposes. Table 4 compares the performance of the various wind tunnel contraction shapes.

The shapes that produced the best flow uniformity were the original Bell and Mehta fifth-order polynomial ($f(\xi)=1.0$); the Brassard and Ferchichi transformation with $f(\xi)=x/L$; and the

Downloaded 03 Jun 2010 to 171.66.16.156. Redistribution subject to ASME license or copyright; see http://www.asme.org/terms/Terms_Use.cfm

MTL contraction. The shape that achieved the largest available flow area (smallest boundary layer thickness) was the Brassard and Ferchichi transformation with $f(\xi)=0.5$. However, this was achieved at the expense of flow uniformity, which exceeded our nominal limit of 1% in this case. The modified shape increased the flow velocity along the wall, thereby reducing the boundary layer thickness. However, as the same mass flux must pass through the contraction, an increased velocity gradient exists across the exit plane, resulting in higher flow nonuniformity.

Separation was found to occur for three of the shapes tested. These were the Brassard and Ferchichi transformations using $f(\xi)=0.3$, $(x/L)^2$, and $(x/L)^3$. The Brassard and Ferchichi transformation using $f(\xi)=x/L$ gave the best total performance based on flow area and uniformity. However, the improvement was marginal compared with the $f(\xi)=1.0$ case. By allowing higher flow nonuniformity, progressively larger flow areas are available using selected Brassard and Ferchichi transformations. However, care must be taken with regard to flow separation. The UTAS shape was similar in performance to the $f(\xi)=0.7$ contraction shape.

On balance, however, the original Bell and Mehta fifth-order polynomial gives good all-round performance and any improvement in flow area will be achieved at the expense of flow uniformity. Interesting future work would be to use an optimization procedure to derive new forms of $f(\xi)$ to achieve the best possible contraction performance.

4 Conclusions

A potential flow solver and laminar viscous solver have been coupled for the purposes of wind tunnel contraction design. A variety of contraction shapes were numerically investigated and compared. Shapes included recently suggested polynomial modifications of the original Bell and Mehta fifth-order polynomials. The numerical evaluations of the shapes have concluded that, on-balance, the original Bell and Metha fifth-order polynomial shape provides good all-round performance. The suggested modifications typically increased the inviscid flow area at the expense of flow nonuniformity.

Acknowledgment

This work has been generously supported by the Sir Ross and Sir Keith Smith Fund of South Australia. The author would like to thank Dr. Rick Morgans for his suggestions regarding the numerical modeling.

References

[1] Bell, J. H., and Mehta, R. D., 1988, "Contraction Design for Small Low Speed Wind Tunnels," NASA Contractor Rep. No. NASA-CR-177488.

[2] Brassard, B., and Ferchichi, M., 2005, "Transformation of a Polynomial for a Contraction Wall Profile," J. Fluids Eng., **127**, pp. 183–185.

[3] Mehta, R. D., and Bradshaw, P., 1979, "Design Rules for Small Low Speed Wind Tunnels," Aeronaut. J., **73**, pp. 443–449.

[4] Lindgren, B., and Johansson, A., 2002, "Design and Evaluation of a Low-Speed Wind-Tunnel With Expanding Corners," Royal Institute of Technology, Department of Mechanics, Sweden, Technical Report.

[5] Sargison, J. E., Walker, G. J., and Rossi, R., 2004, "Design and Calibration of a Wind Tunnel with a Two Dimensional Contraction," *Proceedings of the 15th Australasian Fluid Mechanics Conference*, The University of Sydney, Sydney, Australia.

[6] Jasak, H., Weller, H. G., and Nordin, N., 2004, "In-Cylinder CFD Simulation Using a C++ Object Orientated Toolkit," SAE Technical Paper No. 2004-01-0110.

[7] Cebeci, T., and Bradshaw, P., 1977, *Momentum Transfer in Boundary Layers*, McGraw-Hill, New York.

Downloaded 03 Jun 2010 to 171.66.16.156. Redistribution subject to ASME license or copyright; see http://www.asme.org/terms/Terms_Use.cfm